



Proceedings of the



INTERNATIONAL CONFERENCE ON BIO SIGNALS, IMAGES AND INSTRUMENTATION

March 14th to 16th, 2013



ICBSII - 2013

Department of Biomedical Engineering
SSN College of Engineering

Old Mahabalipuram Road
SSN Nagar - 603 110
Tamil Nadu, India

Proceedings of the



International Conference on Biosignals, Images and Instrumentation



Department of Biomedical Engineering
SSN College of Engineering

ICBSII - 2013
(March 14th - 16th)

Editorial Board

Chief Editor : Dr. A. Kavitha

Co- Editors : Akshaya Chandrasekaran

Vishnupriya K.

Saranya Priyadharshini D.

Sowdhami S.

Contents

From the President's desk.....	ix
Mrs. Kala Vijayakumar	
From the Principal's desk.....	x
Dr. S.Salivahanan	
Convener's Message.....	xi
Dr. A. Kavitha	
Message from the Conference Secretary.....	xii
Dr. V. Mahesh	
Conference Organizing Committee.....	xiii
Technical Advisory Committee.....	xv
Review Committee.....	xvi
Student Organizing Team.....	xviii

Keynote Speakers

Emilio Gomez Gonzalez.....	II
Recent advances in non-invasive and image-guided surgery	
Niranjan D. Khambete.....	IV
Clinical Engineering in India	
Srinivasan Rajagopalan	VI
Precision Medicine: From Hype to Hope	
D. Vasudevan.....	VIII
Advances in Neurophysiological Investigations and their Relevance and Application to Clinical Neurology	



G. Kumaramanicavel.....	IX
Walking through the Human Genomic Technology Highway and its Application in Medicine	
B. Ganesh.....	XI
Lasers in Ophthalmology	
Sushil Chandra.....	XII
Combining Physiological monitoring and Neurocognition	

Research Papers

1. Segmentation and Disentangling of Clumps of Chromosomes	
MR Anuja, E. Loganathan, Nirmalan Madian.....	1
2. Applications of Image Processing Techniques for the Detection of Eye Diseases	
R.Manjula Sri, K.M.M. Rao.....	8
3. Detection and Classification of Lesions in Retinal Images	
G. Mohanapriya, S. Vasanthi.....	15
4. Detection and Feature Selection of Abnormal Retinal Vessels using Fundus Image by Genetic Algorithm	
B. Deepthimaris, A. Amsaveni.....	25
5. A New Chaotic Image Encryption Scheme using Random Permutation and Logistic Map	
T.Gopalakrishnan, S.Ramakrishnan, R.Ranjith Kumar.....	34
6. Enhancement of Diabetic Retinopathy Imagery Using Histogram Equalization techniques	
Srinivasan Aruchamy, Rukhmini Roy, Partha Bhattacharjee.....	44
7. Analysis of Classification Techniques for Microarray Cancer data using Support Vector Machines	
C. Arunkumar, S. Ramakrishnan.....	55

8. An Accurate Approach Using Neural Network for Plaque Characterization C.Ganesh, P. John vivek, S.Sridevi.....	65
9. Real Time Diagnosis of Respiration Rate using Single Lead ECG K.Ramya, V.Kalaivani.....	76
10. Analysis of Heart Rate Variability in Normal Pregnancy and Postpartum S. Veerabhadrappa, T. Anoop Lal Vyas, Sneha Anand.....	84
11. Parkinson's Disease Diagnosis Using Self-Adaptive Resource Allocation Network (SRAN) and Extreme Learning Machine (ELM) Classifier A. Suganya , M. Sivachitra , S. Vijayachitra.....	92
12. Soft Computing as a tool for Classification of Cardiovascular Abnormalities S. Dilip Kumar, M. PallikondaRajasekaran, B. Perumal.....	101
13. Cardiac Arrhythmia Diagnosis System Using Data Mining Techniques R.Lakshmi Devi, V. Kalaivani.....	109
14. Unconstrained and Constrained Control of Drug Infusion System for Patients under Critical Care using Linear Model Predictive Control Strategy S.A.Nirmala, RanganathMuthu, B. VeenaAbirami.....	118
15. Design Considerations for Differential Amplifiers in Bio impedance Measurements Padma Batra, Rajiv Kapoor.....	126
16. A Novel DWT-LSB Watermarking Scheme for Fingerprint Authentication with Increased Security using RSA algorithm S.PradhebaaRubinaa, S.Usha.....	135
17. Patient Monitoring System for the Identification of Cardiac Abnormalities using Genetic Algorithm N.Sathiya Rani, K. Vimala.....	145

18.Noise Reduction Using FIR Filter in Cochlear Implants P.Mithradevi, J.Indra, N.Kasthuri.....	155
19.A New Adaptive Wavelet Shrinkage for Speckle Noise Removal in Ultrasound Scan Images Using Inter and Intra Scale Dependencies P. Nirmaladevi, R. Asokan, P.S.Sudarsana.....	165
20.A Novel Awareness and Alertness Implementation on Biometric Authentication in Moving Vehicle B. Hema, R. Sundaraguru.....	175
21.Detection and Segmentation of Optic Disc in Retinal Images K. Gogila Devi, S. Vasanthi.....	186
22.Implementation and Testing of Median and MMSE Filters on the TMS320C6713DSK for Rician Noise Removal in MR Images J. Papitha ,D.Nedumaran.....	195
23.Hepatitis B Disease Diagnosis Using Meta-Cognitive Neural Network and Extreme Learning Machine R. Madhuvathani, M. Sivachitra, S. Vijayachitra.....	206
24.A Smart Phone Based Heart Rate Monitor Dennis Joe Harmah, D. Kathirvelu.....	214
25.Changes in Steering Wheel Grip Interface Pressure during Simulated Driving Rahul Bhradwaj,Mohan Jagannath, VenkateshBalasubramanian.....	221
26.Development of Multiparametric Patient Monitoring System using ZigBee with an Emergency Alarm VageeshV.Kantli, L.H. Anjaneya, MallikarjunS.Holi.....	229
27.ECG Signal Processing Using LabVIEW V. Nageshwar, Y. Padmasai , S. Nagarjuna Chary , L.V.Rajani.....	236

28.Multiple sclerosis lesion segmentation in brain MR images based on a hybrid of Markov random field and Ant colony optimization	
V. Divya, G. Kavitha.....	246
29.Comparison of Segmentation Techniques for Identification of Microcalcification clusters in Breast Tomograms	
Rajalakshmi Thyagarajan, S. Murugavalli.....	255
30.Medical Image Fusion Using Evolvable Histogram Equalization	
S.Kalimuthu,A.Nandini.....	262
31.FPGA implementation of a Genetic Algorithm based Scheme for Optimal Anaesthetic delivery	
S. Supraja, M. Varun, K. Kamalanand.....	269
32.Retinal Image Analysis for Vessels and Exudates using Curvelet Transform and Clustering Techniques	
A. Anitha Christina , S.Kuzhaloli ,M.S.Godwin Premi.....	276
33.Gabor Image Enhancement Algorithm for AFIS and Machine Vision Applications	
M. Selva Kumar, D. Nedumaran.....	284
34.Finite Element Analysis Of Lumbar Spine with dynamic stabilization device	
Abhishek Singh, S.Karuppudaiyan , D.KingslyJeba Singh.....	294
35.Design and Implementation of Micro Thermo Electric Generator for Bio Implantable Devices	
Y. Jeyashree, PhebaCherian, A.Vimala Juliet, E. Paul Braineard.....	302
36.Patient Safety Automation Using Secured Steganography and DSP Automatic Control	
PrabaharanRajagopal, SubhaAustalakshmi.....	311
37.Neural Network based Handwritten Script Recognition	
Jose Anand, Helen Samuel, H. C. Parimala.....	316

38.Bedside Fall Detection and Patient Limb Movement Detection using Near Infrared Sensor	
Subash Padmanaban, Suryah Suresh.....	325
39.Texture Based Feature Extraction from Mammogram Images to Classify Different Masses & Comparison of Various Classification Techniques	
S.Sivarajanji , R.Prem Kumar.....	331

*Dedicated
to
all Staff and Students
of
the Department of
Biomedical Engineering*

From the President's desk



Mrs. Kala Vijayakumar

President, SSN Institutions

The numerous achievements of SSN College of Engineering are a direct result of the institution's strong backbone of staff and students. Academic excellence apart, the institution also strives to instill in its students traits such as critical thinking, work ethic and the sense of responsibility towards society. Every aspect of SSN, from the campus to the libraries, is aimed at ensuring the holistic development of its students. The Research Centre at SSN and its success is a testimony to the emphasis laid on research and development.

Biomedical Engineering as a discipline is truly multi-disciplinary and offers varied research avenues. We also observe that in this day and age, it has become imperative to stay abreast with all the latest developments in technology. The importance is two-fold when the technology is linked with healthcare. Taking cognizance of this fact, the BME department's initiative to host an International Conference certainly deserves appreciation.

On behalf of the SSNCE administration, I congratulate BME and also wish that such initiatives are the first of many to come.

Mrs. Kala Vijayakumar
Chief Patron, ICBSII – 2013.

From the Principal's desk



Dr. S. Salivahanan

Principal, SSN College of Engineering

The SSN Group of Institutions has emerged to be one of the best private educational institutions in the country in terms of academics, infrastructure and extra-curricular achievements. The main aim of SSN is to make a positive difference to the society through education. Biomedical engineering is indeed a holistic discipline and successfully integrates engineering technology with healthcare. The Biomedical Engineering Department of the college with its unique course objectives has brought glory to the institution through its various successes.

The department's inclination toward research has to be appreciated and the fact that the enthusiasm is prevalent in students and teachers alike is commendable. The department has also signed various memorandums with many companies and medical colleges to facilitate students in the path of their research.

The Biomedical Engineering Department continues its trail of success by organizing The International Conference on Bio Signals, Images and Instrumentation-ICBSII in a manner befitting the stream. I congratulate the entire team at BME for planning this to perfection and wish them all the very best!

Dr. S. Salivahanan
Patron, ICBSII – 2013.

Convener's Message



Dr. A. Kavitha

Head, Department of Biomedical Engineering
SSN College of Engineering

It is with tremendous pride that I present the International Conference on Bio Signals, Images and Instrumentation-ICBSII, 2013. To simply state that this feeling is shared by my colleagues and students would amount to a gross understatement. Words, however, can only achieve so much.

The Biomedical Engineering fraternity is one which is oblivious to the boundaries of institutions, states, countries, etc. This is understandable, given that the field of study is intertwined with medicine and healthcare. The outcomes of research assume a whole new level of importance and significance. The discipline also sees growth on a regular basis, an aspect which is exciting while being challenging.

The department constantly strives to keep pace with the developments by organizing numerous workshops, conferences, seminars and project exhibitions. Another event worthy of mention is the annual technical symposium 'Srishti' which is a repeat success. The symposium provides students with a chance to compete on a technical front and also presents an amazing networking opportunity.

The International Conference on Biosignals, Images and Instrumentation (ICBSII), organized by SSN College of Engineering, is a multi-disciplinary academic event aimed at bridging the industry-institution gap. The conference provides a platform for academics, students, clinicians and researchers to observe, discuss and showcase advancements in biomedical research.

They say teamwork divides the tasks and multiplies the success. I hope that the success of the conference sets a new benchmark in academia.

Dr. A. Kavitha
Chair Person, ICBSII – 2013.

Message from the Conference Secretary



Dr. V. Mahesh

Associate professor, Department of Biomedical Engineering
SSN College of Engineering

The International Conference on Bio Signals Images and Instrumentation (ICBSII 2013) is being conducted to unveil the efforts of researchers, engineers and scholars and trot out the outcomes and observations of their research activities to the prominent people in the field of Biomedical Engineering. The Conference is also aimed at accentuating the advancements and current trends in the industry to make the undergraduate students to concenter their ideas in terms of projects and product development.

The conference serves as a platform for diverse disciplines of medicine, engineering, healthcare and software to congregate in the same venue to elevate the medical and healthcare industry to greater standards. The conference also turns out to be a forum for the scientists, researchers and scientists from all over the world to share their ideas, experiences, findings and conclusions of their work in due course of their scientific research.

I extend my sincere gratitude to the Management of SSN College of Engineering, Ms. Kala Vijayakumar, President, SSN Institutions and Dr. Salivahanan, Principal, SSN College of Engineering for granting the department a wondrous opportunity to organize and conduct this prolific occasion and for helping us to take it forward to the global level.

I immensely thank the delegates from different places and various professions for their honourable presence and for their inspirational talks. I convey my huge gratitude to Dr. Emilio Gomez Gonzalez from University of Seville, Spain for inaugurating the occasion, Dr. Sushil Chandra from the DRDO, Dr. Srinivasan Rajagopalan from Mayo Clinic, USA, Dr. Niranjan Khambete from SCTIMST, Trivandrum, Dr. D. Vasudevan from The Brain, Spine and Nerve center, Chennai, Dr. G. Kumaramanicavel from Narayana Nethralaya, Bangalore and Dr.B.Ganesh from Karpaga Vinayaga Medical College for their gracious presence and motivational speech.

I also thank the entire faculty and the students of Department of Biomedical Engineering for joining hands in making this event a smashing success!!!!

Dr. V. Mahesh
Secretary, ICBSII – 2013.

Conference Organizing Committee

Chief Patron:

Mrs. Kala Vijayakumar,

President

SSN Institutions

Patron:

Dr.S. Salivahanan,

Principal

SSN College of Engineering

Chairperson:

Dr.A. Kavitha,

Head, Department of Biomedical Engineering

SSN College of Engineering, Chennai

Secretary:

Dr.V. Mahesh

Treasurers:

Dr.S. Pravin Kumar

Dr. R. Subashini

Joint Secretaries:

Dr. Sachin Gowrishankar Sarate

Dr. Mallika Jainu

Organizing Team:

Dr. Guruprakash Subbiahdoss

Mrs.B. Geethanjali

Mr. R. Sivaramakrishnan

Mr.P. Manoj Niranjan

Mrs.M. Dhanalakshmi

Ms.R. Nithya

Mrs.A. Gowri

Technical Advisory Committee

International Advisory Committee

Dr. Dhan Kuppuswamy, USA

Dr. Emilio Gomez, Spain

Dr. Jesu Christopher J., South Africa

Mr. Michel Owayjan, Lebanon

Dr. Naveed Syed, Canada

Dr. Ramji S., Northern Ireland

Dr. Sekar Raju, China

Dr. Tania Douglas, South Africa

Dr. Vijayalakshmi Mohan Seenivasan, USA

National Advisory Committee

Dr. Ramakrishnan S., IIT Chennai

Dr. Niranjan D. Khambete, SCTIMST, Trivandrum

Dr. Jenega, JNTU, Hyderabad

Dr. Vasudevan D., Brain and Spine Center, Chennai

Dr. Sujatha C.M., Anna University, Chennai

Dr. Kavitha G., MIT, Chennai

Dr. Ravindra Mohan E., Global Hospital, Chennai

Prof. Kumaramanickavel, Narayana Nethralaya, Bangalore

Dr. Sudhir, Sundaram Medical Foundation, Chennai

Dr. Rose C., CLRI, Chennai

Review Committee

1. Dr. C.M. Sujatha

Department of Electronics and Communication Engineering
College of Engineering, Guindy
Anna University, Chennai

2. Dr.G. Kavitha

Department of Electronics
MIT Campus,
Anna University, Chennai

3. Dr.U.S. Raghupathy

Department of Electronics and Instrumentation Engineering
Kongu Engineering College, Coimbatore

4. Dr.A. Kavitha

Department of Biomedical Engineering
SSN College of Engineering, Chennai

5. Dr.S. Pravin Kumar

Department of Biomedical Engineering
SSN College of Engineering, Chennai

6. Dr.V.Mahesh

Department of Biomedical Engineering
SSN College of Engineering, Chennai

7. Dr. Najumunnisa Jamal

Department of EIE
B.S. Abdur Rahman University, Chennai

8. Mr.N. Sri Madhava Raja

Department of Electronics and Instrumentation Engineering
St. Joseph's College of Engineering, Chennai

9. Ms. Ebenezer Priya

Department of Instrumentation
MIT Campus,
Anna University, Chennai

10. Ms. A.Mythili

Department of Instrumentation
MIT Campus,
Anna University, Chennai

Student Organizing Team

Food Committee

Sheshank S., Final Year

Jeya Prakash P.S., Final Year

Ganesh K., Final Year

Hall Arrangement Committee

G. Santosh, Third Year

Sanjay, Third Year

Srikanth M., Final Year

Sai Dhayanand A., Final Year

Deepak N., Final Year

Renita A., Final Year, MOC for the Inauguration

Memento Committee

Sanjay, Third Year

Transportation Committee

Surya Kumar, Third Year

Sudhakar, Third Year

Guru Prasanth, Third Year

Prabhakaran, Third Year

Cultural Committee

Shruthi S., Final Year

Achudhan S.M., Final Year



Registration Committee

Prasannaa V., Final Year

Lakshmi A., Final Year

Archana J., Final Year

Sabariya M., Final Year

Guest House/Accommodation Committee

Moorthy B., Final Year

Manoj M., Final Year

Rajalakshmi V., Final Year

Rajashree, Third Year

Arun E., Third Year

Photography Committee

Vignesh, Third Year

Pravin Richard Ebenezer C., Final Year

Arthi D., Final Year

Conference Proceedings Committee

Akshaya C., Final Year

Vishnupriya K., Final Year

Swetha S., Final Year

Saranya Priyadharshini D., Final Year

Sowdhami S., Final Year

Priyadharshini B., Final Year

International Conference on Bio Signals, Images and Instrumentation

ICBSII 2013

Keynote Talks



Recent advances in non-invasive and image-guided surgery

- Prof. Dr. Emilio Gómez-González

Abstract

Medical imaging has experienced an increasingly fast development given by the generalization of ultrasound, computed tomography, magnetic resonance and radioisotope imaging capable of showing anatomy, morphology, metabolism and function of tissues and structures. Their combination with information technologies and the advent of novel visualization devices have further allowed imaging to enter the operating room and integrate multidisciplinary approaches to diagnosis and therapeutics. Augmented reality, navigation devices, image processing and robotics are discussed as surgical planning and intraoperative guidance defined first steps of an evolving road towards minimally- and non-invasive surgery within the new paradigms of molecular imaging and personalized medicine in the XXI century.

Cone beam computed tomography and magnetic resonance guided surgery are explained as well as ultrasonic-based localization and 3D visualization and planning devices. Motorized surgical microscopes and surgeon helmets allowing for image injection are analyzed together with fluorescent imaging. Endoscopy approaches to minimal incision and natural-orifice procedures are presented together with advanced systems based on video pills and robots. Contrast imaging and biomarkers are discussed as biomedical optics evolves to virtual biopsy. Features of the four different levels of integration at the operating room are explained and smaller, mobile units are also presented.



Dr. Emilio Gómez-González
University of Seville,
Spain

Prof. Dr. Emilio Gómez-González has a background in Physics since 1991. In 2001, he founded -and directed thereafter-the “*Interdisciplinary Physics Research Group (GFI)*” at the Engineering School of the University of Seville, Spain. Currently, the GFI has over 40 members and collaborators of many different profiles: physicist, engineers and physicians (neurosurgeons, neurologists, hepatologists, radiologists and others), biochemist, biologist and psychologist. The GFI has developed over 30 national and international research projects and keeps active collaboration with top-level hospitals of Seville, the National Accelerator Center, and multinational and local companies within the Scientific and Technological Park in Seville. His research lines have been mainly centered in physics applied to medicine, including the design and development of surgical instrumentation and technology specific for neurosurgery and fetal surgery and methods and algorithms for simulation and computer aided diagnosis, neuronavigation, neuromonitoring of evoked potentials, fluorescence

Non-invasive surgery is discussed including precise energy delivery to the target by radiation (in radiosurgery) and by high intensity and focused ultrasound beams guided by ultrasound and by magnetic resonance imaging. Novel applications in gynecology, oncology, neurology and neurosurgery are presented. Principles of closed-loop image-guided procedures are discussed and their technological features are addressed.

Medical robotics devices, types and technologies are described as surgical robots evolve to autonomous systems and even to *surgeon* robots. New frontiers to be explored are presented as actual challenges of applied science and engineering in medicine.

Clinical Engineering in India

- Dr. Niranjan D. Khambete

Abstract

Healthcare delivery systems in India have evolved over the years resulting in a mix of government funded public healthcare system and those set up by charitable organisations and private corporate groups. The high quality of training of doctors and nursing professionals from India is well accepted fact all over the world. In recent years, attention is also being directed towards improving and formalising training of the allied health professionals through establishment of the National Institute of Allied Health. Furthermore, significant efforts have been made to improve the quality of healthcare delivery by introducing Quality Management Systems. The process of hospital accreditation has made significant progress as indicated by a steady increase in the number of hospitals accredited by the National Accreditation Board for Hospitals and Healthcare Systems, since its establishment in 2006. The passing of the Clinical Establishment Act, 2010, by the Indian Parliament has been another important milestone towards ensuring minimum standards of quality for all healthcare systems.

In spite of these strengths reported above and recent quality improvement initiatives in the Indian healthcare system, one aspect that seems to have attracted less attention from the healthcare system leaders and policy makers is the need to have effective HTM systems and ensure safe use of medical devices. This is particularly challenging when an estimated 75% of medical devices in India are imported and 30% of the medical equipment were found to be “out of service” by a recent study covering one of the largest public hospital network in South India. Significant issues exist with repair and condemnation of the equipment and are attributed to



Dr. Niranjan D. Khambete

SCTIMST,
Trivandrum, India

Dr. Niranjan D. Khambete received his B. E. in Instrumentation Engineering from College of Engineering Pune, his M. Tech. in Biomedical Engineering in from Indian Institute of Technology, Bombay and his PhD in Engineering in, from The University of Sheffield, UK. He worked as a Graduate Engineering Trainee in Medical Electronics Division of Larsen and Toubro Limited, India. Since 1992, he has been working as an Instrumentation Engineer in the present Institute, an ‘Institute of National Importance’ with a tertiary care hospital and a leading Biomedical Technology Development and Research center of the country. Dr. Khambete has been actively involved and leading efforts aimed at obtaining a formal recognition to the Clinical Engineering profession and promoting safety of medical equipment in the country. In 2010, he received the WHO Patient Safety Award for his paper on medical device safety in hospitals at a conference in London. He has been closely involved in development of academic and training curriculum for the first of its kind Three-Institute joint M. Tech. Clinical Engineering programme with IIT M and CMC Vellore, and continues to work as a Coordinator for this programme.

process and procedure failures in equipment management and vendor management, sub-optimal user training, lack of safety testing and preventive maintenance. Recently, concerns have also been raised in newspaper reports regarding medical equipment safety. The absence of formal training opportunities and certification systems for Clinical Engineers also seems to be contributing to these suboptimal HTM practices.

Recently, efforts are being made to initiate discussion among all the stake holders of the health care system to address the need for strengthening the HTM situation in India. A clear consensus seems to emerge from various Clinical Engineering Workshops and subsequent expert group meetings that an urgent and definite action is essential to initiate effective Healthcare Technology Management (HTM) practices in all healthcare sectors and actively promote medical device and equipment safety in India. This paper reviews all these efforts and highlights the outcomes.

Precision Medicine: From Hype to Hope

- Dr. Srinivasan Rajagopalan

Abstract

The digital age is witnessing irreversible advances in almost every sphere of science and technology- more so in medicine, where significant progress in the ability to effectively diagnose, treat and cure disease have been made at a remarkable pace. Nevertheless, while the island of medical knowledge has increased so has the shore of ignorance. As Sir William Osler pointed out, "*medicine is [and continues to be] a science of uncertainty and an art of probability*". Uncertainty is a common thread that ties down all the players in the web of life and death. Patients cannot tell exactly how they feel or since when they started feeling a certain [abnormal or even normal] way. The mere presence of a white coat in the room affects their physiological behavior. Physicians and nurses cannot repetitively and reproducibly tell what they observe in a patient. Laboratory results are wrought with errors. Radiologists' performance not only depends on their experience but also in the setting where they accrue their experience. Pathology, despite the potential of serving as a surrogate to the reality, depends on the site and manner of tissue harvest. Even if pathology is a surrogate ground truth, pathologists are not. Physiologists do not yet fully understand the precise working of the human body. Medical researchers cannot precisely characterize how diseases alter the ethiology of the body. Pharmacologists do not fully understand the mechanisms accounting for the drug efficacy. Epidemiology is dependent on the esoteric of statistics. What statistics reveals is suggestive, but what they conceal is vital.

Dr. Srinivasan Rajagopalan

Asisstant Professor, Mayo Clinic
College of Medicine

Dr.Rajagopalan currently heads a multi-disciplinary team of scientists, engineers and clinicians to develop unique clinical frameworks for automatic understanding of medical images and triaging the patients to the most relevant clinical pathway. This paradigm has shown promise in a number of specialties. Most notably the techniques invented, developed and deployed by DrRajagopalan is routinely used in the clinical assessment of lung diseases at Mayo Clinic. Physicians in the departments of Radiology, Pathology and Thoracic diseases regard this capability as heralding an important new advance in the clinical assessment of this complicated diseases. Captivated by the intellect and the efficacy of this tool, these specialists fondly refer to DrRajagopalan as "*Doctor's Doctor*". The same technology is showing great promise in applications in gastroenterology, orthopedic surgery, neurology and liver and kidney disease. It is not overstated to single out Dr. Rajagopalan as the resident expert at Mayo in quantitative medical image understanding.

Notwithstanding the above mentioned shortcomings, the innate nature of uncertainty in medicine has been recognized and effectively managed. Consequently, disease management is being revolutionized through the emerging practice of P4 (Predictive, Pre-emptive, Participatory and Personalized) medicine. The unwritten mantra behind P4 medicine is the optimal navigation through the data->information->knowledge->wisdom pipeline. The success and strides in machine learning serves as a viable predicate to realize the goals of P4 medicine. However, the success in machine learning still lags behind the current potential, and even farther from the visionary but reachable horizon of hopeful expectations and vision for computational medicine. There are two major hurdles to overcome: 1) putting the patient first, to target and focus on specific and relevant individual patient needs, and 2) effective, expedient translation from basic research and engineering prototypes to clinical application. Progress toward fully realizing these goals varies in pace and delivery of expected results, in spite of the intrinsic advantages offered by high spatial and temporal resolution imaging. This advanced technology provides not just a patient-specific dataset, but rather a faithful surrogate of the patient to facilitate more rapid development of an individualized, focused, validated solution expediently translated into clinical utility and patient application.

This talk will emphasize imaging science and technology engineering as related to effective production and translation of working, validated prototypes and their integration into relevant healthcare workflows and solutions focused on the individual patient. Putting the patient first insures that whatever the pathway to success, the objective and solution have positive impact on the well-being of the patient. Planning a successful translational system incorporates upfront the ideal patient surrogate (as represented by a high resolution, faithful image). This talk will also describe and illustrate several specific clinical individual “patient-first” examples of approaches and systems wherein success was achieved by using near-ideal patient surrogates- faithful specific full 3D or 4D images of the patient.

Advances in Neurophysiological Investigations and their Relevance and Application to Clinical Neurology

- Dr. D.Vasudevan

Abstract

From the time of the ancients, well into the eighteenth century past the dark ages, electricity was regarded as a strange mystical power. It was differentiated from magnetism in 1600 by Gilbert, but its nature remained a mystery. Gradually its relation to the nervous system emerged, first from the effect of its application to the human body and later from the discovery that muscle, nerve and brain could be sources of this power. The first technique became the precursor of electrotherapy and the latter the forerunner of electrodiagnosis. From electrodiagnosis proceeds the current application of use of neural signals to control computers and eventually to be able to physically move or manipulate machines. In its initial stages now, this field holds tremendous promise in the form of a variety of possible applications both in the field of clinical medicine as well as in other aspects of our daily life. Some of the salient aspects are discussed.



**Dr. D.
Vasudevan**

The Brain, Spine
and Nerve
Center

Dr D Vasudevan completed his MD in Medicine; DM in Neurology. He is currently a consultant Neurologist and Clinical Neurophysiologist at The Brain, Spine and Nerve Centre, Chennai. Earlier he worked as a Professor of Neurology at Sri Ramachandra Medical College, Chennai and went to hold the position of Professor and Head : Department of Neurology, Narayana Medical College, Nellore. He is also the Examiner for DM neurology at Dr MGR Medical University and University of Mumbai and is a principal Investigator in numerous clinical trials in Epilepsy, Stroke, Parkinson's Disease, Diabetic Neuropathy etc.

Walking through the Human Genomic Technology Highway and its Application in Medicine

- Dr. G. Kumaramanickavel

Abstract

Human genome project initiated in 1989 is a major global effort to (i) sequence the entire human genome and (ii) to map the human genes causing various diseases from blindness to cancer. Current state of knowledge was achieved by various technological inventions, innovations and advancements made in the last half a century. High throughput DNA sequencing and microarray methodologies, married to analysis software algorithms enabled us to reach the goal of completing one of the objectives much ahead of time, namely sequencing the entire human genome.

The fields of genetics and molecular biology started in Feb 1953 with the discovery of the structure of the DNA double helix coil by the Nobel Prize winners James Watson and Francis Crick at the Cavendish Laboratory, Cambridge. At which point of time sequencing DNA was a hard task, which needed herculean effort, a fat sum of money and enormous amount of time. However today, with the next generation sequencing techniques, it is done with much ease and comfort for a fraction of not only effort but also money and time.



**Dr.
G.Kumaramanickavel**

Narayana Nethralaya,
Bangalore

Prof. Govindasamy Kumaramanickavel, for the last two decades, works on ocular genomics - primarily involved in gene mapping, mutational screening and association studies including genomewide in complex and Mendelian ophthalmic diseases. He carried out two major (*glaucoma and diabetic retinopathy*) epidemiological and genetic projects comprising of 20,000 subjects. Has been facilitating cross-faculty integration of clinicians, epidemiologists, sociologists and vision scientists. Was a key member of a successful ocular gene mapping team at the University of Otago, Dunedin, New Zealand. Later, joined the Department of Genetics at Sankara Nethralaya with two technicians in Jan 1996 and left the same as head with 18 staff members in Apr 2009. PhD examiner for many universities both in India and overseas. Has done genetic counseling for nearly 9000 new patients with ocular genetic diseases and teaches genetics for ophthalmologists and para-ophthalmic courses. He is now on a mission to persuade ophthalmologists to undertake PhD and do research and also wants to create many genetics and medical research centers in India and Asia.

Currently we know that about 14,000 single gene disorders, like color blindness and a multitude of complex disorder genes for diseases like cancer to hypertension are being identified to alleviate the human suffering. So far 6237 disease causing genes have been identified and are available for diagnostics. Major effort is underway to treat human diseases through gene therapy and spectacular achievements have been made so far in research and hopefully it should enter the clinical arena in a few years from now.

Lasers in Ophthalmology

- Dr. B. Ganesh

Abstract

In this era of scientific advancement in every field of medicine, it would be imperative for biomedical engineering students, to know not only the advances but also how each machine works. The field of ophthalmology is growing phenomenally and is now a superspeciality with its own subspecialties like cornea, glaucoma, retina etc. The growth has been aided by the use of modern gadgets, like specular microscope, Optical coherence tomogram, perimetry etc., for both diagnostic and theraperutic purposes. Now, Lasers have also become an integral part of the speciality in providing therapeutic care to the patients. In this address, I would like to highlight the principles, advantages and disadvantages of various lasers that are currently being used in the field of ophthalmology to treat various ocular conditions. The talk will also give a brief look into the potential areas of research to expand the treatment horizons. For better understanding of the mechanism in lasers, short video clips of various laser procedures has also been included.



Dr.B Ganesh

Karpagavinayagar
Medical College and
research institute

Dr. Ganesh Balasubramaniam did his Bachelor of Science (B.S.), Zoology, in Madras University he has also done his M.B.B.S, Diploma in ophthalmic medicine and surgery and M.S in ophthalmology. Was offered a fellowship in Ophthalmology at Sankara Nethralaya and also in Intra Ocular Lens at Aravind Eye Hospital. Was awarded FAICO fellowship award and AGARWAL GOLD MEDAL ORATION award for outstanding contribution to the field of ophthalmology. He has been selected as a vice president of the Indian Intraocular and Implant Society, later he was selected as a president of Indian Intraocular Implant and Refractive Society. Has presented papers in both national and international conferences for the past 15 years. His research projects include Clinical drug trial by ALCON Laboratories. His community services includes organizing various eye camps and performed over a hundred surgeries with IOL implantation. Member of Editorial board for the Tamilnadu ophthalmic journal and Indian Intraocular Implant and refractive society member also an Executive committee member of Indian Intra Ocular and Implant Society.

Combining Physiological Monitoring and Neurocognition

- Dr. Sushil Chandra

Abstract

Cognition indeed refers to the mental process by which external or internal input is transformed, reduced, elaborated, stored, recovered, and used. As such, it involves a variety of functions such as perception, attention, memory coding, retention, and recall, decision-making, reasoning, problem-solving, imaging, planning and executing actions. Furthermore, these processes can to some extent be observed or at least empirically probed, leading to scientific investigation by means of methods akin to those of the natural sciences.

Neuroscientists received impressive help in studying the functionalities of the human brain by means of electrophysiology and Imaging. The significance of the electroencephalogram (EEG) for investigating neuro-cognitive functions was already recognized by its discoverer, Hans Berger himself. Other electrophysiological parameters i.e. ECG (Electrocardiography) and GSR (Galvanic skin responses) are basic indicators of stress and are also correlated with memory and other cognitive abilities.

Dr. Sushil Chandra

Head, Dept. of Biomedical Engineering,

Dr. Chandra holds a senior Scientist position (Scientist- F) with 26 years of experience in INMAS-DRDO and heads the Dept. of Biomedical Engineering. His current research focus includes Cognitive Science, Biomedical Engineering and applications in defence R&D. Recent work addressed Biosensors, Defence Electronics, Tropo communication, Telemedicine, Image Compression and Rehabilitation. Prepared Government Reports for Adaptive Variable Data Rate Modem for High Frequency Communication, Digital Tropo Communication System. Interested in implementation/Operation/execution/Tech nology Management / Technology Departments of Large Scale Social/vocational/Engineering Setup e.g. ; International collaborated NGOs, Technical empowerment for All. Acted at senior level for partnerships/collaboration with various international Organization, NGOs, social Society, Government Department. Coordinated, a large no. of project of research project between various professional & educations institutes & INMAS (Biomedical Engg.)Visiting Faculty/Advisor/consultancy/Invited Lectures at various engineering colleges for Biomedical Engineering, bio Medical Technology, Disaster Management. Published various Technological Articles in professional Journals. Authored the Book, "Topics in Electromagnetic Waves".

Many studies have been published for stress and its effect on cognitive abilities. The rapid improvement of other brain- imaging methods such as positron emission tomography (PET) and functional magnetic resonance imaging (fMRI) have critically revolutionized the field of neuroscience and cognitive science. Other methods as Magnetoencephalography (MEG), functional near infrared spectroscopy (fNIR) have been introduced and increased no. of monitoring methods in real time cognitive task processing. In EEG various specific brainwaves reflects activity of cognitive brain. Visual and advanced properties of these brain waves signify cognitive brain states. However most important and most directional approaching technique is Event related potentials (ERP) in psychophysiology. ERP's can be used to distinguish and identify psychological and neural subprocesses involved in complex cognitive, motor, or perceptual tasks. They present an intriguing possibility to obtain information about how the intact human brain processes signals and prepares actions. These all techniques of physiological monitoring now became essential for cognitive and Psychophysiological studies. Explorations of basic insights in brain and functional/event related is now critically dependent on these physiological techniques.

International Conference on Bio Signals, Images and Instrumentation

ICBSII 2013

Research Papers

Segmentation and Disentangling of Clumps of Chromosomes

Anuja MR¹, Loganathan E¹, Nirmala Madiam¹

K S R College of technology

Tiruchengode

anujamr1989@gmail.com, loguhelp21@gmail.com, nirmalaootty@gmail.com

Abstract

Classification is a widespread procedure in cytogenetics to assess the possible presence of genetics defects. The procedure is lengthy and repetitive, so that an automatic analysis would greatly help the cytogeneticist routine work. Still, automatic segmentation and full disentangling of chromosomes are open issues. We propose an automatic procedure to obtain the separated chromosomes, which are then ready for a subsequent classification step. The segmentation is carried out by means of a space-variant thresholding scheme, which proved to be successful even in presence of hyper- or hypofluorescent regions in the image. Then, the tree of choices to resolve touching and overlapping chromosomes is recursively explored, choosing the best combination of cuts and overlaps based on geometric evidence and image information.

Keywords

Adjacent chromosomes, chromosome analysis, image segmentation, karyotyping, overlapping chromosomes.

1. Introduction

The analysis of human chromosomes can be used to obtain information about genetic disorders. In normal human being, there are 23

pairs of chromosomes which include 22 pairs of autosomes and 1 pair of sex chromosomes. These may be in the form of touching or overlapping chromosomes, figure 1(a), 1(b). The first step that has to be taken in analysing[1] a chromosome image is the segmentation of chromosomes and chromosome clusters from the image background. We propose here a fully automatic and effective method to segment and disentangle chromosomes from prometaphase images, without any assumption on their number or dimension distribution. To achieve this, we propose a space variant thresholding scheme to segment chromosome objects from the background. Then, we describe a novel yet simple measure of single-chromosome likelihood (SCL), to evaluate whether an object is a single chromosome or a cluster, and to score each object. For each cluster, several disentangling hypotheses are generated, evaluated, and recursively analysed therefore generating a hypothesis tree. The tree of disentangling hypotheses is explored online during its generation, with an additional branch-and-bound strategy to keep the computational complexity low. The problems associated with various methods like level set formulation, voting method, watershed transform, Delaunay triangulation described in [2], [3] & [4], can be overcome with the help of

our approach. In the case of Delaunay triangulation, more lines are drawn which becomes very complex in separating the chromosomes. As a result, (i) computational complexity is reduced to an almost linear complexity; (ii) the number of free parameters is drastically reduced; and (iii) a more complex clump can now be decomposed, which was almost impossible to do during our previous implementation.



Fig 1(a): overlapping chromosome



Fig 1(b): touching chromosome

The analysis consists of mainly two main steps, segmentation and separation of chromosomes. The separation of overlapped or touching chromosomes is shown in figure 2.

The automatic chromosome identification method we propose is based on a preprocessing stage, whose aim is to separate from the background the chromosomes and chromosome



Fig 2: Separated chromosomes

clusters, which are then passed on to the cluster disentangling stage. Each object (either chromosome or cluster) is analyzed to test whether it is composed by a single chromosome or if it has to be split by means of a single-chromosome likelihood, it is based on the availability of the chromosome axis, whose extraction is done and performs a novel measure. Each object that does not pass the test becomes the root of a tree, where each node represents one of several cuts and overlaps hypotheses, generated based on geometrical and image evidence. Each node is recursively analyzed until each leaf of the tree is evaluated as a single chromosome. Then, the best overall combination of hypotheses gives the final disentanglement.

1.1 Detection of points of maximum curvature

The maximum curvature is calculated with the help of the formula,

$$K = ((x'y'' - y'x'') / (x'^2 - y'^2)^{3/2})$$

Where x and y are coordinates of the boundary points, x' and y' represents the first derivatives, x'' and y'' represents the second derivatives. We denote the ith point of local maximum curvature as v_i and jth point of local maximum as v_j.

1.2 Main chromosome axis identification

With the help of a vessel tracking algorithm [5], the best hypothesis is selected. The tracking scheme is shown in figure 3.

It consists of three procedures:

1.2.1 Interactive initialisation

- (i) Pointing one or several points of vessels, or
- (ii) by defining a Region of Interest (ROI) further explored to detect the vessels inside.

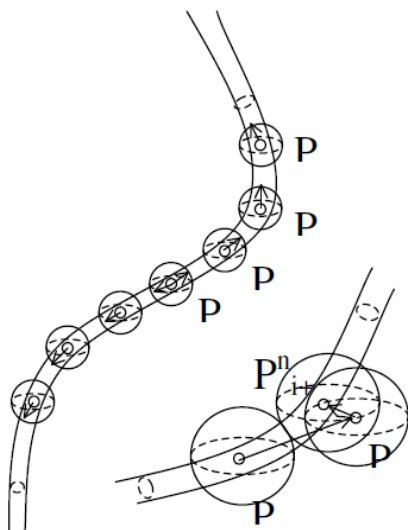


Fig 3: Vessel tracking scheme

1.2.2 Vessel tracking

Any new point (including the initial one) is iteratively adjusted and, when centered, the vessel orientation and its size are being estimated. The next point estimation is then calculated along the estimated direction, the incremental displacement depending on the vessel size and curvature.

The algorithm for vessel tracking algorithm is shown below:

Step 1: start

Step 2: choose P_0 ; $i=0$;

Step 3: check whether P_i is an element of vessel.

Step 4: if yes go to step 5 else goto step 7

Step 5: correct the P_i position;

Step 6: $i=i+1$;

Step 7: end

1.2.3 Stopping strategy

The tracking stops when several conditions, which are detailed below, are not fulfilled any more (too small vessel, gap along a vessel, ...). However, the procedure can be locally reinitialised by searching another vessel segment that crosses the faces of a cubic window centered on the last detected point. In such a way, highly curved vessel, local artefact or abnormalities can be bypassed.

1.3 Single chromosome likelihood

The object is marked as a cluster if the axis has a change in curvature sign and the difference between the maximum and the minimum curvature is greater than an empirical threshold $th_K=0.2$. We then identify the two most prominent peaks and estimate their contrast with respect to the surrounding area. Whenever there are other peaks showing similar contrast, we consider the blob as a cluster. Hence, given a blob C with area A_C and with the description of its axis given by the curve $a(l)=[x(l), y(l)]$ onto which the curvature $K_a(l)$ is computed, the score of C is,

$$SCL(C) = 0; \quad \text{if bulges or S shape}$$

$$=9 - \int K_a(l)dl; \quad \text{if } A_C < th_A$$

$$=10 - \int K_a(l)dl; \quad \text{otherwise}$$

so that a blob presenting more than two bulges estimated according to Section III-C has score zero, whereas all other blobs have scores depending on the integral of the contour curvature of their axis. The second condition states that blobs with an area smaller than th_A have a lower score, in order to avoid the splitting of blobs into too many tiny parts. The area threshold th_A was heuristically set at 150 pixels.

1.4 Generation of candidate splits

As a preliminary analysis for each cluster, by looking at the most prominent local minima of the contour curvature k (those with value lower than a threshold $th_K = -0.15$), we derive a set $K = \{k_i, i=1:N_K\}$ of points on the contour suggesting the possible presence of touching and overlaps, as previously proposed [10], [11].

1.4.1 Touching Chromosomes Through Dark Paths

Often, the contact area along adjacent chromosomes has a low but nonzero intensity, due to some fluorescence diffusion from the surrounding chromosomes. Therefore, a path of pixels darker than those belonging to the adjacent chromosomes may be found.

1.4.2 Overlapping Chromosomes

From the set K of selected local minima of the curvature k of a blob C all segments entirely contained in C and connecting every two points in K are considered. Since overlaps areas have a rhomboid shape, we look for quadruplets of lines forming a polygon of dimension coherent with the chromosomes diameters and with two pairs of almost parallel sides. Each segment $tij = [kj - ki]$ is defined by its starting and ending points ki and kj , and its orientation can be

easily derived. The distance between two segments tij and tmn , can be defined as in [11] using the metrics,

$$d(tij, tmn) = (tij \times tlm)/|tij|$$

All pairs of segments whose distance is less than $th_C = 1.2 \times ad$ pixels, and whose orientations differ by less than $\pi/6$ are considered; ad is the average diameter of the single chromosomes in the image. If no single chromosome has been found yet, ad is set to the empirical value of 45 pixels.

1.5 Generation and exploration of the hypothesis tree

The automatic chromosome identification method proposed is based on a preprocessing stage whose aim is to separate from the background the chromosomes and chromosome clusters, which are then passed on to the cluster disentangling stage. Each object (either chromosome or cluster) is analyzed to test whether it is composed by a single chromosome or if it has to be split by means of a single-chromosome likelihood. It is based on the availability of the chromosome axis.

Given a set of N chromosomes, $C_M = \{C_i; i=1, \dots, N\}$ that results from the disentanglement of a cluster with M splits, its fitness is evaluated as,

$$\Delta(C_M) = \omega_1 \cdot \log((\sum_{i=1:N} SCL(C_i))/N) + \omega_2 \cdot \log M$$

Where ω_1 and ω_2 are weights summing to 1 and empirically set to 0.2 and 0.8, respectively.

Each object that does not pass the test becomes the root of a tree, where each node represents one of several cuts and overlaps hypotheses, generated based on geometrical and image evidence. Each node is recursively analysed until each leaf of the tree is evaluated as a



single chromosome. Then, the best overall combination of hypotheses gives the final disentanglement.

2. Experimental Results

The separation of touching and overlapping chromosomes can be done with the help of hypothesis tree approach. The input image based on touching chromosome and its corresponding contour plots are shown in figure 4 and 5 respectively.



Fig 4: input image

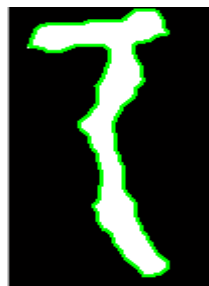


Fig 5: contour plot

The input image related to overlapping chromosome is shown in figure 6 and its corresponding contour plots are shown in figure 7 respectively.



Fig 6: overlap image

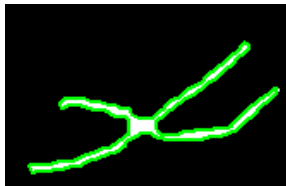


Fig 7: contour plot

The concave and convex points of touching and overlapping chromosomes are shown in figure 8 and 9.

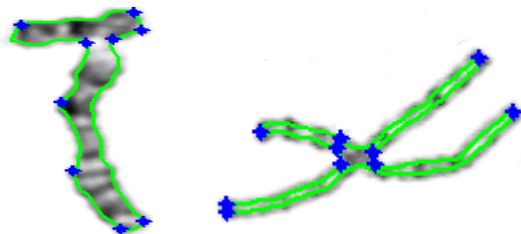


Fig 8. Curvature points

The curvature points of touching and overlapped chromosomes are plotted in a graph as shown in figure 10 and 11 respectively.

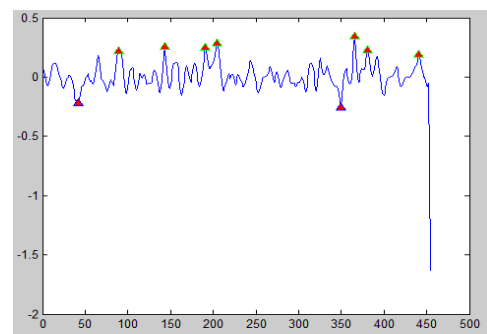


Fig 10. Maximum and minimum curvature points of touching chromosomes

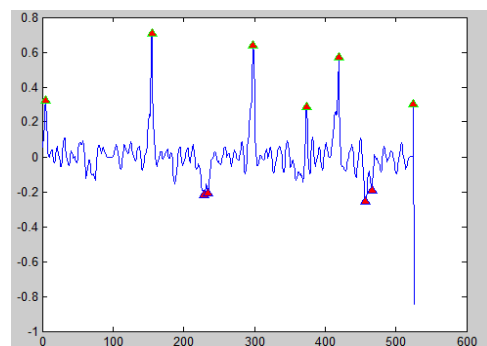


Fig 11. Maximum and minimum curvature points of overlapped chromosomes

After the above step, vessel tracking approach is done for both type of chromosomes whose results are shown in figure 12.

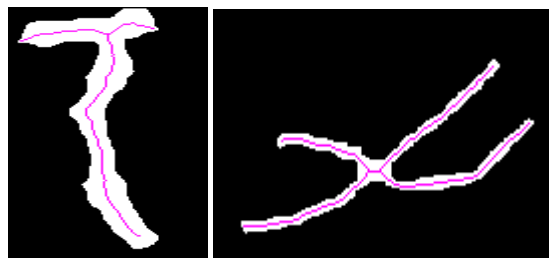


Fig 12. Vessel tracking approach for touching and overlapped chromosomes

Then a hypothesis of the given chromosome image is done. The various hypothesis on touching chromosome is shown in figure 13.

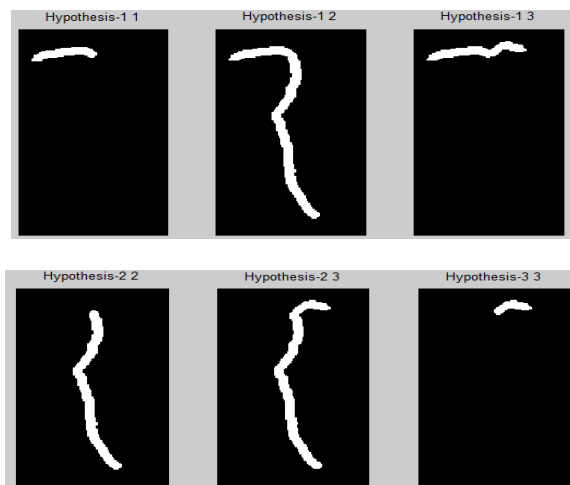


Fig 13. Hypothesis for the touching chromosome image

The hypothesis for overlapped image is given in figure 14.

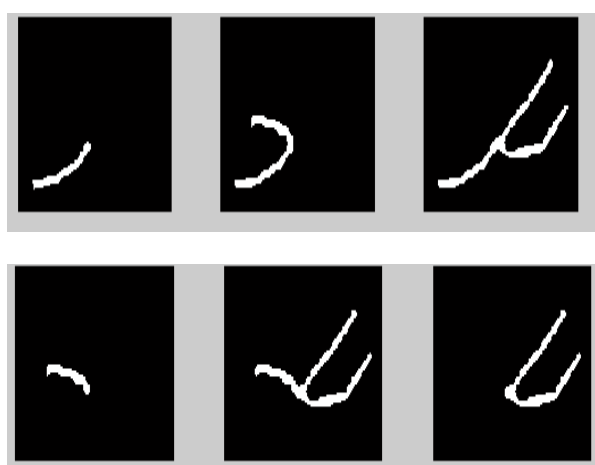


Fig 14. Hypothesis for the overlapped chromosome image

After this, we are selecting the desired hypothesis based on the vessel tracking algorithm. This helps in determining the best separation of touching and overlapping chromosomes. The desired output related to touching chromosome is shown in figure 15.

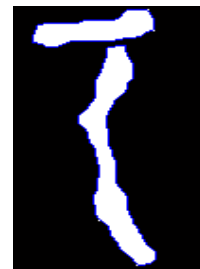


Fig 15. Separated chromosomes

The overlapped section of the chromosome is shown in figure 16 and the corresponding separation is given in figure 17 and 18.



Fig 16: overlapped section

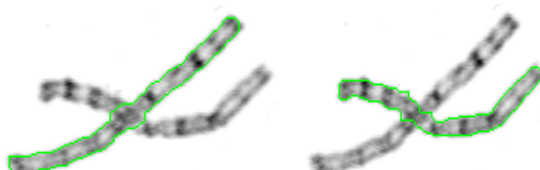


Fig 17. Separation1



Fig 18: separation 2

3. Conclusion

In this paper, we proposed a new approach for segmenting clumps of chromosomes by using the points of maximum curvature. Based on hypothesis tree approach, it ensures that at each step only the best split of a blob is performed. Compared to algorithms like Delaunay triangulation and watershed, hypothesis tree is the most accurate approach to separate chromosomes easily. More number of chromosomes can be separated with this approach. To the best of our knowledge, this is the first method to simultaneously tackle segmentation, overlaps, and adjacencies, providing a tool able to automatically analyze an image, and whose results can be handed over with minimal human intervention to a classifier for automatic karyotyping.

4. References

- [1] J. Graham and J. Piper, Automatic Karyotype Analysis. Totowa,NJ: Humana, 1994, pp. 141–185.
- [2] Hang Chang, Qing Yang, and Bahram Parvin, “Segmentation of heterogeneous blob objects through voting and level set formulation,” Pattern Recognition Letters, vol. 28, pp. 1781–1787,2007.
- [3] Bahram Parvin, Qing Yang, Ju Han, Hang Chang, B Rydberg, and M.H. Barcellos-Hoff, “Iterative voting for inference of structural saliency and characterization of subcellular events,” IEEE Transactions on Image Processing, vol. 16, no. 3, pp. 615–623, March 2007
- [4] Luc Vincent and Soille Pierre, “Watersheds in digital spaces: An efficient algorithm based on immersion simulations,” IEEE Transactions of Pattern Analysis and Machine Intelligence, vol. 13, no. 6, pp. 583–598, June 1991.
- [5] E.Grisan, A. Pesce, A. Giani, M. Foracchia, and A. Ruggeri., “A new tracking system for the robust extraction of retinal vessel structure,” in Proc. 26th Annu. Int. Conf. IEEE-EMBS. New York: IEEE Press, 2004, pp. 1620–1623.
- [6] Ramesh Jain, Rangachar Kasturi and Brian G.Schunck, “Machine Vision” Mc Graw-Hill, 1995
- [7] Rafael C. Gonzalez and Richard E.Woods, “Digital image processing”, Pearson Education, 2008
- [8] Dr.Amit Konar, “Artificial Intelligence and Soft Computing”, CRC, 1999.
- [9]Dr.Amit Konar, “Computational Intelligence- Principles, Techniques and Applications”, Springer, 2005.
- [10] X. Shunren, X. Weidong, and S. Yutang, “Two intelligent algorithms applied to automatic chromosome incision,” in Proc. IEEE Int. Conf. Acoust., Speech, Signal Process., '03. (ICASSP '03), Apr., pp. 697–700
- [11] G. Agam and I. Dinstein, “Geometric separation of partially overlapping nonrigid objects applied to automatic chromosome segmentation,” IEEE Trans. Pattern Anal. Mach. Intell., vol. 19, no. 11, pp. 1212–1222, Nov. 1997.

Applications of Image Processing Techniques for the Detection of Eye Diseases

R.Manjula Sri¹, K.M.M. Rao²

¹Department of EIE, VNR Jyothi IET, Hyderabad, India

²Department of EEE, BITS-Pilani-Hyderabad Campus, Hyderabad, India

rmanjulasri@gmail.com, kundamrao@gmail.com

Abstract

This paper describes the application of image processing techniques for automatic detection of eye diseases. Large percentages of people suffer from eye diseases in rural and semi urban areas in India as well as world over. Image processing techniques greatly help diagnosing various eye diseases. Low cost instrumentation system coupled with internet and mobile enabled network connectivity and image processing techniques help patients in rural and semi urban areas to access well equipped and sophisticated hospitals in cities. The main objective of this work is to design a simple inexpensive retinal image analysis system for a large number of people in a village or a cluster of villages without the need for travelling a long distance for diagnosis. As a part of the low cost instrumentation system design the authors have developed the suitable software to detect Glaucoma, Age related Macular Degeneration (AMD), Diabetic Retinopathy(DR) with image processing techniques using LabVIEW, and achieved better accuracy, sensitivity and specificity.

Keywords

Image Enhancement, Registration, Fusion, Segmentation, Feature extraction, ophthalmic diseases.

1. Introduction

With the tremendous improvements in the Medical imaging techniques, Image Processing simplifies the diagnosis of eye diseases, there by assisting ophthalmologists for quick diagnose of the diseases [1][2]. In this work, the authors simulated various image processing techniques for the detection of commonly observed eye diseases viz. Age related Macular Regeneration (AMD), Glaucoma and Diabetic Retinopathy(DR) using LabVIEW. The image processing techniques for the detection of different eye diseases include Enhancement, Registration, Fusion, Segmentation, Feature extraction, Pattern matching, Classification, Morphology, Statistical measurements and Analysis [3][4].

Image registration is an important feature in medical imaging for change in detection. It has many potential applications in the retinal diagnosis. Image registration is a process of aligning two images into a common coordinate system. In medical imaging based diagnosis, it is essential to combine data from

different images and the images are to be geometrically aligned for better analysis and more accurate measurements. The process of mapping points from one image to another image is called image registration. The images to be aligned may be taken at different times or taken with different imaging devices [5]. Image fusion is an approach to combine information acquired from number of imaging devices. The goal of image fusion is to integrate contemporary multi-sensor, multi-temporal or multi-view information into a single image, containing all the information. The multi sensing imaging technology results in large volumes of data. Image fusion effectively reduces the data volume , helps in effective analysis and better results[6]. Segmentation is a process of subdividing an image into its constituent parts such as objects, region containing pixels of similar properties and contiguous regions perceived by humans. Classification is labeling of a pixel or group of pixels based on the grey values and other statistical parameters. Image classification is perhaps the most important technique of digital image analysis, which includes the estimation of statistical parameters based on the gray-level intensities of the image pixels. The image analysis functions are used to understand the content of the image.

In the earlier research inverse segmentation [7], adaptive thresholding [8], histogram normalization and adaptive segmentation, and circular Hough transform[9] were used for the detection of macula and drusens. For the detection of Glaucoma matched filter, curvelet transform, fuzzy c-mean clustering, artificial neural networks, k-NN regressor, pyramidal decomposition, edge detection, entropy filter and feature vector [10-15] were used. The techniques used for: blood vessel enhancement

and detection of hard exudates(HE), Cotton Wool Spots(CWS), Micro Aneurisms(MA) and hemorrhages were segmentation ,edge detection, mathematical modeling, feature extraction, classification, pattern recognition and texture analysis [16-20].

2. Eye Diseases and Detection Methodologies

Age related macular degeneration, diabetic retinopathy and glaucoma are the most frequently observed eye diseases in rural and semi urban areas. AMD is degeneration of the macula, which is a part of the retina, responsible for the sharp, central vision needed to read, drive and for face recognition. Glaucoma is characterized by the progressive degeneration of optic nerve fibers and that leads to structural changes of the optic nerve head (ONH), slowly diminishing neuro-retinal rim. Diabetic retinopathy is a complication due to diabetes. DR leads to several abnormalities like MA, hemorrhages, HE, CWS, venous irregularities, new vessels and macular edema. All these lead to vision loss or blindness, if not detected at early stage.

For the detection of AMD one method is localizing Macula, then localizing the abnormal regions and non- homogeneous textures on macula. Another method is detection and segmentation of drusens. For the detection of Glaucoma optical disc(OD) and cup are localized and ratio of cup to disc diameters or areas is calculated. For Glaucomatous eye the ratio is more than 0.3.

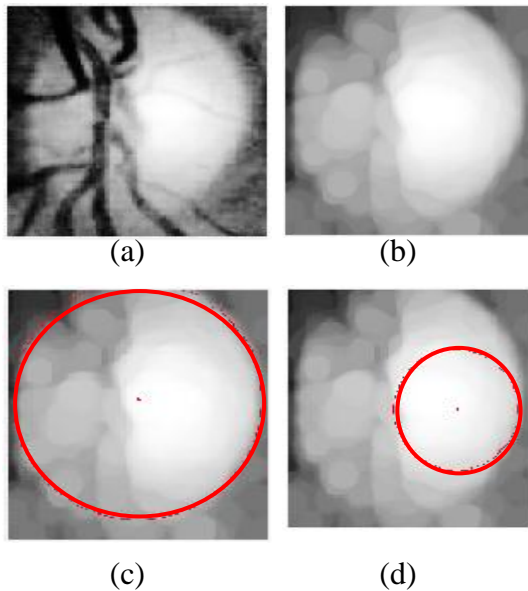


Figure 1: (a) histogram equalization
(b) morphology and median filter (c)
Circle fitting by outside to inside
pixels (d) Circle fitting by inside to
outside pixels

The methods used for the detection of diabetic retinopathy are vessel extraction, localization of MA, HE, Hemorrhages, CWS and Identifying oozing of blood vessels and irregularities in the blood vessels.

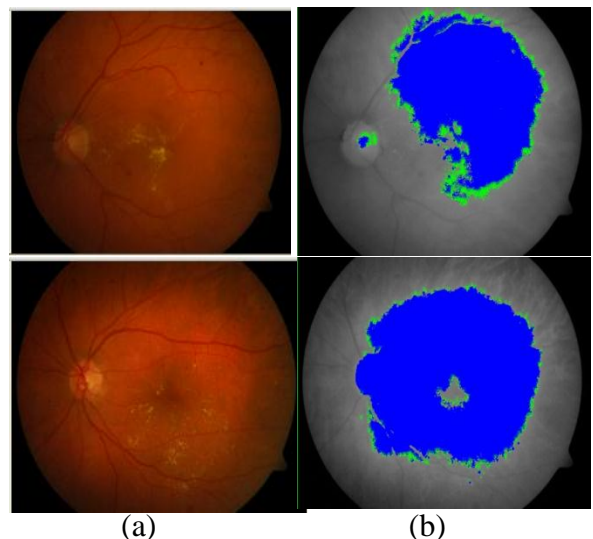
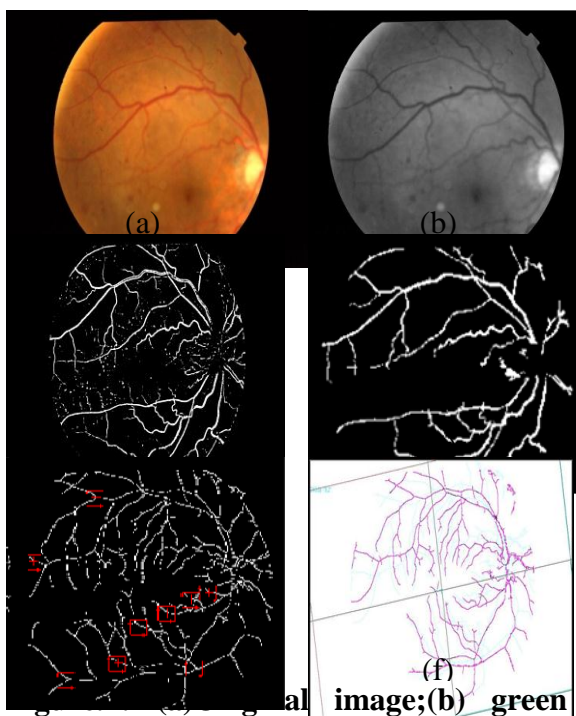


Figure3:(a) original image (b) kNN-
Classifier output to detect Hard
Exudates in(a)



plane extraction to convert into gray scale image (c) Thresholding to convert in to binary image,(d) Morphology to remove small objects;(e)Y-feature extraction;(f)Registration with Golden template matching.

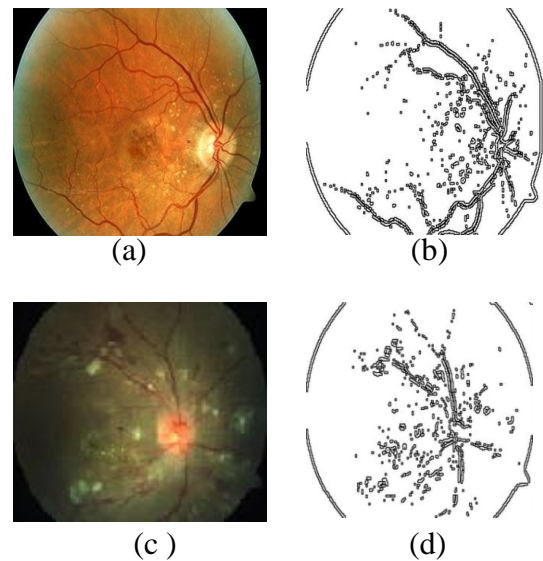


Figure.4: (a)original image of
Hypertensive DR;(b) vessel extracted
image of (a) ; (c)original image of
AMD ;(d) vessel extracted image of (c)

3. Implementation

As part of the soft ware development the authors have implemented few image processing techniques and algorithms to detect retinal disorders using LabVIEW software. For the detection of glaucoma, OD and cup are localized using circle fitting tool and their diameters are measured. Cup to disc diameters ratio is calculated to identify glaucomatous eyes. The corresponding images are shown in figure 1. For the detection of lesions two flourscein images are collected with a time delay of 10 seconds. The two images are extracted to green plane, threshold and morphological operators are applied to enhance the vessels. The two enhanced images are fused synchronizing the Y-features- to identify discontinuities in the die flow. Figure 2 shows (b) Green plane extraction, (c) Thresholding, (d) Morphology, (e) Y-feature extraction and (f) Registration on (a) Original image. To detect hard exudates from an image of diabetic retinopathy, three different classifiers: maximum images mean distance, Nearest Neighborhood (NN) and k-NN classifiers were trained and images were tested. The k-NN classifier has given better results. The original and resultant are shown in figure 3. Green points show the pixels, where hard exudates are detected. Diameter of retinal blood vessels plays an important role in identifying the retinal disorders. Morphological methods are applied to enhance blood vessels and diameters are measured using measurement tool of LabVIEW. The resulting images are shown in figure 4.

4. Results and Discussion

The main theme of this work is to design a simple inexpensive system, easily operated by any trained technician and to employ image processing techniques for automatic detection and analysis of eye diseases of large number of patients. The authors have developed and tested the software to demonstrate that image processing can help meeting the challenges of healthcare for rural and semi urban population. The authors have developed software for OD analysis; feature extraction ; fusion of angiographic images for the detection of lesions; k-NN classifiers for detection of hard exudates; blood vessel enhancement for the detection of vessel based eye diseases. The resultant images are shown in figures 1 to 4. For the testing of Lesions, detection of Glaucoma, Blood vessel enhancement the clinical images from Maxivision Eye Hospital and Padmavathy Nertralaya, Hyderabad are used with their permission. For the detection of Hard Exudates with k-NN classifier, DRIVE database with 80 images has been considered out of which 30 images contain Hard exudates. The k-NN Classifier has given an Accuracy of 92.5%, Sensitivity of 96.1 %, and Specificity of 90.7%. The statistical results of the measurement of blood vessel diameters for the detection of vessel based eye diseases are shown in Table1. Table2 shows the cup to disc ratio measurement for the identification of Glaucoma. Table 3 shows the identification score with a classification score of 1000 with k-NN classifier with k=8, for five images with HE.

Table 1: Average Thick and Thin Vessel diameters measured using mathematical morphology method.

Sn o	Retina l	Thick Vessels	Thin vessels
1	NDR*	169.3	82.0
2	NDR(196.5	55.5
3	HDR(143.6	66.1
4	HDR(139.4	65.3
5	NPDR	134.9	55.5
6	NPDR	132.3	82.0
7	PDR(0	169.3	55.5
8	PDR(1)	156.9	56.3

*NDR: Normal Diabetic Retinopathy;
 HDR: Hypertensive Diabetic Retinopathy;
 PDR: Proliferative Diabetic Retinopathy
 NPDR: Non- Proliferative Diabetic Retinopathy

Table 2: cup and disc radii, areas and CDR with circular fit method for different cases.

	Regi on	Radius	Rad ius	Are a	CD R
Cas e1	Disc	138.7	0.81	2.01	0.41 04
	Cup	88.81	0.52	0.86	
Cas e2	Disc	138.7	0.81	2.01	0.34 12
	Cup	80.86	0.47	0.71	
Cas e3	Disc	140.7	0.82	2.15	0.22 02
	Cup	66.04	0.38	0.47	
Cas e4	Disc	136.4	0.80	2.02	0.42 39
	Cup	88.84	0.52	0.86	
Cas e5	Disc	137.8	0.81	2.06	0.39 32
	Cup	86.45	0.50	0.81	
Cas e6	Disc	139.2	0.81	2.10	0.41 06
	Cup	89.21	0.52	0.86	
Cas e7	Disc	140.0	0.82	2.14	0.26 64
	Cup	72.26	0.42	0.57	

Table 3: The identification score with

Ima	Image	Image	Imag	Imag
636	760	835	656	462
636	738	385	773	842
395	176	0	830	745
636	754	655	97	722
455	430	818	631	691
379	463	818	423	823
717	740	818	631	146
140	660	823	842	716

5. Acknowledgements

The authors thank doctors at Maxivision Eye Hospital and Padmavathy Netralaya, Hyderabad and for providing data base and for their valuable suggestions. Thank Principal, VNRVJIET-Hyderabad for encouraging the research work and providing the facilities. Thank Director, BITS-Pilani- Hyderabad for encouraging research in medical image processing.

6. References

- [1] R.Manjulasri and KMM Rao, "Review of image processing and tele ophthalmology research projects world over" in Technology Spectrum Journal, November 2010 pp.42-48.
- [2] KMM Rao,"Image Processing For Medical Applications" , Proceedings of the 14th World Conference on Non- Destructive Testing, Delhi, 8-13 December 1996.Vol. 2,pp. 1219 – 1224
- [3] R.ManjulaSri,KMM Rao, "Novel Image Processing Techniques to Detect Lesions using LabVIEW", IEEE Conference Publications on Annual IEEE India Conference INDICON.Publication Year: 2011 , Page(s): 1-4

- [4] Viralkumar Bulsara, Surabhi Bothra, Poonam Sharma, K.M.M.Rao, "Low Cost Medical Image Processing System for Rural/Semi Urban Healthcare", IEEE Conference Publications on Recent Advances in Intelligent Computational Systems (RAICS), Publication Year: 2011 , Page(s): 724 - 728
- [5] NI Vision Concepts Manual, National Instruments, November 2005.
- [6] Austin , " Digital Image processing using Mathematical Link for LabVIEW", A demo developed for NI week 2002 August 14-16, 2002.
- [7] Cemal Köse,U gur , Sevika Okyay and Gençlioğlu "Automatic segmentation of age-related macular degeneration in retinal fundus images", in Computers in Biology and medicine , Vol.38 (2008) ,pp. 611 – 619.
- [8] K. Rapantzikos, M. Zervakis,K. Balas "Detection and segmentation of drusen deposits on human retina: Potential in the diagnosis of age-related macular degeneration" in Medical Image Analysis, Vol.7(2003) ,pp. 95–108
- [9] Maryam Mubbashar, Anam Usman, M. Usman Akram, " Automated System for Macula Detection in Digital Retinal Images", 33rd Annual International Conference of the IEEE EMBS, Boston, Massachusetts USA, August 30 - September 3, 2011
- [10] Aliaa Abdel-Haleim Abdel-Razik Youssif, Atef Zaki Ghalwas, and Amr Ahmed SabryAbdel-Rahman Ghoneim Optic Disc Detection From Normalized Digital Fundus Images by Means of a Vessels' Direction Matched Filter-IEEE Transactions On Medical Imaging, Vol. 27, No. 1, January 2008
- [11] Mahdad Esmaeili, Hossein Rabbanin and Alireza Mehri Dehnavi: "Automatic optic disk boundary extraction by the use of curvelet transform and deformable variational level set model" in Pattern Recognition, Vol. 45 (2012) , pp. 2832–2842
- [12] Meindert Niemeijer, Michael D. Abràmoff and Bram van Ginneken" Fast detection of the optic disc and fovea in color fundus photographs" in Medical Image analysis, in press.
- [13] Rashid Jalal Qureshi et al. "Combining algorithms for automatic detection of optic disc and macula in fundus images; Computer Vision and Image Understanding ,Vol. 116 (2012) ,pp. 138–145
- [14] Chih-Yin Ho,Tun-Wen Pai, Hao-Teng Chang and Hsin-Yi Chen, " An automatic fundus image analysis system for clinical diagnosis of glaucoma",-2011 International Conference on Complex, Intelligent, and Software Intensive Systems.
- [15] Zhuo Zhang et al. "MRMR Optimized Classification for Automatic Glaucoma Diagnosis"-33rd Annual International Conference of the IEEE EMBS, Boston, Massachusetts USA, August 30 - September 3, 2011.
- [16] Jorge J.G.Leandro, Roberto M Cesar Jr and Herbert F.Jelinek.," Blood Vessels Segmentation in Retina : Preliminary Assessment of the Mathematical Morphology and of the Wavelet Transform Techniques", Conference proceedings: Brazilian Symposium on Computer Graphics and Image Processing - SIBGRAPI , pp. 84-90, 2001

- [17] Attila Budai, Georg Michelson and Joachim Hornegge, “ Multiscale blood vessel segmentation in retinal fundus images”, ConfereceProceedings-BVM 2010,Aachen,pp261-265.
- [18] M. E. Martinez-Perez, A. D. Hughes, S. A. Thom, A. A. Bharath and K. H. Parker, “ Segmentation of Blood Vessels from Red-free and Fluorescein Retinal Images: In *Medical Image Analysis*.vol. 11 (1),pp. 47-61, 2007
- [19] Cemal Kose, Ugur Sevik, Cevat Ikibas and Hidayet Erdol,“ Simple methods for segmentation and measurement of diabetic retinopathy lesions in retinal fundus images”, in computer methods and programs in biomedicine(2011) in press.
- [20] A.Sopharak,B.Uyyanonvara,S.Barman and T.H.Williamson“Automatic detection of diabetic retinopathy exudates from non-dilated retinal images using mathematical morphology methods” in Computerized Medical Imaging and Graphics ,Vol. 32 (2009) pp. 720–727.

Detection and Classification of Lesions in Retinal Images

Mohanapriya.G¹, Vasanthi.S¹

¹K.S. Rangasamy College of Technology, Tiruchengode

mohanapriyagaja@gmail.com, vasanthiramesh@gmail.com

Abstract

Automatic recognition of Diabetic Retinopathy (DR) lesions and age-related macular degeneration (AMD) lesions in retinal images are a fundamental step for early detection and screening in large population. In which, the red lesion microaneurysms is the earliest sign of DR and the presence of bright lesion drusen is the main characteristic of early AMD. An efficient framework for detection and classification of lesions in ocular fundus images is proposed. An optimal filter framework can automatically generate features space derived from a set of reference image samples which includes typical target lesion, positive and negative lesion confounders. These reference samples are obtained from either an expert driven or a data driven approach. A testing approach is performed by training the samples to detect red lesion microaneurysms and by training it to differentiate drusen from the other bright lesions stargardt's disease flecks. The proposed method is fast, provides an instantaneous feedback to the patient.

Keywords

Microaneurysms, Drusen, Lesion Detection, Retinal Image, Diabetic Retinopathy (DR), Age-Related Macular Degeneration (AMD)

1. Introduction

Diabetic-related eye disease is a major cause of preventable blindness in the world. It is a complication of diabetes which can also affect various parts of the body. When the small blood vessels have a high level of glucose in the retina, the vision will be blurred and can cause blindness eventually. This is known as diabetic retinopathy (DR). Microaneurysms are the earliest clinical sign of the diabetic retinopathy. Microaneurysms appeared as small dark round dots on the fundus images. They are small bulges developed from the weak blood vessels. The number of microaneurysms would increase with the stage of the retinopathy. Hence, the regular screening is essential in order detect the early stages of diabetic retinopathy for timely treatment to prevent or delay further deterioration. The most of the automated detection of DR is the detection of early sign as microaneurysms[1-9]. The number of studies being carried out for accurate detection of MAs, i.e. the retinal online challenge (**ROC**) microaneurysm detection competition was recently held in order to compare different algorithms on the same data where the difficulty was with the detection of MA from small blood vessel and differentiating MA close to vessel [10].

On the other hand, Age-related macular degeneration (AMD) is the leading cause of



irreversible vision loss among the elderly in developed countries and the third leading cause worldwide. AMD is a disease associated with aging that gradually destroys sharp, central vision. Because older people represent an increasingly larger percentage of the general population, vision loss from AMD is a growing public health problem. Drusens are tiny yellow or white accumulations of extracellular material that build up in Bruch's membrane of the eye. The presence of a few small drusen is normal with advancing age, and most people over 40 have some hard drusen. However, the presence of larger and more numerous drusen in the macula is a common early sign of AMD. Many studies have demonstrated that early treatment can reduce the amount of DR and AMD cases mitigating the medical and economic impacts of the disease. Several methods of detecting drusen and other bright lesions in fundus images have been proposed, using mathematical morphology [11], histogram-based adaptive local thresholding [12], background removal and histogram-based thresholding [13], or pixel classification [14]. In prior attempts, one of the main challenges is to differentiate drusen from other bright lesions. In particular, differentiation of drusen from Stargardt's disease flecks because of similar looking [15].

Even though several algorithms have been developed, detection of lesions still produce false positives and false negatives. The negative lesion confounders (false positives)

where the lesions structure are visually similar but not the original, like vessel portions detected falsely as microaneurysms. The positive lesion confounders (false negatives) where some of the lesions are missed to detect the true lesions like the lesion close to or fused to some specific structures such as vessels or other lesions. Therefore the detection process is not optimal.

2. Methodology

This paper proposed a new optimal filter framework (shown in Fig.1) for effective automated detection and segmentation of lesion like microaneurysms and differentiating drusen from flecks. The optimal filter generates the feature space for classification from the reference samples. The design of the filter is by either mathematical modelling the both lesions and their confounders or by using the directly annotated image samples.

2.1 Mathematical Shape model of Samples

Modelling the shapes of lesions like microaneurysms and drusen are by using the Gaussian distribution function. The Intensity distribution model would frame the image samples. $I(u,v)$ is the intensity of the image at the pixel location (u,v) .

$$\text{Intensity}(r; \beta, \delta) = I(u,v) = \delta e^{-r^\beta} \quad \dots\dots (1)$$

$$r = \sqrt{\left(\frac{u}{\alpha_1}\right)^2 + \left(\frac{v}{\alpha_2}\right)^2} \quad \dots\dots (2)$$

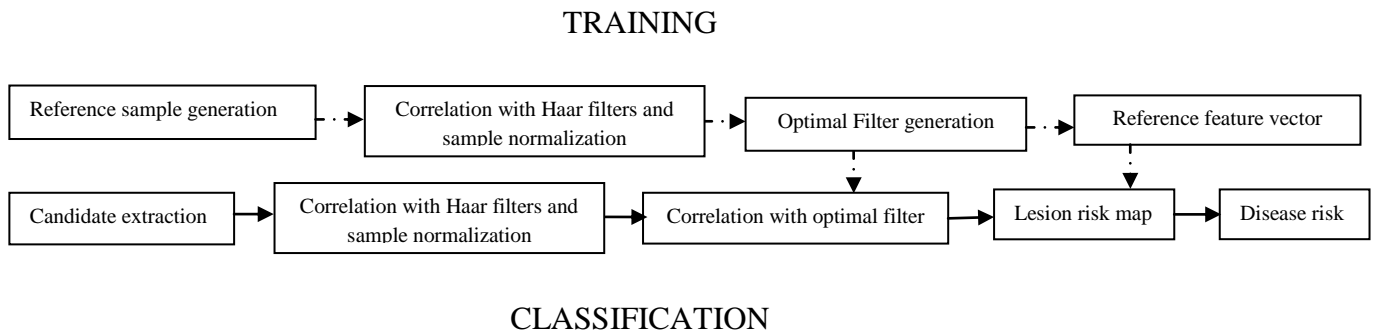


Fig.1 Flow diagram of the proposed method.

Where β is a shape parameter modelling the sharpness of the contours (when $\beta=2$ generates the Gaussian function) and δ is the amplitude models contrast with the image background ($\delta = 1$ for drusen, $\delta = -1$ for microaneurysms). α_1, α_2 , shows the minor and major axis. θ represents the angular orientations for the ellipsoid shape.

For the mathematical model based generation of samples, it is not possible to generate all the possible lesion samples from all possible images. So sample model is performed with the common lesion confounders. Intensity distribution models for lesion confounders is for both Microaneurysm detection and Drusen detection, which are

- Common positive lesion confounder
- Common negative lesion confounder

Drusen, the bright lesions typical of ARMD, and the pisciform deposits or flecks typical of Stargardt disease, are both similar in color and size but differ in shape, with drusen displaying a more rounded shape, whereas the flecks in SD often have a more elongated, fishtail shape [15].

The negative lesion confounder chosen for drusen detection is flecks.

$$\text{Intensity}(r; \beta, \delta) = \delta e^{-r^\beta}; \delta = 1 \dots (3)$$

$$\text{Intensity}(r_1; \beta, \delta); u > 0, \text{tail of flecks} \dots (4)$$

$$\text{Intensity}(r_2; \beta, \delta); u \leq 0, \text{head of flecks} \dots (5)$$

$$r_1 = \sqrt{\left(\frac{u}{\alpha_1}\right)^2 + \left(\frac{v}{\alpha_2}\right)^2} \dots (6)$$

$$r_2 = \sqrt{\frac{u^2+v^2}{(\alpha_2)^2}} \dots (7)$$

The common negative lesion confounder choosen for microaneurysms are linear vessel, vessel branch and vessel overlaps. For the linear vessel portion $r = \left|\frac{v}{\alpha}\right|$ for normalized distance. For the vessel branch and vessel overlaps, linear vessels meet at the center of the model whose intensities distributions are fused. Since two vessels are overlap, the intensity is darker at the center of the model.

The common positive lesion confounders for microaneurysms are two types which are modelled. microaneurysms either close to a vessel or connected to it and microaneurysms either close to another microaneurysms. The common positive lesion confounder for drusen detection is modelled where drusen either close to other drusen or fused to other drusen.

The intensity distribution of all the lesions and lesion confounder were modelled, samples were generated from each intensity distribution model as by choosing the scale parameter. The scale for the generated samples can be selected based on an estimation of the typical size of the lesions and lesions confounders in images. The generated image samples can be defined as circular patches of radius R times as wide as the typical lesion size($R = 3$). Gray-level model of the image samples are transformed into color image using intensity color mapping which can be used to improve further the presented greylevel modelling of the lesions.

2.2 Direct Image Sampling:

An advanced physical model of the lesion which are created, is completely predicting the visual appearance of the lesion and lesion confounders. Such a model is highly complex and it requires substantial domain knowledge. In direct sampling or data driven approach, the target typical lesions and positive lesion confounders can be annotated directly from the images. An annotated comprises an indication of the center of the lesion, or segments the lesion.

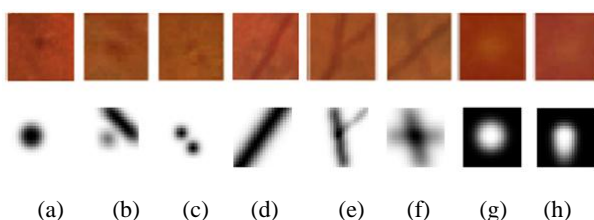


Fig. 2 The mathematical model of image samples are generated similar to that of the example samples in the spatial domain. The first six samples come from the microaneurysm detection problem: (a) typical lesion, (b), (c) positive lesion confounders and (d), (e), (f) negative lesion

confounders. The last two samples come from the drusen (g) versus flecks (h) differentiation problem.

2.3 Correlation with Haar filter:

To make the reference samples less sensitive to noise and background variability of the retinal images, correlating the reference samples with two 2×2 Haar filter; horizontal filter (H) and vertical filter (V). Two transformed images were thus obtained. This step leads to the highest signal-to-noise ratio when characterizing candidate bright lesions in fundus images; while preserving the shape of the bright lesions.

The noise from the samples is removed by Haar filter. The image samples are decomposed into horizontal filter coefficient and vertical filter coefficient which is generated by correlation of Haar filter and dilated into image scale.

2.4 Sample Normalization:

The reference samples characterize the range of variations for the shape, the intensity and the colour of the lesions. The intensity of the object can be normalised across the samples. Normalising the intensity can reduce the dimensionality of the problem without affecting the quality of the image sample representation. After normalisation, the two differently contrasted image samples become similar.

The Intensity at the centre of the model simply needs to be set to one in the mathematical model based sample generation. Normalizing the intensity of the samples directly extracted from images is not difficult. For the reliable

estimation of the lesion intensity, the intensity distribution in the target sample is matched to the intensity distribution in the average sample using the least mean squared algorithm, with high SNR.

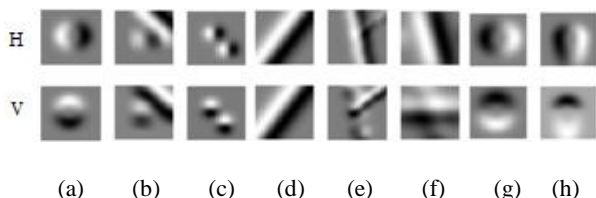


Fig.3 After correlating the example samples (Fig.2) with Haar filter, horizontal Haar filter (1st row) and vertical Haar filter (2nd row) are generated.

2.5 Optimal Filter Generation:

The reference samples are the maximal representativeness of all the lesions and lesion confounders, provided that those are with high signal-to-noise ratio and are normalized. A compact filter set is created derived from a large number of instances of the models, as follows: instances of lesion models were generated from equations, setting $\beta= 2$ and $\delta= -1$, based on preliminary studies, and by varying sizes α_1 and α_2 . When a sample S to its nearest neighbour sample in set of reference sample is generated with least mean square sense then the classification performance tends towards optimality. The distance between the image region around each pixel and each filter is obtained by the Euclidian distance between their projections onto the optimal filter set, after normalization.

The normalized transformed space can be used as a feature space for classification with K-NN classifier [16]. The collection of reference samples can be relied upon to find the filter

generating the optimal feature space as the training set for classifying new samples which can be provided by Principal Component Analysis (PCA).

Principal components analysis (PCA) is a technique that can be used to simplify a dataset. PCA is a way of identifying patterns in data, and expressing the data in such a way as to highlight their similarities and differences [17]. In PCA, to create the mean centered data vector, the mean image is to be subtracted from each image of the data set. It is very easy to compute the covariance matrix from the mean centered data matrix. The principal components are found by calculating the eigenvectors and eigenvalues of the data covariance matrix. PCA is an orthogonal linear transformation that transforms the set of samples into new coordinate system where the eigenvector with the highest eigenvalue is the principle component of the data set. The first highest value is placed at the first coordinate; the second value is at the second coordinate, etc. and thereby ordering from highest to lowest. These principal components can be the optimal filter transformed as an optimal feature space.

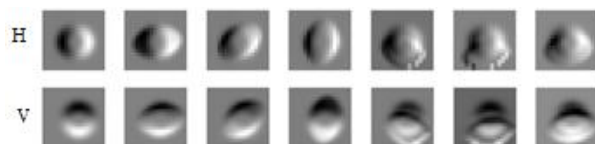


Fig.4 Optimal filter generated for microaneurysms detection with various range of parameters using mathematical model based approach. The upper part (resp. the lower part) of each filter is correlated with horizontal (resp. vertical) Haar filters.

3. Proposed Lesion Detector

The image can be processed as follows:

1) A pre-processing step, where candidate extraction is performed by both direct image sampling method and with the set of sample generated which are used to identify and normalize candidate target lesions in image.

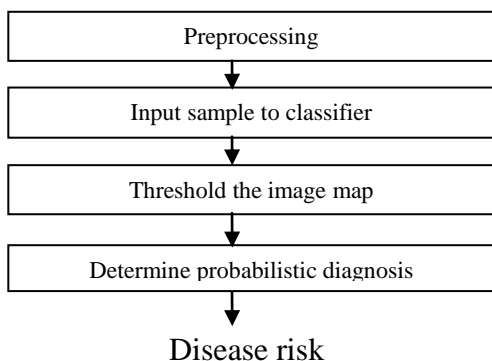


Fig.5 Flow of the proposed lesion detector

2) After normalization, samples selected in the pre-processing step are input to the classifier. A lesion risk map is obtained by computing the risk of presence of the target lesion by the classifier for that sample.

Risk of presence $\rho(S)$ is computed for each new sample S . $\rho(S)$ derives from the distance between two samples S and representative samples R where S and R are projected on each PCA component. The distance between these two samples is simply defined as the Euclidean distance between their projections on the optimal set of filters. Then k-Nearest Neighbour search can be performed to find the most similar reference samples.

3) For the segmentation of the lesions, the risk map is thresholded, and the connected components of the foreground samples are identified by using morphological labelling process. All connected components are

considered as an automatically detected lesion and that lesions are assigned with a risk value.

4) If a probabilistic diagnosis for the entire image is required, the risk values assigned to each automatically detected lesion are fused. Then combined risk is referred to as the disease risk. When a single type of lesions is detected, the probabilistic diagnosis for the image can be defined as the maximum risk of presence of a target lesion.

4. RESULTS AND DISCUSSION

The performance of the proposed method was tested on detection of two lesions in fundus disease. microaneurysms and drusen (differentiated from flecks).

4.1 Microaneurysms Detection:

For the detection of microaneurysms, a set of 50 images are obtained from various experts. The retinal images are captured using zeiss fundus camera. The original size of the different retinal images is resized into 1280×1024 pixels. The original image is converted into greyscale retinal image (Fig.6 (a)) which is segmented and connected foreground samples are identified using morphological labelling. After segmentation, the risk map calculated by the classifier is applied to each segmented image and performed the classification process to detect microaneurysms using KNN classifier. The negative lesion confounders identified are the linear vessels (Fig 6 (b)).

The computation times were obtained with the image samples to be tested where results shows that the computation time increases with the number of sample increases (Fig.8).

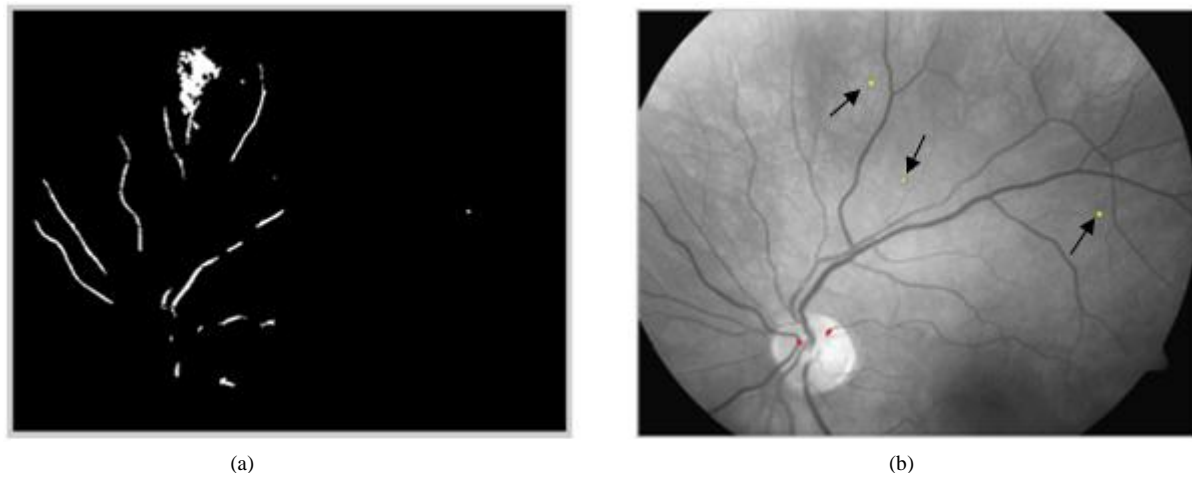


Fig. 6 The segmented greyscale image (a) of the original retinal image for microaneurysm detection and the detected microaneurysms(yellow colour) with false detected lesions (red colour).

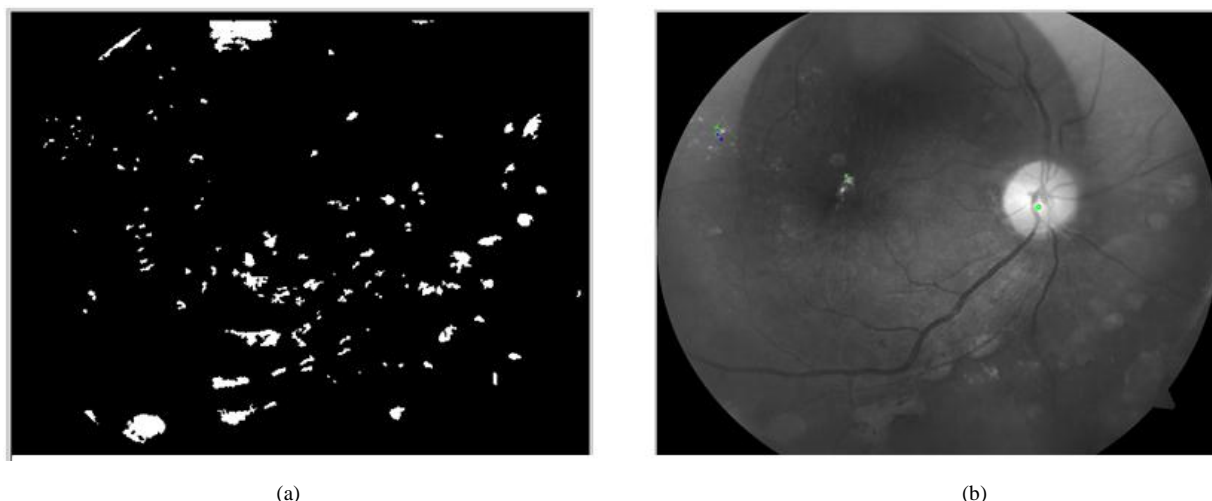


Fig. 7 The segmented greyscale image (a) of the original retinal image for drusen detection and the detected drusen (green colour) differentiated with flecks (blue colour).

But it shows that the processing of retinal image takes less than a second and this proposed new method is faster compared with the previous approach taking several minutes.

4.2. Drusen versus Flecks Classification:

For the classification of drusen and Stargardt's disease (SD) flecks, a set of images were obtained from fundus experts captured using the same camera. The original images acquired in size of 2196×1958 are

resized as mentioned above. The greyscale retinal image is segmented (Fig.7 (a)). Some set of samples are annotated directly from the images as the training samples. By using the KNN classifier, the drusen and flecks are classified with the risk value assigned (Fig 7 (b)).

The computation time for the drusen detection is also plotted with the image samples (Fig.9). The performance of the proposed method also provides the fast result in differentiating the drusen and stargardt's disease flecks.

Both the mathematical model based approach and direct driven approach are performed well. If one does not required spending more time in modelling new shapes with the use of human expert, the direct driven approach can be preferred.

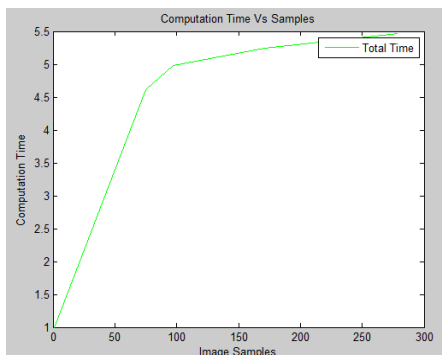


Fig.8 Microaneurysm time vs. samples computation

Here X-axis represents the number of image samples to be tested from the set of images after segmentation and Y-axis represents the computation time (sec) to detect microaneurysms from the total 300 samples in just 5 images.

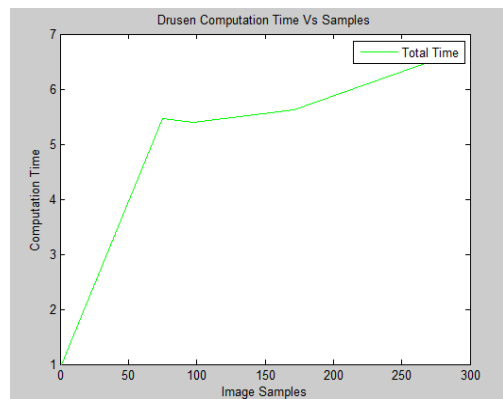


Fig.9 Drusen computation time vs. samples

Here X-axis represents the number of image samples to be tested from the set of testing images after segmentation and Y-axis represents the computation time (sec) to detect drusen from 275 samples.

This method of optimal filter generation is performed for two different important lesions in eye diseases such as microaneurysms and drusen. In which the main concentration for drusen detection is only the differentiation of drusen from stargardt's disease flecks by setting values $\beta=2$ and $\delta= 1$ for modeling the drusen and for flecks by using equation (3),(4),(5),(6),(7) and the same procedure is followed for generating the optimal filter of drusen.

There are few limitations in this paper. It actually uses only the shape as feature not the colour or intensity. Second, the reference samples are obtained by a single expert.

5. Conclusion

Early detection of lesions and timely treatment can reduce the severity of the retinal disease and prevent the vision loss. An optimal filter framework for the detection of lesions in retinal images, derived through factor analysis of the lesions and their confounders, has been

performed and was successfully applied to two important retinal image analysis problems such as diabetic retinopathy (microaneurysms) and age-related macular degeneration (drusen). Potentially, this optimal filter framework can be applied to other lesion detection problems in retinal images, where rapid system development and instantaneous performance are required.

6. References

- [1] T. Spencer, J. A. Olson, K. C. McHardy, P. F. Sharp, and J. V. Forrester, "An image-processing strategy for the segmentation and quantification of microaneurysms in fluorescein angiograms of the ocular fundus," *Computers and Biomedical Research*, vol. 29, no. 4, pp. 284–302, Aug. 1996.
- [2] J. H. Hipwell, F. Strachan, J. A. Olson, K. C. McHardy, P. F. Sharp, and J. V. Forrester, "Automated detection of microaneurysms in digital red-free photographs: A diabetic retinopathy screening tool," *Diabetic Medicine*, vol. 17, no. 8, pp. 588–594, Aug. 2000.
- [3] L. Gang, O. Chutatape, H. Lui, and S. M. Krishnan, "Abnormality detection in automated mass screening system of diabetic retinopathy," in *Proceedings of 14th IEEE Symposium on Computer-Based Medical Systems*, 2001, pp. 132–137.
- [4] M. Larsen, J. Godt, N. Larsen, H. Lund-Andersen, A. K. Sjølie, E. Agardh, H. Kalm, M. Grunkin, and D. R. Owens, "Automated detection of fundus photographic red lesions in diabetic retinopathy," *Invest. Ophthalmol. Vis. Sci.*, vol. 44, no. 2, pp. 761–766, Feb. 2003.
- [5] M. Niemeijer, B. van Ginneken, J. Staal, M. S. A. Suttorp-Schulzen, and M. D. Abramoff, "Automatic detection of red lesions in digital color fundus photographs," *IEEE Trans. Med. Imaging*, vol. 24, no. 5, pp. 584–592, May 2005.
- [6] A. D. Fleming, S. Philip, K. A. Goatman, J. A. Olson, and P. F. Sharp, "Automated microaneurysm detection using local contrast normalization and local vessel detection," *IEEE Trans. Med. Imaging*, vol. 25, no. 9, pp. 1223–1232, Sept. 2006.
- [7] T. Walter, P. Massin, A. Erginay, R. Ordonez, C. Jeulin, and J.-C. Klein, "Automatic detection of microaneurysms in color fundus images," *Med. Image Anal.*, vol. 11, no. 6, pp. 555–566, Dec. 2007.
- [8] G. Quellec, M. Lamard, P. M. Josselin, G. Cazuguel, B. Cochener, and C. Roux, "Optimal wavelet transform for the detection of microaneurysms in retina photographs," *IEEE Trans. Med. Imaging*, vol. 27, no. 9, pp. 1230–1241, Sept. 2008.
- [9] A. Mizutani, C. Muramatsu, Y. Hatanaka, S. Suemori, T. Hara, and H. Fujita, "Automated microaneurysm detection method based on doubling filter in retinal fundus images," in *Proceedings of SPIE Medical Imaging 2009: Computer Aided Diagnosis*, vol. 7260, pp. 72601N-1–8, Feb. 2009.
- [10] M. Niemeijer *et al.*, "Retinopathy online challenge: Automatic detection of microaneurysms in digital color fundus

- photographs," *IEEE Trans. Med. Imaging*, vol. 29, no. 1, pp. 185–195, Jan. 2010.
- [11] A. Barthes, J. Conrath, M. Rasigni, M. Adel, and J. P. Petrakian, "Mathematical morphology in computerized analysis of angiograms in age-related macular degeneration," *Med. Phys.*, vol. 28, pp. 2410–2419, 2001.
- [12] K. Rapantzikos, M. Zervakis, and K. Balas, "Detection and segmentation of drusen deposits on human retina: Potential in the diagnosis of age-related macular degeneration," *Med. Image Anal.*, vol. 7, pp. 95–108, 2003.
- [13] R. T. Smith, J. K. Chan, T. Nagasaki, U. F. Ahmad, I. Barbazetto, J. Sparrow, M. Figueroa, and J. Merriam, "Automated detection of macular drusen using geometric background leveling and threshold selection," *Arch. Ophthalmol.*, vol. 123, pp. 200–206, 2005.
- [14] M. Niemeijer, B. van Ginneken, S. R. Russel, M. S. A. Suttorp- Schulten, and M. D. Abràmoff, "Automated detection and differentiation of drusen, exudates, and cotton-wool spots in digital color fundus photographs for early diagnosis of diabetic retinopathy," *Inv. Ophthalmol. Vis. Sci.*, vol. 48, pp. 2260–2267, 2007.
- [15] S. Walia and G. A. Fishman, "Natural history of phenotypic changes in stargardt macular dystrophy," *Ophthalmic Genet.*, vol. 30, pp. 63–68, 2009.
- [16] M. D. Abràmoff, W. L. M. Alward, E. C. Greenlee, L. Shuba, C. Y. Kim, J. H. Fingert, and Y. H. Kwon, "Automated segmentation of the optic nerve head from stereo color photographs using physiologically plausible feature detectors," *Invest Ophthalmol. Vis. Sci.*, vol. 48, no. 4, pp. 1665–1673, Apr. 2007.
- [17] I. T. Jolliffe, "Principal Component Analysis," in *Statistics*, ser. Springer Series, 2nd ed., NY: Springer, 2002.

Detection and Feature Selection of Abnormal Retinal Vessels using Fundus Image by Genetic Algorithm

¹Deepthimaris.B, ¹Amsaveni.A

¹Department of ECE

Kumaraguru College of Technology

Coimbatore- 641049.

deepthi_maris@yahoo.com, amsaveni_a@yahoo.com

Abstract

Diabetic-related eye disease is a major cause of preventable blindness in the world. It is a complication of diabetes which can also affect various parts of the body. When the small blood vessels have a high level of glucose in the retina, the vision will be blurred and can cause blindness eventually. This is known as diabetic retinopathy. Regular screening is essential in order detect the early stages of diabetic retinopathy for timely treatment to prevent or delay further deterioration. This project describe a method for automatically detecting new vessels on the optic disc using retinal photography. Abnormal vessels are segmented using region based segmentation. Feature parameters are measured based on texture and shape. Texture properties are measured using GLCM (Gray Level Co-Occurrence Matrix). Shape based parameters are measured using moment invariant. Thus set of parameters are extracted based on Gray level Co-Occurrence Matrix (GLCM) and moment invariant methods. Valid features are extracted using Genetic algorithm (GA). The objective of this project is to develop a computer-based approach to detect the different diabetic retinopathy stages using fundus images.

Keywords

Diabetic Retinopathy (DR), Optic Disc, Moment invariant, Gray level Co-Occurrence Matrix (GLCM), Genetic algorithm (GA).

1. Introduction

Diabetes is fast becoming an epidemic around the world and especially in the Indian society. This is leading to Diabetes related disorders like Diabetic Retinopathy (DR). When the small blood vessels have a high level of glucose in the retina, the vision will be blurred and can cause blindness eventually. The main mechanism by which vision is lost due to diabetic retinopathy is proliferative retinopathy. Proliferative retinopathy is the more serious condition as it involves the development of new vessels which are prone to bleed and ultimately retinal detachment occurs.

These complications if not dealt with on time can lead to lot of disability on the part of the patient and huge cost and work load on the specialists and the government. Hence there is a need to develop an automated diagnostic system to expedite the work of the practitioner and reduce morbidity of the patients. Figure.1 shows a typical retinal image labeled with various

feature components of Diabetic Retinopathy. Microaneurysms are small saccular pouches caused by local distension of capillary walls and appear as small red dots. This may also lead to big blood clots called hemorrhages. Hard exudates are yellow lipid circular region from where the blood vessels emanate is called the optic disk. The fovea defines the center of the retina, and is the region of highest visual acuity. These deposits appears as bright yellow lesions. The bright spatial distribution of exudates and microaneurysms and hemorrhages, especially in relation to the fovea can be used to determine the severity of diabetic retinopathy.

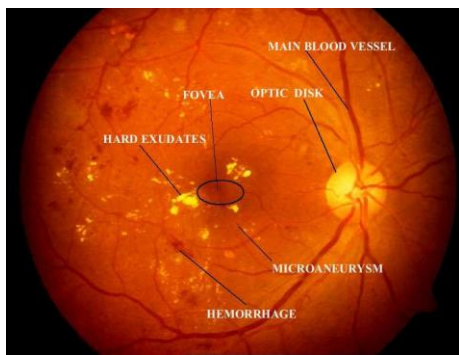


Figure1. Illustration of various features on a typical retinopathic image.

2. Related Work

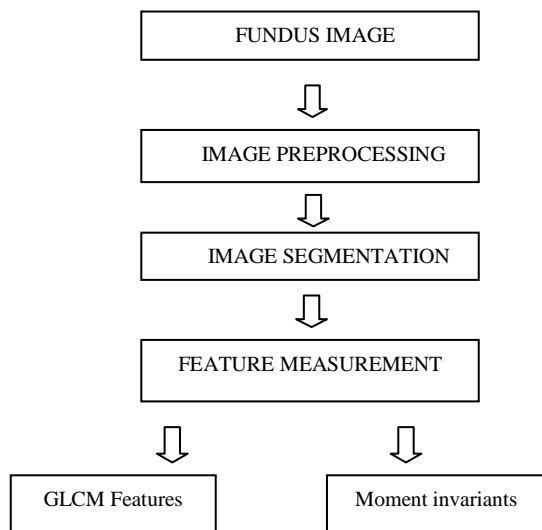
Detection of microaneurysm by using the diameter closing and an automatic threshold scheme[2]. Some investigations have been made for detecting haemorrhages and exudates. This uses the high grey level variation for detecting exudates. Some methods that uses neural network-based shape recognition to detect venous bleeding[7]. In this paper proposed method by combining the prior works of Optic Disc Segmentation and detection of new vessels to detect disease Proliferative Diabetic Retinopathy. Since the optic disc is the entry point of most of the

blood vessels, focused on the attention towards the optic disc. A number of studies regarding the detection of microaneurysm is the sign of diabetic retinopathy[5][8]. The work was based on the algorithm that enhances the features and classifies it as based on the intensity and size of the features[8].

Analyzing the performance of different matching algorithms with respect to the detection of blood vessels in the retinal images for both gray level and color images[9]. Blood vessels detection using 2D Gaussian matched filtering gives the complete and continuous vessel map of the blood vessels[15].

Many of the features such as blood vessel, exudates and optic disk are accurately measured using morphological operations[6].It also classifies the segmented regions into disjoint classes, exudates and non-exudates and comparing the performance of various classifiers[4][6] by using Back-propagation neural network (BPNN), the Bayesian neural network (BNN).

3. Methodology



4. Pre Processing

Patient movement, poor focus, bad positioning, reflections, inadequate illumination can cause a significant proportion of images to be of such poor quality as to interfere with analysis. Blood vessels are extracted in this paper for the identification of diabetic retinopathy. The contrast of the fundus image tends to be bright in the centre and diminish at the side, hence preprocessing is essential to minimize this effect. Preprocessing of such images can ensure adequate level of success in the automated abnormality detection.

4.1 The Green Plane Extraction

The green color plane is used in the analysis since it shows the best contrast between the blood vessels and retina. Next, the color space of the image is adjusted to gray image, extracting only the intensity component of the original image.

4.2 Resampling

Resampling refers to change the pixel dimensions of an image primarily for viewing. Nearest neighbor determines the grey level from the closest pixel to the input coordinates, and assigns that value to the output coordinates. This method is considered as the most efficient in terms of computation time and it doesn't make any gray level changes in the image.

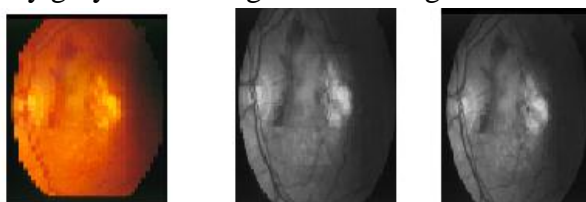


Figure 2. Illustration steps of preprocessing:
(a) Input image (b) The Green channelled image (c) Resampled image.

5. Segmentation

The consequence is that watershed transformations produce usually over-segmented image.

Segmentation using the watershed transform works better if we can identify or "mark" foreground objects and background locations. The watershed transform can be classified as a region-based segmentation approach.

5.1 Marker Controlled Watershed Segmentation

Marker-controlled watershed segmentation follows some basic procedure to compute a segmentation function by computing foreground markers background markers. Modification of the segmentation function so that it only has minima at the foreground and background marker locations. Hence it is the watershed transform of the modified segmentation function. Segmentation using the watershed transform works better if you can identify, or "mark," foreground objects and background locations. Usually external markers, or pixels belong to the background and internal markers specify the target location.

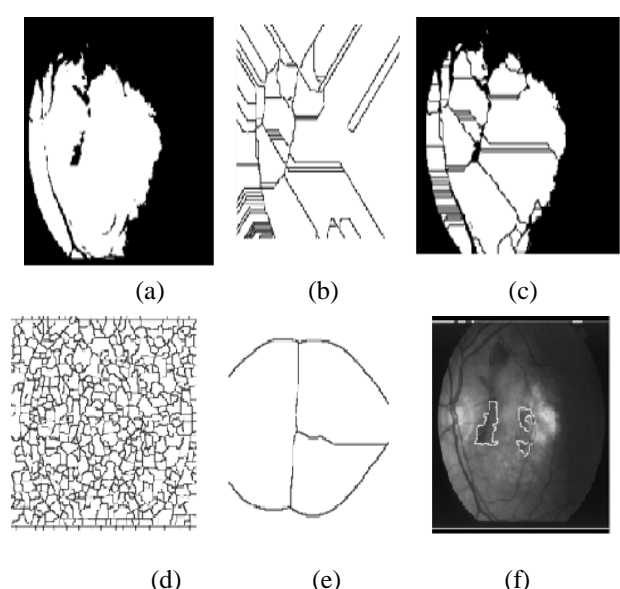
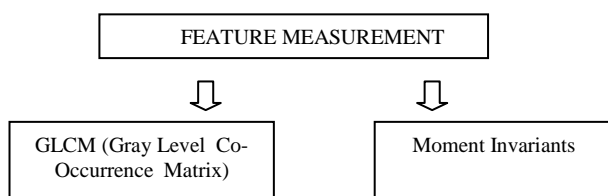


Figure 3: Illustration of watershed segmentation on an image of data set (a)

Binary image, (b) Distance transformed image, (c) Superimposed image, (d) Watershed transformed image, (e) Markercontrolled image, (f) Marker controlled watershed transformed image.

6. Feature Extraction

The aim of the feature extraction stage is characterized by means of feature vector, a pixel representation in terms of some quantifiable measurements which may be easily used in the classification stage.



6.1 Moment Invariants:

Moment invariants have been frequently used as features for image processing shape recognition. Moments can provide characteristics of an object that uniquely represent its shape. Hu (Hu, 1962), that first set out the mathematical foundation for two-dimensional moment invariants. The invariant features can be achieved using central moments, which are defined as follows:

Table 1. Moment Invariant feature values for Various images.

Moment Invariant Features	Original Image	After Filter	After Binary	After Noise	After Edge
M1	6.189765	6.228532	6.029539	6.468739	
M2	18.73726	19.95227	18.34357	23.12302	
M3	25.20876	26.33469	25.35447	26.97498	
M4	23.05345	22.50894	22.22065	25.98606	
M5	47.73730	47.09200	47.79942	54.92515	
M6	35.91640	33.16931	32.13368	37.88696	
M7	47.68054	48.28983	47.26928	52.60156	

$$p,q = 0,1, \dots$$

$$\mu_{pq} = \int(x - \bar{x})(y - \bar{y})f(x,y)dxdy \quad \dots(1)$$

$$\bar{x} = m_{10}/m_{00}$$

$$\dots\dots\dots(2)$$

$$\bar{y} = m_{01}/m_{00}$$

$$\dots\dots\dots(3)$$

The pixel point (\bar{x}, \bar{y}) are the centroid of the image.

The normalized central moments are defined as follows:

$$\eta_{pq} = \mu_{pq}/\mu_{00} \quad \dots\dots\dots(4)$$

$$\gamma = [(p+q)/2]+1 \quad \dots\dots\dots(5)$$

μ_{pq} computed using the centroid of the image is equivalent to the μ_{pq} whose center has been shifted to centroid of the image. Therefore, the central moments are invariant to image translations. In terms of the central moments, the seven moments are given as,

$$M_1 = (\eta_{20} + \eta_{02}),$$

$$M_2 = (\eta_{20} - \eta_{02})^2 + 4\eta_{22}$$

$$M_3 = (\eta_{30} - 3\eta_{12})^2 + (3\eta_{21} - \eta_{03})^2,$$

$$M_4 = (\eta_{30} + \eta_{12})^2 + (\eta_{21} + \eta_{03})^2,$$

$$M_5 = (\eta_{30} - 3\eta_{12})(\eta_{30} + \eta_{12})[(\eta_{30} + \eta_{12})^2 - 3(\eta_{21} + \eta_{03})^2] + (3\eta_{21} - \eta_{03})(\eta_{21} + \eta_{03})$$

$$[3(\eta_{30} + \eta_{12})^2 - (\eta_{21} + \eta_{03})^2],$$

$$M_6$$

$$= (\eta_{20} - \eta_{02})[(\eta_{30} + \eta_{12})^2 - (\eta_{21} + \eta_{03})^2] + 4\eta_{11}(\eta_{30} + \eta_{12}) \\ (\eta_{21} + \eta_{03}),$$

$$M_7 = (3\eta_{21} - \eta_{03})(\eta_{30} + \eta_{12})[(\eta_{30} + \eta_{12})^2 - 3(\eta_{21} + \eta_{03})^2] - (\eta_{30} + 3\eta_{12})(\eta_{21} + \eta_{03})$$

$$[3(\eta_{30} + \eta_{12})^2 - (\eta_{21} + \eta_{03})^2].$$

$$\dots\dots\dots(6)$$

6.2 .Gray Level Co-occurrence Matrix

In 1973, Haralick introduced the co-occurrence matrix and his texture features which are the most popular second-order statistical features. Texture features can be extracted in several methods, namely: statistical, structural, model-based, and transform information. Each method has different techniques. Best algorithm to extract texture features is the use of Gray Level Co-occurrence Matrices (GLCMs). Texture is a significant feature of an image that has been widely used in medical image analysis, image classification, automatic visual inspection, content-based image retrieval, and remote sensing. The GLCM defines the probability of joining two pixels i and j with distance d .

Haralick proposed two steps for texture feature extraction:

1. First step is computing the GLCMs and
2. Second step is calculating texture features using the calculated GLCMs.

This technique is useful in a wide range of image analysis especially in biomedical techniques for obtaining exact feature sets. The well-known algorithm to extract texture features is the use of Gray Level Co-occurrence Matrices (GLCMs).

The GLCM contains the second-order statistical information of spatial relationship. Statistical measures such as correlation, energy, entropy, homogeneity and sum of square variance are computed based on GLCM. GLCM features are calculated in terms of directions and distances. The size of GLCM is given by number of gray level in an image. statistical methods.

$P(i,j)$ - probability corresponding to the i th row and j th column.

μ_i, μ_j – mean.

σ_i, σ_j - standard deviation.

Table 2. GLCM Features and corresponding formulae

Features	Explanation	Formula
Entropy	Entropy measures the statistical randomness	$\sum \ln(P_{ij})P_{ij}$
Energy	It is known as uniformity of ASM (angular second moment) is the sum of squared elements from the GLCM.	$\sum (P_{ij})^2$
Homogeneity	Measure the distribution of elements in the GLCM with respect to the diagonal	$\sum P_{ij} / ((1+(i-j)^2))$
Correlation	Measures the joint probability occurrence of the specified pixel pairs	$\sum P_{ij} (i-\mu)(j-\mu) / \sigma_i \sigma_j$
Cluster Shade	Local variation in GLCM.	$\sum P_{ij}(i-j)^2$
Cluster prominence	An elevation (or) projection.	$\sum ((i-\mu_i)+(j-\mu_j))^4 c(i,j)$
Dissimilarity	Instance of difference.	$\sum P_{ij}(i-j)$
Variance	Sum of the squared distances of each term in the distribution from the mean.	$\sum \sum (i-\mu)^2 p(i,j)$
Max probability	Max probability of occurrence.	$\max(P_{ij})$
Autocorrelation	Measures the coarseness of image	$\sum \sum P_{ij} / (1+ i-j)$

Table 3. GLCM Feature values for various images

Features	Line Filter	Ring Filter	2nd Ring Filter	Grayscale
Maximum probability	0.3645	0.4494	0.4255	0.3653
Contrast	0.0930	0.0825	0.1877	0.0921
Correlation	0.9437	0.9293	0.9517	0.9615
Cluster prominence	29.973	21.643	28.673	26.712
Cluster shade	0.9978	2.2594	3.7651	2.6731
Dissimilarity	0.0779	0.0819	0.0576	0.0674
Energy	0.2779	0.332	0.6743	0.8435
Entropy	1.5309	1.4106	0.9258	1.4571
Homogenet iy1	0.9633	0.4591	0.9242	0.7633
Homogenet iy2	0.9626	0.4944	0.9424	0.6543
Auto correlation	5.756	4.5094	6.4356	4.9867
Variance	5.7596	4.5096	6.9876	6.94

7. Feature Selection

As a commonly used technique in data preprocessing, feature selection selects a subset of informative attributes or variables to build models describing data. By removing redundant and irrelevant or noise features, feature selection can improve the predictive accuracy and the comprehensibility of the predictors or classifiers. In this paper, we propose a framework based on a genetic algorithm (GA).

Feature selection techniques study how to identify and select informative (discriminative) features for building models which can interpret data better. Feature selection can reduce the computational cost by reducing dimensionality of data, improve the prediction performance and the comprehensibility of the models by eliminating redundant and irrelevant (probable noise) features.

7.1. Genetic algorithm

Genetic algorithms (GAs), a form of inductive learning strategy, are adaptive search techniques initially introduced by Holland (1975). Genetic algorithms derive their name from the fact that operations are similar to the mechanics of genetic models of natural systems.

7.2. Genetic operators

(1)Selection : Features are selected according to their fitness value. This involves that a features with a higher fitness value will have a higher probability of contribution in the next generation.

(2)Crossover : It is a procedure in which a highly fit-ting chromosome is given an opportunity to reproduce by exchanging pieces of its genetic information with other highly fitting chromosomes.

(3) Mutation : This is often applied after crossover by randomly altering some genes to individual parents.

7.3. Working Principle of Genetic Algorithm (GA)

Step I : [Start] Generate random population suitable solution for the problem (feature set values).

Step II : [Fitness] Evaluate the fitness function.

Step III : [New population] Create a new population by repeating the steps until the new population is complete.

- (a) Selection
- (b) Crossover
- (c) Mutation

Step IV: [Replace] Use new generated population for a further run of the algorithm.

Step V : [Test] If the end condition is satisfied, stop, and return the best solution in current population.

Step VI : [Loop] Go to step 2.

8. Simulation result of GA

Name	Size	Bytes	Class
In node status 1	163x1	1304	Double
Gene names 1	1x19	1236	Cell
Num samples	1x1	8	Double
Num variables	1x1	8	Double
Sample names	163x1	11084	Cell
Signal	163x9	24776	double

Sample names : 163 (fundus image samples).

Genes name: F1,F2,...,F19 (19 Features combining both GLCM Moment invariants). Signal : 163x 19 (19 feature values for 163 images).

Optimization Terminated : Time Limit exceed.

Selected Features

F6

F7

F10

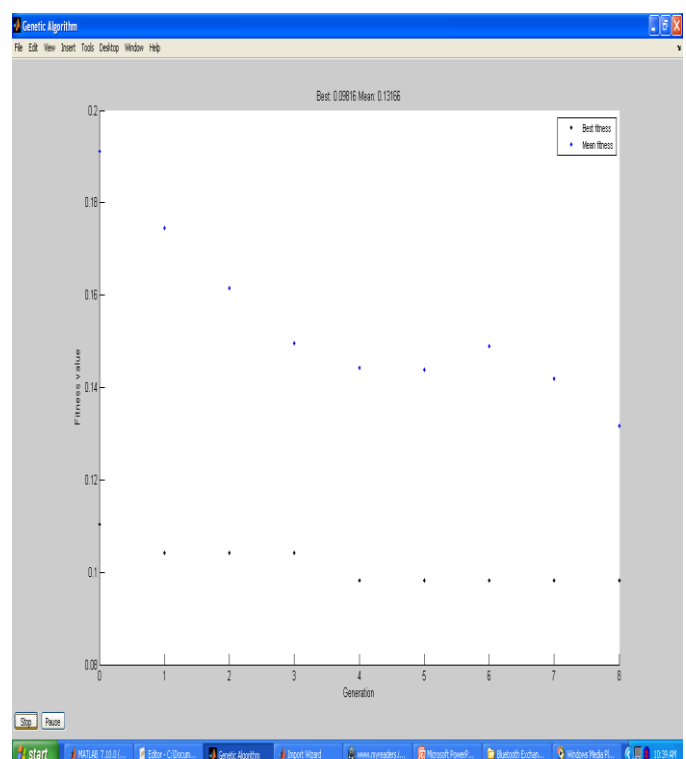


Fig 4. Plot function of GA (Fitness Function Vs Generation)

8.1 Characteristics of Fitness Function Vs Generation

Gives the plot of both mean fitness values and best fitness values across the generations.

Best fitness value : 0.09816 ,

Mean fitness value : 0.13166.

Generation	F count	Best f(x)	Mean f(x)	Stall Generations
1	200	0.1043	0.1665	0
2	300	0.1043	0.151	1
3	400	0.09816	0.1397	0
4	500	0.09816	0.1351	1
5	600	0.09816	0.1229	2
6	700	0.09816	0.1317	3
7	800	0.09816	0.1256	4
8	900	0.09816	0.1209	5
9	1000	0.09816	0.1161	6

9. Conclusion

Marker controlled watershed segmentation segments the abnormal blood vessels. Then feature extraction involves extracting feature values from various fundus images. Valid features are extracted using genetic algorithm(GA) work can be extended by selecting classify them based on abnormalities which will demonstrate an automated system which is able to distinguish normal and abnormal vasculature on the optic disc. It could form part of a system to reduce manual grading and a workload or a tool to prioritize patient grading queues.

10. References

- [1] Keith A. Goatman, Alan D. Fleming, SamPhilip, Graeme J. Williams, John A. Olson, and Peter F. Sharp. "Detection of New Vessels on the Optic Disc Using Retinal photographs", IEEE transaction on medical imaging, vol. 30, no. 4, April 2011.
- [2] Fleming, K. A. Goatman, S. Philip, G. J.Williams, G. J. Prescott, G. S. Scotland,

P. Mc Hamee, G. P. Leese, W. Wykes, P. F. Sharp, and J. A. Olson, "The role of haemorrhage and exudate detection in automated grading of diabetic retinopathy," Br. J. Ophthalmol., vol.94, no. 6, pp. 706–711, 2010.

[3] M. Niemeijer, M. D. Abràmoff, and B. van Ginneken, "Fast detection of the optic disc and fovea in color fundus photographs," Med. Image Anal., vol. 13, pp. 869–870, 2009.

[4] B. Niemeijer, B. V. Ginneken, S. R. Russel, M. S. A. Suttorp- Schulten, and M. D. Abramoff, "Automated detection and differentiation of drusen, exudates and cotton-wool spots in digital color fundus photographs for diabetic retinopathy diagnosis," Investigate Ophthalmol. Vis.Sci., vol. 48, pp. 2260–2267, 2007.

[5] H. F. Jelinek, M. J. Cree, J. J. G. Leandro, J. V. B. Soares, R. M.C. Jr, and A.Luckie, "Automated segmentation of retinal blood vessels and identification of proliferative diabetic retinopathy," J. Opt. Soc. Am. A, vol. 24, pp. 1448–1456, 2007.

[6] G. S. Scotland, P. McNamee, S. Philip, A. D. Fleming, K. A. Goatman, G. J. Prescott, S. Fonseca, P. F. Sharp, and J. A. Olson, "Cost-effectiveness of implementing automated grading within the national screening programme for diabetic retinopathy in scotland," Br. J. Ophthalmol., vol. 91, pp. 1518–1523, 2007.

[7] L. Gang, O. Chutatape, and S. M. Krishnan, "Detection and measurement of retinal vessels in fundus images using amplitude modified second- order Gaussian filter,"

- IEEE Trans. Biomed. Eng., vol. 49, pp. 168–172, Feb. 2008.
- [8] Li H, Chutatapee O. “Automated feature extraction in color retinal images by a model based approach,” IEEE Trans. Biomed. Eng 51:246 –254, Feb.2004.
- [9] Alireza Osareh, Bita Shadgar, and Richard Markham,” A Computational-Intelligence-Based Approach for Detection of Exudates in Diabetic Retinopathy Images”, IEEE Trans. on Information Technology In Biomedicine, Vol. 13, no. 4, July 2009.
- [10] D. Fleming, S. Philip, K. A. Goatman, J. A. Olson, and P. F. Sharp,“Automatic detection of retinal anatomy to assist diabetic retinopathy screening,” Phys. Med. Biol., vol. 52, pp. 331–345, 2007.
- [11] Hoover, V. Kouznetsova, and M. Goldbaum, “Locating blood vessels in retinal images by piecewise threshold probing of a matched filter response,” IEEE Trans. Med. Imag., vol. 19, no. 3, pp. 203–210, Mar. 2000.
- [12] F. Zana and J. C. Klein, “Segmentation of vessel-like patterns using mathematical morphology and curvatures evaluation,” IEEE Trans. Image Process., vol. 10, no. 7, pp. 1010–1019, Jul. 2001.
- [13] J. J. Staale, M. D. Abr’amoff, M. Niemeijer, M. A. Viergever, and B.V. Ginneken, “Ridge based vessel segmentation in color images of the retina,” IEEE Trans. Med. Imag., vol. 23, no. 4, pp. 501–509, Apr. 2004.
- [14] M. A. Bamashmas, B. Matlhaga, and G. N. Dutton, “Causes of blindness and visual impairment in the west of scotland,” Eye, vol. 18, pp. 257–261, 2004.
- [15] K. Faciy, E. Cummins, K. Macpherson, A. Morris, L. Reay, and J. Slattery, Organisation of services for diabetic retinopathy screening health technology assessment report 1 (Technical Report Health Technology Board for Scotland Glasgow) 2002.
- [16] S. Wild, G. Roglic, A. Green, R. Sicree, and H. King, “Global prevalence of diabetes: estimates for the year 2000 and projections for 2030,” Diabetes Care, vol. 27, pp. 1047–1053, 2004.
- [17] Osareh, M. Mirmahdi, B. Thomas, and R. Markham, “Automated identification of diabetic retinal exudates in digital colour images,” Br. J. Ophthalmal., vol. 87, pp. 1220–1223, 2003.
- [18] C. I. Sánchez, M. García, A. Mayo, M. I. López, and R. Hornero, “Retinal image analysis based on mixture models to detect hard exudates,” Med. Image Anal., vol. 13, pp. 650–658, 2009.
- [19] Kocur and S. Resniikoff, “Visual impairment and blindness in Europe and their prevention,” Br. J.Ophthalmol., vol. 86, pp. 716–722, 2002.
- [20] Guyyon and A. Elisseeff, “An introduction to variable and feature selection,” J. Mach. Learn. Res., vol. 3, pp. 1157–1182, 2003.

A New Chaotic Image Encryption Scheme using Random Permutation and Logistic Map

T.Gopalakrishnan¹, S.Ramakrishnan², R.Ranjith Kumar¹

¹Department of Electrical and Electronics Engineering

²Department of Information Technology

Dr. Mahalingam College of Technology, Pollachi

tgkme@yahoo.com, ram_f77@yahoo.com, rranjithkumar7@gmail.com

Abstract

In this paper we propose a secure image encryption scheme that is based on chaotic logistic map iteration and pseudo random permutation. The main advantages of this scheme are the usage of large key space to resist the brute force attack and encrypt the images with any quantization level. An external key of 159 bit is used for the encryption. Confusion and diffusion process is used to strengthen the scheme. The experimental, statistical, key space and key sensitivity analyses show that the proposed scheme is efficient and robust for real time image encryption and transformation.

General Terms

Chaotic cryptography for secured encryption.

Keywords

Random permutation, chaotic map, entropy, correlation and image encryption.

1. Introduction

Owing to the growth of World Wide Web and technologies there is an increase in the transmission and processing of digital images. Fields like medical, Army, industry, multimedia etc., are mostly deal with the transmission of the digital images. After the escalation of internet there are millions of images transferred through the internet by the above mentioned fields. Even in personal millions of images are stored and transmitted through the internet every day. To ensure secure transmission we need a technique called encryption. These techniques protect our information from the eavesdropper. So many encryption schemes have been proposed during the last years. Some of these encryption schemes are based on scan pattern methodology [12], random permutations, random phase encoding and chaos maps etc. Among these due to the intrinsic and ergodicity characteristics chaotic map based encryption schemes provide an appropriate response in secure image encryption. Since the map is greatly sensitive to the initial conditions it provides more complexity in confusion and diffusion stages in encryption. It also satisfies the speed required in Real-time. Due to the strong correlation between

the image pixels only permutation of their position will not

give the required levels of security. To obtain a robust encryption scheme we need to confuse and diffuse the position and values of the pixels respectively. For a best

encryption scheme the conditions like key space, keysensitivity, and randomness of cipher must be satisfied by the encryption scheme [2]-[4]. A first application for transmitting signals using chaos was proposed by Pecora and Carroll[8]. They showed that two similar chaotic circuits can have their trajectories synchronized. Then, the message to be sent is masked in one of the chaotic signals. During transmission, this message is extracted using a synchronous circuit, usually by the receiver. Following the improvements in chaos based signal transmission, M.S.Baptista have proposed a cryptographic scheme [1] that completely based on a chaotic logistic map given below,

$$X_{n+1} = bX_n(1-X_n) \quad (1)$$

In Ref [1] the encryption scheme is only proposed for text messages. After this proposal so many methods based on the chaotic maps have been proposed. Baptista proposed a cryptosystem for the text messages. The message to be encrypted is a text composed by some alphabet. The portion of the attractor is partitioned and associated with the alphabets. Cipher text for the text to be encrypted is produced by iterating the Eqn (1) until the trajectory falls into the region corresponds to the alphabet. The main drawbacks in Baptista's methods are, Length of the cipher text is greater than the plaintext and the time complexity. This method is the

base for all cryptographic proposals found at the present.

References [3] and [4] show the encryption schemes differ from the Baptista's. These are based on confusion and diffusion of image pixels. In both the papers chaotic maps were used to do the above said operations. Different maps are used to do the confusion and diffusion process respectively.

In this paper we propose an encryption scheme based on random permutation and chaotic function. The chaotic function used here is the Logistic map, same as in Ref [1]. The initial condition and the parameter b are used as keys for the encryption. Two chaotic functions are used in this scheme with different keys to increase the key space as well as the complexity of prediction. The experimental and performance analysis results show that the proposed scheme is secure and robust. In section 2 we discuss the proposed encryption method in detail. Section 3 experimental results of the proposed scheme.

2. The Proposed Encryption Method

2.1 Random permutation

Generally, the pixels in an image will have strong correlation with their neighbor pixels; especially with their adjacent ones. To increase the quality of the cipher text this correlation must be broken. To achieve this we are using random permutation. In this proposed scheme the image of size $N_1 \times N_2$ is selected, first the position of the pixels is changed using the random permutation. The eavesdropper can know the original histogram of the image from the permuted one but it is impossible to perform the brute force attack



since the number of possible permutations is comparatively large [11]. In our case it is $N!$, where $N = N_1 \times N_2$. That represents the eavesdropper will never get the original image from the permuted one due to the large N . The overall encryption scheme is shown in the Figure 1. In our method both gray scale and color image are used.

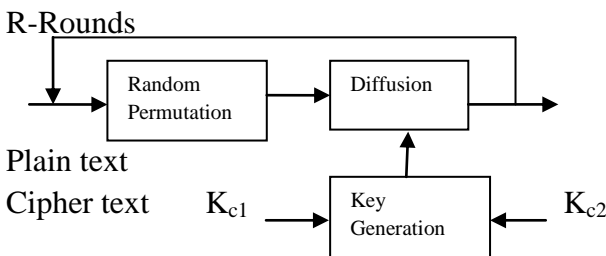


Figure 1. Proposed encryption scheme.

As already discussed a best encryption scheme will prefer the confusion and diffusion of the pixels. Random permutation is done for the confusion part alone. After applying the random permutation the diffusion part starts where the chaotic maps are used. The permutation sequence is sent to the receiver via a secured channel.

2.2 Diffusion using chaotic maps

Two Logistic maps are used here. The equations are similar to that of the equation (1). the two keys consists of the initial condition and the parameter value b . Let us consider the following functions be used in our scheme,

$$y_{n+1} = b_1 y_n (1 - y_n) \quad (2)$$

$$z_{n+1} = b_2 z_n (1 - z_n) \quad (3)$$

Where b_1 and b_2 are the parameters of the maps represented by (2) and (3).these

parameter values ranges from 3.6-4[1]. The initial condition and the value of the parameter act as a key for encryption. Since we are dealing with two maps we are using two keys K_{c1} and K_{c2} each of size 74 bits. Using these two keys the diffusion masks of size N , which is the size of the image, is generated [6]-[9].

The output from the random permutation block is masked by the masks created by the Y and Z maps. This process is repeated until the required constraints have met. The purpose of the key generator is to generate individual keys to the permuted pixels using the keys K_{c1} and K_{c2} . The cipher image obtained from the above step is again given as a plain image to the permutation block. The number of rounds(R) carried out in this method are three. The number of Rounds to be used for encryption is,

$$R = \text{Floor} \left[\frac{128}{\log_2 L} \right] + 1 \quad (4)$$

Where L indicates the number of ciphers produced by the key space. The value of the round number R cannot be applied for all kind of images. For our scheme, using the above equation the number of rounds satisfying the encryption standard i.e., the number of Rounds used is 1. As from the Table 1 we can find that at Round 1 itself the value of NPCR and UACI attains its necessitated values.

3. Experimental Results

3.1 Key space analysis

For today's computers the sufficient key size must be greater than or equal to 2^{128} . This condition is must to avoid brute force attacks[10]. In the proposed scheme key of size 159 is used and it satisfies the condition.

The following test is performed to check the sensitivity of the key,

1. A 512x512 gray scale image is encrypted with the keys K_{c1}/K_{c2} (0.0011223344556677/0.998877665 5443322).
2. Keys are slightly changed to be 0.0011223344556676/0.998877665 5443321 is used to encrypt the image.
3. The two resulting ciphers are compared pixel-by-pixel.

There is a difference of 99.62% between the two ciphers for each round i.e., for R=1,1 and 3. This analysis shows that if a slightly modified key is used (or) a key nearly equal to the original key is used to decrypt the image, the process fails completely.

3.2 Differential attack

To resist the differential attacks the cipher image must be very sensitive to the

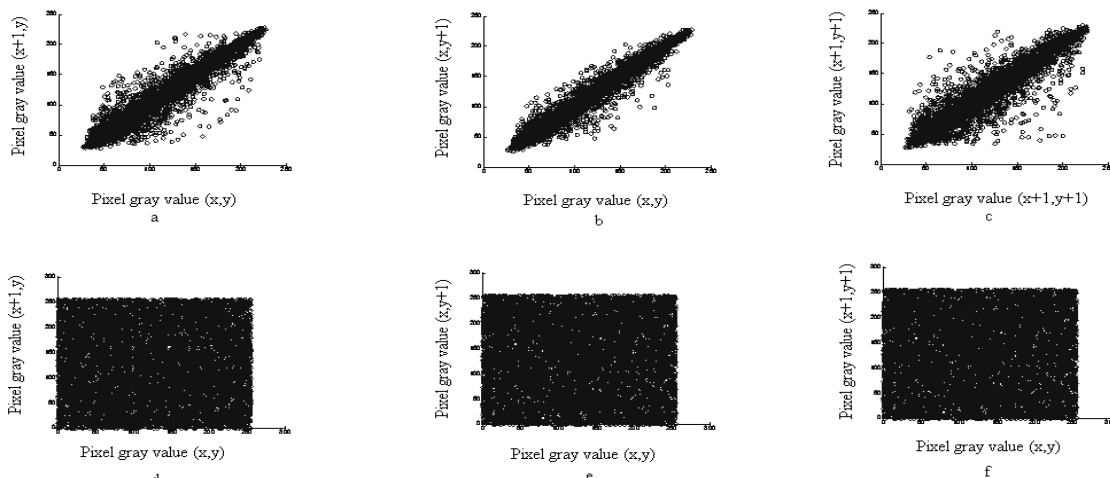


Figure 4. correlation of two adjacent pixels (a) Horizontal direction of the plain image (b) Vertical direction of plain image (c) Diagonal direction of plain image (d)Horizontal direction of the cipher image (e)Vertical direction of cipher image (f)Vertical direction of cipher image.

small change in the plaintext. The common measures used to measure this sensitivity are NPCR (Number of pixel change rate) and UACI (unified average changing intensity). They are given by the following equations,

$$NPCR = \frac{\sum_{i,j} D(i,j)}{W \times H} \times 100\% \quad (5)$$

$$UACI = \frac{1}{W \times H} \left[\sum_{i,j} \frac{|C_1(i,j) - C_2(i,j)|}{255} \right] \times 100\% \quad (6)$$

Where C_1 and C_2 are the cipher images whose plain images have a slight difference in one pixel. $C_1(i, j)$ denotes the position of pixel in C_1 . W and H are width and height of the cipher image. $D(i,j)$ is determined as 1, if $C_1(i,j)=C_2(i,j)$, otherwise $D(i,j)=0$. NPCR is measured between the two ciphers having slightly different plain images i.e., one pixel change between the plain images.

Table 1 The NPCR and UACI values for different rounds.

IMAGE	R=1		R=2		R=3	
	NPCR	UACI	NPCR	UACI	NPCR	UACI
Lena (gray)	0.9956	0.3179	0.9959	0.3332	0.9962	0.3341
CT Scan Image (gray)	0.9954	0.3206	0.9961	0.3340	0.9961	0.3346
X ray Image (color)	0.9946	0.3280	0.9953	0.3354	0.9961	0.3350
Lena (color)	0.9951	0.3280	0.9953	0.3354	0.9961	0.3350
Athens (color)	0.9953	0.3244	0.9959	0.3340	0.9961	0.3351
Bob cat (color)	0.9950	0.3327	0.9957	0.3352	0.9961	0.3348

Table 2 Time Complexity Comparison.

Image size	R-Value		Entropy of key space(bits)		Encryption/Decryption(s)	
	Ref[3]	Our scheme	Ref[3]	Our scheme	Ref[3]	Our scheme
64 x 64	18	3	270	159	0.03/0.04	0.44/0.22
128 x 128	20	3	340	159	0.14/0.15	0.50/0.26
256 x 256	22	3	418	159	0.90/0.96	0.68/0.44
512 x 512	24	3	504	159	7.86/8.02	1.4/1.17
1024 x 1024	26	3	598	159	44.50/45.72	4.29/4.01

The resulting NPCR and UACI values are tabulated in Table 1. The proposed system needs one round to achieve the high performance $\text{NPCR} \geq 0.995$ and $\text{UACI} \geq 0.333$. Therefore the proposed system can resist the differential attack if $R \geq 1$.

3.3 Statistical analysis

3.3.1 Histogram analysis

A histogram of an image simply shows the distribution of the gray levels. We can see the distribution of each pixel in an image. There is a possibility of estimating the image from its histogram. To reduce the possibility the histogram must be changed during the encryption.

The figure shows the histograms of the original and encrypted images. The figure 2 (a) and (b) shows the original and encrypted image respectively, figure 2(c) and (d) shows the histograms of the corresponding images. The figure 3 (a) and (b) Plain image and encrypted image of CT scan of Head (c) and (d) are the Histogram of the plain and encrypted image. The figure 4 (a) and (b)

shows the color image (X-ray of heart) and its encrypted Image. Figure 4(c), (d) and (e) shows the histograms of red, green and blue channels, Figure 4 (f), (g) and (h) shows the encrypted red, green and blue channel histograms. These images are encrypted by using keys $K_{C1}/K_{C2}(0.12345678901234567/0.9876543210987654)$. The results show that the histogram of the image is equally distributed and the eavesdropper can't predict the original histogram of the image.

3.3.2 Correlation of adjacent pixels:

To be a best encryption scheme the correlation between the pixels must be broken. This analysis shows the correlation between the randomly selected pairs of both plain image and cipher image [5]. This analysis carried out by following the procedures, Randomly 10,000 pairs are selected and they are selected like they are horizontally and vertically adjacent. The correlation is calculated by the following equations,

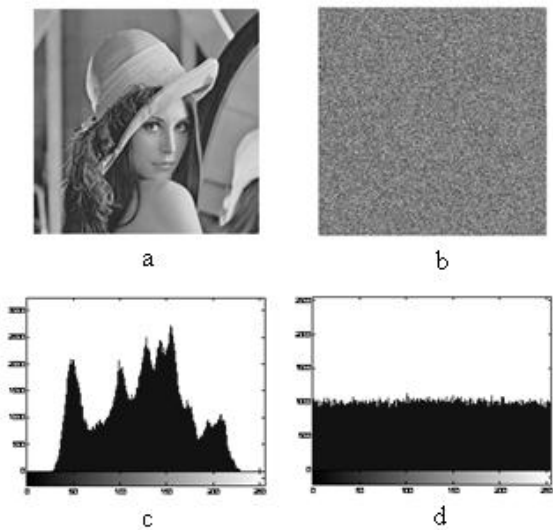


Figure 2 (a) Plain image (b) encrypted image (c) Histogram of plain image (d) Histogram of encrypted image.

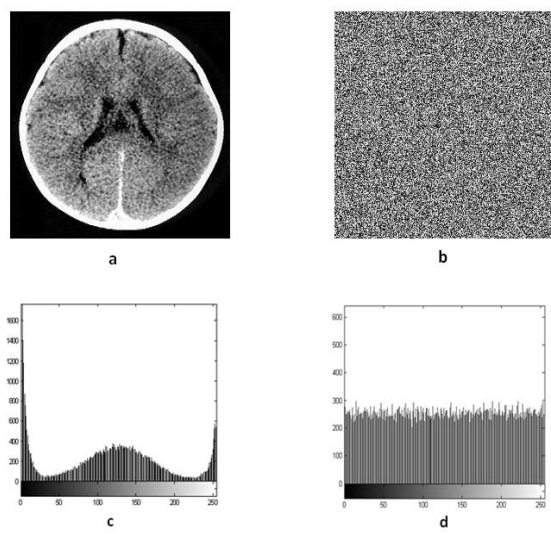


Figure 3 CT Scan of Head (a) Plain image (b) encrypted image (c) Histogram of plain image (d) Histogram of encrypted image.

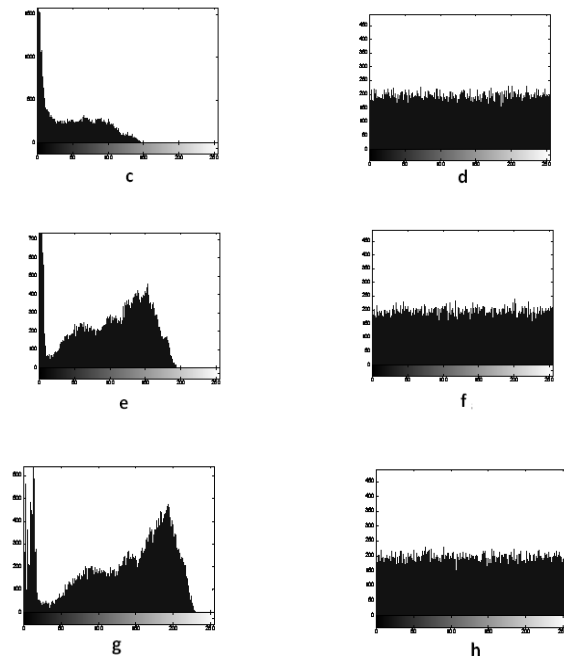
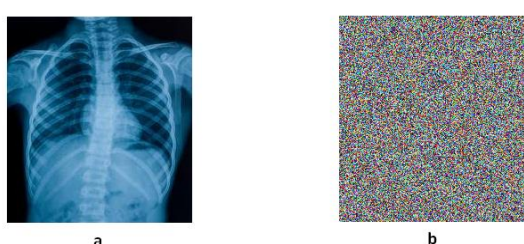


Figure 4 (a)plain image (b)encrypted image(c)Histogram of red channel (d)Histogram of green channel(e)Histogram of blue channel (f)Histogram of encrypted red channel(g) Histogram of encrypted green channel (h) Histogram of encrypted blue channel.

$$Cov(x, y) = E\{(x - E(x))(y - E(y))\} \quad (7)$$

$$r_{xy} = \frac{\text{cov}(x, y)}{\sqrt{D(x, y)} \sqrt{D(y)}} \quad (8)$$

Where x and y are the gray level values of the two adjacent pixels in the image,E(x) and D(x) are the mean and standard deviation of the corresponding gray level values.The correlations of vertical, diagonal and horizontal adjacent pixels are plotted. Figure4 (a)-(f) shows the results of the correlation of the adjacent pixel analysis.

3.3.3 Information entropy analysis

The entropy of a message source can be measured by,

$$H(m) = \sum_{i=0}^{M-1} p(m_i) \log \frac{1}{p(m_i)} \quad (9)$$

Where M is total number of symbols, $p(m_i)$ represents the probability of occurrence of symbol m_i and log denotes the base 2 logarithm so that the entropy is expressed in bits. For a random source emitting the 256 symbols, its entropy is equal to 8bits. For the cipher images, the entropies are also equal to that of the plain image. This shows that the cipher is resistive to entropy attack.

3.3.4 Correlation coefficient

The correlation coefficient is a measure that determines the degree to which two variable's movements are associated. It simply determines the interdependence of two variables. The formula for calculating the correlation coefficient is,

$$R_{xy} = \frac{\text{cov}(x, y)}{\text{std}(x) \times \text{std}(y)} \quad (10)$$

The correlation coefficient will vary from -1 to +1. A -1 indicates perfect negative correlation, and +1 indicates perfect positive correlation. 0 indicates no linear relationship. Table 3 shows the correlation coefficient of three ciphers produced by slightly varying keys k1, k2 and k3. The results in Table 3 shows that there is no correlation between the ciphers.

3.3.5 Time complexity

The time complexity of the proposed method is examined finally. several images of different sizes are taken into account and the proposed scheme is performed on these images. This analysis is achieved on Intel(R) Pentium(R) Dual-core Processor 2.30GHz with 1024MB RAM personal computer. The method is coded and simulated in MATLAB (R2009a). The results are shown in Table 2. The table compares the time complexity of Ref[3] and the proposed scheme. Ref[3] uses Intel(R) Pentium(R) M Processor 1.73MHZ with 2048 MB RAM personal computer. In Ref[3] the algorithm is coded in C. The results show that although our scheme took more time than Ref[3] for small size images it sounds good for the larger ones.

Table 3 Analysis on Correlation Coefficients

Image	Correlation coefficient
Lena	
k1/k2	0.0046
k1/k3	0.00043
k2/k3	-0.0025
X ray Image	
k1/k2	0.0012
k1/k3	-0.0021
k2/k3	0.0051
CT Scan Image	
k1/k2	0.0002
k1/k3	-0.0021
k2/k3	0.0014

4. Conclusion

A new encryption scheme proposed is based on random permutation and standard logistic map. Various analysis have been done to prove the security level of proposed encryption scheme. A good encryption scheme should satisfy the key space $\geq 2^{128}$, to resist the brute force attack and it should be more sensitive to the slight change in the key. The proposed scheme has the above qualifications as it has the key space of 2^{159} (approximately 3.5×10^{44} keys). By using these keys with chaotic map the proposed method have a greater sensitivity to the minute change in the key. The proposed scheme has proved the NIST tests and guarantees a negligible correlation between the pixels in the cipher. The statistical, key space and key sensitivity analysis shows that the proposed method is robust and provides secure image transformation. Finally to conclude that the proposed scheme is efficient one for the applications that require secure transformations of images with various images such standard test image and medical images with secret keys.

References:

- [1] Baptista M.S. ‘Cryptography with chaos’, Physics Letter A, Vol 240(1-2), pp. 50-54, March 1998.
- [2] Bourbakis,S , Alexopoulos C, “Picture data encryption using SCAN pattern”, Pattern Recognition, Vol.25, No.6, pp. 567–581, June 1992.
- [3] Francois M ,GrosgesT , Barchiesi D , Erra R. “A new image encryption scheme based on a chaotic function”, Signal Processing: Image Communication, Vol.27, Issue 3, pp. 249–259, March 2012.
- [4] Kwok-Wo Wong, Bernie Sin-Hung Kwok, and Wing-Shing Law., “A Fast Image Encryption Scheme based on Chaotic Standard Map”, Physics Letters A, pp. 2645–2652, April 2008.
- [5] Li S, Li C, Chen G,Bourbakis N.G., Lo K.T., “A general quantitative cryptanalysis of permutation-only multimedia ciphers against plaintext attacks”, Signal Processing: Image Communication Vol.23, No.3, pp. 212–223, March 2008.
- [6] Lian SG, Sun J, Wang Z., “Security analysis of a chaos-based image encryption Algorithm”, PhysicaA,Vol 351, No 2-4, pp-645-661, June 2005.
- [7] Lian SG, Sun J, Wang Z. “A block cipher based on a suitable use of chaotic standard Map”, Chaos, Solitons and Fractals; Vol 26, No.1, pp.117-129, Oct 2005.
- [8] Louis M. Pecora and Thomas L. Carroll,” Synchronization in chaotic systems”, Physics Review Letter, Vol.64, pp. 821–824, Jan 1990.
- [9] Pareek N.K, Patidar V, Sud K.K., “Discrete chaotic cryptography using external Key”, Physics Letter A,Vol 309, pp. 75-82, March 2003.
- [10] VinodPatidar, N.K.Pareek, G.Purohit, K.K.Sud, “A robust and secure chaotic standard map based pseudorandom permutation-substitution scheme for image encryption”, Optics Communications, Vol 284, pp. 4331–4339, September 2011.
- [11] Wong WK, Lee LP, Wong KW,”A modified chaotic cryptographic method” Computer Physics

- Communication, vol.138, pp. 234–236,
Aug 2001.
- [12] Wong KW, “A fast chaotic
cryptography scheme with dynamic
look-up table”, Physics Letter A, Vol,
298, pp. 238–242, June 2002.

Enhancement of Diabetic Retinopathy Imagery Using Histogram Equalization techniques

SrinivasanAruchamy, Rukhmini Roy, ParthaBattacharjee

Cybernetics Group

CSIR – CMERI, Durgapur

sriniwaspsg@gmail.com, rukhmini.roy788@gmail.com, partha11cmeli@gmail.com

Abstract

Diabetic retinopathy is a serious eye disease originating from diabetes mellitus and the most common cause of blindness in the developed countries. Early detection and treatment can prevent such condition or in other words aggravation of the diseases patients may be arrested. The ocular images produced by fluorescent oscilloscope are often noisy and low in contrast making it difficult for doctors to precisely detect the inherent abnormalities. In the present paper, we propose to use different contrast enhancement techniques like histogram equalization, dualistic sub image histogram equalization, brightness preserving bi-histogram equalization, contrast limited adaptive histogram equalization and compare those techniques to check which is best suited to aid the detection of retinal changes. The effectiveness of the proposed techniques is evaluated using widely accepted methods like Absolute Mean Brightness Error, Peak Signal to Noise Ratio and Entropy. Finally a considerable improvement in the enhancement of the Diabetic Retinopathy image is achieved by contrast limited adaptive histogram technique.

Keywords

Contrast enhancement, histogram, PSNR, AMBE

1. Introduction

Diabetic Retinopathy (DR) is one of the most common eye diseases which occur due to diabetes. It damages the small blood vessels in the retina resulting in loss of vision. The risk of the disease increases with age and therefore, middle aged and older diabetics are prone to Diabetic Retinopathy [1]. According to the World Health Organization (WHO), a total of 20.8 million people i.e. 7 percent of the population suffer from diabetes, out of which only 14.6 million cases are diagnosed in the United States. Further, the risk of blindness in patients with diabetes is 25% more than those not having DR. A large part of Indian population also has diabetes with DR steering it to the sixth biggest cause of vision impairment in the country [2]. Early detection of the disease by regular check up is particularly important to prevent vision loss. Color fundus [3] images are used by ophthalmologists to study this disease. For doctors, it is very important to clearly detect and distinguish the blood leakages, hemorrhages and lesions from amongst the numerous blood vessels present in eye [1]. An

important feature of this disease is that, detectable changes take place in the retina, as shown in Fig. 1, which can be cured using laser treatment, if detected at an early stage. Usually, retinal images captured from fluorescence oscilloscope are of low gray level contrast [4] because of the poor acquisition process.

A well known fact is that image enhancement techniques improve the quality of retinal images. Enhancing the image improves the image quality so that the processed image is better than the original image for a specific application or to achieve a set of objectives. The purpose of image enhancement is to improve the interpretability and perception of information in image for human viewers and to provide better (processed) input for other automated image processing techniques.

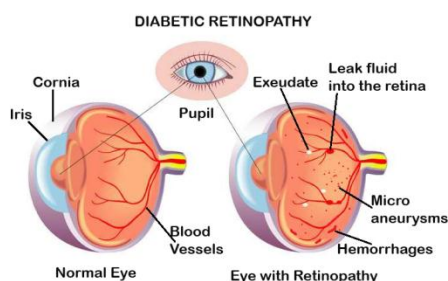


Fig 1: Observable changes in diabetic retinopathy affected eye as compared to that of the normal eye

Several methods for detection of abnormality in ocular images appear in literature. Zhitao Xiao et. all [4] proposes to extract the features to detect DR from phase information of the image by which phase congruency, phase based symmetry, symmetric phase congruency and improved integrated feature congruency values are analyzed. Lazer and Hajdu[5] find the presence of microaneurysm(MA) in retina using MA score map and thresholding method.

Noronha, K. and Prabhakar N. K. [6] have done a detailed review on image processing techniques for retinal imaging and discussed the sensitivity, specificity and positive predictive accuracy of different methods. Yagmuret all [7] proposed a method to recognize different retinopathy related deformations using wavelet based artificial neural network which has multilayer perception structure and back propagation algorithm. Vijayakumari et al[8] extracted the image of blood vessel of different thickness using morphological operations (open and close). Sizes of the exudates [19]are detected by using different structural element in morphology. The Works discussed so far are focused on detection and classification of ocular problems. Retinal images are usually acquired with digital fundus camera. Despite the controlled condition under which imaging takes place, there are many patient-dependent aspects which are difficult to control. Thus, most retinal images suffer from non-uniform illumination. Some of the contributing factors are (a) The curved surface of the retina, because of which entire retinal regions cannot be illuminated uniformly, (b) Imaging requires a dilated pupil. The degree of dilation is highly variable across patients. (c) Unexpected movements of the patient's eye. The bright flash-light makes the patient move the eye away from the view of the camera involuntarily. (d) Presence of other diseases such as cataract which can block the light reaching the retina. These factors cause large variation in luminosity and contrast within and across images. Regarding the enhancement of retinal images few studies have been published. Retinal image enhancement using curvelet transform(a geometrical transformation using anisotropic scaling and directionality) is proposed by Candes et al [9].

Miri et al [10] used multi-resolution tools using a non linear function to modify the curvelet coefficients. Techniques based on matched filtering are ideal in enhancing low contrast blood vessels over a limited area but the computation becomes complex with image size [11,12]. This process is attractive in enhancing the global contrast of an image, but not suitable, when features of interest occupy a relatively narrow range of gray scale.

As mentioned above,a wide range of image processing techniques are available for diagnosis and classification of retinopathy related diseases. For a reliable diagnosis, whether manual or automated, the contrast of a fundus image plays a significant role in all the above studies and the results of such studies are prone to error. Very few studies are there for enhancement of DR imagery. Piezer et al.[13] uses Adaptive Histogram Equalization (AHE) to overcome the drawbacks of Histogram Equalization, especially for images with varying contrast. They explained the diagnostic capability of AHE on chest CT scan. Kim et al[14] use brightness preserving bi histogram equalization to overcome the drawback of changing brightness of an image (mainly due to the flattening property of the histogram equalization). Zimmerman [15] showed by ROC studies on CT chest studies that CLAHE with moderate limitation of contrast enhancement allows as effective detection of simulated Gaussian lesions as CLAHE with no such limitation (AHE).The idea behind the present work is to exploit the effectiveness of CLAHE in early detection of retinopathy in diabetic patients.

2. Research Background

In the present section we discuss issues that are in close relation to Diabetic Retinopathy

with an emphasis on the medical research background. Towards the end, we provide the comparative study of different contrast enhancement techniques for retinopathy imagery.

Retinopathy is a progressive disease, which can advance from mild stage to proliferative stage. There are three stages: (i) early stage called non-proliferate diabetic retinopathy (NPDR), (ii) maculopathy[16] and (iii) progressive or proliferate retinopathy [16]. These stages of DR are shown in Fig. 2.The early stage is further classified as mild NPDR and moderate to severe NPDR. In mild NPDR, signs such as microaneurysms [17], dot and blot hemorrhages[18] and hard or intra-retinal exudates[19] are seen in the retinal images. In the early stage, the vision is rarely affected and the disease can be identified only by regular dilated eye examinations. In moderate to severe NPDR, the signs discussed in mild NPDR are present in excess and in addition to this cotton wool spots, venous beading, venous loops and Intra-retinal micro vascular abnormalities (IRMA) are observed. Cotton wool spots [19] are essentially infections in the nerve fiber of retina.

Diabetic Maculopathy is a stage where fluid leaks out of damaged vessels and accumulates at the center of the retina called macula causing permanent loss of vision. Proliferatediabetic retinopathy, which is defined as the growth of abnormal new vessels (neovascularization) on the inner surface of the retina. The above stages can be seen clearly in Fig. 2 which shows different changes that take place in the retina of a DR patient over a period of time.

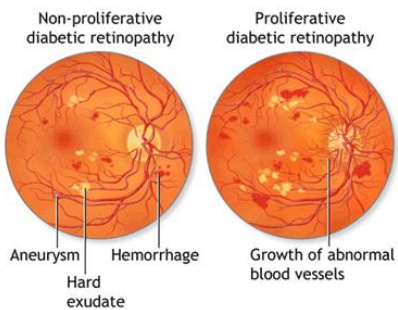


Fig 2: Main stages of Retinopathy with the disorders

3.Image enhancement Techniques

3.1Histogram Equalization

Histogram equalization is the one of the well-known methods for enhancing the contrast of given images in accordance with the sample distribution of an image. In general, histogram equalization moderates the density distribution of the resultant image and enhances the contrast of the image. As a consequence, histogram equalization has an effect of stretching dynamic range. In this context we define X as an image vector as follows.

$X = \{X(i, j)\}$ is an image with L discrete gray levels $\{X_0, X_1, \dots, X_{L-1}\}$, where $X(i, j)$ is the intensity of the image at the 2D position (i, j) and $X(i, j) \in \{X_0, X_1, \dots, X_{L-1}\}$. $H(X) = \{n_0, n_1, \dots, n_k, \dots, n_{L-1}\}$ is the histogram of image X , where n_k is the number of pixels whose gray level is X_k .

Consider the input image X . Based on the histogram $H(X)$, The probability of the occurrence of a pixel of level k in the image is

$$p_x(k) = p(x = k) = n_k/n, (0 < k < L) \quad (1)$$

Where L is the total possible number of gray levels in the image, n is the total number of pixels in the image, n_k is the number of

occurrences of gray level k , and $p_x(k)$ is the image histogram for pixel value k .

The cumulative distribution function [20, 21] corresponding to p_x can be defined as

$$cdf_x(k) = \sum_{j=0}^k p_x(j) \quad (2)$$

which is also accumulated normalized histogram of the image. The cdf must be normalized to [0,255]. The general histogram equalization formula may be written as

$$h(v) = round((cdf(v) \div (M \times N)) \times (L - 1)) \quad (3)$$

where $M \times N$ is the expression for the number of pixels present in the image and L is the number of grey levels used (in most cases 256). Thus, histogram equalization remaps the input image over the entire dynamic range $[X_0, X_{L-1}]$.

3.2Brightness Preserving Bi-Histogram Equalization[22]

The BBHE first decomposes an input image into two sub-images based on the mean of the input image. One of the sub-images is the set of samples less than or equal to the mean whereas the other one is the set of samples greater than the mean. Then the BBHE equalizes the sub-images independently based on their respective histograms with the constraint that the samples in the formal set are mapped into the range from the minimum gray level to the input mean and the samples in the latter set are mapped into the range from the mean to the maximum gray level. The resulting equalized sub-images are bounded by each other around the input mean, which has an effect of preserving mean brightness.

Denote by X , the mean of the image X and assume that $X_m \in \{X_0, X_1, \dots, X_{L-1}\}$. Based on the mean, the input image is decomposed into two sub images X_L and X_U as

$$X = X_L \cup X_U \quad (4)$$

where

$$X_L = \{X(i,j) | X(i,j) \leq Xm, \forall X(i,j) \in X\} \quad (5)$$

$$X_U = \{X(i,j) | X(i,j) > Xm, \forall X(i,j) \in X\} \quad (6)$$

The sub-image \mathbf{X}_L is composed of $\{X_0, X_1, \dots, Xm\}$ and the other sub-image \mathbf{X}_U is composed of $\{X_{m+1}, X_{m+2}, \dots, X_{L-1}\}$.

Subsequently, the respective probability density functions of the sub-images \mathbf{X}_L and \mathbf{X}_U are

$$p_L(X_k) = n_l^k / n_l \text{ where } k=0,1,\dots,m \quad (7)$$

$$p_U(X_k) = n_u^k / n_u \text{ where } k=m+1, m+2, \dots, L-1 \quad (8)$$

in which and represent the respective numbers of X_k in $\{X\}_L$ and $\{X\}_U$ respectively. Note that

$$n_L = \sum_{k=0}^m n_k^l, n_U = \sum_{k=m+1}^{L-1} n_k^u$$

The cumulative density functions for $\{X\}_L$ and $\{X\}_U$ are then defined as

$$c_l(x) = \sum_{j=0}^k p_L(X_j), \\ c_u(x) = \sum_{j=m+1}^k p_U(X_j) \quad (9)$$

Where $X_k=x$, $C_L(X_m)=1$ and $C_L(X_{L-1})=1$

$$\text{The mean of the histogram is } \sum f_i X_i / \sum f_i \quad (10) \\ n_L = \sum_{k=0}^m n_k^l$$

where X_i is the histogram of the image and f_i is the frequency of occurrence. The transform functions exploiting the cumulative density functions are

$$f_L(x) = X_0 + (X_m - X_0)c_L(x) \quad (11)$$

$$f_U(x) = X_{m+1} + (X_{L-1} - X_{m+1})c_U(x) \quad (12)$$

Based on these transform functions, the decomposed sub-images are equalized

independently and the composition of the resulting equalized sub-images constitute the output of the BBHE. That is, the output image of the BBHE, Y , is finally expressed as

$$Y = \{Y(i,j)\}, Y = f_L(X_L) \cup f_U(X_U) \quad (13)$$

$$\text{where } f_L(X_L) = \{f_L(X(i,j)) | \forall X(i,j) \in X_L\}$$

$$f_L(X_L) = \{f_L(X(i,j)) | \forall X(i,j) \in X_L\} \quad (14)$$

$$f_U(X_U) = \{f_U(X(i,j)) | \forall X(i,j) \in X_U\} \quad (15)$$

If $0 < C_L(x), C_U(x) < 1$ it is easy to say that $f_L(X_L)$ equalizes the sub image X_L over the range (X_0, Xm) whereas $f_U(X_U)$ equalizes the sub images X_U over the range (X_{m+1}, X_{L-1}) . As a consequence, the input image X is equalized over the entire dynamic range (X_0, X_{L-1}) with the constraint that the samples less than the input mean are mapped to (X_0, Xm) and the samples greater than the mean are mapped to (X_{m+1}, X_{L-1}) .

3.3 Dualistic Sub-Image Histogram Equalization [23]

DSIHE is similar to BBHE except that the threshold for histogram segmentation is the median of the input image.

The median of the histogram may be expressed by

$$\sum_{i=0}^{L-1} f_i \quad (16)$$

If the result of the equation (16) is even then the middle value is calculated using

$$M = \frac{\frac{1}{2} \sum_{i=0}^{L-1} f_i + \frac{1}{2} (\sum_{i=0}^{L-1} f_i + 1)}{2}$$

else

$$M = \frac{\sum_{i=0}^{L-1} f_i + 1}{2}$$



where f_i histogram of the image, M is middle value of the histogram, then the median is by summing the frequencies up to middle value. Then the input histogram $H(X)$ is partitioned into two sub-histograms $HL(X)$ and $HU(X)$ based on median. Each of $HL(X)$ and $HU(X)$ is then equalized independently as BBHE.

3.4 Contrast Limited Adaptive Histogram Equalization

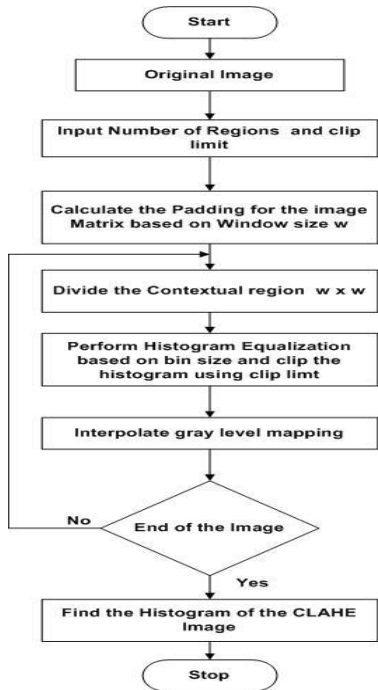


Fig 3: Flowchart of CLAHE

This algorithm is an improvement of the AHE algorithm[24]. The CLAHE divides the original image into contextual regions, where histogram equalization was made on each of these sub regions. These sub regions are called tiles. The neighbouring tiles are combining by using a bilinear interpolation [11] to eliminate artificially induced boundaries. This could give much better contrast and provide accurate results.

4 Metrics For Grayscale Images

4.1 Absolute Mean Brightness Error (AMBE)

It is the difference between original and enhanced image AMBE(X,Y)=|XM-YM|,[17] where XM is the mean of the input image and YM is the mean of the output image. A small value of AMBE indicates better brightness preservation in the output image.

4.2 Peak Signal to Noise Ratio (PSNR)

A large value of PSNR indicates better contrast enhancement in the output image.

The PSNR [17] has been computed as, $PSNR = 10 \log_{10}(L - 1)^2 / MSE$, where MSE is the mean square error and it is defined as

$$MSE = 1/(m \times n) \sum_{i=0}^{m-1} \sum_{j=0}^{n-1} [I(i,j) - K(i,j)]^2$$

4.3 Entropy

In this work the characterization of the texture of the input image was done by measuring entropy [23,25] using the formula

$$Ent = \sum_{i=1}^n p(x_i) \log_b p(x_i) \quad (19)$$

where p is the pdf and X_i is the histogram count. The result is shown in fig 6.

5. Result And Analysis

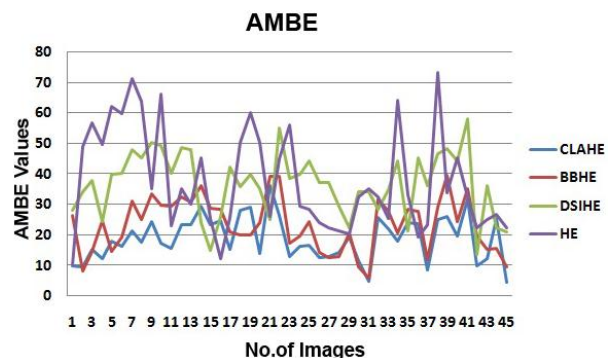


Fig 4: AMBE values of enhanced images

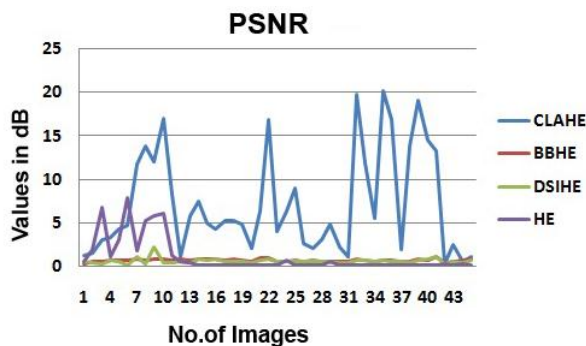


Fig 5: PSNR values of enhanced images

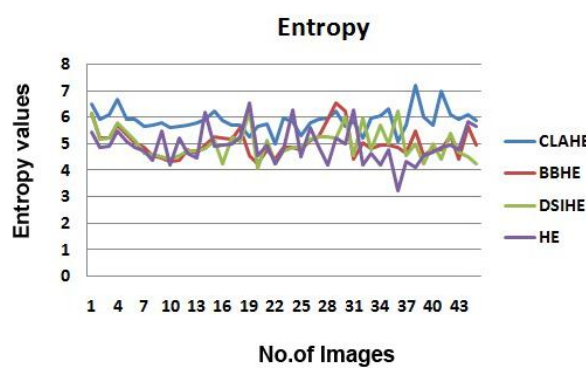


Fig 6: Entropy values of enhanced images

Nearly 45 DR images tested with four different image enhancement techniques. The input images are taken from Messidor digital retinal database [26]. A few enhanced images

are shown in fig 7, fig 8 to 10. The black arrow marks in these figures show the observable differences for NPDR images from fig 7 to fig(9). Fig 10 and 11 shows the PDR image with abnormal blood vessel growth.

As a last step, to perform the assessment of different enhancement techniques mentioned above, the image quality evaluation parameters like AMBE (fig 4), Entropy (fig 5), PSNR (Fig 6) is calculated for nearly 45 images and the comparative study has been described through the plotted graphs. Smaller value of AMBE indicates lesser loss of information during enhancement. Therefore in terms of AMBE, CLAHE gives the best result compared to other methods. As CLAHE is having the maximum entropy, we can say that contrast distribution is much more in case of CLAHE compared to other three equalization techniques. PSNR is used to assess the degree of contrast enhancement. Greater PSNR indicates better image quality [27]. So, in terms of PSNR also CLAHE is showing the best result.

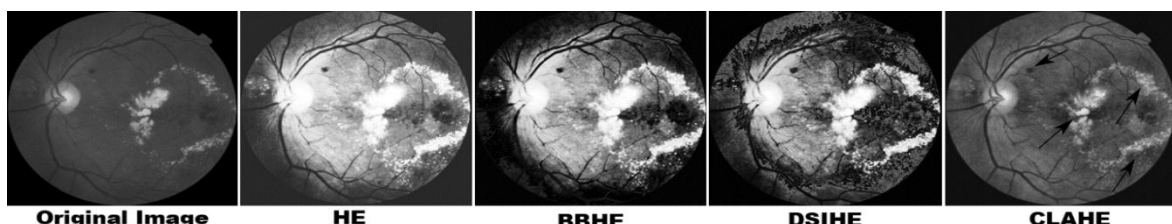


Fig 7: Microaneurysms and Exudates appear brighter in CLAHE

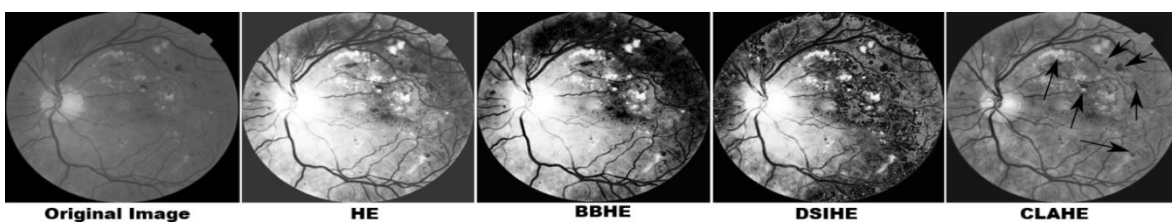


Fig 8: Haemorrhages and cotton wool spots (moderate NPDR)

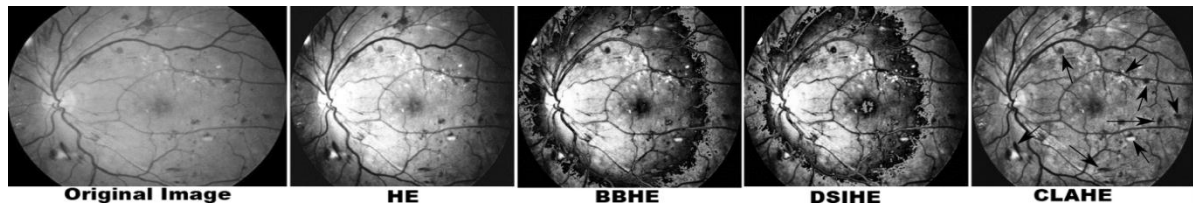


Fig 9: Severe NPDR(with microaneurysms, haemorrhages and exudates)

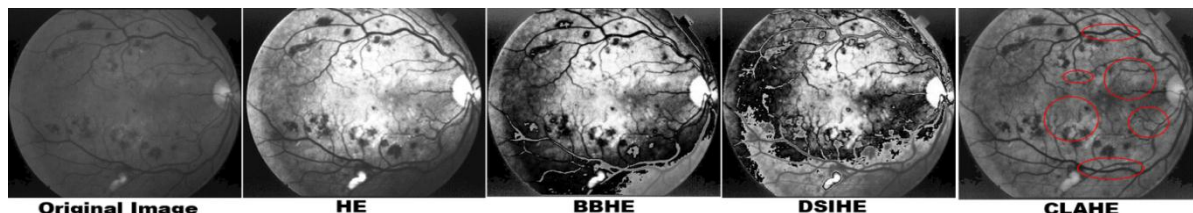


Fig 10: Severe PDR(neovascularisation)

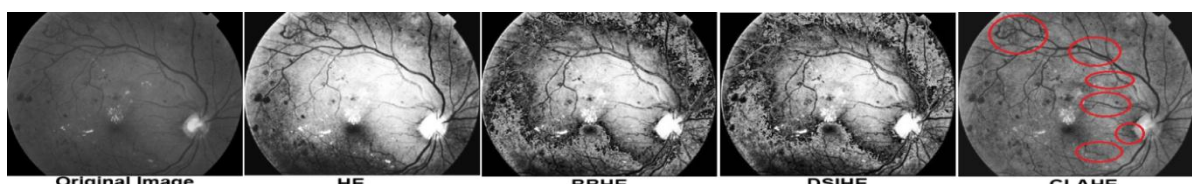


Fig 11: Intra-retinal micro vascular abnormalities (IRMA) appear brighter in CLAHE

6. Conclusion

In this paper, a frame work of image enhancement, based on histogram equalization has been presented. An effort has been made to establish that for DR imagery measuring the values of AMBE, PSNR and Entropy are fruitful. Number of practical experiments of real time DR images has been presented. From the experiment results, it is found that CLAHE performs better than other techniques. This work will help ophthalmologist to identify the pathological symptoms in the retina. In our future work colour fundus images will be taken and new parameters will be considered for the evaluation of enhancement techniques. New mathematical models will also be developed for better comparison purpose.

7. Acknowledgments

The authors would like to thank Dr. Debdulal Chakraborty, Consultant (Incharge Vitreo Retina Services), Disha Eye Hospital Kolkata

for his professional help to this research work and Messidor Digital Retinal Database for providing retina images.

8. References

- [1].K. J. Frank and J. P. Dieckert, “Clinical review of diabetic eye disease: A primary care perspective,” Southern Medical Journal, vol. 89, no. 5, pp. 463–470, May 1996.
- [2].WHO reports on Diabetics [online] Available :<http://www.icoph.org/downlod>s.
- [3].Sinthanayothin, J. F. Boyce, H. L. Cook and T.H. Williamson, “Automated location of the optic disk, fovea ,and retinal blood vessels from digital color fundus images”, British Journal of Ophthalmology, Vol. 83,

- No. 8, 1999, pp.902-910. Journal of Cognitive Neuroscience, Vol. 3, No. 1,1991, pp. 70-86.
- [4].Zhitao Xiao,Jun Wu, Qian Zhao and Jiangtao Xi “Diabetic Retinopathy Fundus Image Processing Based on Phase Information,” IEEE International Conference on Control, Automation and Systems Engineering (CASE),2011.
- [5].Istvan Lazer and Andras Hajdu, “Microaneurysm detection in retinal images using a rotating cross-section based model,” IEEE International Symposium on Biomedical Imaging: From Nano to Macro, 2011.
- [6].Noronha, K. and Prabhakar Nayak, K. “Fundus image analysis for the detection of diabetic eye diseases-a review,” IEEE International Conference on Biomedical Engineering (ICoBE), 2012.
- [7].Yagmur, F.D. Karlik, B. and Okatan, A. “Automatic recognition of retinopathy diseases by using wavelet based neural network,” First International Conference on The Applications of Digital Information and Web Technologies, 2008. ICADIWT 2008.
- [8].Kumari, V.V Suriyaharayananm, N. and Saranya, C.T. “Feature Extraction for Early Detection of Diabetic Retinopathy,” International Conference on Recent Trends in Information, Telecommunication and Computing (ITC), 2010.
- [9].E. Candès, L. Demanet, D. Donoho and L. Ying, “Fast Discrete Curvelet Transforms,” *Unpublished*.
- [10]. Miri M S, Mahloojifar A, “A Comparison Study to Evaluate Retinal Image Enhancement Techniques,” *IEEE International Conference on Signal and Image Processing Applications*, pp. 90-94,2009.
- [11]. Hoover,V.Kouznetsova, and M. Goldbaum,”Locating blood vessels in retinal images by piecewise threshold probing of a Matched filter response,” *IEEE Trans. Med. Imaging*, vol. 19, no. 3, pp. 203-210, 2000.
- [12]. T.S. Lin, M.H. Du, and J.T. Xu, “The Preprocessing of subtraction and the enhancement for biomedical image of retinal blood vessels,” *J.Biomed. Eng.*, vol. 20, no. 1, pp. 56-59, 2003.
- [13]. John B. Zimmerman Stephen M Pizer, Edward V.Staab,J.Randilph Perry, William Mccartney and Bradley C.Brenton, “An Evaluation of the Effectiveness of Adaptive Histogram Equalization for Contrast Enhancement,” *IEEE Transaction on Medical Imaging* Vol 7, No.4 December 1988.
- [14]. Y.-T. Kim Contrast Enhancement Using Brightness Preserving Bi-Histogram Equalization Contrast Enhancement Using Brightness Preserving Bi-Histogram Equalization yeong-taekgi

- member, IEEE
- [15]. Zimmerman, JB, SB Cousins, ME Frisse, KM Hartzell, MG Kahn, "A Psychophysical Comparison of Two Methods for Adaptive Histogram Equalization", *J. Dig. Im.*, 2(3), 1989.
- [16]. J.J. Kanski, Clinical Ophthalmology: A Systematic Approach, London, Butterworth - Heinemann, 1989.
- [17]. J. H. Hipwell, F. Strachan, J. A. Olson, K. C. McHardy, P.F. Sharp, and J.V. Forrester, "Automated detection of micro aneurysms in digital red-free photographs: A diabetic retinopathy screening tool," *Diabetic Med.*, vol. 17, no. 8, pp. 588–594, 2000
- [18]. Saiprasad Ravishankar, Arpit Jain, A.M. 2009. Automatic feature extraction for early detection of diabetic retinopathy in fundus images. CVPR.
- [19]. R. Phillips, J. Forrester, and P. Sharp, "Automated detection and quantification of retinal exudates," *Graefe's Arch. Clin. Exp. Ophtalmol.*, vol. 231, pp. 90–94, 1993.
- [20]. Rubina Khan and Madki M R, "Comparison and analysis of various histogram equalization techniques," *International Journal of Engineering Science and Technology (IJECT)* ISSN:0975-5462, Vol.4 No.4 April 2012.
- [21]. Mohammad SalehMiri and Ali Mahloojifar, "A Comparison study to evaluate retinal image Enhancement techniques," *IEEE International Conference on Signal and Image Processing Applications.*, 2009.
- [22]. Yeong-Taeg Kim, "Contrast enhancement using brightness preserving bi-histogram equalization," *IEEE Transaction Consumer Electronics*, vol.43,no.1, pp. 1-8, Feb. 1997.
- [23]. Yu Wan, Qian Chen and Bao-Min Zhang, "Image enhancement based on equal area dualistic sub-image histogram equalization method," *IEEE Transactions Consumer Electronics*, vol.45, no. 1, pp. 68-75, Feb.
- [24]. K. Zuiderveld Contrast Limited Adaptive Histogram Equalization. P. Heckbert *GraphicsGems IV*, Academic Press 1994, ISBN 0-123361559.
- [25]. Sandeepkumar and Puneet Verma, "Comparison of Different Enhanced Image Denoising with Multiple Histogram Techniques," *International Journal of Soft Computing and Engineering (IJSCE)* ISSN: 2231-2307, Vol.2 May 2012.
- [26]. <http://messidor.crihan.fr/description-en.php>

- [27]. Heechang Kim, Sangjun Park, Jin Wang, Yonghoon Kim, JechangJeong, “Advanced Bilinear image interpolation based on edge features” First International Conference on advances in Multimedia-2009.
- [28]. P.Rajavel “Image Dependent Brightness Preserving Histogram Equalization”, IEEE Transactions on Consumer Electronics, Vol. 56, No. 2, May 2010.

Analysis of Classification Techniques for Microarray Cancer data using Support Vector Machines

Arunkumar.C¹, Dr.Ramakrishnan.S²

¹Department of Information Technology, Amrita Vishwa Vidyapeetham, Coimbatore

²Department of Information Technology, Dr.Mahalingam College of Engineering Technology, Pollachi.

c_arunkumar@cb.amrita.edu, ram_f77@yahoo.com

Abstract

Classification is a prediction or learning problem in data mining. Given a collection of records called the training set, the goal of classification is to find a model that should be capable of assigning the given data set into different classes as accurately as possible. In this paper, an analysis of different classification techniques using Support Vector Machines based on microarray cancer data is presented. The data set chosen for this analysis is the microarray gene expression data which is a set of 7086 and 7457 different genes of 4 persons and 18 persons suffering from adenoma/carcinoma Cancer (abnormal) and 4 and 18 persons (normal) respectively. The results are analyzed based on all the genes and also based on the prominent genes based on Feature selection approach. The classification rate is higher when a few hundred genes are considered than thousands of genes.

Keywords-classification,microarray, gene expression data, distance measure, proximal SVM, Newton SVM

1. Introduction

1.1 Motivation

Cancer medically known as malignant neoplasm covers a broad group of diseases caused by unregulated growth of the cells. There are about 200 different types of cancers that occur in humans [6]. According to a recent survey conducted in India, the three most fatal cancers are oral, stomach and lung cancer [7]. There were about 5 lakh deaths in 2010 due to cancer in India. Some of the ways to reduce the cancer deaths are to reduce the use of tobacco related products and also to devise mechanisms to detect cancer at the early stages itself. In the area of research, the major issues of focus are on the agents that cause genetic changes in cells, precise nature of the genetic damage and the set of affected genes and the consequences of genetic changes in the cell biology that may lead to the progress of cancer. The main motivation of this analysis is to detect the kind of genes that are responsible for the cause of cancer and in turn to reduce the mortality rate caused by cancer.

2. Classification Methods

Classification methods are broadly classified into Supervised Classification and Unsupervised classification.

2.1 Supervised and Unsupervised Classification

Supervised classification is the process of performing classification based on predefined categories (training set) and it maps the results of classification to predefined classes. Labeling is the key to supervised classification. The task in supervised learning is to search for patterns and construct mathematical models. In the unsupervised classification technique, there is no labeling done. Infact labeling needs to be done automatically. It tries to find the hidden structure in unlabeled data. Classification in an unsupervised environment is done based on

the content and the taxonomy is created “on-the-fly”. There is no apriori knowledge available on the data set. Supervised classification tries to find the connection between two sets of observations. The difficulty of the learning task increases exponentially in the number of steps between the two sets and that is why supervised learning cannot, in practice, learn models with deep hierarchies. In unsupervised learning, the learning can proceed hierarchically from the observations into even more abstract levels of representation. Each additional hierarchy needs to learn only one step and therefore the learning time increases (approximately) linearly in the number of levels in the model hierarchy [14]. Several Classification methods exist. The pictorial representation of the traditional classification methods is shown in Fig 1:

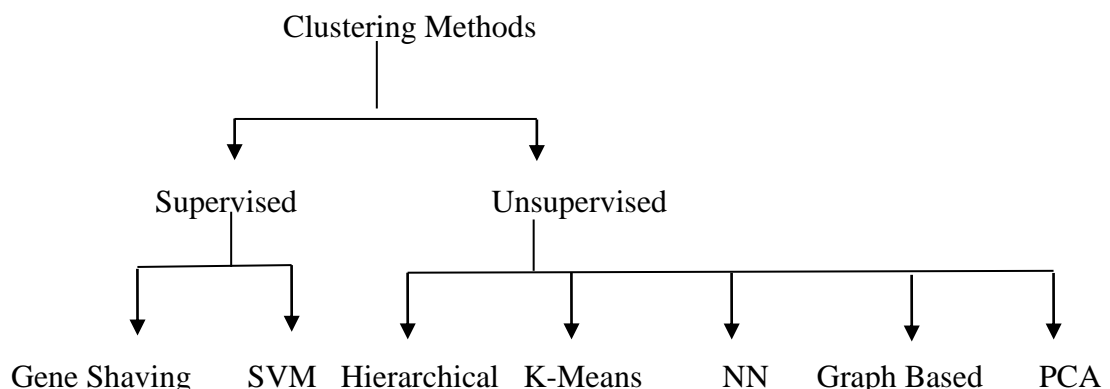


Figure 1. Traditional Methods of Classification

2.1.1 Support Vector Machines

The Support Vector Machines (SVM) is a supervised learning technique. The classification process takes place based on the reference vectors that are known in advance. Gene expression vectors are mapped from the expression space to a higher level feature space. The distance measurement is based on

the mathematically based kernel function which then performs the process of classification and clustering. If the kernel function is not chosen properly, SVM will not be able to find an optimal separating hyperplane in feature space. SVM is linear since it makes use of the hyperplane to separate the two distinct classes. The

separating hyperplanes are selected so that the margin between the separating surfaces that split the positive and negative feature vector space is maximum. This is done to avoid overfitting. After the separating hyperplanes are selected, then the computational burden gets reduced greatly as the computation of the decision function involves the inner dot product of the points in the feature space. The advantage of SVM is that it is possible to train a non-linear, generalizable set with a small training data set. It exhibits robust performance even under noisy conditions for multiple biological analysis data. The disadvantages of SVM are the computational complexity involved in the training, selection of the kernel function and other parameters [2][10].

3. Implementation Using Support Vector Machines

3.1 Princeton Gene Expression Project Cancer Data

The Princeton Gene Expression project microarray data is used for this comparative study. The dataset used are the Adenomas cancer data and carcinoma Normal Data. The Adenoma Cancer Data file consists of 8 columns of data. The first four columns represent the gene expression levels of patients with Cancer and the next four columns represent the gene expression levels of patients without cancer (normal patients). A total of 7086 different genes are taken into consideration. Adenoma is benign tumor of glandular origin. There is a possibility that they could progress to malignant form if left untreated for in the early stages. Similarly in the second data set used for the study, the

carcinoma (cancer) normal data contains records of 18 patients suffering from cancer and data of 18 normal patients. The dataset contains a wide variety of data ranging from 10% to 100% of tumorous genes. It also contains the data of both male and female. The age group of the patients analyzed ranges from 35 to 85. The data present in the dataset are unprocessed data meaning they are not normalized to any scale.[16]

3.2 Feature Extraction

The data that is taken from the Princeton microarray database is raw data. This dataset contains thousands of gene information. Out of the thousands of different genes available for analysis, only a few hundred genes contain relevant information to identify whether a tissue is cancerous or not [3]. In order to extract the features, we use a specific algorithm as in [20]. The sample results are tabulated as under in Table 1. The different steps followed to extract the relevant genes are:

1. Obtain the mean of the expression values for each gene of cancerous samples and mean of the expression values for each gene of normal samples.
2. Obtain absolute difference between the mean of cancerous samples and the mean of normal samples.
3. Arrange the genes based on absolute difference in decreasing order.
4. Select Top 250 genes.

5. Apply the following formula on selected 250 genes.

$$F(x_i) = (\mu(\text{cancerous}) - \mu(\text{normal})) / (S(\text{cancerous}) + S(\text{normal}))$$

where μ is the mean and S is the standard deviation.

6. Select 200 genes with highest absolute $F(x_i)$ scores as our top features.

Table 1. Sample Dataset of Feature Extraction

Normal(1)	Normal(2)	Normal(3)	Normal(4)	Mean	STDEV	Abs Diff of Mean	Add STDEV	Abs Diff/ADD STDEV
361.29	592.04	471.38	444.27	467.2443	95.47043	361.9600576	3.3983986	106.5090065
705.59	771.65	749.92	656.48	720.9075	50.99847	663.1135372	11.070606	59.89857464
227.26	436.65	306.94	239.33	302.5489	96.03305	220.0679359	5.0084692	43.93916138
627.40	1130.35	755.90	952.49	866.5361	220.9145	1211.311171	36.720799	32.98705939
-31.08	-61.10	-127.56	-306.19	-131.483	123.2531	159.6310716	5.0144411	31.83426966

3.3 Classification using Proximal Support Vector Machines

The genes selected from Feature Extraction are fed as the input to the Proximal SVM. A standard support vector machine performs classification by assigning the given input sequence to one of the two disjoint half spaces and the points are classified by assigning them to the closer of the two planes in feature space. Also a standard SVM consumes a large amount of computational time to solve a linear or quadratic equation. In Proximal Support Vector Machine (PSVM), also termed as regularized least squares is a simple and efficient algorithm to perform classification on larger datasets [10]. The proximal SVM takes a matrix A as the input, the variable d which takes one of the two values 1 or -1. The positive sign indicates cancerous genes and a negative sign indicates non-cancerous genes. The variable 'k' represents the folding factor. The variable 'nu' is the weighting factor that takes as input any value as -1, 0 or any other number. The value -1 indicates easy

estimation, 0 indicates hard estimation. The default value of 'nu' is 0. The mandatory variables in this algorithm are A , d and k . [6][7]

Our first experiment involves the use of 300 different genes from the Adenoma Cancer Set and also the simultaneous use of all the 7086 genes of the Adenoma Cancer dataset. The experiment involves the data of 4 patients suffering from cancer and 4 normal patients. The input matrix A involves 300 rows of gene data where the first 150 genes represents the values of genes of patients suffering from cancer and the value of ' d ' is fixed as 1. The subsequent 150 genes represents the gene data of normal patients and the value of ' d ' is fixed as -1. Similarly the input matrix A involves 14172 rows of gene data where the first 7086 genes represents the values of genes of patients suffering from cancer and the value of ' d ' is fixed as 1. The subsequent 7086 genes represents the gene data of normal patients and the value of ' d ' is fixed as -1. The value of ' k ' is assumed to be 1, 3, 5 and 8 for comparison

purposes. The algorithm uses a 3-fold method (if $k=3$) where the input data set is split into 3 sets and the cross validation is performed on

the dataset. This would improve the accuracy of the training and the testing dataset. The results are pictorially represented as under:

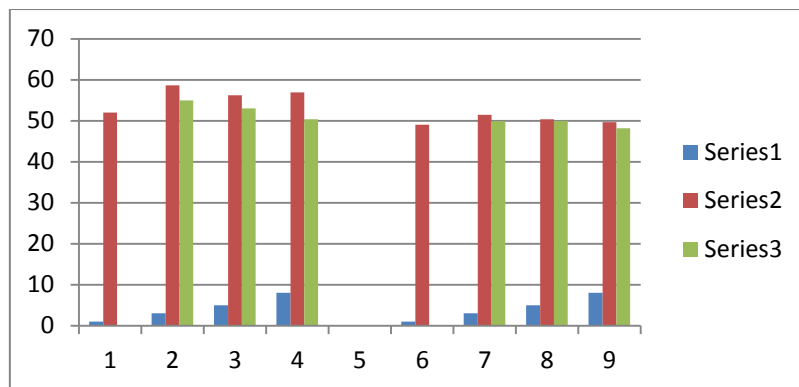


Figure 2. Results of PSVM on adenoma (percentage)

It can be clearly noticed from the above diagram that the training and classification accuracy is higher in the left side of the diagram than the right side. The left side of the Figure 2 is obtained by taking into account the most significant 300 genes after the feature selection process whereas the right side of Figure 2 is obtained by using all 14172 genes to train and test the classifier. Since the value of k is 1 in the first case, the entire dataset was used for training purposes. Hence the value of testCorr in the above diagram is 0.

Our second experiment involves the use of 7457 different genes from the Carcinoma Dataset. The experiment involves the data of 18 patients suffering from tumor and 18 normal patients. The input matrix A involves 300 rows of gene data where the first 150

genes represents the values of genes of patients suffering from cancer and the value of 'd' is fixed as 1. The subsequent 150 genes represent the gene data of normal patients and the value of 'd' is fixed as -1. Similarly the input matrix A involves 14914 rows of gene data where the first 7457 genes represents the values of genes of patients suffering from cancer and the value of 'd' is fixed as 1. The subsequent 7457 genes represents the gene data of normal patients and the value of 'd' is fixed as -1. The value of ' k ' is assumed to be 1, 3, 5 and 8 for comparison purposes. The algorithm uses a 3-fold method (if $k=3$) where the input data set is split into 3 sets and the cross validation is performed on the dataset. This would improve the accuracy of the training and the testing dataset. The results are pictorially represented as under

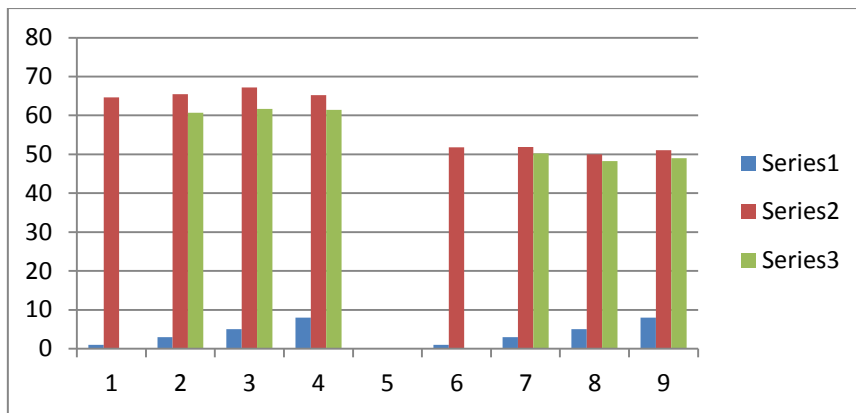


Figure 3. Results of PSVM on Carcinoma(percentage)

It can be clearly noticed from the above diagram that the training and classification accuracy is higher in the left side of the diagram than the right side. The left side of the Figure 3 is obtained by taking into account the most significant 300 genes after the feature selection process whereas the right side of Figure 3 is obtained by using all 14914 genes to train and test the classifier. Since the value of k is 1 in the first case, the entire dataset was used for training purposes. Hence the value of testCorr in the above diagram is 0.

3.4 Classification using Finite Newton Method for Lagrangian Support Vector Machines

A standard support vector machine performs classification by assigning the given input sequence to one of the two disjoint halfspaces and the points are classified by assigning them to the closer of the two planes in feature space.

Also a standard SVM consumes a large amount of computational time to solve a linear or quadratic equation. In Newton Support Vector Machine (NSVM), is a simple and efficient algorithm to perform classification on larger datasets [18][23][24]. This algorithm converges in a maximum of 6 to 7 iterations. The Newton SVM takes a matrix A as the input, the variable d that takes one of the two values 1 or -1. The positive sign indicates cancerous genes and a negative sign indicates non-cancerous genes. The variable ‘k’ represents the folding factor. The variable ‘nu’ is the weighting factor that takes as input any value as -1, 0 or any other number. The value -1 indicates easy estimation, 0 indicates hard estimation. The default value of ‘nu’ is 0. The mandatory variables in this algorithm are A ,d and k.

The same dataset as used in the first experiment of PSVM is used here. The results are pictorially represented as under:

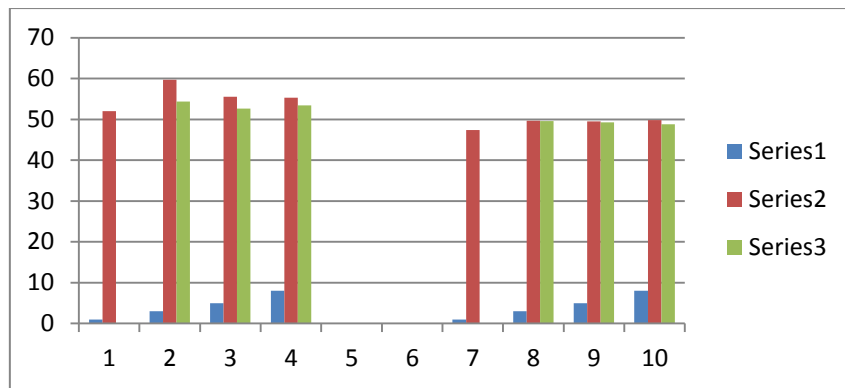


Figure 4. Results of NSVM on Adenoma(percentage)

It can be clearly noticed from the above diagram that the training and classification accuracy is higher in the left side of the diagram than the right side. The left side of the Figure 4 is obtained by taking into account the most significant 300 genes after the feature selection process whereas the right side of Figure 4 is obtained by using all 14172 genes

to train and test the classifier. Since the value of k is 1 in the first case, the entire dataset was used for training purposes. Hence the value of testCorr in the above diagram is 0.

The same dataset used in the second experiment in PSVM is used here. The results are pictorially represented as under:

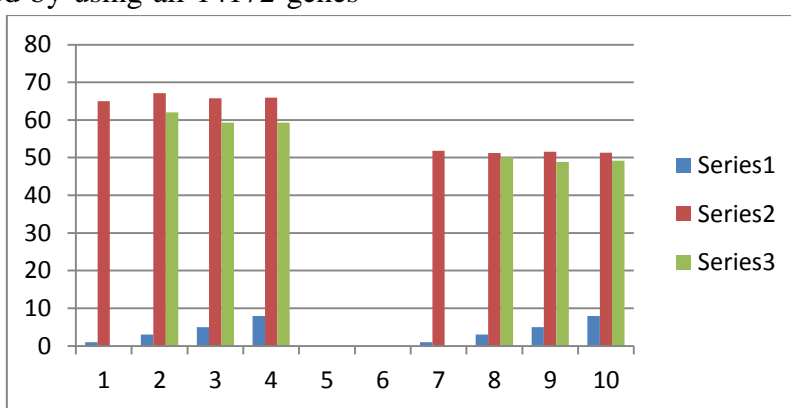


Figure 5. Results of NSVM on Carcinoma (percentage)

It can be clearly noticed from the above diagram that the training and classification accuracy is higher in the left side of the diagram than the right side. The left side of Figure 5 is obtained by taking into account the most significant 300 genes after the feature selection process whereas the right side of Figure 5 is obtained by using all 14914 genes to train and test the classifier. Since the value

of k is 1 in the first case, the entire dataset was used for training purposes. Hence the value of testCorr in the above diagram is 0.

4. Results And Discussion

The results of PSVM and NSVM on the Adenoma and Carcinoma Dataset is tabulated in Table 2. It shows the results for different

values of k applied on the feature extracted dataset and the entire dataset. It is clearly evident from the table that the training and

testing correctness for the Feature Extracted Data set are much better than using the entire dataset for training and testing.

Table 2. Results of Classification using PSVM and NSVM

ADENOMA - PSVM								
Dataset Type	Feature Extracted Dataset				Entire Dataset			
Value of K	K=1	K=3	K=5	K=8	K=1	K=3	K=5	K=8
Training Correctness	52	59.1667	57.4167	55.6178	48.4053	50.7056	49.1798	49.7924
Testing Correctness	0	54.6667	51	52.3826	0	50.6139	49.0685	48.3135
CARCINOMA - PSVM								
Dataset Type	Feature Extracted Dataset				Entire Dataset			
Value of K	K=1	K=3	K=5	K=8	K=1	K=3	K=5	K=8
Training Correctness	64.6667	69.3333	65.9167	65.333	51.8104	51.3275	50.7577	51.1523
Testing Correctness	0	60	60.6667	59.3439	0	50.4494	48.6053	48.3906
ADENOMA - NSVM								
Dataset Type	Feature Extracted Dataset				Entire Dataset			
Value of K	K=1	K=3	K=5	K=8	K=1	K=3	K=5	K=8
Training Correctness	52	57.8333	56.4167	55.142	48.9275	51.3971	50.2505	50.6078
Testing Correctness	0	49.3333	49	52.3115	0	50.3528	49.1109	49.4497
CARCINOMA - NSVM								
Dataset Type	Feature Extracted Dataset				Entire Dataset			
Value of K	K=1	K=3	K=5	K=8	K=1	K=3	K=5	K=8
Training Correctness	65	66.8333	65.6667	65.5237	51.8104	50.7376	51.2303	51.4205
Testing Correctness	0	61	64.6667	61.3442	0	49.1686	49.1553	49.2425

5. Conclusion

The two classification techniques of Support Vector Machines namely Proximal SVM and Newton SVM for two different microarray datasets are analyzed. The maximum accuracy of the training and testing dataset is found to be 67%. The output of the classifiers clearly depicts that all human genes are not responsible for the cause of cancer. Subsets of genes from the larger dataset are responsible for cancer. The key to identifying and classifying cancer is the feature selection process that selects a subset of genes based on ranking and then the feature rich genes are fed as input to the classifier which trains and tests the data based on the specific algorithms. Further techniques/ensemble methods can be used to increase the accuracy of classification of the Support Vector Machines.

Supervised techniques produce better results than non-supervised techniques because the knowledge of the training data set is available. The undeterministic character of the several clustering algorithms also makes them unreliable. The main challenge is to find the distance/proximity measure. Gene expression data contains a lot of clusters that are highly connected. The algorithms should be capable of handling these situations. The algorithms should also be able to operate under a noisy environment as most of the gene expression data that is captured would contain noise[25]. The performance and validation of other techniques that would also involve the use of ensemble methods will be presented in the future publications.

6. References

[1] Yang, A.C.; Hui-Huang Hsu; Ming-Da Lu, Applying gene ontology to microarray gene expression data analysis,

International Conference on System Science and Engineering, 421-426, 2010

- [2] Tang, Yuchun; Zhang, Yan-Qing; Huang, Zhen, Development of Two-Stage SVM-RFE Gene Selection Strategy for Microarray Expression Data Analysis, IEEE/ACM Transactions on Computational Biology and Bioinformatics, Vol 4, Issue 3, 365-381, 2007
- [3] Huang, D.; Chow, T.W.S.; Ma, E.W.M.; Jinyan Li, Efficient selection of discriminative genes from microarray gene expression data for cancer diagnosis, IEEE Transactions on Circuits and Systems, Volume 52, Issue 9, 1909-1918, 2005
- [4] Maji.P, Mutual Information-Based Supervised Attribute Clustering for Microarray Sample Classification, IEEE Transactions on Knowledge and Data Engineering, Volume 24, Issue 1, 127-140, 2012
- [5] Lei Yu; Yue Han; Berens, M.E. , Stable Gene Selection from Microarray Data via Sample Weighting, IEEE/ACM Transactions on Computational Biology and Bioinformatics, Vol 9, Issue 1, 262-272, 2012
- [6] Ghorai, S.; Mukherjee, A.; Sengupta, S.; Dutta, P.K., Cancer Classification from Gene Expression Data by NPPC Ensemble, IEEE/ACM Transactions on Computational Biology and Bioinformatics, Vol 8, Issue 3, 659-671, 2011
- [7] Guang-bin Huang; Hongming Zhou; Xiaojian Ding; Rui Zhang, Extreme Learning Machine for Regression and Multiclass Classification, IEEE Transactions on Systems, Man, and



- Cybernetics, Part B: Cybernetics, Vol 42, Issue 2, 513-529, 2012
- [8] <http://en.wikipedia.org/wiki/Cancer>
- [9] <http://www.ncbi.nlm.nih.gov/pubmed/22460346>
- [10] <http://bioinfo.mbb.yale.edu/mbb452a/intro>
- [11] Cluster Analysis an introduction for marketing, media and public affairs analyst, IPSOS Strategic Marketing, October 2009
- [12] Joe Assouline, "Clustering strategies and other descriptive statistics applications"
- [13] http://home.dei.polimi.it/matteucc/Clustering/tutorial_html/
- [14] http://users.ics.aalto.fi/harri/thesis/valpola_thesis/node34.html
- [15] Miao Li, Biao Wang, Zohreh Momeni, and Faramarz Valafar, "Pattern Recognition Techniques in Microarray Data Analysis", Proceedings of the International Conference on Mathematics and Engineering Techniques in Medicine and Biological Sciences 2002, Las Vegas, Nevada, June 24-27, 2002, Pages 610-616
- [16] <http://genomicspubs.princeton.edu/oncology/>
- [17] Glenn Fung and Olvi L. Mangasarian, "Proximal Support Vector Machine Classifiers"
- [18] Glenn Fung & O. L. Mangasarian, "Finite Newton Method for Lagrangian Support Vector Machine Classification"
- [19] Feng Chu and Lipo Wang, "Applications of Support Vector Machines to Cancer

- classification with microarray data", International Journal of Neural Systems, Vol. 15, No. 6, 475–484, 2005
- [20] Seeja.K.R, Shweta, "Microarray Data Classification Using Support Vector Machine", International Journal of Biometrics and Bioinformatics (IJBB), Volume (5): Issue (1): 2011
- [21] <http://www.ncbi.nlm.nih.gov/books/NBK6624>
- [22] Michael J. Duffy, Zoë D. Kelly, Aedín C. Culhane, Sallyann L. O'Brien and William M.Gallagher, DNA Microarray-Based Gene Expression Profiling in Cancer: Aiding Cancer Diagnosis, Assessing Prognosis and Predicting Response to Therapy, Current Pharmacogenomics, Vol. 3, No. 4, 2005
- [23] Xiong Fu-song, NLSSVM: Least Square Support Vector Machine based on Newton optimization, IEEE International Conference on Computer Science and Automation Engineering (CSAE), 140-144, 2011
- [24] Ruopeng Wang; Hongmin Xu; Hong Shi, Newton's Method for L^∞ Support Vector Machine Via Smoothing technique, Sixth International Conference on Natural Computation, Vol 1, 436-440, 2010
- [25] Mitra, S.; Das, R.; Hayashi, Y., Genetic Networks and Soft Computing, IEEE/ACM Transactions on Computational Biology and Bioinformatics, Vol 8, Issue 1, 94-107, 2011

An Accurate Approach Using Neural Network for Plaque Characterization

C.Ganesh, P. John vivek, S.Sridevi

Department of Electronics and Communication Engineering,

Paavai Engineering College,

Namakkal.

csganesh86@gmail.com, johnvivek2020@gmail.com, balasriya@gmail.com

Abstract

Computer-aided diagnosis (CAD) has become one of the key research subjects in medical imaging and diagnostic radiology. In this paper, Computer-aided diagnosis (CAD) of carotid atherosclerosis into Symptomatic or Asymptomatic or Normal (without plaque) has been proposed. Deposition of plaques results in the hardening of arteries and leads to atherosclerosis, stroke. The success of treatment for stroke depends on the quality of the diagnosis system and also carotid surgery carries risk for the patient. The proposed Diagnosis system can make a factual difference in the treatment of atherosclerotic cardiovascular diseases. Ultrasound imaging is cost effective and affordable and therefore is a excellent choice for image acquisition which is used in this paper. The system involves pre-processing of the ultrasound image which is subjected to feature extraction using DWT technique and significant features are extracted. Selected features are then fed to the neural network classifier for classification. It uses a database of images for training the classifier. Neural networks can handle problems with very many parameters, and they

are able to classify objects well even when the distribution of objects in the N-dimensional parameter space is very complex. It has good classification accuracy with multi classification ability and hence it is preferred.

Keywords – Carotid atherosclerosis, Cardio vascular, Computer aided diagnosis, Neural networks, Discrete wavelet transform.

1. Introduction

Computer Aided Diagnosis (CAD) is a system in medicine that assists doctors in the analysis of medical images. Imaging techniques in X-ray, MRI, and ultrasound diagnostics yield a great deal of information, which the radiologist has to analyze and evaluate comprehensively in a short time. These systems help scan digital images, e.g. from computed tomography, for typical appearances and to emphasize noticeable sections, such as possible diseases. It combines elements of artificial intelligence and digital image processing with radiological image processing. They might become a very important part of clinical workflows and clinical decision making processes for several reasons. First, the use of a CAD system provides an objective second opinion without



the need for a second physician. This can save costs as well as time. Secondly, in contrast to physicians, CAD systems will always offer a constant quality for the decision support. Finally, CAD systems can use multimodal knowledge databases which can comprise more information than any physician could ever keep in mind. Carotid stenosis is a narrowing of the carotid arteries, the two major arteries that carry oxygen-rich blood from the heart to the brain. Also called carotid artery disease, carotid stenosis is caused by a buildup of plaque inside the artery wall that reduces blood flow to the brain. The process of plaque buildup is called atherosclerosis. Carotid stenosis is a major risk factor for stroke and can lead to brain damage. The carotid artery begins at the aorta in the chest as the common carotid and courses up through the neck to the head. Near the larynx, the common carotid divides into the external and internal carotid arteries. The external carotid arteries supply blood to the face and scalp. The internal carotid arteries supply blood to the brain. The most common location of atherosclerotic plaque buildup is the carotid bifurcation, where the common carotid divides into the internal and external carotid arteries. . Normal healthy arteries are flexible and have smooth inner walls. As we age, hypertension and small injuries to the blood vessel wall can allow plaque to build up. Plaque is a sticky substance made of fat, cholesterol, calcium, and other fibrous material. Over time, plaque deposits inside the inner wall of the artery can form a large mass that narrows the lumen, the inside diameter of the artery. Atherosclerosis also causes arteries to become rigid, a process often referred to as "hardening of the arteries." Currently, disease severity and selection of patients to be considered for endarterectomy is based on previous occurrence of clinical

symptoms (e.g., stroke, transient ischemic attack, amaurosis fugax) and the degree of stenosis caused by the plaque. There is a substantiation that carotid endarterectomy in patients with asymptomatic carotid stenosis will reduce the incidence of stroke [1]. Patients with stenosis of less than 50 percent did not benefit from surgery. Patients with severe stenosis (70 percent) had a strong benefit from endarterectomy [2]. Measurement of echolucency, together with the degree of stenosis, will improve the selection of patients for carotid endarterectomy [12]. Ultrasound imaging is a non-invasive medical test that helps physicians spot and treats medical conditions. The most common imaging format for general use is B-mode, in which the image is constructed and displayed on the monitor as a gray-scaled, two-dimensional image or cross-section of the target organ that is moving in real time. In this paper, the classification of carotid in to Symptomatic, Asymptomatic and condition without plaque i.e Normal is achieved by feature extraction using discrete wavelet transform (DWT) and multiclassification is achieved through neural network classifier.

2. Materials And Methods

The block diagram of the proposed system for classification using Discrete wavelet transform based feature extraction and neural network based classification is shown below,

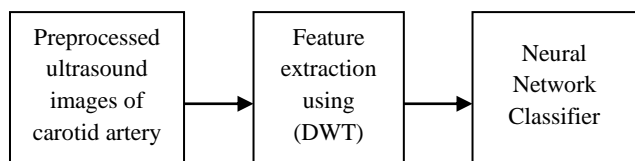


Fig 1: Block diagram of the proposed neural network based classification system for plaque

The ultrasound images of carotid plaque are pre-processed and subjected to feature extraction using DWT technique. The obtained features are fed as input to the Neural Network classifier for multiclassification.

2.1 Carotid plaque ultrasound image acquisition and Preprocessing

Ultrasound imaging, also called ultrasound scanning or sonography, involves the use of a small transducer (probe) and ultrasound gel to expose the body to high-frequency sound waves. Ultrasound is safe and painless, and produces pictures of the inside of the body using sound waves. Ultrasound examinations do not use ionizing radiation (as used in x-rays). It is also cost effective, it is most widely used for diagnosis and hence it is preferred for image acquisition. Database of images with symptomatic, asymptomatic plaque and normal (without plaque) was created. The plaques from patients having retinal or hemispheric symptoms (unstable plaques), such as stroke, transient ischemic attack (TIA), were grouped as symptomatic plaques. Asymptomatic plaques (stable) were from patients who had no stroke symptoms in the past. The unstable plaque has a thin, fibrous cap that contains large number of macrophages and T lymphocytes but small number of Smooth Muscle Cells (SMC) i.e. bottom panel. The stable plaque has a thicker cap with large number of smooth muscle cells and less inflammation (top). This is shown in the Figure 2. The ultrasound images of carotid artery belonging to the cases: Symptomatic, Asymptomatic and Normal (without plaque) are shown in Figure 3. Rupture of the plaque surface, often with thrombosis superimposed, occurs frequently during the evolution of coronary atherosclerotic lesions. It is probably

the most important mechanism underlying the sudden, rapid plaque progression responsible for acute coronary syndromes. Patients with symptomatic carotid artery disease were found to have more frequent plaque rupture, fibrous cap thinning and fibrous cap foam-cell infiltration when compared with the asymptomatic group. Plaque rupture was seen in 74% of asymptomatic plaques and in only 32% of plaques from asymptomatic patients. Fibrous cap thinning was noted in 95% of symptomatic plaques and 48% of asymptomatic plaques. No significant differences were found between the two groups with respect to plaque haemorrhage [3].

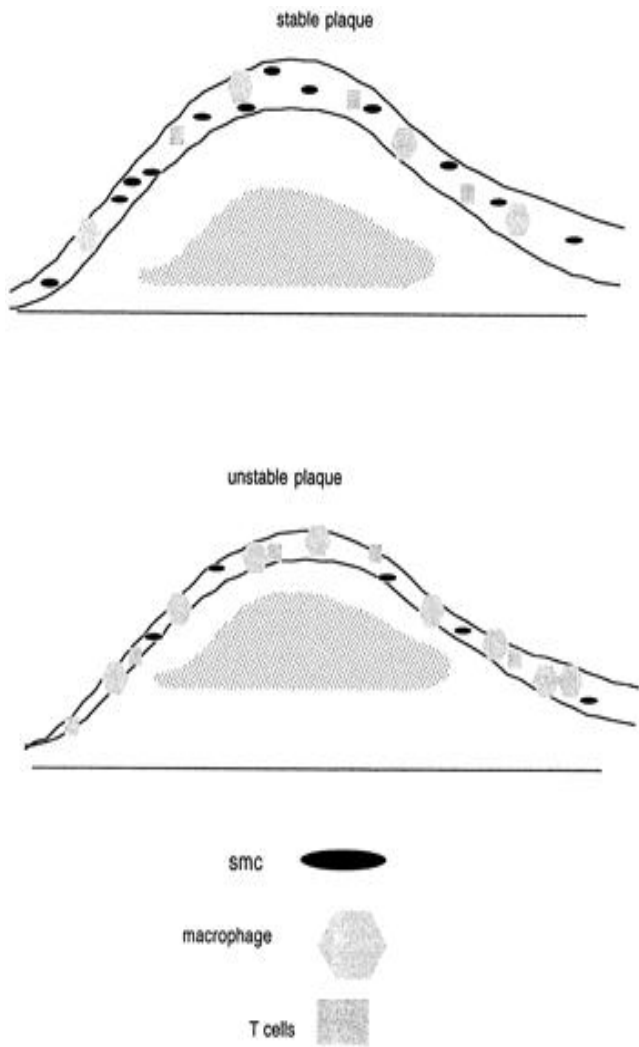


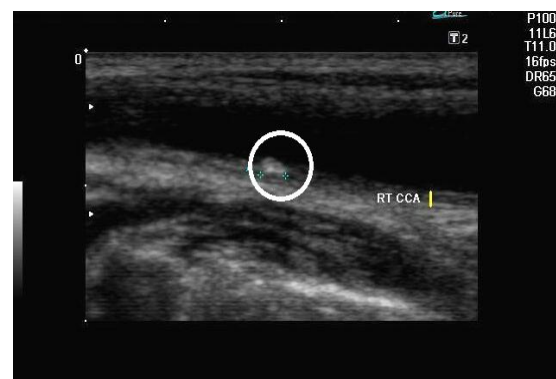
Fig 2: Stable and Unstable plaques

2.1.1 Region Of Interest selection

Region of interest selection plays a vital role to select only those areas where plaque formation takes place typically. It is carried out by a trained medical practitioner before carrying out the feature extraction step. Hence, Region of interest selection is done manually. Selected ROI constitutes only less percentage of image frame. The symptomatic, asymptomatic plaques, normal artery images are shown in the Figure 3(a), 3(b) and 3(c) and their corresponding ROI's are shown in Figure 4.



(a)



(b)



(c)

Fig 3: (a) Symptomatic, (b) Asymptomatic plaques and (c) Normal carotid arteries

2.2 Feature extraction

In image processing, feature extraction is a special form of dimensionality cutback. When the input data to an algorithm is too large to be processed and it is suspected to be disreputably redundant (e.g. the same measurement in both feet and meters) then the input data will be transformed into a condensed representation set of features (also named features vector). Transforming the input data into the set of features is called feature extraction. If the features extracted are carefully chosen it is expected that the features set will extract the relevant information from the input data in order to perform the desired task using this reduced depiction instead of the full size input. When performing analysis of complex data one of the major problems stems from the number of variables involved. Analysis with a large number of variables generally requires a large amount of memory and computation power or a classification algorithm which overfits the training sample and generalizes poorly to new samples.

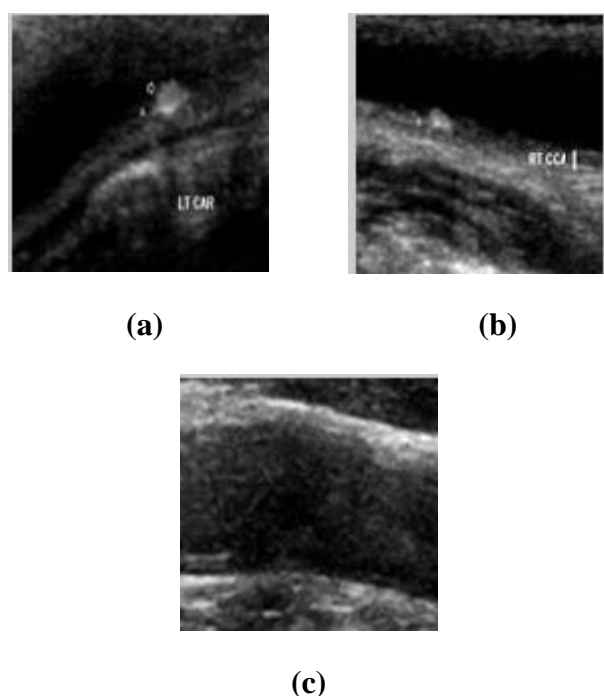


Fig 4:ROI's of (a)Symptomatic, (b)Asymptomatic plaques (c) Normal carotid artery

Feature extraction is a general term for methods of constructing combinations of the variables to get around these problems while still describing the data with sufficient accuracy. 2-D DWT and averaging algorithms are used for feature extraction in this system. The Wavelet Transform, at high frequencies, gives good time resolution and poor frequency resolution, while at low frequencies, the Wavelet Transform gives good frequency resolution and poor time resolution. The wavelet transform (WT) has gained widespread acceptance in signal processing and image compression. Because of their inherent multi-resolution nature, wavelet-coding schemes are especially suitable for applications where scalability and tolerable degradation are important. Wavelet transform, decomposes a signal into a set of basis functions. These basis functions are called wavelets which are obtained from a single prototype wavelet (called mother wavelet by dilations and shifting). The wavelet transform is computed separately for different segments of the time-domain signal at different frequencies. Multi-resolution analysis: analyzes the signal at different frequencies giving different resolutions. MRA is designed to give good time resolution and poor frequency resolution at high frequencies and good frequency resolution and poor time resolution at low frequencies. Good for signal having high frequency components for short durations and low frequency components for long duration .e.g. Images and video frames.

2.2.1 Multi-Resolution Analysis using Filter Banks

Wavelets can be realized by iteration of filters with rescaling. The resolution of the signal, which is a measure of the amount of detail information in the signal, is determined by the filtering operations, and the scale is determined by up sampling and down sampling (sub sampling) operations. The DWT is computed by successive low pass and high pass filtering of the discrete time-domain signal .This is called the Mallat algorithm or Mallat-tree decomposition. The DWT based feature extraction gives better classification results[4].The DWT transform of a signal x is determined by sending the signal through the low-pass filter defined by the transfer function $g[n]$ and the high-pass filter defined by the transfer function $h[n]$. The output of the high-pass filter $D[n]$ is known as the detail coefficients.

$$D[n] = \sum_{k=-\infty}^{\infty} x[k]h[2n - k] \quad (1)$$

The output of the low-pass filter $A[n]$ is known as the approximation coefficients given by,

$$A[n] = \sum_{k=-\infty}^{\infty} x[k]g[2n - k] \quad (2)$$

The 1-D DWT can be extended to 2-D transform using separable wavelet filters. With separable filters, applying a 1-D transform to all the rows of the input and then repeating on all of the columns can compute the 2-D transform. When one-level 2-D DWT is applied to an image, four transform coefficient sets are created. As shown in Figure 5, the four sets are LL, HL, LH, and HH, where the first letter corresponds to applying either a low pass or high pass filter to the rows, and the second letter refers to the filter applied to the columns.

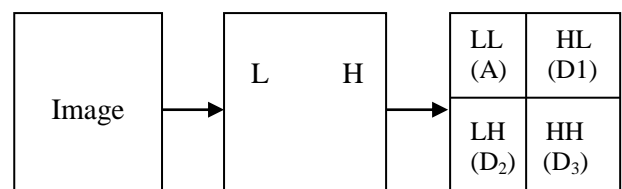


Fig 5: 2D-DWT decomposition Row & Column wise

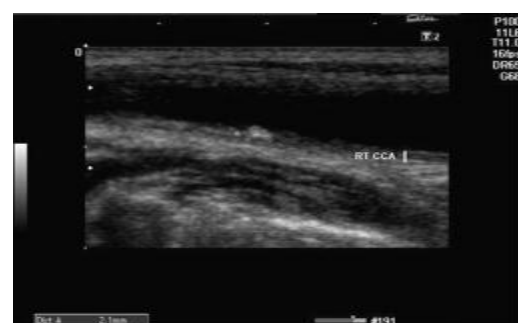
A – Approximated coefficient.

D1 – Detailed coefficient (Vertical: 90 degree)

D2 – Detailed coefficient (Horizontal: 0 degree)

D3 – Detailed coefficient (Diagonal: 45 degree)

The input carotid artery image and its corresponding decomposition levels are shown in the following Figure 6. There are a number of basis functions that can be used as the mother wavelet for Wavelet Transformation. Since the mother wavelet produces all wavelet functions used in the transformation through translation and scaling, it determines the characteristics of the resulting Wavelet Transform.



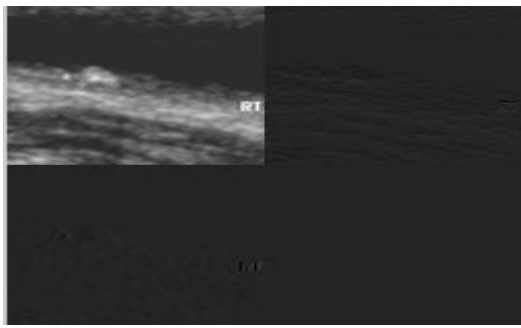


Fig.6: Input image of carotid artery and wavelet transformed image

In the case of the biorthogonal wavelet filters which is used in this paper, the low pass and the high pass filters do not have the same length. The low pass filter is always symmetric, while the high pass filter could be either symmetric or anti-symmetric. The coefficients of the filters are either real numbers or integers.

2.2.2 Feature vectors

2.2.2.1 Covariance (Cov):

Covariance function takes the intensity values along the rows and columns of an image and returns a matrix called covariance matrix. In MATLAB it is computed using the function: cov(x), if x is a vector, it returns the variance of x. For matrix input X, where each row is an observation, and each column is a variable, cov(X) is the covariance matrix.

$$\text{Cov}(x_1, x_2) = E[(x_1 - \mu_1)^*(x_2 - \mu_2)] \quad (3)$$

2.2.2.2 Standard deviation (Sigma, σ):

It represents how much variation exists from the average or mean. A low standard deviation indicates that the data points tend to be very close to the mean whereas high standard deviation indicates that the data points are spread out over a large range of values. In MATLAB if X is a

matrix; Std(X) returns a row vector containing the standard deviation of the elements of each column of X.

$$S = \left(\frac{1}{n-1} \sum_{i=1}^n (x_i - \bar{x})^2 \right)^{\frac{1}{2}} \quad (4)$$

2.2.2.3 Entropy

The entropy or average information of an image can be determined approximately from the histogram of the image. The histogram shows the different grey level probabilities in the image. The entropy is useful, for example, for automatic image focusing: as the state of focusing of an image varies, so does its entropy. It is calculated in matlab for an image using the function entropy (I) returns E, a scalar value representing the entropy of grayscale image I. Entropy is a statistical measure of randomness that can be used to characterize the texture of the input image. Entropy is defined as,

$$-\sum(p.*\log2(p)) \quad (5)$$

Where p contains the histogram counts returned from imhist.

2.2.2.4 Average (Avg):

Takes the average values (intensity) of the feature vectors.

$$\text{Avg}(D_2) = \frac{1}{N*M} \sum_{x=N} \sum_{y=M} |D_2(x, y)| \quad (6)$$

$$\text{Avg}(D_1) = \frac{1}{N*M} \sum_{x=N} \sum_{y=M} |D_1(x, y)| \quad (7)$$

2.2.1.5 Energy (E):

Takes the energy of the intensity values

$$E = \frac{1}{N^2 * M^2} \sum_{x=N} \sum_{y=M} (D_1(x, y))^2 \quad (8)$$

2.3 Classification using Neural Network

Neural network is a mathematical model inspired by biological neural networks. A neural network consists of an interconnected group of artificial neurons, and it processes information using a connectionist approach to computation. In most cases a neural network is an adaptive system that changes its structure during a learning phase. Neural networks are used to model complex relationships between inputs and outputs or to find patterns in data. A neuron is an information-processing unit that is fundamental to the operation of a neural network. Figure 7 shows the basic structure of an artificial neural network. Which consists of set of inputs applied to the nodes, they are processed and weight updation is done to make the actual output equalize with the desired output. Finally the signals from various nodes are summed up and a suitable activation function is applied. The activation function is also referred to in the literature as a squashing function in that it squashes (limits) the permissible amplitude range of the output signal to some finite value. Typically, the normalized amplitude range of the output of a neuron is written as the closed unit interval [0, 1] or [-1, 1].

2.3.1 Back propagation:

Back propagation is a common method of training artificial neural networks so as to minimize the objective function. Arthur E. Bryson and Yu-Chi ho described it as a multi-stage dynamic system optimization method in 1969. It is a supervised learning method, and is a generalization of the delta rule. It requires a dataset of the desired output for many inputs, making up the training set. It is most useful for

feed-forward networks (networks that have no feedback, or simply, that have no connections that loop).

Inputs

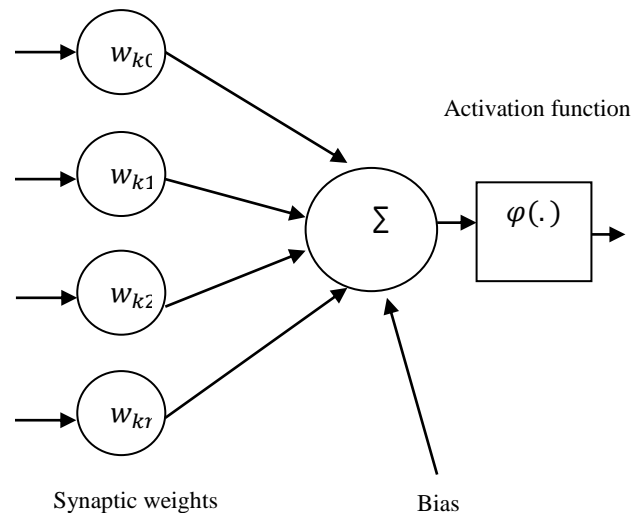


Fig 7: Layered structured of a neural network for classification

This term is an abbreviation for "backward propagation of errors". For better understanding, the back propagation learning algorithm can be divided into two phases: propagation and weight update. Propagation Phase: It involves, forward propagation of a training pattern's input through the neural network in order to generate the propagation's output activations and backward propagation of the propagation's output activations through the neural network using the training pattern's target in order to generate the deltas of all output and hidden neurons. Weight Update Phase: For each weight-synapse multiply its output delta and input activation to get the gradient of the weight, Bring the weight in the opposite direction of the gradient by subtracting a ratio of it from the weight. The sign of gradient vector of a weight indicates where the error is increasing, this is why the weight must be updated in the opposite

direction. Propagation phase and weight update phase are repeated until the performance of the network is satisfactory i.e efficient classification of plaques. The input applied to the neural network are the set of features obtained using discrete wavelet transform and the output of the network is the classification result i.e symptomatic, asymptomatic and normal cases. Initially the neural network is trained with the database of images, then test images are applied for a perfect classification.

3. Classification Performance

Classification performance of the neural network based CAD system is determined by three terms: Accuracy, Sensitivity and Specificity. Accuracy is the measure of percentage of correct classifications. Sensitivity reflects the percentage of symptomatic correctly classified as symptomatic and the Specificity represents asymptomatic correctly classified as asymptomatic. The system is said to have a high performance if both sensitivity and specificity are high. The following Figure8 shows the diagnosis result of the proposed CAD system that classifies the plaque formed in the carotid artery in to Symptomatic, Asymptomatic and Normal cases. The classification result displayed in the message box differentiates the three different plaque cases referred in this paper.

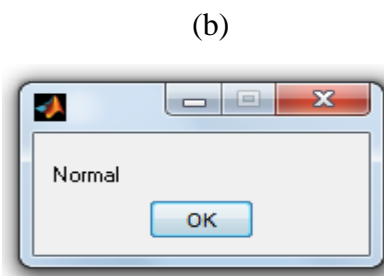
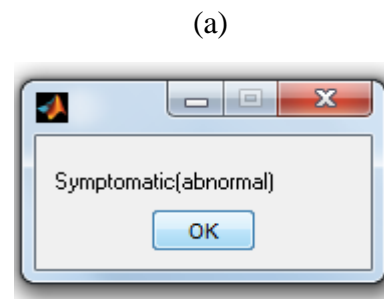
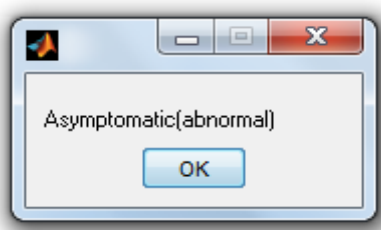


Fig 8: Message box that displays the diagnosis result as (a) Asymptomatic (b) Symptomatic and (c) Normal carotid artery images classification

Table I
Symptomatic, Asymptomatic And Normal Image Features Obtained Using The Feature Extraction Step

Features	Asymptomatic images	Symptomatic images	Normal images
Avg (D1)	0.1003	0.0727	-0.2345
Avg (D2)	0.1852	0.1411	0.2194
Energy	0.0047	0.0051	0.0034
Entropy	0.9979	0.9462	0.2419
Standard Deviation	33.72	28.4137	14.7079
Covariance	167.84	77.81	187.36

The table1 shown above displays the values of various features that are extracted from the Symptomatic, Asymptomatic and Normal carotid artery images. It can be observed form the table that the standard deviation for the asymptomatic image is higher than the other two and so is the value for the entropy. These set of values differ according to the image which is given as the input to the proposed CAD system.

4. Discussion

Classification of carotid atherosclerosis into symptomatic and asymptomatic is very important in case of medical diagnosis. Treatment varies between symptomatic and asymptomatic plaques. So the diagnosis of plaque is very important. The CAD system has to be trained with a database of images (training images) and test images to be diagnosed, which are classified using a neural network as symptomatic or asymptomatic or normal cases. Once plaque is detected, the treatment options to unblock the stenosis include carotid artery stenting (CAS) and carotid endarterectomy In the case of the plaque ROI classification, an accuracy of 83.7% has been registered by the SVM classifier [4]. An another system for the classification of plaque using laws' texture and energy features using neural network classifier is also developed by Mougiakakou [5]. The texture and motion patterns of carotid atherosclerosis features were extracted and fed to a fuzzy C-means classifier for classification into symptomatic and asymptomatic plaques [6].Plaque classification is also done analysing the plaque's structure i.e its morphology [7]. Texture based classification of plaque has achieved a classification accuracy of 73.1% [8]. Another method of classification of

plaque by applying motion analysis on B-mode ultrasound images was proposed by Chan [10].Quantitative analysis of ultrasound images of carotid plaque based on visual classification is presented[11] as the one of the analysis method applied for plaque.

5. Conclusion

In medical image processing the crucial task is to differentiate a normal condition and abnormal condition by carrying out a proper diagnosis which combines digital image processing and artificial intelligence system like neural network. Diagnosing plaques in to symptomatic and asymptomatic is critical in selecting patients for undergoing surgery to remove the plaque. The task of diagnosing plaque involves experienced physicians and radiologists. This manual dependency for diagnosis can be lessened by the use of CAD system discussed in this paper. This CAD system uses DWT for feature extraction (5 features) and neural network for plaque classification. Future work in this regard will deal with the use of some other classifiers and more related features for the classification using other feature extraction techniques. This method of classification in medical imaging can be applicable to the diagnosing of other medical conditions as well and the other future work includes making of the ROI selection to be done automatically instead of a manual selection.

6. Acknowledgment

We would like to thank all the staff members of our college who have helped us by providing the key ideas for the successful completion of this work on plaque classification.

7. References

- [1] S. N. Cohen, J. L. Blackshear, F. L. Silver, J. P. Mohr, B. K. Lal, and J. F. Meschia, "Stenting versus endarterectomy for treatment of carotid-artery stenosis," *New England J. Med.*, vol. 363, no. 1, pp. 11–23, Jul. 2010.
- [2] Henry J.M. Barnett et.all, "Benefit of carotid endarterectomy in patients with symptomatic moderate or severe stenosis," *New England J. Med.*, March 2012.
- [3] S. Carr, A. Farb,W. H. Pearce, R. Virmani, and J. S. Yao, "Atherosclerotic plaque rupture in symptomatic carotid artery stenosis," *J. Vascular Surg.*, vol. 23, no. 5, pp. 755–765, May 1996.
- [4] U. Rajendra Acharya, Oliver Faust, S. Vinitha Sree, Filippo Molinari, Luca Saba, Andrew Nicolaides, and Jasjit S. Suri, Senior Member, IEEE, "An Accurate and Generalized Approach to Plaque Characterization in 346 Carotid Ultrasound Scans", *IEEE transactions on instrumentation and measurement*, vol. 61, no. 4, april 2012.
- [5] Stavroula gr. Mougiakakou, Spyretta golemati, Ioannis gousias,Aandrew n. Nicolaides and Konstantina s. Nikita, "Computer-aided diagnosis of carotid atherosclerosis based on ultrasound image statistics, laws' texture and neural networks", *Ultrasound in Med. & Biol.*, Vol. 33, No. 1, pp. 26–36, 2007.
- [6] Stoitsis J, Golemati S, Nikita KS, Nicolaides AN. "Characterization of carotid atherosclerosis based on motion and texture features and clustering using fuzzy c-means", *Engineering in Medicine and Biology Society, 2004. Vol 1, IEMBS '04.*
- [7] E. Kyriacou, M. Pattichis, C. S. Pattichis, A. Mavrommatis, C. I. Christodoulou, S. Kakkos, and A. Nicolaides, "Classification of atherosclerotic carotid plaques using morphological analysis on ultrasound images," *J. Appl. Intell.*, vol. 30, no. 1, pp. 3–23, 2009.
- [8] C. I. Christodoulou, C. S. Pattichis, M. Pantziaris, and A. Nicolaides, "Texture based classification of atherosclerotic carotid plaques," *IEEE Trans. Med. Imag.*, vol. 22, no. 7, pp. 902–912, Jul. 2003.
- [9] <http://www.mayfieldclinic.com/PE-CarotidStenosis.htm>
- [10] Chan KL. "Two approaches to motion analysis of the ultrasound image sequence of carotid atheromatous plaque". *Ultrasonics* 1993;31: 117–123.
- [11] Wilhjelm JE, Grønholdt MLM, Wiebe B, Jespersen SK, Hansen LK, Sillesen H. "Quantitative analysis of ultrasound B-mode images of carotid atherosclerotic plaque: correlation with visual classification and histological examination". *IEEE Trans Med Imaging* 1998;17:910–922.
- [12] Marie-Louise M. Grønholdt, MD, PhD, Børge G. Nordestgaard, MD, DMSc, Torben V. Schroeder, MD, DMSc, Sissel Vorstrup, MD, DMSc, Henrik Sillesen, MD, DMSc "Ultrasound Echolucent Carotid Plaques Predict Future Strokes", American Heart Association, April 2011.

Real Time Diagnosis of Respiration Rate using Single Lead ECG

K.Ramya¹, V.Kalaivani ²

Computer science & Engineering,

National Engineering College,

Kovilpatti.

ramyaraj25@gmail.com¹,kalai.nec@gmail.com²

Abstract

Respiration rate is the respiratory signal or the respiratory knowledge. The numeral methods are applied to derive a respiratory signal from the ECG. The efficacy of this monitoring method has been improved by deriving respiration and it is previously based on overnight polysomnography studies where patients are stationary or the use of multi lead ECG systems. In this paper, ECG features of Heart rate variability (HRV) and ECG-derived respiration (EDR) including ECG filtering methods are examined using single lead ECG. This ECG features are compared with the simultaneously recorded respiratory signal, it can estimate from the RR-interval, R-wave time duration and R-wave amplitude. The calculated values are evaluated using discrete wavelet transform. The time domain measures like MeanRR, SD_{RR}, Maxrate, Minrate, RMSDD, SDEDR, MeanEDR, pNN50, NN50 values are calculated. The obtain result reflect the Respiration variability (RV). These RV measures are able to differentiate between the first resting period and the periods following the respiration rate.

Keywords – Discrete wavelet transform, Heart rate variability, ECG-Derived Respiration, Respiration Variability.

1. Introduction

Respiration rate is an interesting physiological process. Numeral scheme to obtain a respiratory signal include impedance sensors, pressure sensors and a thermistor in the nose. There are two common disadvantages of using these methods: 1) It is involved might interfere with natural physiological breathing. 2) It is cannot be used for certain clinical purposes, for example, ambulatory or long-term monitoring in naturalistic settings. In clinical perspective, development of the convenient method for record or estimate respiratory signals is important. ECG is the most well-known, feasible, and an accessible tool in diagnostic respiration rate, during ECG recording no extra equipment is needed. The ECG based respiration rate calculation contains the two facts 1) the positions of ECG electrodes on the chest surface move relative to the heart. 2) transthoracic impedance varies at the lungs fill and empty, during the recording of the ECG. The respiration rate calculation mainly based on the two ECG features (i.e) Heart rate variability (HRV) and ECG-derived respiration (EDR). These ECG features are two prominent physiological functions which are both modulated by fluctuations of the autonomic nervous system (ANS). Amendment of these modulations may appear during ageing or during the progress of a disease (e.g. sleep-disordered breathing). The electrocardiogram

(ECG) recording the heart rate time series may be derived with high accuracy and provides a basis to analyze the heart rate variability (HRV). Accordingly, HRV has been used extensively as a non-invasive tool to investigate the autonomic control of the cardiovascular system. Many characteristic features of heart rate variations in health and disease have been discovered in the past and further will be explored. ECG-Derived Respiration measurement method is to monitor the respiration rate from the available ECG sources. The EDR calculation mainly based on the R-wave amplitude, QRS-complex, R-wave time duration and beat to beat interval based calculated.

This paper contains the following sections, the II-section explain the related work of this paper, III-section describe the ECG signal processing, IV-section express the wavelet Techniques and V-section describe the result of this paper.

II. Related work

A constructive appraisal of ECG-derived respiration techniques provides the groups algorithms [11] into categories based on beat morphology, heart rate, or a combination of both. This sector is included on algorithm evaluation, which stresses the importance of comparing the derived respiratory information with a simultaneous recording of the respiration signal. The Fourier transforms and spectral features based EDR values [3] analyzed. Kernel principal component analysis based algorithm is developed [1] which derive the EDR value and this value analyzed using Eigen and entropy value. Principal Component Analysis technique

based three different algorithms derived [10]. These algorithms are mainly used to analysis the ECG-derived respiration. The automatic respiration rate analysis using ambulatory based single lead ECG signal [5], this ECG signal recording mainly based on the holter monitor, it describes the HRV based analysis of respiration rate. The HRV and ECG amplitude values based respiration rate is calculated [2]. The HRV features based the respiration rate is calculated [6]. In this paper, HRV and EDR features based the respiration rate is analyzed by using discrete wavelet transform.

2. Ecg Data Processing

The Figure-1 represents the Real time respiration rate diagnosis system. This system contains the automated de-noising, ECG-derived respiration and Heart rate variability features extraction. This system mainly used to diagnosis respiration rate values.

3.1 ECG- Data collection

The database collection is the one of the most important part in signal processing. We have tested using Physionet Apnea-ECG Database [13]. This database contains totally 35 subjects sleep studies. The ECG signal recordings were visually scored by an expert for sleep apnea/hypopnea events on the basis of respiration per minute basis. This 35 subjects recordings (30 men, 5 women) were arranged in three groups: Group A recordings the 20 subjects with clear occurrence of sleep apnea (100 min or more), Group B (borderline) recordings (five subjects) with some degree of sleep apnea (between 5 and 99 min) and Group C (control) recordings

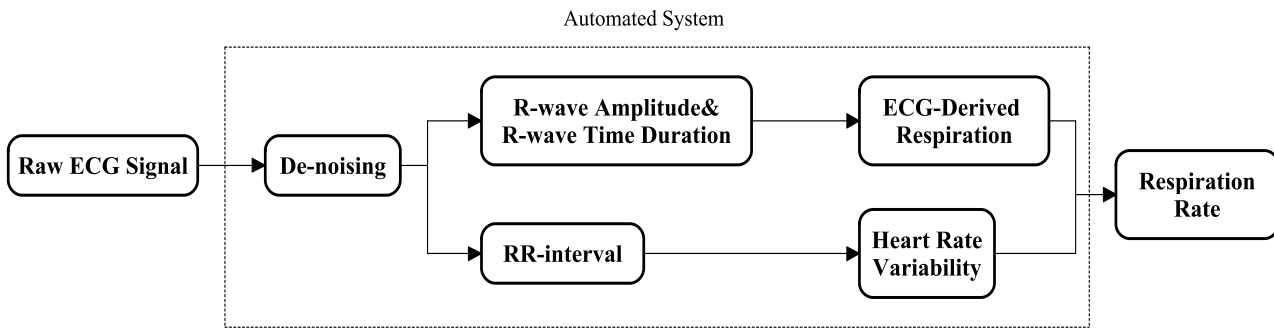


Fig-1: Real time Respiration Rate diagnosis system

3.1.1 Preprocessing of ECG signals

The ECG signal mainly having different types of noise, like frequency interference, baseline drift, electrode contact noise, polarization noise, muscle noise, internal amplifier noise and motion artifacts (Movement of electrode). ECG artifacts are the noise induced to ECG signals that result from movements of the real time electrodes. The most common problems in ECG signal processing is baseline wander removal. The removal of baseline wander is required in the analysis of the real time ECG signal to minimize the changes in beat morphology. The respiration and electrode impedance changes due to respiration are important sources of baseline wander in most types of ECG recordings. The baseline wander of frequency content is usually in a range well below 0.5Hz. The baseline drift can be eliminated without changing or disturbing the characteristics of the waveform. The median filters (200-ms and 600-ms) to eliminate baseline drift of ECG signal [2]. The process is as follows:

- a) The real time ECG signal is processed with a median filter of 200-ms width to remove QRS complexes and P waves
- b) Resulting signal is then processed with a median filter of 600-ms width to remove T waves. ECG signal resulting from the

second filter operation contains the baseline of the ECG signal.

- c) Subtracting the filtered signal from the original signal and a signal with baseline drift can be obtained.

The before and after removal of baseline wander signal sample beats from record No. a01 of Apnea-ECG Database are shown in Fig.2 where X-axis represents number of samples and Y-axis indicates the amplitude of signal in mV.

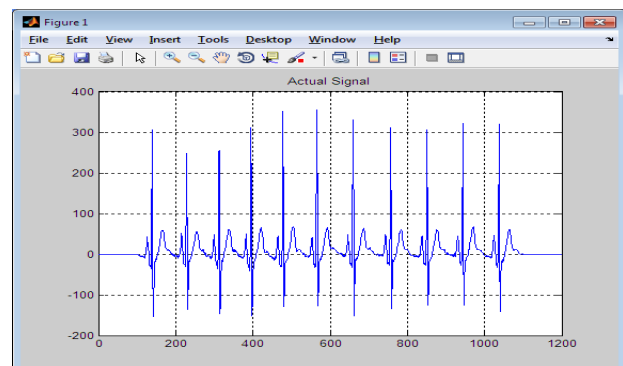


Fig. 2(a): Samples beats from record No.a01

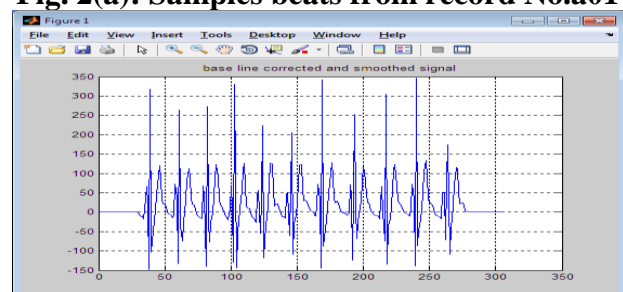


Fig. 2(b): Beats after removal of baseline wander

Wavelet Technique

The wavelet transform (WT) provides a new dimension to signal processing and event detection. The time-frequency localization properties, the wavelet transform is an efficient technique tool for analyzing non-stationary ECG signals. It provides a description of a signal in a timescale domain, analogous to a time-frequency domain, allowing the representation of temporal features at multiple resolutions. The WT is achieved by the decomposition of the signal over dilated (scale) and translated (time) versions of a prototype wavelet. The prototype wavelet function is Mother Wavelet function and it is used for the analytical requirements. The Discrete Wavelet Transform (DWT) Mother wavelet function defined as:

$$\varphi_{a,b} = \frac{1}{\sqrt{a}} \varphi\left(\frac{x-b}{a}\right) \quad a, b \in \mathbb{R}, a > 0 \quad (1)$$

Where

a=coefficient of time translation,

b=coefficient of scale (compression),

X= It is the baseline wander noise removal ECG signal,

R= It is the wavelet space,

The DWT contains number of families like Haar, Daubechies, Biorthogonal, Coiflets, Symlets, Morlet, and Mexican Hat. The Daubechies (DB4) filter has been found to give details more accurately signal features [12],[7],[9]. This wavelet shows similarity with QRS complexes and energy spectrum is concentrated around low frequency noises. The DB4 filter contains number of levels based coefficient values and each level contains the wavelet function. The mother wavelet applied into the four levels of DB4 filter, it is used to calculate the features of the ECG signal. The Fig 3 has shown the coefficient levels of the

DB4 filter. This coefficient level split into two type's approximation coefficient and detail coefficient. The detail level coefficient values are used to calculate the ECG feature value.

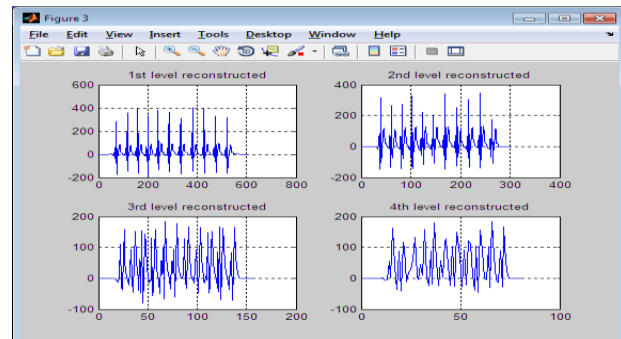


Fig 3: The DB4 filter coefficient levels

4.1 ECG-Derived respiration (EDR)

We evaluated EDR by two methods:

1. Based on the extraction of the R wave amplitude (RWA) after the subtraction of the ECG baseline.
2. Based on the calculation of the R wave duration (RWD), defined in

4.1.1 R-wave Amplitude (RWA)

The R-wave amplitude is calculated by using the five point derivative function [4]. It gives the QRS-complex slope information. The five point derivative with the transfer function is

$$H(x) = (1/8T)(-X^{-2} - 2X^{-1} + 2X^1 + X^2) \quad (2)$$

The amplitude response is

$$|H(\omega T)| = (1/4T)[\sin(2\omega T) + 2\sin(\omega T)] \quad (3)$$

The equation (2) difference response is

$$y(nT) = (1/8T)[-z(nT - 2T) - 2z(nT - T) + 2z(nT + T) + z(nT + 2T)] \quad (4)$$

The frequency response of this derivative (4) gives the slope value of QRS-complex in linear format. The after differentiation process the signal is squared point by point. The equation of this operation is

$$y = [z(nT)]^2 \quad (5)$$

This function makes all data points positive and does nonlinear amplification of the output of the derivative emphasizing the higher frequencies.

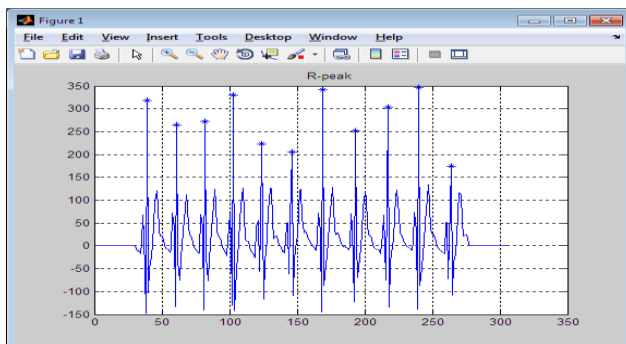


Fig 4(b): Thre R-peak marked value

5. Features Derived From Hrvand Edr

RR-interval is a distance of two successive top R-waves. The EDR is the combination of both Ramp and R-peak values. These values based number of feature parameters are calculated:

- Maximum respiration rate per minute of RR-interval and EDR
- Minimum respiration rate per minute of RR-interval and EDR
- Standard deviation for respiration rate per minute of RR-interval and EDR
- Mean for respiration rate per minute of RR-interval and EDR
- Root of mean of sum of squared difference of adjacent RR-intervals (RMSSD),
- Two pNN50 measures is defined as each NN50 measure divided by the total number of NN value
- The NN50 measure is defined as the number of pairs of adjacent NN where the second respiration rate exceeds the first respiration rate by more than 50 ms

6. Results

The 1-min time duration ECG signal recording represents Figure 2, it is acquired from polysomnogram studies. The ECG signal common noise is removed from the median filter. The ECG signal features are HRV and EDR values are derived from DWT function. The decomposition levels of DB4 filter removes other low frequency noise in the ECG signal (Figure 3). RWA value is calculated from the derivative and squaring function. RWD values are analyzed using Moving window integration and also R-peak value based RR-interval (HRV) values are analyzed. This HRV and EDR value based respiration variability time domain features are RMSSD, Mean, Standard Deviation, Maxrate, Minrate, pNN50 and NN50 calculated. Among 70 acquired database data, five sample patient's ECG features of RR-interval, R-wave amplitude and R-wave time duration are listed as table. RR Interval, R-wave amplitude, R-wave time duration sampled data are listed in Table-1, Table-2, and Table-3 and in those data the first three patients are disease affected time domain features and rest of them are normal time domain features. This respiration rate diagnosis system is supportive to end user and might be commercialized. It does not affect the natural physiological signal. This paper couldn't support the long term monitoring signal. This respiratory variability features gives input to the classification process, hence it provides the acceptable result.

7. Conclusion

The HRV and EDR information is very useful for ECG classification, analysis, diagnosis, and authentication and identification performance. The HRV can also serve as an input to a system that allows automatic cardiac diagnosis. The

main advantage of this kind of detection is less time consumption compared to Holter monitor based ECG signal. Several techniques are used for respiration calculation. The discrete wavelet transform based respiration rate computation gives the precise values. This respiration

variability is mainly used to diagnosis the sleep apnea disease. The future enhancement process of this paper is applied to the respiration variability features to detect the stress testing and Atrial fibrillation disease diagnosis process.

Table 1. Heart rate variability based Time domain features (Seconds)

Patients	MeanRR	MinRR	MaxRR	HR	SDRR	RMSSDRR	NN50	pNN50
1	102.4138	155	167	3.7005	57.9165	57.4150	55	0.9483
2	105.9074	130	206	2.7033	38.3141	37.9577	51	0.9444
3	127.8913	140	309	3.8178	54.5838	53.9872	45	0.9783
4	74.7722	72	85	0.7834	2.6129	2.5959	58	0.6753
5	82.4861	77	88	0.7279	2.1163	2.1015	55	0.7639

Table 2. R-wave amplitude based Time Domain Features (micro volt)

Patients	MeanRamp	MinRamp	MaxRamp	SDRamp	RMSSDRamp	NN50	pNN50
1	0.6830	0.3000	1.2008	0.1110	0.1099	42	0.5636
2	0.6067	0.3045	1.3457	0.1145	0.1135	44	0.5148
3	0.6295	0.4045	1.1188	0.1035	0.1027	44	0.6667
4	0.7804	0.5154	1	0.1246	0.1236	47	0.7581
5	0.7235	0.5022	1	0.1043	0.1036	50	0.8452

Table 3. R-wave Time Duration based Time Domain Features (Seconds)

Patients	MeanRwt	MinRwt	MaxRwt	SDRwt	RMSDRwt	NN50	pNN50
1	43.9661	24	74	20.4560	20.2819	53	0.8983
2	39.1455	15	65	15.7273	15.5837	60	0.8696
3	49.0435	27	80	15.8350	15.7199	60	0.8600
4	60.6250	33	51	10.4497	10.3779	66	0.9041
5	62.9324	37	56	10.1691	10.0934	64	0.9649

8. References

- [1] Defy Widjaja Carolina Varon Alexander Caicedo Dorad Johan A.K. Suykens and Sabine Van Huffel, Fellow. "Application of Kernel Principal Component Analysis for Single-Lead-ECG-Derived Respiration" IEEE Transactions on Biomedical Engineering, 2012, Vol.59 No.4 pp.1169-1176.
- [2] Dirk cysarz, Rroland zerm, Henrik bettermann, Matthias fru" hwirth, Maximilian moser and Matthias kro" z "Comparison of Respiratory Rates Derived from Heart Rate Variability, ECG Amplitude, and Nasal/Oral Airflow", Annals of Biomedical Engineering, Dec 2008, Vol. 36, No. 12, pp. 2085–2094.
- [3] Dorfman Furman G. Shinar Z. Baharav A. and Axelrod S. "Electrocardiogram Derived Respiration during Sleep" IEEE transactions on Computers in Cardiology, 2005, Vol.32, pp.351-354.
- [4] Justin Boyle, Niranjan Bidargaddi, Antti Sarela, and Mohan Karunanithi "Automatic Detection of Respiration Rate From Ambulatory Single-Lead ECG", IEEE transactions on information technology in biomedicine, Nov 2009, vol. 13, no. 6, pp.890-896.
- [5] LingengZhao, S. Reisman, T. Findley, "Respiration derived from the electrocardiogram during heart rate variability studies", Proceedings of the 16th Annual International Conference of the IEEE Biomedical Engineering, Nov 1994, Vol.1 pp. 123-124.
- [6] N.V.Thakor J.G.Webster and W.J.Tompkins, "Estimation of QRS complex power spectra for design of a QRS filter", IEEE Transcations on Biomedical Engineering, Nov1986,Vol.BME-31, no.11, pp.702706.

- [7] P.D.Chazal, C.Heneghan, E.sheridan, R.Reilly, P.Nolan, M. O'Malley, “Automated processing of the single-lead electrocardiogram for the detection of Obstructive sleep apnea”, IEEE Transaction Biomedical Engineering, 2003, 50(6):686-689.
- [8] P.D.Khandait, N.G.Bawane and S.S.Limaye, “Features Extraction of ECG signal for detection of cardiac Arrhythmias”, International Journal of Computer Applications, 2012, pp.6-10.
- [9] T.Penzel, “The Apnea-ECG database Comput.Cardiol”, 2000, Vol.27, pp.255- Philip de Chazal Maria O.Dwyer and Richard B. Reilly, “Automatic Classification of Heartbeats Using ECG Morphology and Heartbeat Interval Features” IEEE transactions on biomedical engineering, 2004, Vol.51, No.4, pp.686-6
- 258.S.Z. MAhmoodabadi, A. Ahmadian and M.D. Abolhasani, “ECG feature Extraction using Daubechies Wavelets”, Proceedings of the fifth IASTED International conference on Visualization, Imaging and Image Processing, 2005, pp. 343-348.
- [10] R. Bailon, L. Sornmo, and P. Laguna, “ECG-derived respiratory frequency estimation,” in Advanced Methods and Tools for ECG Analysis, G. Clifford, F. Azuaje, and P. McSharry, Eds. Norwood, MA: Artech, 2006,pp. 215–244.

Analysis of Heart Rate Variability in Normal Pregnancy and Postpartum

¹Veerabhadrappa S. T,¹ Anoop Lal Vyas,² Sneha Anand

¹ Instrument Design Development Centre

² Centre for Biomedical Engineering

Indian Institute of Technology, New Delhi

veeru.st@gmail.com, alvyas@iddc.iitd.ac.in, sneha@cbme.iitd.ac.in

Abstract

This paper presents the study and comparison of linear and non-linear heart rate variability analysis in normotensive pregnant and postpartum women. The ECG is recorded for 124 pregnant women in all three trimesters and 32 women in postpartum. The HRV analysis is carried out based on its spectral, approximate entropy (ApEn) and correlation dimension (CD). The significant differences are found in the LF/HF ratio, ApEn and CD indices change during pregnancy. It is observed that, in normal pregnancy the LF/HF ratio significantly increases as the pregnancy progresses. The results can be used to quantify the HRV to detect the cardiovascular changes and sympathetic activity in pregnant and postpartum women.

Keywords:

Pregnancy, heart rate variability, Entropy, Correlation Dimension

1. Introduction

It is known that normal pregnancy results in profound maternal hemodynamic changes to adjust to increased volume load [1]. The increased intravascular volume is needed to create utero placental circulation for the developing and growing fetus. This

physiological adaptation in pregnancy is complex, involving cumulative effect of various regulatory organs. The physiological alterations in volume homeostasis and cardiovascular system are together. These changes are detectable at the end of 4 weeks and are nearly complete in the first half of pregnancy. It has been suggested that hemodynamic changes during pregnancy occur through autonomic control mechanisms, but the actual role of the autonomic nervous system during pregnancy is not fully understood [1] [2].

Recent studies have shown that baroreflex control of vasomotor sympathetic activity is similar to those of renal and cardiac sympathetic activity under physiological conditions. The sympathetic activity has found to be increased in women with normal pregnancy and was even greater in hypertensive pregnant women during the third trimester of gestation [3]. In contrast to the sympathetic activation, peripheral vascular resistance was found to be even lower in normal healthy pregnant women during their late pregnancies. These findings suggest that the transduction of sympathetic action into vascular resistance is attenuated during pregnancy. In recent years, the study of cardiac autonomic modulation in human subjects has been greatly facilitated by the

development of computer-based methods for spectral analysis of heart rate variability (HRV) and spontaneous baroreflex (SBR) function [3][4][5].

It is reported that, increased heart rate results in decreased BP during pregnancy [6]. It is also shown that systolic and diastolic blood pressures and augmentation index decrease in normal pregnancy [7].

The researchers have demonstrated that the heart rate variability decreases during pregnancy. The ANS activity shifts from lower vagal to sympathetic modulation in late pregnancy and these alterations occur in early pregnancy in case of Pregnancy Induced Hypertension (PIH), diabetes and preeclampsia. Early detection of lower sympathovagal balance can predict the occurrence of this dysfunction in later stages of pregnancy. The ANS plays an important role in adaptation of the maternal body to nurturing the fetus. It is therefore important to understand the sequential changes in the autonomic nervous activity [4] [5]. It is shown that the sympathetic activity remains unchanged in the first trimester of pregnancy [2]. The increased sympathetic activity during pregnancy can be explained by a true increase in the activity of higher sympathetic centres and the sympathetic activity is somewhat decreased in pregnant women in the case of threatened preterm delivery and immediately before normal delivery [4] [5].

2. Subjects

We performed a cross sectional study involving 25 subjects in the first trimester, 47 in second trimester, 52 in third trimester pregnant women and 32 women in postpartum (within a week). The subjects were consented from the routine antenatal clinic and hospital staff who agreed to participate. All pregnant

women had normal pregnancies. The parameters like maternal age, weight, blood pressure status were recorded. This study was cleared and approved by the bioethical committee. Further all women gave written informed consent for collecting their data. The demographic characteristics of the study population are presented in Table 1.

Table 1: Demographic characteristics of the study population

	I	II	III	Postpartum
Age (Years)	23.11 ±2.96 1	22.09 ±2.29 6	23.06 ±2.86 7	23.74 ±2.661
Weight (kgs)	45.57 ±6.80 1	47.54 ±5.31 6	52.47 ±6.45 8	44.12 ±2.736
Gestational age (weeks)	10.8 ±2.20 3	20.4 ±3.12 5	32.38 ±3.02 4	2.476 ±1.721 days
SBP(mmhg)	116 ±8.13 7	116.1 ±7.32 4	115.7 ±7.50 3	118.4 ±5.448
DBP(mmhg)	76.1 ±5.61	75.02 ±7.49 2	74.4 ±7.40 9	77.97 ±4.601

3. Data Analysis and Methods

The ECGs were recorded using National Instrument's data acquisition card and signal express software from Labview. The signals were recorded at a sampling frequency of 500 Hz with a resolution of 12 bits per sample. The HRV was calculated by measuring the RR interval. The HRV analysis was carried out in frequency domain and using non-linear techniques such as approximate entropy and correlation dimension.

3.1 Frequency domain Analysis

The power spectrum was estimated by parametric method. The HRV spectral power was calculated in very low frequency (VLF), low frequency (LF) and high frequency (HF) components. The VLF represents the power in frequency band (0.0033 - 0.04) Hz. The low frequency (LF) range of (0.04-0.15) Hz has been attributed to the actions of both sympathetic and parasympathetic nervous activities, whereas the higher frequency (HF) range of (0.15- 0.4) Hz is solely due to the parasympathetic nervous activities. The LF/HF ratio was considered to reflect sympathovagal balance. The LF and HF were measured in normalised units and emphasise the controlled and balanced behavior of the two branches of the autonomic nervous system [8][9][10].

3.2 Approximate Entropy (ApEn) analysis

Approximate entropy measures complexity of a time series and is calculated according to the algorithm first proposed by Pincus in 1991[11]. The approximate entropy depends on the two input parameters embedded dimension m and tolerance window r along with the length of the series N . The larger value of ApEn corresponds to more irregular data and lower value of ApEn indicates more similarities in the RR series [8]. The ApEn of each data set can be calculated as follows. For a given signal $x(n) = [RR(1), RR(2), \dots, RR(N)]$, where N is the total number of RR intervals.

- 1) Form m -vectors, $X(1)$ to $X(N-m+1)$ defined by

$$X(i) = [x(i), x(i+1), \dots, x(i-m+1)] \quad (1)$$

where $i = 1, 2, \dots, (N-m+1)$

- 2) Calculate the distance between vectors $X(i)$ and $X(j)$, as the absolute maximum difference between their scalar components.

$$d[X(i), X(j)] = \max_{k=0, m-1} [|x(i+k) - x(j+k)|] \quad (2)$$

- 3) Define a quantity $C_r^m(i)$ for each i , for $i=1, 2, \dots, (N-m+1)$

$$C_r^m(i) = \frac{V^m(i)}{N-m+1} \quad (3)$$

where $V^m(i) = \text{number of } d[X(i), X(j)] < r$

- 4) Calculate $\Phi^m(r)$ by taking natural logarithm of each $C_r^m(i)$ and average it over i as defined in step 2

$$\Phi^m(r) = \frac{1}{N-m+1} \sum_{i=1}^{N-m+1} \ln(C_r^m) \quad (4)$$

Increase the embedded dimension to $m+1$ and repeat the steps 1-4

- 5) Calculate ApEn values for a finite data length

$$ApEn(N, m, r) = \Phi^m(r) - \Phi^{m+1}(r) \quad (5)$$

As mentioned earlier, the calculation of ApEn requires a priori knowledge of two unknown parameters. The embedded dimension length $m=1$ or $m=2$ and tolerance window r was set between 0.15 and 0.25 times the standard deviation of the time series. In most of the studies where ApEn was applied to analyse physiologic signals, the parameters m and r are set according to the Pincus [11]. In our study, we choose value of m as 2 and r as 20% of the standard deviation of the RR series.

3.3 Correlation Dimension (CD) analysis

Correlation dimension is a quantitative measure of the complexity of the deterministic system. Methods based on chaos theory have been applied in tracking HRV signals and predicting the onset events such as Ventricular Tachycardia detecting congestive heart failure situations. Correlation Dimension (CD) is one of the most frequently used measures of fractal dimension. This method gives information on the minimum number of variables required to model the underlying system. The correlation dimension of each data set can be calculated as follows. From a defined RR series ($RR_j; j = 1; 2; \dots; N$) with N points, an m -dimensional phase space is constructed according to Taken's theorem [13] [14], obtaining: $x_n = (RR_n, RR_{n+d}, RR_{n+2d}, \dots, RR_{n+(m-1)d})$ where $n = 1, 2, \dots, (N - (m - 1)d)$, d is the time delay and m is the embedded dimension. Grassberger and Procaccia showed that correlation dimension CD can be obtained from

$$CD = \lim_{r \rightarrow 0} \frac{\log_2 C_m(r)}{\log_2(r)} \quad (6)$$

Where $C_m(r)$ is the correlation summation which measures the number of points x_j that are correlated with each other in a space of radius r . In other words, it measures the space occupied by a set of points. CD is obtained using the distance between each pair of points $d(i, j) = |x_i - x_j|$. With reference to the phase-space plot, X-axis represents the heart rate $X[n]$ while the Y-axis represents the heart rate after a delay $X[n + d]$. Using the minimal mutual information technique, the choice of an appropriate delay can be calculated.

$$C_m(r) = \lim_{N \rightarrow \infty} \frac{2}{N(N-1)} \sum_{n=1}^N \sum_{k=1}^N \theta(r - |x_n - x_k|) \quad (7)$$

Where θ is the Heaviside step function and r is the correlation length. In this study we chosen

$r = 0.2$ times standard deviation of the time series, embedded dimension $m=5$ and delay $d=3$.

4. Results and Discussion

The ECGs were recorded and the complete results for all subjects were included in the analysis. The heart rate of 91.44 ± 7.315 , 93.34 ± 6.812 , 100.8 ± 10.12 and 75.25 ± 7.331 were observed in I, II, III trimester and postpartum respectively. It is seen that there is no significant change in the heart rate from I to II trimester. However significant increase, almost 7.5% was seen from II to III trimester. The heart rate came down appreciably about 25% soon after delivery. Further the HRV analysis were carried out in frequency domain and using non-linear techniques such as approximate entropy and correlation dimension and are presented in the following sections.

4.1 Spectral Analysis

The spectral analysis of heart rate variability techniques are employed to evaluate cardiovascular changes in postpartum and pregnancy. The values of LFnu, HFnu, LFHF ratio in postpartum and during all the three trimesters are as shown in Table 2. The mean and standard deviation of LF, HF and LF/HF ratio are as shown in Fig.1. In the frequency domain, the LFnu increases and HFnu decreases progressively as gestational age increases when compared to the postpartum. The LF/HF ratio was significantly higher during pregnancy than in the postpartum. In normal pregnancy, insignificant change have been observed in LFnu, HFnu and LF/HF ratio in three trimesters ($P=0.3992$). The frequency domain parameters are insufficient to provide insights into the ANS activity during different phases of pregnancy. Our findings are

consistent with an increase in the sympathetic activity of the autonomic nervous system in all the three trimesters of pregnancy. It is reported that, decrease in time domain HRV parameters and there is no change in frequency domain during the pregnancy [2]. However, our findings and observation made by other authors show that the sympathetic activity increases in the first trimester, reaching a maximum at the end of the second trimester [5]. An increase in the sympathetic activity in pregnant women is considered to be caused by chronic stress and due to systemic vasodilatation. In our opinion, the increased sympathetic activity during pregnancy can be explained by true increase in the activity of higher sympathetic centres. Our findings show that the sympathetic activity increases during the pregnancy which decreases immediately after normal delivery.

Table 2: Heart rate variability parameters

Parameters	I	II	III	Postpartum
LFnu	0.449 8 ± 0.10 66	0.471 5 ± 0.10 85	0.5191 ±0.161 4	0.3262 ±0.0848 9
HFnu	0.289 7 ± 0.10 12	0.02790 ±0.10 17	0.2494 ±0.064 97	0.3991 ±0.1123
LF/HF	1.604 ± 0.524 2	1.764 ± 0.54 40	1.924 ± 0.568 0	0.8878 ± 0.3304

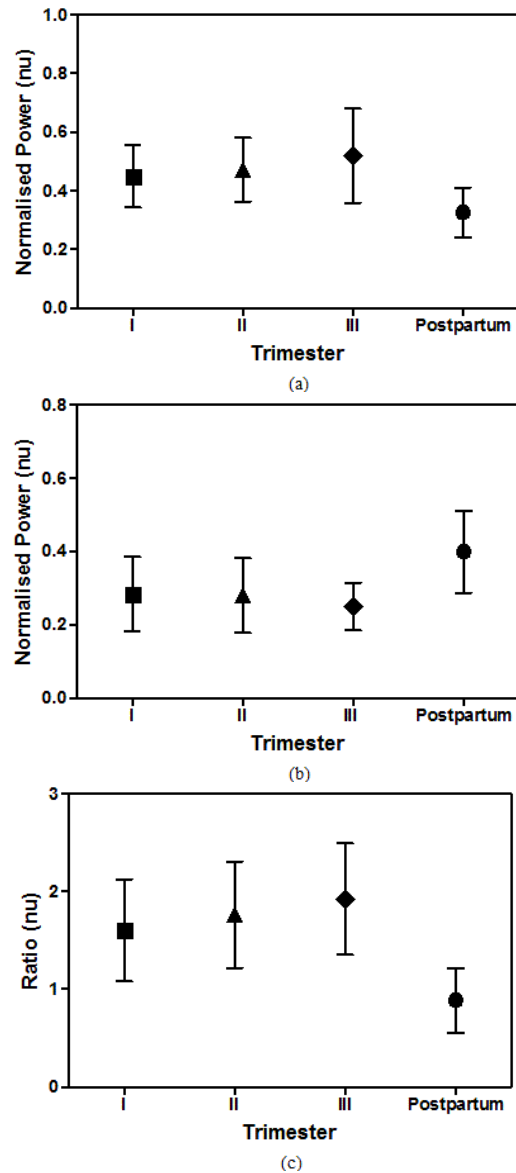


Fig. 1. The Mean and standard deviation of (a) LF, (b) HF, (c) LF/HF ratio

4.2 Nonlinear Analysis

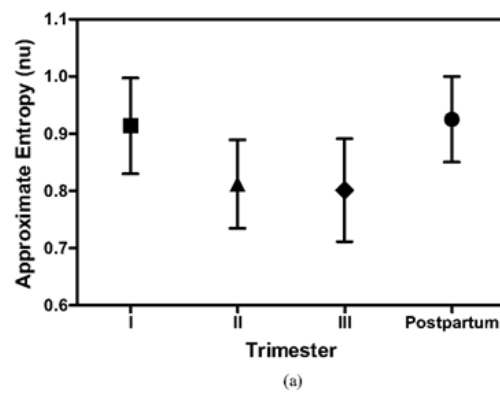
The mean and standard deviation of ApEn for the four groups are reported in Table 3 and Fig. 2a. The mean ApEn value was higher in postpartum women than the pregnant women ($P \leq 0.001$). The ApEn increases as the more number of frequency components in the signal [11] [12]. The increased value of ApEn indicates the increased complexity in the heart rate variability. The ApEn is significantly

lower in pregnancy than in the postpartum. In normal pregnancy, ApEn significantly changes in I trimester (0.9135 ± 0.0838 , vs. 0.8119 ± 0.0772 , $P \leq 0.0001$; 0.8013 ± 0.0898 , $P \leq 0.0001$ respectively) as compared to II and III trimester of pregnancy and insignificant in II trimester (0.8119 ± 0.0772 , vs. 0.8013 ± 0.0898 , $P \geq 0.5251$) as compared to III trimester. There were significant differences between postpartum and normotensive pregnant women group ($p < 0.0001$) data sets with regard to the nonlinear measures of HRV. The ApEn also found to be measured significantly in postpartum state as compared to the state of pregnancy.

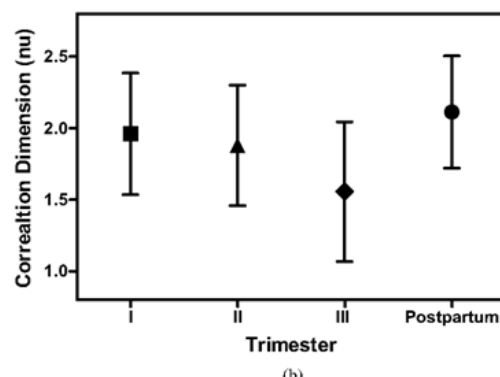
The correlation dimension for three trimesters and postpartum is listed in Table 3 and Fig. 2b. The CD values examined for the correlation values were obtained with delay=3 and embedded dimension $m=5$. The CD found to be significantly lower during pregnancy than in the postpartum. In normal pregnancy, the CD significantly changes in III trimester (1.556 ± 0.4882 , vs. 1.880 ± 0.4223 , $P \leq 0.005$; 1.959 ± 0.4245 $P \leq 0.005$ respectively) as compared to II and I trimester during pregnancy, while there is insignificant changes in II trimester (1.880 ± 0.4223 , vs. 1.959 ± 0.4245 $P \geq 0.4519$) as compared to I trimester. The CD values are significantly decreased in the third trimester than the first and second trimesters and increased immediately after delivery. These results agree with other studies done in diabetic and cardiac pathology [13] [14]. This evidence shows that HRV is more dynamic and chaotic in third trimester compared to I and II trimester and postpartum group. The result clearly reveals reduction in ApEn and CD is a strong indicator of the regularity increment in the heart rate and the complexity of HRV.

Table 3: Mean and SD of Approximate Entropy, Correlation Dimension

Paramete rs	I	II	III	Postpart um
Approximate Entropy	0.9135 ± 0.083 76	0.8119 ± 0.0772 9	0.8013 ± 0.0898 73	0.9248 ± 0.0747 98
Correlation Dimension	1.959 ± 0.4245 5	1.880 ± 0.4223 23	1.556 ± 0.4882 82	2.113 ± 0.3917



(a)



(b)

Fig. 2: The Mean and SD of Approximate entropy, Correlation Dimension

5. Conclusion

The preliminary studies demonstrate the association of narmotensive pregnancy with decreased HRV. The change in the HRV shows that sympathetic activity increases in

pregnancy as gestation age progresses and decreases immediately after the delivery. It was shifted to a significantly lower sympathetic and higher parasympathetic activity immediately after delivery. These result showed a significant decrease in LF/HF ratio and increase in ApEn and CD in postpartum than pregnancy due to vascular constriction produced by discharge of vagal tone. The results obtained using nonlinear techniques contribute significant changes compared to the frequency domain HRV indices during all three trimesters. The ApEn and CD can be used to quantify the HRV to detect the cardiovascular changes and sympathetic activity in all phases of pregnancy.

6. Acknowledgements

Authors wish to thank District Health and Family Welfare officer Davanagere for their support and I would like to acknowledge support extended by Dr. Chandrakala Medical Officer and staff, Maternity centre, Bhashanagara, Davanagere during data collection.

7. References

- [1]. Errol R. Norwitz and Julian N Robinson, "Pregnancy Induced Physiologic Alterations", Critical care Obstetrics, 5th Edition, 30-52, 2010.
- [2]. D. Chamchad, J C Horow, L Nakhamchik and V A Arkoosh, "Heart rate variability changes during pregnancy: an observational study", International Journal of Obstetric Anesthesia, 16, 106–109, 2007.
- [3]. Melanie J. BLAKE, Allison MARTIN, Brad N. MANKTELOW, Charles ARMSTRONG, Aidan W. HALLIGAN, Ronney B. PANERAI and John F. POTTER, "Changes in baroreceptor sensitivity for heart rate during normotensive Pregnancy and the puerperium", Clinical Science, 98, 259–268, 2000.
- [4]. C.-D Kuo, G.-Y Chen, M.-J. Yang, H.-M Lo, and Y.-S. Tsai, "Biphasic changes in autonomic nervous activity during pregnancy", British Journal of Anesthesia, 84, 323-329, 2000.
- [5]. S. V. Khlybova, V. I. Tsirkin, S. A. Dvoryanskii, I. A. Makarova, and A. N. Trukhin, "Heart Rate Variability in Normal and Complicated Pregnancies", *Human Physiology*, Vol. 34, No. 5, pp. 625–632, 2008.
- [6]. Simone A. Smith, Jonathan M. Morris, FRACOG, DDU, Eileen D. M. Gallery, "Methods of assessment of the arterial pulse wave in normal human pregnancy", American Journal of Obstetrics and Gynecology 190, 472-476, 2004.
- [7]. Maria L. Macedo, Daniele Luminoso, Makrina D. Savvidou, Carmel M. McEniry, Kypros H. Nicolaides, "Maternal Wave Reflections and Arterial Stiffness in Normal Pregnancy as Assessed by Applanation Tonometry", *Hypertension* 1-5, April 2008
- [8]. U. Rajendra Acharya, K. Paul Joseph, N. Kannathal, Choo Min Lim and Jasjit S. Suri "Heart rate variability a review", Medical & Biological Engineering & Computing, 44: 1031-1051, 2006.
- [9]. Gary G Berntson, J Thomas Bigger, Dwain L. Eckberg, Paul Grossman, Peter G. Kaufmann, Marek Malik, Haikady N Nagaraja, Stephen W. Porgesw, J. Philip Saul, Peter H. Stone and Mauits W. Vander Molen, "Heart rate variability: Origins methods and interpretive caveats", Psychophysiology, 623-648, 1997.

- [10] Task Force of the European society of Cardiology and North American Society of Pacing and Electrophysiology, “Heart rate variability standards of measurement, physiological interpretation and clinical use”, *European Heart Journal*, 17, 354-381, 1996.
- [11] Pincus SM, “Approximate entropy as a measure of system complexity”, *proceedings national Academic science, USA*, vol88, 2297-2301, March1991.
- [12] Roberto Hornero, Mateo Aboy, Daniel Abásolo, James McNames, and Brahm Goldstein, “Interpretation of Approximate Entropy: Analysis of Intracranial Pressure Approximate Entropy during Acute Intracranial Hypertension”, *IEEE TRANSACTIONS ON BIOMEDICAL ENGINEERING*, VOL. 52, NO. 10, OCTOBER 2005 1671-1680.
- [13] Raul Carvajal, Neils Wessel, Montserrat Vallverdu, Pere Caminal and Andreas Voss, “Correlation dimension analysis of heart rate variability in patients with dilated cardiomyopathy”, *Computer method and programs in Biomedicine*, 133-140, 2005.
- [14] Casaleggio and A Corana, “Correlation dimension estimation from electrocardiograms”, *Chaos solutions and fractals*, vol 5, 713-726, 1995.

Parkinson's Disease Diagnosis Using Self-Adaptive Resource Allocation Network (SRAN) and Extreme Learning Machine (ELM) Classifier

¹Suganya.A , ²Mrs.Sivachitra.M , ³Dr.Vijayachitra.S

¹ Department of Applied Electronics

² Department of Electronic and Electrical Engineering

³ Department of Electrical and Instrumentation Engineering

Kongu Engineering College, Perundurai

suganyanbalagan@gmail.com, sivachitra@kongu.ac.in, svijayachitra@kongu.ac.in

Abstract

This paper proposes the application of Self-Adaptive Resource Allocation Network (SRAN) and Extreme Learning Machine (ELM) for Parkinson's disease classification. This is the first paper to apply the concept of self-regulated learning algorithm and Extreme Learning Machine (ELM) for Parkinson's disease classification. Also Genetic Algorithm (GA) is applied for optimizing the parameters to get better classification efficiency. Self-regulated learning algorithm uses self adaptive error based control parameters for altering the training data sequence, evolving the network architecture and learning the network parameters. Repeated learning samples stored in the network database are removed with the help of this algorithm, hence training time and over flow problems are avoided. SRAN algorithm uses explicit classification error in growing/ learning criterion and discarding similar samples, which provides better generalization performance whereas ELM is the neural network which is a three step

algorithm without tuning mechanism that works with fast speed. This ELM network uses sigmoid activation function. The result shows the comparison of efficiency for both the network for Parkinson's disease classification.

Keywords - Resource allocation network, Self adaptive control parameters, Sequential learning, Binary category classification.

1. Introduction

Parkinson's disease is a progressive nervous system disorder that affects the movement, including speaking and writing [3]. Symptoms develop gradually and may start off with ever so slight tremors in one hand. People with Parkinson's disease also experience stiffness and they cannot carry out things in hand. Parkinson's disease belongs to a group of condition called movement disorders and it describes a variety of abnormal body movements that have a neurological basis
URL:http://en.wikipedia.org/wiki/Parkinson's_disease.



The symptoms of Parkinson's disease usually begin gradually, slowly and often randomly with reduced sensation. It causes problems with movement, cognitive problems, neurobehavioral problems, as well as sensory and sleep difficulties. Each sufferer will be affected differently with a unique set of symptoms. Patients also tend to respond differently to treatment. Some patients may experience tremor (shaking) as their primary symptom, while others may not have tremors, but have balance problems. The symptoms of Parkinson's disease are caused by a loss of nerve cells in a part of the brain called the substantia nigra (literally means "black substance"). The dopaminergic cells are responsible for producing dopamine. URL:http://en.wikipedia.org/wiki/Parkinson's_disease. Dopamine is a neurotransmitter which helps in transmitting the messages from the brain that control and coordinate body movements. Dopamine allows the substantia nigra and another area of the brain, the corpus striatum to communicate and coordinate proper muscle movement.

Self – adaptive Resource Allocation Network (SRAN) classifier is a feed forward network. Neural networks (NN) are powerful tools that can capture the underlying relationship between the input and output data by learning. Architecture selection is a very important aspect of neural network model selection. The objective of architecture selection algorithm is to find the smallest architecture that accurately fits the true function described by the training data. In doing so, architecture selection algorithms have to balance network complexity with goodness of fit of the function being approximated. A too large architecture may accurately fit the training data, but may have bad generalization due to over fitting of the

training data. On the other hand, a too small architecture will save on computational costs, but may not have enough processing elements to accurately approximate the true function. The complexity of finding the minimal architecture increases further, when the training data set is not defined prior to the learning process. To solve this problem, various different approaches like regularization, network construction, learning algorithm were developed [7].

The self regulated control parameters identify the sample 't' with maximum information. The learning process of SRAN involves allocation of new hidden neurons as well as adjusting network parameters. If the sample 't' does not satisfy the learning criteria, then the current sample is stacked at the rear end of the sequence [1].

The paper is organized as follows: Section II briefly describes the data set information. Section III describes the sequential learning concept and SRAN classifier. Section IV describes the Extreme Learning Machine (ELM) concept and section V explains about the GA which are used for optimization problems. Section VI shows the results from this study using SRAN classifier. Section VII summarizes the conclusion.

II. Data Set information

Parkinson's dataset contains only two classes as output classes. The dataset contains 22 features with 195 instances and it is taken from UCI machine learning repository [2]. This data set is composed of a range of biomedical voice measurements from 31 people, 23 with Parkinson's disease. The main aim of the data is to discriminate healthy people from those with PD, based on the "status" column which is set to 1 for PD and 2

for healthy. The data set have been separated as 80 % for training and 20 % for testing [3].

III. Sequential learning and SRAN classifier

In this section, the sequential learning concept and then SRAN classifier are described. Sequential learning is better than batch learning algorithm as they do not require retraining whenever a new data is arrived. Sequential learning algorithm uses all training samples one by one and only once. If the training dataset contains more similar data, then resultant classifier has poor generalization due to over fitting. Also, the sequence in which the training samples presented to the sequential algorithm affects the performance and the problem dependent algorithm control parameters changes the approximation ability of the network.

The SRAN classifier uses radial function network as a basic building block. The controlled parameters in proposed algorithm are self regulated, so they are fixed and are problem independent. The control parameters alter the sequence in which the SRAN classifier approximates the decision function, based on the difference between the information contained in each sample and the knowledge acquired by the network. If the difference is higher, the earlier a sample participates in learning. If the difference is lesser, the samples are pushed into the rear end of the sample data stack. These samples are later used to fine tune the network parameters. Also, the samples with redundant information are discarded from the training dataset. Thus, the finally realized network is compact and provides better generalization performance [9].

In sequential learning algorithm, the training samples arrives one at a time and the network updates its parameters based on the difference in knowledge sample is either

- Used for network training immediately
- Pushed to the rear end of the stack for learning in future
- Deleted from the dataset

The SRAN learning algorithm begins with zero hidden neurons and adds new hidden neuron based on the information present in the current sample. The sequence of the training sample is controlled internally using self regulated control parameters.

Advantage of SRAN classifier

- The control parameters are self regulated.
- The self regulated control parameters alter the sequence of training sample presentation, such that the network approximates the decision function accurately.
- Samples with redundant information are deleted from the training set and thus it avoids over training, reduces learning time and minimizes the computational effort.
- The self regulated control parameters result in selection of fewer neurons and efficient network structure.

Sequential learning algorithms differs from classical radial basis function training rules in which they combine new centre allocation with weight updating in a single routine [8]. Sequential learning algorithm uses all training samples one by one and only once. If the training dataset contains more similar data, then resultant classifier has poor generalization due to over fitting. Also, the sequence in which the training samples presented to the sequential algorithms affects the performance. And the problem dependent



algorithm control parameters changes the approximation ability of the network. These difficulties are overcome by SRAN classifier.

A. SRAN Architecture

The basic building block of SRAN is RBF network [8] as shown in fig.1. SRAN is sequential learning algorithm and starts with no hidden neuron and builds the necessary number of hidden neurons based on the information contained in the current sample. SRAN has a self regulating scheme which controls the learning process by proper selection of the training samples [9].

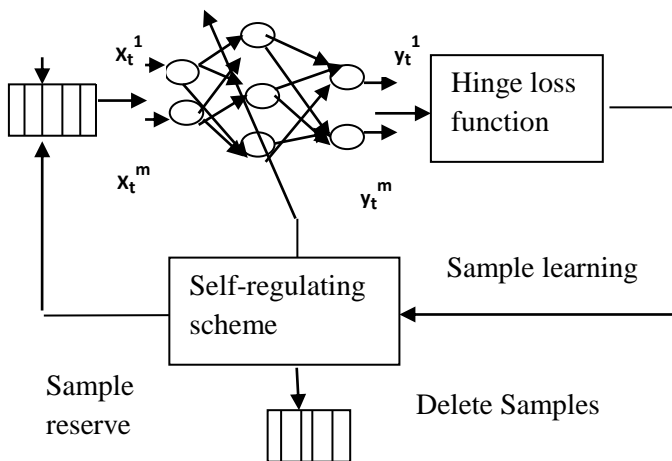


Fig.1. Architecture of SRAN Classifier

B. Self Regulating Scheme

Based on the magnitude and absolute phase error of each sample in the training sequence, the self regulating scheme performs one of the following actions [7].

a. Deletion

If the absolute maximum error $E = \max_{i=1,2,\dots,n} |e_i|$ is less than 0.05, then the sample is deleted without being used and thus prevents over training.

b. Growing

The following criteria must be met for an observation (x_t, y_t) to be used to add a new hidden neuron to the network.

$$C \neq C \text{ and } E \geq \eta_a \quad (1)$$

where E is the absolute maximum error in the current sample, and η_a is the self adaptive growing threshold.

The growth control parameters are adapted based on the current sample error (e). Depending on the error that contributes to neuron growth, the respective growth control parameters are updated as

$$\eta_a = \delta \eta_a - (1 - \delta) E \quad (2)$$

where δ is the parameter that controls the slope of decrease of the control parameter. If the growing criterion is satisfied, then a new hidden neuron is added and its parameters are set as

$$a_{K+1} = e; \quad \mu_{K+1}^c = x_t; \quad \sigma_{K+1}^c = k \|x_t - \mu_{nr}^c\| \quad (3)$$

where k is positive constant which controls the overlap between the hidden neurons nr is the nearest neuron to the current sample, and c is the actual class label of the current sample.

When a new hidden neuron is added, the dimensionality of error covariance matrix $P_{(t)}$ is increased to

$$P_{(t)} = \begin{bmatrix} P_{(t-1)} & 0 \\ 0 & P_0 I \end{bmatrix}$$

where I is identity matrix, and p_0 is an estimate of uncertainty in the initial values assigned to the parameters. The dimensionality of identity matrix is equal to the number of parameters introduced by the new hidden neuron [9].

c. Learning

The network parameters ($w = [\alpha_0, \alpha_1, \mu^1, \sigma^1, \dots, \alpha_k, \mu_k^1, \sigma_k^1]$) are updated if the following criteria is satisfied

$$C == \hat{C} \text{ and } E \geq \eta_l$$

where η_l is the self adaptive learning control parameter. Here, the self adaptive learning threshold. Is adapted based on the knowledge present in the current sample as

$$\eta_l = \delta \eta_l - (1 - \delta) E$$

where δ is the parameter that controls the slope of decrease of the control parameter.

d. Sequence altering

If the current sample does not satisfy the growth and learning criteria, then the sample pushed to the rear end of the stack, to be presented to the network, in future. These samples can be used to fine tune the network parameters, when all the available samples in the dataset are presented. Any new sample arriving in the sequence is stacked behind the current last sample.

IV. ELM classifier

ELM is a three-step algorithm without tuning mechanism. The learning speed of ELM is extremely fast [5] and it can be used as a classifier. It is the network which contains only one hidden layer and the input layer to hidden layer weights can be chosen randomly. The hidden layer to output layer weights can be calculated analytically. ELM can be able to work for all bounded nonconstant activation functions. ELM can be used to obtain the solution in a direct manner and hence it needs very less time for training since there is no requirement of parameter tuning. It can be used for difficult classification applications. In

this, many types of hidden nodes can be used and ELM with RBF nodes needs more number of nodes than ELM with additive nodes. For architectural and additional details of ELM refer [5].

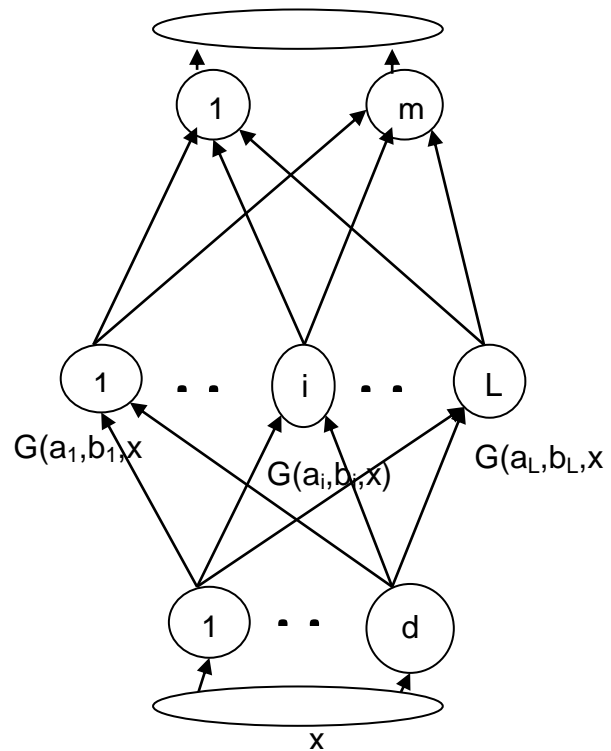


Fig.2. ELM Architecture

One of the typical implementation of ELMs is to apply random computational nodes in the hidden layer, which may be independent of the training data. Different from traditional learning algorithms for neural networks, ELM not only tends to reach the smallest training error but also the smallest norm of output weights.

V. Genetic Algorithm

The genetic algorithm is perhaps the most well-known of all evolution based search techniques [10]. Genetic algorithms are widely used to solve complex optimization problems where the number of parameters and constraints are large and the analytical

solutions are difficult to obtain. In recent years, many schemes for combining genetic algorithms and neural networks have been proposed and tested. A detailed survey on evolving neural networks using genetic algorithms can be found in schaffer et al. (1992)[11]. In this paper we use the algorithm for parameter optimization which will provide better generalization performance [12].

A genetic algorithm for any particular optimization problem must have the following components [6]:

- String representation
- Population initialization
- Selection function
- Genetic operators
- Fitness function and
- Termination function

The components of the genetic algorithm are described below.

A. String representation

String representation is the process of encoding a potential search node (solution) as a string. The string representation depends on the structure of the problem in a genetic operators used in the algorithm [12].

B. Selection function

In a genetic algorithm, new search nodes for the next generations are selected from the existing set of search nodes (population). The selection process plays an important and critical role. Using genetic operators, a probabilistic selection is performed based upon the fitness of existing search nodes, such that the better search nodes have a higher chance of being selected. It is possible that a search node in the population can be selected more than once for producing new search nodes [12].

C. Genetic operators

Genetic operators provide the basic search mechanism of the genetic algorithm. The operators are used to create search nodes based on existing search nodes in the population. New search nodes are obtained by combining or rearranging parts of the old search nodes and a new search node obtained may give a better solution to the optimization problem. These operators are analogous to those which occur in the natural world: crossover and mutation [12].

a. Crossover operator

Crossover operator is a primary operator in genetic algorithm. The role of a crossover operator is to recombine information from two selected search nodes to produce two new search nodes. It improves the diversity of the solution [12].

b. Mutation operator

The mutation operator alters one solution to produce a new solution. The mutation operator is needed to ensure diversity in the population, and to overcome premature convergence and local minima problems [12].

D. Fitness function

The objective of the optimization is to find the best set of parameters that maximizes the classification efficiency. The effectiveness can be determined by evaluating the training and testing efficiencies of the SEAN classifier [6].

E. Termination criterion

In genetic algorithm, the evolution process continues until a termination criterion is satisfied. The most widely used termination criterion is the maximum number of generations [12].

Hence the genetic algorithm has been applied for optimizing the parameters in order to improve the testing efficiency and it has

been compared with the Extreme Learning Machine (ELM). GA gives the best solution for the classifier and it is mostly used for complex optimization problems.

VI. Performance Measures

In this paper, we use the global measures such as overall and average efficiencies as a performance measure. The statistical measures are given in confusion matrix. The performance is indicated by the percentage classification which tells us how many samples belonging to a particular class have been correctly classified. The average and overall classification efficiency for SRAN and ELM are defined as

$$\eta_a = \frac{1}{n_c} \sum_{i=1}^{n_c} \eta_i \quad (4)$$

$$\eta_o = \frac{1}{N^T} \sum_{i=1}^{n_c} q_{ii} \quad (5)$$

where n_c is the total number of classes and N^T is the number of testing samples.

The Overall efficiency for ELM classifier can be obtained as below:

Table I
Classification Results of SRAN Classifier Applied for Parkinson's Disease Dataset

Class type	Dataset	SRAN		ELM	
		Confusion matrix	Overall efficiency	Confusion matrix	Overall efficiency
Binary	Parkinson's Disease	76	7	0.87273	65
		14	68		18
				12	70
					0.82

It is the ratio between number of samples correctly classified and total number of samples.

$$\text{Traeff} = \frac{\text{Number of samples correctly classified}}{\text{Total number of samples}}$$

ELM has been used for comparing the performance of SRAN classifier applied to binary datasets. Table I presents the overall efficiency of SRAN and ELM classifier. It can be observed that SRAN Classifier has better efficiency when compared to ELM classifier.

VII. Conclusion

This paper has presented a new approach for Parkinson's disease classification using SRAN classifier and ELM. Using self regulative control parameters, the self adaptive nature of the algorithm identifies the reduced training data sequence and produces a compact network. The SRAN uses misclassification error and hinge loss function. The performance of SRAN has been studied with binary dataset. Based on these studies, it can be concluded that SRAN uses the reduced training sample sequence which avoids over training and it produces a compact network with better generalization while ELM has fast speed. Apart from few fields for which we have applied, SRAN can also be applied for different fields.

VIII. Acknowledgement

I greatly thank the authors Dr.Suresh Sundaram(Professor, Nanyang Technological university, Singapore) and also Dr.R.Savitha(Research associate, Nanyang Technological University, Singapore) for supporting us with their valuable suggestions.

IX. References

- [1] Anchana khcmphila and Vccra boonjing. "Parkinson's disease classification using neural network and feature selection", World Academy of science, Engineering and Technology 64 2012.
- [2] Asuncion.A and D.J.Newman. "UCI machine learning repository",2007.URL <http://www.ics.uci.edu/~mlearn/ML Repository.html>.
- [3] David GIL A, Magnus Johnson B, "Diagnosing Parkinson by using artificial neural network and support vector machine", Global Journal of Computer Science and Technology, 2010.
- [4] Freddie Astrom, Rasit koker, "A parallel neural network approach to prediction of parkinson's disease", 2011.
- [5] Guang-Bin Huang,Qin- YuZhu,Chee-Kheong siew, Extreme Learning Machine: Theory and Applications Neurocomputing 70 (2006) 489-501.
- [6] Mahanand.B.S, Suresh.S, Sundararajan.N, "Identification of brain regions responsible for Alzheimers disease using Self-Adaptive Resource Allocation Network ". Neural networks 32 (2012) 313-322, Elsevier 2012.
- [7] Suresh.S, keming dongg, H.J.Kim, "A sequential learning algorithm for self adaptive resource allocation network classifier", Neuro computing 73 (2010)3012-3019.
- [8] Lu.Y, Sundararajan. N, Saratchandran. P, "A sequential learning scheme for function approximation using minimal radial basis function (RBF) neural networks", Neural computing.9(2)(1997),pp.461-478.
- [9] Sudha. S, Sivachitra.M, Vijayachitra.S "Self-adaptive resource allocation network classifier applied for classification problem", Neural computing, 2012.
- [10] Saraswathi.S, Sundaram.S, Sundararajan.N, Zimmermann.M, Nilsen-Hamilton.M, ICGA-PSO-ELM approach for accurate multiclass cancer classification resulting in reduced gene sets in which genes

- encoding secreted proteins are highly represented, Computational Biology and Bioinformatics, IEEE/ACM Transaction on 8 (2), 452-463, 2011.
- [11] Schaffer, J.D., whitley, D., Eshelman, L.J., 1992. “Combination of genetic algorithms and neural networks: a survey of the state of the art. Proceedings of International Workshop on combinations of genetic algorithms and neural networks”, vol. 1; 1992, pp.1-37.
- [12] Suresh. S, Saraswathi. S, Sundararajan. N. “Performance enhancement of extreme learning machine for multi-category sparse data classification problems”. Engineering applications of Artificial intelligence 23 (2010) 1149-1157.

Soft Computing as a tool for Classification of Cardiovascular Abnormalities

¹Dilip Kumar.S, ¹Pallikonda Rajasekaran.M, ²Perumal.B

¹Department of Instrumentation and Control Engineering,

²Department of Electronics and Communication Engineering,

Kalasalingam University.

sdilipkumar29@gmail.com, mpraja80@gmail.com, palanimet@gmail.com

Abstract

Classification of Electrocardiogram (ECG) for Cardio-Vascular Abnormalities (CVA) in the process of diagnosis is inevitable. In this paper we propose a scheme to integrate Principal Component Analysis (PCA) with Neural Networks (NN) for classification of ECG Signals. A Neural Network (NN) with Back Propagation Algorithm is deployed as classifier. ECG samples consisting of Normal signals and three abnormal signals are taken from physionet arrhythmias database for our experiments. The PCA is used to minimize ECG signals into weighted sum of basic components that are statistically mutual independent. Thus PCA is used for dimensionality reduction of data. Here a comparison of performance of Neural Network (NN) and Principal Component Analysis (PCA) with Neural Network (NN) are investigated. Principal Component Analysis (PCA) eliminates the least considerable data values, hence helps in improving the performance in classification of ECG signals. The results obtained suggest that Principal Component Analysis (PCA) with Neural Network (NN) performance is faster and better than Neural Network (NN) Classifier alone.

Keywords

Principal Component Analysis (PCA), Electrocardiogram (ECG), Neural Network (NN). Cardio-Vascular Abnormalities (CVA)

1. Introduction

ECG signal has been intensively used by cardiac surgeons to efficiently diagnose the Cardiovascular Diseases (CVD) for the last seven decades. Traditionally the automatic analysis of ECG signals, including delineation, was taking place online on bulky, high performance beside cardiac monitors, or performed offline during a pre-processing stage after ambulatory ECG recording using wearable, yet obtrusive, ECG data loggers. Maintaining and updating such a system for every new abnormality is intrinsically complex. This introduces a problem of finding a simple and fast solution toward heart disease classification from ECG that raises alert to cardiac specialist as soon as a cardiac disease is recognized. But the issues faced in ECG analysis of one patient differ with other patients ECG waveforms; due to this the performance of classifiers will be low during training of data.

2. Related Works

It is known that from years, researchers have proposed various methods for ECG beat Classification using Neural Network (NN) classifier [1][2][3]. By convention back propagation Neural Networks (BPNN) is used. The important feature of BPNN is its ability to recognize and classify ECG signals; the shortcoming with this method is slow convergence to local and global minima. To outcome this problem, Hybrid Neural Networks was proposed by researchers.

In [4] Dipti Patra *et al* had applied Integration of fuzzy c-means (FCM), Principal Component Analysis (PCA) and Neural Networks for Classification of ECG data, in which training the fuzzy layer by fuzzy c-means algorithm. Fuzzy c-means clustering algorithm divides the data into fuzzy functions that with overlap with one another. Applying PCA to the obtained data, results in dimensionality reduction of the data, which results in elimination of insignificant data values present. Hence the reduced matrix is the input for NN and the classification for ECG Arrhythmias are obtained.

In [6] Atena Sajedin *et al* had applied a trainable Neural Network model for ECG beat classification, in which topologies of multilayer perceptrons neural networks are designed. Comparative analyses of combination of different topologies are performed. In [8] Wei Jiang *et al* had applied Block-based Neural Networks (BbNN) for ECG signal Classification, in which BbNNs are utilized for personalized health monitoring.

In [5] Dayong GAO *et al* had applied ECG Arrhythmia Identification using a Neural Network based on a Bayesian Framework, in

which Bayesian framework is based on logistic regression model and the back propagation algorithm. Here a dual threshold method is applied to determine false alarm signals. In [7] Philip Langley *et al* had applied Principal Component Analysis (PCA) for analyzing Beat-to-beat changes in ECG features, in which Coherence and correlation are obtained for the ECG features.

In this paper, we evaluate the performance of Neural Network and the integration of Principal Component Analysis (PCA) with Neural Network for ECG features. The proposed structure consists of layer of feature extraction with Principal Component Analysis (PCA) and classification by Neural Networks using Back Propagation Neural Network (BPNN) Algorithm. Principal Component Analysis (PCA) performs the extraction of Principal Components from the raw data and the multilayer perceptron works as a final classifier. Initially the raw data for ECG is trained for Neural Network by varying the sigmoid function, number of hidden layers, training function.

But in Principal Component Analysis (PCA) the raw data is reduced and the principal components obtained are given as input to Neural Network. It is observed from the results obtained that performance of Principal Component Analysis (PCA) with Neural Network (NN) is more generalized and faster in computation than Neural Network (NN) alone.

3. ECG Signal Classification Methods

For classification of ECG signals based on their arrhythmias, various solutions were



presented in the literature. We present integration of Principal Component Analysis (PCA) with Neural Network (NN) and compare the performance of the model with Neural Network (NN). The data set is the prerequisite for the Neural Network (NN); the data set is obtained by taking the ECG values from four different subjects for Normal wave, Arrhythmia Wave, Ventricular Tachyarrhythmia, Supra Ventricular Arrhythmia from physionet database www.physionet.org [9]. A set of thousand values are taken from subjects the values are put in columns and output classifiers [0 0 0 1], [0 0 1 0], [0 0 1 1], [0 1 0 0] are marked for corresponding input values. The input values and the output classifiers are shuffled and the data set can be utilized for Neural Network (NN). Similarly this raw data is used in Principal Component Analysis (PCA) for dimensionality reduction and the output obtained is the input for Neural Network (NN) training, thus classification of ECG signals based on cardiovascular abnormalities is done.

3.1 Neural network classifier

The classifier implemented for this work is a standard, feed forward, Neural Network (NN) with error back propagation algorithm with two or more hidden layers and output layer. The activation function for all units is the asymmetric sigmoid function. Training the network is accomplished by initializing all weights to small, random values and then performing a gradient-descent search in the network's weight space for a minimum of a squared error function of the network's output. The error obtained will be the difference of the network's output and the target value for each input vector. For the experiments, the target values were set to [0 0 0 1] for the Normal ECG wave, [0 0 1 0] for the Arrhythmia

Wave, [0 0 1 1] for the Ventricular Tachyarrhythmia wave, and [0 1 0 0] for the Supra ventricular Arrhythmia.

The steps for performing NN are,

- [1] Load the data set.
- [2] Specify the sigmoid function, training function, Number of hidden layers.
- [3] Specify data for training and testing.
- [4] Mean Square Error for training and testing are obtained.

Classification of cardiovascular abnormalities is obtained using Neural Network.

3.2 Principal component analysis

Principal Component Analysis (PCA) is a mathematical procedure that uses an orthogonal transformation to convert a set of observations of possibly correlated variables into a set of values of linearly uncorrelated variables called principal components. The number of principal components is less than or equal to the number of original variables. This transformation is defined in such a way that the first principal component has the largest possible variance (ie, accounts for as much of the variability in the data as possible), and each succeeding component in turn has the highest variance possible under the constraint that it be orthogonal to (i.e., uncorrelated with) the preceding components. Since Principal Component Analysis (PCA) is known for its dimensionality reduction technique gives the linearly correlated variables where its matrix dimensions are reduced, which gives high accuracy, and quick computation.

The steps for performing PCA are,

- [1] Load the input raw data set.
- [2] Find the mean from the data set.
- [3] Subtract the mean from individual components.
- [4] Compute the Covariance from the data.
- [5] Determine the Eigen vectors and values of the Covariance matrix.
- [6] Principal Components are chosen and the matrix is formed.

The most assumption made in PCA for dimensionality reduction is to obtain the Principal Components from the principal axes which consists of relevant information. Thus computational time will get reduced. To this model reduced matrix Neural Network with Back Propagation is performed.

4 Proposed Method

In this paper, the proposed method is divided into three steps: (A) ECG dataset formation, (B) Dimensionality reduction, (C) Classification by Neural Networks.

4.1 ECG dataset formation

For our experiment, ECG samples such as Normal wave, Arrhythmia Wave, Ventricular Tachyarrhythmia, Supra Ventricular Arrhythmia are obtained from physionet database www.physionet.org [9]. The data values are taken from signal before and after R peak, since this region consists of vital information values of Heart. Data are obtained from four subjects each for four beat types. Output classifier is marked and the data are shuffled. To this dataset 75% of data is trained and 25% of data will be tested.

4.2 Dimensionality reduction

The dataset formed will be of raw data and it is required to obtain the principal components from the dataset. Hence by using PCA to the dataset the dimension of the dataset is reduced without compromising the feature vector. The most assumption made in PCA for dimensionality reduction is to obtain the Principal Components from the principal axes which consists of relevant information. Thus computational time of the process will get reduced.

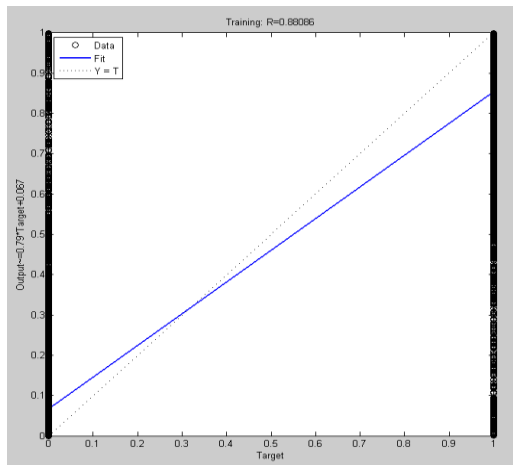


Fig .1 Regression plot of NN

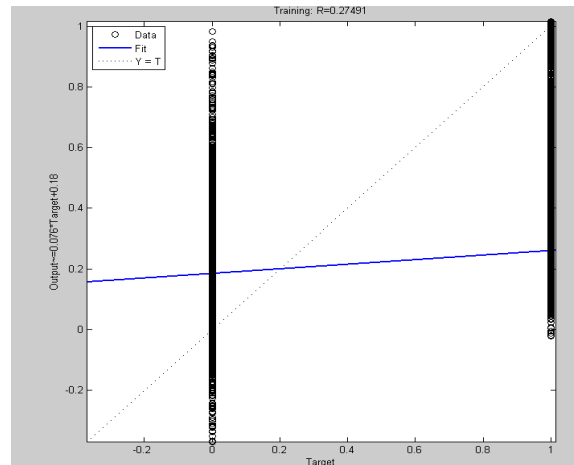


Fig.2 Regression plot of PCA-NN

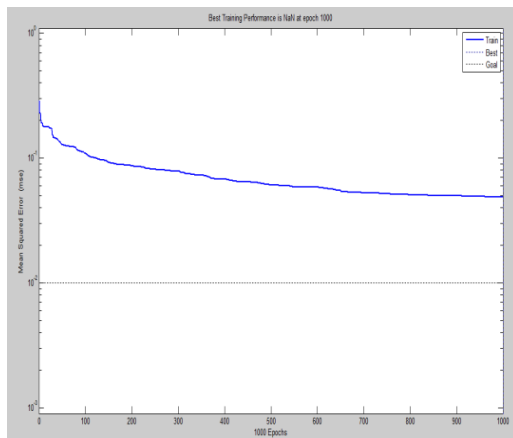


Fig 3.Performance plot of NN

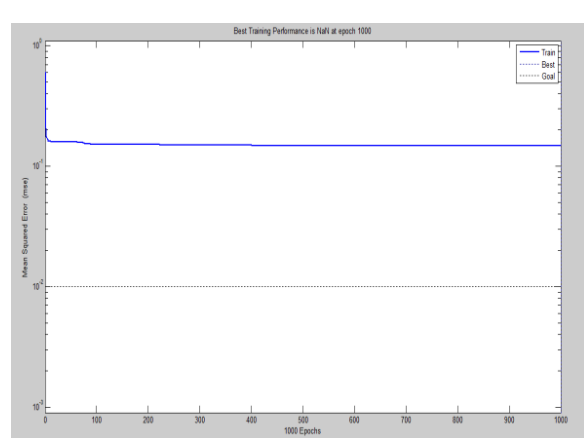


Fig 4. Performance plot of PCA-NN

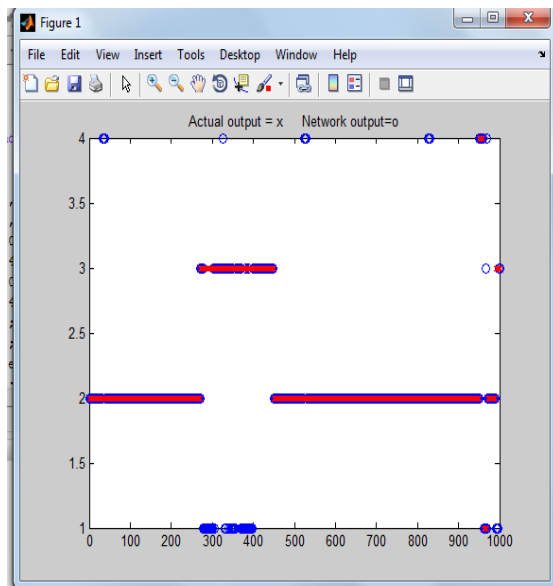


Fig 5. Classification of NN

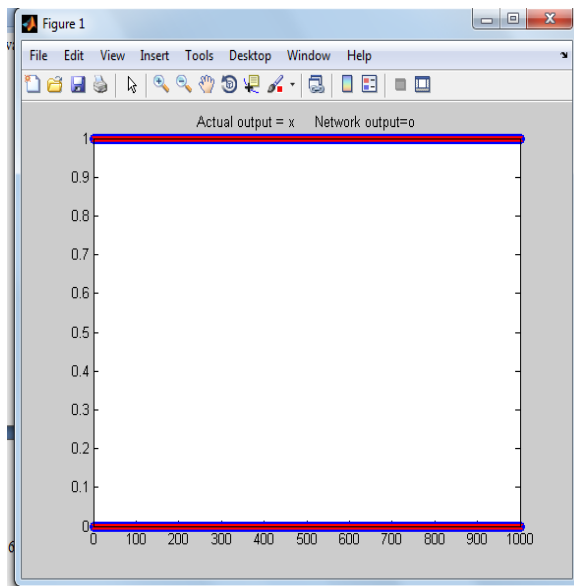


Fig 6 Classification of PCA-NN

Table 1. Tabulation of NN and PCA-NN results

S.NO	Parameters	NN	PCA-NN
1	No of Hidden Layers	19	12
2	No of iterations	1000	1000
3	Sigmoid Function	tansig	tansig
4	Training Type	Trainscg	Trainscg
5	MSE training	0.0487	0.0933
6	MSE testing	0.018	0.092
7	Computation time (sec)	64.4908	71.8385
8	% Correctly Classified	90%	100%

4.3 Classification by Neural Networks

For our experiment back propagation Neural Network (NN) is used. In which the Neural Network (NN) structure consists of three layer structure. The three layers are input layer, hidden layer and output layer. The data obtained as a result of PCA is given as input to the input layer of Neural Network. The no of hidden layers can be varied from 3-20. The output layer consists of four neurons, where ECG signals of four types are to be classified. In our study tansig is sigmoid function and training type is Scaled Conjugate Gradient. The weight and bias values are updated with a learning rate of 0.01.

5 Results

We got the samples from different subjects for four types of ECG Beats from physionet database. The obtained samples comprises of

4000x8 data matrix where 8 columns represents the input and output classifiers. By applying PCA to the data matrix, model reduced matrix is obtained. Neural Network (NN) training is done to the model reduced matrix. This PCA-NN structure when compared with NN depicts the variation in classification of ECG Beats. Moreover the numbers of hidden layers are less in PCA-NN than NN structure alone. The error obtained during training and testing are less in PCA-NN. It is observed that PCA-NN structure is performing well than NN structure. The comparison of results is depicted in table 1. The Fig 1, 2 represents the regression plots of Neural Network and Principal Component Analysis with Neural Network. Fig 3, 4 represents the performance plots of Neural Network and Principal Component Analysis with Neural Network. Fig 5,6 represents the classification of Neural Network and Principal Component Analysis with Neural Network. The table depicts the results which are ought to be well performing structure of NN and PCA-NN. The value obtained is concluded by obtaining the values by varying the parameters (viz) No of Hidden layers, sigmoid function, Training Type.

6 Conclusions and Future Work

In this study, the integration of PCA-NN structure performs well for the cardiovascular abnormalities classification than the conventional Neural Network (NN) classifier alone. Previously using Neural Network (NN) classifier alone for the data increases the computational time. This is curbed and the performance of the overall system is

improvised in PCA-NN structure. By making a comparative analysis of PCA-NN and NN structure it is observed that the Performance of PCA-NN structure is well served in recognizing and classification of ECG waves with better accuracy and higher computational rate. Further as a part of future work other soft computing techniques can be employed for the classification of cardiovascular abnormalities.

7 Acknowledgments

We thank The Department of Instrumentation & Control Engineering of Kalasalingam University,(Kalasalingam Academy of Research and Education), Tamil Nadu, India for permitting to use ECG setup available in Biomedical Laboratory, which was setup with the support of the Department of Science and Technology (DST), New Delhi under FIST Program.

8 References

- [1] Acharya, R., Bhat, P. S., Iyengar, S.S., Roo, A. & Dua, S., "Classification of heart rate using aritificial neural network and fuzzy equivalence relation," The Journal of the pattern Recognition Society, 2002.
- [2] De Chazal, P., & Reilly, R. B., "Automatic classification of ECG beats using waveform shape and heart beat interval features," In IEEE international conference on acoustic,speech and signal processing (ICASSP '03), vol. 2, pp. 269-272, Hong Kong, China, 2003
- [3] Osowski, S & Linh, T. H., "ECG beat recognition using fuzzy hybrid neural network," IEEE Trans Biomed Eng. 2001 Apr;48(4):1265-71.
- [4] Dipti Patra, Manab Kumar Das,Smita Pradhan "Integration of FCM, PCM and Neural Networks for Classification of ECG Arrhythmias" IAENG International Journal of Computer Science, 36:3,IJCS_36_3_05.
- [5] Dayong Gao, Micheal Madden, Micheal Schukat, Des Chambers, and Gerard Lyons "Arrhythmia Identification from ECG Signals with a Neural Network Classifier Based on a Bayesian Framework" In the Twenty-fourth SGAI International Conference on Innovative Techniques and Applications of Artificial Intelligence, December 2004.
- [6] Atena Sajedin, Shokoufeh Zakernejad, Soheil Faridi, Mehrdad Javadi and Reza Ebrahimpour " A Trainable Neural Network Ensemble for ECG Beat Classification" Proceedings of the International Conference on Neural Networks (ICNN2010), Amsterdam, Netherland, Publication year 2010, Page no 28-30
- [7] Philip Langley, Emma J.Bowers, and Alan Murray "Principal Component Analysis as a Tool for Analyzing Beat-to-Beat Changes in ECG Features: Application to ECG Derived respiration" IEEE Trans Biomed Eng. 2010 Apr;57(4):821-9. Epub 2009 Apr
- [8] Wei Jiang, Seong G.Kong, and Gregory D.Peterson "ECG Signal Classification using Block-based Neural Networks" Neural Networks, 2005. IJCNN '05. Proceedings. 2005 IEEE International Joint

Conference on 31 July-4 Aug. 2005, page
(s) 326 - 331 vol. 1.

[9] www.physionet.org from where data are
obtained

Cardiac Arrhythmia Diagnosis System Using Data Mining Techniques

R.Lakshmi Devi ¹, Dr.V. Kalaivani²

National Engineering College,

Kovilpatti, Tutticorin District,

¹lakshmideviit31@gmail.com, ²kalai.nec@gmail.com

Abstract

Heart disease is the major cause of death around the world. Heart disease is any type of disorder that affects the function of Heart. The deaths due to heart disease occur because of high workload, mental stress, smoking, physical inactivity and other problems. Several heart diseases which affect the human are Heart valve disease, congenital heart disease, Myocardial Infarction and Congestive heart failure. An arrhythmia is one type of heart disease. Arrhythmia is an irregular heartbeat. During Arrhythmia the heart may beat too fast, too slowly or too irregularly. Generally the Arrhythmia disease is diagnosed by ECG analysis. ECG signal has noise that should be removed for correct diagnosis which is a time consuming task. To reduce the time consumption the Heart Rate Variability analysis, a non-invasive measure, which reflects the variation over time of the interval between consecutive heartbeats, is proposed. The Heart Rate Variability features are used for diagnosis of arrhythmia disease. Data mining is a computer assisted technique which analyzes large quantity of data and extract meaningful information quickly. Therefore the data mining techniques Classification and Regression Tree is used for the cardiac arrhythmia diagnosis system using the Heart Rate Variability features. The Classification using Classification and Regression Tree provides 97.56% of accuracy.

Key words

Data mining, Heart Rate Variability, RR interval, Heart Disease, Arrhythmia.

1. Introduction

There are several diseases which affects the human are cancer, Polio, Asthma, Chicken Pox, Diabetes, Influenza, and Heart disease. Among the several diseases which are affecting the human severely, heart disease is a life-threatening one. Heart disease is the major cause of death due to mental stress, inactivity and poor diet. Several diseases that affect the heart are Cardio vascular disease, congenital heart diseases, congestive heart failure and Ischemic diseases. The general causes of heart diseases are Heredity, Physical Inactivity, and High Blood pressure, High Cholesterol, Mental Stress, Alcohol, Smoking and Diabetes.

An arrhythmia is a problem with the rate or rhythm of the heartbeat. In arrhythmia, the heart can beat too speedy, too slowly, or with an irregular rhythm. A heartbeat that beats too fast is called tachycardia. A heartbeat that beats too slowly is called bradycardia. A heart beat that beats too irregularly is called as Flutter or Fibrillation. Arrhythmia may feel like fluttering or a brief pause. For Arrhythmia diagnosis, Heart Rate Variability, a non-invasive measure, which reflects the variation over time of the interval between

consecutive heart beats, is used. Heart Rate Variability measures are used for other investigations, such as for the diagnosis of Obstructive Sleep Apnea Syndrome, and for the analysis of the relationship between HRV and the menstrual cycle in healthy young women, and for the detection of congestive heart failure.

The timely diagnosis of arrhythmia is essential to prevent from death. To diagnose the arrhythmia efficiently, the analysis used are the ECG analysis and Heart Rate variability analysis. ECG analysis means to diagnose the arrhythmia using ECG signal features. Heart Rate Variability features are calculated from the R-R interval.

ECG is used to measure the rate and regularity of heartbeats, as well as the size and position of the chambers, the existence of any harm to the heart.

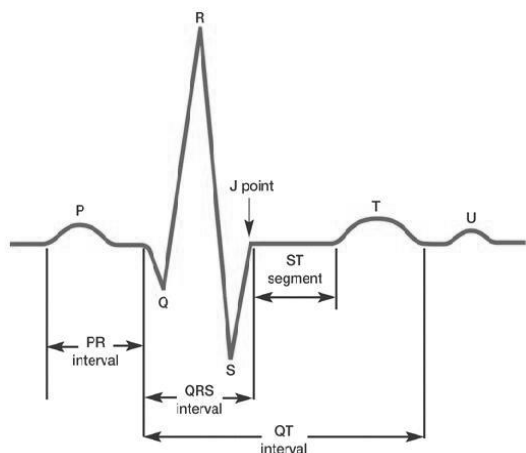


Figure.1 Normal ECG Signal

ECG signal contains five characteristic peaks and valleys, arbitrarily labeled with successive letters of the alphabets: P, Q, R, S, and T, as shown in Figure. 1.

Another important feature to diagnose the cardiac arrhythmia is the Heart Rate Variability features. Heart Rate Variability analysis is non-invasive measure, which reflects the variation over time of the interval between consecutive heartbeats. The Heart Rate Variability features are extracted from the RR interval. R-R interval is the interval from the peak of one QRS complex to the peak of the next QRS complex. The following Figure. 2 shows the R-R interval.



Figure.2 RR Interval

Data mining has been widely used in the field of medical, to include patient diagnosis records to help to identify best practices. It includes classification, clustering, association rule mining and prediction. Our work attempts to predict the arrhythmia disease on Heart Rate Variability features using data mining classification techniques.

2. Literature Survey

Large number of work is carried out in finding out efficient methods of medical diagnosis for various diseases. Our work is an attempt to efficiently diagnose the arrhythmia

diseases. Abhilasha et. al., (2012) developed arrhythmia detection system on a mobile platform to diagnose different type of arrhythmia [1]. The types of arrhythmia detected are Bradycardia, Tachycardia, Premature ventricular contraction and

Premature Atrial contraction. Mohamed Ezzeldin et. al., (2012) proposed an arrhythmia classification by using the hybrid techniques such as trigger learning and ECG parameter customization. In this paper J48 classification algorithm is used for classifying types of arrhythmia [9]. Yakup et. al., (2011) proposed an arrhythmia recognition and classification system. The K-Nearest Neighbour algorithm is used for classification [12]. Leandro Pecchia et. al., (2011) investigate the discrimination power of Short-term Heart Rate Variability Features for Heart disease diagnosis. The authors also investigate the discrimination power of standard long-

term heart rate variability (HRV) measures for the diagnosis of chronic heart failure (CHF). And the authors developed the remote health monitoring system to diagnose the heart disease using the Heart Rate Variability features [6][7][8]. For classification the Data mining Classification and Regression Tree is used. The rest of the section is arranged in following manner. Datasets used for arrhythmia detection, Extraction of HRV Time domain features, Extraction of HRV Frequency domain features and Classification using CART. Finally the implementation results are discussed.

3. Framework Of Cardiac Arrhythmia Diagnosis System

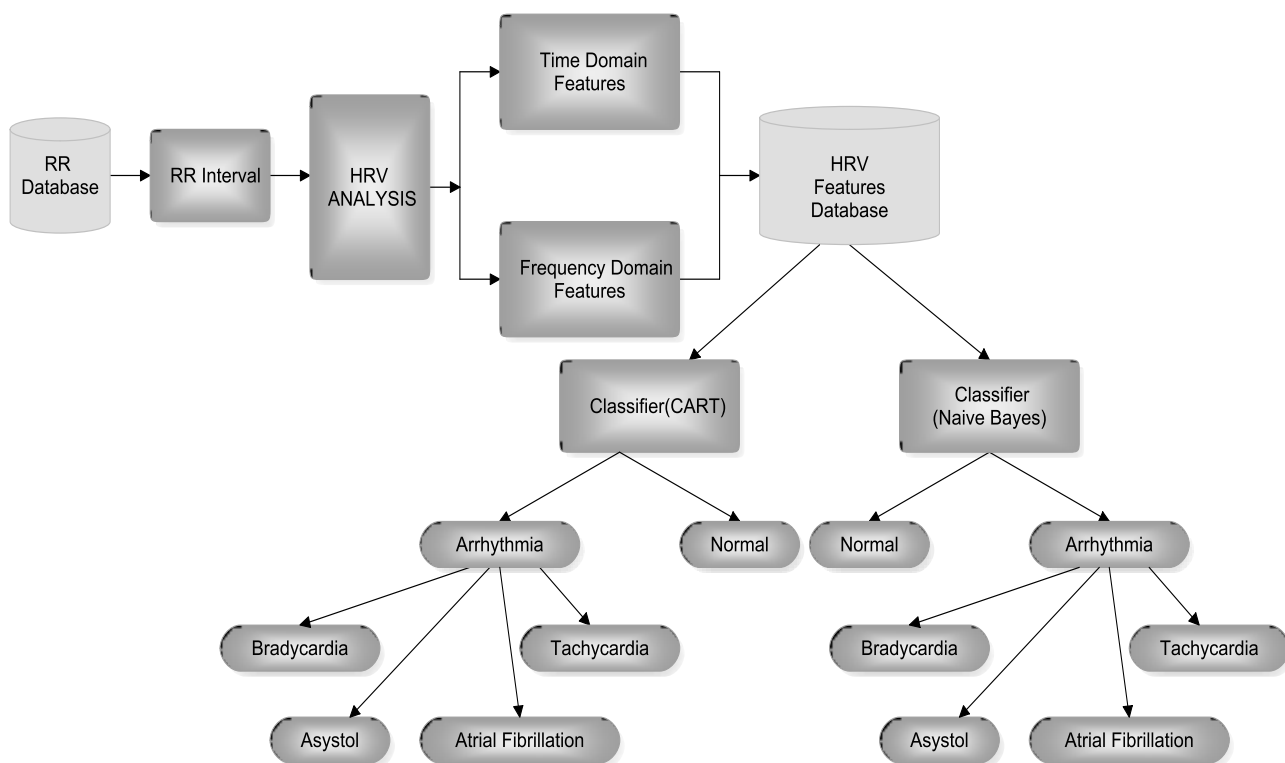


Figure.3 The Architecture of Cardiac Arrhythmia Diagnosis System

It is proposed to develop a cardiac arrhythmia diagnosis system using data mining techniques. The Figure. 3 shows the

architecture of Cardiac Arrhythmia diagnosis system. Arrhythmia is an irregular heartbeat. The heart beats slowly, quickly or irregularly.

The Arrhythmia disease is diagnosed using Heart Rate Variability features. Heart Rate Variability features are calculated from the RR interval of the ECG signal. RR interval is the interval between one peak of the QRS complex to the next peak of the QRS complex. From the RR intervals the HRV time domain and frequency domain features are calculated and used for the classification of arrhythmia. Classification and Regression Tree is used for the classification because it provides an easy to understand description of classification procedures, in terms of intelligible ‘if then’ rules. After classifying the arrhythmia disease, the system further classifies different types of arrhythmias such as Bradycardia, Tachycardia, Asystole and Atrial Fibrillation.

The proposed work consists of the following modules.

The modules are

- Extraction of Time domain features
- Extraction of Frequency domain features
- Classification of Arrhythmia disease
- Classification of type of arrhythmia

3.1 Dataset

For extracting the time domain and frequency domain features, the RR interval is the major input to the HRV analysis. The RR intervals are collected from Physionet’s MIT-BIH arrhythmia RR interval database and Normal sinus rhythm RR interval database. The MIT-BIH Arrhythmia RR interval database contains RR interval of the arrhythmia affected patients. It contains RR interval for 48 records. The Normal Sinus Rhythm RR interval database contains the RR interval of the normal persons. It contains RR interval for 54

records. All the original ECG records were digitized at 128 samples per second.

3.2 Extraction of Time Domain features

A number of standard statistical time-domain HRV measures are calculated from the RR intervals. The measures

are Average of all Normal to Normal interval (AVNN), Standard deviation of Normal to Normal interval (SDNN), Root of mean of sum of squared difference of consecutive NN intervals (RMSSD), Standard deviation of average of all NN intervals (SDANN), The count of consecutive intervals having difference of x ms (NNx), and the percentage of NNx (pNNx). The features are calculated using the following formulas.

AVNN

AVNN is the average of all NN intervals in the dataset. The average of of RR intervals can be calculated as,

$$AVNN = \frac{1}{N} \sum_{i=1}^N RR_i$$

Where N is the total number of RR intervals and RR_i is the ith RR interval.

SDNN

SDNN means standard deviation of all RR intervals. The standard deviation is the root-mean-square (RMS) deviation of its values from the mean.

$$SDNN = \sqrt{\frac{1}{N} \sum_{i=1}^N (RR_i - \bar{RR})^2} \quad (1)$$

Where RR_i is the RR interval \bar{RR} is the mean value of the RR_i.

$$\bar{RR} = \frac{RR_1 + RR_2 + \dots + RR_N}{N} \quad (2)$$

Where N is the total number of RR intervals.

NNx

NNx is the count of adjacent RR intervals that are differed by more than x ms.

$$NNx = \sum_{i=1}^N \{ |RR_{i+1} - RR_i| > x \text{ ms} \} \quad (3)$$

Where N is the total number of RR intervals.

pNNx

pNNx is the percentage of differences between adjacent NN intervals that are > x ms. pNNx is calculated by dividing the NNx by the total number of RR intervals.

$$pNNx = \frac{NNx}{N} \cdot 100 \quad (\%) \quad (4)$$

Where N is the total number of RR intervals.

RMSD

RMSD is the square root of the mean of sum of differences of successive RR intervals. It is described as,

$$RMSD = \sqrt{\frac{1}{N-1} \sum_{i=1}^N (RR_{i+1} - RR_i)^2} \quad (5)$$

Where N is the total number of RR intervals.

3.3 Extraction of Frequency Domain features

Frequency domain features are calculated by Fast Fourier transform. The feature Very Low Frequency (VLF) is calculated over 0 to 0.04 and Low Frequency (LF) between 0.04 and 0.15, High Frequency between 0.15 and 0.4 and the total power between 0 and 0.4. Then the ratio of Low frequency and high frequency (LF/HF) is calculated.

The Fast Fourier transform is determined using the following equation.

$$F(u) = \frac{1}{N} \sum_{x=0}^{N-1} f(x) e^{-j2\pi ux/N} \quad (6)$$

Where N is the total number of RR intervals.

The power spectrum can be calculated as,

$$P(u) = R^2(u) + I^2(u) \quad (7)$$

$R^2(u)$ is the real part and $I^2(u)$ is the imaginary part of the digital signal.

3.4 Classification Of Arrhythmia Disease

The Heart Rate Variability features are used to classify the normal or arrhythmia disease. For classification of arrhythmia, the Classification and Regression tree is used. CART resembles a stepwise feature selection, as at each splitting it tries to obtain the most relevant information from the part of the space it is working on. However, one feature may not be included in the final tree because its effect was masked by other variables. Classification and regression tree is one of the decision tree which the impurity measure Gini index used as the splitting criterion. The Gini index can be calculated as,

$$GINI(D) = 1 - \sum_{i=0}^m P_i^2 \quad (8)$$

Where P_i is the probability of a tuple in D belongs to class C_i , and D is the dataset.

Gini index considers a binary split for each attribute. If Binary split on a partitions the data into D_1 and D_2 , the gini index of D with partitioning is,

$$Gini_A(D) = \frac{|D_1|}{|D|} Gini(D_1) + \frac{|D_2|}{|D|} Gini(D_2) \quad (9)$$

Hence the CART algorithm uses the binary split for selecting the split point. To select the split point for continuous attributes, the attributes are arranged in an order then the midpoint between each pair of adjacent values are taken as possible split points. The point giving the minimum Gini index for a continuous-valued attribute is taken as the split-point of that attribute. The point giving minimum Gini index is selected as the split point for that attribute.

The Reduction in impurity can be calculated as

$$\Delta Gini(A) = Gini(D) - Gini_A(D) \quad (10)$$

The attribute that maximizes the reduction in impurity is selected as the splitting attribute.

The accuracy of the classifier is the percentage of the test data that are correctly classified by the classifier. The confusion matrix is a useful tool for analyzing the classifier performance. The terms used for analyzing the classifiers ability are True positive, true negative, False positive and false negative. True positive means that the positive tuples that were correctly classified by the classifier. True negative means that the negative tuples that were correctly classified by the classifier. False positive means the negative tuples that were incorrectly classified. False negative means that the positive tuples that were incorrectly classified. The accuracy measures are sensitivity, specificity, precision and accuracy. The table 1 shows the accuracy measures.

Table 1. Accuracy Measures

Measure	Formula
Sensitivity	$\frac{TP}{TP + FN}$
Specificity	$\frac{TN}{TN + FP}$
Precision	$\frac{TP}{TP + FP}$
Accuracy	$\frac{TP + TN}{TP + TN + FP + FN}$

3.5 Classification of Types of Arrhythmia

First the classifier classifies the normal or arrhythmia disease and then further classifies different types of arrhythmia. The different types arrhythmia classified are Bradycardia, Tachycardia, Asystole and Atrial Fibrillation. Bradycardia refers to a heart rate that below the normal range. A heart rate below 60 beats per minute is bradycardia. Tachycardia refers to a heart rate that exceeds the normal range. A heart rate above 100 beats per minute is bradycardia. Atrial Fibrillation is a too

irregular or rapid heartbeat. The heart rate between 100 to 175 beats per minute is Atrial Fibrillation. Atrial Fibrillation occurs if fast, unsystematic electrical signals cause the heart's two upper chambers called the atria to fibrillate which means to contract very fast and irregularly. Asystole means there is no heartbeat.\

4. Results

Heart Rate Variability features are determined using Matlab software. The Heart Rate Variability features are calculated from the RR intervals. The RR intervals are stored in an ibi (inter beat interval) file format. It then processes the RR intervals for calculating the HRV features. The Time Domain Features AVNN, SDNN, RMSSD, NNx, pNNx and Frequency Domain features VLF, LF, HF and LF/HF are calculated using the standard formulas.

4.1 Time Domain Features

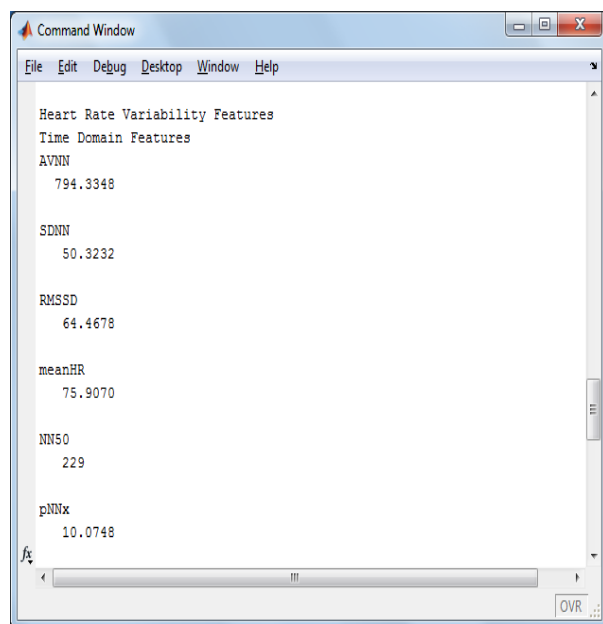


Figure. 4 Extraction of Time Domain Features

The Figure 4 shows the result of extraction of time domain heart rate variability features. The mean and standard deviations of all NN

intervals are calculated using the above formulas.

4.2 Frequency Domain Features

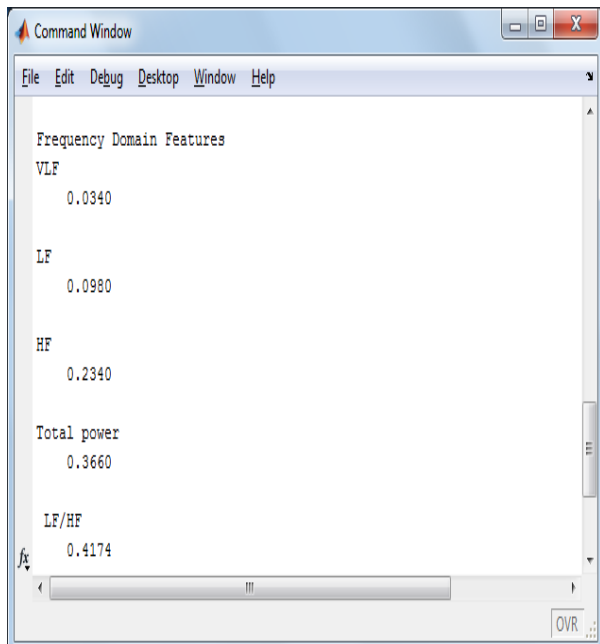


Figure. 5 Frequency Domain Features

The Figure 5 shows the frequency domain features calculated from the RR intervals. The features are VLF, LF, HF, LF/HF and Total power.

4.3 CART Decision Tree for Cardiac Arrhythmia Diagnosis

The extracted Heart Rate Variability features are used for building the classifier. The classifier is learned and the tree grown using Gini index as splitting criterion. The CART tree is implemented in MATLAB software. The attributes present in the HRV database are continuous attributes. Hence the CART algorithm uses the binary split for selecting the split point. To select the split point for continuous attributes, the attributes are arranged in an order then the midpoint between each pair of adjacent values are taken as possible split points. The point giving the minimum Gini index for a continuous-valued attribute is taken as the split-point of that

attribute. The features selected by the algorithm to classify the arrhythmia disease are LF/HF, VLF and SDNN. These three features are used for the classification of Arrhythmia disease.

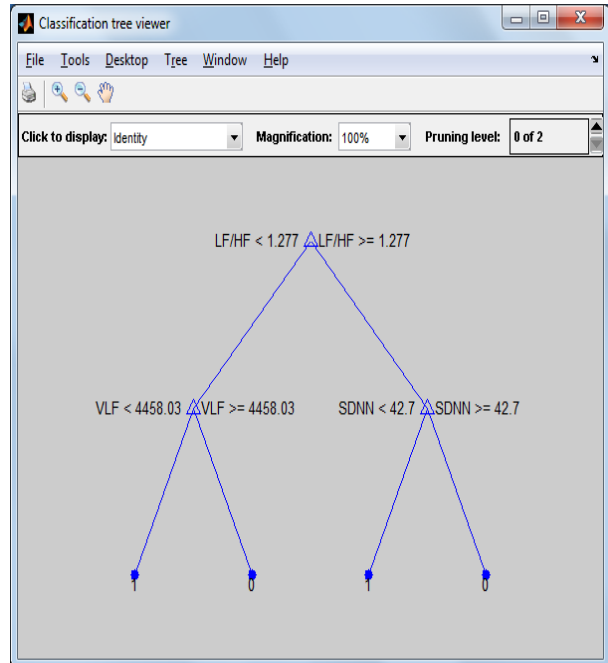


Figure. 6 Classification and Regression Tree for Cardiac Arrhythmia Diagnosis

The Figure 6 shows the Classification and Regression tree for cardiac arrhythmia diagnosis system. The Tree has the following nodes to classify the arrhythmia disease are ratio of low frequency to the high frequency, Very low frequency and standard deviation of NN intervals. The paths from the first node to each terminal one are a graphical representation of a set of "if... then..." rules. For instance, the rule can be formed as "if LF/HF is less than 1.277 and VLF less than 4458.03 then the subject is classified as Arrhythmia" and "if LF/HF is less than 1.277 and VLF greater than 4458.03 then the subject is classified as Normal". Other rules are "if LF/HF is greater than 1.277 and SDNN less than 42.7 then the subject is classified as Arrhythmia" and "if LF/HF is greater than 1.277 and SDNN greater than 42.7 then the

subject is classified as Normal". The Accuracy measures of the classifier are sensitivity, specificity, precision and accuracy. Sensitivity is the true positive rate, Specificity is the false positive rate. Accuracy of the classifier is the percentage of tuples that are correctly classified by the classifier.

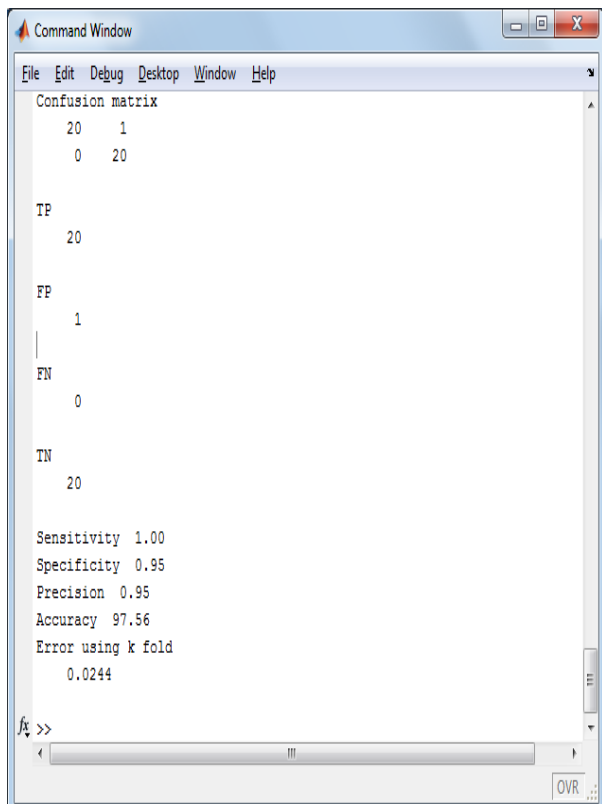


Figure. 7 Accuracy Measures of the Classifier

The Figure 7 shows the accuracy measure of the classifier. The classifiers performance can be evaluated from the above measures such as sensitivity, specificity, precision and accuracy. Leandro Pecchia et al used the Heart Rate Variability features to diagnose chronic heart failure and attained the accuracy of 96.39% and precision of 100%. The proposed system attained the accuracy of 97.56% and precision of 95%.

5. Conclusion

The major challenge in the heart disease diagnosis is the timely diagnosis and accurately identifying particular disease. To

make it easy and accurate, the diagnosis of arrhythmia can be done using the Heart Rate Variability features. The classification of arrhythmia disease based on HRV features are performed using Classification and Regression Tree. The CART is the human understandable tree like structure in terms of if then rules. The tree provides the simple if then rules for the classification of arrhythmia disease. In future, the work is extended to use some other classification models to classify arrhythmia and also classify different types of arrhythmia diseases. The Classification using Classification and Regression Tree provides 97.56% of accuracy.

6. References

- [1] Abhilasha M. Patel. Pankaj K. Gakare. A. N. Cheeran (2012) 'Real Time ECG Feature Extraction and Arrhythmia Detection on a Mobile Platform', International Journal of Computer Applications Vol. 44 No.23 pp. 40-45.
- [2] Anbarasi. M, Anupriya. E, Iyengar .N.C.H.S.N. (2010) 'Enhanced Prediction of Heart Disease with Feature Subset Selection using Genetic Algorithm' International journal of Engineering Science and Technology Vol.2, No.10, pp. 5370-5376.
- [3] Asha Rajkumar, Mrs. G.Sophia Reena (2010) 'Diagnosis of Heart Disease Using Data mining Algorithm' Global Journal of Computer Science and Technology Vol. 10 No. 10 pp. 38-43.
- [4] Chaittail S. Dangare, Sulabha S. Apte (2012) 'Improved Study of Heart Disease Prediction System using Data Mining Classification Techniques', International Journal of Computer Applications Vol. 47 No.10 pp.44-48 .

- [5] Chin-Teng Lin, Kuan-Cheng Chang, Chun-Ling Lin, Chia-Cheng Chiang, Shao-Wei Lu, Shih-Sheng Chang, Bor-Shyh Lin, Ray-Jade Chen, Yuan-Teh Lee and Li-Wei Ko (2010) ‘An Intelligent Telecardiology System Using a Wearable and Wireless ECG to Detect Atrial Fibrillation’ IEEE Transactions on Information Technology in Biomedicine, Vol. 14, No. 3, pp. 726-733.
- [6] Leandro Pecchia. Paolo Melillo. Mario Sansone. and Marcello Bracale (2011) ‘Discrimination Power of Short-Term Heart Rate Variability Measures for CHF Assessment’ IEEE Transactions on Information Technology in Biomedicine, Vol. 15. No.1 pp. 40-46.
- [7] Leandro Pecchia. Paolo Melillo and Marcello Bracale (2011) ‘Remote Health Monitoring of Heart Failure with Data Mining via CART Method on HRV Features’ IEEE transactions on biomedical engineering Vol.58 No.3 pp. 800-804.
- [8] Leandro Pecchia. Paolo Melillo. Mario Sansone. and Marcello Bracale (2011) ‘Discrimination Power of Short-Term Heart Rate Variability Measures for CHF Assessment’ IEEE Transactions on Information Technology in Biomedicine, Vol. 15. No.1 pp. 40-46.
- [9] Mohamed Ezzeldin A. Bashir, Dong Gyu Lee. Meijing Li. Jang-Whan Bae. Ho Sun Shon. Myung Chan Cho. and Keun Ho Ryu (2012) ‘Trigger Learning and ECG Parameter Customization for Remote Cardiac Clinical Care Information System’ IEEE transactions on information technology in biomedicine Vol. 16 No. 4 pp. 561-571.
- [10] Paolo Melillo. Roberta Fusco. Mario Sansone. Marcello Bracale. Leandro Pecchia (2011) ‘Discrimination power of long-term heart rate variability measures for chronic heart failure detection’ Journal on Springer Medical and Biological Engineering Vol.49 pp.67–74.
- [11] Shivajirao M. Jadhav. Sanjay L. Nalbalwar. Ashok A. Ghatol (2012) ‘Artificial Neural Network Models based Cardiac Arrhythmia Disease Diagnosis from ECG Signal Data’ International Journal of Computer Applications Vol. 44 No.15 pp.8-13.
- [12] Yakup Kutlu and DamlaKuntalp (2011) ‘A multi-stage automatic arrhythmia recognition and classification system’ Journal on Elsevier Computers in Biology and Medicine Vol.41, No. 41, pp. 37-45.

Unconstrained and Constrained Control of Drug Infusion System for Patients under Critical Care using Linear Model Predictive Control Strategy

¹S.A.Nirmala, ²Ranganath Muthu, ¹B. Veena Abirami

¹ Kumaraguru College of Technology, Coimbatore.

² SSN College of Engineering, Kalavakkam.

madavsri@gmail.com, ranganathm@ssn.edu.in, veenaabirami@yahoo.com

Abstract

Critical care patients whether undergoing surgery or recovering in intensive care units require drug infusion to regulate physiological variables such as blood pressure, cardiac output, heart rate and degree of consciousness. The rate of infusion of each administered drug is critical, requiring constant monitoring and frequent adjustments. In this paper, the control of the drug infusion system is implemented using model predictive controller (MPC) with a state-space model. Simulation studies are carried out for constrained and unconstrained cases and the results obtained are satisfactory.

General Terms

Biomedical Instrumentation and Control

Keywords

Drug infusion system, mean arterial pressure, cardiac output, model predictive control

1. Introduction

In critical care units, physicians maintain certain patient state variables within an acceptable operating range by infusing several

drugs. Many of these states are not measured directly and must be inferred. These physiological states are maintained within acceptable ranges by infusing drugs and/or intravenous fluids. Typically, the drugs and fluids are infused manually using drip intravenous (IV) lines, or using programmable pumps, which deliver constant infusion rates or an infusion rate profile. For example, in the case of patients with congestive heart failure, hemodynamic variables such as mean arterial pressure (MAP) and cardiac output (CO) are of primary importance and are maintained using sodium nitroprusside (SNP) and dopamine (DPM).

The infusion rate of SNP and DP is critical, requiring close attention and frequent adjustments. Manual control can be very tedious and time-consuming. The need for improved care of patients requires a feedback control system to efficiently and accurately regulate MAP and CO. Clinical experiments reported in the literature have shown that such an automated procedure is safe, effective and often superior to manual methods (Gao et al, 2003). Figure 1 shows the schematic diagram for the closed loop drug infusion system.

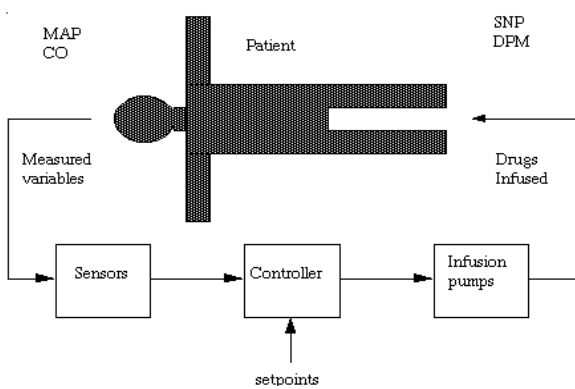


Figure 1 Schematic diagram of the drug infusion system

A variety of control methods have been proposed and tested. These methods can be classified into three categories: 1. Fixed gain linear control such as PID and optimal control, 2. Adaptive linear control such as minimum variance, pole placement, model reference control, self-tuning control and multiple model adaptive control etc and 3. Rule based control such as fuzzy logic control (Gao et al, 2003, Boldisor et al, 2011). While adaptive control strategies rely on using a nominal model with on-line adaptation, model predictive approaches depend on the accuracy and availability of a model capable of predicting the patient response.

The goal of the drug infusion control system is to manipulate the flow rate of the drugs SNP and DP to maintain the MAP and the CO at their set-points. In this paper, the control objective is to regulate simultaneously MAP and CO by automated infusion of inotropic and vasoactive drugs using MPC.

Model based predictive control, which can be implemented quite naturally on constrained multivariable systems, has been considered in this paper for drug delivery. An important issue in the design of drug infusion systems is

the need to impose bounds on dosages and infusion rates to avoid overdosing or drug toxicity. The primary advantage of the MPC is its ability to handle constraints explicitly. Its optimization-based framework allows computation of the optimal infusion rates subject to input and output constraints (Rao et al).

However, any new idea in the patient-care field cannot be put to use without proper testing and validation. Since animal experiments are a lengthy and expensive process, it is often preferable to use simulation. The success of the simulation depends on the simulation model used to mimic the patient conditions. The study was limited to imposing constraints on the manipulated variables i.e. flow rates of SNP and DP.

The paper is structured as follows: Section 2 discusses the patient model used in this study; in section 3, the MPC strategy is elaborated; Section 4 elaborates on the simulation study done on the closed loop control of drug infusion system with a state-space model. Results and discussions are presented in section 5.

2. Process Description

Yu et al (1992) modelled the hemodynamic system by a two-input two-output first order systems with delays. He proposed the equation (1) to represent the plant model.

$$\begin{bmatrix} \Delta MAP \\ \Delta CO \end{bmatrix} = \begin{bmatrix} \frac{K_{11}e^{-T_{11}s}}{\tau_{11}s + 1} & \frac{K_{12}e^{-T_{12}s}}{\tau_{12}s + 1} \\ \frac{K_{21}e^{-T_{21}s}}{\tau_{21}s + 1} & \frac{K_{22}e^{-T_{12}s}}{\tau_{22}s + 1} \end{bmatrix} \begin{bmatrix} SNP \\ DP \end{bmatrix} \quad (1)$$

Where, the gains K_{ij} represent the patient sensitivity to the drug, τ_{ij} the corresponding

Parameter	Typical value
K_{11}	-6
T_{11}	0.75
τ_{11}	0.67
K_{12}	3
T_{12}	1
τ_{12}	2
K_{21}	12
T_{21}	0.75
T_{21}	0.67
K_{22}	5
T_{22}	5
τ_{22}	1

time constants and T_{ij} the corresponding time delays between drug infusion and the response of the system. Typical values are shown in Table 1 (Bequette, 2003).

Table 1 Nominal values and ranges of model parameters

Using the transfer function model given in equation (1), the open loop characteristics was studied. The corresponding response is shown in Figure 2. From figure 2, it is inferred that the infusion of SNP decreases the MAP and increases the CO and the infusion of DP increases both MAP and CO.

3. Model Predictive Control

MPC is a control strategy that has developed largely in the recent years. MPC

fundamentally depends on a model of the system to be controlled. In general, a predictive control algorithm solves on-line an optimal control problem subject to system dynamics and variable constraints. Consider the system model given equation (2).

$$\begin{aligned} x(k+1) &= Ax(k) + Bu(k) + Gd_p(k) \\ y(k) &= Cx(k) + Du(k) + Hd_m(k) \end{aligned} \quad (2)$$

Where,

$x(k) \in \mathbb{R}^{nx}$ are the states, $u(k) \in \mathbb{R}^{nu}$ are manipulated inputs and $y(k) \in \mathbb{R}^{ny}$ are the measured outputs.

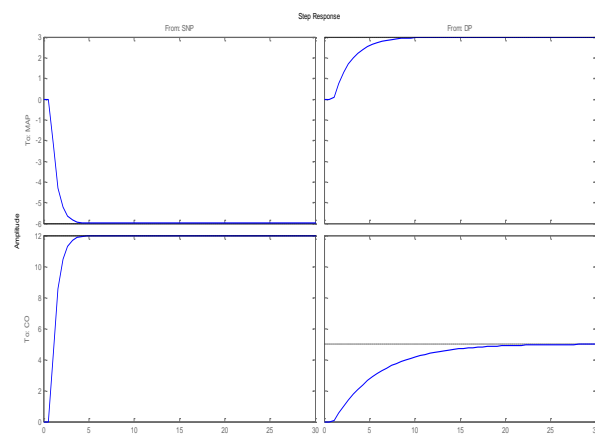


Figure 2 Open loop response of the drug infusion system

The vectors $d_p(k)$ and $d_m(k)$ are the unmeasured disturbances to the state dynamics (process noise) and to the outputs (measurement noise), respectively. The controller predicts the future behaviour of the actual system over a time interval defined by a lower and an upper prediction horizon, denoted by N_w and N_p , respectively. Figure 3 shows the basic principle of the MPC strategy.

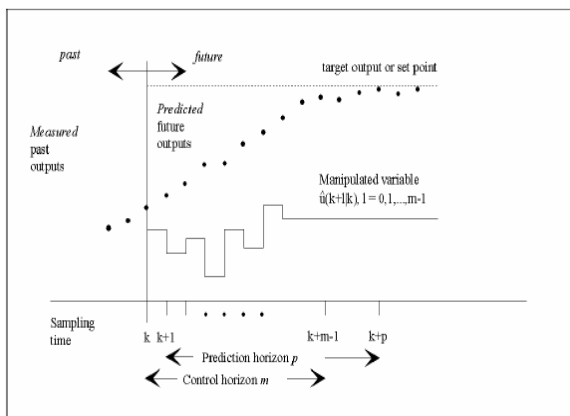


Figure 3 Basic Principle of the MPC Strategy

The optimal input to the plant is calculated by minimizing a cost function defined along the prediction horizon. This is usually specified as a sum of quadratic future errors between the reference trajectory and predicted plant output, and the predicted control effort given by equation (3).

$$J(k) = \sum_{i=N_w}^{N_p} \| \hat{y}((k+i)/k - r(k+i)) \|^2 Q(i) + \sum_{i=0}^{N_u-1} \| \Delta u((k+i)/k) \|^2 R(i) \quad (3)$$

Subject to constraints specified on the inputs, outputs and inputs increments given in equation (4).

$$\begin{aligned} u_{\min} &\leq u(k) \leq u_{\max} \\ y_{\min} &\leq y(k) \leq y_{\max} \\ \Delta u_{\min} &\leq \Delta u(k) \leq \Delta u_{\max} \end{aligned} \quad (4)$$

Where

$Q(i)$ is a positive definite error-weighting matrix;

$R(i)$ is a positive semi-definite control-weighting matrix;

$\hat{y}((k+i)/k)$ is the vector of the predicted output signals;

$r(k+i)$ is the vector of the future set-point;

$\Delta u((k+i)/k)$ is the vector of future control actions.

The presence of disturbances and plant/model mismatch are taken into account by implementing a feedback measurement and a receding horizon strategy, which means that only the first element of the computed control sequence is applied to the plant. At the next sampling interval, both the control horizon and the prediction horizon move one-step ahead and the entire cycle of state estimation, output prediction and optimization is repeated using the new measurements from the plant.

The tuning parameters of the MPC controller are the cost function weighting matrices R and Q , the control horizon N_u , the prediction horizon N_p and the sampling time T_s . The prediction horizon N_p determines the number of output predictions that are used in the optimization calculation. A long prediction horizon leads to better performance and has a stabilizing effect, but increases the computational burden.

The control horizon N_u determines the number of future control actions that are calculated at each optimization step. In general, a short control horizon leads to a controller that is moderately insensitive to uncertainties and modelling errors, whereas a long control horizon results in unnecessary control action and long computation time. The matrix Q penalizes the tracking errors and guides the servo performance of the control system. The matrix R is a move suppression factor that changes the aggressiveness of the controller and assures a smooth control action. A smaller sampling time, T_s , results in more aggressive control, while a larger sampling time results in less aggressive action.

Usually, the tuning of these parameters, in order to guarantee good performance, stability and robustness, is carried out by simulation, even if the approaches for developing model predictive control tuning rules exist (Camacho et al, 2004).

3.1 State-space model as prediction model

For the design of a linear MPC, a linearised approximation for the nonlinear model in equation (1) should be obtained. In this study, the transfer function model in equation (1) is linearised and a linear state-space model of the drug infusion system is obtained and used as the prediction model.

4. Closed Loop Study Of Drug Infusion System With MPC

Closed loop simulations were carried out on the drug infusion with MPC strategy without constraints, and after applying constraints on the manipulated variable with the linear state-space model as the prediction model.

4.1 Response of the drug infusion system with unconstrained MPC Strategy for a step change in the hemodynamic variables

Step changes of 10 mmHg and 5 ml/hr with initial values of zero were applied to the variables MAP and CO respectively. Figure 4 shows the response of the system without applying any constraints on the manipulated variables.

4.2 Response of the drug infusion system with constrained MPC Strategy for a step change in the hemodynamic variables

Constraints imposed on the manipulated variables mimic a real time system where the rate of change of drug flow cannot respond faster to the change in the set-point of the controlled variable, due to physical limitations of the final control element. The response of the drug infusion system was studied for a step change of 10 mmHg and 5 ml/hr with initial values of zero in the variables MAP and CO respectively, with constraints imposed on the rate of flow of the drugs SNP and DP, the two manipulated variables. Figure 5 shows the response obtained.

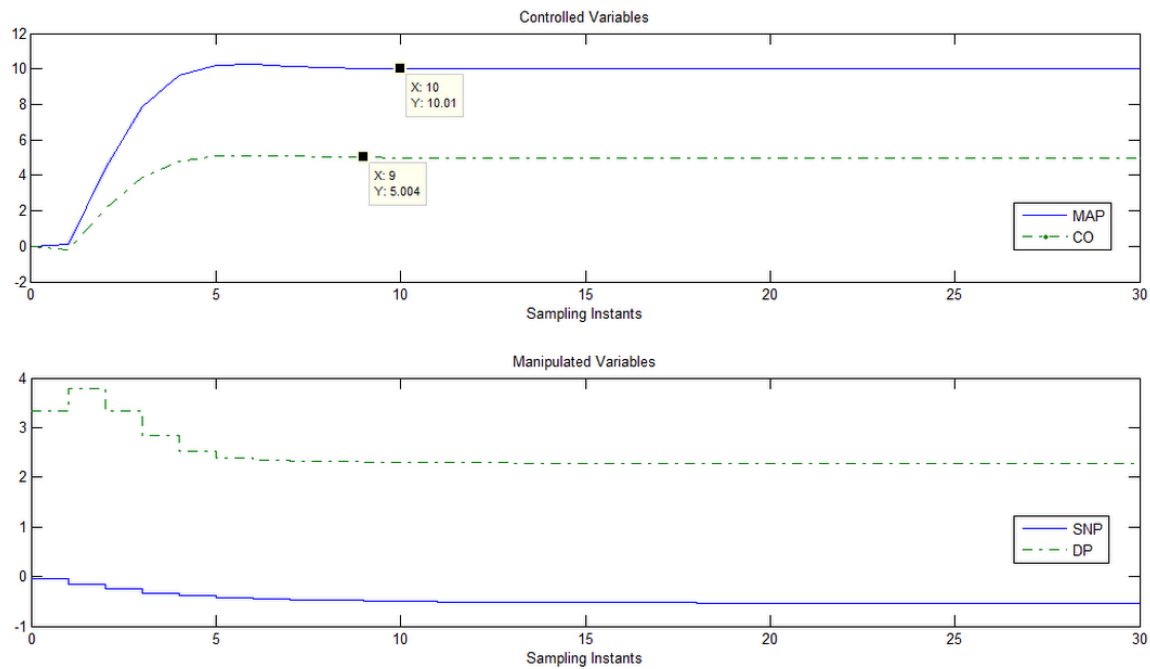


Figure 4 Response of the drug infusion system for a step change in the hemodynamic variables MAP and CO with unconstrained MPC using the state space model

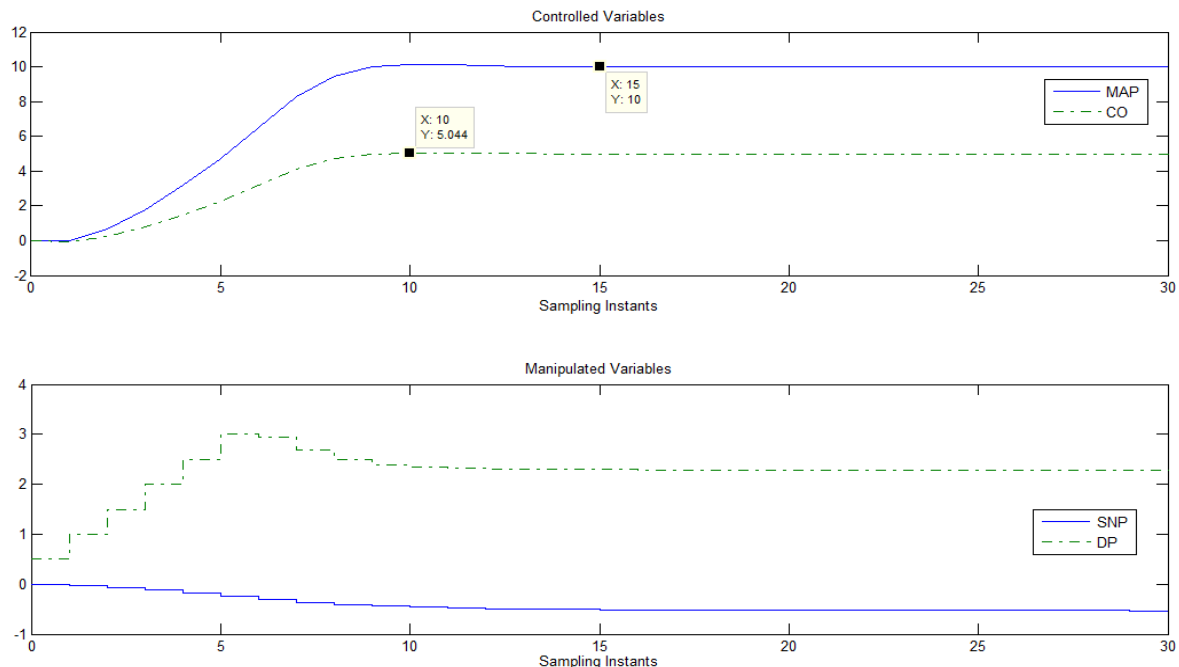


Figure 5 Response of the drug infusion system for a step change in the hemodynamic variables MAP and CO with constrained MPC using the state space model

5. Results and Discussion

In all the simulations, the initial conditions for MAP and CO are zero. This simulates a steady-state initial condition. A comparative study was done on the performance of the model predictive controller with and without constraints.

From figure 4, it is observed that for the system without constraints on the manipulated variables, the rate of change of drug flow is very fast. From figure 5, it can be seen that there is a uniform change in the variation of the drug flow rate due to the limitations of the final control element. Figures 4 and 5 shows that the unconstrained system settles down faster than the constrained system.

6. Conclusion

The inherent characteristics of the MPC to handle the multivariable system with constraints are demonstrated in this study. The main drawback in the application of the constraints is that the output takes a longer time to attain the new set-point due to the constraints. This is acceptable, as in real-time system, the physician applies these constraints.

7. References

- [1] Yang Gao and Meng Joo Er (2003), "Adaptive Fuzzy Neural Modeling and Control Scheme for Mean Arterial Pressure Regulation", IEEE International Conference on Intelligent Robots and Systems, pp. 1198-1203, Las Vegas, Nevada, USA.

- [2] Cristian N. Boldisor, Vasile Comnac, Simona Coman, Sorin Grigorescu (2011), "A Combined Experience and Model Based Design Methodology of a Fuzzy Control system for Mean Arterial Pressure and Cardiac Output", 18th IFAC World Congress, Vol. 18, Part 1, pp. 2889-2894, Milano, Italy.
- [3] M. Araki, E. Furutani (2005), "Computer control of physiological states of patients under and after surgical operation", Annual Reviews in Control, Vol. 29, No. 2, pp. 229–236.
- [4] Ramesh R. Rao, Brian Aufdehiede, B. Wayne Bequette (1999), "Multiple model predictive control of Hemodynamic variables: An Experimental study", American Control Conference, 2, 1253-1257.
- [5] C. Yu, R. Roy, H. Kaufman, and B. Bequette (1992), "Multiple-model adaptive predictive control of mean arterial pressure and cardiac output", IEEE Trans. in Biomedical Engineering, Vol. 39, No. 8, pp. 765-778.
- [6] Wayne Bequette B. (2003), "Process Control, Modeling, Design and Simulation", Prentice Hall of India Pvt. Ltd.
- [7] E. F. Camacho and C. Bordons (2004), "Model Predictive Control", Springer-Verlag, London.
- [8] Edgar T.F., D.M. Himmelblau, and L. Lasdon (2001), Optimization of Chemical Process, 2nd edition, McGraw-Hill, New York.
- [9] Selahattin Ozcelik and Kaufmanx (1999), "Multi-Drug Infusion Control Using a Robust Direct Adaptive Controller for Plants with Time Delays", 7th

Mediterranean Conference on Control and
Automation (MED99), pp. 989-1006,
Haifa, Israel.

Design Considerations for Differential Amplifiers in Bio impedance Measurements

Padma Batra¹, Rajiv Kapoor²

¹Mewar University, Chittorgarh, ²Delhi Technological University, Delhi

¹ padmabatra61@gmail.com

Abstract

We have analysed the Common Mode Rejection Ratio (CMRR) for differential amplifiers used in bioimpedance measurement systems and derived the complete equations for the case when OPAMPS have finite differential and common mode gains. In principle, passive ac-coupling networks that include no grounded components have an infinite CMRR, but they must provide a path for input bias currents. This paper analyses how component tolerances limit the CMRR and affect the transient response of different networks. Experimental results and various measurements support our theoretical predictions. The best CMRR is obtained when the differential gain is concentrated in the input stage, but it decreases at frequencies above 1 kHz because of the reduced CMRR for the differential stage at these frequencies.

Keywords— differential amplifiers, passive filters, ac-coupling, CMRR, biopotential amplifiers.

1. Introduction

External bioimpedance measurement on the body uses sinusoidal carrier signals from 10 kHz to 100 kHz. We study the systems that work at a single frequency. The parameter measured is tissue impedance, which is usually in a zone or part where it varies with time. The amplitude of the signal injected is limited for safety regulations to 1 mA at 10 kHz or up to 10 mA at 100 kHz. Typical values

of impedance obtained are very small, and, therefore, the need arises for the amplification of the signal obtained before any further processing.

OPAMP based differential amplifiers are a common building block in bioimpedance measuring systems. At higher frequencies, discrete transistors usually replace OPAMPS. Differential amplifiers are valuable because of their ability to reject power-line and other common mode interference which follows from their high common mode rejection ratio (CMRR).

In this paper, we analysed the CMRR performance of an amplifier with little variations in a basic differential amplifier circuit. First, a theoretical analysis shows what parameters determine the CMRR then we present experimental results that verify the theoretical models developed. We have paid particular attention to phase measurements as they have emerged as being very important in determining whether or not we are obtaining the best CMRR in a given circuit. The tradeoffs between component tolerances, CMRR and transient responses are identified and assessed by experimental measurements.

2. Common mode rejection ratio

The circuit model for 4 terminal bioimpedance measurement systems when using a single ended current source in Fig.1 is analysed to explain the need for high CMRR.



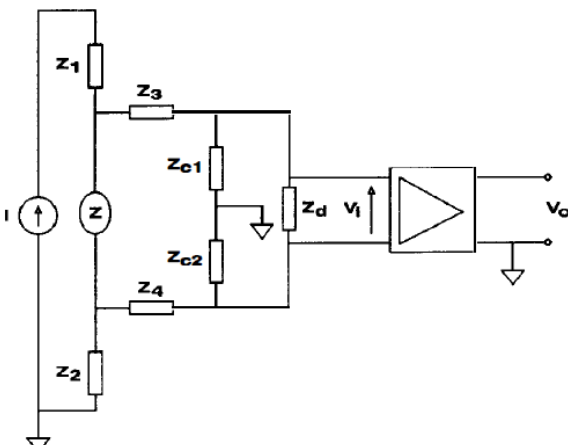


Fig 1. Circuit model for four terminal bioimpedance measurements using a single ended current source

A. Infinite Differential and Common Mode Input Impedances

Assuming both the differential and common mode input impedances to be infinite, the amplifier output voltages

$$V_o(s) = H_D(s)I(s) \left\{ Z(s) + \frac{1}{CMRR_A(s)} \left[\frac{Z(s)}{2} + Z_2(s) \right] \right\} \quad (1)$$

Here, $H_D(s)$ is the amplifier differential transfer function, $CMRR_A(s)$ is common mode rejection ratio and $Z_2(s)$ is the current injection electrode impedance.

Equation (1) shows that only a perfect differential amplifier would result in a zero offset and gain error. In order to evaluate the minimal $CMRR_A$ required in fig (1), we should know Z_2 and its variations. According to [2] we can assume Z_2 to be from $6k\Omega \parallel 10\text{ nF}$ at 10 kHz to $600\Omega \parallel 2\text{ nF}$ at 100 kHz, for thoracic impedance plethysmography. To have a 1% offset error, $CMRR_A$ must be atleast about 70dB.

B. Finite Differential and Common Mode Input Impedances

The next step is to determine the system common mode rejection considering finite input impedances. It is well known that in differential systems the total CMRR reduces to a value lower than the CMRR for the amplifier without any input imbalances. In bioimpedance measurements, the situation is different from that of biopotential amplifiers as described in [3]: firstly the common and differential mode voltages here are due to the same current (the one being injected), whereas when amplifying biopotentials the most concern is about power line interference; secondly, the ratios between electrode and amplifier input impedances are different from those encountered at low frequencies.

Taking into account the imbalances in electrodes and common mode impedances we define

$$Z_3 = Z_e + \Delta Z_e/2 \quad (2a)$$

$$Z_4 = Z_e - \Delta Z_e/2 \quad (2b)$$

$$Z_{c1} = Z_c + \Delta Z_c/2 \quad (3a)$$

$$Z_{c2} = Z_c - \Delta Z_c/2 \quad (3b)$$

Where the subindex "e" stands for electrode and "c" stands for common mode. Using the results from [3], we finally have

$$\frac{1}{CMRR_T} \approx \frac{1}{CMRR_A} + \frac{Z_e}{Z_c} \left\{ \frac{\Delta Z_c}{Z_c} + \frac{\Delta Z_e}{Z_e} \right\} \quad (4)$$

The common mode input voltage is determined here mainly by Z_2 . Therefore, the reduction of Z_2 is an important problem. Feeding back the common mode voltage to the current source (by driving its floating ground) or to the body so that no net current flows through Z_2 is a solution. If the bandwidth is not restricted to about 10 kHz it can result in oscillations.

From (4) we deduce that $CMRR_T$ is a complex number. The minimal value of $CMRR_T$ in order to achieve low errors must be judged by considering its phase angle. We have shown that at frequencies above 10 kHz, the output signal due to a common mode signal for the three OPAMP instrumentation

amplifier is -90° or $+90^\circ$ out of phase with the common mode input signal [5]. Further, at the measurement frequencies, both electrode and common mode input impedances have large capacitive components. As a result the phase for CMRR_T will strongly depend on the relative value of impedance imbalances: the lower these are the closer the phase of CMRR_T will be zero. Equation (4) shows that the effect of a given electrode imbalance is smaller for higher common mode input impedances. Therefore, this is another important parameter in amplifier design.

3. Fully differential passive ac-coupling networks

Fully differential ac amplifiers can easily be designed by placing an ac-coupling network in front of a fully differential dc amplifier [1]. Such a network, however, must have a high common mode rejection ratio (CMRR) to keep the overall CMRR high.

A. Coupled Single-Ended Filters (Network 1)

Fig. 1 shows a fully differential ac-coupling network built by joining two single-ended, high-pass filters and connecting the common node to the ground through a high-value resistor R_B [8]. Ideally, R_B should be infinite to achieve an infinite CMRR, but its maximal value is dictated by the input bias currents of the amplifier.

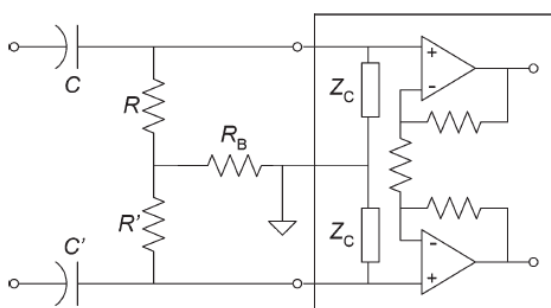


Fig. 2. Fully differential passive ac-coupling network built by connecting two single-ended, high-pass filters whose common node is grounded through a high value resistor.

If the ensuing common-mode impedances Z_C are large enough, the differential-to-differential gain is given in (1), shown at the bottom of the next page, which for matched components ($R = R_-$, $C = C_-$, and hence, $\tau = RC = R_-C_- = \tau_-$) simplifies to

$$G_{DD}(s) = \frac{1 + (\tau + 2\tau_B)s}{[1 + (2\tau_B)](1 + \tau s)} = \frac{\tau s}{1 + \tau s} \quad (5)$$

where $\tau_B = R_B C$. This transfer function corresponds to a first order high-pass filter. The CMRR for unmatched components when the ensuing common-mode input impedance Z_C is included is

$$\text{CMRR}(s) = \frac{(R + 2RB)CZ_C}{Z_C \frac{\Delta R}{R} + (Z_C + R + 2RB) \frac{\Delta C}{C} + (R + 2RB) \frac{\Delta Z_C}{Z_C}} \quad (6)$$

The effect of unmatched components has only been considered in the denominator because its influence on the numerator is irrelevant. If Z_C is mostly determined by the common-mode input impedance C_{IN} , (6) can be rewritten as:

$$\text{CMRR}(s) \approx \frac{\frac{\tau + 2\tau_B}{\Delta C / C + \Delta R / R} s}{1 + (\tau_{IN} + 2\tau_B, IN) \frac{\Delta C / C + \Delta C_{IN} / C_{IN}}{\Delta C / C + \Delta R / R} s} \quad (7)$$

where $\tau_{IN} = R C_{IN}$, and $\tau_{B,IN} = R B C_{IN}$. At frequencies well below $f_c \approx 1/[2\pi(R + 2RB)C_{IN}]$, the CMRR increases by 20 dB/dec according to

$$\text{CMRR}_{LF}(s) \approx \frac{(\tau + 2\tau_B)S}{\Delta R / R + \Delta C / C} \quad (8)$$

whereas at frequencies well above f_c , the CMRR reaches the limit value

$$\text{CMRR}_{HF}(s) \approx \frac{C / C_{IN}}{\Delta C / C + \Delta C_{IN} / C_{IN}} \quad (9)$$

B. Cascade-Reversed Single-Ended Filters (Network 2)

Fig. 2 shows a fully differential ac-coupling network built by cascade-connecting two single-ended high-pass filters with reverse polarity [6, p. 376]. The low-pass version of this circuit has been used for some time in analog front ends for data acquisition [7].

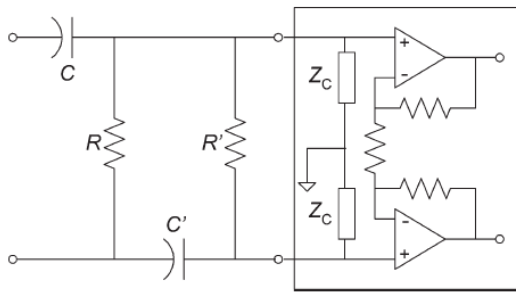


Fig. 3. Fully differential passive ac-coupling network built by cascading two single-ended, high-pass filters with reverse polarity.

If the ensuing common-mode impedances Z_C are large enough, the differential-to-differential gain corresponds to a second-order high-pass filter. Hence, the low-frequency rejection is better than that of Network 1.

Since, there is no current path to the ground (bias currents flow to the ground through the signal source), the CMRR for the ac-coupling network alone is infinite, even for unmatched components. If finite input capacitances from each amplifier input to the ground are considered, the CMRR is

$$CMRR(s) = \frac{\tau(1 + C/C_{IN})s + 1/2}{\tau(\Delta C_{IN}/C_{IN} + \Delta C/C)s + 1} \quad (10)$$

whose extreme values at very low and very high frequencies, respectively, are

$$CMRR_{LF}(s) \approx \tau(1 + C/C_{IN})s + 1/2 \quad (11)$$

which is limited even for perfectly matched capacitances, and

$$CMRR_{HF}(s) \approx \frac{1 + C/C_{IN}}{\Delta C/C + \Delta C_{IN}/C_{IN}} \quad (12)$$

which is quite close to that for network 1.

c. Coupled Single-Ended Filters Connected to the Input Common-Mode Voltage (Network 3)

Fig. 4 shows a fully differential ac-coupling network built by joining two single-ended, high-pass filters whose common node is connected to the input common-mode voltage obtained by an ungrounded passive voltage adder [8].

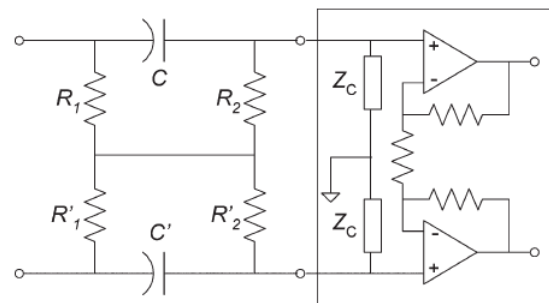


Fig. 4. Fully differential passive ac-coupling network built by mirroring two single-ended, high-pass filters whose common node is connected to the common-mode input voltage obtained through an ungrounded passive voltage adder.

If the ensuing common mode impedances Z_c are large enough the differential to differential gain corresponds to a first order high pass filter and no matching is required for R_1 and R_1' to obtain high frequency response.

The CMRR for this network would be infinite if the input common-mode impedances of the ensuing amplifier were ideal. If Z_c is mainly determined by stray capacitances C_{IN} then we have the following expression for CMRR.

$$CMRR(s) \approx \frac{C}{C_{IN}} \times \frac{1+2\tau}{\Delta R/R + \Delta C_{IN}/C_{IN} + 2\tau(\Delta C/C + \Delta C_{IN}/C_{IN})s} \quad (13)$$

Whose extreme values at very low and very high frequencies, respectively are

$$CMRR_{LF}(s) \approx \frac{C/C_{IN}}{\Delta R/R + \Delta C_{IN}/C_{IN}} \quad (14)$$

$$CMRR_{HF}(s) \approx \frac{C/C_{IN}}{\Delta C/C + \Delta C_{IN}/C_{IN}} \quad (15)$$

$CMRR_{LF}$ is larger than that for the networks 1 and 2, whereas $CMRR_{HF}$ is uncapped and can become very large for matched capacitances.

D. Another Proposed Active dc Suppression Amplifier Circuit without Grounded Resistor

The circuit shown in fig 5.uses an integrator in a feedback loop around the difference amplifier [1], [6]. The system has two ac-coupled stages: the front differential ac-coupling network and the high pass difference amplifier. The overall transfer function is

$$T(s) = \frac{s\tau_2}{1+s\tau_2} \frac{s\tau_i A V_0}{1+s\tau} \quad (16)$$

Where $\tau_i = R_i C_i$ and $A V_0 = 1 + 2R_4/R_3$. The first factor in (16) corresponds to the passive ac-coupling network and the second factor corresponds to the amplifier and dc restoration circuits.

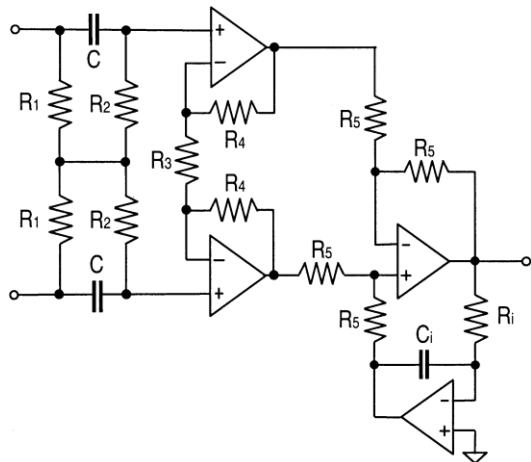


Fig. 5. Proposed amplifier circuit, which has two ac-coupling stages, a passive input stage, and an active dc suppression circuit.

The simple, novel, ac-coupled front end for biopotential measurements in Fig. 5 is a fully differential passive-coupling network that does not include any grounded resistor, hence, resulting in a high CMRR. The proposed network enables the design of a high gain for the input stage of biopotential measurement systems, thus leading to implementations with a reduced number of stages, which are particularly convenient for low power applications. Because the common-mode voltage is dc coupled, the proposed circuit also suits single-supply operation.

A single-supply ECG amplifier with a gain of 1001, built according to the design rules proposed and tested for transient and frequency response, and CMRR, fulfilled the requirements in [10], including a CMRR of 123 dB at 50 Hz.

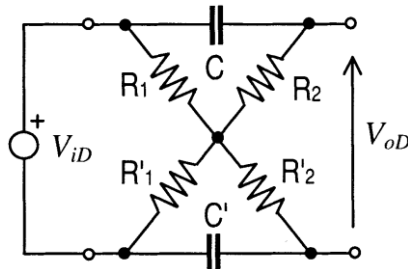


Fig. 6. Proposed fully differential ac-coupling network that does not include any grounded resistor.

The fig. 6 is an alternative drawing of the proposed passive ac-coupling network in fig. Because it is a fully differential circuit, differential and common-mode voltages define four transfer functions. The main transfer function G_{DD} is the quotient between the Laplace transforms of the differential output voltage V_{OD} and the differential input voltage V_{ID} . The circuit gain is given by the following expression [8]

$$G_{DD} = \frac{1}{s + 1/\tau_2} \quad (17)$$

where $\tau_2 = R_2 C$.

E. Another Circuit with dc Output Voltage Feedback and no Grounded Component

Fig. 7 shows a simplified model of the proposed biopotential amplifier [4]. It includes a fully differential feedback network with two attenuators, one located at the input of the integrator stage and the other at its output. Assuming a negligible error voltage at the op amps inputs (this implies infinite gain op-amps), the ratio between differential-mode input and output voltages ($=G_{DD}$, differential input to differential output gain) is

$$A(s) = \frac{\alpha\beta s\tau}{1 + s\tau} \quad (18)$$

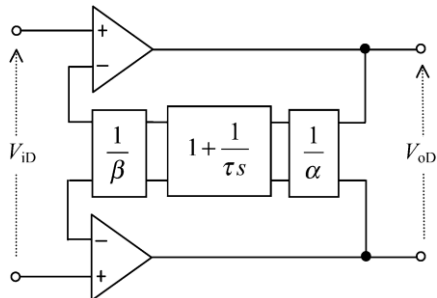


Fig. 7.Fully differential circuit for dc suppression implemented by feeding back the dc output voltage using a fully differential network.

Fig. 8. Is a possible implementation of the circuit shown above. Assuming $R_1=R_1'$, $R_2=R_2'$, $R_4=R_4'$, $R_T=R_T'$ and $C_T=C_T'$, we have

$$\alpha = 1 + 2R_4/R_3 \quad (19a)$$

$$\beta = 1 + 2R_2/R_1 \quad (19b)$$

$$\tau = R_T C_T \quad (19c)$$

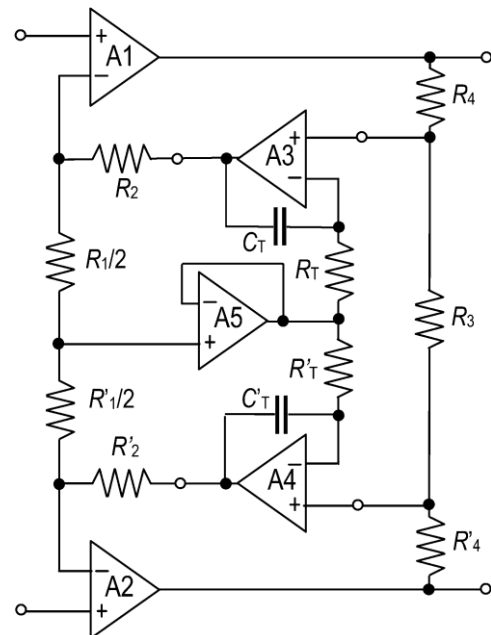


Fig. 8.Implementation of the method in Fig. 7. Because the proposed topology does not include any grounded component, its CMRR is ideally infinite.

The passive component mismatches do not degrade the CMRR. Given that the proposed circuit has no connections to ground, and disregarding stray capacitances, no current flows when applying a common-mode input voltage. In fact, all circuit nodes reach this potential regardless of eventual mismatches in passive components due to their tolerance. Hence, the differential output is zero, which means $G_{DC}=0$ (common mode input to differential output gain), and the CMRR ($=G_{DD}/G_{DC}$) is infinite. In practice, however, mismatches in differential and common-mode op amp open loop gain limit the global CMRR [5]. A good choice to minimise opamp mismatches is to use dual IC models which yields typical CMRR values greater than 100 dB at 50 Hz even for general purpose opamps.

4. Experimental Results and Discussion

The first three passive ac-coupling networks in Figs. 2-4 have been built and tested for the following component values: $R =$

$R' = 1 \text{ M}\Omega$, $R_B = 10 \text{ M}\Omega$, $C = C' = 100 \text{ nF}$ (Network 1);

$R = R' = 2.8 \text{ M}\Omega$, $C = C' = 100 \text{ nF}$ (Network 2) ; and $R_1 =$

$R_2 = 1 \text{ M}\Omega$, $C = C' = 100 \text{ nF}$ (Network 3). These values were selected to set the same high-pass corner frequency of about 1.6 Hz for the three networks. Resistors and capacitors had a $\pm 5\%$ tolerance. The instrumentation amplifier (IA) connected to the network output was AD620AN, whose relevant parameters had the following typical values: $I_{BIAS} = 0.5 \text{ nA}$, $I_{OS} = 0.3$, $V_{OS} = 30 \mu\text{V}$, $C_{IN} = 2 \text{ pF}$, and $CMRR = 135 \text{ dB}$ at dc for $G = 1000$. The maximal CMRR that can be measured with our setup is limited by the CMRR of this IA. Therefore, we have experimentally characterized this CMRR from dc to 1 kHz and verified that it is greater than 115 dB. To keep C_{IN} small, IC pins were directly soldered to input components so that no printed circuit board lands would be involved in the connection. Fig. 9 shows the CMRR for the three networks analyzed.

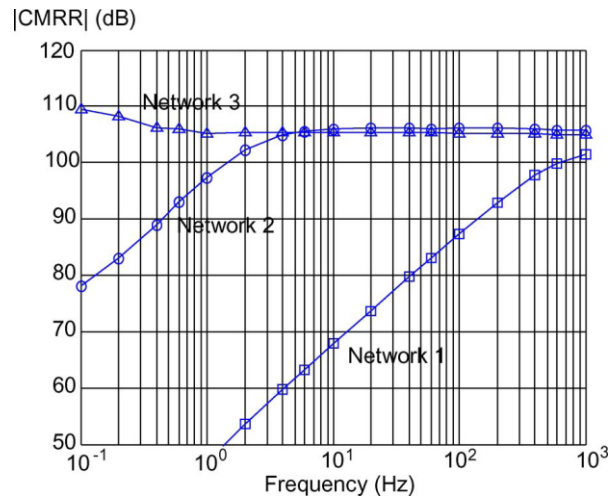


Fig. 9. Cmrr For The Three Ac-Coupling Networks In Figs2-4

The following table summarises a comparative behaviour of the CMRR at low and high frequencies as well as the offset

voltages due to input bias currents for the threenetworks (1-3).

Table I
Low And High Frequency Cmrr Behavior And Offset Voltages Due To Input Bias Currents For The Networks (1-3)

	Network 1	Network 2	Network 3
$CMRR_{LF}$	$\frac{(\tau + 2\tau_B)s}{\Delta R + \Delta C} \frac{s}{R + C}$	$\tau \left(1 + \frac{C}{C_{IN}} \right) s + \frac{1}{2}$	$\frac{C/C_{IN}}{\Delta R + \Delta C} \frac{s}{R + C_{IN}}$
$CMRR_{HF}$	$\frac{C/C_{IN}}{\Delta C + \Delta C_{IN}} \frac{s}{C + C_{IN}}$	$\frac{1 + \frac{C}{C_{IN}}}{\Delta C + \Delta C_{IN}} \frac{s}{C + C_{IN}}$	$\frac{C/C_{IN}}{\Delta C + \Delta C_{IN}} \frac{s}{C + C_{IN}}$
V_{bias}	$ I_{BIAS1}R - I_{BIAS2}R' $	$ I_{BIAS2}R' $	$ I_{BIAS1}R_2 - I_{BIAS2}R_2' $

For a worst-case condition, with a $\pm 5\%$ tolerance in passive components and a $\pm 10\%$ tolerance in input-amplifier impedance, the theoretical CMRR values at 50 Hz are 70 dB (Network 1) and 105 dB (Networks 2 and 3).

Thus the three proposed networks improve the CMRR value of industry-standard ac-coupling circuits that have separate connections from each

signal terminal to the ground. The limited input impedance of network 3 can reduce the CMRR.

Implementing the complete circuit of single-supply ECG amplifier [8] based on the circuit explained in fig. 5, the frequency response so obtained is given in fig. 10.

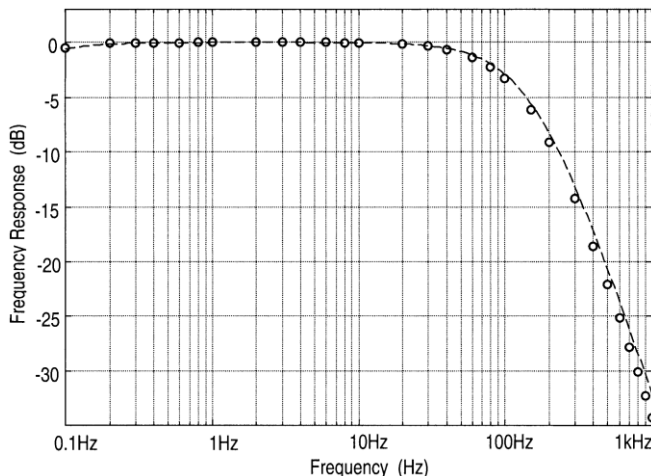


Fig. 10. Frequency response of the ECG amplifier in Fig. 3. The analytic expression is in dashed line and experimental data with markers.

The amplifier shown in fig. 8 has been built by using metal film resistors with 1% tolerance for R_1 to R_4 , 10% tolerance for R_T and 10% tolerance for capacitors C_T .

5. Conclusion

We have analyzed five differential ac coupling networks that do not use separate grounded components for each signal line and, hence, achieve a very high CMRR. None of the networks rely on matched passive components. The network 2 (Fig. 3) and network 3 (Fig. 4) yield a better CMRR than network 1 (Fig. 2). The proposed network in Fig. 5 has a reduced number of stages convenient for low power applications and is also suitable for single-supply operations. Lastly, the proposed DC

suppression circuit in Fig. 8 , in addition to ac coupling, provides a simple method for fast restoring the dc level of biopotentials. Also the absence of any grounded passive component makes the CMRR of the amplifier insensitive to the tolerance of passive components. A circuit implementation with a single 5V power supply yields 102dB CMRR at 50 Hz.

6. Acknowledgment

This work is supported by Department of Electronics and Communication Engineering, Krishna Institute of Engineering & Technology, Ghaziabad.

7. References

- [1] Oscar Casas, E. M. Spinelli, R. Pallas-Areny, “Fully Differential AC-Coupling Networks: A Comparative Study”, IEEE Trans. Instrum. Meas., vol. 58, Jan. 2009.
- [2] T.Yamamoto and Y.Yamamoto, “Electrical properties of the stratum corneum” , Med. Biol. Eng., vol. 14, pp. 151-158, Mar. 1976.\
- [3] A.C. Meeting van Rign, A.Peperanf C. A. Grinbergen, “High-quality recording of bioelectric events”, Med. Biol. Eng. Comput., vol. 28, pp. 389-397, 1990.
- [4] E. M. Spinelli, Nolberto Martinez, Miguel Angel Mayosky and R. Pallas-Areny, “A Novel Fully Differential Biopotential Amplifier with DC Suppression”, IEEE Trans. Biomed. Eng. Vol. 51, Aug. 2004.
- [5] R. Pallás-Areny and J. G. Webster, “Common mode rejection ratio in differential amplifiers”, IEEE Trans. Instrum. Meas., vol. 40, pp. 669-676, 1991.
- [6] R. Pallás-Areny and J. G. Webster, Analog Signal Processing. New York: Wiley, 1999.

- [7] B. M. Gordon, The Analogic Data-Conversion Systems Digest.Wakefield, MA: Analogic, 1977, p. 38.
- [8] E. Spinelli, R. Pallàs-Areny, and M. Mayosky, “AC-coupled front-end for biopotential measurements,” IEEE Trans. Biomed. Eng., vol. 50, no. 3, pp. 391–395, Mar. 2003.
- [9] H. W. Smit, K. Verdon, and C. A. Grimbergen, “A low-cost multichannel preamplifier for physiological signals,” IEEE Trans. Biomed. Eng., vol. BME-34, pp. 307–310, Apr. 1987.
- [10] American National Standard ANSI/AAMI EC38:1998, Ambulatory Electrocardiographs. Arlington, VA: Association for the Advancement of Medical Instrumentation, 1999.

A Novel DWT-LSB Watermarking Scheme for Fingerprint Authentication with Increased Security using RSA algorithm

S.Pradhebaa Rubinaa, S.Usha

Department of Electronics and Electrical Engineering,

Kongu Engineering College, Perundurai.

rubinaasrec@gmail.com, sushamangal@gmail.com

Abstract

In this paper, the Digital watermarking schemes comprising both the spatial and frequency domain approach is used to watermark the fingerprint image into the face image for secure transmission of fingerprint image. The security in the network is being increased by the transmitting the cipher text image of the watermarked image using RSA algorithm with the minutiae point as the key. Such that the hacking of key can be avoided during transmission since the key can be generated only by the authenticated person. At the receiver side the cipher text is again decrypted and the watermarked image can be obtained. And the fingerprint image is recovered from the watermarked image using the inverse process. The Stillness of the watermarking scheme is measured by the Peak Signal to Noise Ratio and the Quality Index. The proposed method is developed using MATLAB (2010b).

Index Term

Cipher text, DWT, Watermarking, LSB watermarking, PSNR, RSA algorithm.

1. Preface

In contemporary era, digital information transformation has a great impact on human life. Hefty information content can be stored and transmitted with security. A mass data of governments, military information, e-passport applications are to be transmitted securely through internet. The confidentiality in information is being maintained by various techniques such as cryptography, watermarking and stenography.

Biometrics based recognition techniques uses physiological characteristics that are becoming consistently popular compared to traditional techniques like identification cards or passwords. The main reason for this reputation is the ability of the biometrics to discriminate the authorized person and a pretender who illegally try to acquire license [4] [5]. The biometric techniques such as fingerprint, face, iris, voice, etc, offer a reliable method for personal identification, the problem of security and integrity of the biometrics data pose several security problems. Consider if the biometric data is stolen and replaced by another then the legally authorized person is restricted to access at the juncture. So the biometric data has to be secured during transmission. In most of the applications the biometric data is secured by either watermarking or cryptography method [1] [6]



[9]. This paper comprises the combination of both the watermarking and cryptography for secure transmission of the biometric data such as the fingerprint image.

Digital Watermarking is the process of hiding or embedding an unapparent data into the specified data. The unapparent data is the watermark and the specified data is the cover work. This cover work can be an image, audio or a video file. This embedded unapparent data can be extracted from the multimedia at the receiver side for security purposes. Watermarks can be embedded using spatial domain or a transform domain [3].

Embedding the watermark into spatial domain component of the original is straight forward method. LSB scheme is one of the examples of spatial domain which modifies the lower order bits of cover image to embed the watermark. It has the advantage of low complexity and easy implementation but problem with this scheme is low security, because it is possible to remove the watermarked image easily by setting all LSBs or pixels to zero.

In Transform domain technique the original cover image is transformed into transform coefficients by using various transforms like DCT, DFT and DWT etc. Nowadays discrete wavelet transform is widely used due to its multi resolution property and its robustness against various attacks. [2]

The DWT Transform divides the image into 4 sub-bands cA, cH, cV and cD. The message or the secret information is embedded into the mid-frequency range due to its robustness compared to the lower and high frequency sub-bands.

Cryptography is the practice and study of hiding information into unreadable form. Modern cryptography interconnects the disciplines of arithmetic, computer science, and engineering. Applications of cryptography include ATM cards, computer passwords, e-passport, e-driving license and electronic commerce. Cryptology former to the modern age was almost synonymous with encryption, the conversion of information from a readable state to unintelligible state. The sender retained the ability to decrypt the information and therefore avoid unwanted persons being able to read it. [8][7]

The most common, public key cryptography implementation is RSA algorithm named after three MIT mathematicians who developed it — Ronald Rivest, Adi Shamir, and Leonard Adleman. RSA today is used in hundreds of software products and can be used for key exchange, digital signatures, or encryption of small blocks of data. In the proposed method one of the minutiae points derived from fingerprint and is used as key for the RSA algorithm.

2. Proposed Method

In the proposed digital image watermarking scheme the watermark is embedded using discrete wavelet transform and LSB algorithm. The algorithm is composed of watermark embedding process, key generation from minutiae point of fingerprint, formation of cipher text image using RSA algorithm, extracting watermark image from the cipher text using RSA algorithm and watermark extraction process.

The intact of the project can be divided into two phase. The transmission phase and the reception phase.

2.1) Transmission Phase

In the transmission phase the fingerprint image will be embedded in the face image using LSB-DWT and the watermarked image will be encrypted using RSA algorithm using minutiae point as the key and the cipher text image will be transmitted in the network. The flow in the transmission side will be shown in the Fig.1

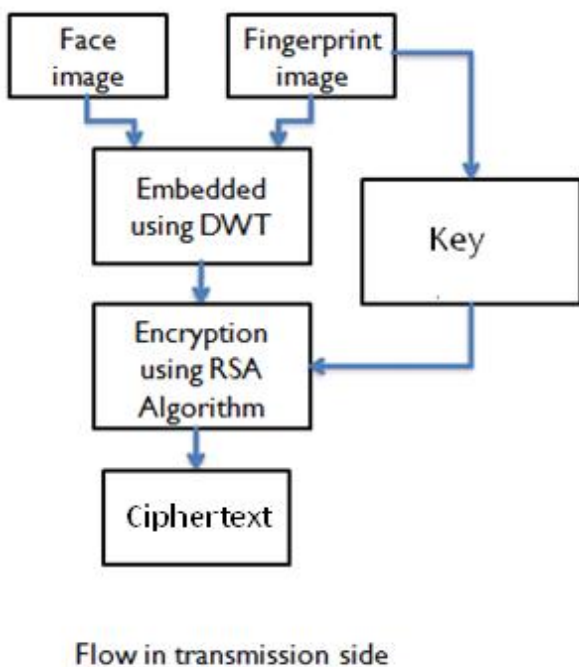


Fig.1 Flow in Transmission side

Step 1: The original face image of size 512X512 is taken and is divided into 64 blocks of size 64X64 each. And the texture information is calculated for each block. (The selection of size of the image depends on the application. Consider for e-passport application the resolution is approximately 512X512). And the fingerprint image of size 256X256 is taken and divided into 16 blocks

of size 64X64 each. Among the 64 blocks of the face image 16 highest texture information blocks are selected. For each high texture information blocks DWT is applied. The watermarks are generated by LSB algorithm. Since, the mid frequency sub-band coefficients are less sensitive to attacks, the generated watermark of the fingerprint is embedded into the mid frequency sub-band of the DWT cover image. By applying inverse DWT and concatenating the blocks, the watermarked image is obtained. The watermark embedding process is shown in the Fig.2

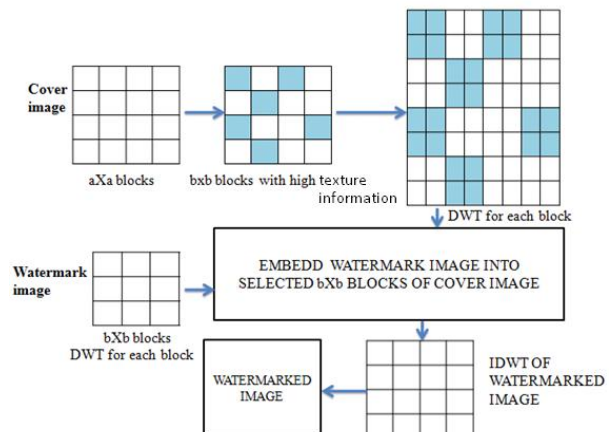


Fig.2 Watermarking Block Diagram

Step 2: Each fingerprint will have its unique bifurcation and termination points. The bifurcation and termination points are taken from the data base and one point which satisfies the prime number concept is used to derive the public key and private key for the proposed method.

Step 3: The cipher image is formed by using RSA encryption algorithm for which the inputs are Watermarked image and public key derived by using STEP 2. The figure 3 shows the formation of Cipher text Image

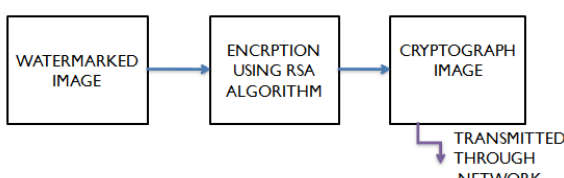


Fig.3 Formation of Cipher text Image

RSA Algorithm:

Step 1: Key Generation

1. Choose 2 distinct random prime numbers : $p:q$
(In the proposed method p and q are one minutiae point of fingerprint image)
2. Compute $n = pxq$
3. Compute $f(n) = (p-1)(q-1)$ (Euler's totient function)
4. Choose an integer e , for $1 < e < f(n)$ and $\text{gcd}(e:f(n)) = 1$
5. Compute $d \equiv e^{-1} \pmod{f(n)}$
6. Publish the public encryption key : (e,n)
7. Keep secret private decryption key : (d,n)

Step 2: Encryption

1. To encrypt a message the sender has to:
2. Obtain public key of recipient $(e:n)$
3. Represent the message as an integer m in $[0:n-1]$
4. Compute : $c = m^e \pmod{n}$

Step 3: Decryption

To decrypt the cipher text c the recipient:

- 1) Uses his private key $(d:n)$
- 2) Computes : $m = c^d \pmod{n}$

Using this algorithm the cipher text of the watermarked image is formed and transmitted securely in the network.

2.2) Reception Phase

In the reception phase the cipher text image will be decrypted into watermarked image and the watermark will be recovered. The recovery process is shown in Fig.4.

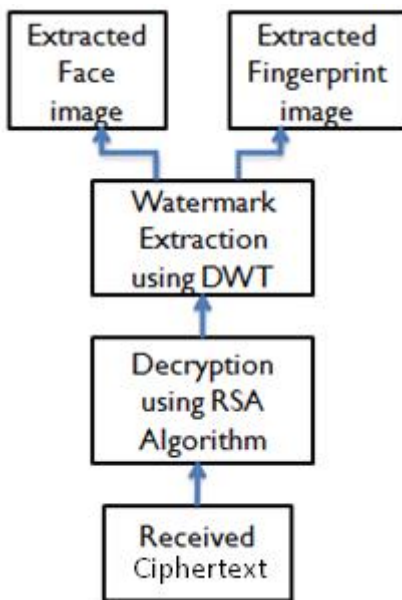


Fig.4 Flow in Reception Side

Step 1: The private key will be generated from the authenticated fingerprint image using minutiae point at the receiver side. Using the RSA algorithm watermarked image will be extracted from the ciphertext image using the key. The decryption of the ciphertext image is shown in Fig.5.

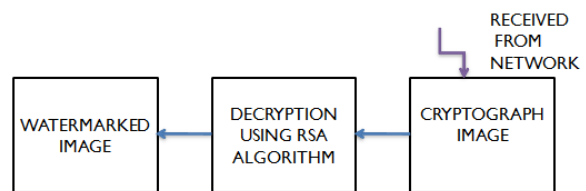


Fig.5 Decryption of Ciphertext Image

Step 2: The received watermarked image of size 512X512 is divided into 64 blocks and the texture information is calculated. Among the 64 blocks 16 blocks having highest texture information is selected. For each high texture information blocks DWT is applied. The LSB of the watermarked image is extracted from the mid-frequency sub-band and it is made as MSB for the new image and IDWT is taken for the new image which is the recovered message image (fingerprint). By concatenating the blocks the fingerprint will be recovered. PSNR is calculated to measure the imperceptibility of the watermarking scheme. The watermark extraction process and the recovery of fingerprint is shown in Fig.6

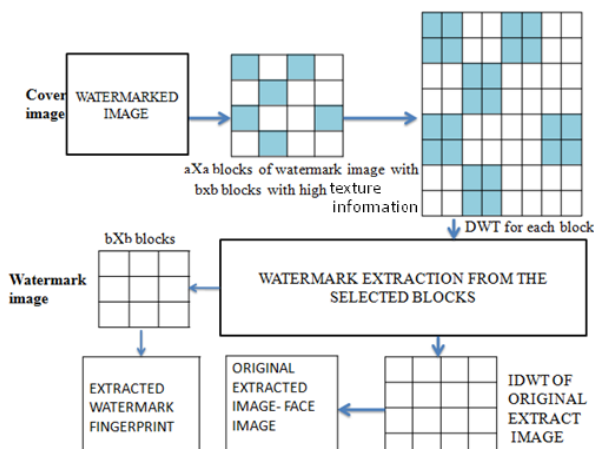


Fig.6 Extraction of Watermarked Image

3. Scrutiny

The proposed method is found to be successful for 120 face image and 200 fingerprint images from the data base. The transmission phase is shown with a standard image and the watermarked result is shown in the Fig.7.

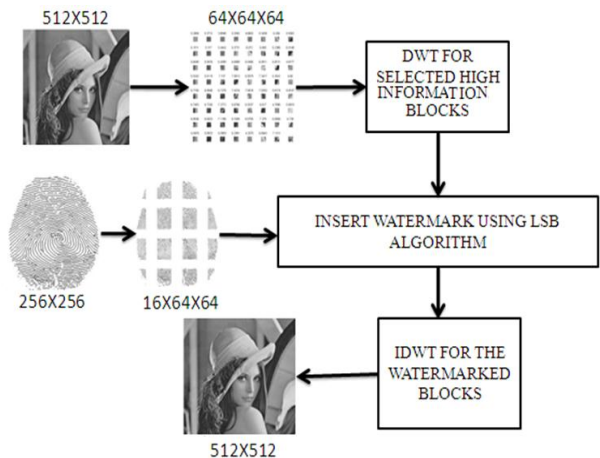


Fig.7 Example for Watermarking

Using the RSA algorithm the watermarked image is encrypted into ciphertext image with the minutiae point as a key.

And the ciphertext image will be transmitted in the network. In most of the watermarking techniques the key for the watermark will be send as another data in the network. So by hacking the watermarked image and the key the network hackers may easily retrieve the secret information from the watermarked image. In this proposed work since the watermarked image is encrypted and the minutiae point of the fingerprint is used as key there is no need to transmit the key in the network and the secret information will be retrieved only by the authenticated person from the received ciphertext. The conversion flow of encryption and decryption of the ciphertext image is shown in Fig.8

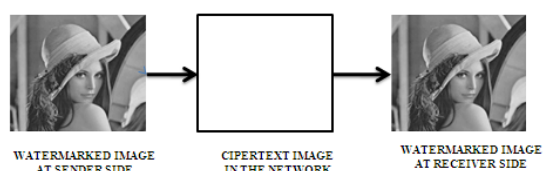


Fig.8 Example for formation of Ciphertext image formation and its Extraction

The decrypted image or the watermarked can be used as multiple-biometric-recognition. Where the face and fingerprint is used together as the biometrics for personal identification.

By the inverse process of the DWT and LSB watermarking scheme the embedded fingerprint image can be recovered which is shown in Fig.9

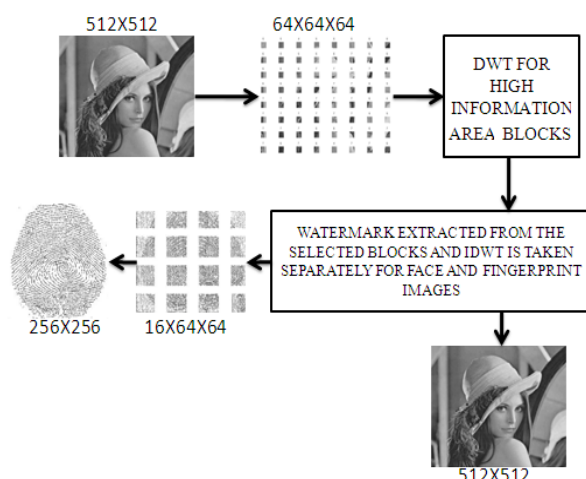


Fig.9 Example for Extraction of Fingerprint Image

The Peak Signal to Noise Ratio (PSNR) and the Quality Index (QI) relates the quality of the image against the noise. The PSNR and QI are calculated for the watermarked image, recovered fingerprint image and the recovered face image. For Lena Image (Standard Image)

PSNR of watermarked image	-47.2876
QI of watermarked image	-0.9998
PSNR of recovered fingerprint	-60.6418
QI of recovered fingerprint	-0.7737
PSNR of extracted face image	-47.1391
QI of extracted face image	-0.9995

From the database some of the results with their Peak Signal to Noise Ratio and Quality Index are shown in the Table 1.

4. EVALUATION OF ROBUSTNESS OF LSB-DWT COMPARED TO LSB AND DWT ALGORITHMS FOR VARIOUS ATTACKS

The watermarked image should be able to withstand various types of attacks so that the original characteristics of fingerprint can be recovered. The PSNR and QI of the recovered fingerprint and the watermarked image of the LSB-DWT algorithm is compared with LSB and DWT algorithm. The comparison graph of the algorithms without attack is the graph is shown in Fig.10, 11, 12.

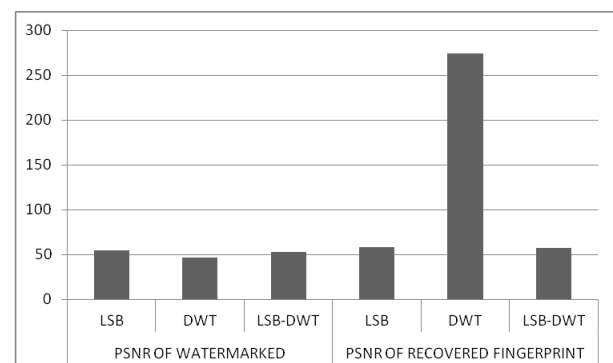


Fig.10 PSNR of LSB, DWT, LSB-DWT Without Attacks

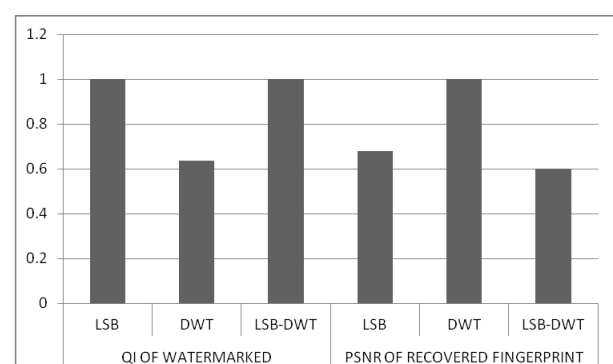


Fig.11 QI of LSB, DWT, LSB-DWT Without Attacks

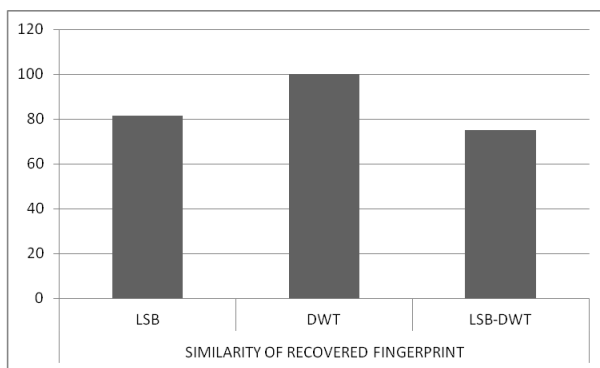


Fig.12 Similarity Of The Recovered Fingerprint Of LSB, DWT, LSB-DWT Without Attacks

The PSNR, QI and Similarity of the recovered Fingerprint is shown in the Graph for various attacks. The stability despite of various attacks shows the robustness of the recovered image. The robustness shows that the image can withstand various kinds of attacks such as Gaussian, Speckle, Salt&Peper, Rotation. The results are shown as Graph in Fig.13, 14, 15

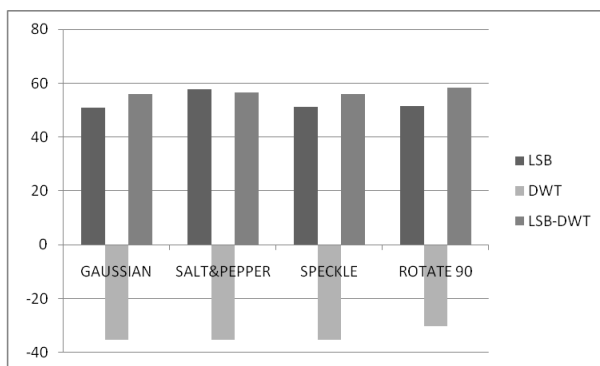


Fig.13 PSNR Of Recovered Fingerprint For Various Attacks

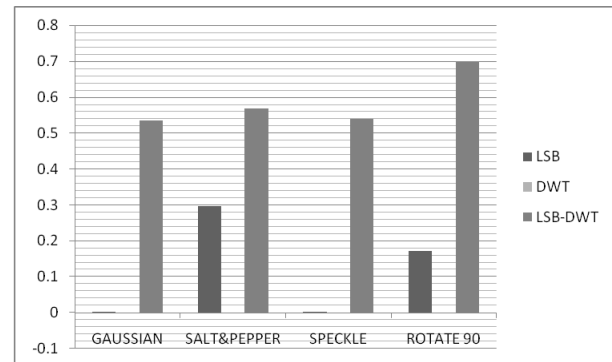


Fig.14 QI Of Recovered Fingerprint For Various Attacks

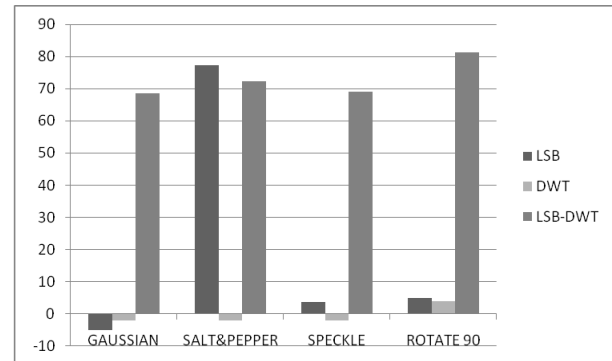


Fig.15 Similarity Of Recovered Fingerprint For Various Attacks

From Fig.10 to Fig.12 it is difficult to analyse whether DWT or LSB-DWT is stable. It seems that DWT is better than other results. But when the watermarked image is exposed to attacks the LSB and DWT algorithms does not provide robustness compared to the proposed algorithm LSB-DWT which can be noted from Fig.13 to Fig.15. Thus the robustness of the proposed algorithm has been proved.

Table 1 Database Results

IPI & FI	WI	CI	RFPI	RFI
 	 PSNR- 43.536 QI-0.9998		 PSNR- 59.6926 QI-0.6958	 PSNR- 43.4016 QI-0.9999
 	 PSNR- 43.2588 QI-0.9993		 PSNR-61.0232 QI-0.7837	 PSNR- 43.1564 QI-0.9997
 	 PSNR- 43.8811 QI-0.9991		 PSNR- 61.8008 QI- 0.8031	 PSNR- 43.7387 QI-0.99900
 	 PSNR- 48.9332 QI-0.9995		 PSNR- 61.7502 QI-0.7824	 PSNR- 48.9028 QI-0.9989
 	 PSNR- 50.9527 QI-0.9989		 PSNR-60.7314 QI- 0.7693	 PSNR- 50.8916 QI-0.9991
 	 PSNR- 49.7564 QI-0.9999		 PSNR-61.1408 QI-0.8128	 PSNR- 49.7409 QI-0.9997

6. Conclusion

This paper presents a novel DWT-LSB based watermarking algorithm to improve the solidity of biometric data. The proposed method embeds the watermark bits in high-texture information blocks using both the spatial domain and the frequency domain. And the security has been increased by RSA algorithm where the private key can be generated only by the authenticated person. Hence the security of the biometric Image has been increased considerably by using the combination of Watermarking and Cryptography.

The method provides a good Peak Signal to Noise Ratio and a high Quality Index for the watermarked and recovered images. Various attacks over watermark image have been analyzed and compared with the other spatial and frequency domain algorithms which shows that the proposed algorithm is more robust compared with the other algorithm.

7. Reference

- [1] Ameya K. Naik, Raghunath S. Holambe, 'A Blind DCT Domain Digital Watermarking for Biometric Authentication', proceeding of International Journal of Computer Applications (0975 - 8887) Volume 1 – No. 16,2010
- [2] Baisa L. Gunjal,R.R. Manthalkar, 'An overview of transform domain robust digital image watermarking algorithms',Journal of Emerging Trends in Computing and Information Sciences, (2010-2011), Volume 2 No. 1 ISSN 2079-8407
- [3] Cox, IJ,Miller,ML & Bloom,JA2002,Digital Watermarking,
- MorganKaufmannPublisher,San Francisco,CA,USA.
- [4] Jain.A, Pankanti.S, and Bolle.R, eds., luwer, "BIOMETRICS: Personal Identification In Networked Society", 1999.
- [5] Khan. M. K, Zhang. J. S., Tian. L., 'Chaotic Secure Content based Hidden Transmission of Biometric Templates', Chaos, Solitons, Fractals, Vol.32, No.5, pp:1749 1759, 2007.
- [6] MayankVasta, Richa Singh, AfzelNoore, Max M.Houck and Keith Morris, 'Robust biometric image watermarking for fingerprint and face template protection' IEICE Electronics Express, Vol.3,No.2, 23-28,2006
- [7] Moi, S.H., Rahim, N.B.A.; Saad, P.; Sim, P.L.; Zakaria, Z.; Ibrahim, S. , 'Iris Biometric Cryptography for Identity', Document Soft Computing and Pattern Recognition, 2009. SOCPAR '09. International Conference of Computing
- [8] Ramaswmay.G, Vuda, Srinivasarao, "A Novel Approach Of Cryptography And Watermarking Using To Protect GIS Data", Journal of Theoretical and Applied Information Technology, JATIT, (2005-2010), ISSN: 1817-3195 / E-ISSN: 1992-8615
- [9] Biometrics for Enhanced Security', this paper appears in Control, Automation, Communication and Energy Conservation. INCACEC 2009M, International Conference.
- [10] Nik Shahidah Afifi Md. Taujuddin, Nur Adibah Binti Lockman, "Image Compression Using Wavelet Algorithm",

Patient Monitoring System for the Identification of Cardiac Abnormalities using Genetic Algorithm

N. Sathiya Rani¹, K. Vimla²

Department Computer Science and Engineering,
National Engineering College,
Kovilpatti.

¹n.sathiya90@gmail.com, ² vimala.arivalagan@gmail.com

Abstract

Now-a-days, many diseases are reducing the life time of the human. One of the major diseases is cardiovascular disease (CVD). It has become very common perhaps because of increasingly busy lifestyles. The rapid development of mobile communication technologies offers innumerable opportunities for the development of software and hardware applications for remote monitoring of cardiac disease. Compressed ECG is used for fast and efficient. Before performing the diagnosis, the compressed ECG must be decompressed for conventional ECG diagnosis algorithm. This decompression introduces unnecessary delay. In this paper, we introduce advanced data mining technique to detect cardiac abnormalities from the compressed ECG using real time classification of CVD. When the patient affect cardiac disease, at the time hospital server can automatically inform to patient via email/SMS based on the real time CVD classification. Our proposed system initially uses the data mining technique, such as Genetic algorithm for attribute selection and Expectation Maximization based clustering. In this technique are used to identify the disease from compressed ECG with the help of telecardiology diagnosis system.

Keywords

Cardiovascular disease (CVD), Data mining, Genetic algorithm, EM based cluster, Classification, Telecardiology.

1. Introduction

Recent trends and developments in wireless technologies, mobile phones are play an important role to become an effective tool for cardiovascular monitoring. The Electro Cardio Gram (ECG) plays a key role in cardiac patient monitoring and diagnosis. In the industrialized world, it is estimated that millions of people die due to various cardiac heart disease annually. The key to treat these diseases is timely detection. Since ECG is the most commonly recorded signalin the patient monitoring [2] and examination Process, it becomes important to be able to reliably and quickly detect cardiac diseases from ECG analysis.

In the medical mining, huge amount of data generated by healthcare transactions are too complex and voluminous to be processed and analysed by traditional methods. Data mining provides methodology and technology to transform these data in to useful information for decision making. The main aim of healthcare management, the data mining applications can be developed to better identify and track chronic disease states and high risk patients, design the appropriate interventions, and reduce the number of hospital admission and claims. Data mining applications are developed to evaluate the effectiveness of medical treatments. By the comparing and contrasting causes, symptoms and courses of the treatments, data mining can deliver an analysis of which treatments is best



for particular diseases and cost effective. Remote Patient Monitoring (RPM) refers to a wide variety of technologies designed to manage and monitor a range of health conditions. Data security and optimization of wireless communication between devices of the system [12] are very important in the home monitoring. In the existing system compressed ECG must be decompressed before performing for every ECG packet introduces unnecessary delay and patient's mobile phone only received the analog signal from health care monitoring device to hospital server in continuous manner. However, this continuous mode of data transfer generates network traffic and causes internet expensive and computational burden on the hospital server.

Our proposed system plays an important role in reducing the delay and provides a fully automatic monitoring facility for the cardiac patient who requires on-going monitoring facility. The aim of this approach is to detect cardiac abnormalities from the compressed ECG using real time classification of CVD. Data mining techniques can be placed with in wireless monitoring facility to alert the patient. This technique running on the hospital server generates a set of constraints for representing each abnormality. Fig 1 depicts the proposed system where the attribute selection using genetic algorithm and EM based clustering are applied first to retrieve a set of constraints within the hospital server. The patient's mobile phone later uses these set of constraints (e.g., ventricular flutter/ fibrillation, premature ventricular contraction, atrial fibrillation, etc.) to classify abnormal beats in real time. With the help of real time classification, emergency message are informed automatically to the patient's mobile phone whenever a life-threatening cardiac abnormality is detected. Some of the related researches are explain in Section 2.

Attribute selection using genetic algorithm and EM based clustering are provided in Section 3.

2. Related Works

There are many researches are going in analyzing ECG signals in national and international level. For example, the telemedicine facilities have been developed for diagnosis through the Internet. Usually attribute selection [14] is done for selecting the features from the compressed ECG. Expected Maximization (EM) [10] clustering technique is used to create normal and abnormal ECG

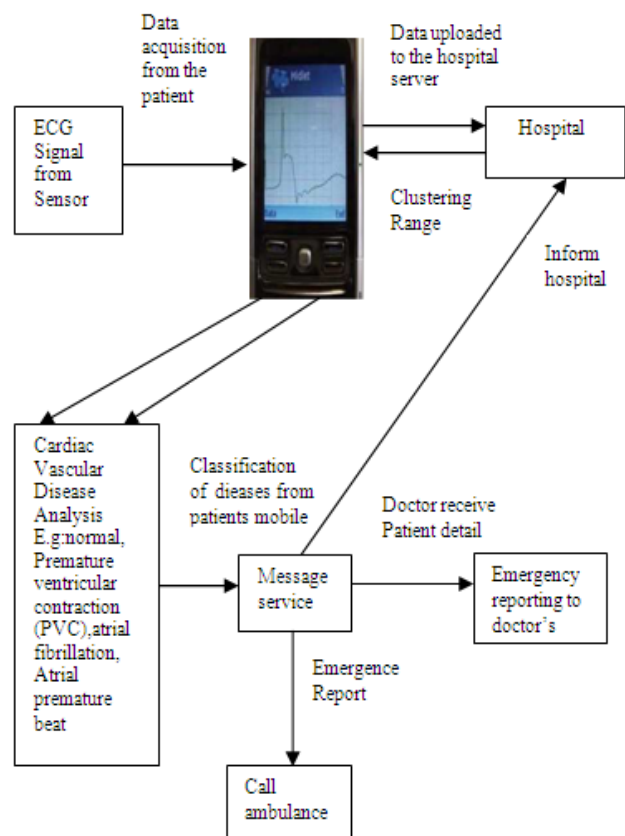


Fig 1: Cardiovascular Abnormality Diagnosis Process

clusters. The threshold value of ECG signal determination is done using Wavelet transform coefficients [11].

For Remote Health Care monitoring, the compression of ECG signals are essential. For compression new wavelet-based [1] ECG compression technique is implemented and this technique is tested using several records taken from the MIT-BIH Arrhythmia database. Also, wavelet transform method is

used to achieve high compression ratios (CR) and a low percent root mean square difference (PRD). Using smartphone-based wearable CVD-detection platform, real-time ECG acquisition and display, feature extraction, and beat classification are done.

Noise is present usually in ECG pattern and the noise reduction process is an important task in ECG signals. Such noises are difficult to remove using typical filtering procedures. So many noise reduction technique is developed in international level such as efficient analytical tool [5] which is a technique for averaging of cardiac cycles which is increasing signal to noise ratio.

Usually the parameters are given as the inputs from medical practitioner directly on to the mobile phone. The score [10] is calculated by miniature java based software running inside the mobile phone. Based on the score, level of urgency is determined by the intelligent program. At the end, specialists are contact automatically by messaging services. Moreover, the results of the scoring are transmitted to the hospital server.

The small capacitive electrodes integrated into a cotton T-shirt together with a signal processing and transmitting board on a two-layer standard printed circuit board design technology. The entire system [17] has small size, is thin, and has low power consumption compared to recent ECG monitoring systems. In addition, appropriate signal conditioning and processing is used to remove motion artifacts. The acquired ECG signals are compared with the obtained using conventional glued-on electrodes, and are easily read and interpreted by a cardiologist.

Prototype Intelligent Heart Disease Prediction System (IHDPS) [14] are developed in national level using data mining technique such as Decision trees, Navie Bayes, Neural Network. Also, biometric systems have been developed using ECE using data mining (DM) techniques like attribute selection and clustering. The biometric template has lesser

in size compared to other forms of biometrics like face, finger, retina, etc.

The ECG signal is filtered using digital filtering techniques to remove power line interference and base line wander. Support Vector Machine (SVM) [18] is used as a classifier for detection of QRS complexes in ECG

An Efficient DDC algorithm has been developed over existing modified Amplitude Zone Time Epoch Coding (AZTEC) technique, named as improved modified AZTEC [13] and tested on Common Standard for quantitative Electrocardiography (CSE) database. The performance has been evaluated on the basis of compression ratio (CR), percentroot-mean-square difference (PRD) and fidelity of the reconstructed signal. A comparison of the wavelet-derived features of compressed and original signals has been used for performance evaluation of the compressed signal.

The ultimate aim of this proposed work is to provide a remote healthcare monitoring system for Faster Identification of Cardiac Abnormalities from Compressed ECG using advanced data mining approach. It is proposed to implement the data mining techniques on a hospital server that will generate a set of constraints for representing each of the abnormalities. Then, the patient's mobile phone receives these set of constraints and employs a rule-based system that can identify each of abnormal beats in real time.

3. System and Method

This system provides an efficient telecardiology diagnosis system for both patients and doctors for fast identification and treatment of the diseases. As we can see from Figure 1, the patient mobile phone receives the compressed ECG signal from the health care monitoring through bluetooth. The compressed ECG packets are sent to the hospital server through SMS/MMS/HTTP in



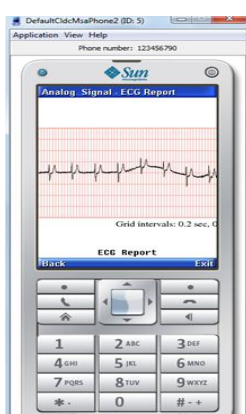
digital format. After receiving the compressed ECG, the hospital server perform the disease recognition task with data mining techniques such as attribute selection and EM based clustering. Hospital server generates a range for particular disease. Based on the range, diseases are identified using rule based classification techniques.

3.1 Patient's mobile phone

In the proposed system plays an important role in reducing the delay by performing diagnosis directly from the compressed ECG and mobile phone receive the digital format ECG from health care monitoring device to hospital server using HTTP. The telecardiology framework provides a fully automatic monitoring facility for the cardiac patient who requires ongoing monitoring facility. Healthcare monitoring to mobile phone communication was performed using bluetooth. Java 2 Micro Edition in net beans language was used for programming the small miniature program called midlet. Figure 2 shows different snapshots of our Midlet implementation of mobile phone based telecardiology application.



(a) Main Screen on Patient's Mobile



(b) Drawing ECG in Patient's Mobile



(c) Viewing ECG Samples in Patient's Mobile

Fig 2: Our Implementation of mobile phone based wireless telecardiology

3.2 Attribute Selection on Hospital Server

In the proposed system, Genetic Algorithm is used for the attribute selection. The attribute selection process is used to reduce the dimensionality of the analysed data, it will speed up learning algorithms, improves the performance of data mining techniques (e.g., learning time, predictive accuracy, etc.), and improves the comprehensibility of the output. The genetic algorithm (GA) is an optimization and search technique based on the principles of genetics and natural selection. A GA allows a population composed of many individuals to evolve under specified selection rules to a state that maximizes the fitness. A genetic algorithm mainly composed of three operators: selection, crossover, and mutation.

In selection, a good string (on the basis of fitness) is selected to breed a new generation from compressed ECG digital values. Roulette wheel selection method is used to select the parent in randomly. Individuals are given a probability of being selected that is directly proportionate to their fitness. Two individuals are chosen randomly based on these probabilities and produce offspring. Table 1 shows that fitness value for each chromosome.

The fitness function evaluated for each individual, providing fitness values, which are the normalized. Normalization means dividing the fitness value of each individual by the sum of all fitness values, so that the sum of all resulting fitness values to 1. The population is sorted by the descending fitness value. After the selection process, crossover is performed.

Table 1. Calculate the fitness value for each phenotype

Genotype	Phenotype	Fitness
Parent 1 : 1001010		
Parent 2 : 0100101	0.331 - 0.835	0.109 0.697
Parent 3 : 1101010	1.339 - 0.300	1.790 0.090
Parent 4 : 0110110	0.488	0.238
Parent 5 : 1001111	.	.
.	1.591	2.531
Parent 300 : 0001101		

Crossover is a process of taking more than one parent solutions and producing a child solution from them. Two-Point Crossover will generate a two cut-point in given two parents and recombines the first part of first parent with the second part of the second parent to create one offspring and then recombines the second part of the first parent with the first part of the second parent to create a second offspring.

Mutation alters a string locally to maintain genetic diversity from one generation of a population of chromosomes to the next. In

Table 2. Generate the new generation (Child)

Genotype	Genotype	Phenotype	Fitness
	Child1:0001 001		
Parent 6: 00 011 01	Child2:1101 110	-1.685	2.839
Parent 3:11 010 10	Child3:1001 111	1.433	2.054
Parent 5: 10 011 11	Child3:1001 111	0.898	0.806
Parent 6: 00 011 01	Child4:0001 101	-1.654	2.736
Parent 2: 01 001 01	Child5:0101 001	1.339	1.793
Parent 1: 10 010 10	Child6:1000 110	0.677	0.458

each generation, the population is evaluated and tested for termination of the algorithm. Mutation occurs during evolution according to a user-definable mutation probability. This probability should be set to low. Table 2 shows that generate a new generation using crossover and mutation. Based on the genetic algorithm best fitness values are generated from the total fitness value.

Algorithm 1: Genetic Algorithm

Step 1 : Randomly select two parents : P1,P2 from R,
and place them in to matting pool
Step2 : Apply the suggested two-point crossover
operation on the selected two parents P1,P2
to generate two new offspring say : O1,O2.
Step 2.1 : Insert two offspring (O1, O2) into new population.
Step 3 : For mutation, select one individual based on the fitness value.
Step 3.1: Insert mutation into new population.
Step 4 : Combine the crossover and mutation, produce the offspring.
Step 5 : If the desired number of generations is not completed, go to Step 1. Otherwise end.

Algorithm 1: EM based Clustering

Step 1:

Start with initial value of mean (μ), standard deviation (σ) and probability (P).

Step 2:

Loop (For each iteration i - Number of instances)

Calculate the probability of each element belong to each cluster C₁, C₂...C_N.

$$P(C_K/x_i) = \frac{P(C_K)P(x_i/C_K)}{P(x_i)}$$

The Probability of P (x_i/C_K) can be modeled using any distribution function for the commonly used normal (Gaussian) distribution; it can be given by,

$$P(x_i/C_K) = N(\sigma_{C_K}, \mu_{x_i})$$

Update the mixture parameters on the basis of the new estimates.

$$P_{C_K} = \sum_{i=1}^n \sum_{K=1}^N \frac{P(C_K/x_i)}{n}$$

$$\mu_{C_K} = \sum_{i=1}^n \sum_{K=1}^N \frac{x_i P(C_K/x_i)}{P(C_K/x_i)}$$

$$\sigma_{C_K} = \sum_{i=1}^n \sum_{K=1}^N \frac{P(C_K/x_i)(x_i - \mu_{C_K})^2}{P(C_K/x_i)}$$

End loop

On the other hand, M-step updates or reestimates the probability values by calculating the log likelihood data. As shown in Algorithm 2, our implementation of EM revolves around the idea that every single ECG packet Corresponding to a Particular CVD is assigned to a cluster for identify the disease. We assume that there are N number of clusters (C₁, C₂, C_N) representing N number of diseases. At the beginning of the algorithm2, step1 represents the initial value of the mean, standard deviation for each of the patient Step 2 denote the value of the standard deviation



and the mean are refined and updated. Step 3 produce the final value for mean and standard deviation. At the end of this process, we will have the same number of mean and standard deviations as the number of cardiac anomalies.

3.4 Rule Based Technique on a mobile phone

Using the proposed technique, one or more diseases can be successfully identified. Γ represents the constraint set for N number of diseases. Each element within Γ (i.e., an individual disease) contains the actual frequency constraints. If a patient is recommended for ongoing monitoring, then during the holter monitoring the doctors could have already obtained the patient's normal and multiple abnormal ECG traces, from where the constraints are computed within the hospital server (before the patient is monitored wirelessly). Then, normal and CVD-affected ECG traces can be fed to our Data Mining (DM) model (i.e., the model that executes on hospital server) to obtain the constraint set (Γ_i) for all the cases (i.e., normal and all the abnormal cases). Equation (1) shows the constraint set (Γ_i) for an individual case, where $i = 0, 1, 2, \dots, N$, N is the maximum number of diseases, and M is the total number of attributes for that particular disease. The number of attributes depends on the attribute selection procedure on each patient. Equation (2) shows the mean values of each attribute (i.e., for all M attributes). On the other hand, Equation (3) shows the standard deviations against the mean values μ_i . Therefore, Equation (4) demonstrates the valid ranges of each cluster (e.g., normal beat, ventricular tachyarrhythmia, premature ventricular beats,

etc.). These constraint set can efficiently be calculated from the proposed DM.

$$\Gamma = \{\Gamma_1, \Gamma_2, \Gamma_3, \dots, \Gamma_N\} \quad (1)$$

$$\Gamma_i = \{f_1^i, f_2^i, f_3^i, \dots, f_M^i\} \quad (2)$$

$$\mu_i = \{\mu_1^i, \mu_2^i, \mu_3^i, \dots, \mu_M^i\} \quad (3)$$

$$\sigma_i = \{\sigma_1^i, \sigma_2^i, \sigma_3^i, \dots, \sigma_M^i\} \quad (4)$$

$$f_M^i = \mu_M^i \pm \sigma_M^i \quad (5)$$

Patient's mobile can execute a rule-based system following the condition specified by Equation (5) to detect particular abnormality. s_m is the value of the m_{th} attribute. F is the set containing the frequency counts of encoding ECG signal. Based on the condition set out by Equation (6), the compressed ECG packet of the patient can be classified as belonging to a particular class i (where, $i = 1, 2, 3, \dots, N$).

$$\forall s_{min} \in F : (\mu_m^i - \sigma_m^i) \leq s_m \leq (\mu_m^i + \sigma_m^i) \quad (6)$$

Patient's mobile phone transmits the compressed ECG packets to the hospital at a convenient time. On receipt of the compressed ECG, the hospital server calculates the constraints and forwards it to the patient's mobile phone. The patient's mobile phone then performs continuous monitoring or beat classification. When abnormal beat is detected, the mobile phone activates the messaging services.

4. Results and Discussions

In our experimentation the compressed ECG samples are collected from MIT-BIH (Massachusetts Institute of Technology - Beth Israel Hospital) physiobankdatabase.



Table 3: Sample output

Physio net Database and Entry	Number of Samples	Best Fitness value using GA	Cluster	Beat Classification
CU 01	300	278	Class 1	Ventricular Flutter
CU09	300	274	Class 2	Atrial Fibrillation
200	300	280	Class 3	Atrial Premature beat
208	300	292	Class 4	Premature Ventricular Contractation

The programs for patient to doctor communication were performed with Midlet implementation using netbeans IDE 7.0.1. Healthcare monitoring to mobile phone communication was performed using bluetooth. On the other hand, patient to doctor / patient to server / server to doctor mobile phone communication via MMS, SMS and HTTP were performed. Data mining techniques are running on hospital server using netbeans. Our experimentation attribute selection using genetic algorithm produce a 278 best fitness value from 50820 total fitness for ECG samples.

Send SMS/ Email

Name:	Rani
Email:	rani@gmail.com
Disease Diagonized:	Diagnosed Disease is:PVC
	<input type="button" value="Post"/>

Name:	Rani
Phone:	9876543210
MSG:	PVC
	<input type="button" value="Send"/>

Fig 3: Hospital Server Transmit the Message to Patient Mobile Phone

The quality and performance of the EM based algorithm becomes very good when a huge dataset. EM based clustering calculate the mean and standard deviations from the best fitness value. The diseases are classified from the clustering range. After the disease classification, the hospital server inform to patient's mobile phone. Figure 3. shows the hospital server send the message to the patient's mobile phone via HTTP and SMS. If the patient condition critical, automatically call to the ambulance.

5. Conclusion

Patient's mobile phone transmits the compressed ECG packets to the hospital at a convenient time (e.g., may be once a week, when Internet connectivity is available). This model is suitable whenever there is bandwidth restriction on the Internet (i.e., continuous monitoring by the hospital server is not possible). On receipt of the compressed ECG segments, the hospital server calculates the constraints (i.e., Γ values) and forwards it to the patient's mobile phone. The patient's mobile phone then performs continuous monitoring or beat classification. This work could be enhanced as identification of the patient and retrieval of the patient's previous records for doctor analysis.

6. References

- [1] AlshamaliA ,Ghaith T, "Combined coding and adaptive thresholding algorithms for ECG compression", 5th IEEE transaction on GCC Conference March 2009, pp.1-3.
- [2] Bount M. Batra M. Capella N. Ebling R. jerome R. Martin M.Nidd M.Niemi M. and Wright S. (2007) , "Remote health care monitoring using Personal Care Connect", IBM Systems Journal Vol. 46 No 1.
- [3] Dihu Chen, Sheng Yang, "Compression of ECG signal using video codec technology-like scheme", Journal of Biomedical Science and Engineering Vol.1, No:1, May 2008, pp.22-26.
- [4] EbrahimNemati, M. Jamal Deen, and Tapas Mondal, McMaster "A Wireless wearable ECG Sensor for Long-Term Applications", IEEE Communications Magazine,January 2012.
- [5] FahimSufi ,Ibrahim Khalil "Faster person identificationusing compressed ECG in time critical wireless telecardiologyapplications",Journal of Network and Computer Application,Vol.34, Issue 1, January 2011.
- [6] Fahim Sufi, Ibrahim Khalil , AbdunNaserMahmood,"clustering based system for instant detection of cardiac abnormalities from compressed ECG", Journal ExpertSystems with Applications: An International Journal ,Vol.38, Issue 5, May, 2011.
- [7] Hamid SadAbadia, MasoodGhasemia, Ali Ghaff aria "Mathematical algorithm for ECG signal denoising using window analysis", IEEE transaction Biomed Pap Med FacUnivPalacky Olomouc Czech Repub. 2007, 151(1):73–78.
- [8] JoseGarcía, Ignacio Martínez, Leif Sörnmo, Member, IEEE, Salvador Olmos, Associate Member, IEEE, Angel Mur, and Pablo Laguna, "Remote Processing Server for ECG-Based Clinical Diagnosis Support", IEEE Transactions On Information Technology in Biomedicine, Vol. 6, No. 4, December 2002, pp.277-284.
- [9] Joseph J, Oresko, "Real-Time Cardiovascular DiseaseDetection Via electrocardiogram Processing", IEEEtransactions on information technology in biomedicine, Vol. 14, No. 3, May 2010, pp.734-740.
- [10] KarupothulaMadhavi Latha1 , Shiramshetty Gouthami2 ,P. Ranjith Kumar," Scoring System Approach for Assessment of Critical Illness using Mobile Phones",International Journalof Distributed and Parallel Systems (IJDPS) Vol.3, No.1, January 2012.
- [11] Mamaghanian H, Khaled N, AtienzaD,Vanderghenst P, "Compressed Sensing for Real-Time Energy-Efficient ECGCompression on Wireless Body Sensor Nodes" , IEEE Transactions on Biomedical Engineering Volume: 58 Issue: 9, Sept. 2011,pp.2456-2466.
- [12] MarcinBajorek. andJedrzej Nowak. (2011), "The role of amobile device in a home monitoring healthcare system",Conference On Computer Science and Information Systems.
- [13] NibeditDey, Tripada Prasad Dash, Sriram Dash,"ECG Signal denoising by Functional Link Artificial NeuralNetwork(FLANN)", International Journal of Biomedical Engineeringand Technology, Vol. 7, No.4 December 2011, pp. 377 - 389.
- [14] Palaniappan S, Awang R, "Intelligent heart disease prediction system using data mining techniques", IEEE/ACS



International Conference on Computer Systems and Applications, 2008. AICCSA 2008, ISBN:978-1-4244-1967-8.

- [15] Physiobank: Physiologic signal archives for biomedical research (2009). [online]. Available: <http://www.physionet.org/physiobank/>
- [16] Ranveig Nygaard, Gerry Melnikov, and Aggelos Katsaggelos, “A Rate Distortion Optimal ECG Coding Algorithm”, IEEE Transactions On Biomedical Engineering, Vol. 48, No. 1, January 2001, pp.28-40.
- [17] S. S. Mehta and N. S. Lingayat , “Comparative study of QRS detection in single lead and 12-lead ECG based on entropy and combined entropy criteria using support vector machine”, Journal of Theoretical and Applied Information Technology.
- [18] Vinod Kumar a, S.C. Saxena b, V.K. Giri a, Dilbag Singh, “Improved modified AZTEC technique for ECG data compression: Effect of length of parabolic filter on reconstructed signal”, Computers and Electrical Engineering, pp. 334–344, 2005.
- [19] Ying Zhang and Hannan Xiao, “Bluetooth-Based Sensor Networks for Remotely Monitoring the Physiological Signals of a Patient”, IEEE Transactions On Information Technology In Biomedicine, Vol. 13, No. 6, November 2009, pp.1040-1048.

Noise Reduction Using FIR Filter in Cochlear Implants

¹P.Mithradevi, ²J.Indra, ³N.Kasthuri

¹ Department of Electronics and Electrical Engineering

²Department of Electronics and Instrumentation Engineering

³ Department of Electronics and Communication Engineering

Kongu Engineering College, Erode.

mithra.kavi@gmail.com, jindu@kongu.ac.in, nkasthuri@kongu.ac.in

Abstract

The use of auditory models in cochlear implant speech processing strategies aims to improve cochlear implanter's perception of speech. Current speech processing strategies for cochlear implants use an IIR filter bank which decomposes the audio signals into multiple frequency bands each associated with one electrode. It produces unstable output and also does not confer any solution for noise reduction. Noise causes severe effects in cochlear implants. The proposed method focuses on reduction of noises in cochlear implants. The aim of the proposed method is to reduce the noise in cochlear implants and improve the speech perception by using the FIR filter bank. The design consists of eight FIR filters with eight channels. Each channel contains different frequency bands. The filter bank designed is successfully tested using speech signal extracted from Noizeous corpus speech database.

Keywords:Cochlear implant, IIR, FIR, Auditory models

1. Introduction

Human communication relies on taking in complicated perceptual information from the

outside world through the hearing sense and interpreting that information in a meaningful way [10]. The part that deals with hearing is called the cochlea and it consists of a bony tube about 33 mm in length, coiled upon itself for two and a half turns. The basilar membrane in the cochlea is responsible for splitting the input signal into different frequencies. The location of inner hair cells along the basilar membrane determines the hair cells optimal response to various frequencies. When sound signal is transmitted in the form of travelling wave in cochlea, the hair cells at the apex respond to low frequencies whereas hair cells at the base respond to high frequencies as shown in figure.1

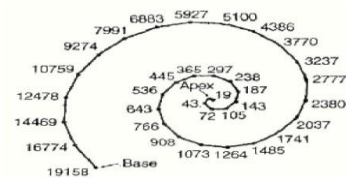


Fig.1 The structure of Basilar membrane showing the speech frequencies at apex and base

Hearing impairments are clinically categorized into two major groups: conductive and sensineurial disorders [10]. The impairment

levels are determined with respect to the Pure tone Threshold Average (PTA) in decibels (db). Problems at the external or middle ear that block or degrade sound transmission from the external ear to the cochlea are the cause of conductive hearing loss. Today, replacement of the middle ear bones and other sophisticated correlative procedures are available for conductive hearing loss patients. Sensineural hearing loss involves changes in the inner ear that result in a change in sensitivity to sound. The loss of hair cells in the cochlea due to exposure to loud sound or heavy drug treatment is the most common sensineural impairment. Damage of hair cells also results in subsequent degeneration of the adjacent auditory neurons [8].

If the hair-cell and auditory nerve damage are excessive, the connection between the central nervous system and the external world is lost and the person who has such level of loss is recognized as being profoundly deaf(PTA>91db).However, some amount of living auditory neurons can still exist in the cochlea, even with extensive loss of hair cells. Direct electrical stimulus of these neurons can create a sound sensation in profoundly deaf people. These electronic neural stimulus systems are called cochlear prostheses. Profoundly deaf people are assumed to be good candidates for cochlear implant devices if they have some degree (<30%) of open-set speech recognition ability with best-fit hearing aids [10].

The major problem that occurs in the cochlear device is noise. It is due to inability of reduction of noise in the signal processing unit of the cochlear device. In this paper, an effective FIR filter for the reduction of noise in the cochlear implant device is proposed.

2. Cochlear Implant

Cochlear implants have been very successful in restoring partial hearing to profoundly deaf people and are only appropriate for people who receive minimal or no benefit from a conventional hearing. It provides partial hearing by stimulating the auditory nerve cells, and thereby circumventing malperformance of the transmission of acoustic sound into neural impulses. The implant electrically stimulates neurons directly to provide information about sound to the brain. It is the only widely available medical device designed to restore a human sense. It is the imitation of normal hearing human cochlea. The implant can effectively transmit information to the brain about the loudness of the sound, which is a function of the amplitude of the stimulus current, and the pitch, which is a function of the place of the cochlea being stimulated.

2.1 Block diagram of the cochlear implant Device

The general block diagram of cochlear implant speech processor is shown in fig 2. The input source is speech signal; it can be picked up by the microphone [10]. Then the speech signal can be filtered and passed into the different channels of the cochlear implant. Speech processor is the heart of the cochlear implant. Channel 0 transmits the lower frequency, while channel 7 transmits the higher frequency.

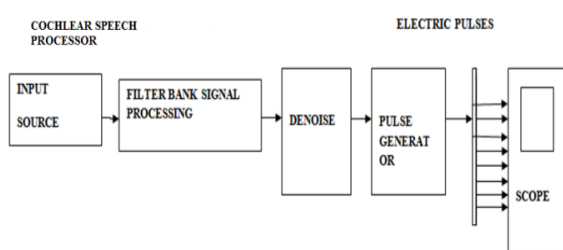


Fig.2 Cochlear speech processor

2.2 Noise in the Cochlear Device

The input speech signal is corrupted with noise. Noise can be of different types such as additive noise, reverberation noise, echo noise and babble noise. It degrades the ability of hearing.

3. Filter Design

Current speech processing strategies for cochlear implants use an IIR filter bank which decomposes the audio signals into multifrequency bands each associated with one electrode [11]. The proposed system consists of non uniformly spaced 8 channel FIR filter bank model for cochlear implants. The design has the advantage of linear phase frequency response. The speech signal is passed through a bank of band pass filters whose coverage spans the frequency range of interest in the signal which is from 100-5500Hz. Generally the number of filters in the filter bank depends on the number of channels which in turn depend on the number of stimulating electrodes. Hence the filter bank consists of 8 channels of band pass FIR filter as depicted in the following fig 3.

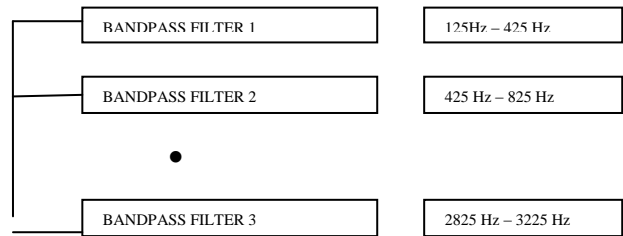


Fig. 3 Filter bank model for speech processor

3.1 Filter Structure

A finite-duration impulse response filter has a *system function* of the form [11]:

$$H(z) = b_0 + b_1 z^{-1} + \dots + b_{M-1} z^{1-M} = \sum_{n=0}^{M-1} b_n z^{-n} \quad \dots \quad (1)$$

Hence the *impulse response* $h(n)$ is

$$h(n) = \begin{cases} bn & 0 \leq n \leq M-1 \\ 0 & \text{else} \end{cases} \quad \dots \quad (2)$$

And the *difference equation* representation is
 $y(n) = b_0 x(n) + b_1 x(n-1) + \dots + b_{M-1} x(n-M+1)$

$\dots \quad (3)$
Which is a linear convolution of finite support.

The *order* of the filter is $M-1$, while the *length* of the filter is M . For linear phase FIR filters, the filter coefficients are symmetric or anti-symmetric. So for an N -th order filter, the number of multiplications can be reduced from N to $N/2$ for N even and to $(N+1)/2$ for N odd. The output of the filter is given as,

$$y[n] = h[0]x[n] + h[1]x[n-1] + h[2]x[n-2] \dots + h[M-1]x[n-M-1]$$

..... (4)

In this design Direct Form I structure of FIR filter is chosen.

4. Filter Coefficients Generation

FIR filter is designed as a bandpass filter of order 8 with the sampling frequency of 8 kHz. The block diagram of proposed FIR filter bank is shown in fig 4.

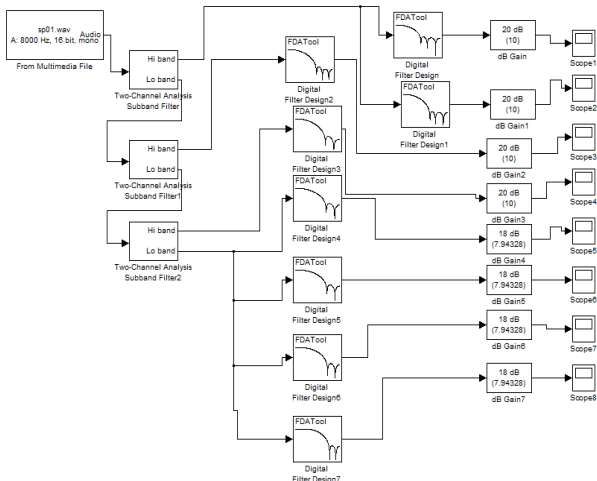


Fig.4 Filter bank processing

The filter bank consists of eight band pass FIR filters. Each FIR filter consists of one channel and each having different frequencies. The pure input speech signal (8000Hz) and noisy speech signal can be given to the two channel analysis subband filter. It gives the low frequency signals to the first four channels of filter bank and high frequency signal to the next four channels of the filter bank. Filter design and analysis [8] is shown in fig 5.

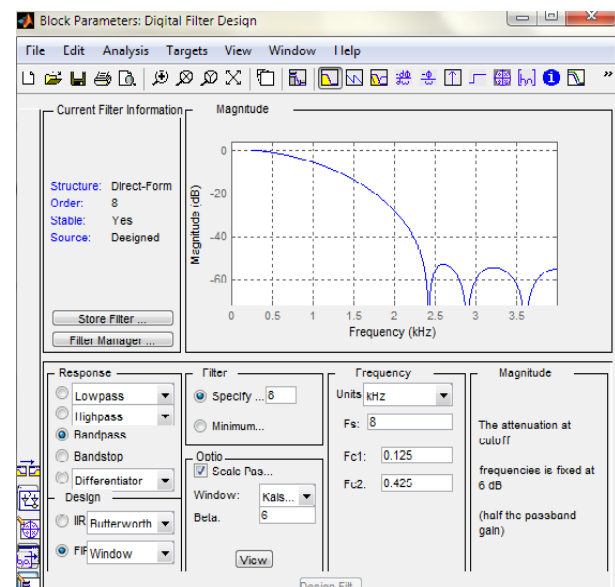


Fig .5 Filter Design and analysis

4.1 Two channel analysis subband filter

The Two-Channel Analysis Subband Filter block decomposes the input into high-frequency and low-frequency subbands, each with half the bandwidth and half the sample rate of the input.

4.2 Filter Design Algorithm using Kaiser Window

The design of band pass filter using Kaiser Window has been carried out based on the following steps.

Step1:

The ideal frequency response of a band pass filter is taken as

$$H(e^{jw}) = \begin{cases} 0 & \text{for } 0 \leq |w| < w_{c1} \\ 1 & \text{for } w_{c1} \leq |w| < w_{c2} \\ 0 & \text{for } w_{c2} \leq |w| < w_{sf}/2 \end{cases}$$

.....(5)

The design consists of two transition bandwidths, that is $B_1 = \min [(\omega_{p1} - \omega_{s1}) (\omega_{s2} - \omega_{p2})]$, where $(\omega_{p1} - \omega_{s1})$ and $(\omega_{s2} - \omega_{p2})$ are the initial and later transition

edge frequencies of the band pass filter. The cut-off frequencies are given by $\omega_{c1} = \omega_{p1} - B_t / 2$ [11].

Step 2:

Assuming that the pass band ripple is approximately equal to the stop band ripple, that is $\delta_p \approx \delta_s$ and on a basis of $\delta = \min(\delta_p, \delta_s)$, the length N is compared using,

$$N = -20 \log(\sqrt{\delta_p \delta_s}) - 13/14.6(\omega_s - \omega_p)/2\pi \quad \dots \dots \dots (6)$$

Step 3:

Kaiser window is used with $\beta = 6$. A Kaiser window is used which has an adjustable parameter β that controls the stop band attenuation and an independent parameter N that controls the transition width [11]. Kaiser window is widely used for the spectral analysis and filter design applications.

The kaiser window sequence is given by,

$$w_k = \begin{cases} \frac{I_0(\beta \sqrt{1 - \left(\frac{2k}{N} - 1\right)^2})}{I_0(\beta)} & 0 \leq k \leq N \\ 0 & \text{otherwise} \end{cases} \quad \dots \dots \dots (7)$$

Where β is an adjustable parameter, and $I_0(x)$ is the modified zeroth order Bessel function, which can be expanded in to the following series.

$$I_0(x) = 1 + \sum_{r=1}^{\infty} \left[\frac{x^r}{r^r} \right] r/r! \quad \dots \dots \dots (8)$$

4.3 Frequency Specifications of Channels

The proposed method consists of eight channels. Each channel consists of different frequencies. The frequency specifications of the eight channels are given below in table 1.

Table 1 Frequency range of eight channels

Channel no	Freq. range
1.	125-425
2.	425-825
3.	825-1225
4.	1225-1625
5.	1625-2025
6.	2025-2425
7.	2425-2825
8.	2825-3225

The frequency range of 20Hz-20000 kHz [12] is the ability of human hearing range. But the normal persons are able to hear the sound at the range of 125 Hz. So the channel 1 is designed at the frequency range of 125 Hz to 325 Hz. The band pass FIR filter passes the signal only in this range. The other channels also do similar operation. The frequency range of the input signal is 8000 Hz with SNR value of 15 db. After the input signal is processed into the filter bank, the output of the filter bank is amplified. SNR of the output signal is calculated using the formula as

$$\text{SNR} = 20 \log \frac{\text{signal power}}{\text{noise power}}$$

(Noise power)



..... (9)

Finally SNR value for output of each channel is calculated. Output SNR value is slightly increased than the input SNR value. The noise present in the input signal is reduced by the FIR filter bank and also it increases the SNR value of the speech signal.

5. Simulation Results

The following results show the reduction of noise in the speech signal and increase in SNR value in the FIR filter bank. The noise signal (Babble noise 5 dB, 10 dB, 15 dB), which is taken from the NOIZEOUS speech corpus database, is given to the filter bank. The below figure 6 shows the output of noise signal (Babble noise(5dB)) with SNR value of 15db.

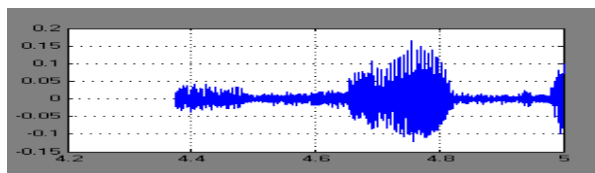


Fig.6 Output of noisy speech signal

The above noisy speech signal is given to the FIR filter bank.

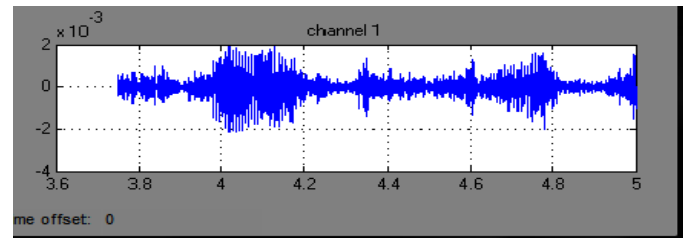


Fig.7 Filtered output of channel 1

Channel 1 is designed at the frequency range of 125Hz-425Hz. The noise speech signal (8000HZ) is given to the first FIR filter (channel 1). The output of the filter is shown above in fig.7.SNR value of channel 1 is 17db with the sampling frequency of 8 kHz.

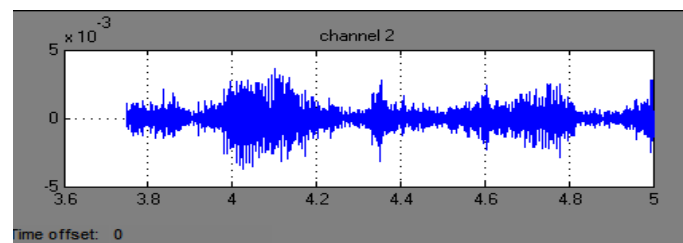


Fig.8 Filtered output of channel 2

Channel 2 is designed at the frequency range of 425Hz-825Hz. The noisy speech signal (8000Hz) is given in to the second FIR filter (channel 2) and the output of channel 2 is shown in fig 8.It gives the SNR value 17.2 db

with the sampling frequency of 8 kHz.

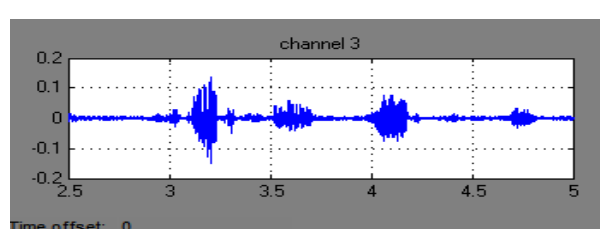


Fig.9 Filtered output of channel 3

Channel 3 is designed at the frequency range of 825Hz-1225Hz. The noisy speech signal (8000Hz) is given to the third FIR filter (channel 3) and the output of channel 3 is

obtained with the SNR value of 17dB which is shown in fig 9.

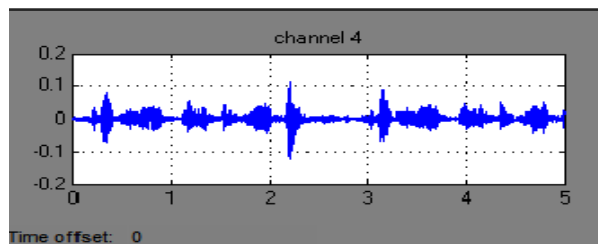


Fig.10 Filtered output of channel 4

Channel 4 is designed at the frequency range of 1225Hz-1625Hz. The noisy speech signal (8000Hz) is given to the fourth FIR filter (channel 4). The output of channel 4 is obtained with the SNR value of 17.3 dB. It is shown in fig.10.

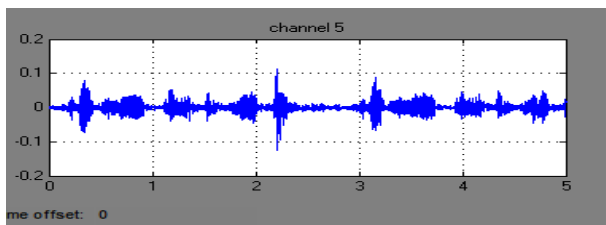


Fig.11 Filtered output of channel 5

Channel 5 is designed at the frequency range of 1625Hz-2025Hz. The noisy speech signal (8000Hz) is given to the fifth FIR filter (channel 5). The output of channel 5 is obtained with the SNR value of 19 db. It is shown in fig.11.

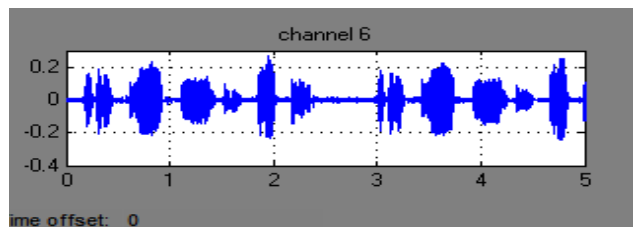
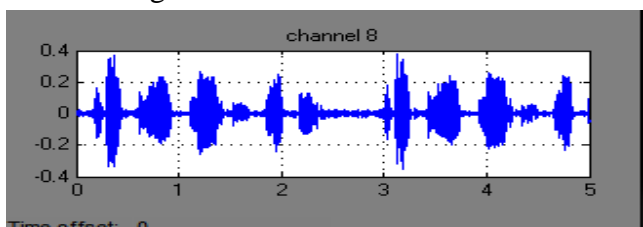


Fig.12 Filtered output of channel 6

Channel 6 is designed at the frequency range of 2025Hz-2425Hz. The noisy speech signal (8000Hz) is given to the sixth FIR filter (channel 6) and the output of channel 6 is obtained with the SNR value of 19.2 db. It is shown in fig.12.

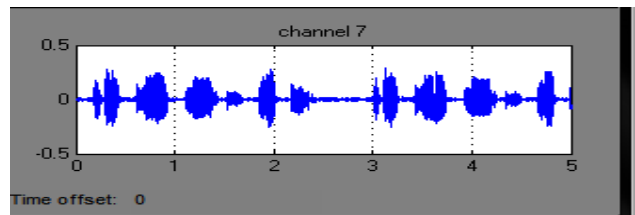


Fig.13 Filtered output of channel 7

Channel 7 is designed at the frequency range of 2425Hz-2825Hz. The noisy speech signal (8000Hz) is given to the seventh FIR filter (channel 7) and the output of channel 7 is obtained with the SNR value of 19.5 db. It is shown in fig.13.

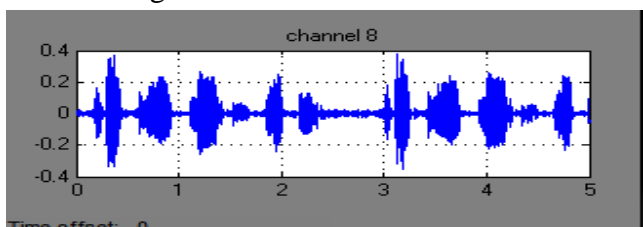


Fig.14 Filtered output of channel 8

Channel 8 is designed at the frequency range of 2825Hz-3025Hz. The noisy speech signal (8000Hz) is given to the eighth FIR filter (channel 8) and the output of channel 8 is obtained with the SNR value of 19.2 db which is shown in fig.14. The spectrogram of 8 channel filter bank for the noise signal is given below in fig.15.

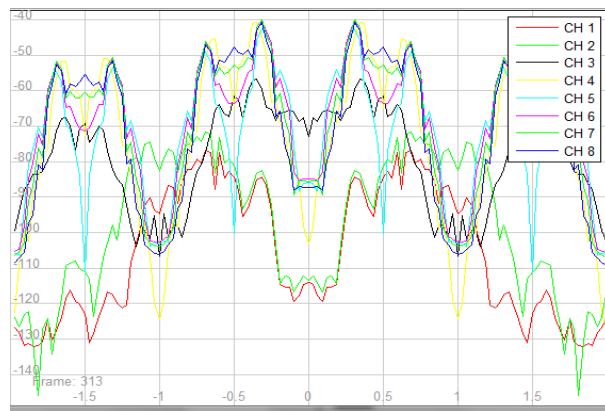


Fig.15 Output of 8 channel filter bank

6. SNR Values for Different Noise Signals

Noise signal - Babble noise (5 dB)								
Input noise signal	ch-1	ch-2	ch-3	ch-4	ch-5	ch-6	ch-7	ch-8
Signal (15dB)	17 dB	17.2 dB	17 dB	17.3 dB	19 dB	19.2 dB	19.5 dB	19.2 dB

Noise signal – Babble noise (10 dB)								
Input noise signal	ch-1	ch-2	ch-3	ch-4	ch-5	ch-6	ch-7	ch-8
Signal (15dB)	19 dB	18 dB	17.9 dB	20 dB	18 dB	21 dB	20 dB	21 dB

Noise signal – Car noise (5 dB)								
Input noise signal	ch-1	ch-2	ch-3	ch-4	ch-5	ch-6	ch-7	ch-8
Signal (15dB)	19.2 dB	19 dB	19 .5 dB	20 dB	22 dB	21 dB	22 dB	22 dB

Noise signal – Car noise (15 dB)								
Input noise signal	ch-1	ch-2	ch-3	ch-4	ch-5	ch-6	ch-7	ch-8
Signal (15dB)	20 dB	19 dB	21 dB	22 dB	22.4 dB	22.9 dB	22.9 dB	23 dB

7. Conclusion

Speech processing unit of cochlear implant is designed by the Band pass FIR filter bank. The filter bank is tested by the speech signals

obtained from the AURORA database and Noizeus corpus. The output of the speech processing unit shows that the FIR filter reduces the noise present in the speech signal and it increases its SNR value.

8. References

- [1] Amira Derbel,Mohamed Ghorbel,Mounir Samet, Ahmed Ben Hamida (2009),‘Implementation of strategy based on auditory model based transform speech processing on DSP dedicated to cochlear prosthesis’, IEEE, fourth international symposium on computational intelligence and intelligent informatics, pp. 143-148
- [2] Amparo Albalate et al (2006) , ‘Signal analysis by using Adaptive Filter Banks in cochlear implants’,IEEE conference on biomedical circuits and systems, pp. 210-213.
- [3] Apurva Mishra, Allyn E. Hubbard (2002), ‘A Cochlear Filter Implemented with a Field-Programmable Gate Array’IEEE Transactions on circuits and systems—ii: analog and digital signal processing, Volume. 49, no. 1, pp. 54-60.
- [4] Blake S. Wilson, Michael F. Dorman (2008), ‘Cochlear implants: Current designs and future possibilities’, Journal of Rehabilitation Research & Development, Volume 45, No. 5, pp. 695-730.
- [5] Daniel Schurzig, Robert F. Labadie, Andreas Hussong, Thomas S. Rau,Robert J. Webster (2012), ‘Design of a Tool Integrating Force Sensing With Automated Insertion in Cochlear Implantation’, IEEE/ASME Transactions on mechatronics, Volume. 17, no. 2, pp. 381-389.
- [6] Fan-Gang Zeng, Stephen Rebscher, William Harrison, Xiaoan Sun, Haihong Feng (2008), ‘Cochlear Implants: System Design, Integration, and Evaluation’, IEEE conference on biomedical circuits and systems, Volume. 1, pp. 115-142.

- [7] Hugh McDermott (1998), ‘A Programmable Sound Processor for Advanced Hearing Aid Research’ IEEE Transactions on Rehabilitation Engineering, Volume 6, Issues. 1, pp. 53-59.
- [8] K.Rajalakshmi.A.Kandasamy (2012), ‘VLSI Architecture of Digital Auditory filter for speech processor of cochlear implant’, International Journal of computer Applicatons, Volume 39, No.7, pp. 19-27.
- [9] Pamela T. Bhatti, and James H. McClellan, Fellow (2011), ‘VLSI Architecture of Digital Auditory filter for speech processor of cochlear implant, IEEE Transactions on education, Volume. 54, no. 4.
- [10] Philipos C.Loizou (1999), ‘Signal processing techniques for Cochlear implants’, IEEE transaction on Engineering in medicine and biology, Volume. 18, No. 3, pp. 34-46.
- [11] P.Mahalakshmi, M.R.Reddy (2010), ‘Signal Analysis by using FIR Filter banks in cochlear implant prostheses’, International conference on system in medicine and biology, pp. 253-258.
- [12] Rekha V. Dundur, M.V.Latte, S.Y. Kulkarni, M.K.Venkatesha (2008), ‘Digital Filter for cochlear implant implemented on FPGA’, PWASET IEEE Transaction on Circuits and Systems II: Analog and Digital Signal Processing, Volume. 39, pp 468-472.
- [13] Supavit Muangjaroen, Thaweesak Yingthawornsuk (2007), “Comparison of Speech response of Normal hearing listener and cochlear implanted patient”, IEEE multipic Conference, pp. 1-9.
- [14] Vipan Kakkar (2010), ‘Low Power Architecture for Cochlear Implant’, International Journal of Engineering Science and Technology, Volume.2, page No.51-58.

A New Adaptive Wavelet Shrinkage for Speckle Noise Removal in Ultrasound Scan Images Using Inter and Intra Scale Dependencies

P. Nirmaladevi¹, Dr.R. Asokan², P.S.Sudarsana¹

¹Department of Electronics and Communication Engineering, Kongu Engineering College Perundurai

² Kongunadu College of Engineering & Technology, Thottiam, Trichy

nirmaladevi@kongu.ac.in, asokece@yahoo.com, pssudarshana@gmail.com

Abstract

In this paper a new adaptive thresholding function is proposed for image denoising in the translational invariance wavelet domain. The inter-scale and intra-scale dependencies among the wavelet coefficients at different scales are exploited to improve restoration in noise corrupted image. The noisy image is decomposed into many levels to obtain different sub bands. A spatially adaptive threshold is selected and is used in the new adaptive thresholding function to shrink the noisy wavelet co-efficient. The simulation results on ultrasound scan image shows that this method yields better visual quality and Peak Signal to Noise Ratio (PSNR). To prove the efficiency of this method, we have compared with various denoising methods.

General Terms

Bio medical Image processing, Speckle Noise, Wavelet Transform, Ultrasound Images

Keywords

Stationary Wavelet transform, Inter and Intra scale dependencies, Adaptive Threshold function, Image denoising.

1. Introduction

Speckle noise is a multiplicative noise. SAR, Medical ultrasound imagery and laser images are said to contain speckle noise. The presence of speckle degrades the quality of images and they become unsuitable for further processing. Image denoising is an essential preprocessing step. The main objective of image denoising is (i) to remove the unwanted noise present in the images (ii) to preserve the edges and fine details (iii) to improve the visual quality of the images.

Speckle noise results due to the constructive-destructive interference of the coherent ultrasound pulses that are backscattered from the tiny biological tissues. Ultrasound images are formed by transmitting a sound wave and receiving the echoes that are reflected from the biological tissues, give rise to a granular pattern in the imaging data. This may obscure some of the important image features and hence it becomes a tedious process for the physician to make a diagnosis [7].

Many spatial domain approaches have been developed for despeckling including Lee, Frost and Kuan Filters. In Lee and Kuan filters the output of a centre pixel in a window is the

average intensity of the pixels within the window. Frost filter produces output by forming an exponential kernel.

Recent investigations in the literature [2], [3], [5],[13],[16], [18] show a significant use of wavelet transform for denoising, called non linear filtering. Wavelet denoising attempts to remove noise and preserve the signal details irrespective of its frequency content.

Denoising by thresholding in wavelet domain was developed by Donoho [1]. Thresholding is a non-linear technique, which can operate on one wavelet coefficient at a time. The standard thresholding methods are hard thresholding and soft thresholding. In thresholding, the coefficient is smaller than the threshold are made zero or shrunk towards zero otherwise it is kept or modified. Soft thresholding preserves the smoothness and fixed bias is also present.

The experimental results of Coifman and Donoho , show that the shift invariant wavelet denoising is better than shift variant wavelet denoising. The Stationary wavelet transform overcomes the lack of translation-invariance property of the discrete wavelet transform by removing the down samplers and up samplers in the wavelet transform. SWT is a redundant scheme as the output of each level has the same number of samples as the input. Small image details can be revealed in finer scales and it can be determined by inter-scale dependencies which involves two adjacent scales [4], [12]. Chen [18] found that we could get better result by translation invariant multi wavelet denoising than translation invariant single wavelet denoising. Xiaogang Dong et al [5] proposed an improved thresholding method to reduce the fixed-bias.

A new adaptive thresholding function [5] is used in this paper which is a combination of

hard and soft thresholding functions. The denoising performance of [5] is enhanced by utilizing the secondary wavelet properties of inter and intra scale dependency among the wavelet co-efficients to identify the homogenous regions in the transformed co-efficients [6], [8],[10]. A subband adaptive threshold is employed in the adaptive threshold function for shrinking the wavelet coefficients. The performance measures like PSNR and visual quality are found to improved compare to the existing soft and hard thresholding techniques.

This paper includes following sections. Section II explains intra- and inter-scale dependencies among the wavelet co-efficients Section III explains the proposed new adaptive thresholding function. Section IV is about the proposed noise removal algorithm and section V discusses the performance improvement of the proposed method over the existing techniques.

2. Inter and Intra Scale Dependencies

The Secondary wavelet transform properties are intra-scale dependency and inter-scale dependency. The dependency between same sub band is called intra-scale dependency and different sub band is called as inter-scale dependency which involves two adjacent scales.

Fig.1 shows one level decomposition of stationary wavelet transform. It is an undecimated wavelet transform which preserves the shift invariance property.

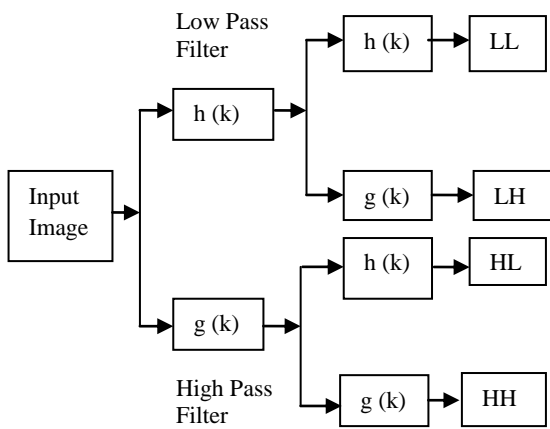


Fig.1: One level decomposition of stationary wavelet Transform

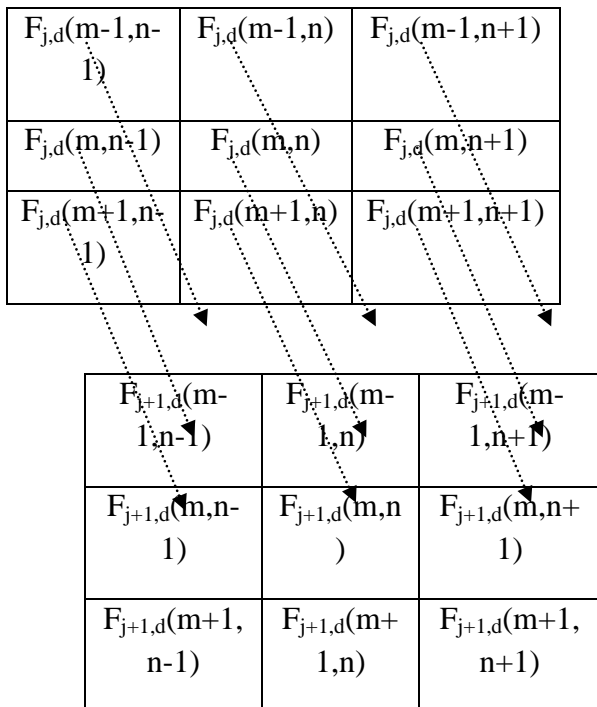


Fig.2: Inter scale and Intra scale dependency among adjancent level co-effcents

In fig.2 [11] j is the finest scale and $j+1$ is the coarsest scale of wavelet decomposition. Coarsest scale coefficients are parent coefficients and finest scale coefficients are child coefficients. If the magnitude of parent

coefficient is small then the magnitude of child coefficient must be small. This property of wavelet co-efficients is used as a measure of homogenous regions in the images. The large magnitude wavelet coefficients produced at finer scales are more likely to yield significant parents at coarser scales. However, the coefficients caused by noise would decay rapidly along scales. Also, estimating the data locally by using the correlation of wavelet coefficient in the local neighborhood have been widely used in the denoising algorithms [23]. Through the literature it is found that intra scale and inter scale dependencies exist among wavelet coefficients within and across the wavelet decomposition scales (i.e., the wavelet coefficients are not only correlated with their neighbours in a subband, but also the adjacent wavelet scales are strongly correlated in general). Therefore, wavelet intra and inter scale dependency information have been combined in the proposed method to improve the performance of restoration.

3. Wavelet Denoising Technique

In image processing wavelet based denoising technique consists of the following steps:

- Decomposing the image into various sub bands at various levels
- Shrink the wavelet co-efficients using soft or hard thresholding function
- Reconstruct the restored image by applying inverse wavelet transform.

In wavelet domain, noise is associated with small magnitude coefficients. Important image structures are contained within the magnitude of the high coefficients. Therefore a suitable threshold is applied to make the small magnitude coefficients to zero and large magnitude coefficients are scaled towards zero. This is done because the coefficients that has

mostly noise component are to be reduced to negligible values while the coefficients that contain signal components are to be reduced less.

3.1 Thresholding Functions

There are two types of traditional thresholding functions.

3.1.1. Soft Thresholding Function

$$\begin{aligned} \widehat{W}(j,k) &= sgn(|W_{j,k}|)(|W_{j,k}| - \lambda) \quad |W_{j,k}| \\ &\geq \lambda \\ &= 0 \\ &\quad |W_{j,k}| < \lambda \dots(1) \end{aligned}$$

3.1.2. Hard Thresholding Function

$$\begin{aligned} \widehat{W}(j,k) &= W_{j,k} \quad |W_{j,k}| \geq \lambda \\ &= 0 \quad |W_{j,k}| < \lambda \\ &\dots\dots\dots(2) \end{aligned}$$

Where, $W_{j,k}$ stands for the wavelet coefficients, λ stands for the threshold value, $\widehat{W}_{j,k}$ stands for the restored wavelet coefficients.

3.2 New Adaptive Thresholding Function

The traditional hard and soft thresholding has the following shortcomings. In the hard threshold method, the wavelet coefficient processed by the threshold value have discontinuous point on the threshold λ and $-\lambda$, which may cause Gibbs shock to the useful reconstructed signal. In the soft-thresholding method, its continuity is good, but when the wavelet coefficients are greater than the threshold value, there will be a constant bias between the wavelet coefficients that have been processed and the original wavelet coefficients, making it impossible to maintain the original features of the images effectively.

In order to improve the denoising performance the fixed bias may be reduced, but cannot be

reduced to zero (Hard Thresholding Function). Hence the co-efficients are estimated between $|W_{j,k}| - \lambda$ and $W_{j,k}$. Therefore a weighted method is used to construct the new adaptive threshold function defined [5] as follows:

$$\begin{aligned} \widehat{W}_{j,k} &= sgn(W_{j,k})(|W_{j,k}| \\ &- \left(1 - \exp\left(\frac{-m}{|W_{j,k}|^2 - \lambda_j^2}\right)\right)\lambda_j \\ &\quad \text{For} \end{aligned}$$

$$\begin{aligned} |W_{j,k}| &\geq \lambda_j \\ &= 0 \quad \text{for} \\ &|W_{j,k}| < \lambda_j \dots\dots\dots(3) \end{aligned}$$

Where m is a positive constant. When $m = \infty$, the thresholding function approaches the soft thresholding and when $m = 0$ it approaches hard thresholding function.

3.3 Parameter Selection for Thresholding

The threshold λ if it is a constant parameter then it will result in too many kill of the wavelet coefficients. Therefore λ for the adaptive threshold function is selected as subband adaptive exploiting inter and intra scale dependency.

The subband adaptive threshold is given by

$$\lambda_j = \beta T_B \dots\dots\dots(4)$$

Where β is a subband adaptation parameter given by

$$\beta = \sqrt{\frac{\log M}{2^j}} \dots\dots\dots(5)$$

Here M is the total no. of coefficients and j is the current level of decomposition.

Thus the estimation of signal threshold exploits the intra scale dependency of wavelet coefficients in the subbands.

3.3.1. Intra Scale Dependency Model

Wavelet coefficient dependencies exist within and also across the sub bands. Adjacent subband coefficients exhibit strong correlation. Small magnitude coefficients at coarser scales yield insignificant descendants at finer scale. In contrast, large magnitude wavelet coefficients at finer scales have significant parents at coarser scales. The coefficients that are affected by noise decay rapidly across scales. Xu et al. multiplied the adjacent wavelet scales to sharpen edge structures while weakening noise. Sadler et al. analyzed the product of multiscale wavelet coefficients and used them to step detection and estimation.

The threshold T_B is defined as

$$T_B = \begin{cases} \frac{\hat{\sigma}_n^2}{\hat{\sigma}_x^2} & , \hat{\sigma}_n^2 < \hat{\sigma}_x^2 \\ \max(|Y_k|) & , \hat{\sigma}_n^2 \geq \hat{\sigma}_x^2 \end{cases} \dots \dots \dots (6)$$

Noise variance $\hat{\sigma}_n^2$ is estimated as follows:

$$\hat{\sigma}_n^2 = \left(\frac{\text{median}(|Y_i|)}{0.6745} \right)^2 \dots \dots \dots (7)$$

Y_i belongs to subband HH1.

3.3.2. Inter scale Dependency Model

σ_x^2 is the signal variance. The estimation of data locally is the most widely used methodology in image denoising algorithms. Chang et al. proposed a spatially adaptive wavelet thresholding scheme based on context modelling. Each wavelet coefficient is modeled as a mixture of Generalized Gaussian Distribution variables with unknown slowly spatially varying parameters. The estimation of

these parameters is carried out as a function of its neighbouring coefficients.

The signal variance $\hat{\sigma}_x^2$ can be estimated using the standard deviation given below:

$$\hat{\sigma}_x = \sqrt{\max(\hat{\sigma}_y^2 - \hat{\sigma}_n^2, 0)} \dots \dots \dots (8)$$

Where $\hat{\sigma}_y^2 = \frac{1}{N_s} \sum_{k=1}^{N_s} Y_k^2$, where N_s is the no. of coefficients in the subband.

In this paper a new inter scale dependency model is proposed.

$$W_j(m) = 0 \text{ if } W_{j+1}\left(\frac{m}{2}\right) \leq t_j \dots \dots \dots (9)$$

(i) For the coarsest scale $j+1$ of decomposition, define a weight matrix U_j with all entries 1 and multiply with wavelet coefficients.

(ii) For the finest scale j of decomposition define a weight matrix U_j with zero entries where the coefficients in the $j+1$ level are above the adaptive threshold t_j and with entries as 1 otherwise. Multiply with the corresponding finest scale wavelet coefficients.

The adaptive threshold t_j is defined as $t = \alpha \cdot \hat{\sigma}_n$ (10)

Where α is the positive constant having the value 2.

The signal variance is then estimated as given in equation. Thus the variance estimated for finest scale now exploits the inter scale dependency of wavelet coefficients.

3.4 Algorithm

The following steps are to be processed for the noise removal in ultrasound images.

Step 1: Decompose the input noisy image to J levels by applying stationary wavelet transform.

Step 2: Estimate the noise variance using equation (7)

Step 3: Estimate the signal variance for all the subbands at different levels exploiting inter and intra scale dependencies using equation (8)

Step 4: Estimate the threshold using equation (6)

Step 5: Apply the new adaptive thresholding function to shrink the wavelet co-efficients

Step 6: Reconstruct the image by taking inverse wavelet transform

4. Results and Discussions

Experiments were conducted on several ultrasound scan for different noise variances. Daubechies wavelet is used for decomposition. Too many level of decomposition reduces the reconstruction accuracy. Therefore two or three levels of decomposition is sufficient for a better performance.

The performance is measure with three parameters: Peak-Signal to Noise ratio (PSNR), Structural Similarity Index Measure (SSIM) and Equivalent Number of Looks (ENL). Simulation results and restored images are presented below:

$$PSNR = 10 \log_{10} \left[\frac{255^2}{MSE} \right] dB$$

$$MSE = \frac{1}{MN} \sum_{i=1}^M \sum_{j=1}^N (X(i,j) - P(i,j))^2$$

$$ENL = \frac{1}{H} \sum_{i=1}^H \frac{\mu^2}{\sigma^2}$$

$$SSIM(x, y) = \frac{(2\mu_x\mu_y + C_1)(2\sigma_{xy} + C_2)}{(\mu_x^2 + \mu_y^2 + C_1)(\sigma_x^2 + \sigma_y^2 + C_2)}$$

μ_x is the average of x and μ_y is the average of y
 σ_x^2 is the variance of x and σ_y^2 is the variance of y

$2\sigma_{xy}$ is the covariance of x and y

$$C_1 = (K_1 \cdot L)^2, \quad C_2 = (K_2 \cdot L)^2; \quad K_1 = 0.01, \\ K_2 = 0.03$$

L is the dynamic range of pixels

The image used for simulation is ultrasound fetal image with dimension 512x512.



Fig.3 Original Image

Variance	0.01	0.02	0.05	0.1
Noisy	34.99	32.93	31.03	30.13
Soft Thresholding	36.27	34.15	31.99	30.93
Adaptive with Bayes	38.53	36.35	34.07	32.70
Proposed	39.76	37.53	34.97	33.40

Table 1. Comparison of PSNR values for different noise variances

Variance	0.01	0.02	0.05	0.1
Noisy	0.97	0.94	0.87	0.78
Soft Thresholding	0.97	0.95	0.89	0.81
Adaptive with Bayes	0.98	0.96	0.93	0.88
Proposed	0.98	0.97	0.95	0.89

Table 2. Comparison of SSIM values for different noise variances

Variance	0.01	0.02	0.05	0.1
Noisy	1.67	1.64	1.56	1.44
Soft Thresholding	1.68	1.65	1.57	1.46
Adaptive with Bayes	1.70	1.69	1.65	1.59
Proposed	1.71	1.69	1.67	1.63

Table 3. Comparison of ENL values for different noise variances

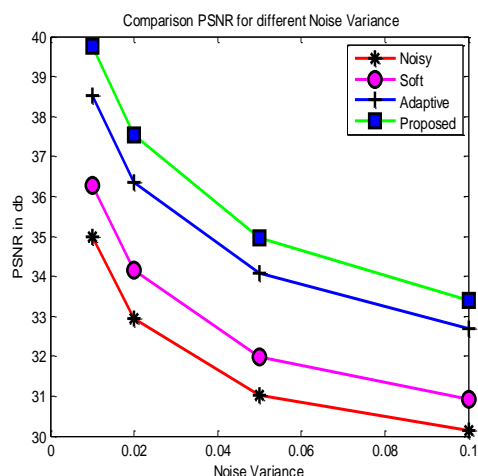


Fig 4. Comparison of PSNR for different Noise Variances

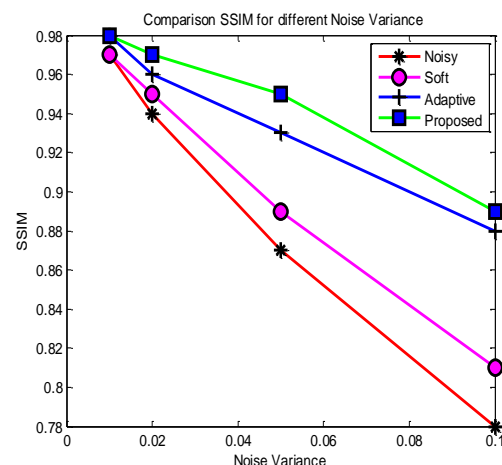


Fig 5. Comparison of SSIM for different Noise Variances

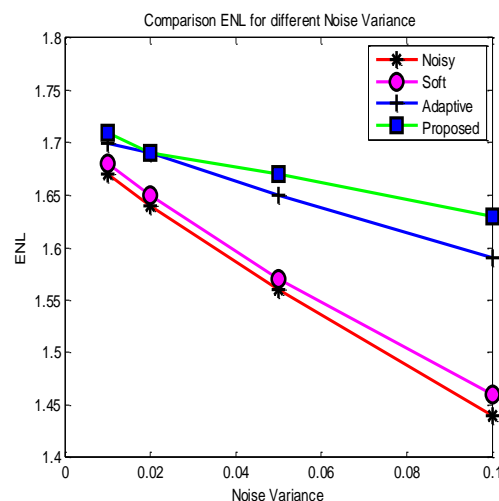


Fig 6. Comparison of ENL for different Noise variances

The improvement in visual quality of images is shown below:

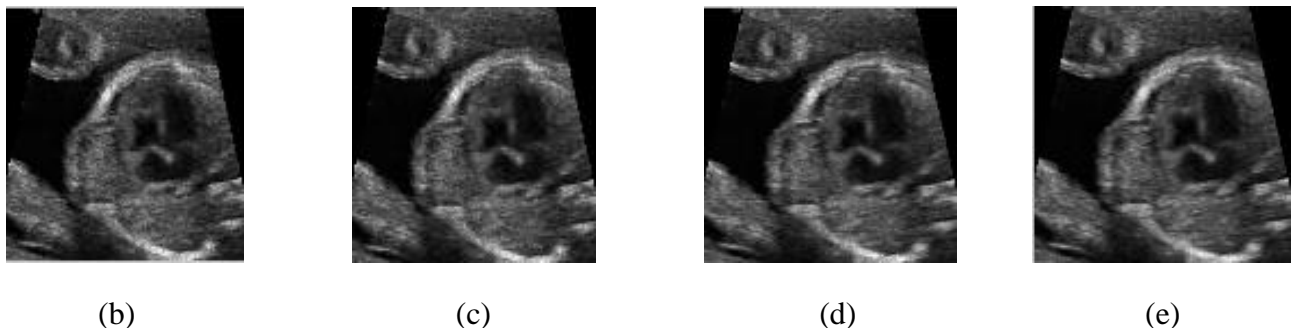


Fig 7. Visual quality for Noise variance 0.01

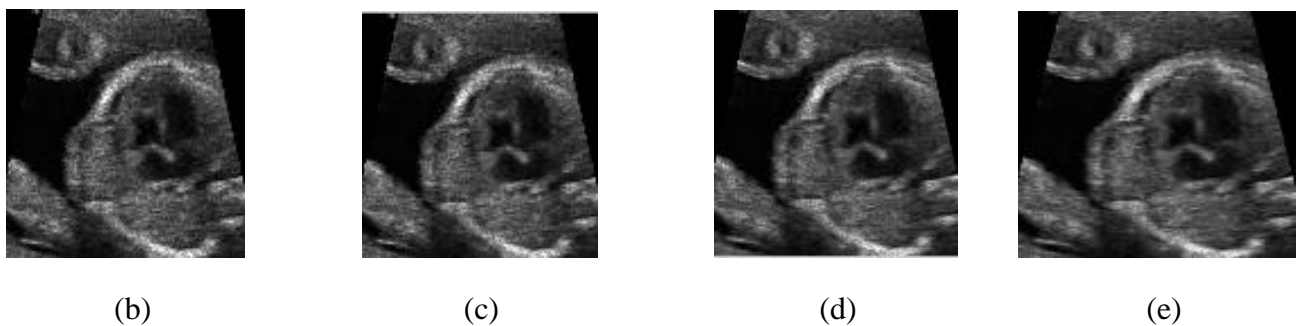


Fig 8. Visual quality for Noise variance 0.02

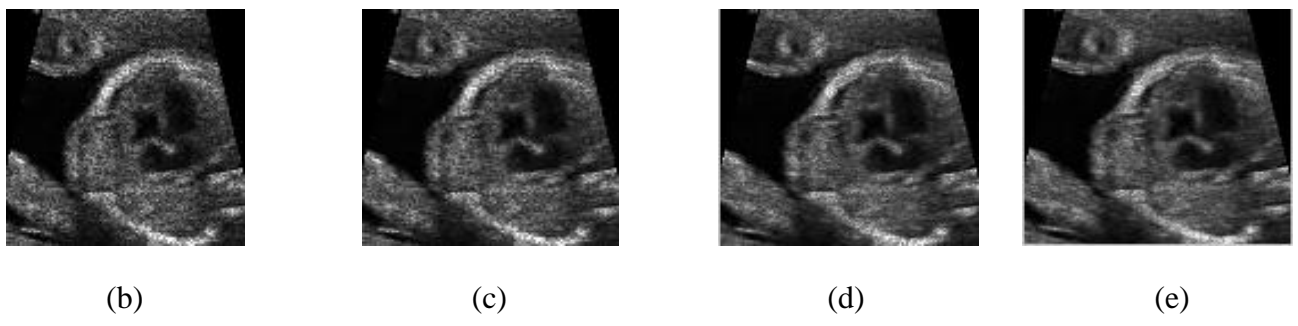


Fig 9. Visual quality for Noise variance 0.05

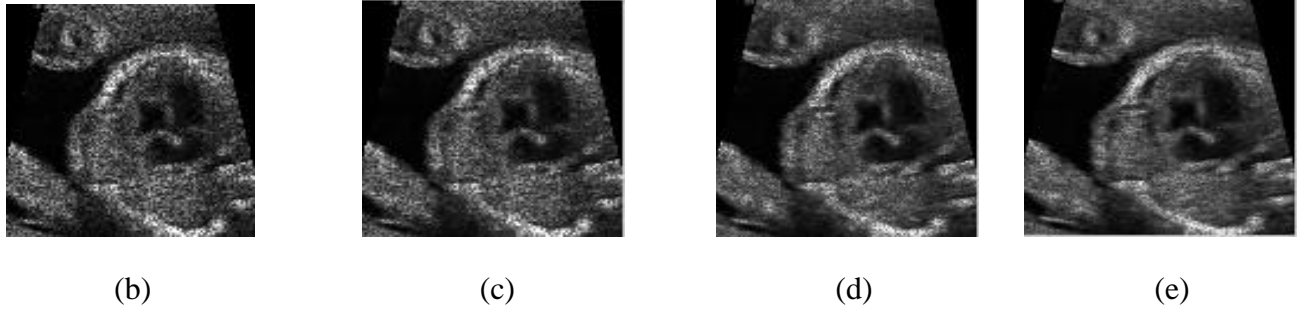


Fig 10. Visual quality for Noise variance 0.1

In Fig.7 to 10. (b) is the noisy image, (c) is the output of Soft Thresholding, (b) is the output of Adaptive Thresholding function without

exploiting intra and inter scale dependencies and (d) is the output of the proposed method. The existing algorithm is modified using

secondary wavelet properties and a subband adaptive threshold. The image used for simulation is ultrasound fetal image. From the comparison tables and the visual quality of the output images, it is seen that the performance of the proposed filter outperforms the other filters discussed.

5. Conclusion

In this paper an efficient adaptive thresholding function based wavelet shrinkage is proposed. The proposed method utilizes a subband adaptive threshold and also exploits inter and intra scale dependencies of the wavelet coefficients. The denoising efficiency depends on how much correct information is conveyed from the coarser scale to its adjacent finer scale. If a significant edge point occurs at a finer scale then it is expected that a corresponding edge point will appear with the same sign at coarser scale. Otherwise, a coarser scale may be decremental to finer scale estimation.

4. References

- [1] David L Donoho, 1995, De-noising by soft thresholding, *IEEE Transactions on Information Theory*, 41(3) , pp.613–627.
- [2] Zhaojun Cai, Tee Hiang Cheng, Chao Lu and K.R.Subramanian,2001, Efficient wavelet-based image denoising, *IEEE Electronics Letters*, vol.37,No.11, May 2001, pp. 683-685.
- [3] H. R. Tizhoosh, 2005,“Image Thresholding using type II fuzzy sets,” *Pattern Recognition*, 38, 2363-2372 .
- [4] Meena Srinivasan , S.Annadurai, 2006, “A Novel Inter and Intra scale wavelet denoising with arbitrary windows,” *GVIP Journal*, Volume 6, Issue 2, 2006, pp.63-67.
- [5] Xiaogang Dong et al, 2010,“An Improved Method of Image Denoising Based on Wavelet Transform,” International conference on CMCE, pp.167-170.
- [6] U. D. Dwivedi and S. N. Singh , 2010, “Enhanced Detection of Power-Quality Events Using Intra and Interscale Dependencies of Wavelet Coefficients,” *IEEE transactions on Power delivery*, vol. 25, no. 1, January 2010, pp.358-366.
- [7] Senthil Kumar,2005, “Performance Improvement in the Bivariate models by using modified marginal Variance of noisy observations for Image denoising applications,” *World Academy of Science, Engineering and technology* 11 , pp.103-107.
- [8] Sudha.S, Suresh.G.R, Sukanesh.R 2009, ‘Comparative study on Speckle Noise suppression techniques for Ultrasound Images’, *International Journal of Engineering and Technology*, vol.1, No.5.
- [9] Alavandan.J, Santhosh Baboo.S 2012 ‘ Enhanced Speckle Filters for SonarImages Using Stationary Wavelets and Hybrid Inter- And Intra- Scale Coefficient Dependency’, *Global Journal of Computer Science and Technology*, Volume 12 Issue 2 version 1.0,pp.12-19.
- [10] Lei Zhang, Paul Bao, Xiaolin Wu, 2003 ‘Hybrid Inter- and Intra-wavelet Scale image restoration ’, *Pattern Recognition* 36,pp.1737-1746.
- [11] Prabakar Puvanathasan , Kostadinka Bizheva 2007, ‘Speckle noise reduction algorithm for optical coherence tomography based on interval type II

- fuzzy set', Vol. 15, No. 24 Optical Express,pp. 15747-15758.
- [12] Jianhua Yang, Rong Fengb, Wei Deng, 2011, A New Algorithm of Image Denoising Based on Stationary Wavelet Multi-scale Adaptive Threshold, Proceedings, International conference on Electronic&Mechanical and Information Technology.
- [13] Jappreet kaur et al, 2011,'Survey of despeckling Techniques for Medical Ultrasound Images', Int. J. Comp. Tech. Appl., Vol 2 (4), 1003-1007
- [14] Gaoyong Luo, 2006, Fast Wavelet Image Denoising Based on Local Variance and Edge Analysis, Int. Journal of Electrical and Computer Engineering, 1:6
- [15] Levent Sendur, Ivan W. Selesnick, Bivariate Shrinkage Functions for Wavelet-Based Denoising Exploiting Interscale Dependency, IEEE Transactions On Signal Processing, Vol. 50, No. 11.
- [16] Sabahaldin A. Hussain, Sami M. Gorashi, 2012, Image Denoising based on Spatial/Wavelet Filter using Hybrid Thresholding Function, International Journal of Computer Applications, Vo.42, No.13, March 2012
- [17] Hyun-Young Go, Ji-Bum Lee, Hyung-Hwa Ko, 2006, Wavelet Based Image Denoising Using Intra Scale Dependency, Proceedings of the 6th WSEAS International Conference on Multimedia Systems & Signal Processing, Hangzhou, China, April 16-18, 2006 (pp56-61)
- [18] Pei Chen and David Suter, 2004, Shift-Invariant Wavelet Denoising Using Interscale Dependency, MECSE-2-2004
- [19] T.Ratha Jeyalakshmi and K.Ramar. 2010, 'A Modified Method for Speckle Noise Removal in Medical Ultrasound Images' International Journal of Computer and Electrical Engineering, Vol. 2, No. 1, February, 2010 1793-8163
- [20] Juan Liu And Pierre Moulin, Analysis Of Interscale And Intrascale Dependencies Between Imagewavelet Coefficients
- [21] Jamal Saeedi , Mohammad Hassan Moradi, Karim Faez, 2011, A new wavelet-based fuzzy single and multi-channel image denoising, Elsevier, Image and Vision Computing 28 (2010) 1611–1623
- [22] M.Vijay, L.Saranya Devi, 2012, Image Denoising by Multiscale - LMMSE in Wavelet Domain and Joint Bilateral Filter in Spatial Domain, International Journal of Soft Computing and Engineering (IJSCE) ISSN: 2231-2307, Volume-2, Issue-1

A Novel Awareness and Alertness Implementation on Biometric Authentication in Moving Vehicle

Hema.B, Sundaraguru.R

PSN College of engineering and technology,
Tirunelveli.

hema.shivam@gmail.com, sugursg@yahoo.co.in

Abstract

Driver drowsiness is among the leading causal factors in traffic accidents occurring worldwide. In this project an advance robust wireless Bluetooth communication system is used to control the vehicle and prevent the accident. There are two distinct methods which are eye movement monitoring and bio-signal processing are used to monitor the driver safety through analyzing the information related to fatigue. An infrared sensor and respiration, heart rate sensor are connected with controller, which is continuously reading the bio signal of the driver. An interface Bluetooth module continuously transmits the bio signal with the help of microcontroller. In the receiver side an android based Dynamic Bayesian Network is used to monitor the information of the driver status. An alertness alarm is initiated if the driver fatigue is believed to reach a defined threshold.

General Terms - Android based smart phone, Dynamic Bayesian network, and fatigue.

1. Introduction

Sensor and network-based information technology growth has widened the reach of

wireless sensor networks into countless areas such as healthcare monitoring, remote control monitoring, wildlife monitoring, detection of military explosion, intelligent home monitoring devices, and environment observation and forecasting system [1]–[2]. In 2012, National Highway Traffic Safety Administration (NHTSA) records say that there were 33,808 vehicle causalities. Those accidents are due to driver fatigue which was reported by over 56,000 people. This results in 1800 deaths, 73,000 injuries and 14.5 billion dollars public property loss. It is difficult to estimate that how many accidents were really caused by driver fatigue. According to police, a fatigued driver and drunk driver had a same behavior like reacting slowly; go off from lanes, and carelessly slowing or speeding up the vehicle. Driver Fatigue is caused by four main reasons. The reasons are sleep, work, physical condition, and time of day. Normally people work more in day time and taking a rest in night time. If rest times not enough to a person, the fatigue will cause.

A fuzzy-control massage seat was developed to keep drowsy drivers awake by Lai et al. [3]. (Luis et al. [4]) developed a nonintrusive prototype computer vision system for monitoring driver's attentiveness in real-time. A system with visual, cognitive, and decision making functions for elderly drivers to recognize various objects encountered



during driving was proposed by Kasukabe *et al.* [5]. A traffic-simulation model was designed in a vehicle which is equipped with an adaptive cruise-control (ACC) and lane departure warning (LDW) system for monitor a driver behavior in a real traffic environment by Pauwelussen *et al.* [6]. A system with two fixed cameras to capture images of the driver and the road respectively, and then the images were mapped to global coordinates to monitor the driver sight line is proposed by Lee *et al.* [7]. These authors found four distinctive driving patterns through analysis by a hidden Markov model (HMM). The reliability of steering behavior to detect driver fatigue by multi wavelet packet energy spectrum using a support vector machine (SVM) was designed by Zhao *et al.* [8]. A video sensor based eye-tracking and blink-detection system with Haar-like features and template matching for an automated drowsiness warning system was developed by Lee *et al.* [9]. Drowsiness has a greater effect on rule-based driving tasks than on skill-based tasks using a Bayesian network (BN) paradigm through simulator-based human-in-the-loop experiments was proposed by Yang *et al.* [10].

A latent variable to represent the attributes of individual drivers for recognizing the emotional state of drivers using four sensors, specifically for respiration, skin conductance, temperature, and blood pressure was developed by Wang *et al.* [11]. The design of an electrocardiograph (ECG) and photoplethysmograph (PPG) sensor to measure the driver's metabolic condition was developed by Shin *et al.* [12]. An overall design of classification based on multiple features such as electroencephalography (EEG) signals, steering wheel correction movements, lateral position, average velocity

change trends and weaving, position within the traffic lane and analysis results on recorded videos was presented by Bouchner *et al.* [13]. The drowsiness-related information extracted from electrooculogram (EOG), EEG and ECG signals to classify driver attentiveness was maximized by Khushaba *et al.* [14]. A brain-computer interface (BCI) system that can analyze EEG signals in real time to monitor a driver's physiological and cognitive states was proposed by Lin *et al.* [15]. Bundele *et al.* [16] proposed a neural network approach to classify mental fatigue and drowsiness in driver, where they focused on skin conductance and pulse oximetry. A first-order HMM to compute the dynamics of BN for compiling information about multiple physiological characteristics such as ECG and EEG to infer the level of driver fatigue was designed by Yang *et al.* [17]. Meanwhile, a system to analyze a driver's eye-lid movement, jaw movement, and variation in pulse was developed by Deshmukh *et al.* [18]. An intelligent system that compiled physiological data acquired from a sensor on the steering wheel, as well as mechanical data from a simulation platform to evaluate a driver's level of attentiveness was developed by Giusti *et al.* [19]. Additionally, a method for detecting a driver's distraction and drowsiness levels by analyzing several parameters using an artificial neural network (ANN) was proposed by Eskandarian *et al.* [20]. Liang *et al.* [21] proposed similar fusion approaches can be applied using SVM, which is a data mining method for detecting cognitive distraction using driver eye movement. Driver stress in term of physical appearance using a visual sensor, physiological conditions collected from emotional mouse, and behavioral data from

user interaction activities by using DBN was developed by Zhang *et al.* [22].

There is more number of methods for detection of driver fatigue in real time. The first method is monitoring the driver's physiological signals such as brain waves, heart rate, respiration rate, as well a variety of physiological signals. The second factor is monitoring the physical changes of driver such as mouth for yawning, head position, sagging posture, eye open or close status, and a variety of other factors. The third method is sensing the driver operation and vehicle behavior such as steering wheel movement and driver condition. The fourth method is monitoring the response of the driver. In these paper only two methods is taken for driver fatigue detection. These two method is more reliable, robust and non intrusive. This makes the driver to feel most comfortable.

2. System Architecture

There are four modules consists of hardware and software for driver monitoring complete system design. The modules are bio sensor module, microcontroller module, and android application development and information fusion by DBN.

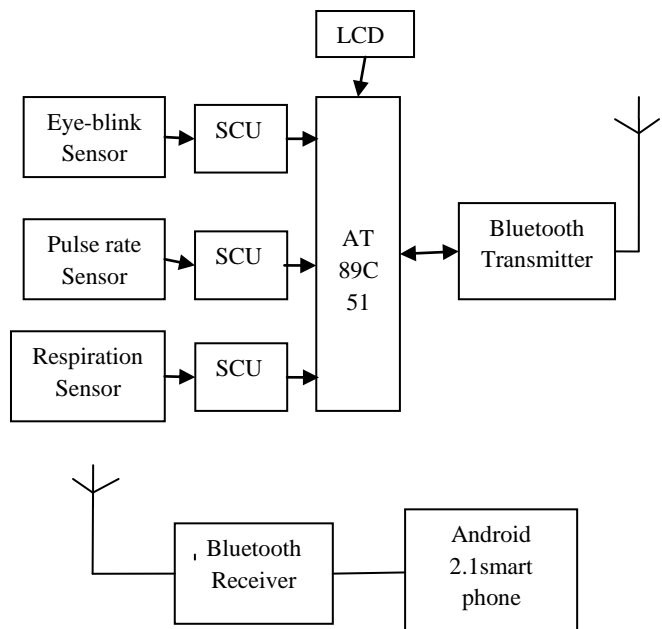


Fig 1: Block diagram overview of system architecture

The DBN in android based smart phone receives the bio signal value from Bluetooth transmitter. DBN fusions the parameter and calculate the probabilistic value. The DBN gives the final output as the status of driver alertness. The warning alarm is initiated to alert the driver if the output reached particular threshold.

2.1 Eye-blink sensor

Eye-blink sensor is used to monitor the alertness of driving person through eye lid movement status. When the person feels drowsy or when he is unconscious the eye lid will be in closed position. An IR sensor consists of IR transmitter and receiver. IR receiver is used as the sensing unit. The IR transmitter continuously transmits the infrared rays towards the eye ball. When the eye lid is closed due to drowsiness the signal is reflected by the eye lid to the receiver. The sensor is connected with the microcontroller. Every 3

seconds the eye blink is monitored. When the sensing occurs, according to DBN result the alarm will be sounded for alertness.

2.2 Pulse rate sensor

Pulse Rate Sensor monitors the flow of blood through a part of the body. It continuously monitors the driver's heart rate. It is also connected to microcontroller. The heart rate is the number of heart beats per minute. Normal heart rate of the person is 65 to 75 beats per minute. Every 5 seconds the heart rate is monitored. When the heart rate is goes down from normal, according to DBN result alarm will be sounded for alertness.

2.3 Respiration sensor

A respiration sensor also connected with controller which is continuously reading the respiration of driver. Driver's respiration is continuously monitored for every 30 seconds. When respiration goes down from normal, according to DBN result alarm will be sounded to alert the driver.

2.4 Signal conditioning unit

The signal conditioning unit accepts input signals from the analog sensors and gives a conditioned output of 0-5V DC corresponding to the entire range of each parameter. It also accepts the digital sensor inputs and gives outputs in 10 bit binary with a positive logic level of +5V. The calibration voltages* (0, 2.5 and 5V) and the health bits are also generated in this unit.

Microcontrollers are widely used for control in electronics system. It provides real time control by processing analog signals obtained from the system. In between a

control circuit and hardware unit there is a suitable isolation is needed to be designed. A signal conditioning unit acts as an interface circuit in between hardware and control unit.

2.5 SMCL-LCD

AT89C51 is the 40 pins, 8 bit Microcontroller which is manufactured by Atmel group. It has the flash type reprogrammable memory. By using this we can erase the program within few minutes. It has 128 bytes internal Random Access Memory and 4kb on chip Read Only Memory. The 32 I/O pin as arranged as port 0 to port 3 each has 8 bit bin. Port 0 contain 8 data line (D0-D7) as well as low order address line (AO-A7). Port 2 contain higher order address line (A8-A15). Port 3 contains special purpose register such as serial data transmitter/receiver register SBUF, two external and three internal interrupt sources, and two 16 bit timers (T0, T1), control registers. It has clock and oscillator circuit also.

The heart of the micro controller is the circuitries which generate the clock pulse. The micro controller has the two pins of XTAL1 and XTAL2 which are connected to crystal oscillator. The clock frequency of the microcontroller is the crystal frequency.

Here we interface LCD display to microcontroller through port0 and port2. LCD control lines are connected in port2 and Data lines are connected in port0. Liquid Crystal Display has 16 pins in which first three and 15th pins are used for power supply. 4th pin is RS (Register Selection). 5th pin is Read/Write. This pin has value of 1 means read operation is done. If it is low means it performs write operation. 6th pin is act as enable pin. Remaining pins are data lines. In

microcontroller Port (1.0 and 1.1) pin is connected to eye-blink sensor and respiration sensor output value and Port (3.0 and 3.1) pin is connected to Bluetooth transmitter hardware module. Microcontroller is worked as a coordinator of all function

2.6 Bluetooth transmitter

Bluetooth transmitter module in hardware gets the bio parameters value from microcontroller. Bluetooth is an open wireless technology standard for exchanging data over short distances (using short wavelength radio transmissions) from fixed and mobile devices, creating personal area networks (PANs) with high levels of security. Here it acts as a wireless network instead to RS-232 data cables. It don't have synchronization problem. Frequency-hopping spread spectrum is one of the radio technologies which are used by Bluetooth. The data transmission rate is up to 79 bands (1 MHz each) in the range 2402-2480 MHz it uses 2.4 GHz short-range radio frequency band.

Generally Bluetooth is a packet-based protocol. It has a master-slave structure. One master may communicate at a time 7 slaves in a piconet. In piconet all devices share the master's clock. Packet exchange is based on the master defined basic clock which notes at 312.5 μ s intervals. The two slot pair has a 1250 μ s. In Bluetooth the master transmits packets in even slots and receiver transmits in odd slots; the slave receives packets in even slots and transmits packets in odd slots. In all cases the master begins to transmit even slots and the slave transmits the odd slots.

2.7 Android based smart phone

The smart phone has the facilities like 3G/4G connectivity, Wi-Fi connectivity, Bluetooth connectivity, accelerometer w/compass, ambient light sensor, proximity sensor, GPS, Gyroscope, and GSM.

2.8 Android architecture

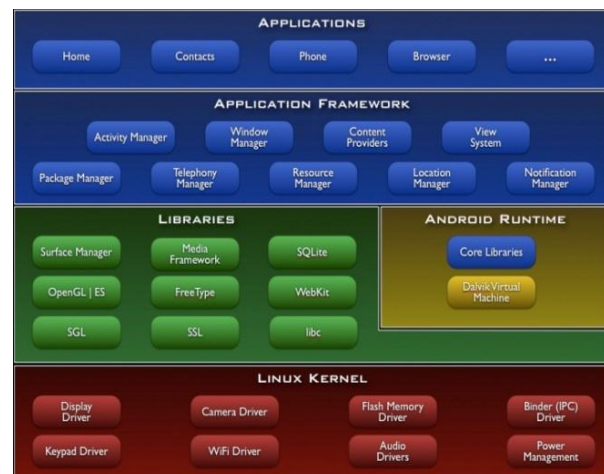


Fig 2: Android architecture

In smart phone particularly Android OS is selected for this work. Because Android is an open source operating system which is created by Google specifically for use on mobile devices (cell phones and tablets). It is Linux based (2.6 kernels). It can be programmed in C/C++ but most application development is done in Java. It has open source libraries like SQLite, Web Kit and OpenGL.

The benefits of Android OS over other mobile OS are it has familiar programming environment. The Android development tools are open source. It is free even for commercial use. Android has a simple and powerful SDK (Software Development Kit). It has no licensing, distribution, or development fees.

Android development over many platforms Linux, Mac OS, windows is possible.

2.9 Android application development

There are three tools used for Android application development. The first tool is Eclipse Platform. It is the platform upon which the plug-in runs. The second tool is Android Emulator it is used to implement the Android virtual machine and used to test and debug android applications. The third tool is Android SDK. Here the Android Developer Tools (the Eclipse plug-in) is installed by the Android SDK.

In Android, applications are packaged in .apk format and it is downloaded to mobile and installed. The .apks contains .dex files (byte codes), manifest and other files. Manifest contains security, link, hardware access and minimum OS related information etc.

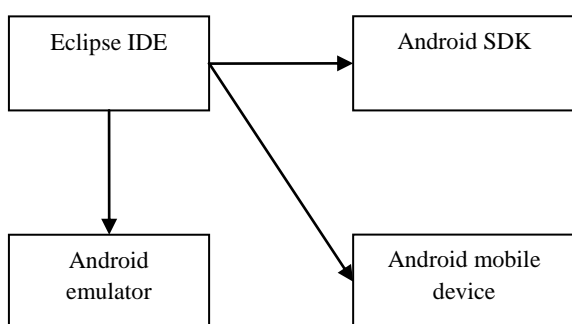


Fig 3: Android application development

2.10 Dynamic Bayesian network

There are various parameters can be used to detect the driver alertness level. Here those parameters are divided into two groups: eye blink parameters and bio signal. In our work, a dynamic Bayesian network paradigm is programmed in smart phone is used for driver fatigue analysis. DBN paradigm is a

probabilistic graphical model. It uses different mathematical techniques to integrate a given input data. The main reason for adapting DBN is that it has an ability to integrate distinct categories of parameters. The final output of the system defining the driver status at a specific time is estimated with a dynamic Bayesian network paradigm.

2.11 DBN algorithm & implementation

The parameters for fatigue level analysis is blink frequency(BF), blink rate(BR), percentage of eye closure(PC), average eye closure speed(AC), heart rate variability(HV), root mean square(RM), first-order-derivation(FD), power spectrum density(PD), Respiration (RESP), Temperature (TEMP). DBN calculates its probability based on density of joint probability function which is the product of the individual density function and parent variables conditional function. The joint probability density function can be written as, $P(Y_1 = y_1, \dots, Y_N = y_N) = \prod_{i=0}^N P(Y_i = y_i | Y_{\text{parent}} = y_{\text{parent}})$. Here each Y_v is a parent of Y_u . In this case, Y_v is the parent node. In this the input parameters are declared. Y_u is the child node. In this status of the driver is declared. The correlations for parameters are calculated for to detect the dependencies relationships among them.

The Pearson's correlation among the parameters are defined as, $\rho_{X,Y} = E[(X\mu_X)(Y - \mu_Y)] / (\sigma_X\sigma_Y)$ where μ_X and μ_Y is the mean of X and Y parameters. Meanwhile, σ_X and σ_Y stand for the standard derivation for X and Y parameters. The correlation value is zero if the parameters are totally independent. The negative sign expresses the inverse relationship between the parameters.

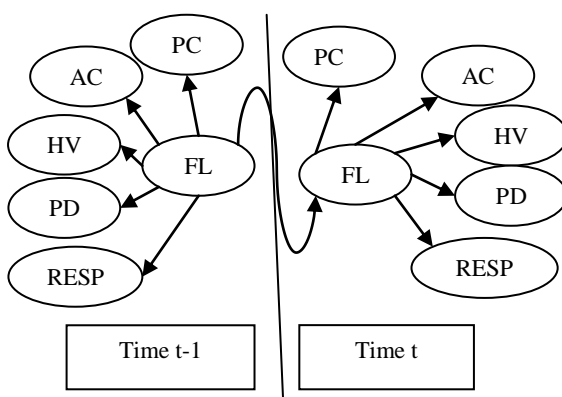


Fig 4: Structure of DBN with five parameters as input of parent nodes and the final output of child nodes

BF and BR shows the closest linear relationship while calculating the correlation value. The high correlation parameters should be removed to reduce the repeated calculation. Finally, the selected highly independent parameters are PC, AC, PD, HV and RESP as inputs to the DBN paradigm. DBN calculation is written using java eclipse language in android platform and it is implemented in android based smart phone. The driver bio parameters are given to smart phone by using Bluetooth transmitter. The DBN in smart phone combined the parameters and calculates the result of single probabilistic value. The calculated probabilistic value is 0.95.

In order for the DBN to perform analysis, a conditional probability table (CPT) is required for each and every parent node. Conditional probability is defined as it is the probability of an event occurring given that another event has already occurred. Experiment's data is filtering for any incomplete or missing parts is necessary before a CPT can be constructed. Some of the eye blinks captured are not able to process due to the sudden huge movement of driver or

affected by the changes of light in the surrounding environment. Moreover, parts of the heart & respiration rate signals are missing sometimes. When constructing the CPT, only meaningful data is extracted and labeled.

3. Experiments and Evaluation Details

The eye blink and respiration sensors are placed in a helmet which was wore by the driver and the pulse rate sensor is connected to helmet via driver's finger. During the experiment the helmet is wore by the driver.

The experimental evaluation details are given below: Figure 5 shows the overall hardware kit architecture for driver fatigue level monitoring.



Fig 5: Hardware kit for driver fatigue level monitoring



Fig 6: Android based smart phone monitoring system for driver alertness

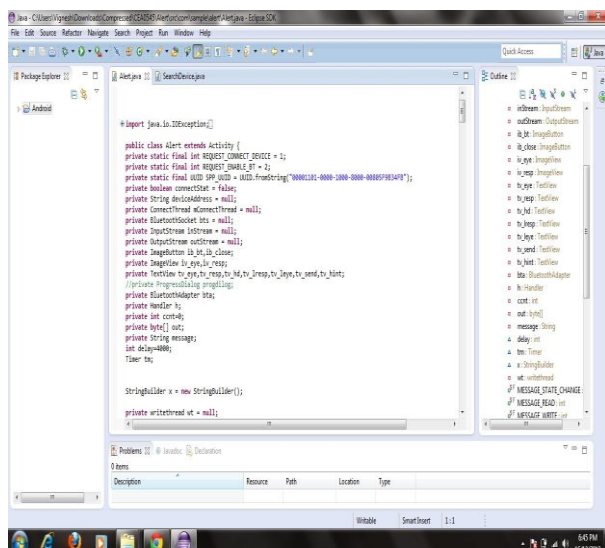


Fig 7: Screenshot for the android programming using eclipse for driver alert monitoring

Case 1: Both the eye blink and bio signal value is normal.

The DBN in android mobile calculates the combined probability value of received parameters. In normal case the result of DBN is below the threshold value. So the status ‘Driver Safe’ will be displayed in the mobile screen.

Case 2: When eyes are closed due to drowsiness.

In this case the final result of DBN is above the threshold level. But the alarm waits 3 seconds for eye opening and afterwards the alarm will be sounded to alert the driver and others. Same time driver’s ‘Eyes closed’ status is displayed in the mobile screen. The corresponding LED will be set ON.



Fig 8: The snapshot of driver's eyes are closed due to drowsiness

Case 3: When respiration or heart pulse go down.

When heart rate or respiration level goes down below the normal level, the DBN produces the probability figure which was above the threshold level. In this case the alarm waits 5 seconds for normal beats of heart and respiration. If the abnormal condition continues, alarm will be on. In the same time the driver’s ‘Heart rate is Abnormal’ or ‘Respiration is Abnormal’ will be displayed in the mobile screen. The corresponding LED will be set ON.



Fig 9: The snapshot of driver's respiration in abnormal status.

4. Result

The system is effectively designed. It takes a quick action to avoid an accident. Dynamic Bayesian Network programmed in smart phone performs the statistical analysis according to the extracted information. This approach avoids the false detection rate that annoys the driver. For a true detection only it initiates the alarm. The driver status is continuously displayed in the mobile.

5. Conclusion

A fatigue monitoring system was designed and implemented in Android-based smart phone. The final output of the system produces the driver status in specific time by using dynamic Bayesian network paradigm. The system can take a quick action to avoid accidents. It is more reliable and can be easily implemented in all automobiles. In future work we have planned to implement a system that will give alert to the nearby vehicles by giving proper indication and also stop the vehicle gradually, if the driver is not in

position to control the vehicle due to his physical condition. Then the condition of the driver will also be informed to nearby emergency ambulance, base station and the rescue guards.

6. References

- [1] N. CSU, "A survey of sensor network applications," IEEE Communication. August 2002.
- [2] M. Ying, "Application of sensor networks," Department of Computer Science, Friedrich-Alexander-Univ. Erlangen Nuremberg, Nuremberg, Germany, May 2005.
- [3] R. L. Lai and C. L. Liu, "A fuzzy control massage seat for awaking drowsy drivers", in 2006.
- [4] L. M. Bergasa, J. Nuevo, M. A. Sotelo, R. Barea, and M. E. Lopez, "Real-time system for monitoring driver vigilance," March 2006.
- [5] T. Kasukabe, M. Hiraoka, O. Yamamoto, M. Yamada, and T. Nakano, "Development of system for comprehensively measuring driving ability for elderly safe driving" in May 2009.
- [6] J. Pauwelussen and P. J. Feenstra, "Driver behavior analysis during ACC activation and deactivation in a real traffic environment, June 2010.
- [7] J. D. Lee, J. D. Li, L. C. Liu, and C. M. Chen, "A novel driving pattern recognition

and status monitoring system”, December 2006.

[8] S. F. Zhao, G. H. Xu, and T. F. Tao, “Detecting driver’s drowsiness using multi wavelet packet energy spectrum,” in October 2009.

[9] Y. S. Lee and W. Y. Chung, “Video sensor based eye tracking and blink detection to automated drowsy driving warning system using image processing,” July 2010.

[10] J. H. Yang, Z. H. Mao, L. Tijerina, T. Pilutti, J. F. Coughlin, and E. Feron, “Detection of driver fatigue caused by sleep deprivation,” July 2009.

[11] J. Wang and Y. Gong, “Recognition of multiple drivers’ emotional state,” in December 2008.

[12] H. S. Shin, S. J. Jung, J. J. Kim, and W. Y. Chung, “Real time car driver’s condition monitoring system,” November 2010.

[13] P. Bouchner, R. Pieknik, S. Novontny, J. Pekny, M. Hajny, and C. Borzová, “Fatigue of car drivers - detection and classification based on experiments on car simulators,” in September 2006.

[14] R. N. Khushaba, S. Kodagoda, S. Lal, and G. Dissanayake, “Driver drowsiness classification using fuzzy wavelet-packet-based feature extraction algorithm,” January 2011.

[15] C. T. Lin, Y. C. Chen, T. Y. Huang, T. T. Chiu, L. W. Ko, and S. F. Liang, “Development of wireless brain computer interface with embedded multitask

scheduling and its application on real-time driver’s drowsiness detection and warning,” May 2008.

[16] M. M. Bundele and R. Banerjee, “Detection of fatigue vehicular driver using skin conductance and oximetry pulse: A neural network approach,” 2009.

[17] G. S. Yang, Y. Z. Lin, and P. Bhattacharya, “A driver fatigue recognition model based on information fusion and dynamic Bayesian network”, May 2010.

[18] S. V. Deshmukh, D. P. Radake, and K. N. Hande, “Driver fatigue detection using sensor network,” February 2011.

[19] A. Giusti, C. Zocchi, and A. Rovetta, “A noninvasive system for evaluating driver vigilance level examining both physiological and mechanical data,” March 2009.

[20] A. Eskandarian and R. A. Sayed, “Analysis of driver impairment, fatigue, and drowsiness and a unobtrusive vehicle-based detection scheme December 2005.

[21] Y. L. Liang, M. L. Reyes, and J. D. Lee, “Real-time detection of driver cognitive distraction using support vector machines,” June 2007.

[22] W. H. Liao, W. H. Zhang, Z. W. Zhu, and Q. Ji, “A real-time human stress monitoring system using dynamic Bayesian network,” June 2005.

[23] W. Y. Chung, Y. D. Lee, and S. J. Jung, “A wireless sensor network compatible wearable u-healthcare monitoring system



- using integrated ECG, accelerometer and SpO2,” August 2008.
- [24] A. Shabtai, Y. Fledel, U. Kanonov, Y. Elovici, and S. Dolev, “Google android: A state-of-the-art review of security mechanisms,” 2009.
- [25] Z. L. Zheng and F. Yang, “Enhanced active shape model for facial feature localization,” July 2008.
- [26] C. Zocchi, A. Rosetta, and F. Fanfold, “Physiological parameters variation during driving simulations,” September 2007.
- [27] H. Park, S. Oh, and M. Hahn, “Drowsy driving detection based on human pulse wave by photoplethysmography” 2009.
- [28] Q. Wu, B. X. Sun, B. Xie, and J. J. Zhao, “A perclos-based driver fatigue recognition application for smart vehicle space,” October 2010.

Detection and Segmentation of Optic Disc in Retinal Images

Gogila Devi.K¹, Vasanthi.S¹

K.S.Rangasamy College of Technology, Tiruchengode

devi.kanivcet@gmail.com, vasanthiramesh@gmail.com

Abstract

Image segmentation plays an vital role in image analysis for diagnosis of various retinopathic diseases. For the detection of glaucoma and diabetic retinopathy the manual examination of the optic disc is the standard clinical procedure. The proposed method is to use the circular transform to automatically locate and extract the optic disc (OD) from the retinal fundus images. The circular transform uses the radial line operator which uses the multiple radial line segments on every pixel of image. The maximum variation pixels along the each radial line segments are taken to detect and segment OD. The input retinal images are preprocessed before applying circular transform

Keywords

Optic disc, Detection and Segmentation, Circular transform, Radial line segments

1. Introduction

Digital photography of the retinal image is used as a screening tool for patients suffering from sight threatening diseases such as Diabetic retinopathy (DR) and Glaucoma. The automatic screening system for retinal image diagnosis consist of reliable and efficient detection of normal features like optic disc, blood vessels and fovea in the retinal images are required. And also OD location helps to build a retinal coordinate system that can be used to determine the position of other retinal

abnormalities, such as exudates, drusen, and hemorrhages.

In literature a very few work have been reported about the location of optic disc and they haven't addressed about the boundary of optic disc. OD localization methods can be classified into two main categories, appearance-based methods and model-based methods. Appearance-based methods identify the location of the OD as the location of the brightest round object within the retinal image. The optic disc represents the beginning of the optic nerve and is the point where the axons of retinal ganglion cells come together. The optic disc is also the entry point for the major blood vessels that supply the retina. The techniques that uses this property of OD are such as intensity thresholding [1] and [2], highest average variation [3], matched spatial filter [4], and principle component analysis [5]. For detection of optic disc, the optic disc center have been previously approximated as the centroid of the largest and brightest connected object in a binary retinal image obtained by thresholding the intensity channel. Reza *et al.* [6] also used the watershed transformation for OD segmentation. In [7], the approach is based on considering the largest area of pixels having highest gray level in the images for optic disc detection. In [8], stated a method to detect the location of the OD by detecting the area in the image which has the highest variation in brightness. As the optic disc often appears as a bright disc covered in dark

vessels the variance in pixel brightness is the highest there.

Some other methods were based on the anatomical structure that all major retinal blood vessels radiate from the OD. The matching of the expected directional pattern of the retinal blood vessels is used as OD detection algorithm and the retinal blood vessels are segmented using a simple and standard 2-D Gaussian matched filter [9]. In [10], the two methods were described and combined. In the first method calculation of fuzzy and then applies the hypothesis generation. The second method equalizes the illumination of the image's green plane and then applies the hypothesis generation. The hypothesis generator returns either a location for the optic disc or no location at all. The matching of the expected directional pattern of the retinal blood vessels is used as OD detection algorithm and the retinal blood vessels are segmented using a simple and standard 2-D Gaussian matched filter.

In [11] the optic disc was located by means of mathematical morphology filtering techniques and watershed transformation. This method was tested against a database of 30 retinal images out of that in 27 the exact contours were found. The parametric active contour model was used to detect the Colour morphology in lab colour space followed by the contour detection snakes based on an external image field called Gradient Vector Flow was reported in [12].

The proposed technique circular transform works for the all kind of retinal fundus images with the pathological lesions, image artifacts, exudates, haemorrhages etc. In the proposed work the circular transform detect and segment OD simultaneously where other state of art methods uses different methods for OD detection and segmentation. Circular

transform is not only used for OD detection, it can also be used to detect circular shaped objects such as blood vessels in the fundus images.

2. Methodology

There were a set of 25 images collected from Aarthy Eye Hospital, Karur. Those fundus images were captured using the Carl Zeiss fundus digital camera with photographic angles of 20°, 30° and 50°. The aim of this work is to detect and extract the exact boundary of optic disc using circular transform. The preprocessing steps are histogram equalization, converting the RGB (Red Green Blue) image into RG (Red Green) image, down sampling, median filtering, reducing the search space for optic disc detection. Circular transform uses the radial line operator. The radial lines operate on the every pixel of the image and find the variation among the each line segment and the pixel with maximum variation on all line segments are taken into account for optic disc detection and segmentation.

2.1 Preprocessing

The first step in the preprocess is histogram equalization, to distribute the contrast equally in the image. This method usually increases the global contrast of the images, especially when the usable data of the image is represented by close contrast values. Due to this adjustment, the intensities can be better distributed on the histogram. This allows for areas of lower local contrast to gain a higher contrast. Histogram equalization accomplishes this by effectively spreading out the most frequency intensity values. For the given retinal input image Fig. 1 is histogram



equalized with the reference image Fig. 2 and the matched image in Fig. 3 is obtained with globally distributed contrast over the image.

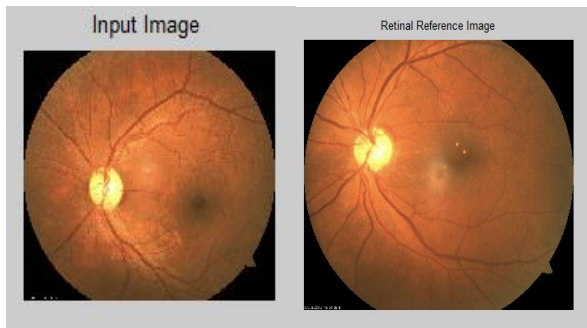


Fig.1

Fig. 2

Input Retinal Image Input reference image



Fig. 3. Obtained Match Image

Fig. 4 represents the image histogram where it plots the number of pixels for each tonal value. The horizontal axis represents the tonal variations, while the vertical axis represents the number of pixels in that particular tone. As the blue color component of the retinal image contains only little information about the optic disc detection the blue color is eliminated from RGB image. The intensity of the image is obtained by combining the green and red colour component of the image by the equation,

$$I = c I_r + (1-c) I_g \quad \dots \dots (1)$$

where I_r represent the red colour component and I_g represents the green colour component of the image and c represents the constant value which is maintaining the weights of I_r and I_g .

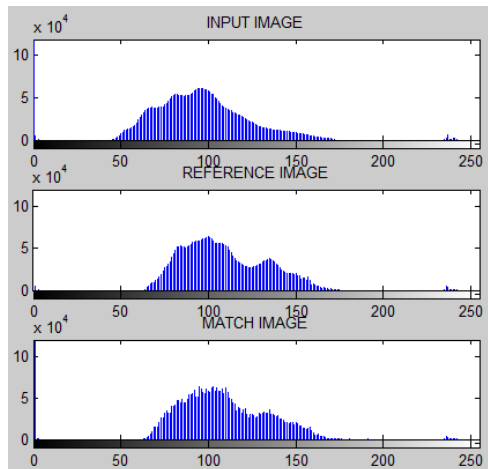


Fig. 4.Histogram analysis of the input, reference and match image

The retinal vessels are more stronger in I_g , so to suppress the green colour component the I_r is set with more weight . The constant c value is chosen as 0.75 for the proposed preprocessing steps. The individual red, green and blue colour component planes are shown in Fig. 5. The intensity converted image is shown in Fig.6.

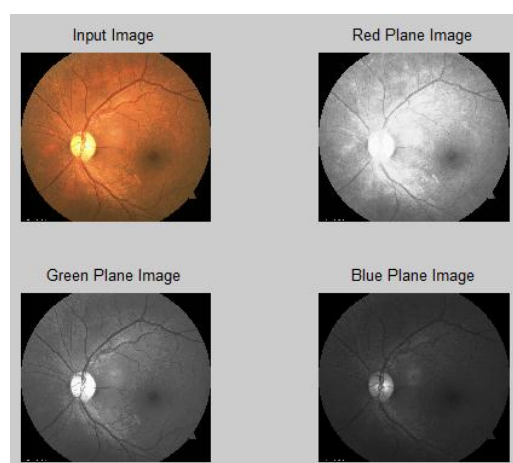


Fig. 5. Individual colour planes

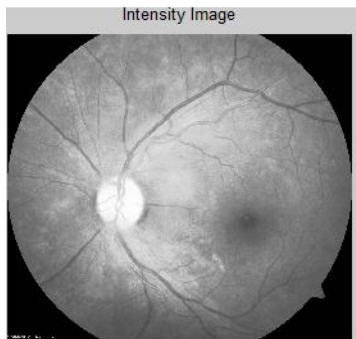


Fig. 6. Intensity Converted Image

Next step is the downsampling of the image to reduce its size and computational cost. Downsampling of an image reduces the number of samples that can represent the signal. In this work, the downsampling is done with the factor of 0.25. The downsampled image is shown in Fig. 7.

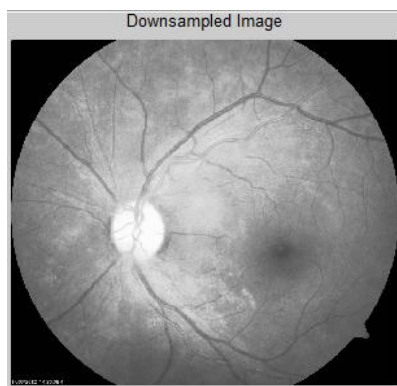


Fig. 7. Downsampled Image

The median filter is used to eliminate the speckle noise and also the small image variation in the retinal blood vessels. The main idea of the median filter is to run through the pixel entry by entry, replacing each entry with the median of neighboring entries. The pattern of neighbors is called the window or template, which slides, over the entire signal or image. The pixel at the center will be replaced by the median of all pixel values inside the window. The operation of a median filter is explained in Fig. 8. For every input image the binary template as like in Fig. 9 is created for its own in order to avoid complications. Thus the window is applied to every pixel of image. All

the pixels of the window are arranged in ascending order the middle value of sequence is replaced to the window. Thus median operation of an image is performed.

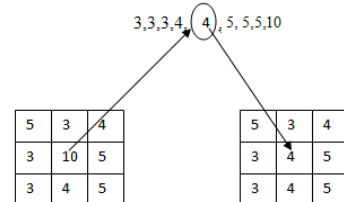


Fig. 8. Representation of median filter

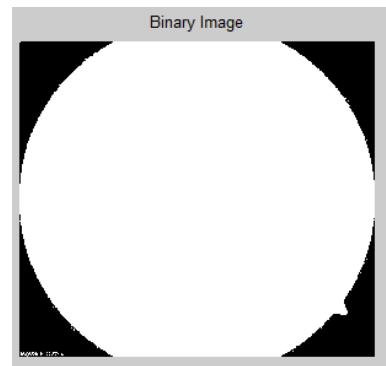


Fig. 9. Binary template for Fig. 1

The obtained median filtered image is free from speckle noise and low frequency blood vessel variation as in Fig. 10.



Fig. 10. Median Filtered Image

Inorder to reduce the search space for the optic disc detection , the optic disc probability map was obtained. Here the brightest 20% pixels

was extracted for OD detection and segmentation. The methodology is projection of image variation and image intensity along the horizontal and vertical direction.

$$HPM(x) = (HG(x,y) - VG(x,y)) \cdot I(x,y) \quad \dots\dots\dots(2)$$

$$VPM(y) = (HG(x,y) + VG(x,y)) \cdot I(x,y) \quad \dots\dots\dots(3)$$

where $HG(x,y)$ represents the image gradient along the horizontal direction, $VG(x,y)$ represents the image gradient along the vertical direction, $I(x,y)$ represents the intensity image, R represents the number of rows in image, C represents the number of columns image. And finally the probability along the horizontal and vertical directions are combined to form the optic disc probability map.

$$OPM(x,y) = HPM(x) \cdot VPM(y) \quad \dots\dots\dots(4)$$

In reference with Mahfouz's method [13] the brightest 20% pixels are extracted for optic disc detection is shown in Fig. 11.

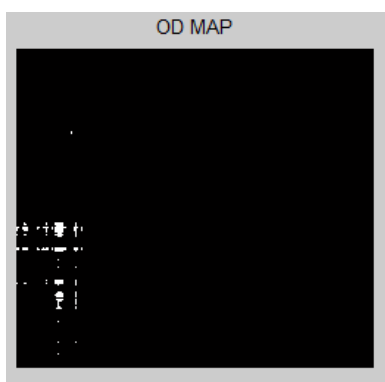


Fig.11.Optic Disc Probability Map

2.2 Circular Transform

Here the OD assumption is that, it is circular region. The circular transform uses the multiple oriented radial lines segments as in Fig. 12 applicable for all pixels of the image to find image variation along those radial lines. The maximum image variation pixels(PMs) along each radial line are taken. The PMs with zero and negative variation are eliminated because they are not belonging to OD. The remaining pixels are filtered based on distance transform.

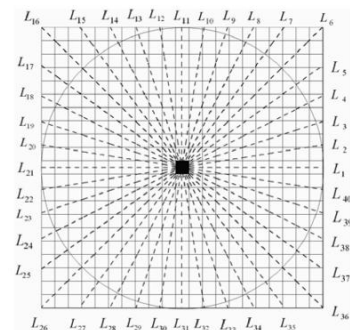


Fig. 12. Representation of radial line operator

In radial line representation n is the number of radial lines and p is the length of each radial lines. The image variation along each radial line is calculated by subtracting the each pixel with its neighboring. The image variation is obtained using the formula,

$$IV(x_{i,j}, y_{i,j}) = I(x_{i,j-1}, y_{i,j-1}) - I(x_{i,j+1}, y_{i,j+1}) \quad (4)$$

where, $i = 1, 2, \dots, n$, $j = 1, 2, \dots, p$.

The pixel $(x_{i,j}, y_{i,j})$ has its neighbouring position pixels are

$(x_{i,j-1}, y_{i,j-1})$ and $(x_{i,j+1}, y_{i,j+1})$. These image variation will be positive because the OD will be brighter than surrounding regions. The position of the PMs for a pixel at (x_0, y_0) along the n evenly oriented line segments are indexed by a vector as,

$$M(x_0, y_0) = [m_1, \dots, m_i, \dots, m_n] \quad (5)$$

where m_i indicates the position of the PM along the i^{th} radial line segment. The maximum image variation along the radial line segments can be denoted as,

$$\begin{aligned} IV(x_0, y_0) &= [iv(x_{1,m1}, y_{1,m1}), \dots, iv(x_{i,mi}, y_{i,mi}), \\ &\dots, \\ &iv(x_{n,mn}, y_{n,mn})] \end{aligned} \quad (6)$$

For a pixel at (x_0, y_0) , the distance of the PMs are determined using the vector as,

$$S(x_0, y_0) = [s_1(x_0, y_0), \dots, s_i(x_0, y_0), \dots, s_n(x_0, y_0)] \quad (7)$$

and the $d_i(x_0, y_0)$ is the distance of (x_0, y_0) to PM of the i^{th} radial line segment at $(x_{i,mi}, y_{i,mi})$ can be obtained using the formula ,

$$s_i(x_0, y_0) = (((x_{i,mi} - x_0)^2 + (y_{i,mi} - y_0)^2)^{1/2}) \quad (8)$$

Some pixels may be lie outside the OD boundary due to retinal vessels or presence of abnormalities, so they have to be eliminated based on OD constraints. The PMs with the zero and negative variations are to be eliminated. After that distance threshold is made to minimize the number of pixel. The final OD map is obtained by,

$$OD(x, y) = (\sum IV''(x, y)) / (\sum (S''(x, y)) - (S''(x, y))^2)^{1/2} \quad (9)$$

where $IV''(x, y)$ is maximum variation and $S''(x, y)$ is maximum distance of PMs. With these PMs, the pixel at the global peak is the OD center and the remaining are used with fitting

method for OD boundary extraction. The final optic disc map is obtained by combining,

$$ODM = OPM \cdot OD \quad \dots \dots \dots (10)$$

The OD map is mapped into retinal image for extracting the optic disc boundary. The downsampled retinal input image with PMs for OD boundary are shown in Fig. 13. The PMs on the downsampled median filtered image are then marked on the original input retinal image. The obtained PMs are connected together to extract the optic disc boundary. The segmented optic disc boundary is shown in Fig. 14.

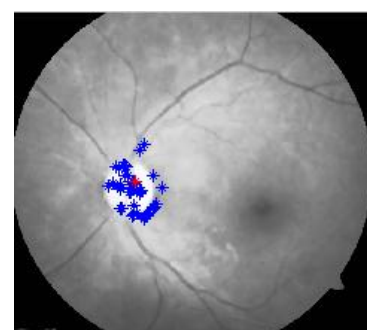


Fig. 13. Marked PMs on the median filtered image

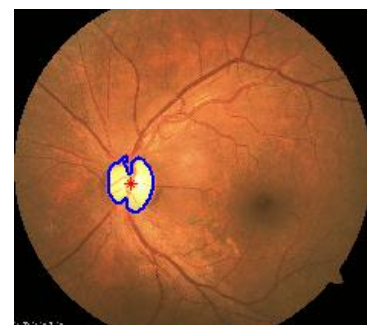


Fig. 14. Segmented Optic disc using the PMs

2.3. Feature Extraction

The optic disc diameter and distance of macula were found as features. The average optic disc diameter(DD) obtained was 70 to 100 pixels. For segmentation of macula first the search area was defined. In standard retinal image the macula will be present at two times the optic disc diameter, so the width of search area is 2DD. In obtained search area the part with lowest intensity is taken as macula, macula present the darkest portion of image. The segmented macula is shown in Fig. 15.

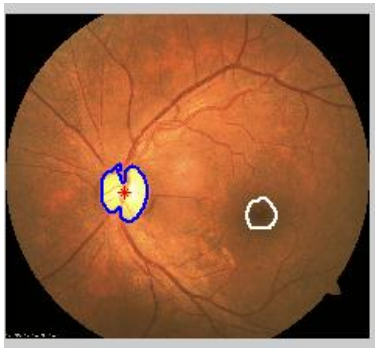


Fig. 15.Segmentation of optic disc and macula

2.4. Classification of Optic Disc

2.4.1. Support Vector Machine

A support vector machine (SVM) is a supervised type of learning methodology that classifies the set of input data by analyzing their features. The SVM classifier is trained with the features extracted to classify the optic disc in retinal images. On the basis of prediction SVM classifies which input data set belongs to which class. In this work the classes defined were the segmented part is optic disc or not. The decision making function is,

$$f(x)=\text{sign}((w.x)+b)$$

.....(11)

where w represents the weight of the hidden nodes and b represents the bias of the hidden nodes.

2.4.2. Extreme Learning Machine

Extreme Learning Machine is the feed forward network, which consists of three layers. This is similar to SVM the only difference is, in ELM the input weights and hidden biases are randomly generated instead of tuned. Thereby the nonlinear system is converted to a linear system,

$$H\beta=T$$

.....(12)

Where β -Weight vector between hidden layer neurons and the output layer neuron, T - Target vector for training dataset, H -hidden layer output matrix.

$$H=\{h_{ij}\}(i=1,2,\dots,N)(j=1,2,\dots,K)$$

.....(13)

$$h=g(w.x+b)$$

.....(14)

Where $g(x)$ is the activation function used. In ELM the hidden elements are independent from the training data and target functions, so the training time for classification is less compared with SVM. Fig. 16. represents the time comparison of ELM and SVM.

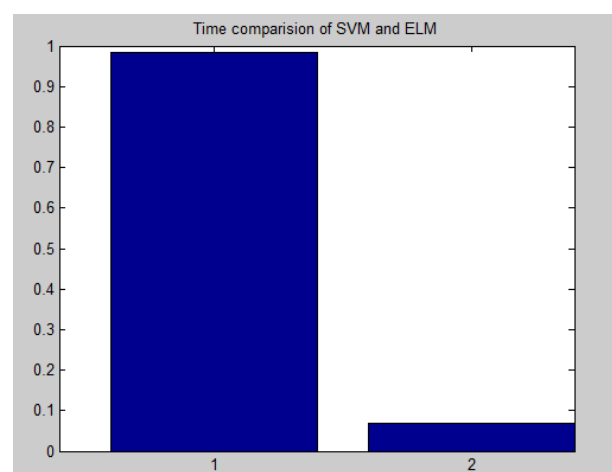


Fig. 16.Time comparison of SVM and ELM

3. Experimental Results

This section presents the PM markings and segmentation results of the optic disc. In the proposed work for the radial line operator , the number of radial line segments used are 180. As each of the radial line segments operate on pixels present on their own line segment and performs the variation difference on the pixels which are present adjacent. The maximum image variation of the pixels along each line segment are marked as PMs. This work uses 180 radial line segments and thereby 180 PMs are marked.

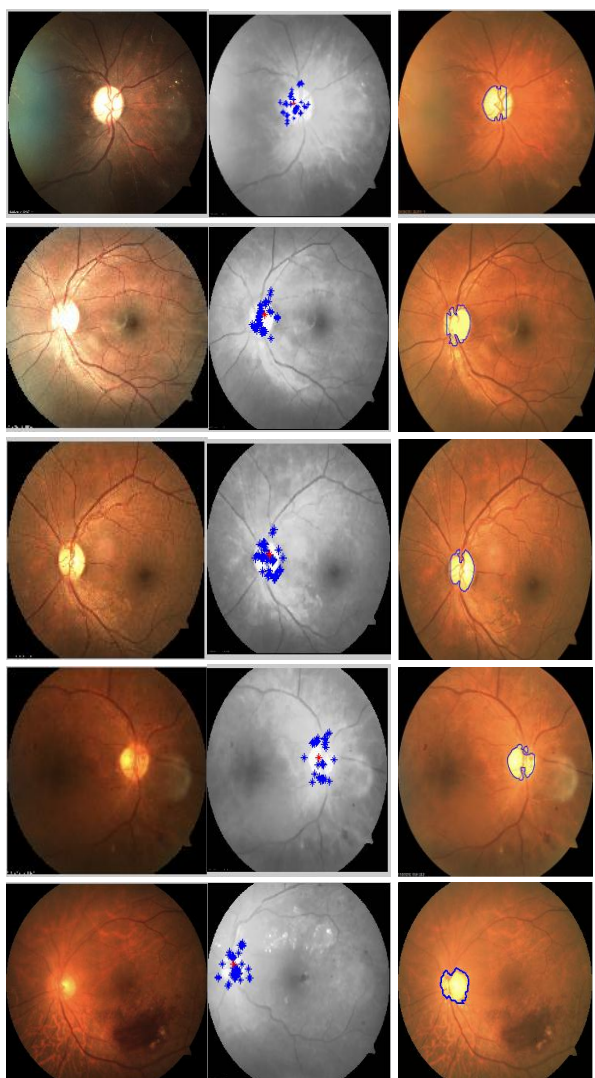


Fig. 17.First column represents the given retinal images, middle column represents obtained PMs on the retinal image and third column represents the segmented OD

Some of the PMs are eliminated by two filtering stages. In first filtering stage, the PMs with zero and negative variations are eliminated because they represent the macula and the retinal blood vessel. In second filtering stage, distance transform is used. The resulting PMs are used to extract the boundary of OD as shown in Fig. 17.

4. Conclusion

Thus the OD center and OD boundary was obtained simultaneously using the single method circular transform. This technique can applied to the image having lesions and with imaging artifacts such as illusions, hazing etc and can accurately detect OD with radial line function. The circular transform is used to locate the OD more accurately than the methods using the anatomical structures such as blood vessels and optic nerves.

5. References

- [1] S.Tamura,Y.Oka moto and K. Yanashima,1998 “Zero crossing interval correction in tracking eye-fundus blood vessels,” in *Proc. Int. Conf.Pattern Recogit.*, pp. 227–233.
- [2] Z. Liu, O. Chutatape, and S. M. Krishnan, 1997“Automatic image analysis of fundus photograph,” in *Proc. Conf. IEEE Eng. Med. Biol. Soc.*, pp.524-525, (Nov 1997).

- [3] M. Goldbaum, S. Moezzi, A. Taylor, S. Chatterjee, J. Boyd, E. Hunter, and R. Jain, 1996“Automated diagnosis and image understanding with object extraction, object classification, and inferencing in retinal images,” in *Proc. Conf. IEEE Int. Conf. Image Process.*, pp. 695–698, (Sep 1996).
- [4] C. Sinthanayothin, J. F. Boyce, H. L. Cook, and T. H. Williamson, 1999 “Automated location of the optic disk, fovea, and retinal blood vessels from digital color fundus images,” *Br. J. Ophthalmol.*, vol. 83, pp. 902–910, (Aug. 1999).
- [5] H. Li and O. Chutatape, 2004“Automatic feature extraction in color retinal by a model based approach,” *IEEE Trans. Biomed Eng.*, vol. 51, no. 2, pp. 246–254(Feb. 2004).
- [6] A. W. Reza, C. Eswaran, and S. Hati, 2008 “Automatic tracing of optic disc and exudates from color fundus images using fixed and variable thresholds,” *J. Med. Syst.*, vol. 33, pp. 73–80.,
- [7] S. Tamura, Y. Okamoto and K. Yanashima, 1988 “Zero-crossing Interval Correction in Tracking Eye-fundus Blood Vessels”, *Pattern Recognition*, Vol. 21, No.3, pp.227-233.,
- [8] S. Sekhar, W. Al-Nuaimy, and A. K. Nandi, 2008 “Automated localisation of retinal optic disk using Hough transform,” in *Proc. Int. Symp. Biomed. Imag.: Nano Macro*, pp. 1577–1580.
- [9] A. Youssif, A. Z. Ghalwash, and A. Ghoneim, 2008“Optic disc detection from normalized digital fundus images by means of a vessels’ directionmatched filter,” *IEEE Trans. Med. Imag.*, vol. 27, no. 1, pp. 11–18, (Jan. 2008).
- [10] A. Hoover and M. Goldbaum, 2003“Locating the optic nerve in a retinal image using the fuzzy convergence of the blood vessels,” *IEEE Trans. Med. Imag.*, vol. 22, no. 8, pp. 951–958, (Aug. 2003).
- [11] Walter, T., Klein, J. C., Massin, P. and Erginay, A. 2002 A contribution of Image Processing to the Diagnosis of Diabetic Retinopathy—Detection of Exudates in Color Fundus Images of the Human Retina. *IEEE Trans. Med. Imag.*, vol. 21, no. 10. 1236-1243.
- [12] Mendels, F., Heneghan, C. and Thiran, J.P. 1999. Identification of Optic disk Boundary in Retinal Images Using Active Contours. *Proc. IMVIP*, 103-115.
- [13] A.E.Mahfouz and A.S.Fahmy, Ultrafast localization of the Optic disc using dimensionality reduction of the search space, in *Int. Conf. Med. Image Computing Computer – Assisted Intervent.*, 2009, vol. 5761, pp. 985-992.
- [14] Guang-Bin Huang, Extreme Learning Machine for Regression and Multiclass Classification, *IEEE Trans. on systems, man, and cybernetics—part b: cybernetics*, vol. 42, no. 2, Apr. 2012.

Implementation and Testing of Median and MMSE Filters on the TMS320C6713DSK for Rician Noise Removal in MR Images

J. Papitha ,D.Nedumaran

Central Instrumentation and Service Laboratory,

University of Madras,

Guindy Campus,Chennai.

dnmaran@gmail.com,dnmaran@yahoo.com

Abstract

MR images are corrupted by Rician distributed noise. This paper presents an MMSE and Median filter techniques for removing the Rician noise present in MR images. The algorithms were developed in the Texas Instruments Code Composer Studio and implemented on the TMS320C6713 Digital Signal Processor Starter Kit (DSK). Further, the algorithms were tested on various brain MR images and the performance of the algorithms were studied by visual inspection as well as calculated performance metrics.

Keywords

Median filter, MMSE filters, MRI, Rician Noise, TMS320C6713 DSK.

1. Introduction

Magnetic Resonance Imaging (MRI) is a routine imaging modality used to view various soft tissues of the body. The MR images are affected by an artifact called Rician noise, which is originated from radio frequency inhomogeneity and intensity deviation of the magnetic field. The removal of Rician noise has been attempted by the biomedical engineers and researchers using various

hardware and software techniques. This paper presents the Median and Minimum Mean Squared Error (MMSE) techniques for Rician noise removal in the TMS320C6713 DSP environment.

Median filter is a digital non-linear filter for removing the impulse noise and for preserving the edge details effectively. It is run through the signal entry by entry and replacing each entry with the median of neighboring entries. Lee and Kassam proposed a Modified Trimmed Mean (MTM) filter based on the data dependent modification of linear filter and the performance of the filter was found to be better than the M filters [1]. Qiu presented an improved recursive Median filter for image processing applications using minimized two-term cost function, which exhibited improved mean square error over the standard recursive medium filters [2]. Wang and Zhang demonstrated a Progressive Switching Median (PSM) filter method using progressive impulse detection and the noise filtering procedures for removing the salt-and-pepper impulse noise, which showed a better performance over the standard median filters for highly corrupted images [3]. Chan et al proposed an adaptive median filter to detect pixel corrupted by salt-

and-pepper impulse noise and restored those pixel information using objective function and edge-preserving regularization term [4]. Ghandeharian et al proposed the Modified Adaptive Center Weighted Median (MACWM) filter using fuzzy clustering of partitioning vector space for identifying the center weight of each block and least mean square (LMS) algorithm for training the center weight of each block [5]. This technique exhibited better performance over the standard impulse filter techniques. Castro and Donoho showed a two-stage median filter based on increasing the SNR at the fine scale and exploiting the nonlinearity of the median filter at the coarse scale, which outperforms other traditional median filters in an asymptotic framework [6]. Coupe et al proposed a Robust Median Absolute Deviation (RMAD) estimator in the wavelet domain and correcting the estimator iteratively using the SNR of the image, which was tested for Rician noise removal on real and synthetic images. The experimental results exhibited improvements in accuracy and robustness [7]. Kizrak and Ozen developed Histogram-Partitioning Median-Filtering Fingerprint-Recognition Algorithm (HMFA) and tested on fingerprint images through ensemble averaging of the mean square error [8].

A minimal mean square error (MMSE) is a common measure of estimator quality, which minimizes the mean square error (MSE) and variance among unbiased estimators. Klein et al proposed finite impulse response (FIR) MMSE decision feedback equalizer (DFE) based on the loss of orthogonality caused by the multipath channel as well as intersymbol interference (ISI) [9]. Aja-Fernández et al., derived a closed-form solution for the linear minimum mean square error (LMMSE) estimator using the local variance, the local

mean, and the local mean square value, which reduces the Rician noise in MR images dynamically through iteration and exhibits good performance in noise removal as well as feature preservation [10]. Jiang et al analyzed the various applications of zero forcing (ZF) and MMSE equalizers for wireless multi-input and multi-output (MIMO) systems [11]. Lee and Kim developed a nonlocal MMSE de-noising filter to minimize the mean square error (MSE) of noisy nonlocal neighbors. It ignores overlapping blocks during de-noising of each block and search non-local neighbors from the entire input image and the external codebook to improve the performance [12].

The rest of the paper presents the details of the Median and MMSE filter based methods for Rician noise present in MR images. The paper is organized as follows: In Section II, a brief review of the Rician noise is given. In Section III, the implementation methodology of the proposed algorithm in the TMS320C6713 DSK is discussed. Section IV discusses about the basics of Median and MMSE filter and its functional parameters. Section V and VI discuss the testing and comparison of the proposed technique. Finally, section VII discusses some of the concluding remarks arrived out of this study.

2. MRI Noise Reduction

Magnetic Resonance (MRI) images are affected by noise and artifacts due to the complex MR image formation and factors exotic to physiological requirements, which affect image quality and are visible on the resulting MRI. De-noising is a challenging problem in MRI and researchers have been attempting several strategies to remove the noise and improve the quality for accurate



clinical diagnosis. It is well known that magnetic resonance (magnitude) image data obeys a Rician noise distribution. The Rician probability density function of Rician distribution is given by

$$p(x) = \frac{x}{\sigma^2} \exp\left(\frac{x^2 + A^2}{-2\sigma^2}\right) I_0\left(\frac{xA}{\sigma^2}\right) \quad (1)$$

where x is a noisy-image intensity of Rician distribution, I_0 is the zero-order modified Bessel function of the first kind, σ is standard deviation and A is the true image intensity value.

Verma and Sharma conducted a comparative study among Bilateral, Bilateral Median and Gaussian filters for removing the noise present in MR images. They found that the bilateral median filter shows the best results for noise removal in MR images in terms of the estimated parameters viz., peak signal-to-noise ratio (PSNR), mean square error (MSE) and contrast to noise ratio (CNR) values [13]. Jaya and Thanushkodi described a new transformation model (NTM) for detection of tumor. They applied block based weighted median filtering for each pixel and compared the intensity pair of each block in MRI without disturbing the edges [14]. Hu et al proposed a combined linear filter (mean filter) with a nonlinear filter (median filter) and showed the filter performance in preserving the edges and removing the noise in MR images, effectively [15]. Lalitha and Latte developed modified spatial median filtering (MSMF) technique based on the window size and threshold of the non-noisy pixels under the mask, which exhibited an impulsive noise suppression without blurring edges in MRI images [16].

3. TMS320C6713 DSK

The Texas Instruments TMS320C6713 Digital Signal Processor based Starter Kit (DSK) is a dedicated tool capable of doing number crunching operations involved in complex signal and image processing applications. It has a USB interface with JTAG emulation port, which provides a reliable communication interface between the host computer and the DSK. In addition, it supports VLIW architecture with 32-bit integer/floating point operations. Further, the DSK is designed to provide PC host applications to boot software onto the DSK and to permit the data transfer using Host Port Interface [17]. Kaymak et al proposed the Normalized Least Mean Square (NLMS) algorithm and implemented on the TMS320C6713 DSK (DSP) as an adaptive digital filter for removing dental drill noise [18]. Zapata and Ruiz demonstrated a median filter model simulated using Simulink and tested on a signal having glitches. Using RTDX instrumentation (CCS) and MATLAB tools, the signal was sent and visualized in real-time [19]. Employing the TMS320C6713 DSK and MATLAB/SIMULINK tools, several signal processing applications have been reported in the literature [20-21]. In this work, Median and MMSE filters are designed in the MATLAB and ported in the DSK for testing the suitability of the Rician noise removal algorithm in the DSK environment for real-time implementation.

4. Filter Techniques

4.1. Median Filter



Median filter is an averaging kernel, which produces an output pixel mean intensity with respect to the neighborhood around the pixel.

Mathematically median is defined as,

For the observation having an odd number of data (N), Median is represented as,

$$\text{Median} = \frac{N+1}{2}$$

(2)

For the observation of an even number of data (N), Median is represented as,

$$\text{Median} = \text{average of } \left(\frac{N}{2} \right) \text{ and } \left(\frac{N+1}{2} \right)$$

(3)

Median of a group data having continuous frequency distribution is represented as,

$$\text{Median} = l + \frac{\frac{N}{2} - c.f}{f} \times h$$

(4)

where l is the lower limit of median class, f is the frequency of median class, $c.f.$ is the cumulative frequency of pre-median class, h is the size of median class and N is the total numbers of items [22].

For the computation of median, we have taken a 3x3 kernel in the matrix image. Since the median filter is a rank filter, the output is chosen in i^{th} pixel intensity of neighboring pixels, where the index i is simply the middle point. If the neighborhood is sorted in ascending order, and the index i is chosen to be the first element, then the filter is a minimum filter. If the last element is chosen, the filter is a maximum filter. Passing an image through a minimum filter is known as erosion (dark areas in the image) and

maximum filter is called as image dilation (bright areas in the image) [23].

For implementing the median filter in the TMS320C6713 DSK, DMA is used for sending page blocks of image data into internal RAM and then scan-lines are filtered. The processed pixels are paged out to external RAM via DMA. For initializing the input image buffer with a noisy image, the program written in C communicated with the DSK via linker command file and a header file. The median filter routine works in a row-major fashion. The first two columns of the processed image are meaningless and should be ignored from the output image for getting better representation of the processed image.

4.2. MMSE Filter

The MMSE filter provides the noise variance, which is estimated by calculating the noise "power" from the mean of all the local variances of the input data. This filter can be used to remove both additive white noise and Rician noise. Consider an image $f(i,j)$ with a neighborhood pixel L of size ($NH \times NH$). Let σ_n^2 be the noise variance, μ_L be the local mean, and σ_L^2 be the local variance. The linear MMSE filter output $g(i,j)$ is given by,

$$g(i, j) = \left(1 - \frac{\sigma_n^2}{\sigma_L^2} \right) f(i, j) + \frac{\sigma_n^2}{\sigma_L^2} \mu_L$$

(5)

Here, the σ_n^2 parameter represents the variance of a background area of the image containing noise. Implementation of the MMSE algorithm generally performed in two phases. If the noise variance is known in advance, then the two phases could be



collapsed into one, which should result in a performance boost.

For implementing the MMSE filter algorithm, the statistics of neighboring pixels such as local mean and local variance are computed and stored. Then, the weighting factor (the ratio of the noise variance to the local variance) for linear interpolation between the input pixel and local mean is calculated, when the current pixel meets the MMSE criterion. This is performed using fixed-point Newton-Raphson iteration employing lookup tables in the TMS320C6713DSK [23].

5. Comparison Methods

To estimate the performance of the algorithm, several performance measures are reported in the literature. In this work, mean square error, peak signal to noise ratio, probabilistic rand index, global consistency error, normalized absolute error, image quality index, average SNR and image variance are estimated. The features of these performance metrics are discussed in the following sub-sections.

5.1 MSE and Peak Signal to Noise Ratio

Mean Square Error (MSE) is the ratio of the square of the difference between the input and output image to the size of the image. Peak Signal to Noise ratio is the logarithmic value of the ratio of the size of the image and the mean square error of the image, which provides the image quality.

$$PSNR(dB) = 10 \log\left(\frac{255^2}{MSE}\right)$$

(6)

$$MSE = \sum_{i=1}^x \sum_{j=1}^y \frac{|A_{ij} - B_{ij}|}{xy}$$

(7)

where MSE is the mean square error value, 255 is the number of gray scale resolution (8-bit) of the image, x, y are the number of pixels of the MR image, A_{ij} and B_{ij} are the threshold values of the original and the denoised MR images, respectively.

6. Results And Discussion

The Median and MMSE algorithms were developed for the TMS320C6713 DSK using Code Composer Studio 3.1 installed in a Pentium IV 3 GHz processor PC with Window XP operating system. The MR brain images used in this study are taken from Siemens Esaote ARTOSCAN C MRI Machine with a magnetic field intensity of 0.15 Tesla with sample per pixel value 1 attained with 63.677701 imaging frequency. The image data are stored in the DICOM file format.

The algorithm was tested in more than 100 MR images and four different MR images (SP H42.2, SP F29.2, SP A63, SP A5.4) are presented here for estimating the filter performance. The raw image added with Rician noise (RN) of three different standard deviation values (0.0-original image, 0.05, 0.07 and 0.10 Rician noise added images) and their corresponding Median and MMSE filtered images of SP A5.4 MR image are shown in Fig 1. Similarly the raw images with three Rician noise level added images and their corresponding Median and MMSE filtered images of SPH42.2, SP A63 and SP F29.2 are given in Figures 2, 3 and 4, respectively. Visual inspection of the images by the trained radiologist observed that the



Median and MMSE filtered images exhibit more homogeneity and better smoothing improvements over the Rician noise corrupted images.

Further, to compute the performance of the filter quantitatively, peak signal to noise ratio (PSNR) has been calculated for all the four images and are given in Table 1. The calculated PSNR values of both the Median and MMSE filters for the raw and Rician noised images (0.05,0.07,0.1) of all the four MR images are given as a histogram chart as shown in Fig. 5 for easy comparison. For a qualitative comparison of the filter performance, we have computed the parameters of probabilistic rand index (RI), global consistency error (GCE), variation of information (VOI), normalized absolute error (NAE) and image quality index (IQI). The computed values of all the four MR images (and their the Rician noise added images) corresponding to the MMSE and Median filters are given in Tables 2 and 3, respectively. From the filtered images and the calculated performance metrics, it is found that both the MMSE and Median filters remove the Rician noise efficiently and preserves the diagnostic information. Further, the following observations are made out of this study.

- Rand index and image quality index parameters should be 1 for the denoised image retaining most of the information found in the original image. From the Table 2 and 3, the values of both these

parameters estimated for the MMSE and Median filtered images found to have values near 1, which means the filters retain the original information as such after filtering operation.

- The parameters such as global consistency error and normalized absolute error should have small values (<1) for maintaining the homogeneity of the processed image with respect to the original image. For the MMSE and Median filtered images, these values are found to be less than 1, which clearly shows that the denoised images maintain homogeneity and well agree with the original image.
- Similarly, the variation of information was found to be high for the MMSE and Median filtered images. It shows that the Rician noise is removed effectively.

As a result, the MMSE and Median filters are found to be suitable filtering techniques for removing the Rician noise present in MR images. Further, the algorithms were developed and implemented in the TMS320C6713 DSK, which paves the way for real-time implementation in MRI instruments after several field trials.

Rician Noise level	Raw Image	MMSE filtered image	Median filtered image
0.00			
0.05			
0.07			
0.10			

Rician Noise level	Raw Image	MMSE filtered image	Median filtered image
0.00			
0.05			
0.07			
0.10			

Fig 1: Rician noise corrupted, MMSE and Median filtered MR images SP A5.4

Fig 2: Rician noise corrupted, MMSE and
Median filtered MR image SP H42.2

Table 1. PSNR values for MMSE and Median filtered images of all four MR images

Image name	Rician noise value	PSNR value	
		MMSE	Median
SPH42.2	0.0500	31.4682	31.3747
	0.0700	30.3112	30.2018
	0.1000	29.5121	29.3909
SPF29.2	0.0500	31.4008	31.2477
	0.0700	30.2459	30.1228
	0.1000	29.4674	29.3439
SPA63	0.0500	32.2990	32.1356
	0.0700	30.8392	30.6364
	0.1000	29.8206	29.5984
SPA5.4	0.0500	31.2665	31.2327
	0.0700	30.2542	30.1647
	0.1000	29.4581	29.3748

Table 2. Performance Metrics
values for MMSE filtered MR images

Image name	MMSE Filter					
	RN values	RI	GCE	VOI	NAE	IQI
SP H42.2	0.05	0.9748	0.9562	10.3364	0.1046	0.9999
	0.07	0.9759	0.9667	11.0394	0.1272	0.9958
	0.10	0.9765	0.9714	11.6461	0.1501	0.9958
SP F29.2	0.05	0.9748	0.9546	10.366	0.1091	0.9985
	0.07	0.9763	0.9697	11.1911	0.1338	0.9966
	0.10	0.9764	0.9743	11.7429	0.1568	0.996
SP A63	0.05	0.9338	0.9186	9.1332	0.1347	1.0063
	0.07	0.9507	0.9433	10.0415	0.1488	0.9975
	0.10	0.963	0.9596	10.8927	0.1637	0.9944
SP A5.4	0.05	0.9598	0.939	9.9769	0.1294	1.006
	0.07	0.9687	0.9567	10.7046	0.141	0.9961
	0.10	0.9742	0.9677	11.3948	0.1544	0.9939

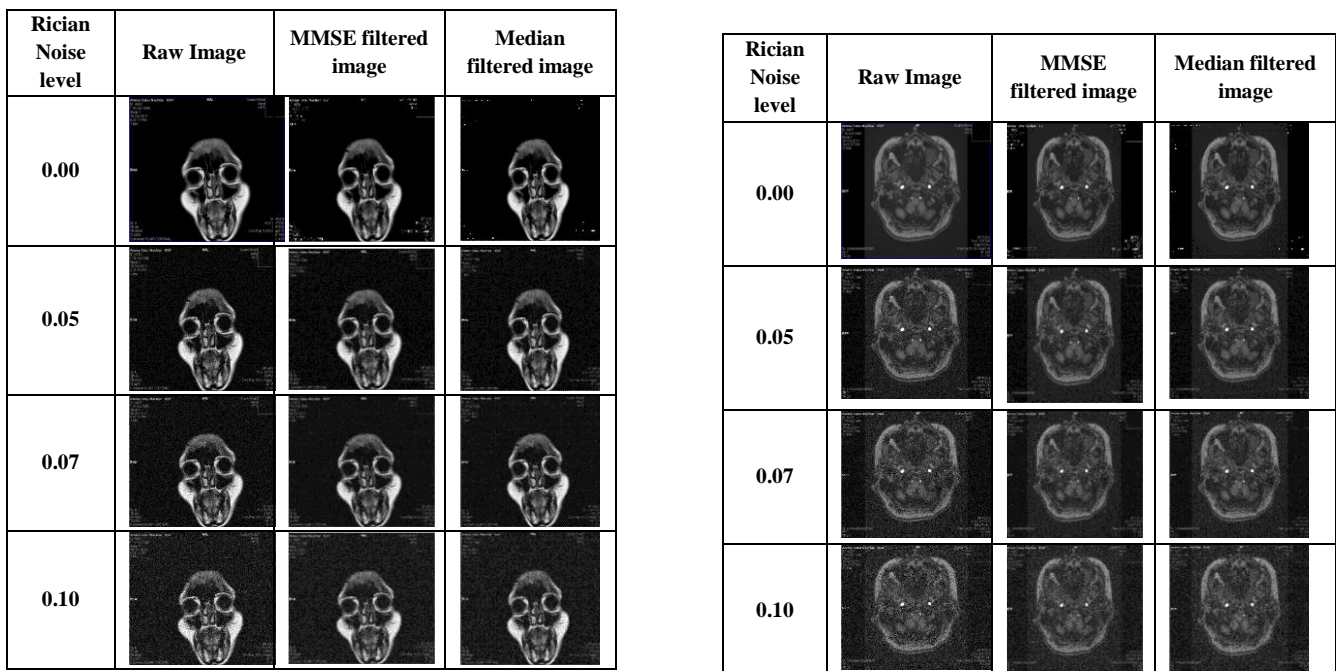


Fig 1: Rician noise corrupted, MMSE and Median filtered MR images SP A5.4

Fig 4: Rician noise corrupted, MMSE and Median filtered MR image SP F29.2

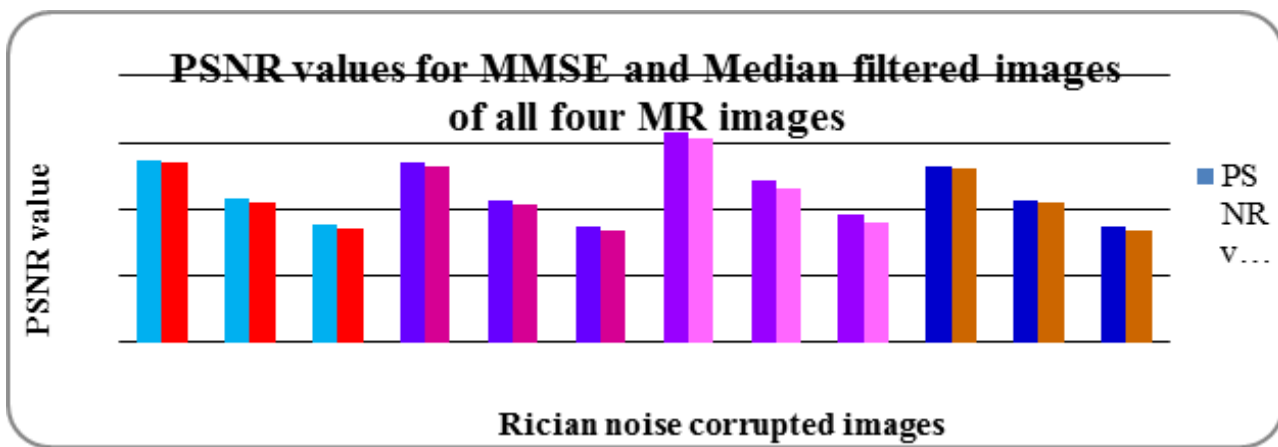


Fig 5: PSNR values of the MMSE and Median filtered images of all four MR images

7. Conclusion

In this work, we have implemented the MMSE and Median filter algorithms in TMS320C6713 DSK environment for removing the Rician noise present in MR images. The performance of filters was estimated both in qualitative and quantitative manner. The results of this study reveal that the MMSE and Median filters removes the signal dependent bias (Rician noise) efficiently, which is evident from the optimum PSNR values as well as the improvements in the contrast of the MR images. The overall performance of MMSE filter is slightly better than the Median filter in terms of PSNR and other parameter values. Also, this study provides some clues/ideas for applying and testing novel filtering techniques intended for improving the performance of the complicated imaging devices like MRI in a cost-effective and simple manner in real-time, since the proposed algorithms were implemented in a real-time DSK platform.

In the future scope of this work, the same DSK platform can be used to study advanced filter algorithms for removing the Rician noise effectively.

8. References

- [1] Lee, Y.H., Kassam, S.A. 1985. Generalized Median Filtering and Related Nonlinear Filtering techniques. IEEE Transactions on Acoustics, Speech and Signal Processing. 33, 3, 672-683.
- [2] Qiu, G. 1996. An Improved Recursive Median Filtering Scheme for Image Processing. IEEE Transactions on Image Processing. 5, 4, 646-648 .
- [3] Wang, Z., Zhang, D. 1999. Progressive Switching Median Filter for the Removal of Impulse Noise from Highly Corrupted Images. IEEE Transactions on Circuits and Systems. Analog And Digital Signal Processing. 46, 1, 78-80.
- [4] Chan, R.H., Ho, C.W., Nikolova, M. 2005. Salt-and-Pepper Noise Removal by Median-type Noise Detectors and Detail-preserving Regularization. IEEE Transactions on Image Processing. IEEE, 14, 10, 1479-1485.
- [5] Ghandeharian, B., Yazdi, H.S., Homayouni, F. 2009. Modified Adaptive Center Weighted Median Filter for suppressing impulsive Noise in Images. International Journal of Research and Reviews in Applied Sciences, 1, 3, 218-227.
- [6] Castro, B.E.A., Donoho, D.L. 2009. Does Median Filtering Truly Preserve Edges Better Than Linear Filtering. The Annals of Statistics. 37, 3, 1172–1206.
- [7] Coupe, P., Manjon, J.V., Gedamu, E., Arnold, D., Robles, M., Collins, D.L. 2009. An Object-based Method for Rician Noise Estimation in MR Images. Medical Image Computing and Computer-Assisted Intervention. 12, 601-608.
- [8] Kizrak, A.M., Ozen, F. 2011. A new median filter based fingerprint recognition algorithm. Procedia Computer Science. Elsevier Ltd, 3, 859–865.
- [9] Klein, A.G., Brown, D.R., Johnson, C.R. 2004. MMSE Decision Feedback Equalization of Orthogonal Multi pulse Modulated Signals. In: Proc. Conf. on Information Sciences and Systems (CISS'04).
- [10] Fernandez, S.A., Lopez, C.A., Westin, C.F. 2008. Noise and Signal Estimation in Magnitude MRI and Rician Distributed Images: A LMMSE Approach. IEEE

- Transactions on Image Processing. 17, 8, 1383-1398.
- [11] Jiang, Y., Varanasi, M.K., Li, J. 2011. Performance Analysis of ZF and MMSE Equalizers for MIMO Systems: An In-Depth Study of the High SNR Regime, IEEE Transactions on Information Theory. 57, 4, 2008 – 2026.
- [12] Lee, C., Kim, C.S. 2012. An MMSE approach to nonlocal image denoising: Theory and practical Implementation. J. Vis. Commun. Image R. Elsevier Inc, 23, 476–490.
- [13] Verma, A., Sharma, B. 2010. Comparative Analysis in Medical Imaging. International Journal of Computer Applications (0975 – 8887). 1, 13, 87-92.
- [14] Jaya, J., Thanushkodi, K. 2010. Exploration on Selection of Medical Images employing New Transformation Technique. IJCSI International Journal of Computer Science Issues. 7,3, 43-48.
- [15] Hu, J.D.C., Hao, H., Chen, J., Ma, Y. 2011. Edge Preserving Filtering by Combining Filters for Magnetic Resonance Image. In: 4th International Congress on Image and Signal Processing. IEEE, 2, 676-681.
- [16] Lalitha, Y.S., Latte, M.V. 2011. A Novel Approach Noise Filtration for MRI Image Sample in Medical Image Processing. International Journal of Computer Science and Communication. 2, 2, 359-363.
- [17] Morrow, M.G., Welch, T.B., Wright, C.H.G. 2006. A Host Port Interface Board to Enhance the TMS320C6713 DSK. In: ICASSP Proceedings. IEEE, 2, 969-972.
- [18] Kaymak, E., Atherton, M.A., Rotter, K.R.G., Millar, B. 2006. Real-Time Adaptive Filtering of Dental Drill Noise Using A Digital Signal Processor, In: 7th International Workshop on Research and Education in Mechatronics. The Royal Institute of Technology, Stockholm.
- [19] Zapata, J., Ruiz, R. 2006. Rapid Development of Real-Time Applications Using MATLAB/Simulink on TI C6000-based DSP. In: Proceedings of the 5th WSEAS International Conference on Education and Educational Technology. Spain, 104-110.
- [20] Golabian, S., Lucas, C., Jamali, M.R., Afrasiabi, M. 2009. Implementation of the Emotional Controller Using DSK TMSC320 Digital Signal Processor. In: CSIT Proceedings, 477-480.
- [21] Vanus, J., Styskala, V. 2011. Application of Variations of the LMS Adaptive Filter for Voice Communications with Control System. Tehnicki vjesnik, 18, 4, 553-560.
- [22] <http://oscience.info/math-formulas/statistics-formulas/>
- [23] Qureshi, S. 2005. Embedded Image Processing on the TMS320C6000™ DSP - Examples in Code Composer Studio™

Hepatitis B Disease Diagnosis Using Meta-Cognitive Neural Network and Extreme Learning Machine.

¹ Madhuvathani.R, ²Mrs.Sivachitra.M , ³Dr.Vijayachitra.S

¹ Department of Applied Electronics

² Department of Electronic and Electrical Engineering

³ Department of Electrical and Instrumentation Engineering

Kongu Engineering College, Perundurai

¹ madhuravisankar.89@gmail.com, sivachitra@kongu.ac.in, svijayachitra@kongu.ac.in

Abstract

Classification problem is used for wide variety of applications like medical diagnosis, pattern recognition, in which the accuracy plays a vital role. This is the first paper in which Meta-cognitive Neural Network (McNN) and Extreme Learning Machine (ELM) is used for the diagnosis of Hepatitis B disease. McNN has two components, namely the cognitive component and the meta-cognitive component. The radial basis function network is the fundamental building block of the cognitive component. The meta-cognitive component controls the learning process in the cognitive component by deciding what-to-learn, when-to-learn and how-to-learn. ELM is a three-step algorithm without tuning mechanism. It could generate the hidden node parameters before training data is fed to them. It is network which contains only one hidden layer. ELM needs very less time for training compared to popular Back Propagation (BP) algorithm. The hepatitis features were obtained from UCI repository of Machine Learning Databases.

Keywords – Meta-cognitive learning, Self regulatory thresholds, Radial basis function network, Sequential learning, Extreme learning machine.

I. Introduction

Hepatitis B is a disease caused by hepatitis B virus (HBV) which infects the liver of hominoids, including humans, and causes an inflammation called hepatitis. Transmission of hepatitis B virus results from exposure to infectious blood or body fluids containing blood. The acute illness causes liver inflammation, vomiting, jaundice and rarely death. Chronic hepatitis B may eventually cause liver cirrhosis and liver cancer—a fatal disease with very poor response to current chemotherapy. The infection is preventable by vaccination. Transmission of the hepatitis B virus (HBV) can occur in one of several ways. It can occur when blood from an infected person enters the body of a person who is not infected. Hepatitis B transmission can also occur through contact with other body fluids, such as semen, vaginal fluids, or saliva. The symptoms of hepatitis B are Fatigue, Excessive tiredness, not feeling very hungry, Nausea or vomiting, Diarrhoea, Muscle pain, Joint pain, Sore throat, Mild abdominal pain, Dark urine, and Light-colored stool. The hepatitis B virus (or HBV) can affect a person with chronic hepatitis B much differently than it would affect someone else. For example,



some people have very bad symptoms of hepatitis B and cirrhosis after many years of having the disease, while others have very few scars.

Meta-cognitive Neural Network (McNN) classifier [5] is a feed forward network. Here, the binary classification problem is dealt with McNN classifier. McNN classifier uses sequential learning algorithm. The training samples arrive one-by-one and the samples are discarded after the learning process. Hence, it requires less memory and computational time during the learning process. In addition, sequential learning algorithms automatically determine the minimal architecture that can accurately approximate the true decision function described by a stream of training samples. Sequential learning has been analyzed for Radial Basis Function Network [1],[2],[3]. Radial basis function networks have been extensively used in a sequential learning framework due to its universal approximation ability and simplicity of architecture. Resource Allocation Network (RAN) was the first sequential learning algorithm [6] developed for function approximation problems. The RAN starts with zero hidden neuron and adds neuron based on the novelty of the input. It uses Least Mean Square (LMS) algorithm for updating the network parameter.

Next sequential algorithms were minimal resource allocation network (MRAN) and Extended MRAN (EMRAN) [3], [7]. A sequential learning algorithm uses all training samples one by one and only once. If the training dataset contains similar data, the resultant classifier has poor generalization performance. An efficient classifier must be capable of judging what samples to learn and when to learn, during the training process. Hence, there is a need to develop a learning algorithm which automatically selects

appropriate samples for learning and adopt best learning strategy to learn them accurately. In human learning, learning process is effective when the learners adopt self-regulation in learning process using meta-cognition [8]. The term meta-cognition is defined in [9] as ‘one’s knowledge concerning one’s own cognitive processes or anything related to them’. Metacognition present in human-being provides a means to address what-to-learn, when-to-learn and how-to-learn. It employs human-like meta-cognition to regulate the sequential learning process, i.e., it learns what it has learnt.

The paper is organized as follows: Section 2 briefly describes the hepatitis dataset. Section 3 describes the McNN classifier. Section 4 describes the ELM classifier .Section 5 describes the results from this study using McNN classifier and ELM. Section 6 summarizes the conclusions.

II. Hepatitis Dataset

In this section, we describe about the Hepatitis dataset.

Hepatitis dataset contains two output classes and it contains 19 features with 155 samples. Out of 155 samples, 75 samples have missing attributes. Here, we have taken 6 significant features out of 19 features [17]. The datasets are obtained from University of California Irvine (UCI) machine learning repository [10].

III. McNN Classifier

In this section, we describe about the McNN classifier.

A. McNN Architecture



McNN architecture is developed based on the Nelson and Narens meta-cognition model [4]. Fig.1 (a) shows the Nelson and Narens meta-cognition model which is analogous to the meta-cognition in human-beings and has two components, a cognitive component and a meta-cognitive component. The information flow from the cognitive component to meta-cognitive component is considered as monitoring, while the information flow in the reverse direction is considered as control. Similar to Nelson and Narens model, McNN has two components as shown in Fig.1 (b), namely the cognitive component and the meta-cognitive component. The cognitive component of McNN is a three layered feed forward radial basis function network with Gaussian activation function in the hidden layer. The meta-cognitive component contains copy of the cognitive component. When a new training sample arrives, the meta-cognitive component of McNN predicts the class label and estimates the knowledge present in the new training sample with respect to the cognitive component. Based on this information, the meta-cognitive component selects a suitable learning strategy, for the current sample. Thereby, addressing the three fundamental issues in learning process: (a) what-to-learn, (b) when-to-learn and (c) how-to-learn.

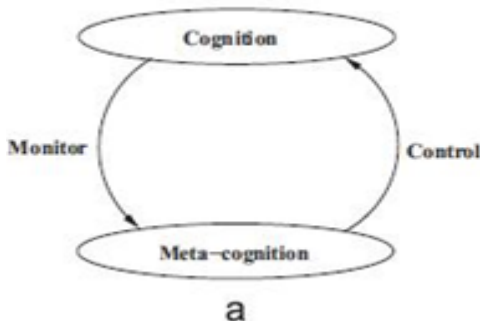


Fig. 1(a) Narens and Nelson model of meta-cognition.

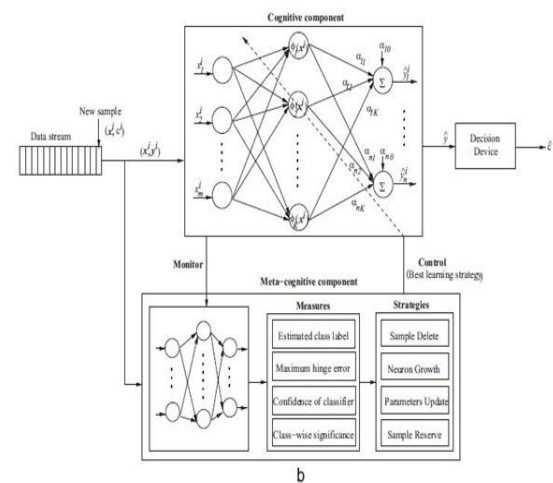


Fig.1 (b) Schematic diagram of McNN learning algorithm.

B. Cognitive component of McNN

The cognitive component of McNN is a three layered feed forward radial basis function network. The input layer maps all features to the hidden layer without doing any transformation, the hidden layer employs Gaussian activation function and the output layer uses a linear activation function. Without loss of generality, we assume that the meta-cognitive learning algorithm builds K Gaussian neurons from i-1 training samples. For given training sample x_i^j , the predicted output ($\hat{y}^i = [\hat{y}_1^i, \dots, \hat{y}_j^i, \dots, \hat{y}_n^i]^T$) of McNN classifier with K hidden neurons is

$$\hat{y}_j^i = \alpha_{j0} + \sum_{k=1}^K \alpha_{jk} \varphi_k(x_i^j), \quad j = 1, 2, \dots, n \quad (1)$$

Where α_{j0} is the bias to the j th output neuron, α_{jk} is the weight connecting the k th hidden neuron to the j th output neuron and $\varphi_k(x_i^j)$ is the response of the k th hidden neuron to the input x_i^j .

C. Meta-cognitive component of McNN

The meta-cognitive component uses estimated class label (\hat{c}), maximum hinge error (E), posterior probability as confidence measure ($\hat{p}(j|x^i)$) and spherical potential based class-wise significance as a measure of knowledge in the new training sample.

D. Learning strategies

The meta-cognitive component devices various learning strategies which directly addresses the basic principles of self-regulated human learning. By selecting one of the following learning strategies for the new training sample, the meta-cognitive part controls the sequential learning process.

a) Sample delete strategy:

Prevents similar samples from being learnt, which avoids over-training and reduces the computational effort. When the predicted class label of the new training sample is same as the actual class label and the confidence level (estimated posterior probability) is greater than expected value then the new training sample does not provide additional information to the classifier and can be deleted from training sequence without being used in learning process. The sample delete criterion is given by,

$$\hat{p}(c|x^i) \geq \beta_d \text{ AND } c == \hat{c} \quad (2)$$

Where, β_d is the deletion, \hat{c} is the estimated class label.

b) Neuron growth strategy:

When the new training sample contains significant information and the estimated class label is different from the actual class label then one needs to add new hidden neuron to

capture the knowledge. The neuron growth criterion is given by,

$$\hat{c} \neq c \text{ AND } \Psi_c(x^i) \leq \beta_c \text{ AND } E \geq \beta_a \quad (3)$$

Where, β_c is the meta-cognitive knowledge threshold.

β_a is the self adaptive meta-cognitive addition threshold.

The β_a is adapted as follows,

$$\beta_a := \delta \beta_a + (1 - \delta) E \quad (4)$$

Where, δ is the slope that controls rate of self-adaptation and is set close to 1.

c) Network parameters update strategy:

Cognitive component parameters $w = [x_0, x_1, \mu^1, \sigma^1, \dots, \mu_k, \sigma_k]^T$ are updated if it satisfies the following criterion,

$$c == \hat{c} \text{ AND } E \geq \beta_u \quad (5)$$

Where β_u is the self adaptive meta-cognitive update threshold. The β_u is adapted based on the prediction error as,

$$\beta_u := \delta \beta_u + (1 - \delta) E \quad (6)$$

McNN uses extended kalman filter (EKF) to update the cognitive component parameters,

$$w' = w + Ge \quad (7)$$

Where e is the error obtained from the hinge loss function and $G \in R^{z^*n}$ is the kalman gain matrix given by,

$$G = PB [R + B^T PB]^{-1} \quad (8)$$

d) Sample reserve strategy: If the new training sample does not satisfy either the deletion or the neuron growth or the cognitive component parameters update criterion, then the sample is pushed to the rear of the training sequence. Since McNN modifies the strategies based on current sample knowledge, these samples may be used in later stage. Ideally, training process stops when no further sample is available in the data stream. However, in real-time, training stops when samples in the reserve remains same.

E. Performance measure

In this paper, we use the global measures such as overall and average accuracies as a performance measures. The statistical measures are given in confusion matrix. The class-wise performance measures like overall/average Efficiency is used for performance.

Per-class classification accuracy is calculated by

$$\eta_a = \frac{1}{n} \sum_{j=1}^n \eta_j \quad (9)$$

Where η_a is the per-class classification accuracy

The over-all classification accuracy is calculated by

$$\eta_o = \frac{\sum_{j=1}^n q_{jj}}{\sum_{j=1}^n N_j} \quad (10)$$

Where η_o is the over-all classification accuracy

IV. ELM Classifier

In this section, we describe about the ELM classifier.

ELMs were originally developed for the SLFNs (Single Layer Feed forward Networks) and then extended to the “generalized” SLFNs. The hidden layer of SLFNs need not be tuned. One of the typical implementation of

ELMs is to apply random computational nodes in the hidden layer, which may be independent of the training data. It is different from traditional learning algorithms; ELM not only tends to reach the smallest training error but also the smallest norm of output weights.

A. Theorem

Given any bounded non constant piecewise continuous function $g : R \rightarrow R$ for additive nodes or any integrable piecewise continuous function $g : R \rightarrow R$ and $\int_R g(x)dx \neq 0$ for RBF nodes, for any continuous target function f and any randomly generated function sequence $\{g_L\}$, $\lim_{L \rightarrow \infty} \|f - f_L\| = 0$ holds with probability one if

$$\beta_L^{(j)} = \frac{e_{L-1}^{(j)}, g_L}{\|g_L\|}, j = 1, \dots, M \quad (11)$$

Theorem can be further extended from additive or RBF hidden nodes cases to “generalized” SLFNs [8, 9]. Given a type of piecewise computational hidden nodes (possibly not neural alike nodes), if SLFNs can work as universal approximator with adjustable hidden parameters, from a function approximation point of view the hidden node parameters of such “generalized” SLFNs can actually be randomly generated according to any continuous sampling distribution. The parameters of these SLFNs can be analytically determined by ELM instead of being tuned. Tuning is actually not required in such generalized SLFNs which include sigmoid networks, RBF networks, trigonometric networks, threshold networks, fully complex neural networks.

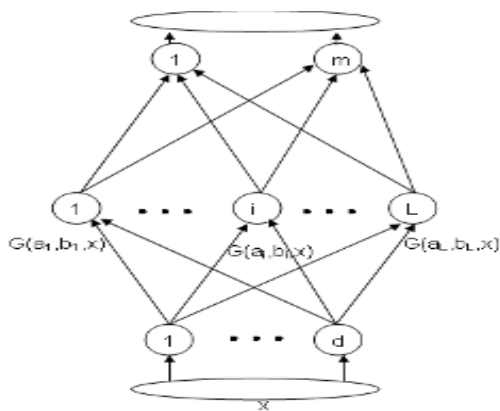


Fig.2 shows the ELM architecture.

The important of ELM Network are the hidden layer of ELM need not be iteratively tuned [11,12], according to feed forward neural network theory [13], both the training error $\|H\beta - T\|$ and the norm of weights $\|\beta\|$ need to be minimized [11,12], the hidden layer feature mapping need to satisfy the universal approximation condition.

B. Classification using ELM classifier

ELM is a three-step algorithm without tuning mechanism. The learning speed of ELM is extremely fast [15] and it can also be used as a classifier [14]. Comparing ELM with conventional learning methods, ELM could generate the hidden node parameters before training data is fed to them. It is network which contains only one hidden layer. The input layer to hidden layer weights can be chosen randomly and hidden layer to output layer weights can be calculated analytically. Unlike traditional gradient-based learning algorithms which only work for differentiable activation functions, ELM can be able to work for all bounded non constant activation functions.

Unlike traditional gradient-based learning algorithms in which issues like local minima, improper learning rate and over fitting, etc are faced, ELM tends to reach the solutions in a straightforward way. The ELM learning algorithm is much simpler than other learning algorithms ELM needs very less time for training compared to popular Back Propagation (BP) algorithm. Compared with BP and Support Vector Machine, ELM implementation of ELM is easier because there is no parameter to be tuned. The classification accuracy of ELM is better than BP and tough classification applications. In ELM many types of hidden nodes (including fuzzy rules, etc) can be used. ELM with RBF nodes needs more number of nodes than ELM with additive nodes. For architecture details and additional details of ELM one can refer [16].

C. Performance measure

The overall efficiency is calculated in ELM by

$$\text{traeff} = \frac{\text{Number of samples correctly classified}}{\text{Total number of samples}}$$

V.Results

In this section, we describe about the results of McNN classifier and ELM.

TABLE.I. Confusion matrix of McNN classifier and ELM for Hepatitis.

Table.II. Results of Mcnn Classifier and ELM for Hepatitis.

		McNN		ELM	
		Predicted			
Actual		1	2	1	2
Training	1	54	0	54	0
	2	4	50	0	54
Testing	1	13	0	13	0
	2	1	12	2	11

	McNN		ELM
	Over-all efficiency	Average efficiency	Over-all efficiency
Training efficiency	0.96296	0.96296	1.00
Testing efficiency	0.96154	0.96154	0.92

VI. Conclusion

This paper proposes the diagnosis of hepatitis B disease with the help of the sequential learning algorithm for Meta-cognitive Neural Network (McNN) based on human meta-cognitive learning principles and Extreme Learning Machine (ELM) for classification problems. The meta-cognitive component in McNN is helpful in choosing suitable strategy for training the cognitive component in McNN. The learning strategies consider sample overlapping condition for proper initialization of new hidden neurons, which helps in minimization of misclassification error. ELM needs less computational time than the conventional neural network. It works with single hidden layer neurons. For this study the acquired classification accuracy of hepatitis disease is

more in McNN classifier than the ELM classifier.

VII. Acknowledgement

We gratefully thank Dr.Suresh Sundaram (Professor, Nanyang Technological University, Singapore) for supporting us with his valuable suggestions.

VIII. References

- [1]Fritzke.B, “Fast learning with incremental radial basis function networks” Neural Process. Lett. 1 (1) (1994) 2–5.
- [2]Huang,L.Chen G.B., “Convex incremental extreme learning machine,” Neurocomputing 70 (16–18) (2007) 3056–3062.
- [3]Lu.Y.W,Sundararajan.N, Saratchandran.P, “A sequential minimal radial basis function (RBF) neural network learning algorithm”, IEEE Trans. Neural Networks 9 (2) (1998) 308–318.
- [4]T.O. Nelson, L. Narens, “Metamemory: a theoretical framework and new Findings”, Psychol. Learn. Motiv. 26 (1990) 125–173
- [5]Sateesh Babu.G, Suresh. S., “Meta-cognitive Neural Network for classification problems in a sequential learning framework”, Neurocomputing 81 (2012) 86–96.
- [6]Savitha.R, Suresh.S,Sundararajan.N, “Self-regulated learning in fully complex valued Radial Basis Function Networks”,Proceedings of the International Joint Conference on Neural Networks,art.No.5596781,2010.
- [7]Platt.J.C, “A resource allocating network for function interpolation” Neural Computing 3(2)(1991)213-225.

- [8]R. Isaacson, F. Fujita, "Metacognitive knowledge monitoring and self-regulated Learning": academic success and reflections on learning, *J. Scholarship Teach.Learn.* 6 (1) (2006) 39–55.
- [9] J.H. Flavell, Metacognitive aspects of problem solving, in: L.B. Resnick (Ed.), *The Nature of Intelligence*, Lawrence Erlbaum Associates, Hillsdale, NJ, 1976, pp. 231–236.
- [10]<http://www.ics.uci.edu/pub/ml-repos/machine-learning-databases/>, 2003.
- [11] Haykin.S., "Neural networks: A comprehensive Foundation", New York: Macmillan, 2nd edition, 1999.
- [12] Hirose.A., "Continuous Complex-Valued Back-Propagation Learning, *Electronics Letters*", 1992 pp.1854–1855.
- [13] Li M.B, G.-B. Huang, P. Saratchandran and N. Sundararajan "Complex-Valued Growing and Pruning RBF Neural Networks for Communication Channel Equalization", *IEEE Proceedings, Vision, Image and Signal Processing*, 2006, pp.411–418.
- [14] S. Suresh, R. V. Babu, H. J. Kim, "No-Reference Image Quality Assessment Using Modified Extreme Learning Machine Classifier," *Applied Soft Computing*, 2009, pp.541–552.
- [15] Guang-Bin Huang, Qin-Yu Zhu,Chee – Kheong siew, "Extreme Learning Machine: Theory and Applications Neurocomputing," 2006, pp.489-501.
- [16] Suresh.S, S. N. Omkar, V. Mani, T. N. Guru Prakash, "Lift Coefficient Prediction at High Angle of Attack Using Recurrent Neural Network," *Aerospace Science and Technology*, 2003, Vol. 7, No. 8, pp. 595–602.
- [17] Tahseen A. Jilani , Huda Yasin , Madiha Mohammad Yasin "PCA-ANN Classification of Hepatitis C patients", *Internal journal of computer applications* feb 2011, volume 14-no7, (0975-8887).

A Smart Phone Based Heart Rate Monitor

Dennis Joe Harmah¹, Kathirvelu D²

Department of Biomedical Engineering,

SRM University, Kattankulathur.

¹joedehaan2005@gmail.com, ²Kathir297@gmail.com

Abstract

The use of mobile communication such as smart phones for monitoring a patient's heart now has a great impact on healthcare in this contemporary world. This system based smart phone will help healthcare professionals such as doctors and nurses to monitor a patient's ECG waveforms as well as some abnormalities like bradycardia and tachycardia. A single-chip microcontroller is used to analyze the patient's heart and this is displayed on the smart phone. This proposed project has an advantage of displaying patient's ECG waveform and heart rate on smart phone using android application. The system uses a microcontroller to capture, reads, stores and displays the condition of the patient's heart rate and ECG signals continuously in real-time. The microcontroller is programmed to analyze the signals and send these signals in packet to a bluetooth to transmit to the smart phone establishing connectivity with the android bluetooth. In this system, the bluetooth is the RF which uses bluetooth over serial protocol and the protocol for transmitting the signals is serial. The system is designed in such a way that detection of ECG signals and any abnormality will be indicated by LED's and Buzzer.

Keywords

Smartphone,ECG,heartrate,android application,bluetooth,microcontroller.

1. Introduction

Heart disease was initially diagnosed using a tape recording of ElectroCardioGram (ECG) signal which is then measured, studied and analysed using a microcomputer. Using ECG signals to diagnose heart disease can be obtained by matching the wave pattern of the ECG signals with a standard or a typical healthy signal and this requires critical complex algorithms, or basic logical decision for characterization of the typical ECG signals in order to process and analyze in depth the heart disease. In most cases, these approaches may require either complicated or simple mathematical analysis to get the required diagnosis. Studying the heart and the signals it generates during our everyday activities for long term basis will help to monitor and group the heart disease depending on how the heart rate is changing during these activities. Many techniques have been developed, implemented and used which restrict the movement of the subject. For example, minicomputer was used in intensive care unit to observe patients or microprocessor-based card was also used in portable system. Here a wire-free system is connected to a hospital minicomputer which allows a subject movement within restricted places in the hospital. Tape systems for

recording ECG signals are bulky, heavy and prone to mechanical failure. In addition, these systems need large batteries. These points are disadvantages to these techniques[1].

ECG Waves and Intervals: The ECG recording consists of two key components-waves (deflections above and below the baseline) and intervals (distances between waves). Each ECG cycle consists of P, Q, R, S, T, and (rarely) U waves. Intervals between the wave that may be measured include QRS complex, QT interval, PR interval, ST segment, and PR segment. Other intervals may be measured. Intervals may sometimes be written as P-R, S-T, etc. Figure 1,2, show the normal ECG tracing(normal sinus rhythm)[2,3,4,].

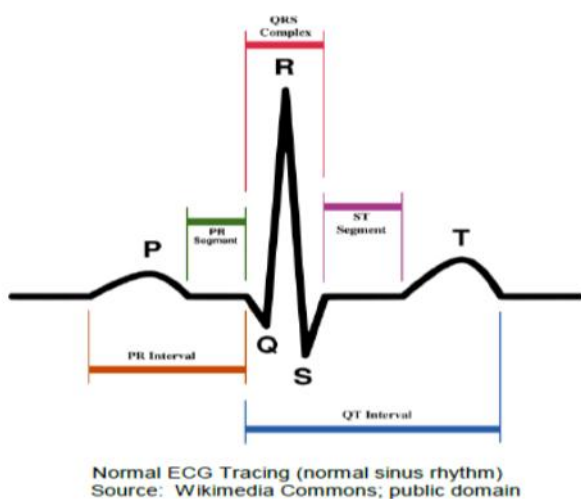


Fig. 1. The normal ECG tracing(normal sinus rhythm).

The introduction of ECG opened a new way and dimension in how to study and analyze the heart, and this allows the cardiac voltages to be measured and recorded. An ECG can be defined as measurement of the surface electrical potential generated by electrical activity in cardiac tissue and the potential between two points on the body surface will change in a characteristic manner at each cardiac cycle, which is a PQRST

waveform. ECG waves are very important to the doctor to know the electrical activities of the heart as well as the condition of the heart. Thus ECG recording, which shows clear P, QRS and T waves, it is possible to obtain a considerable amount of valuable information regarding cardiac activity of the heart. For monitoring ECG signals usually 3 leads are employed and this makes the device simple and becomes user friendly for people who are non-medically trained at the remote places so that when the need of this device arises, even non-medically trained people can easily use them. However, standard number of electrodes attached is twelve for a "diagnostic" purposes but these leads are complex and difficult to be used by the non-medically trained people and therefore need to be handled by only medically trained people or staff. Continuous monitoring of health parameters for long term basis have been expected for patient monitoring, human health care, disease diagnoses and sick prevention. Thus medical professionals such as, doctors, nurses as well as patients demand mobility for user friendly and convenient. This has brought more emphasis on portability of medical devices especially when it comes to patients monitoring and human biotelemetry applications and their importance and therefore researchers need to consider this area. A number of research and developments have already taken place based on medical telemetry systems using wireless communication by means of electromagnetic waves of RF or infrared light which is effective for this condition[5]

The average lifespan has increased nowadays due to the improvement of medical devices and medical care. It has also increased, due to social development, the number of disabilities as a result of various diseases or due to accidents is increasing in our everyday

activities and this has led to need to develop rehabilitation system to assist patients for developing their physical, mental, social ability and independence increased. A small foot-print microcontroller with a built-in analog-to-digital converter(ADC) and low-power consumption was developed by a researcher and this enabled the heart sound signal to be captured by a contact-type microphone which filtered by a band-pass filter and amplified to the level which corresponds to a full-scale input voltage range of the ADC built-in a microcontroller[6].The designing of a wireless real-time monitoring system based on the mobile phone network communication to detect,measure the condition of the heart in real time has had a great mark and improvement in the healthcare. Some of these devices are existing.For example, a system developed by a researcher attaches a portable heart rate sensor to a subject's pulse, and automatically sends a short message for help in accordance with the heart rate monitoring. By using the GSM system as the data transmission network, it transmits the important signs in the old age patient to the monitoring center of the treatment area, community or hospital and provides the medical professionals with diagnosis proof for quick delivery, diagnosing and caring for the patient. As a new monitoring system suitable for remote areas and rural areas as well as the non-medical trained people. This monitor is portable, low cost and good networking as advantage.[7]

Besides these technologies so far, the ECG signals can also be captured on a smart phone with android application. Thus this proposed project is developed to display ECG waveforms and the heart condition of a patient on a Smart Phone using android application. The android application has the following advantages over the already

mentioned ones: It gives clear ECG signals and good resolution, its uses is easy and very simply.

2. Description Of The Hardware System

ATmega8 microcontroller is used for designing and implementation of the hardware with embedded system. This microcontroller is 8-bit based on the AVR RISC architecture and happens to be the main controller of biosignal processing, analysis and transmission. The components used for the construction of this system are of low cost, high precision and low power consumption. It employs three leads with their electrodes which are used to attach to the surface of the patient for capturing ECG signals from the body. The instrumentation amplifier used for conditioning the ECG signals are of high CMRR. The diagram in Figure 2 indicates the block diagram of the system.

2.1. Electrocardiograph (ECG) Machines

There are many types of ECG machines in use today. Most incorporate computer hardware and software that allow for data entry of pertinent patient information. The main components of a basic ECG machine are:

- A cable that splits into individual wires called leads and collects the electrical signals from the skin and transfers them to the machine,
- An amplifier to increase the strength of the received electrical signals.
- Electronics that gather the electrical information and translate it into a readable form,
- Strip recorder with paper, and a stylus.

The stylus reacts to electrical signals from the amplifier and traces the ECG pattern on the

paper. The tracing is made via pen/ink, heat transfer, or laser.

For ECG machines that contain computer hardware and software, there is a visual view of the tracing on a monitor, interpretation of tracings, storage of patient data and test results, and interfaces to transfer information to the patient's electronic medical record.[4].

2.2. Electrodes (Sensors)

Electrodes are usually small plastic tabs that are attached to the skin much like an adhesive bandage. Each electrode is made up of a very thin metal layer (usually stainless steel or silver wire) and a thin layer of gel which is an electrolyte. The electrolyte assists with the transfer of the electrical current from the heart to the ECG machine.

2.3. Lead Wires

This has two meanings: It can mean:

- (i). The wire that connects an electrode to the electrocardiograph machine,
- (ii). A combination of electrodes that form imaginary lines in the body along which the electrical signals are measured.

Each lead is attached to a different electrode and each lead will provide different view of the heart (front to back, side to side, etc.). This proposed project consists of three leads. Figure 2 shows pictures of the lead wires.[4]

2.4. ECG signal processing unit

The ECG acts as a signal sensor which is a low amplitude signal. The raw ECG signal to be observed should be amplified. The ECG signal is amplified by an instrumentation amplifier of high gain which consists of normal Op-Amps such as (TL074). A second order low pass filter constructed with LM324 is used to remove the noise present in the ECG signal and the pure ECG signal is sent

for level detection. A filter built with TL074 is used to pass only the QRS component of the ECG signal. A level detector circuit built with operational amplifier LM358 acts as a comparator to indicate the increase or decrease of heart rate.

2.5. Power supply unit

Power supply is a very important factor in medical devices especially when it comes to proper function of these devices. This system is designed to use rechargeable lithium batteries and this makes the device proactive all the time.

2.6. The Microcontroller

The microcontroller plays a very important role in this project. It processes and analyzes the bio-signals, send them to the bluetooth module based on request of the bluetooth.[9].

2.7. The RF Bluetooth

Bluetooth is a wireless technology standard for exchanging data over short distances (using short-wavelength radio transmissions in the ISM band from 2400–2480 MHz) from fixed and mobile devices, creating personal area networks (PANs) with high levels of security. This Bluetooth used, streamline the activities or process of the microcontroller by sending the packet of biosignals from the microcontroller to the smart phone. A Bluetooth connection is wireless and automatic. It sends biosignal data to the smart phone through serial port by developing a set of commands and responses known as a protocol.

2.8. Android Bluetooth

This will have a user interface to capture biosignals modules on android platform for different time intervals and plot them. Timing supported are 1sec, 3sec, and 6sec, adjustable in user interface. Voltage will be 0-5V as in the

module. the transmitter is for 2 sec so each graphical block is = 2Sec/number of blocks. Analog input is 0 - 5V Max.

3. How the Bio-Signals are Displayed on the Smart Phone.

The three electrodes with their leads are placed on the appropriate locations of the patient. The ECG signals detected from the patient are of very low amplitude are amplified by the instrumentation amplifier of sufficient gain . These ECG voltage signals are amplified, filtered and then compared with fixed threshold (reference voltage) to detect a ECG event. This detected event is indicated by LED & Buzzer. There is a level detector section which gives the state of the QRS complex of the heart. ECG is detected for some period of time and an audio visual alarm system will sound indicating a condition of a bradycardia (low heart rate) if heart rate is below 60bpm. Biosignals go to the ADC of the microcontroller which convert the signals from analog to digital then to the bluetooth module which communicates with the smart phone using bluetooth interface. There is a program running in the microcontroller that constantly reads the ADC channel then converts it into bit packets how the bluetooth module requests then assemble these packets and send them over a serial port to the bluetooth module which also send the same packet to the smart phone and the biosignals are displayed on the phone

4. Results And Discussions

The system is designed to display best ECG signals on the smart phone. The device is first tested in the laboratory to see how the ECG signals are being generated. This is started by fixing the components on a bread board before the are transferred to PCB. Then after that an

experimental testing is done on subject using digital storage oscilloscope. To get proper ECG signals, the skin of the patient must be clean and the three leads electrodes(Red-for right hand,Blue- for left arm and Black-for right leg) must be well fixed on the patients. This is shown in fig.5. The microcontroller ATMEGA8 gives a very good signal analysis and by the help of the Bluetooth these signals are transmitted to the Smart Phone. This is seen in Fig.6. The use of information and communication technology as well as wired and wireless telecommunication equipment and telemedicine servers for transmitting biomedical signals in the healthcare already have impact on disease diagnosis and treatment.

However, the time has come to consider the operating system or softwares used in these devices. This proposed device has advantage of transmitting biosignals to a smart phone using Android platform or Bluetooth. Thus with the development of this device a patient heart rate can be captured on smart phones and the doctor can analyze the abnormalities of the patient's heart.

5. Conclusion

Microcontroller ATMEGA8, is used to process the ECG signals. It is cheap, available, it has low power consumption, and serves as a tool for developing softwares. The signals processed and analyzed , by the means of bluetooth are transmitted to the smart phone. This gives the way for clear ECG signals indicating the condition of the subject's heart. The device is user friendly and makes it possible for the doctor to know the abnormalities of his or her patient. It also give some awareness to the patient to know his or her heart condition. Much effort has been made to produce this device at low cost so that with

installation of the android oscilloscope in these smart phones, anyone can know the condition of his or her heart.

6. Recommendation

In the future work, this proposed system has been limited to few heart conditions but with modification of the software applications and the programming, this device can be used to analyze a lot of heart diseases and abnormalities such as acute myocardial

infarction, asystole, atrial flutter, atrial fibrillation, ventricular fibrillation, ventricular tachycardia, sinus tachycardia, etc. The signals can be transmitted only to a short distance which limit the system for short distance communications. Thus the signal transmission distance has to be improved by implementing advance techniques to carry signals over long distance.

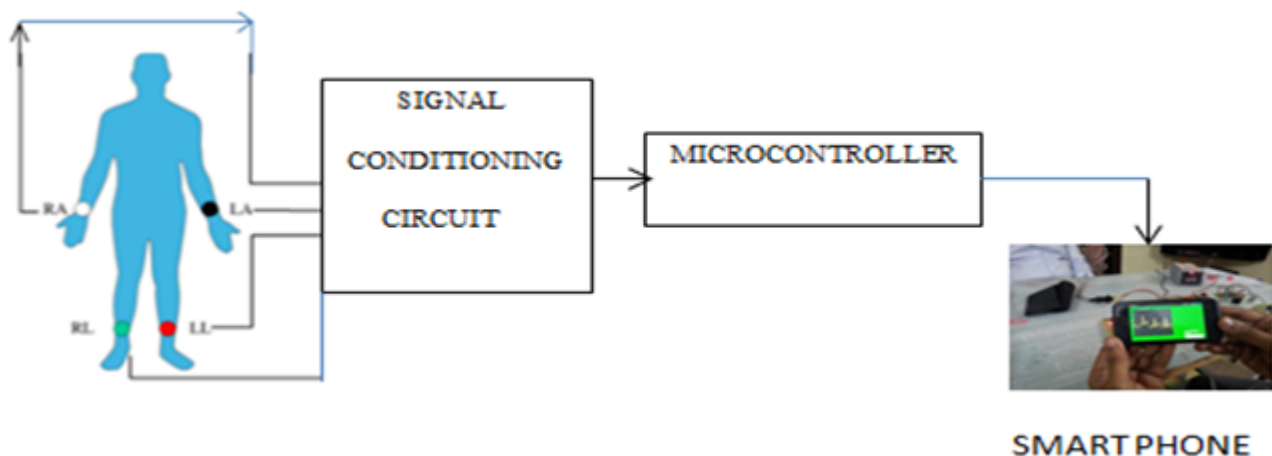


Fig. 2. Block diagram of the Heart Rate System.



Fig. 3. Lead wires.



Fig. 4. Components on PCB



Fig: 5 .ECG signals displayed on Smart Phone

7. References

- [1] Mohamed Fezari, Mounir Bousbia-Salah, and Moudi Bedda, Microcontroller Based Heart Rate Monitor, The International Arab Journal of Information Technology, Vol. 5, No. 4, October 2008.
- [2] Clinical Vectorcardiography, 2nd edition, Te-Chuan Chow, M.D., Robert A. Helm, M.D., & Samuel Kaplan, M.D., Grune & Stratton, 1974.
- [3] New Antiarrhythmic Drugs for Atrial Flutter and Atrial Fibrillation: A Conceptual Breakthrough at last?- F.G, Cosio and E. Delpon, Circulation 105 (3): 276-78, January 2002 .
- [4] National Center for Competency Testing, February 2012.
- [5] Lew C.K. and Moghavvemi, Remote Heart Rate Monitoring System Based on Electrocardiography, 2002 student Conference on Research and Proceedings, Shah Alam, Malaysia.
- [6] Junho Park, Jongman Cho, Junghyeon Choi and Taewoo Nam, A Zigbee Network-based Multi-channel Heart Rate Monitoring System for Exercising Rehabilitation Patients.
- [7] Darwin S. David, Pradeep, Gopalakrishnan, T. Hui Teo, Low Power Low Voltage Digital System for Wireless Heart Rate Monitoring Application. Atmel corporation, 2011.

Changes in Steering Wheel Grip Interface Pressure during Simulated Driving

¹ Rahul Bhradwaj, ² Mohan Jagannath, ¹Venkatesh Balasubramanian,

¹ Department of Engineering Design, IIT Madras

² Department of Biomedical Engineering, SMK Fomra Institute of Technology

rahbhardwaj@gmail.com, jagan.faith@gmail.com, chanakya@iitm.ac.in

Abstract

Driver fatigue has been regarded as potentially unhealthy and considered as one of the major contributing factors of road accident. The driving-induced fatigue results from the combination of physiological and psychological response. This paper presents the driver fatigue detection method by monitoring the driver's grip interface pressure on the steering wheel on the variation in pressure due to fatigue or loosing alertness. Steering grip interface pressure data was obtained by using hand grip pressure measurement system. This study performed on the simulated car, where subjects were asked to drive the car for a period of 60 minutes. Obtained results should permit to appreciate both the steering grip interface pressure time history and the applied force values; more ergonomic solutions and implementations could be possible for driver safety.

General Terms

Driver fatigue, Grip sensor, Steering wheel, Road accident.

Keywords

Grip interface pressure, Driver fatigue, Simulated driving, Monotonous and prolonged driving, Driving posture.

1. Introduction

Driver fatigue has long been identified as one of the major causes of road accident. Every year more than three million accidents involving motor vehicles cause a total of 40000 deaths worldwide. Primary economical loss due to these traffic accidents is estimated to be 651,166,236 USD. It has been estimated that every year about 40% of the road accident happen due to driver fatigue in US and 35% in France. India accounts for as high as 6% of the world's Road traffic accident [1].

There are two approaches presented in the related literature, according to the source of the data used. On the one hand, there are methods based on signals from the driver. These include physiological parameters, such as electroencephalogram, electrocardiogram, electromyogram and skin conductivity [6], whose measure usually requires electrodes to be applied to the driver. Other driver-related signals are eye movement, head position, and facial expression, which can be acquired using cameras and computer-vision [3, 4].



Noninvasive sensors to detect human physiological parameters are becoming more and more important. This is especially useful to monitor driver state as driver-vehicle system is a safety-critical system [2, 12].

Information on drivers' steering wheel grip force as a function of road condition, speed and gender, and an effective grip force measurement system may be valuable to the designers of vehicles, especially to the designers of steering wheel and researchers. For the measurement of grip force, the traditional approach is the use of strain gages [7-9]. This approach, however, requires a specially constructed steering wheel with strain gages applied to the cross-section. In addition, the durability of the strain gage system is limited due to the delicacy of the strain gages. Due to several drawbacks of strain gauges, this study used an alternative method. Capacitive sensors have been also used to estimate driver fatigue while detecting the applied pressure on the steering wheel [5, 15].

Although several promising methodologies for driver fatigue detection have been proposed in literature, much work still needs to be done in the research of effective solutions to their practical implementation. The aim of this study is to estimate the muscular fatigue of the driver using grip interface pressure mapping system.

2. Methods and Materials

2.1 Subject Details

Subjects were 10 undergraduate male students with a mean \pm standard deviation age, height and weight of $21(\pm 4.5)$ years, $1.71(\pm 0.06)$ meters and $59.5(\pm 7.5)$ kilograms respectively.

All subjects were currently licensed drivers with at least 2 years driving experience, self-reported corrected to normal vision and hearing and all were screened for mini-mental state examination. Subjects were instructed not to participate in any heavy training or physical activity 24 hours before their clinical assessment or testing day. All persons were made fully aware of the experimental details before assuming their involvement in the program and signed informed consent that conformed to the ethical guidelines of IIT Madras, India.

2.2 Sensor Placement

The grip pressure measurement system measures and evaluates static and dynamic pressures from grasping objects. This system uses a thin, high-resolution, tactile pressure sensor that can be used directly on a hand or built into a glove. The system provides detailed pressure profiles, forces, and graphical displays for quantitative analysis of driver fatigue. Whether used to improve design for a more ergonomically sound product, study carpal tunnel and repetitive motion syndrome, or analyze the human hold on various tools and steering wheel. These grip pressure sensors were wrapped on to the cotton gloves of left and right hand (Figure 1). So that the driver can wear it easily and can have the good grip on the steering wheel while driving the car. These two sensors are then fetched to the signal acquisition system, and after that acquired signals were seen visually on the computer system which was carried out by the data interface card.



Figure 1. Grip sensor measurement system.

2.3 Driving Simulator

The study was conducted in a driving simulator, 60 minutes for each subject. A realistic, simulator environment (with a steering wheel, foot pedals, and gear lever) was used in conjunction with a computerized driving task ('Need for Speed', Electronic Arts 2010). The video screen presented an 'in-car' view to the driving subject. Subjects were given practice on the simulated driving task prior to participating in the experimental trials. Subjects drove the same simulated track course and while driving, their steering wheel hand grip interface pressure was recorded (Figure 2). Driving speed within a designated criterion range of 35–45 mph while traversing a simulated driving scenario and interacting with other simulated traffic. If a subject's speed varied outside the range, they were reminded to keep their speed within the criterion range.



Figure 2. Driving simulator: A typical participant in use.

3. Grip Pressure Distribution

Grip pressure measurement system is used to process pressure information from the interface board, present the information as a color-coded real-time display, and record the information (as a 'movie') for later review and data analysis. This software allows multiple views of the pressure maps such as the standard 2D view, 2D contoured view, 3D wireframe view, and 3D solid view. Each pressure sensor has eighteen sensing regions that can be individually positioned over important anatomic sections of the fingers and palm. Each sensing region has multiple sensing elements (sensels) for localized identification of pressure points on the hand.

In the data acquisition process, subjects worn the gloves (containing pressure sensor) and applied grip to the steering wheel while simulated driving. The cuffs connect to the sensor, gather the data from the sensor and then process and send this data to your computer via USB connection. After that data being processed using MATLAB version 2009b and required pressure parameters were extracted.

The grip interface pressure time history is very different when the subject simulates the effective driving operation: the grip pressure is averagely high during the initial phase, while in the later phase it is evident the subject's difficulty to maintain the steering wheel control. Another matrix feature is to see the pressure spatial distribution, to understand if there are more solicited hand palm parts. In Figure 3 and Figure 4, the left hand pressure map of the center of force and force of trajectory registered during the simulated driving condition is shown: from the map it is possible to understand the highest pressure values (red colored, from 1500 to 2100 mmHg), corresponding to the fingertips of thumb, index and medium.

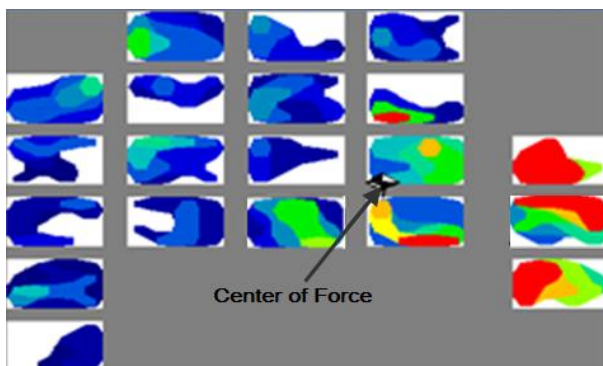


Figure 3. Steering wheel grip interface pressure distribution measured on a left hand. The marker represents the point towards or from which a central force acts.

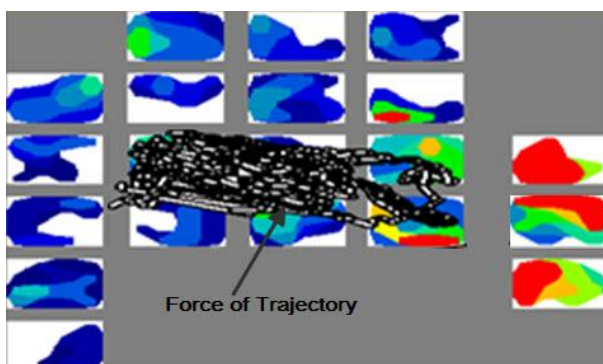


Figure 4. Steering wheel grip interface pressure distribution measured on a left hand. The trajectory represents the path that a moving force follows through space as a function of time.

Force, contact pressure, contact area and center of force [14] were calculated by including only data from sensors that were pressed (i.e. a positive value) at least once, and average (arithmetic mean) values were determined at prescribed interval.

Force: It represents force exerted on steering wheel while driving car. This is very important for the estimating muscles fatigue point of view.

Contact pressure: It represents the pressure exerted by hand on steering wheel while driving the car.

Contact area: It represents the contact area of the hand on the steering wheel while driving the car.

Peak contact pressure: It represents the peak of the pressure while gripping the steering wheel.

Peak force: It represents peak force exerted on the steering wheel.

4. Results and Discussion

The measured grip interface pressure distributions on the steering wheel were examined the change of the average with every 5 minutes. The change of grip interface pressure distributions for long time gripping was remarkably observed.

Total force of the steering wheel, the number of the momentary changes, the area of the contact and peak contact pressure were calculated as grip interface pressure distribution parameters (Table 1). This showed the pressure between driver's hand and

steering wheel included the information about the change of posture and discomfort, and there was a possibility to predict discomfort or fatigue from the grip interface pressure distribution.

Table 1. Mean \pm SD values of steering grip interface pressure parameters obtained during 60 minutes of simulated driving.

Parameter	Right Hand	Left Hand
Contact Area (cm ²)	9.86 (\pm 4.61)	7.78 (\pm 3.97)
Contact Pressure (mmHg)	425.86 (\pm 31.28)	596.28 (\pm 35.01)
Force (N)	70.96 (\pm 11.86)	59.54 (\pm 10.51)
Peak Contact Pressure (mmHg)	1597.13 (\pm 56.05)	2066.62(\pm 64.88)
Peak Force (N)	9.37 (\pm 4.38)	10.6953(\pm 4.7038)

In general, there are mainly two types of driving style of driver: palm driving and thumb driving. In this study, most subjects have the habit of palm driving. In Figure 5, we can see that the center of force is acted on the fore finger in both hands while driving. In Figure 4, we see that the force of trajectory has varied only among fore finger, middle finger and ring finger.

The change of force center position drawn from pressure distribution measurement had the time trend of the load center showing change of driving posture and the momentary change. The correlation between discomfort and the pattern of the pressure distribution was examined. Figure 3 also showed the change of force center position over driven period. The force center position of most subjects moved

downwards on palm. Figure 4 showed the time change of the force trajectory, in which the force center position on hand grip was the distance from steering wheel front edge and the contact point of hand.

Grip interface pressure variable related to the steering wheel was affected by driving time. It indicates that pressure distribution is not uniform when driving period increases. Drivers tend to move more frequently when they feel fatigued and contact pressure values decreases. Similarly contact area starts decreasing during the period of 60 minutes of driving (Figure 5). The contact pressure of the hand decreased as the driving time increased (Figure 6). This implies decreased pressure in corresponding contact area and it causes more discomfort for subject during simulated driving. Long hours of driving discomfort leads to fatigue.

Jin et al. [16] investigated the driver's discomfort based on prediction of body postural change and moving frequency using seat pressure measurement system. As the driving time increased, driver tends to change into sliding down postures with load center position going down and seat pressure distribution decreased thereby causing driving-induced discomfort. This showed that the possibility to predict discomfort from pressure distribution changes while driving. In the present study, the same methodology has been used for analyzing the steering wheel grip interface pressure. While prolonged driving, driver tends to loosened up their grip from steering wheel as they feel fatigue and as a result of that contact area and contact pressure being decreased.

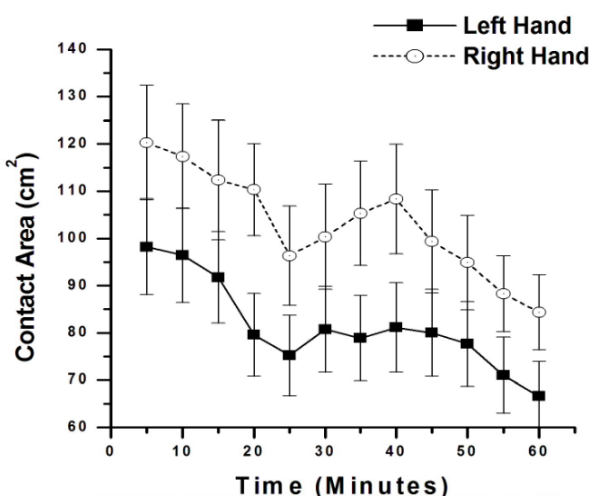


Figure 5. Mean \pm Standard deviation (SD) values of contact area exposed on left and right hand during simulated driving of 60 minutes.

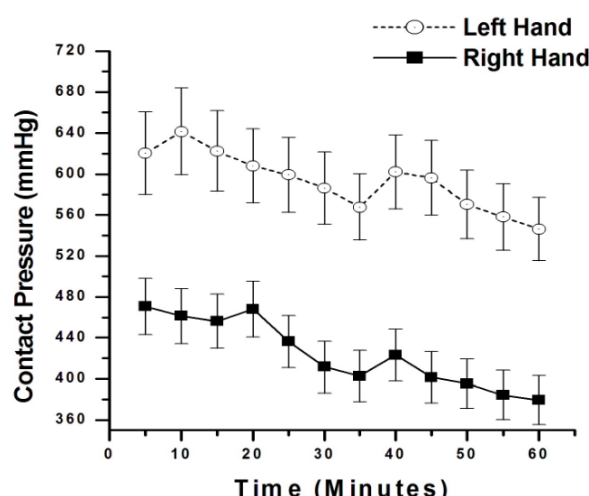


Figure 6. Mean \pm Standard deviation (SD) values of contact pressure exposed on left and right hand during simulated driving of 60 minutes.

From the results, it has been seen that as driven time goes, all the parameters (contact area, contact pressure, force, peak contact pressure, peak force) decrease. This decreasing tendency of all the pressure distribution parameters can be interpreted by two facts. First, after continuous grip of hand on the steering wheel, the normal circulation of the

blood is stopped because of the absence of the circulation, the oxygen content and permeability of the K and Na ions will get reduce across the membrane and it will also leads to lactic acid deposition by certain biochemical process, hence muscles get fatigued [10, 13]. Second, the temperature of the palm is being increased due to continuous folding of hand. Continuous fatigue or decline in performance may occur more rapidly at high temperatures compared with low [11].

The momentary change variable was affected by the driving time, and increased as the driving time increased. Momentary change counted the number of large changes of the grip pressure and force center positions. Increasing of the momentary change means that subjects moved more frequently as driving time passed by. These results show that the driver's hand moving frequency could be used as a quantitative and objective measure to evaluate the driver's discomfort or fatigue. This study showed the possibility of using the hand grip interface pressure distribution as a tool to evaluate driver's discomfort.

The study was performed in simulated driving situations. For a precise and accurate study, the experiments should be performed in a real vehicle on real road environments. Vibrations reflect from on-road driving might affect some of the pressure variables.

5. Conclusion

This study was performed on the application of pressure distribution data for the prediction of the driver's discomfort based on prediction of hand posture change and moving frequency. As the driving time increased, the drivers tend to change into sliding down postures with

force center position going down. So the change of driver's hand postures might be predicted. And further more the drivers tend to move more frequently when they feel discomfort. The frequency of the movement of subjects could be estimated with the momentary change variables of contact pressure and force center position.

This study supports the effectiveness of hand grip pressure distribution for discomfort evaluation. It was clarified that there was a possibility to predict discomfort from steering grip pressure monitoring system while driving. Moreover there was a possibility that variables like the change of the force center position and contact pressure seem to be effective discomfort indicators. Also further studies need to be performed in real on-road driving situations.

6. Acknowledgments

Authors would like to thank all the participants for their time and effort to make this study possible. Authors acknowledge the great help received from the scholars whose articles cited and included in references of this manuscript. The authors are also grateful to authors/ editors/ publishers of all those articles, journals and books from where the literature for this article has been reviewed and discussed. Authors are grateful to ICBSII editorial board members and ICBSII team of reviewers who have helped to bring quality to this manuscript.

7. References

- [1] May, J.F., and Baldwin, C.L., Driver fatigue: The importance of identifying causal factors of fatigue when considering

- detection and countermeasure technologies. *Transportation Research Part F*, Vol. 12, 2009, pp. 218–224.
- [2] Lin, Y., Leng, H., Yang, G., and Cai, H., An intelligent noninvasive sensor for driver pulse wave measurement. *IEEE Sensors Journal*, Vol. 7, No. 5, 2007, pp. 790–799.
- [3] Golfarelli, A., Zagnoni, M., Proli, P., Callegari, S., Talamelli, A., Sangiorgi, E., and Tartagni, M., Acquisition system for pressure sensor network. *Proceedings of IEEE Sensors*, Vol. 2, 2004, pp. 579–582.
- [4] Ji, Q., Zhu, Z., and Lan, P., Real-time nonintrusive monitoring and prediction of driver fatigue. *IEEE Transaction on Vehicle Technology*, Vol. 53, No. 4, 2004, pp. 1052–1068.
- [5] Baronti, F., Lenzi, F., Roncella, R., and Saletti, R., Distributed sensor for steering wheel grip force measurement in driver fatigue detection. *Design, Automation & Test in Europe Conference & Exhibition*, 2009, pp. 894–897.
- [6] Healey, J., and Picard, R., Detecting stress during real-world driving tasks using physiological sensors. *IEEE Transaction on Intelligent Transportation System*, Vol. 6, No. 2, 2005, pp. 156–166.
- [7] Pyykkö, I., Färkkilä, M., Toivanen, J., Korhonen, O., Hyvärinen, J., Transmission of vibration in the hand arm system with special reference to changes in compression force and acceleration. *Scandinavian Journal of Work Environment and Health*, Vol. 2, 1976, pp. 87–95.
- [8] Reynolds, D., Hand-arm vibration: A review of 3 years' research, In: *Proceedings of the International*



- Occupational Hand-arm Vibration Conference*, National Institute for Occupational Safety and Health, Cincinnati. DHEW (NIOSH), Publication No. 77-170, 1977, pp. 99–128.
- [9] Burström, L., and Lundström, R., Absorption of vibration energy in the hand and arm. *Ergonomics*, Vol. 37, No. 5, 1994, pp. 879–890.
- [10] Allen, D.G., Lamb, G.D., and Westerblad, H., Skeletal muscle fatigue: Cellular mechanisms. American Physiological Society, *Physiological Review*, Vol. 88, No.1, 2008, pp. 287–332.
- [11] Enoka, R.M., and Duchateau, J., Muscle fatigue: what, why and how it influences muscle function. *Journal of Physiology*, Vol. 586, No. 1, 2008, pp 11–23.
- [12] de Looze, M.P., Kuijt-Evers, L.F., and van Dieën, J., Sitting comfort and discomfort and the relationships with objective measures. *Ergonomics*, Vol. 46, No. 10, 2003, pp.985–997.
- [13] Reed, M.P., Manary, M.A., and Schneider, L.W., Methods for measuring and representing automobile occupant posture. *SAE Technical Paper*, International Congress and Exposition, Detroit, Michigan, Series No. 1999-01-0959.
- [14] Kyung, G., and Nussbaum, M.A., Driver sitting comfort and discomfort (Part II): Relationships with and prediction from interface pressure. *International Journal of Industrial Ergonomics*, Vol. 38, 2008, pp.526–538.
- [15] Johnson, D.A., and Neve, M., Analysis of possible lower lumbar strains caused by the structural properties of automobile seats: A review of some recent technical literature. *Journal of Manipulative and Physiological Therapeutics*, Vol. 24, No. 9, 2001, pp. 582–588.
- [16] Jin, X., Cheng, B., Wang, B., and Shen, B., Assessment of driver's seating discomfort using interface pressure distribution, *IEEE Symposium on Intelligent Vehicles*, 2009, pp. 1419 – 1424.

Development of Multiparametric Patient Monitoring System using ZigBee with an Emergency Alarm

¹Vageesh V.Kantli, ² Anjaneya L.H., ² Mallikarjun S.Holi

¹ Department of Physics, C.I.T, Gubbi, Tumkur.

² Department of Biomedical Engineering, B.I.E.T., Davangere.

v_kantli@rediffmail.com, anjudvg@yahoo.com, msholi@yahoo.com

Abstract

The patients in the intensive care units (ICU) with critical health condition need a constant monitoring of their body temperature, blood pressure, heart rate and several other physiological parameters. The objective of the present work is to design a working model, which incorporates sensors to measure important body parameters namely the body temperature, respiratory temperature and electrocardiogram (ECG) along with saline level monitoring. The sensors output are conditioned and transmitted through ZigBee to any PC in the hospital which is interfaced with ZigBee receiver, so that the condition of a patient can be analyzed by doctors in any part of the hospital wherever they are. Thus it reduces doctor's workload and also gives more accurate results. Whenever there is an abnormality in a patient, the system will give an alarm signal to doctor, by which doctor can attend the patient immediately. Special software is written in visual basic to display, monitor and record the parameters in separate files with date and time, which will be useful for historical examination of patient and for future references by the doctors.

Keywords : Patient monitoring, ZigBee, microcontroller, ECG

1. Introduction

The objective of any patient monitoring system is to have a quantitative assessment of the important physiological variables of patients

during critical periods of physiological functions [1] [2]. Patient monitoring systems are used for measuring important physiological parameters continuously or at regular intervals automatically. Monitoring is an integral part of the care process together with the administration of therapy. The primary aim of monitoring is to ensure that appropriate care or therapy can be given prior to the onset of complications. Monitoring is therefore a tool that provides early indication of changing patient status, and allows for early intervention, but is also a means by which the effect of interventions and therapies may be recorded, evaluated and controlled. The long term objectives of patient monitoring are to decrease mortality and morbidity rate by [2]:

- Organizing and displaying information in a meaningful form to improve patient care.
- Correlating multiple parameters for clear demonstration of clinical problems.



- Processing the data to set alarms on the development of abnormal conditions.
- Ensuring better care with fewer staff members.

The complete body scanning system deals with real time continuous monitoring and recording of parameters like body temperature, ECG, respiratory temperature as well as their analysis. It also deals with the alarm system for patient call, saline level checking and temperature level. With the advent of computerization in biomedical field, this project has very wide scope, due to the computerized data acquisition, monitoring and control incorporated in it. It reduces the workload of doctors and also gives more accurate results, and decreases mortality and morbidity rate by attending the patient immediately during emergency [3].

2. Methodology

The block diagram of multiparametric patient monitoring system is shown in Fig. 1.

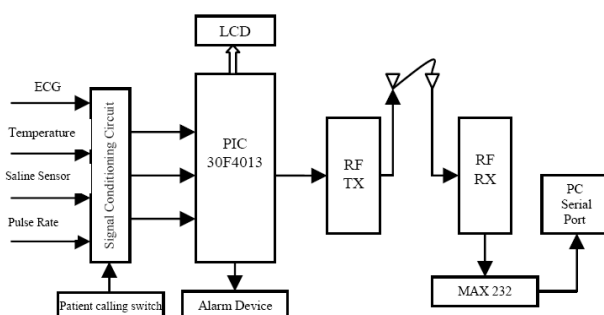


Figure 1: Block diagram of multiparametric patient monitoring system

Measurement of Body Temperature and Respiratory Temperature

Thermistor (bead type) is used for the measurement of body temperature and respiratory temperature. Thermistor is a passive transducer, resistance of which varies inversely

with temperature [4]. In the present work thermistors are mounted on the surface of the body (on hand) and near the nose, and are connected in a potential divider circuits with an excitation voltage. Resistance of the thermistors varies with body temperature which leads change in the output voltage. The output voltage is conditioned, processed, transmitted, displayed and recorded over a distant PC. If the body temperature exceeds the normal temperature and if it is found to be risk for the well being of a patient, an alarm will be triggered by the system to give a caution to doctors. Measurement of airway temperature may help in the respiratory gas concentration monitoring [10]. The changes in the composition of respiratory gas stream may give rise to significant alteration in the thermal conductivity of the stream, and lead to rise or fall in temperature of the element in the path. The thermistor placed at the nostrils will detect the changes in temperature, which enables the system to monitor the changes in the composition of the respiratory gases, in particularly the changes in the concentration of CO₂ [13].

ECG Recording

ECG is recorded by placing body surface plate electrodes with electrode gel in Lead II configuration [2]. Acquired ECG signal is conditioned by an external card and given to the PC through microcontroller. An interactive program in visual basic is developed to read the voltage and time durations of ECG waves and display simultaneously. Any deviation in the normal pattern of ECG, voltage and time duration of different ECG waves will lead to generation of an alarm.

Saline Monitoring System

The block diagram of saline monitoring system is as shown in Fig 2. The infrared emitter and detector are placed on either side and near the neck of saline bottle. As long as saline is present, the path of the infrared rays from emitter are blocked and the infrared detector will not receive any signal and its output will be logical low otherwise output will be logical high. The software is written to give an alarm when the logical high output is given to the microcontroller. A minimum to maximum rays density can be achieved by this circuit. Infrared detector accepts infrared rays if more rays fall on it make the detector as conductor. As long as rays level goes down it finds more insulation level. By practical means an empty bottle was placed and the voltage across the detector was found to be approximately 1V, because more rays fall on it as a beam.

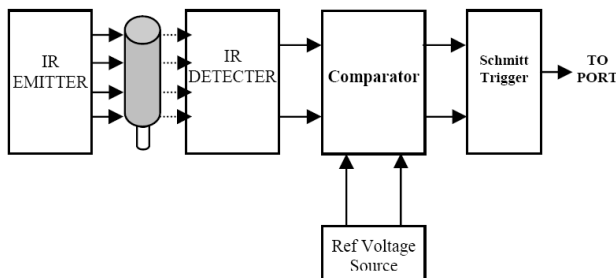


Figure 2 Block diagram of saline monitoring system

When a bottle with saline was placed, spectrum reading we found to be 2V.

$$\begin{array}{ll} \text{Empty Bottle Voltage} & = 1\text{V} \\ \text{Bottle with Saline} & = 2\text{V} \end{array}$$

The LM 339 is used as a differential voltage comparator. It is a very high precision comparator, which can even compare to a precision of 1mV and produce sufficient output. The infrared detector output is connected to the -ve input of the comparator and +ve is

connected to the reference potentiometer, which is varied from 0 to 2.5V. As per the experiments made earlier, empty bottle will give 1V and bottle with saline will give 2V. Voltage across reference potentiometer is set as 1.5V. In general, principle of comparators when the input received is more +ve than the -ve input, the output will become +ve [5]. Whenever input received is more +ve than the +ve input, the output will be low. Now considering the empty bottle condition,

$$\begin{array}{ll} \text{REF Source Voltage} & = 1.5\text{V} \\ \text{Empty Bottle} & = 1\text{ V} \\ \text{Then the output is High} & \end{array}$$

$$\begin{array}{ll} \text{Bottle With Saline} & = 2\text{ V} \\ \text{REF Source Voltage} & = 1.5\text{V} \\ \text{Then the output is Low} & \end{array}$$

By viewing the above data, when saline is present, comparator will produce low output and when no saline the comparator will gives high output. The output of the comparator is connected to the Schmitt trigger to avoid low level triggering and spurious noises. Output of Schmitt trigger is connected to microcontroller and by using software algorithm saline and no saline information will be given on the screen. In case of any abnormality, remedy will be sent for control action and for audio announcing i.e. buzzer.

Patient Calling System

Patient call switch is quite useful for total automation. The reason is while automating the body temperature acquiring ECG and blood pressure. There is no man power is required. So people will not be aware of what is happening inside the patient's room. In case of assistance required for the patient, they can use the switches to call the hospital persons .When the switch is not pressed, switch contact will be

logical high. The other end of the switches is connected to the ground. So whenever the switch is pressed, port will get a logical low. The software is designed in such a way that whenever the port receives a logic low it will produce a call message. When two or more switches are simultaneously pressed all the messages will be displayed one after the other and will be held as long as the switch is pressed. A warning alarm is also raised while the switch is pressed. This enables easy understanding and annunciation. Annunciation means providing legible and audible output for the failure.

Pulse Rate Detection

The block diagram of pulse rate detection is as shown in the Fig 3. A pair of infrared emitter and detector is used for detection of saline level and Heart beat detection. Normally infrared emitters are made up of Gallium Arsenide material which produces infrared rays by accepting electric current. They are also made up of silicon semiconductors. It is quite complex to differentiate the saline color and bottle color because both are same. Only by viewing molecular density of the materials, they can be differentiated. If rays pass through a glass material the output will be like beam, if the same rays pass through a liquid whose viscosity is less than one, it will be a spectrum. Infrared detector accepts infrared rays, if more rays fall on it makes the detector as conductor. As long as rays level goes down it finds more insulation level. Infrared emitter and detector are used.

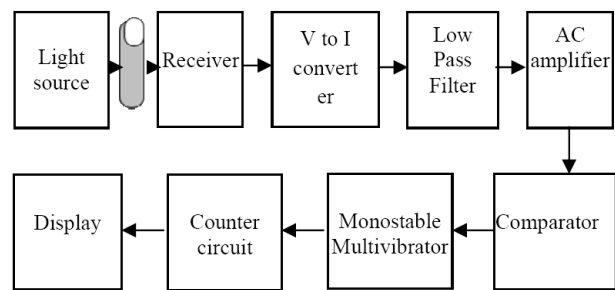


Fig 3 Block diagram of pulse rate detection

3. Hardware Description

PIC Microcontroller (30F4013)

The features are [6] [7], (i) Two 40-bit wide accumulators with optional (ii) Multiply-Accumulate (MAC) operation, (iii) Up to 48 Kbytes on-chip Flash program space, (iv) 16 x 16-bit working register array, and (v) Up to 30 MIPS operation.

MAX 232

The Max 232 is a dual RS-232 receiver/transmitter that meets all EIA RS232C specifications while using only a +5V power supply (See figure 7). It has 2 onboard charge pump voltage converters which generate +10V and -10V power supplies from a single 5V power supply. It has four level translators, two of which are RS232 transmitters that convert TTL\ CMOS input levels into + 9V RS232 outputs. The other two level translators are RS232 receivers that convert RS232 inputs to 5V TTL\CMOS output level. These receivers have a nominal threshold of 1.3V, a typical hysteresis of 0.5V and can operate up to + 30V input. Three main sections of MAX232 are: (i). a dual transmitter, (ii) dual receiver, and (iii).+5V to + 10V dual charge pump voltage converter.

4. ZIGBEE Technology

The block diagram of ZigBee module is shown in Fig 4. The name "ZigBee" is derived from the erratic zigging patterns many bees make between flowers when collecting pollen. This is evocative of the invisible webs of connections existing in a fully wireless environment. ZigBee is the name of a specification for a suite of high level communication protocols using small, low-power digital radios based on the IEEE 802.15.4 standard for wireless personal area networks (WPANs), such as wireless headphones connecting with cell phones via short-range radio. The technology is intended to be simpler and cheaper than other WPANs, such as Bluetooth. ZigBee is targeted at radio-frequency (RF) applications which require a low data rate, long battery life, and secure networking. In the present work point to point communication between the two Zigbee modules is used which operates in a short-range communication between 40 to 120 meters. The power of ZigBee module is about 2 mW when running operation and lower than 1 micro-watt when is in sleep operation modes [11], [12].

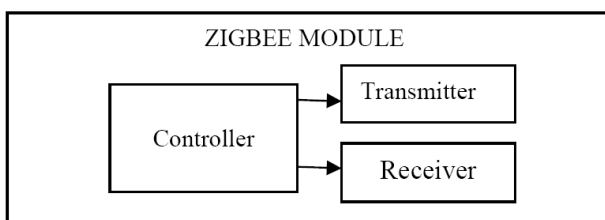


Figure 4 Block diagram of ZigBee module

Features:

- ZigBee targets applications that need low data transmission rates and low power consumption:
 - Moves data only one-fourth as fast as Bluetooth.
 - Can handle hundreds of devices at once.
 - Most promising application is meter reading.
- Current focus is to wirelessly link sensors that are embedded into industrial controls, medical devices, smoke and intruder alarms and building and home automaton.
- On-line recording of all process parameters in the interval selectable by the user, which is most useful for future analysis and failure detection.

5. Software Implementation

The designed and developed multiparametric patient monitoring system requires appropriate software to provide useful diagnostic information and display of important parameters. The Fig. 5 shows the flowchart for part of software implementation. After initialization of PIC microcontroller and

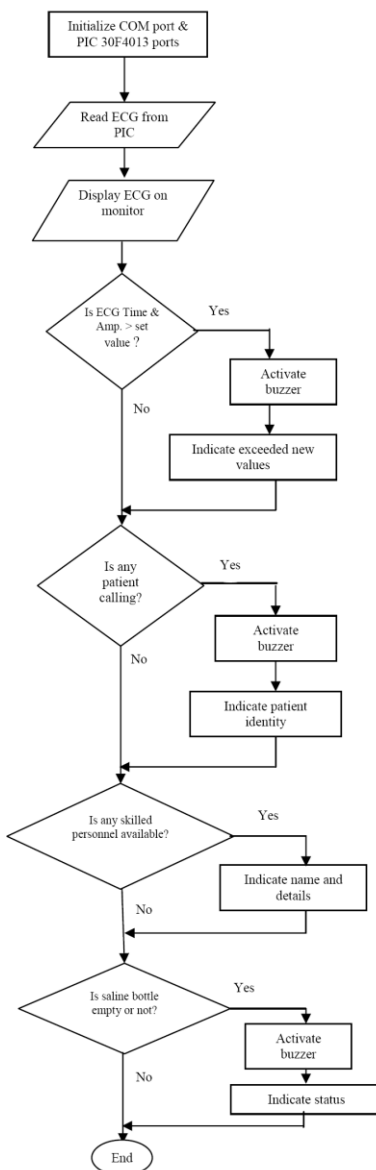


Figure 5 Flowchart showing a part of software implementation

COM port, the data about ECG, pulse rate, saline level and temperature are acquired through signal conditioning unit and their pattern/values/status are displayed online [8] [9]. An extra feature is also incorporated for patient's advantage such as patient calling system and information about the availability of skilled person / nurse with name and other details.

6. Results and Discussion

The Fig. 6 shows the typical output of multiparametric patient monitoring system. The recording shows the instantaneous pulse rate, body temperature, respiratory temperature, ECG and status of saline in the bottle. The display also incorporates the patient name and ID. All the parameters accurately measured,

displayed and transmitted to a system over a distance through ZigBee. For various patient conditions data is acquired, transmitted and monitored. As per the settings under emergency conditions the system is able to generate an alarm to caution the patient attendant and doctor. The data is acquired, transmitted and monitored in 20 subjects and results obtained from the developed system are compared and validated with existing single parameter measuring systems, and found that the results are accurate and are in good agreement with standards. A sample display of the data monitored is show in Fig.6.

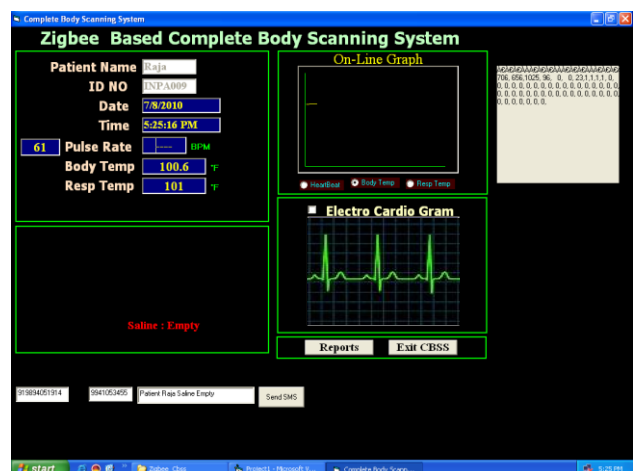


Figure 6 Display of ECG and other parameters

7. Conclusion

The developed system is unique in design to provide diagnostic information about the well being of a person/ patient. The condition of a patient can be analyzed by doctors in any part of the hospital and helps in appropriate therapeutic decisions. Thus, it reduces doctor's workload and also helps to pay immediate attention under emergency conditions.

8. References

- [1]. Konrad L, David J. M, Thaddeus R.F. Fulford-Jones, Alan N, Antony C, Victor S, Geoffrey M, and Matt W., "Sensor Networks for Emergency Response: Challenges and Opportunities", IEEE Pervasive Computing, 3(4), 16-23, 2004.
- [2]. R.S.Khandpur, "Handbook of Biomedical Instrumentation", Tata McGraw Hill, 2004.
- [3]. Schwartz, G.R., "Principles and Practice of Emergency Medicine", King of Prussia, PA: Rittenhouse Book Distributors, 1999.
- [4]. M.Arumugam, "Biomedical Instrumentation", N. Dhanalakshmi Publications, 2006.
- [5]. D.Roy Choudhry and Shail Jain, "Linear Integrated Circuits", New Age International Pvt. Ltd., 2000.
- [6]. J.B.Peatman, "Design with PIC Microcontrollers", PHI 1998.
- [7]. Barrnett C and Cull, "Embedded C programming and the microchip PIC", Thomson Publications, 2004.
- [8]. John G Proakis and Dimtris G Manolakis, "Digital Signal Processing Principles, Algorithms and Applications", PHI, 3rd Edition, 2000,
- [9]. S.Salivahanan, A.Vallaraj and Gnanapriya, "Digital Signal Processing", McGraw-Hill/TMH, 2000.
- [10]. Stephen Z. T, Walter B, Samuel W and Robert D, "Respiratory Monitoring: Recent Developments in Automatic Monitoring of Gas Concentration, Flow, Pressure, and Temperature", Ann Thorac Surg, vol.16, pp. 184-192, 1973.
- [11]. N.Watthanawisuth, T. Lomas, A. Wisitsoraat, A.Tuantranont, "Wireless Wearable Pulse Oximeter for Health Monitoring using ZigBee Wireless Sensor Network", Nanoelectronics and MEMS Laboratory, National Electronics and Computer Technology Center (NECTEC)., Pathumthani, Thailand 12120.
- [12]. Wang Feng Qin, Li.Yang "ZigBee Technology for Designing and Implementing a Remote Medical Monitoring System", International Conference on Computer, Mechatronics, Control and Electronic Engineering (CMCE)., pp. 172-175, 2010.
- [13]. Nagashima T, "Expiratory ventilation and carbon dioxide production measured with a thermistor flow-through system", Nihon Kyobu Shikkan Gakkai Zasshi (Japanese), vol. 34, no.3, pp.281-289, 1996. PMID: 8778467.

ECG Signal Processing Using LabVIEW

¹ Nageshwar V, ² Y Padmasai , ¹ S. Nagarjuna Chary , ² L.V.Rajani

¹ Department of Electronics and Instrumentation Engineering.

² Department of Electronics and Communication Engineering.

VNR VJIET, Hyderabad.

vnagesh1004@gmail.com, ypadmasai@gmail.com, nagarjunachary85@gmail.com, rajani_lv@vnrvjet.in

Abstract

The Electrocardiogram (ECG) waveform is analyzed by the cardiologist in diagnosis of various diseases and monitors the conditions associated with the heart. Generally, the recorded ECG signal is often contaminated by noise and artifacts that can be within the frequency band of interest and manifest with similar characteristics as the ECG signal itself. For the proper realization of the ECG waveform, the ECG signals must be processed to remove the noise signal artifacts. Also, various features of ECG must be extracted for the purpose of diagnosis. ECG signal processing can be roughly divided into two stages by functionality: pre-processing and feature extraction. The pre-processing stage removes or suppresses noise from the raw ECG signal and the feature extraction stage extracts diagnostic information from the ECG signal. In this paper, we propose an effective technique for the denoising of ECG signals corrupted by non-stationary noises using Undecimated Wavelet Transform (UWT) which is implemented with Laboratory Virtual Instrumentation Engineering Workbench (LabVIEW) platform and then QRS complex is extracted. The heart rate variability (HRV) analysis on the R-R interval signal which demonstrates the state of heart and also acts as a powerful non invasive measure of autonomic nervous system

function. The ECG waveforms are obtained from MIT-BIH arrhythmia database. LabVIEW and the related toolkits, advanced signal processing toolkit are used to build the graphical programme for both the stages. The technique is evaluated with MIT-BIH arrhythmia database, which is recorded for 30:06 min with a sampling frequency of 360samples/sec.

Keywords

Electrocardiogram, Pre-processing, Undecimated Wavelet Transform, Heart rate variability (HRV).

1. Introduction

An electrocardiogram (ECG) is a test that records the electrical activity of the heart. ECG is used to measure the rate and regularity of heartbeats, as well as the size and position of the chambers, the presence of any damage to the heart, and the effects of drugs or devices used to regulate the heart (such as a pacemaker). Generally, the recorded ECG signal is often contaminated by noise and artifacts that can be within the frequency band of interest and manifest with similar characteristics as the ECG signal itself. In order to extract useful information from the noisy ECG signals, need to process the raw

ECG signals[3]. ECG signal processing can be roughly divided into two stages by functionality: Pre-processing and feature extraction. The Pre-processing stage removes or suppresses noise from the raw ECG signal and the feature extraction stage extracts diagnostic information from the ECG signal. LabVIEW with its signal processing capabilities provides a robust and efficient environment to resolve ECG signal processing problems. LabVIEW contains the powerful tools for Denoising, analyzing, and extracting ECG signals easily and conveniently. In this paper a algorithm has been developed for filtering ECG signals and detection of P wave, T wave, QRS wave and their onsets and offsets[6].

2. Signal Processing

In this paper we used LabVIEW for signal processing of ECG. Unlike text based programming language, LabVIEW uses the data flow programming, where the flow of data determines execution. The proposed algorithm is implemented in two stages. First, it pre-processes the ECG signal to remove the noise using LabVIEW signal processing tools and second, wavelet transform based approach is used for the QRS complex detection[6]. In the same way, R-peak is detected in the smoothed signal. With reference to R-peak in smoothed signal other features of diagnostic importance mainly RR intervals is found[5]. Based on the RR intervals, heart rate has calculated from that arrhythmias are detected.

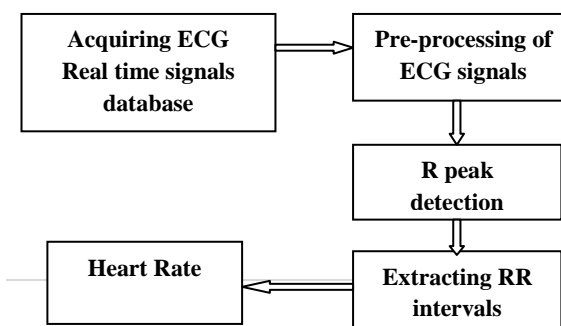


Fig 1: Block Diagram of ECG Signal Processing.

Pre-processing: The aim of pre-processing is to improve the general quality of the ECG for more accurate analysis and measurement. Noises may disturb the ECG to such an extent that measurements from the original signals are unreliable. The main categories of noise are: low frequency base line wander (BW) caused by respiration and body movements, high frequency random noises caused by mains interference (50 or 60Hz) and muscular activity and random shifts of the ECG signal amplitude caused by poor electrode contact and body movements. A number linear and non-linear technique has been developed to eliminate these artifacts. The pre-processing comprises of three steps: removal of base line wander (elimination of very low frequencies) removal of high frequency noise and QRS detection.

2.1 Pre-Processing using wavelet transform

Wavelet Transform: Mathematically speaking, the wavelet transform is a convolution of the wavelet function $\psi(t)$ with the signal $x(t)$. orthonormal dyadic discrete wavelets are associated with scaling functions $\varphi(t)$. The discrete wavelet transform (DWT)[4] can be written as

$$T_{m,n} = \int_{-\infty}^{\infty} x(t) \psi_{m,n}(t) dt \quad (2.1)$$

The scaling function can be convolved with the signal to produce approximation coefficients S . By choosing an orthonormal wavelet basis, $\Psi_{m,n}(t)$, and we can reconstruct the original. The approximation coefficient of the signal at the scale m and location n can be presented by:

$$S_{m,n} = \int_{-\infty}^{\infty} x(t) \varphi_{m,n}(t) dt \quad (2.2)$$

In practice our discrete input signal $S_{0,n}$ is of finite length N , which is an integer power of 2: $N = 2M$. Thus the range of scales that can be investigated is $0 < m < M$. A discrete approximation of the signal can be shown as

$$x_0(t) = x_M(t) + \sum_{m=1}^M d_m(t) \quad (2.3)$$

where the mean signal approximation at scale M is

$$x_M(t) = S_{M,n}\phi_{M,n}(t) \quad (2.4)$$

and the detail signal approximation corresponding to scale m is defined for a finite length signal as

$$d_m(t) = \sum_{n=1}^{2^{M-m}-1} T_{m,n} \psi_{m,n}(t) \quad (2.5)$$

Adding the approximation of the signal at scale index M to the sum of all detail signal components across scales gives the approximation of the original signal at scale index 0. The signal approximation at a specific scale was a combination of the approximation and detail at the next lower scale.

$$x_m(t) = x_{m-1}(t) - d_m(t) \quad (2.6)$$

If scale $m = 3$ was chosen, it can be shown that the signal approximation is given by

$$x_3(t) = x_0(t) - d_1(t) - d_2(t) - d_3(t) \quad (2.7)$$

Corresponding to the successive stripping of high frequency information (contained within the $d_m(t)$) from the original signal at each step. This is referred to as Multiresolution analysis of a signal using wavelet transform, and is the basic of our procedure.

Wavelet Denoising:

Wavelet signal decomposition can be seen as an iterative process whereby a signal is

decomposed into finer resolution signals in time and frequency. First of all, two symmetric filters are created from a “mother” wavelet and a scaling function associated to that wavelet. These filters will provide an orthogonal basis dividing the signal frequency spectrum and generating high and low frequency signals in each iterative step. These signals are decimated by two before the next iterative step. Details on wavelet decomposition can be found in [1]. Figure 2. Illustrate this wavelet decomposition tree of an ECG signal, where the Approximations (A) boxes represent the low frequency components obtained by the low pass filter (LPF), and the D boxes represent the high frequency components obtained by the symmetric high pass filter (HPF).

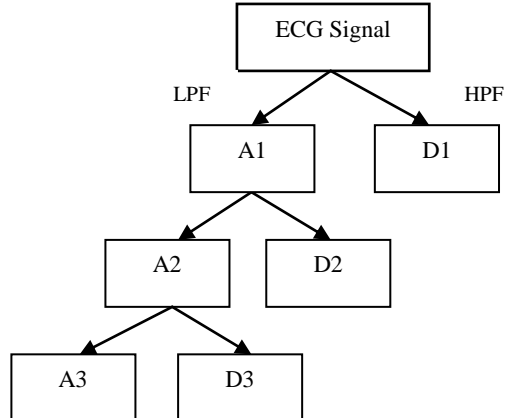


Fig 2: Wavelet Decomposition Tree.

2.2 Removal of Baseline Wandering

Baseline wandering usually comes from respiration at frequency wandering between 0.15 Hz and 0.3 Hz and it can be suppressed by a high pass digital filter. Wavelet transform can also be used to remove the baseline wandering by eliminating the trend of the

ECG signal. The wavelet transform based approach is better because it introduces no latency and less distortion than the digital filter based approach.

The LabVIEW ASPT (Advanced signal processing toolkit) provides the WA Detrend virtual instrument which removes the low frequency trend of the signal.

$$\text{trend level} = \left\lceil \frac{\log_2 t}{\log_2 N} \right\rceil \quad (2.8)$$

Where t is the sampling duration and N is the number of sampling points. The data used here has a sampling duration of 30.06 Min and with a sampling frequency of 360samp/sec, therefore the trend level is 0.61 according to the above equation. Trend level specifies the number of levels of the wavelet decomposition, which is approximately,

$$\text{No. of decomposition level} = (1 - \text{Trend level}) * \log_2 (N) \quad (2.9)$$

and for the data base we are using here it is 8. The WA detrend virtual instrument has an option to specify the wavelet type used for the discrete wavelet analysis. The one selected here is Daubechies(db6) wavelet because this wavelet is similar to the real ECG signal and also Daubechies wavelet being orthogonal wavelet is suitable for signal denoising where as biorthogonal wavelet is suitable for feature extraction. The Daubechies db6 wavelet is shown in Fig. 3

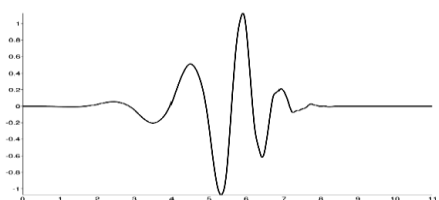


Fig 3: Wavelet Decomposition Tree

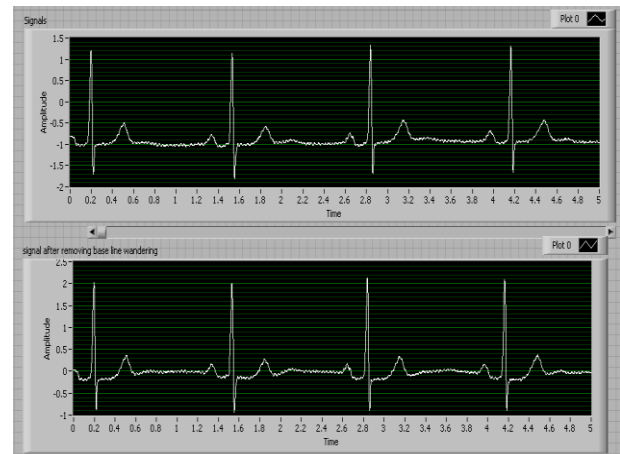


Fig 4: ECG signals before and after Baseline wandering

2.3 Removal of Wideband Noise

After removing baseline wander the resulting ECG signal is more clean and explicit than the original signal. However, some other types of noise might still affect feature extraction of the ECG signal. The noise may be complex stochastic processes within a wideband, so one cannot remove them by using traditional digital filters[3]. To remove the wideband noises, the Wavelet Denoise Express Virtual instrument is used here. The Express Virtual instrument decomposes the ECG signal into several sub bands by applying the wavelet transform and then modifies each wavelet coefficient by applying a threshold or shrinking a function and finally reconstructs denoised signal. From the threshold setting options available, soft thresholding is selected and the thresholding rule selected is ‘universal’ and the Virtual instrument sets the threshold to $\sqrt{2 * \log N}$. The Virtual instrument offers an option to select either discrete wavelet transform or undecimated wavelet transform to denoise the signal. The transform type used is undecimated wavelet Transform (UWT) to denoise the ECG signal.

The UWT has a better balance between smoothness and accuracy than the discrete wavelet transform.

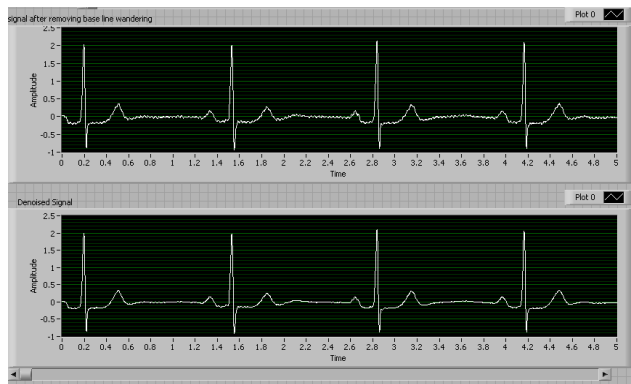


Fig 5: Signal before and after Denoising

3. Methods of HRV Analysis

We used two approaches in this paper.
There are

1. Time Domain Analysis Method
2. Frequency Domain Analysis

3.1 Time Domain Analysis Method

For time series analysis, time domain measures are commonly used. Many measures can be extracted from the original RR interval signals to show the changes in the Autonomic Nervous System (ANS).

We used time domain analysis approach in this paper. The measures which can be finding out in this analysis are:

Table 1 Time Domain Analysis

Variables	Units	Descriptions
Statistical measures		
RR Mean & Std	s	Mean and standard deviation of all RR intervals.

HR Mean & Std	1/min	Mean and standard deviation of all heart rates.
RMSDD	ms	Square root of the mean of the sum of squares of differences between adjacent RR intervals.
NN50 count		Number of pairs of adjacent RR intervals differing by more than 50 ms in all the measurements.
pNN50	%	NN50 count divided by the total number of all RR intervals.
Geometric measures		
HRV triangular index		Total number of all RR intervals divided by the height of the histogram of all RR intervals.
TINN	ms	Baseline width of the minimum square difference triangular interpolation of the highest peak of the histogram of all RR intervals measured on a discrete scale with bins of 7•8125 ms (1/128 s).

The heart rate (H.R) in beats per minute is calculated from the average RR interval(RRI) using the relation

$$H.R = \frac{60}{\text{Average RRI in Seconds}} \quad (3.1)$$

Histogram:

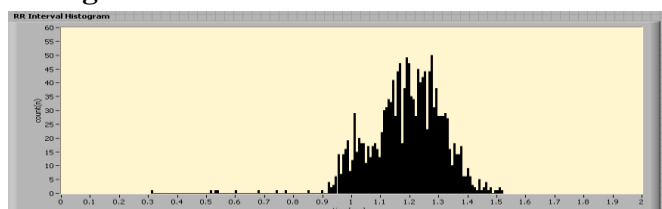


Fig 6: Histogram of RR interval

3.2 Frequency Domain Analysis

The time domain methods are computationally simple, but lack the ability to discriminate between sympathetic and parasympathetic contributions of HRV. These studies of HRV employed the periodogram or fast Fourier transform (FFT) for power spectral density (PSD) estimation procedure consists of two steps.

1. Given the data sequence $x(n)$, $0 \leq n \leq N-1$, the parameters of the method are estimated.
2. Then from these estimates, the PSD estimate is computed. But these methods suffer from spectral leakage effects due to windowing.

The spectral leakage leads to masking of weak signal that are present in the data. The parametric (model based) power spectrum estimation methods avoid the problem of leakage and provide better frequency resolution than nonparametric or classical method. AR method can be used for the analysis of frequency domain. In AR method, the estimation of AR parameters can be done easily by solving linear equations. In AR method, data can be modeled as output of a causal, all pole, discrete filter whose input is white noise. The HF power spectrum is evaluated in the range from 0.15 to 0.4 Hz. This band reflects parasympathetic (vagal) tone and fluctuations caused by spontaneous respiration known as respiratory sinus arrhythmia.

Table 2 Frequency Domain Analysis

Variables	Units	Descriptions
Peak Frequency	Hz	<i>Peak frequencies of the power spectral density (PSD) estimate for the</i>

		<i>VLF, LF, and HF frequency bands.</i>
VLF	ms^2	<i>Power from 0–0.04 Hz.</i>
LF	ms^2	<i>Power from 0.04–0.15 Hz.</i>
HF	ms^2	<i>Power from 0.15–0.4 Hz.</i>
LF Norm	n.u.	<i>LF power in normalized units: LF/(Total Power–VLF)*100.</i>
HF Norm	n.u.	<i>HF power in normalized units: HF/(Total Power–VLF)*100.</i>
LF/HF Ratio		<i>LF [ms^2] / HF [ms^2].</i>

The LF power spectrum is evaluated in the range from 0.04 to 0.15 Hz. This band can reflect both sympathetic and parasympathetic tone.

The VLF power spectrum is evaluated in the range from 0.0033 to 0.04 Hz. The physiological meaning of this band is most disputable. With longer recordings, it is considered to represent sympathetic tone as well as slower humeral and thermoregulatory effects. There are some findings that in shorter recordings VLF has fair representation of various negative emotions, worries, rumination etc.

The TP is a net effect of all possible physiological mechanisms contributing in HR variability that can be detected in 5-min recordings, however sympathetic tone is considered as a primary contributor.

The LF/HF Ratio is used to indicate balance between sympathetic and parasympathetic tone. A decrease in this score might indicate either increase in parasympathetic or decrease in sympathetic tone. It must be considered

together with absolute values of both LF and HF to determine what factor contributes in autonomic misbalance.

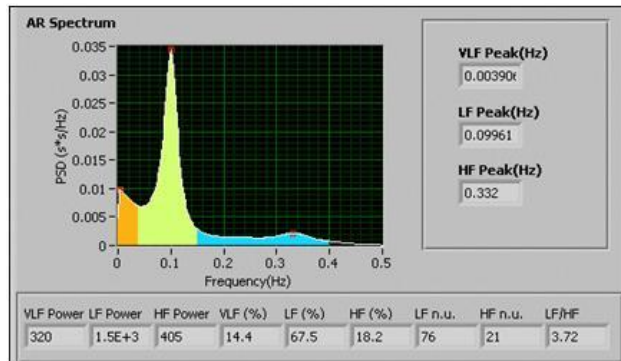


Fig 7: HRV analysis using frequency domain parameters

4. Arrhythmia Classification

The classification of the arrhythmias is based on the heart rate obtained from statistical method: Normal Sinus Rhythm, Bradycardia, Tachycardia and Heart Rate Detection: When heart rate is between 60-100 bpm, the recorded ECG signal is said to have normal sinus rhythm. When heart rate is above 100 bpm, the recorded signal has tachycardia. When heart rate is below 60 bpm, the recorded slow heart rate corresponds to bradycardia. The database is also tested based on A knowledge-based approach to cardiac signal analysis using LabVIEW classified few of the records based on findings as given below:

Table 3 Classification of Arrhythmia

Name of Arrhythmia	Brief Description of the Arrhythmia	Identification Process
Bradycardia	It is critical reduction of heart rate and characterised by normally directed abnormally wide P waves and normal PQ interval	If one R-R interval is greater than 1.5sec (equal to 40 beats per min) and if *RR _t >1.5sec and AR _t >102sec
Tachycardia	This is a serious	An average R to R

	racing of the heart and is characterised by normally shaped and directed P waves with a normal PQ interval	interval less than 0.5sec (120beats per min) AR _t <0.5sec
Type of Arrhythmia	Records from MIT-BIH arrhythmia database	
Bradycardia	Record 123, Female, 63, Lead II Record 106, Female, 24, Lead II Record 117, Female, 69, Lead II Record 124, Female, 77, Lead II	
Tachycardia	Record 203, male, 43, Lead II	
Normal Sinus Rhythm	Records 100,103,105,111,112,115,116,121,122,201,205.	

Case I: a) Time Domain Analysis

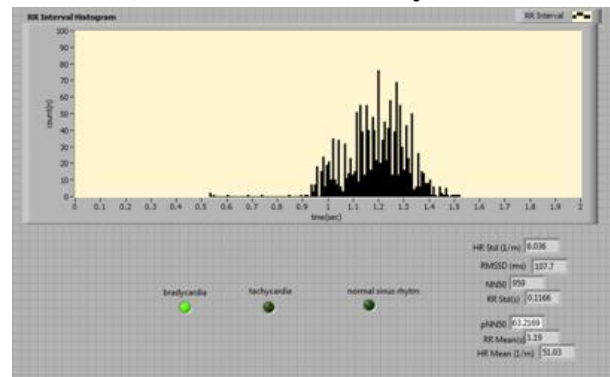


Fig 8: Time Domain Analysis for the record 123 from MIT BIH database.

The arrhythmia found is Bradycardia

Table 4 Inference for the record 123: It is observed that Heart Rate is 51bpm

S. No	Variables	Obtained Value
1	HR Std/min	6.036
2	RMSSD (ms)	107.7
3	NN50	959
4	RR Std(s)	0.1166
5	pNN50	63.2169
6	RR Mean(s)	1.19
7	HR Mean/min	51.03

b) Frequency Domain Analysis

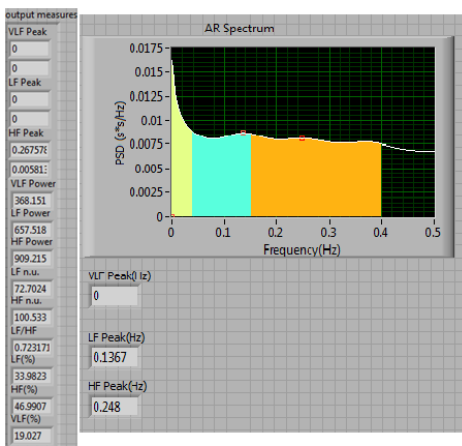


Fig 9: Frequency Domain Analysis for the record 123

Table 5 Inference for the record 123: It is observed that Heart Rate is 51bpm

S. No	Variables	Obtained Value
1.	VLF	0
2.	LF	0.1367
3.	HF	0.248
4.	LF Norm	72.7024
5.	HF Norm	100.533
6.	LF/HF Ratio	0.723171

Case II: a) Time Domain Analysis

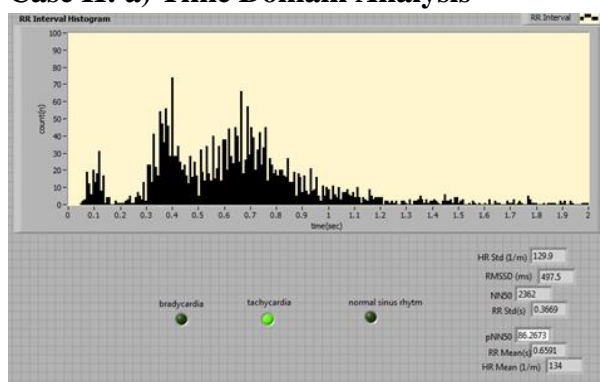


Fig 10: Time Domain Analysis for the record 203

The arrhythmia found is Tachycardia

Table 6 Inference for the record 203: It is observed that Heart Rate is 100bpm.

S. No	Variables	Obtained Value
1	HR Std/min	129.9
2	RMSSD (ms)	497.5
3	NN50	2362
4	RR Std(s)	0.3669
5	pNN50	86.2673
6	RR Mean(s)	1.19
7	HR Mean/min	134

b) Frequency Domain Analysis

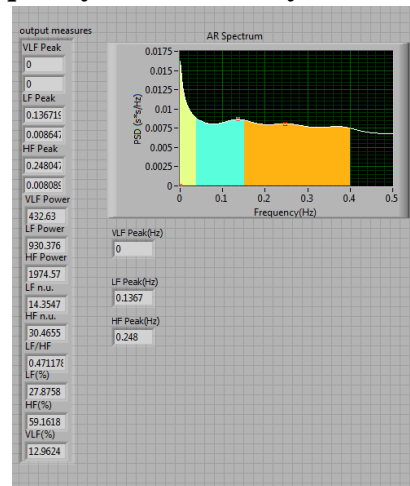


Fig 11: Frequency Domain Analysis for the record 203

Table 7 Inference for the record 203: It is observed that Heart Rate is 100bpm

S. No	Variables	Obtained Value
1.	VLF	0
2.	LF	0.1367
3.	HF	0.248
4.	LF Norm	14.3547
5.	HF Norm	30.4655

6.	LF/HF Ratio	0.471178
----	-------------	----------

5. Conclusion

The extraction of high-resolution ECG signals from recordings contaminated with background noise is an important issue to investigate. The large variety of ECG feature extraction algorithms, and the continuous efforts for their enhancement, proves that universally acceptable solution has not been found yet. Difficulties arise mainly from the huge diversity of the waveform the noise and artifacts accompanying the ECG signals. The main advantage of this graphical programming language is that, it provides a robust and efficient environment and tool for generating very fast, less complex and useful algorithm. Efforts must be made to improve the algorithm. The develop technique to extract all the ECG features that make the report generated from LabVIEW is very effective for physicians to diagnose.

6. Acknowledgement

The authors are thankful to Dr. S Raja Ratnam Professor and Dr. C D Naidu Professors and Principal of VNR VJIET for their constant technical support and encouragement.

7. Reference

- [1]. S. Z. Mahmoodabadi (MSc), A. Ahmadian (Phd), M. D. bolhasani(Phd), "ECG FEATURE EXTRACTION USING DAUBECHIES WAVELETS" Proceedings of the First IASTED, International Conference. Sept 2005
- [2]. Narayana,Rao, A.B, "A KNOWLEDGE-BASED APPROACH TO CARDIAC SIGNAL ANALYSIS USING

LABVIEW" This paper appears in Power, Control and Embedded Systems (ICPCES), 2010. M. Wegmuller, J. P. von der Weid, P. Oberson, and N. Gisin, "High resolution fiber distributed measurements with coherent OFDR," in Proc. ECOC'00, 2000, paper 11.3.4, p. 109.

- [3]. Tan Yun-fu, Du Lei , "STUDY ON WAVELET TRANSFORM IN THE PROCESSING FOR ECG SIGNALS" This paper appears in Software Engineering, 2009. WCSE '09. WRI World Congress on 19-21 May 2009.
- [4]. Manimegalai.P, Bharathi.P, Dr.K.Thanushkodi, "REAL TIME IMPLEMENTATION OF ANALYSIS OF ECG CHARACTERISTIC POINTS USING DISCRETE WAVELETS" Global Journal of researches in engineering" Electrical and electronics engineering Volume 12 Issue ! Version 1.0 January 2012
- [5]. Adib, A. ,Haque, M.A., "ECG BEAT CLASSIFICATION USING DISCRETE WAVELET COEFFICIENTS" This paper appears in Health Informatics and Bioinformatics (HIBIT), 2010 5th International Symposium on 20-22 April 2010
- [6]. K. F. Tan, K. L. Chan', and K. Choi "DETECTION OF THE QRS COMPLEX, P WAVE AND T WAVE IN ELECTROCARDIOGRAM" Advances in Medical Signal and Information Processing, 2000. First International Conference on (IEE Conf. Publ. No. 476)
- [7]. Romania David, V. ; Adochie, F. ; Tudosa, I. "ECG WAVES AND FEATURES EXTRACTION USING WAVELET MULTI-RESOLUTION

ANALYSIS”, Paper appears in: E-Health
and Bioengineering Conference (EHB).

Multiple sclerosis lesion segmentation in brain MR images based on a hybrid of Markov random field and Ant colony optimization

V. Divya¹, G. Kavitha¹

Department of Electronics Engineering

Madras Institute of Technology

Anna University, Chennai

vijayarajandivya@gmail.com, kavithagmit@gmail.com

Abstract

Reliable segmentation of abnormalities such as multiple sclerosis lesions in magnetic resonance brain imaging is important for pharmaceutical trials, decision making for drug treatment or surgery, and patient follow-up. This paper introduces the methodology for the segmentation of brain multiple sclerosis lesions in magnetic resonance images (MRI) using clustering algorithm based on a hybrid of Markov Random Field (MRF) and Ant Colony Optimization (ACO). Combining ACO with MRF algorithm helps in finding the better path using neighborhood information. Therefore, this interaction causes the algorithm to converge to an optimum solution faster. The segmented T1 image is used as a mask over segmented T2 image to segment the multiple sclerosis lesions. Results presented reveal that the hybrid of MRF with ACO outperforms the traditional MRF with Simulated Annealing (SA) both qualitatively and quantitatively.

Keywords

Multiple sclerosis, Markov Random Field, Ant Colony Optimization, Simulated Annealing

1. Introduction

Multiple Sclerosis (MS) is an autoimmune disease of central nervous system. It results in a variety of symptoms from blurred vision to severe muscle weakness and degradation,

depending on the affected regions in brain. Since Magnetic Resonance images provide an excellent spatial resolution and tissue contrast, they are used in a number of applications such as visualization and morphological analysis of the brain. Thus MRIs are used to better understand MS and to quantify its evolution [1].

Manual segmentation of MS lesions in MR images by human expert is time consuming, subjective and is impractical for large amounts of data. Therefore, automatic segmentation is needed as an alternative to manual segmentation. A number of semi-automated and automated methods have been proposed for identification and segmentation of MS lesions using either single or multi channel MR images. Traditional image processing techniques have been widely used in MRI analysis such as threshold techniques [2], region growing techniques, clustering techniques, classifiers and artificial neural networks.

Boudraa et al. [3] proposed an algorithm using FCM algorithm followed post-processing step based on anatomical knowledge to detect lesions. He and Narayana [4] proposed a method based on an adaptive local segmentation derived from morphological grey-scale reconstruction operations to identify both lesion and non-lesion enhancements. Saha et al. [5] automatically determined the number of clusters by introducing genetics into the algorithm.



Yamamoto et al., [6] proposed an automated three stage process involving rule based method followed by level set method then classification was performed using support vector machine.

In recent years, the stochastic models have become more popular in image segmentation. Among the various stochastic models Markov random field (MRF) based model provides better framework for many problems in image segmentation. This is due to the fact that, MRF is based on the notion of neighborhood structure and therefore helps in understanding global interaction through local spatial interactions [7]. Bhattacharya et al.,[8] compared the intensity based fuzzy C-means and Markov random field approaches, both stochastic and deterministic, for the segmentation of brain MR images into three different cortical tissues namely, grey matter, white matter and cerebrospinal fluid. Yousefi et al., [9] proposed a methodology using a hybrid of Markov random fields and Ant colony optimization with gossiping algorithm for normal tissue segmentation in brain MR image.

Among the various MR images, T1-w images are widely used, since they show the best contrast between the three main brain tissues: White Matter, Grey Matter and Cerebrospinal Fluid. The initial tissue segmentation may then be used to help obtain the final lesion segmentation. T2-w and PD-w are the classical images for detecting MS lesions. Another approach is the segmentation of MS lesions using the FLAIR sequence [10]. The multi-channel approaches, on the other hand, use atleast two of the PD-w, T1-w, T2-w, and FLAIR images. One of the benefits of using more than one of the different MR images is that it increases the intensity feature space, producing a better discrimination between brain tissues. Khotanlou et al., [11] proposed a method for MS lesion segmentation using T1 and T2 images based on the modified Fuzzy C-means which uses both the information of pixels and their neighborhoods. Khayatiet

al.,[12] proposed an approach for fully automated segmentation of MS lesions in fluid attenuated inversion recovery (FLAIR) MR images, based on a Bayesian classifier which utilizes the adaptive mixtures method (AMM) and Markov random field. This paper proposes a method for segmentation of multiple sclerosis lesion using T1-w and T2-w images. Section 2 describes the methodology, Section 3 presents the experimental results followed by conclusion.

2. Methodology

Markov Random Field models are of widespread use in a variety of image segmentation tasks as they partition an image into clusters of homogeneous signal value, while controlling the spatial smoothness of the partition. The MRF-based image segmentation method seeks the optimal labeling of the image pixels. The image is segmented by maximizing the a posteriori probability (MAP) of the labeling space given the image data.

The MRF-MAP framework involves solving an energy maximization (or minimization) problem. However this maximization is combinatorial and the energy function is usually non convex and may exhibit many local minima in the solution space. Optimization methods in the MRF model are divided into two categories namely, deterministic relaxation and stochastic relaxation. The first group has reasonable computation burden but depends on initialization intensively and can get trapped in a local minima. The second group is based on Simulated Annealing (SA) and has heavy computation burden but converge to a global minima. This section briefly describes the MRF model for image segmentation.

Suppose $S = \{s_i | i = 1, \dots, row \times col\}$ denotes a two dimensional lattice. The input $X = \{x_i | i = 1, \dots, row \times col\}$, and output $Y = \{y_i | i = 1, \dots, row \times col\}$ on this lattice are such that each site on S



demonstrates a pixel on input image. A subset of S, such as c, in which all s ∈ c are neighbors of one another is called clique. The aim of MRF based segmentation is to assign a label field $y = \{y_s \in \Gamma | s \in S\}$ in which $\Gamma = \{\lambda_i | i=1,2,\dots, \text{number of clusters}\}$. The label field Y is said to be a MRF on lattice S with respect to the neighborhood system $N(s)$ if and only if two below conditions are satisfied. They are as follows:

- i) $P(y) > 0, \forall y \in Y$
- ii) $P(y_i | y_{S \setminus i}) = P(y_i | y_{N(i)}) , i \in S$

The first condition is known as positivity and the second is known as Markovianity. In practice the positivity condition is satisfied and assumed for technical reasons. In the second condition, $S \setminus i$ demonstrates all sites of the lattice S, and $N(i)$ means the neighbors of the site i . In fact, the Markovianity depicts that the label of each site on lattice S depends on its neighborhood set.

The goal of MRF is to find a label field which satisfies maximum a posterior criterion:

$$y^* = \arg \max_{y \in Y} (P(x|y, \theta)P(y|\theta)) \quad (1)$$

where $P(y|\theta)$ is distribution of label field y and according to Hammersley–Clifford theory is equal to Gibbs distribution. Also $P(x|y, \theta)$ is intensity distribution of each cluster and it is defined as a Gaussian distribution with mean μ and variance σ . By replacing these two distributions in MAP criterion:

$$y^* = \arg \max_{y \in Y} \left\{ \frac{1}{\sqrt{2\pi\sigma}} e^{-\left(\frac{(x-\mu)^2}{2\sigma^2}\right)} \frac{1}{Z} e^{-\left(\frac{E(y)}{T}\right)} \right\} \quad (2)$$

where $E(y)$ is the energy function and T is the temperature

$$\begin{aligned} y^* &= \arg \min_{y \in Y} \left(\ln \left(\sqrt{2\pi\sigma} + \frac{(x-\mu)^2}{2\sigma^2} \right) + E(y) \right) \\ &= \arg \min_{y \in Y} (U(y)) \quad \dots \dots \dots (3) \end{aligned}$$

Therefore, the segmentation problem can be posed as a minimization problem (3), in which $U(y)$ is called total energy of the label field y. All of the methods which are introduced in this work use Expectation–Maximization (EM) algorithm in order to estimate mean and variance.

2.1 Markov random fields with Simulated Annealing

Simulated annealing is a Monte Carlo optimization approach based on the principles of thermodynamics, which generates a sequence of Markov chains controlled by gradually decreasing temperature of the system. MRF is a stochastic process in which spatial relations within the image are included in the labeling process through statistical dependence among neighboring pixels. The energy function for a site using the MRF image model is given by

$$\begin{aligned} E(y) &= \sum_{c \in C} \left(\frac{1}{2} \sum_{s=1}^4 v(i,j) \right) \\ v &= \begin{cases} -1 & \text{if } y_i = y_j \\ 1 & \text{if } y_i \neq y_j \end{cases}, i, j \in S \dots \dots (4) \end{aligned}$$

in which $i, j, k \in S$. Fig 1 demonstrates the neighborhood system of the classical MRF.

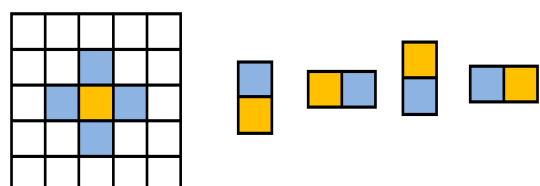


Fig 1: Neighborhood in MRF

The algorithm starts by selecting a random label field which is named w . Each iteration consists of the following steps:

1. Create a new label field (y) by disturbing a label of a site in w .
2. Compute $\Delta U = U(y) - U(w)$ and replace w by y if $\Delta U < 0$ else accepts with the probability of $\exp(-\Delta U/T)$ (analogy with thermodynamics):

$$w = \begin{cases} y & \text{if } \Delta U < 0 \\ y \text{ if } \Delta U > 0 \text{ and } \xi < \exp\left(-\frac{\Delta U}{T}\right) \\ w & \text{otherwise} \end{cases} \quad (5)$$

where ξ is a uniform random number in $[0,1]$.

3. Decrease the temperature and go to Step 2 until the system is frozen. The frozen condition is $\sum |\Delta U_{local}|$ goes to zero.

2.2 Markov random fields with Ant colony optimization

Ants are simple agents individually but the whole colony has a good ability to perform complicated tasks. Using pheromone and heuristic information, each ant constructs a part of solution. Pheromone is a chemical substance, which ants deposit on the edges while transferring in foraging process. Ant colony system updates the pheromone information twice. The first update is performed when an ant moves in constructing of each partial solution. The second update is performed after the move of all ants in each of iterations. Ant colony optimization (ACO) can find better solution than other optimization methods such as simulated annealing [13].

MRF-ACO considers each site as an ant which seeks a food resource. The goal of colony is to find the label field with the optimum energy value. There is a path from each site on the image lattice to the each cluster label. Each ant finds the best path in each iteration probability. Transiting the path, each ant deposits pheromone on the trail. At time $(t +$

$1)$, each ant transits from node s to node λ according to the state transfer probability ($P_{s,\lambda}^{t+1}$) given by:

$$P_{s,\lambda}^{t+1} = \frac{(\tau_{s,\lambda}^t)^\alpha (\eta_{s,\lambda}^t)^\beta}{\sum_{k \in \Gamma} (\tau_{k,\lambda}^t)^\alpha (\eta_{k,\lambda}^t)^\beta} \quad (6)$$

where $\tau_{s,\lambda}^t$ is the pheromone density between site s and λ , $\eta_{s,\lambda}^t$ is the heuristic information between site s and λ . α and β represent the influence of pheromone information and heuristic information respectively.

The heuristic information is given by:

$$\eta_{s,\lambda} = -U_{Ls,\lambda} + |min(-U_{Ls,\lambda})| \quad (7)$$

where $U_{Ls,\lambda}$ is the local energy between site s and cluster λ which is given by

$$U_{Ls,\lambda} = \frac{(x_s - \mu_\lambda)^2}{2\sigma^2} + ln\sqrt{2\pi}\sigma + \sum_{c \in C} V_c$$

$$V_c = \begin{cases} -1 & \text{if } y_i = y_j \\ 1 & \text{if } y_i = y_j \end{cases}, i, j \in S \quad (8)$$

where μ_λ and σ_λ are the mean and variance of the destination cluster.

In ACO the pheromone density is updated twice. The first updation is performed when an ant passes through a path. So the pheromone value of that path should be reinforced locally which is given by:

$$\tau_{s,\lambda}^{t+1} = (1 - \rho) \cdot \tau_{s,\lambda}^t + \rho \cdot \Delta \tau_{s,\lambda} \quad (9)$$

$$\Delta \tau_{s,\lambda} = e^{-|x_s - \mu_\lambda|} \quad (10)$$

where $\tau_{s,\lambda}^t$ is the pheromone density between site s and λ , ρ is the evaporation rate, $\Delta \tau_{s,\lambda}$ is the fitness value of the destination, x_s is the intensity of the source and μ_λ is the mean of the destination cluster. The second updation is done when all ants visit all the nodes and a complete solution is constructed. It is given by:

$$\tau^{t+1} = (1 - \psi) \cdot \tau^t + \psi \left| \frac{\Delta U}{U_{old}} \right| \quad (11)$$

where ψ is the pheromone decay coefficient.



$\Delta U = U_{new\ field} - U_{old\ field}$. So the pheromone matrix is updated globally.

2.3 Multiple sclerosis lesion segmentation

The overall flowchart for lesion segmentation is presented in the Fig 2 T1-w and T2-w images are first segmented followed by masking the segmented T1-w image over the segmented T2-w image for lesion segmentation. The white matter appears as the brightest tissue in T1-w images, the darkest in T2-w images whereas the cerebrospinal fluid is the brightest tissue in T2-w images, but in T1-w it is the darkest tissue. The grey matter appears as the intermediate grey in both T1-w and T2-w images. The MS lesions appear as hypo intense signals as compared to the surrounding healthy white matter tissues in T1-w images whereas it appears as hyper intense signals compared to the healthy WM tissues in T2-w images. So when T1-w image is grouped into three clusters the background and the CSF form a single cluster, grey matter and white matter groups into separate clusters. The white matter region formed in the T1-w image is being used as a mask over the segmented T2-w image and the non white matter region present within the mask represent the lesions.

2.4 Performance Measures

The performance measures used in this work to validate the algorithm are sensitivity, specificity, accuracy and Dice coefficient.

$$\text{Accuracy} = \frac{\text{TP} + \text{TN}}{\text{TP} + \text{TN} + \text{FP} + \text{FN}} \quad (12)$$

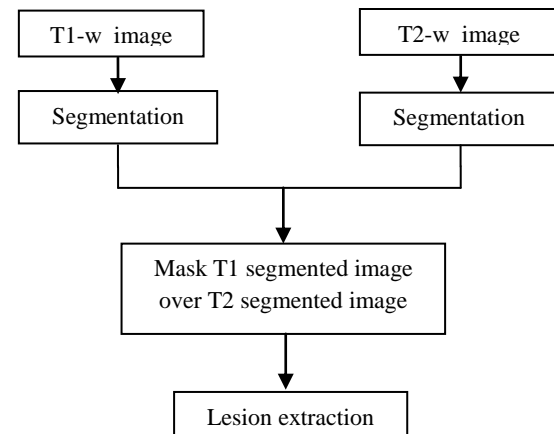


Fig 2: Flowchart for Multiple sclerosis lesion extraction

$$\text{Sensitivity} = \frac{\text{TP}}{\text{TP} + \text{FN}} \quad (13)$$

$$\text{Specificity} = \frac{\text{TN}}{\text{TN} + \text{FP}} \quad (14)$$

$$\text{Dice coefficient} = \frac{2 \times \text{TP}}{2 \times \text{TP} + \text{FP} + \text{FN}} \quad (15)$$

where TP is true positive which represents the number of pixels which are in the ground truth and have been detected, TN is true negative which represents the number of pixels which are not in the ground truth and have not been detected, FP is false positive which represents the number of pixels which are not in the ground truth but have been detected, FN is false negative which represents the number of pixels which are in the ground truth and have not been detected [10].

3. Experimental Results

The proposed method was tested using simulated MR images provided by the BrainWeb Simulated Brain Dataset from the McGill University. The MR images used for the analysis are of voxel size 1.0 mm in-plane and 1.0 mm slice thickness. Table 1 presents the parameters used in image segmentation

using MRF-SA and MRF-ACO. The overall process of MS lesion segmentation is shown in Fig 3.

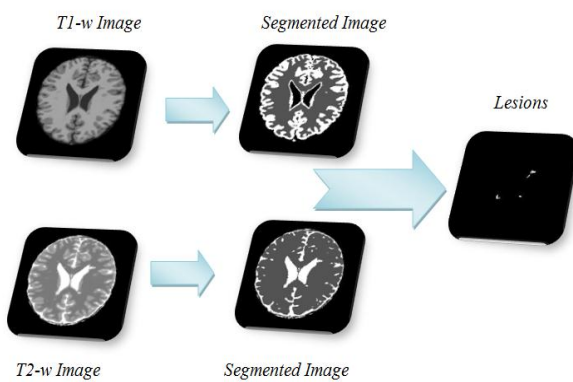


Fig 3: Overall process of lesion segmentation

Fig 4 presents the results obtained for lesion segmentation for various images using MRF-SA, MRF-ACO and the ground truth. Fig 4 a) shows the T1-weighted image for which lesions were detected b) shows the MS lesions detected using MRF-SA c) shows the MS lesions detected using MRF-ACO and d) shows the ground truth.

Table 2 presents the sensitivity, specificity, accuracy for lesion detection using MRF-ACO and MRF-SA. From the table it is observed that the sensitivity of MRF-ACO is higher when compared to the MRF-SA. Higher sensitivity represents the greater ability of the system to reduce the false negatives. Also the sensitivity score of 1 indicates that all pixels

which are lesion in the ground truth were in the observed lesion set. Average accuracy and specificity is nearly equal for both the MRF-ACO and MRF-SA.

Table 1. Parameters for MRF-SA and MRF-ACO

Parameter	MRF-SA	MRF-ACO
Temperature	4	-
Evaporation rate	-	0.1
Pheromone decay coefficient	-	0.1
Heuristic information influence	-	1
Pheromone density influence	-	1

Table 3 gives the comparison of the Dice coefficient for MRF-SA and MRF-ACO, which shows that the average Dice coefficient for MRF-SA is 0.6815 whereas for MRF-ACO it is 0.7745. Dice coefficient close to one represents the exact similarity between the ground truth and the results observed. From the results it is observed that the hybrid MRF-ACO performs better than traditional MRF-SA for MS lesion segmentation

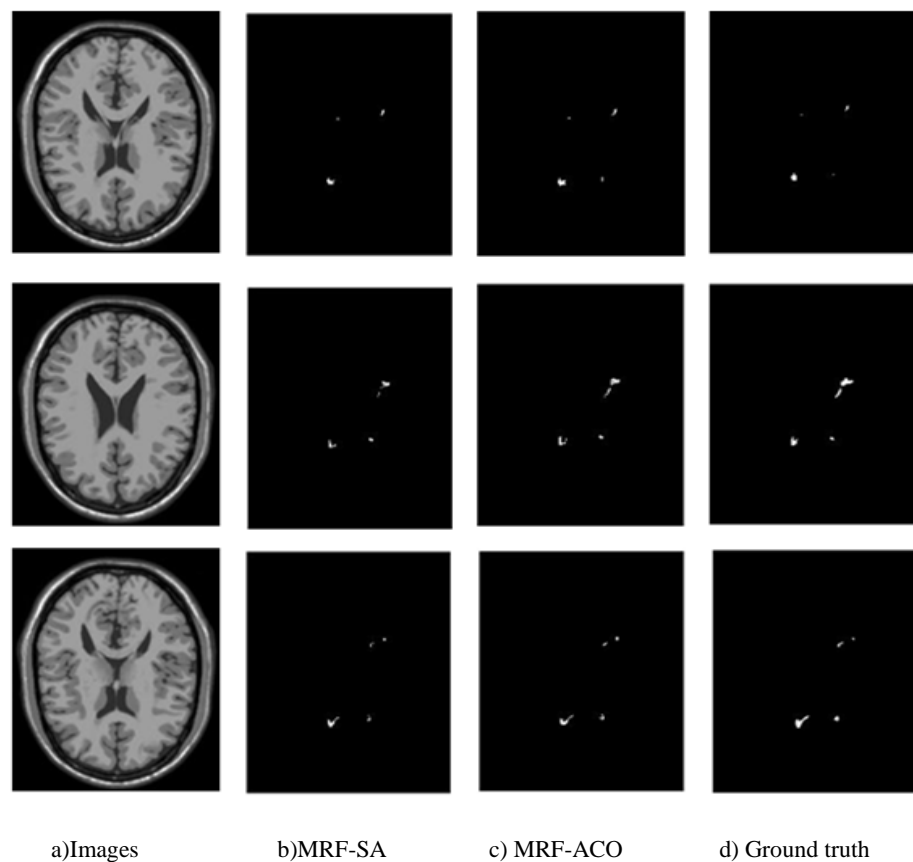


Fig 4: Multiple sclerosis lesion segmentation

Table 2. Performance analysis for multiple sclerosis lesion segmentation

Image s	Sensitivity		Specificity		Accuracy	
	MRF- SA	MRF- ACO	MRF-SA	MRF- ACO	MRF-SA	MRF- ACO
Slice 86	0.5469	0.6563	0.9999	0.9999	0.9992	0.9993
Slice 87	0.6933	0.8133	0.9999	0.9999	0.9994	0.9996
Slice 88	0.7794	0.8382	0.9999	0.9997	0.9995	0.9994
Slice 89	0.7576	0.8182	0.9999	0.9997	0.9997	0.9995
Slice 90	0.6522	0.7174	0.9998	0.9998	0.9994	0.9995
Slice 91	0.5741	0.7407	0.9998	0.9998	0.9993	0.9995

Slice 92	0.619	0.7619	0.9999	0.9998	0.9995	0.9996
Slice 93	0.325	0.9	0.9999	0.999	0.9993	0.9989
Slice 94	0.4783	0.6522	0.9999	0.9998	0.9993	0.9994
Slice 95	0.5176	0.7294	1	0.9999	0.9989	0.9993
Average	0.5812	0.76276	0.99986	0.99973	0.99932	0.9994

Table 3.Comparison of Dice coefficient for lesion segmentation using MRF-ACO and MRF-SA

Images	MRF-SA	MRF-ACO
Slice 86	0.6796	0.7636
Slice 87	0.8062	0.8777
Slice 88	0.8413	0.8261
Slice 89	0.8065	0.7500
Slice 90	0.7317	0.7586
Slice 91	0.6813	0.8000
Slice 92	0.7222	0.7901
Slice 93	0.4727	0.6207
Slice 94	0.6111	0.7317
Slice 95	0.6769	0.8267
Average	0.6815	0.7745

4. Conclusion

MRI brain image segmentation plays an increasingly important role in computer-aided detection and diagnosis of abnormalities in brain. This paper uses a hybrid of Markov Random Field and social algorithms as an unsupervised method for the multiple sclerosis lesion segmentation. The hybrid MRF-ACO is

compared with MRF-SA based on sensitivity, specificity, accuracy and the Dice similarity metric. From the results, it is observed that the hybrid MRF-ACO has better Dice coefficient and sensitivity in comparison with the classical MRF-SA in segmenting the multiple sclerosis lesions in brain MRI. Hence, the hybrid MRF-ACO method has the potential to be used in the real-time computer aided diagnosis systems.

5. References

- [1] García-Lorenzo Daniel, Francis Simon, Narayanan Sridar, Arnold Douglas L., Collins D. Louis, 2013 Review of automatic segmentation methods of multiple sclerosis white matter lesions on conventional magnetic resonance imaging, Med Img Anal 17 (2013) 1–18
- [2] Yang.T, Guan.Y,2011Multi-Threshold MR image segmentation Based on Fuzzy Markov Random Field and Gaussian Curve, Energy Procedia 13(2011) 7355-7361.
- [3] A. Boudraa, S.M.R. Dehak, Y. Zhu, C. Pachai, Y. Bao, J. Grimaud.,2000 Automated segmentation of multiple sclerosis lesions in multispectral MR imaging using fuzzy clustering, Comput. Biol. Med. 30 (1) (2000) 23–40.

- [4] R. He, P.A. Narayana.,2002 Automatic delineation of Gd enhancements on magnetic resonance images in multiple sclerosis, *Med. Phys.* 29 (7) (2002) 1536–1546.
- [5] S. Saha, S. Bandyopadhyay.,2009A new point symmetry based fuzzy genetic clustering technique for automatic evolution of clusters, *Inf. Sci.* 179 (9) (2009),3230–3246.
- [6] Yamamoto.D, Arimura.H, Kakeda.S, Magome.T, Yamashita.Y, Toyofuku.F, Ohki.M, Higashida.Y, Korogi.Y, 2010 Computer-aided detection of multiple sclerosis lesions in brain magnetic resonance images: False positive reduction scheme consisted of rule-based, level set method, and support vector machine, *Comp. Med. Imag. and Graph.* 34 (2010),404–413.
- [7] Roche.A, Ribes.D , Bach.M , Krüger.G.,2011On the convergence of EM-like algorithms for image segmentation using Markov random fields,*Med. Imag. Analy.*, Vol.15, Issue 6, (2011) ,830-839.
- [8] Bhattacharya .M, Chandana. M.,2012Analytical assessment of intelligent segmentation techniques for cortical tissues of MR brain images: a comparative study, *ArtifIntell Rev* 37 (2012) ,69–81
- [9] S. Yousefi , R. Azmi , M. Zahedi.,2012Brain tissue segmentation in MR images based on a hybrid of MRF and social algorithms *Med. Imag. Anal.* 16 (2012), 840–848.
- [10] Lladó. X, Oliver.A, Cabezas.M, Freixenet.J, Vilanova.J.C, Quiles.A, Valls.L, Torrentà.L, Rovira.À.,2012Segmentation of multiple sclerosis lesions in brain MRI: A review of automated approaches, *Inf. Sci.* 186 (2012) ,164–185.
- [11] H. Khotanlou , M.Afrasiabi.,2011Segmentation of Multiple Sclerosis Lesions in Brain MR Images using Spatially Constrained Possibilistic Fuzzy C-means Classification *J.Med. Sig. & Sen.* Vol.1, Issue 3(2011),149-155.
- [12] R. Khayati, M. Vafadust, F. Towhidkhah, S.M. Nabavi.,2008 “Fully automatic segmentation of multiple sclerosis lesions in brain MR FLAIR images using adaptive mixtures method and Markov random field model”, *Comput. Biol. Med.* 38 (3) (2008),379–390.
- [13] Ouadfel, S., Batouche, M.,2003 MRF-based image segmentation using ant colony system. *J. Electron. Lett. Comput. Vis. Image Anal.* 2(2003),12–24.

Comparison of Segmentation Techniques for Identification of Microcalcification clusters in Breast Tomograms

Rajalakshmi Thyagarajan, Dr. S. Murugavalli
Sathyabama University, Panimalar Engineering College, Chennai
raji_312@yahoo.co.in, murugavalli26@rediffmail.com

Abstract

In Digital Breast Tomograms (DBT) obtained from the raw images reconstructed using Filtered Back Projection (FBP) Reconstruction technique are considered in this work, as Filtered back projection is a Fourier Transform based reconstruction technique that produces accurate and less noisy DBT images. Breast is composed of soft non cancerous anatomical structures such as connective tissue, glandular tissue, contractile tissue, chest muscle and skin. Microcalcifications are basically calcium deposits, that tend to be the result of a genetic mutation somewhere in the breast tissue, or they occur due to other conditions also. Features like the size, distribution, form, and density of microcalcifications give clues as to the potentially malignant nature of the tissue where it occurs. Segmentation of a cancerous i.e., an MC region from the non cancerous tissue is a must for analyzing its feature and hence classify as benign or malignant. In our work popular clustering segmentation techniques used for medical images namely the Fuzzy C Means (FCM) and Expectation Maximization (EM), were considered. The comparison of both the methods suggested

that EM method would give more accurate segmentation results. EM segmentation gave greater sensitivity values than FCM. The tomograms were subjected for segmentation of the microcalcification content in each of the slices.

General Terms

Image Processing

Keywords

Digital Breast Tomosynthesis, Microcalcification, Segmentation, Clustering techniques, Fuzzy C Means, Expectation Maximization.

1. Introduction

Breast cancer is the most common cancer diagnosed in women worldwide, ranking second in both sexes combined. An estimated 1.38 million women across the world were diagnosed with breast cancer in 2008, accounting for nearly a quarter (23%) of all cancers diagnosed in women and 11% of the total in men and women. Breast cancer is also the most common cause of death from cancer in women worldwide and ranking fifth in both sexes combined, estimated to be responsible for almost 460,000 deaths in 2008[1]. The above worldwide statistics were taken from

the International Agency for Research on Cancer GLOBOCAN database (version 1.2).

Mortality rate of Breast cancer can definitely be brought down if it is detected early. Early detection of breast cancer is possible by the identification of the fine microcalcifications.

Mammography is the only method that helps in identifying microcalcifications and hence leads to early breast cancer detection among the various methods of breast cancer detection such as MRI, Ultrasound, Mammography, CT scan, etc. But the conventional 2D mammography has a severe limitation of decrease in contrast of structures due to the superimposition of overlying tissue and this leads to false positives and false negatives. Digital Breast Tomosynthesis (DBT), a 3D mammographic technique, is a new modality for breast imaging that overcomes the limitation of planar mammography.

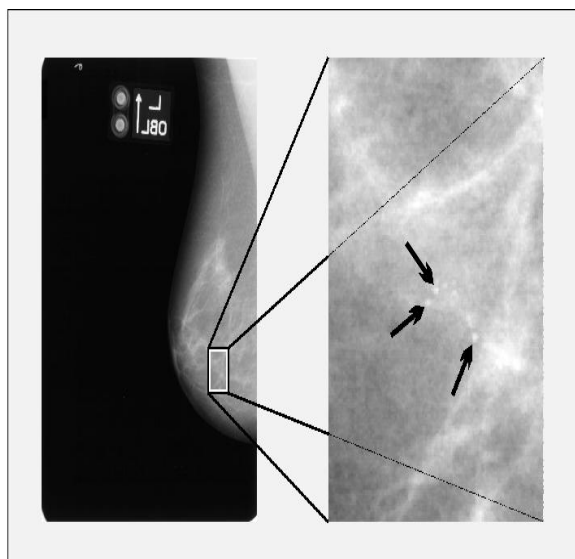


Figure 1: A Region of Clustered Microcalcifications within a Malign Tumor

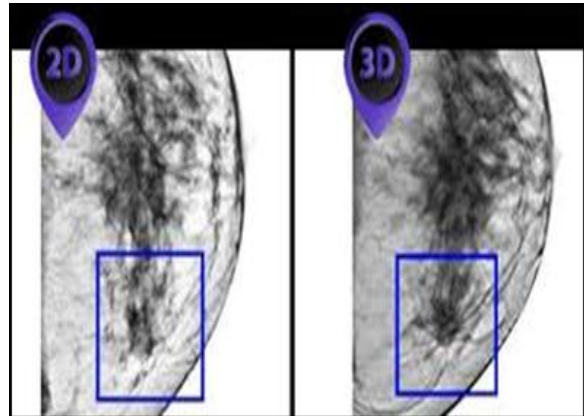


Fig 2: 2-D versus 3-D Mammogram

Digital Breast Tomosynthesis (DBT) is a tomographic technique that permits acquisition of a limited number of projections over a limited angular range with dose levels not exceeding those of conventional tomography. The two dimensional projections can then provide three-dimensional information of the imaged object using simple reconstruction algorithms [2]. Digital Tomosynthesis can prove to be very useful for imaging the breast in an attempt to optimize the detection and characterization of lesions particularly in dense breasts [3] and has the potential to reduce the recall rate [3]. In addition to all the above advantages, DBT can also effectively represent microcalcification clusters at an early stage.

Many important parameters for breast tomosynthesis have an effect on quality of 3D data. They are number of projection images, total dose of the tomosynthesis study, slice thickness, number of slices, type of detector used, radiation source, X-ray tube, quality of X-ray beam, acquisition time, reconstruction algorithms, reconstruction time, compression force, post processing and 3D workstation [5].

2.Method

The 3D reconstruction may result in noisy datasets. In order to eliminate reconstruction noise, a few preprocessing steps namely Bilateral filtering, Unsharp masking and anisotropic diffusion filtering are included to filter the out of plane artifacts, edge, contour and boundary preservation and noise removal. Then segmentation was carried out separately using FCM and EM algorithms. A fuzzy set correspond to continuously - valued logic: All shades of grey between Black (=1) and White (=0). Adaptive histogram equalization is done to the preprocessed image for the purpose of edge enhancement. Then, the Fuzzy C Means is applied to the preprocessed image. Masks generated from FCM clustering resulted in isolated pixels that correspond to pixel gray levels similar to the MC. Hence, Morphological operations were required. They were performed for the removal of salt and pepper noise and residual removal and mask smoothing. Background correction was a must as the MC was mistaken for background pixels and vice versa. It was performed along x-y and y-z plane. Expectation Maximization was then done in two steps namely the E – Step and the M – Step. The EM cycle begins with an Expectation step which is defined by the following equation:

$$E[Z_{ij}] = \frac{p(x=x_i|\mu=\mu_j)}{\sum_{n=1}^k p(x=x_i|\mu=\mu_n)} \quad \text{---(1)}$$

$$= \frac{e^{-\frac{1}{2\sigma^2}(x_i-\mu_j)^2}}{\sum_{n=1}^k e^{-\frac{1}{2\sigma^2}(x_i-\mu_n)^2}} \quad \text{---(2)}$$

Equation(1) states that the expectations or weight for pixel z with respect to partition j equals the probability that x is pixel x_i given that μ is partition μ_i divided by the sum over all partitions k of the same previously described probability. This leads to the lower expression for the weights. The sigma squared seen in the second expression (2) represents the covariance of the pixel data. Once the E step has been performed and every pixel has a weight or expectation for each partition, the M step or maximization step begins. This step is defined by the following equation:

$$\mu_j \leftarrow \frac{1}{m} \sum_{i=1}^m E[Z_{ij}] x_i \quad \text{---(3)}$$

Equation(3) states that the partition value j is changed to the weighted average of the pixel values where the weights are the weights from the E step for this particular partition. This EM cycle is repeated for each new set of partitions until, the partition values no longer change by a significant amount. The algorithm applied to a single tomogram is carried on to a sequence of data for segmentation of microcalcifications from the tomograms. The tomograms were acquired from a private hospital at Chennai from 4 patients.

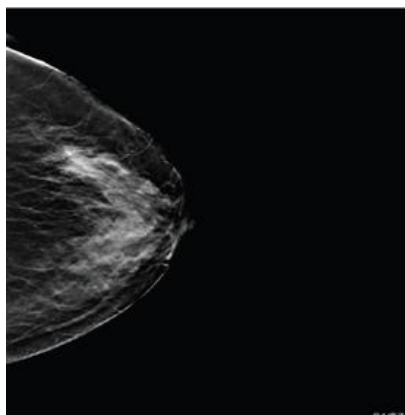


Fig 3: Input Image

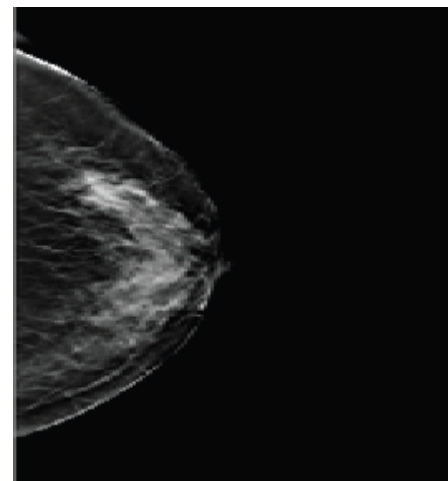


Fig 6: After Median Filtering

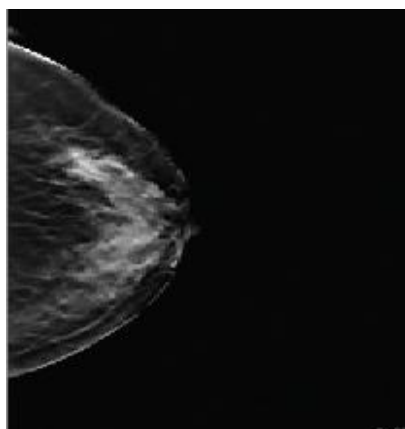


Fig 4: After Bilateral Filtering

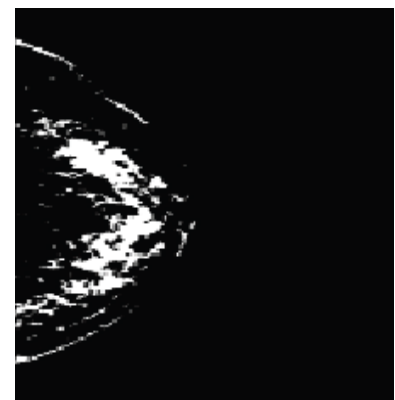


Fig 7: After FCM Segmentation

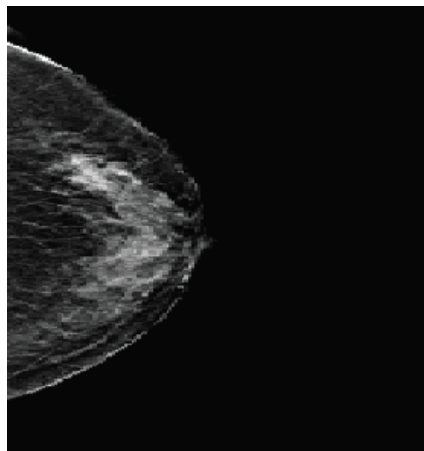


Fig 5: After Unsharp Masking

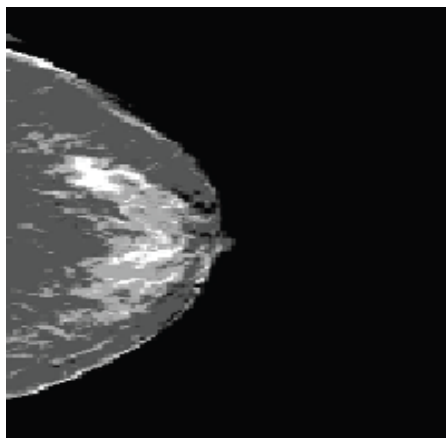


Fig 8: After EM Segmentation

3. Results and Discussions

In this work, FCM and EM segmentation for microcalcification identification is done. Both the segmentation methods have given good results in their own way. The soft tissues of the breast are clearly distinguished from the microcalcifications. The performance of the two clustering techniques is compared with the values of sensitivity calculated. The sensitivity of a clinical test refers to the ability of the test to correctly identify those patients with the disease. Sensitivity is given by, True Positives/(True Positives + False Negatives). A test with 100% sensitivity correctly identifies all patients with the disease.

Out of the 4 samples considered, for Sample 1, the sensitivity value using FCM was found to be 0.9776.

For sample 1, the sensitivity value using Expectation Maximization segmentation, was found to be 0.9801. The performance based on

sensitivity values obtained for Fuzzy C Means and Expectation Maximization were found to be very close. However, for Sample 1, EM scored over FCM with a marginal difference of 0.0025.

Table 1: Sensitivity Values for FCM and EM Techniques

Sample No.	FCM Sensitivity	EM Sensitivity
Sample 1	0.9776	0.9801
Sample 2	0.9802	0.9811
Sample 3	0.9764	0.9802
Sample 4	0.9758	0.9803

After an image is input to MATLAB, it is automatically considered for processing sequentially and gives way for an efficient segmentation. FCM gave good results in case of noisy reconstructed images and EM proved efficient in case of incomplete datasets. EM showed better performance with a sensitivity value of 0.9802 than FCM which has a sensitivity value of 0.9764. However, the difference in performance was marginal. EM not only segmented the microcalcifications but also the other anatomical structures of the breast. The approach discussed in our work is adaptable for efficient and accurate feature extraction using Gray Level Co-occurrence Matrix and classification of tumor cells into malignant and benign which is proposed as our future work.

4. Conclusion

As the next step, we propose to work on the feature extraction in the segmented tomograms. Gray Level Co-occurrence Matrix will be used for the same. Features such auto correlation, energy, entropy, homogeneity are to be extracted which will be given to the classification step where two phases are involved, namely, the training phase and the testing phase. The features extracted from tomograms in training database are compared with the features extracted from the sample tomograms. This will lead to an efficient classification step as well.

5..Acknowledgments

The images accompanied with no personal details such as name, age etcetera of the patients were obtained from a private hospital in Chennai. We thank the private hospital authorities for providing us with the FBP reconstructed 3D mammogram samples for purely research purposes. Since personal details and identity of the patients were not disclosed ethical clearance issues was not addressed.

6.References

- [1] Statistics from the International Agency for Research on Cancer GLOBOCAN database (version 1.2)
- [2] L. Niklason et al., "Digital tomosynthesis in breast imaging", Radiology, vol. 205, pp.399-406, 1997
- [3] X. Gong et al., "A computer simulation study comparing lesion detection accuracy with digital mammography, breast tomosynthesis, and cone-beam CT breast imaging", Med Phys, vol.33, pp.1041-1052, 2006
- [4] D. Gur et al., "Digital breast tomosynthesis:observer performance study", AJR Am J Roentgenol, vol. 193, pp. 586-591, 2009
- [5] Mari Varjonen, "Three-Dimensional Digital Breast Tomosynthesis in the Early Diagnosis and Detection of Breast Cancer", Springer, 2006, Volume 4046/2006
- [6] Berkman Sahiner, Heang-Ping Chan, Lubomir M. Hadjiiski, Mark A. Helvie, Jun Wei, Chuan Zhou, and Yao Lu, "Computer-aided detection of clustered microcalcifications in digital breast tomosynthesis: A 3D approach", Department of Radiology, University of Michigan, Ann Arbor, Michigan 48109 (Received 16 April 2011; accepted 19 October 2011; revised 28 September 2011; published online 9 December 2011)
- [7] Richard H. Moore, Daniel B. Kopans, Heang-Ping Chan, Yi-Ta Wu, Berkman Sahiner, Jun Wei, Mark A. Helvie, Yiheng Zhang, Lubomir Hadjiiski and Ted Way, "Characterization of masses in digital breast tomosynthesis: Comparison of machine learning in projection views and reconstructed slices", Department of Radiology, Massachusetts General Hospital, Boston, Massachusetts 02114 (Received 7 January 2010; accepted 3 May 2010; revised 31 March 2010; published online 15 June 2010)
- [8] Reiser I, Nishikawa RM, Giger ML, Wu T, Rafferty E, Moore RH, Kopans DB, "Computerized detection of mass lesions

- in digital breast tomosynthesis images using two- and three dimensional radial gradient index segmentation.”, 2004 Oct;3(5):437-41.PMID:15453808
- [9] T. Wu, A. Stewart, M. Stanton, T. McCauley, W. Phillips, D. B. Kopans, R. H. Moore, J. W. Eberhard, B. Opsahl-Ong, L. Niklason, and M. B. Williams, “Tomographic mammography using a limited number of low-dose cone-beam projection images,” Med. Phys. 30, pp. 365–380, 2003.
- [10] E. J. Candès, J. Romberg, and T. Tao, “Robust uncertainty principles: Exact signal reconstruction from highly incomplete frequency information,” IEEE Trans. Inf. Theory 52, 2006.
- [11] I. Reiser, J. Bian, R. M. Nishikawa, E. Y. Sidky, and X. Pan, Department of Radiology, The University of Chicago, “Comparison of reconstruction algorithms for digital breast tomosynthesis”, Med. Phys., 33:3781– 3795, 2009
- [12] Mini Das, Howard C. Gifford, Member, IEEE, J. Michael O'Connor, Member, IEEE, and Stephen J. Glick, Member, IEEE, “Penalized Maximum Likelihood Reconstruction For Improved Microcalcification Detection in Breast Tomosynthesis”, 2010 IEEE.
- [13] Weihua Zhou , Xin Qian , Jianping Lu, Otto Zhou c,d, Ying Chen, “Multi-beam X-ray source breast tomosynthesis reconstruction with different algorithms”, Proc. of SPIE Vol. 7622, 76220H · © 2010 SPIE CCC code: 1605-7422/10/\$18 · doi: 10.1117/12.844295

MEDICAL IMAGE FUSION USING EVOLVABLE HISTOGRAM EQUALIZATION

S.Kalimuthu¹,A.Nandini²

Department of Electronics and Communication Engineering,
Saveetha Engineering College, Thandalam, Chennai – 602 105,Tamilnadu,India.

kalimuthusubbarayan@gmail.com

Abstract

A medical medical image enhancement technique to improve the visual appearance based upon evolvable hardware is presented. And then the enhanced image of two different modalities are fused. Improving visual appearance is achieved by evolved histogram stretching transformation. The performance is compared with the classical histogram equalization method using traditional measures of enhancement. And then the results of image fusion after enhancing the image is shown.

Index term-HE-Histogram Equalization, EvoHE-Evolvable Hardware based Histogram Equalization, RMSC-Root Mean Square Contrast, H-Entropy, AMBE-Absolute Mean Brightness Error image enhancement fusion

I .Introduction

Image fusion is the process of combining information from two or more images of a scene into a single composite image that is more informative and is more suitable for visual perception or computer processing [1]. The objective in image fusion is to reduce uncertainty and minimize redundancy in the output while maximizing relevant information particular to an application or task. Given the

Now a day's digital images have enveloped the complete world. The digital cameras which are main source of digital images are widely available in the market in cheap ranges. Sometimes the image taken from a digital camera is not of quality and it required some enhancement[2]. There exist many techniques that can enhance a digital image without spoiling it. First of all, let me tell you that the enhancement methods can broadly be divided in to the following two categories as Spatial Domain Methods, and Frequency Domain Methods[2].

In spatial domain techniques, we directly deal with the image pixels. The pixel values are manipulated to achieve desired enhancement. In frequency domain methods, the image is first transferred in to frequency domain. It means that, the Fourier Transform of the image is computed first. All the enhancement operations are performed on the Fourier transform of the image and then the Inverse Fourier transform is performed to get the resultant image[2].

Before we proceed for the further discussion, I must tell you that we will consider only gray level images. The same theory can be extended for the color images too. A digital gray image can have pixel values in the range of 0 to



255[2]. The basic block diagram of the overall process is shown in the figure given below. The two input images are enhanced using evolvable hardware and then the enhanced images are fused together[3][4].

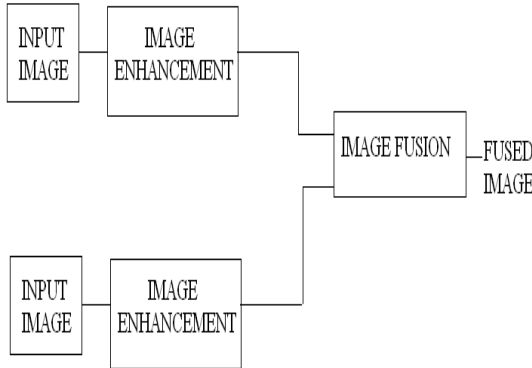


Fig: Block Diagram

II. Evolvable Hardware

In this section, we first present the detail of Evolvable Hardware based Histogram Equalization (EvoHE) [3], and then we will introduce the measures applied for performance comparison[5].

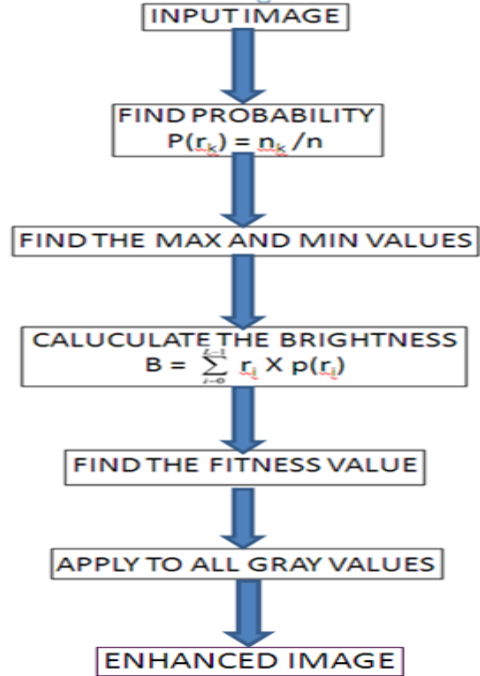


Fig: Steps to Enhance the Image

The probability of each gray value is obtained using the formula

$$p(r_k) = \frac{n_k}{n} \quad k = 0, 1, 2, \dots, L-1$$

- $P(r_k)$ -> Probability of occurrence of gray level.
- n_k -> Total number of pixels with gray level r_k
- n -> Total number of pixels.

The probability is found for all the gray values in the image and are stored in a matrix with the similar size as the input image.[5]

Next step is to find the upper and lower limit of the image, upper and lower limit is the maximum and the minimum value of gray value in the given input image. For example in general for a 8 bit image the image can have value from

0 to 255 then the upper limit is 255 and the lower limit is 0[5]. We can use certain algorithm to find the upper and lower limit of the image because the general case is not applicable every time.

Brightness of the image is calculated using the formula as shown below.

$$brightness = \sum_{i=0}^{L-1} r_i \times p(r_i)$$

Where we already know the r_i and $p(r_i)$ is the gray value and the probability of the gray value respectively. The brightness is found for all the gray values and stored in the matrix form similar to the input image values of the image the gray value should get subtracted by minimum gray value if the brightness of the image is less than or equal to $L/2$ or the maximum value should be get subtracted by the gray value if brightness is greater than $L/2$. This condition is applied to all the gray values and the image is stored. The above paragraph is clearly given in the formula as below,

$$r'_i = \begin{cases} r_i - G_{\min} & brightness \leq \frac{L}{2} \\ G_{\max} - r_i & brightness > \frac{L}{2} \end{cases} \quad i \in [0, L-1]$$

The final step is to find the fitness value that is used to transform the image. Now the new upper limit and lower limit is found for the image obtained by the above transformation. The fitness value is obtained by the formula given below [3][5].

$$fitness = \begin{cases} \frac{G_m}{L-1} & 0 \leq G_m \leq L-1 \\ 0 & otherwise \end{cases}$$

Now after calculating the fitness value we need to apply this value to image and the output image obtained after this transformation is enhanced image obtained using the evolvable hardware[5][6].

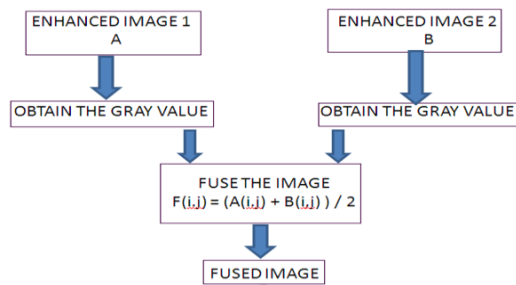


Fig: Steps to Fuse the Images

Now the enhanced image of two modalities of same image are fused together the method for fusing are average method[7] the another technique is the maximum method[8], it is used to scan through the elements of the array and updating a provisional maximum until the last element is reached. Here we going to find the maximum pixel value by comparing the pixels in the two images and the maximum value is used to

form the fused image. Consider two images denoted as $A(i,j)$ and $B(i,j)$ then fusion is done by

$$F(i,j) = \text{Max } (A(i,j), B(i,j))$$

$F(i,j)$ is the fused image[8].

The pixels in the both the images is compared by element by element and maximum value is given to form the fused image like this it continues till the last pixel of the image.

III. Performance Parameters

The three parameters used for the measurement are Entropy, Absolute Mean Brightness Error, and Root mean square Contrast. AMBE should be as low as possible, it is calculated using the formula as shown below

$$AMBE = B(o) - B(p)$$

Where $B(o)$ denotes the mean brightness of the original image and $B(p)$ denotes the mean brightness of the enhanced image. The second measure is the Discrete Entropy it is denoted as the H , entropy is used to measure the content of the image, the larger the entropy value indicates the more detail in the image. The method which has higher entropy is said to be the best method. It is measured using the formula[5].

$$H = \sum_{r=0}^{L-1} p(r) \log_2 p(r) \quad \forall h(r) \neq 0$$

The third measure is the root mean square contrast and it is obtained by the formula as shown below

$$RMSC = \sum_{i=0}^{L-1} (r_i - B)^2 p(r_i)$$

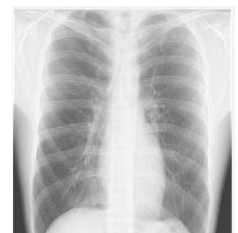
Where B is the mean brightness of the image. The method which has the low RMSC value is said to be the best method[5].

IV. Experimental Results

Image enhancement using Evolvable Hardware algorithm[5] is applied to many X-Ray images and CT scan images and the results are shown in the figure. The figure shows the original image and histogram equalization processed image[9] and the histogram equalization using evolvable hardware processed image are shown[5][6]. After the image has been enhanced the two images are fused using the maximum method and the parameters used to find the best method are calculated and all those three methods are compared and tabulated and shown.



Original image
image

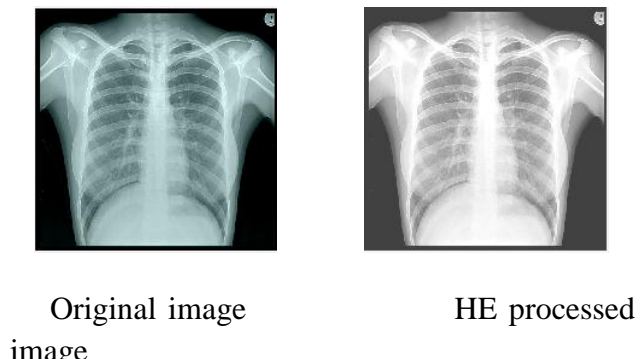


HE processed



EvoHE processed image

(a) chest



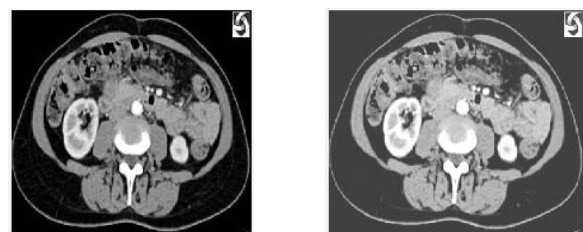
Parameters	HE	Evo HE
AMBE	85	7
Entropy	2.63712	2.72806
RMSC	54	36



(a) Chest

Evo HE processed image

(b) chest 1



EvoHE processed image

(c) CT scan

Fig: Original Image and Enhanced Image

Parameters	HE	EvoHE
AMBE	51	9
Entropy	6.18768	6.40104
RMSC	96	64

(b) Chest 1

Parameters	HE	EvoHE
AMBE	82	6
Entropy	2.7978	2.8942
RMSC	59	39

(c) CT scan

Tabular Column: Comparision of HE and EvoHE

The final two fused images of two different modalities after enhancing output result image is shown in the output

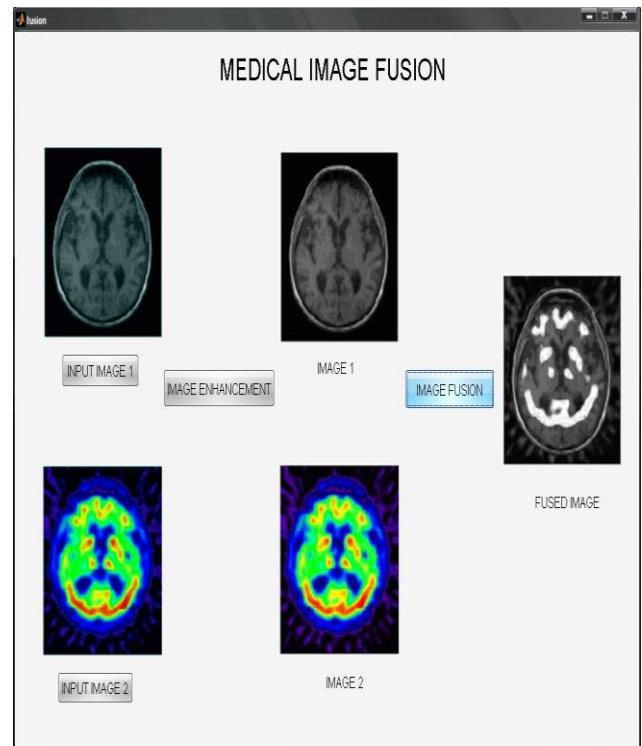


Fig: Output of Two Fused Image

V. Conclusion

Thus we have compared the two enhancement techniques using the three parameters. The histogram equalization and evolvable hardware techniques are used to enhance the image and the process is done using the MATLAB software. The original image and the enhanced image using the two techniques are shown and the parameter values are calculated for both the techniques using the same software and values are compared. Entropy is more in EvoHE than the HE method and the mean brightness deviation is also high when compared with the HE and finally the root means square contrast value is less when compared with HE. On

comparing all these three parameters it is clearly shown that the evolvable hardware technique is best method on comparing with the histogram equalization method. And thus the image is enhanced using EvoHE method and the two images are fused using the maximum method.

VI. References

- [1] P.R. Hill, D.R. Bull and C.N. Canagarajah,” Image Fusion using a New Framework for Complex Wavelet Transforms”, Dept. of Electrical and Electronic Engineering, the University of Bristol, Bristol, BS5 1UB, UK.
- [2] R.C. Gonzalez, R.E. Woods, Digital Image Processing, 2nd ed., Person Education, 2002.
- [3] Gordon Hollingworth, Andy Tyrrell, and Steve Smith “Simulation of Evolvable Hardware to Solve Low Level Image Processing Tasks
- [4] Guihong Qu, Dali Zhang and Pingfan Yan, “medical image fusion by wavelet transform
- [5] Jie Li, “Evolvable Hardware based Gray- level image Enhancement “ 2009 NASA/ESA conference on Adaptive Hardware and systems.
- [6] Jim Torresen “An Evolvable Hardware Tutorial”
- [7] Guihong Qu, Dali Zhang and Pingfan Yan, “medical image fusion by wavelet transform
- [8] modulus maxima”, 13 August 2001 / Vol. 9, No. 4 / optics express 184
- [9] Hojat yeganeh, Ali Ziae, Amirhossein Rezaie, “A Novel Approach for Contrast Enhancement Based on Histogram Equalization” may 13-15, 2008 Kuala Lumpur Malaysia.
- [10] S.Chen, A.R. Ramli, “Minimum mean brightness error bi-histogram equalization in contrast enhancement”, IEEE Trans. On Consumer Electronics. Vol. 49(4), 2003, pp. 1310-1319.

FPGA implementation of a Genetic Algorithm based Scheme for Optimal Anaesthetic delivery

Supraja. S, Varun. M, Kamalanand. K

Dept. of Instrumentation Engg.,MIT Campus, Anna University,Chennai.

ssrimathi11@gmail.com,emvee92@gmail.com,kamalanand@mitindia.edu

Abstract

The administration of adequate anaesthesia is important for avoiding overdosing of patients which results in changes in vital physiological parameters. However, optimization of anaesthetic dosage is challenging due to the inherent patient variability and associated nonlinearities in the system. In this work, the anaesthetic dosage is optimized using Genetic Algorithm (GA) and the compartmental model of Depth of Anaesthesia (DoA). The performance of the developed strategy is compared with the conventional method. Further, the proposed control strategy has been implemented using Field Programmable Gate Array (FPGA) for automated anaesthetic delivery. Results demonstrate that the proposed method is efficient for control of DoA. The percentage accuracy of the proposed strategy was found to be 95.7% with a settling time of 92 seconds. This work appears to be of high surgical relevance since the DoA level plays a vital role in all surgical procedures.

Keywords

Depth of Anaesthesia, Genetic Algorithm, Field Programmable Gate Array

1. Introduction

The monitoring and closed loop control of the depth of anaesthesia is fundamental to most of the surgical procedures. Two major factors

namely the anaesthetic and the surgical stimulation affects the depth of anaesthesia [1]. The anaesthetic comprises analgesia, unconsciousness and muscle relaxation while the surgical stimulation escalates the degree of consciousness by activating the patient's sympathetic nervous system [2]. At present general anaesthetics that include induction agents such as propofol, etomidate and pentothal, inhalation agents such as isoflurane, desflurane and sevoflurane with nitrous oxide and paralyzing agents such as succinylcholine, rocuronium and vecuronium are commercially available.

Adequate depth of anaesthesia is the sufficient amount of the anaesthetic agent that is required to secure unconsciousness and muscle relaxation without affecting vital organ functions of the patient [3]. Although the changes in the physiological parameters like heart rate, respiration rate and lacrimation or diaphoresis indicate the depth of anaesthesia, they are unreliable indicators of the degree of consciousness [4]. For an efficient automated control strategy, it is highly essential to optimize anaesthetic dosage for achieving a balance between insensitivity to pain and maintenance of adequate respiration without cardiac depression [5].

Westenskow D.R (1997) [6] employed a closed-loop PID control scheme to control the



depth of anaesthesia. Sakai T *et al.* (2000) [7] used Bispectral Index (BIS) as the controlled variable and developed a PID control system for propofol administration. Absalom A.R *et al.* (2002) [8] developed a propofol targeting central plasma concentration-controlled infusion system as the control actuator in addition to the control scheme. Anna S and Wen P (2010) [9] employed Internal Model Control techniques to control DoA using BIS as the controlled variable. Abdulla S and Wen P (2012) [10] investigated the use of a robust dead beat controller for DoA control. However, the available control schemes still face few stability problems and optimization of anaesthetic dose is an important field of research.

In recent years, optimization techniques based on evolution and swarm intelligence is used for solving complex optimization problems since such methods are robust, flexible, fault tolerant, scalable and highly parallelizable [11].

The objective of this work is to optimize the anaesthetic dosage using an efficient evolutionary optimization technique known as genetic algorithm, in conjunction with the mathematical model of DoA and to implement the proposed scheme on FPGA for automated anaesthetic delivery.

2. Methodology

2.1 Compartmental model of DOA

2.1.1 Pharmacokinetic (PK) model

The study of the absorption, distribution, metabolism and elimination of the drugs by the human body is defined as pharmacokinetics [12]. To derive the PK model, it is assumed that the human body is divided into several compartments and a homogeneous drug concentration prevails in

each compartment [13]. The following state space model defines the relation between the propofol infusion rate (u) and propofol plasma concentration (c_p^{prop})

$$\left. \begin{array}{l} \dot{x}_1 = A_1 x_1 + B_1 u \\ c_p^{prop} = C_1 x_1 \end{array} \right\} \quad (1)$$

where,

$$A_1 = \begin{pmatrix} -k_{10} & -k_{12} & -k_{13} & k_{21} & k_{11} \\ k_{12} & & -k_{21} & 0 & \\ k_{13} & 0 & & -k_{31} & \end{pmatrix}, B_1 = \begin{pmatrix} \frac{10^4}{3600} \\ 0 \\ 0 \end{pmatrix}, C_1 = \begin{pmatrix} 1 \\ \frac{1}{1000 \times v_1} & 0 & 0 \end{pmatrix}$$

where, k_{10} , k_{12} , k_{13} , k_{21} and k_{31} are the patient specific parameters of the system which influence the BIS sensitivity and v_1 is the volume of the first compartment.

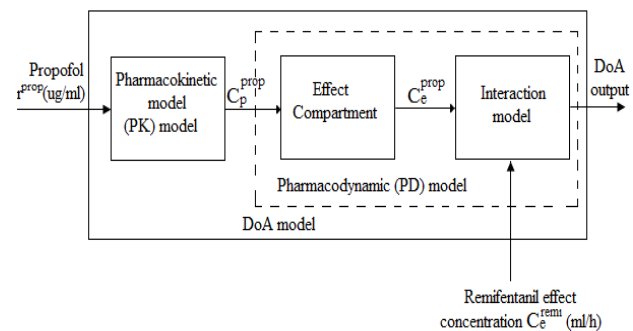


Fig 1: Compartmental DOA model

2.1.2 Pharmacodynamic (PD) model

Pharmacodynamics represents the relationship between drug concentration and the effect of drugs [14]. The following state space model of Pharmacodynamics relates the propofol plasma concentration and the propofol effect concentration.

$$\left. \begin{array}{l} \dot{x}_2 = A_2 x_2 + B_2 c_p^{prop} \\ c_e^{prop} = C_2 x_2 \end{array} \right\} \quad (2)$$

where $A_2 = -K_{e0}$, $B_2 = K_{e0}$ and $C_2 = 1$. The model can be simplified as follows:

$$C_e(s) = \frac{k_{e0}}{s + k_{e0}} C_p(s) \quad (3)$$

where, k_{e0} is the inverse of the effect-site compartment time constant. Further, Hill's equation [15] is used to define the relation between the effect-site concentration (C_e) and DoA output (E).

$$E(t) = E_0 - E_{\max} \frac{C_e^\gamma}{EC_{50}^\gamma + C_e^\gamma} \quad (4)$$

where, EC_{50} is the half-maximal effective concentration and γ is a patient specific parameter of the system. The block diagram of the compartmental DoA model is shown in Fig 1.

2.2 Genetic Algorithm based optimization of anaesthetic dosage

Genetic Algorithm is an evolutionary, adaptive global search optimization technique based on the theory of evolution. The first step in GA involves the selection of an initial population comprising a number of chromosomes [16]. The performance of each chromosome representing the solution to the problem is evaluated by means of a fitness function.

The three main operations involved in GA are selection, crossover and mutation. Crossover and mutation facilitate new chromosomes that are better than their parents. The iterative algorithm is terminated when the optimal solution to the problem is arrived at.

The anesthetic dosage was computed using equation (5)

$$r^{prop}(t) = k_p(q(t) - E(t)) + k_i \int (q(t) - E(t)) dt + k_d \frac{d(q(t) - E(t))}{dt} \quad (5)$$

where, $r^{prop}(t)$ is the propofol infusion rate, $q(t)$ is the desired DoA level and $E(t)$ is the actual DoA level. k_p , k_i , and k_d are the constants to be estimated. The optimal values of $r^{prop}(t)$ were estimated using the following fitness function:

$$\min J = \int_0^t (q(t) - E(t))^2 dt + \int_0^t r^{prop2}(t) dt \quad (6)$$

In this work, the initial population for GA was taken as 200, the number of generations was set at 500 and the probability of crossover and mutation was specified as 0.7.

2.3 Automation of proposed strategy using CompactRIO 9004 FPGA

The huge number of parameters to be monitored in the complex surgical environment overloads the anesthesiologists with information and multitasking needs. Automation of the control strategy eliminates the need for continuous manual monitoring and provides more stable control [17]. The proposed scheme was automated using the NI Compact Rio 9004 module that consists of the following components [18]:

- CRIO FPGA core application for input, output, communication, and control,
- Time-critical loop for floating-point control, signal processing, and point-by-point decision making
- Normal-priority loop for embedded data logging, remote
- Networked host PC for remote graphical user interface, historical data logging and post-processing

The FPGA chip is connected directly to the I/O modules in a star topology thereby providing tremendous scalability and flexibility. The real-time processor is connected to the FPGA chip by a local PCI bus. NI LabVIEW is used to access and integrate all of the components of the reconfigurable I/O architecture.

In addition to the FPGA chip, CompactRIO houses a real-time processor that reliably and



deterministically executes LabVIEW Real-Time applications. In addition, it also offers multirate control, onboard data logging through communication with peripherals and execution tracing.

The DoA level monitored from the patient was connected to the first terminal of the NI 9201 analog input module. The propofol infusion rate as dictated by the control scheme was obtained from the NI 9265 analog output module. The I/O modules had built-in isolation, analog to digital/digital to analog conversion, signal conditioning circuitry, and connectivity for direct connection to industrial sensors/actuators. The proposed strategy was implemented in a timed loop using NI

LabVIEW with FPGA toolkit. The sampling period was set as 1 second. The developed Labview program was converted to VHDL file and compiled into a single bitfile. The bitfile was downloaded into the nonvolatile memory of CompactRIO. Also, a graphical user interface was developed in the PC to monitor DoA level of the patient.

Furthermore data logging algorithm was implemented in the RTC (Real Time Controller) of CompactRIO (CRIo) to log the DoA level periodically into PC dedicated to monitoring through an Ethernet connection. A first in first out memory architecture was built in the CRIo to log the acquired data

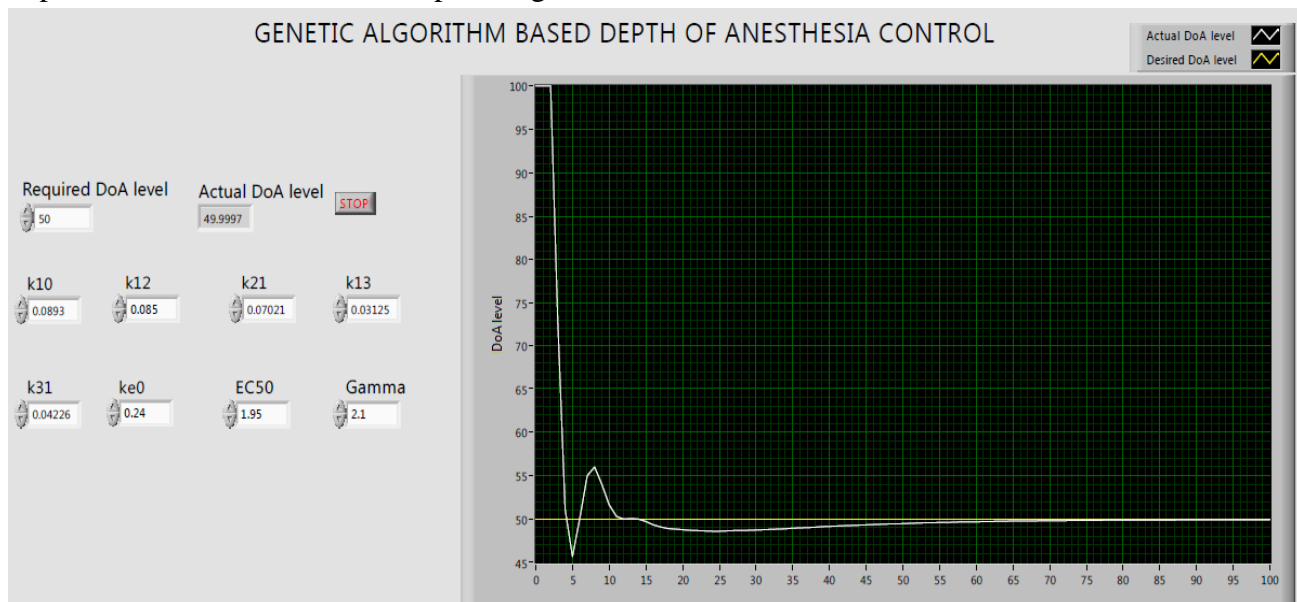


Fig 2: Graphical user interface for automated anaesthetic delivery

periodically. Two network communication paths are employed for the application: one path for sending commands from the user interface to the CRIo hardware and a second path for sending current DoA level from the CRIo hardware to the PC for display.

The developed graphical user interface for the automated scheme is shown in Fig.2. Controls are present to specify the patient specific

physiological parameters that influence the BIS sensitivity and the waveform display depicts the obtained variations in the DoA level as a function of time.

3. Results And Discussions

In this work, the DoA level is measured online and is used as the controlled variable. Initially, the patient is in fully conscious state and the

DoA level is 100%. During surgery, it is necessary to maintain the DoA level between 40% and 60%. The mid value 50% is specified as the desired DoA level for the automated control scheme.

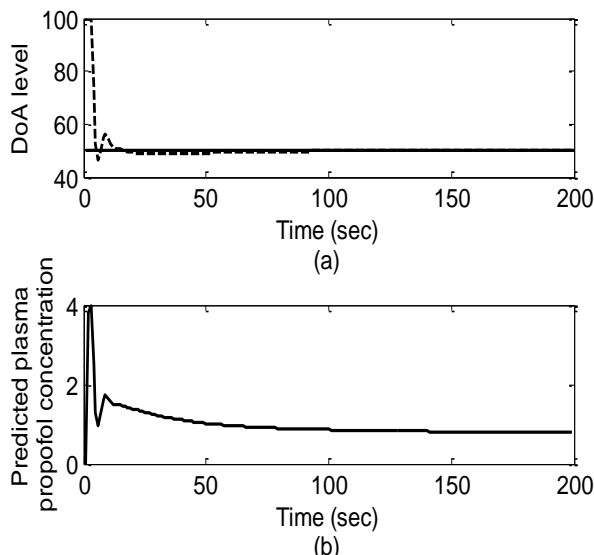


Fig 3: (a) Variation of desired (—) and actual (----) DoA level and (b) predicted plasma propofol concentration shown as a function of time for a patient

The desired DoA level and the variation of the actual DoA level is shown as a function of time Fig 3(a). Similarly, the variation of the predicted plasma propofol concentration estimated from the PK model is shown as a function of time in Fig 3(b). It is seen that the DoA level reduces with increase in the predicted plasma propofol concentration. It is observed that the predicted plasma propofol concentration for the proposed method is maintained between 1 $\mu\text{g}/\text{ml}$ and 5 $\mu\text{g}/\text{ml}$. The lower bound ensures delivery of the anaesthetic drug and the upper bound eliminates overdosing of the patient that may lead to cardiac depression.

Table 1: Performance metrics of the proposed scheme

Performance estimate	Value
Error (%)	4.33796
Settling time (seconds)	92

The mean percentage error between the actual and desired DoA level and the settling time using the proposed strategy is shown in Table 1. It is observed that the desired DoA level for the case considered, is achieved in 92 seconds.

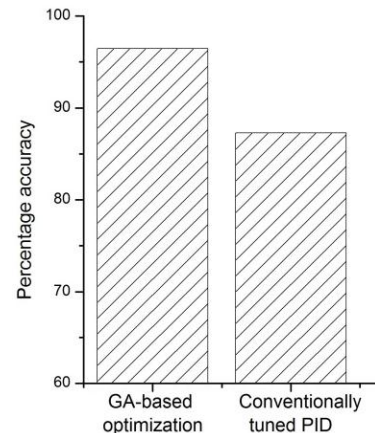


Fig 4: Comparison of accuracy for GA based scheme and conventionally tuned PID.

The performance of the proposed GA based optimization strategy and the conventionally tuned PID controller is compared in Fig 4. It is observed that the proposed scheme is more accurate (95.66204%) than the conventional scheme.

4. Conclusion

In order to ensure sufficient anaesthetic concentration during surgical procedures, it is necessary to regulate the propofol infusion rate to the patient. Generally, the anaesthetist determines the required anaesthetic level by observing the physical signs of the patient. But, these signs fail to be reliable indicators of

DoA thereby warranting the need for an automated, optimization-based strategy that maintains the DoA level effectively by manipulating the propofol infusion rate.

In this work, the compartmental DoA model and genetic algorithm was employed to determine the optimal anaesthetic dosage. The strategy was automated using NI Crio 9004 FPGA module. The results obtained depict that a patient can be brought from the fully conscious state (100% DoA) to the specified DoA level during surgery (40% to 60%) in 92 seconds. Further, the predicted plasma propofol concentration is maintained within the specified limits (1 - 5 µg/ml) with the obtained minimum and maximum values at 1.235 µg/ml and 3.978 µg/ml respectively. Finally, the accuracy has been analyzed using percentage integral error as the performance estimate and the efficiency of the GA based scheme over conventional methods is proved.

This work appears to be important during surgeries as the accurate administration of adequate anaesthetics is essential for maintaining the desired level of unconsciousness without affecting the functioning of vital organs and causing changes in the physiological parameters of the patient. Further, the need for continuous manual monitoring of the various physiological parameters of the patient is eliminated through the automation of the control strategy.

5. References

- [1]Grover, V.K. and Bharthi, N. 2008. Measuring depth of anaesthesia - An overview on the currently available monitoring systems. The Indian Anaesthetics Forum
- [2]Chou, Y.C., Abbod, M.F., Shieh, J.S. and Hsu, C.Y. 2010. Multivariable Fuzzy Logic/Self-organizing for anaesthesia control. Journal of Medical and Biological Engineering. vol. 30(5). 297-306.
- [3]Heier, T. and Steen, P.A. 1996. Awareness in anaesthesia: Incidence, consequences and prevention. Acta Anaesthesiologica Scandinavica. Vol. 40(9). 1073-1086.
- [4]Bressan, N., Castro, A., Bras, S., Ribeiro, L., Ferreira, D.A., Silva, A., Antunes, L. and Nunes, C.S. 2007. Modelling the dynamics of depth of anaesthesia: Cerebral State Index in dogs. Proceedings of the 15th Mediterranean Conference on Control & Automation.
- [5]Sinha, P.K and Koshy,T. 2007. Monitoring Devices for Measuring the Depth of Anaesthesia - An Overview. Indian Journal of Anaesthesia. Vol. 51(5). 365-369.
- [6]Westenskow, D.R. 1997. Fundamentals of Feedback Control: PID, Fuzzy Logic, and Neural Networks. Journal of Clinical Anaesthesia. vol. 9. 33S-35S.
- [7]Sakai, T., Matsuki, A., White, P.F. and Giesecke, A.H . 2000. Use of an EEG-bispectral closed-loop delivery system for administering propofol. Acta Anaesthesiologica Scandinavica. vol. 44. 1007-1010.
- [8]Absalom, A.R., Sutcliffe, N. and Kenny, G.N. 2002. Closed-loop Control of Anaesthesia Using Bispectral Index: Performance Assessment in Patients Undergoing Major Orthopedic Surgery



- under Combined General and Regional Anaesthesia. *Anaesthesiology*. vol. 96. 67-73.
- [9] Anna, S. and Wen, P. 2010. Depth of Anaesthesia Control using Internal Model Control Techniques. Proceedings of the IEEE/ICME International Conference on Complex Medical Engineering. 294-300.
- [10] Abdulla, S. and Wen, P. 2012. Depth of Anaesthesia Control investigation using robust deadbeat control technique. Proceedings of the IEEE/ICME International Conference on Complex Medical Engineering. 294-300.
- [11] Da San Martino, G., Cardillo, F.A., Starita, A. 2006. A new swarm intelligence algorithm for image alignment. Proceedings of Advances in Medical, Signal and Information Processing.
- [12] Alonso, H., Lemos, J.M. and Mendonça, T. A target control infusion method for neuromuscular blockade based on hybrid parameter estimation. *Engineering in Medicine and Biology Society (EMBS) 2008*. 30th Annual International Conference of the IEEE. 707-710.
- [13] Cardoso, N. and Lemos, J.M. 2008. Model Predictive control of Depth of Anaesthesia: Guidelines for controller configuration. *Engineering in Medicine and Biology Society (EMBS) 2008*. 30th Annual International Conference of the IEEE. 5822-5825.
- [14] Bibian, S. 2006. Automation in clinical anaesthesia. University Micro films International, Ann Arbor, MI, USA.
- [15] Munson, E.S. and Bowers, D.L. 1967. Effects of Hyperventilation on the Rate of Cerebral Anaesthetic Equilibration: Calculations Using a Mathematical Model. *Anaesthesiology*. Vol. 28. 377-381.
- [16] Balazs, K., Horváth, Z. and Kóczy, L.T. 2012. Different Chromosome-based Evolutionary Approaches for the Permutation Flow Shop Problem. *Acta Polytechnica Hungarica*. vol. 9(2). 115-138.
- [17] Simanski, O., Schubert, A., Kaehler, R., Jandat, M., Bajoratt, J., Hofmockel, R. and Lampe, B. 2007. Automatic drug delivery in anesthesia: From the beginning until now. Proceedings of the 15th Mediterranean Conference on Control & Automation.
- [18] Rosol, M., Pilat, A. and Turnau, A. 2011. Real-time controller design based on NI Compact-RIO. Proceedings of the International Multiconference on Computer Science and Information Technology. 825–830.

Retinal Image Analysis for Vessels and Exudates using Curvelet Transform and Clustering Techniques

Anitha Christina.A , S.Kuzhaloli ,M.S.Godwin Premi³

Department of Electronics & Telecommunication Engineering

Sathyabama University, Chennai, India

anithaantony.be@gmail.com, kuzhal_oli@yahoo.com ,godwinpremi@yahoo.com

Abstract

Diabetic-related eye disease is a major cause of blindness in the world. The complication of diabetes can also affect various parts of the body. When the small blood vessels have a high level of glucose in the retina, the vision will be blurred and can cause blindness eventually, which is known as diabetic retinopathy. Due to high blood pressure and blockage in the blood flow causes swelling in fundus, leading to the formation of exudates. This method proposes an efficient detection of vessels and exudates for retinal vasculature disorder analysis. Since intrinsic characteristics of retinal images make the blood vessel detection process difficult, this work is aimed to develop a new algorithm to detect the retinal blood vessels effectively. For accurate vessel extraction, green channel is selected. Morphology operators using multi structure elements are applied to the enhanced image in order to find the retinal image ridges. Reconstruction is performed to eliminate the ridges that are not belonging to the vessel tree while thin vessels remain unchanged. Segmentation using clustering technique is performed for exudates detection.

Keywords

Vessels and exudates detection, Morphology operators, Segmentation.

1. Introduction

Diabetic retinopathy is considered as a retinal vasculature disorder that occurs in majority of the patients with diabetes mellitus [1]. Although the diabetes cannot be prevented by itself it can be diagnosed in early stages to avoid complications. According to the estimation made by World health organization (WHO), the number of adults with diabetes would increase from 135 million in 1995 to 300 million in 2025 [2].

This project aims to detect the presence of abnormalities in the retina such as the structure of blood vessels and exudates. The color image of the fundus is captured by DRS and it is being processed for accurate extraction of vessels and exudates which was recommended by doctors for their better observation. Here plane separation and color enhancement techniques are used. The enhanced image is then processed using morphological techniques. Then by using filtering techniques, the unwanted vessels are removed for better vessel extraction. K-means clustering techniques are used for the extraction of exudates.



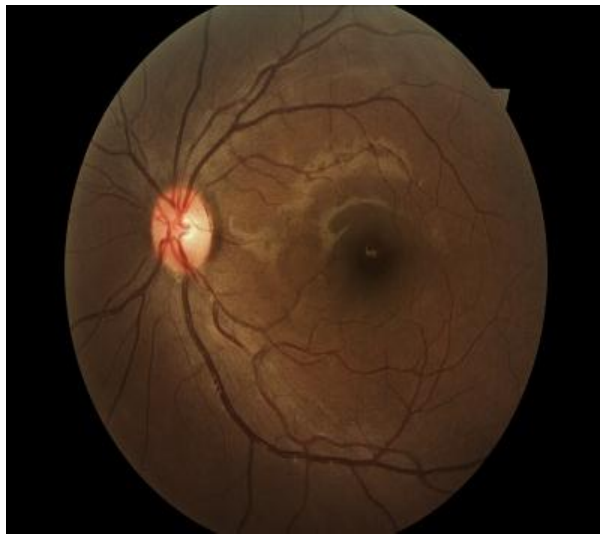


Fig.1 Retinal Image using DRS camera

2. Function Of Human Eye

The human eye is similar to the camera, where the visual information is encoded and then transmitted to the brain through the optic nerve [4]. Fig.1 represents the normal human eye that was captured using DRS camera. Diabetic retinopathy is a complicated disease for diabetic patients, which may lead to loss of vision. Regular screening is essential to detect the early stages of diabetic retinopathy for timely treatment and to avoid further deterioration of vision.

3. Digital Retinography System

Advanced version of fundus camera is the DRS. Fundus images are captured using DRS by non-mydriatic fundus camera with 45° × 40° field of view. It takes less than 30sec to capture an image. It is fully automated device that captures images without pupil dilation. Eye care providers use these images for screening of diabetic retinopathy [9].

3.1 Benefits

Minimal operator skill with software guided operations. Easy to transfer images to network and ipad for remote views[8].

3.2 Technical Specifications

Embedded pc with Wi-Fi and Ethernet connectivity operates at a distance of 37mm and sensor size of 5mpixel. Its sensor resolution is 48 pixels / deg, whereas in fundus camera it is 18.1 mega pixels. Automatic alignment is done using two pupil cameras which captures both the right eye and left eye automatically [9].

4. Proposed System

Here the combination of multi structure morphological process and segmentation technique is used effectively for retinal vessels and exudates detection.

4.1 Detection of vessels

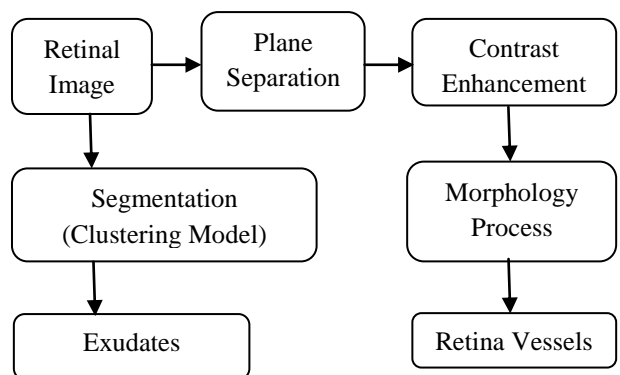


Fig.2 Block diagram for vessel detection

4.1.1 Plane separation

Images will be of three types: binary, gray scale and color image. Here fundus image will be the color image that contains RGB plane. Each plane contains 8bits/pixel. For accurate vessel extraction, green channel will be selected as in Fig.3.

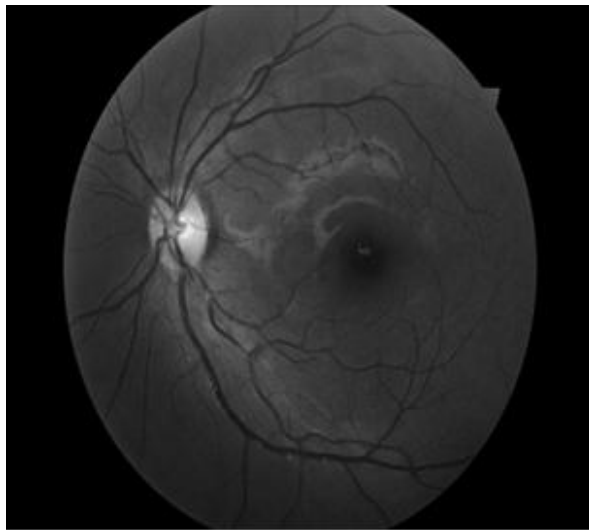


Fig.3 Green plane

4.1.2 Contrast enhancement

The separated plane is then contrast enhanced by using curvelet transform. Curvelet transform is a new multi-scale representation most suitable for objects with curves. Here tiling is performed which transforms curved lines into straight lines known as ‘Ridgelet transform’. Fast discrete curvelet transform (FDCT) uses wrapping technique which is easier than USFFT to modify each co-efficient of an input image. Using maximum co-efficient and standard deviation techniques enhancement factor is found. Enhancement factor is used for adjusting the original co-efficient and then it is matrix multiplied with the original co-efficient to form the modified co-efficient. Inverse FDCT is applied to the modified co-efficient to obtain the enhanced image shown in Fig.4.

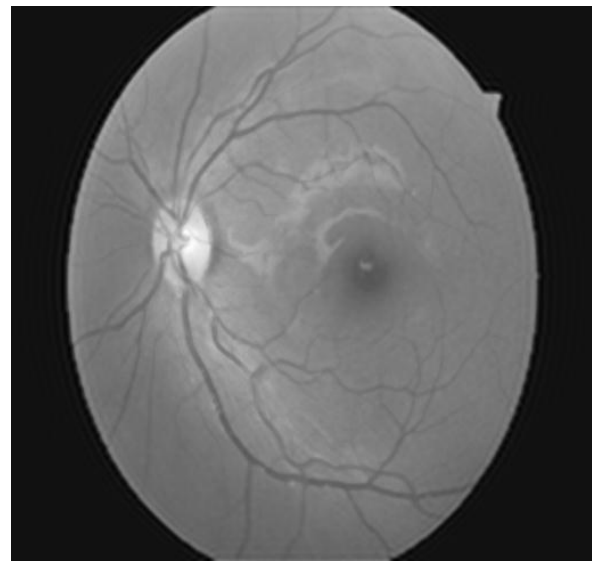


Fig.4 Contrast enhanced image

4.1.3 Morphological processing

Morphological operations are applied on enhanced images for smoothening the vessel part. It processes the image based on shapes using structural element. A structural element is a matrix consisting of only 0s and 1s that can have any arbitrary shape and size. There are several structural elements which are of line shape, square shape, rectangle, diamond, disk and ball shaped. 1s represent neighborhood pixel while 0s represent the background.

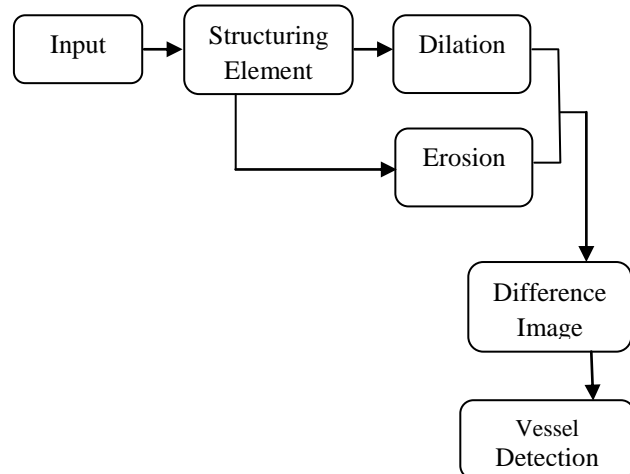


Fig.5 Process flow

4.1.4 Dilation and erosion

Depending on the structural element, the vessel edges are detected by using dilation and erosion process as shown in Fig.6. Dilation is the process of adding a pixel at object boundary based on the structural element. The output pixel value is equal to the maximum of input pixels neighborhood matrix. Erosion is the process of removing the pixel from object boundary based on the structural element. Here the output pixel value is equal to the minimum input pixels neighborhood matrix. Here, the disk structural element is used to dilate and erode the image for vessel extraction. The combination of dilation and erosion operations are performed on image with different structural elements of radius 3 and 6. The dilated and eroded images are subtracted to extract the vessels from retina fundus image.

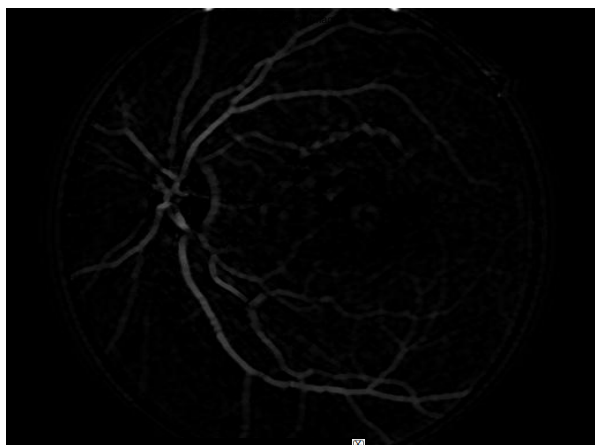


Fig.6 Difference image

4.1.5 Multi-structure morphological elements

Using multi-structure morphology elements the output image is smoothed for reducing distortion from background and increasing the edge sharpness. This is performed by image opening and closing operations with multi-structure elements. This process is known as

'Top-hat transform'. When erosion is followed by dilation then it is known as opening operation while closing operation is the dilation followed by erosion.

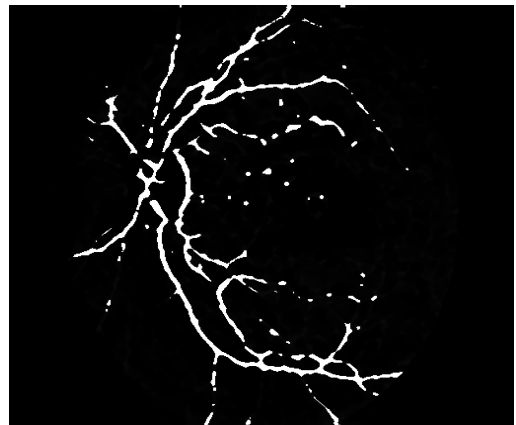


Fig.7 Retinal image with extracted vessels

4.2 Detection of Exudates

Fig.8 represents the fundus image of a patient with exudates and Fig.9 without exudates. These yellow flecks are called exudates. They are the lipid residues of serous leakage from damaged capillaries. The commonest cause is diabetes. Other causes are retinal vein occlusion, angiomas (Von Hippel-Lindau Disease), other vascular dysplasias, and radiation-induced retinal vasculopathy [3].

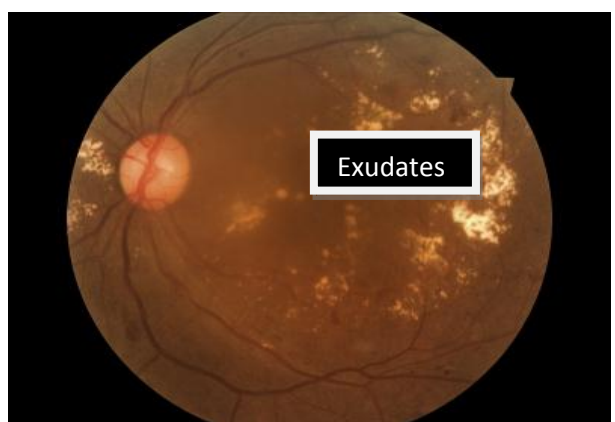


Fig.8 Retinal image with exudates



Fig.9 Retinal image without exudates

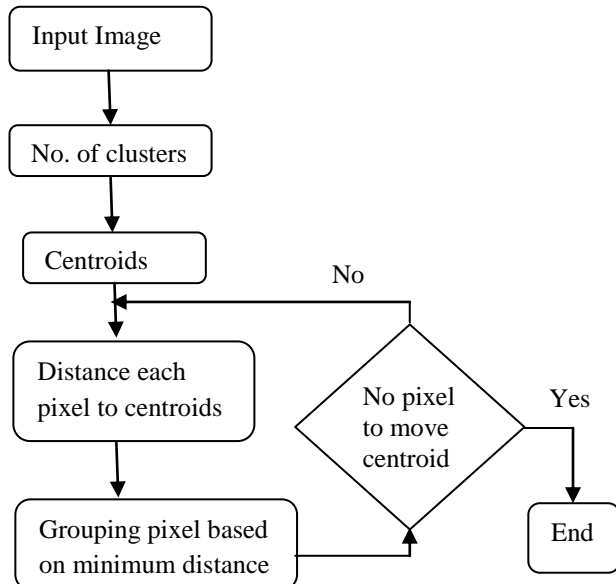


Fig.10 Block diagram for exudates detection

Fig.11 represents the block diagram for exudates detection from the fundus image. Here the input image is partitioned into multiple regions using segment techniques, where the abnormal part in the fundus image will be seen in any one of the region. Using k-means clustering technique, the abnormal parts can be classified. Here k represents number of clusters. First number of clusters will be initialized say c_1, c_2, c_3 and c_4 . Based on the number of clusters, default centroid

value is found for each cluster as shown in eqn (5). Centroid values are initialized by finding the interval value in eqn (1).

$$\text{Interval value} = \frac{\max \text{ iv} - \min \text{ iv}}{\text{no. of clusters}}$$

(1)

Where,

Max iv- Maximum Intensity variation,

Min iv- Minimum Intensity variation

Using intensity variation, the whole abnormal part is detected. Where there was more abnormalities (i.e.) diseased part, the pixel value variation will also be more.

$$\max \text{ iv} = \max (\max (\text{input}))$$

$$\min \text{ iv} = \min (\min (\text{input}))$$

$$a = \begin{bmatrix} c_1 & c_2 & c_3 \\ 1 & 2 & 3 \\ 4 & 5 & 6 \\ 7 & 8 & 9 \end{bmatrix}_{3 \times 3} \quad (2)$$

$$\min(\min(a)) \Rightarrow \min(1\ 2\ 3) \Rightarrow 1 \quad (3)$$

$$\max(\max(a)) \Rightarrow \max(7\ 8\ 9) \Rightarrow 9 \quad (4)$$

By substituting (3) and (4) in (1), Interval value can be obtained.

Assume Interval value=50, then

$$\text{Centroid} = 0 + \text{I.V} = 0 + 50 = 50$$

$$50 + \text{I.V} = 100$$

$$100 + 50 = 150$$

$$150 + 50 = 200 \quad (5)$$

c_1	c_2	c_3	c_4
[]	[]	[]	[]

Grouping pixel based on minimum distance

$$= P_{ij} - \text{Centroid}$$

(6)

Based on the difference between the intensity value of the input and the centroid, each pixel will be partitioned. The pixel value which is the nearest neighborhood of the centroid will be placed in that cluster. The centroids can be updated till the correct segmentation is done. The process will be stopped when there is correct segmentation. This can be found when the updated centroid value and the already stored centroid value become equal.

4.2.1 Post processing

Morphological operations are applied on segmented image for smoothening the exudates part, Fig.12. It processes the image based on shapes and it performs on image using ‘line’ structuring element. Dilation and erosion process will be used to enhance the exudates region by smoothening the unwanted pixels from outside region of exudates part and the output is obtained as shown in Fig.13.

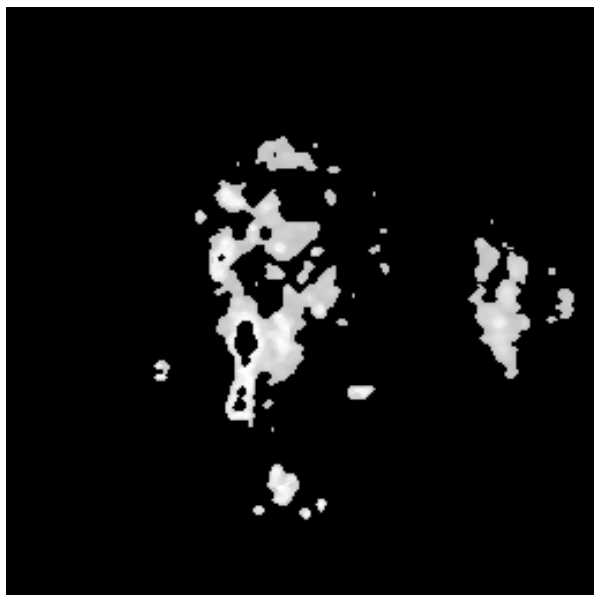


Fig.11 Image before erosion and dilation

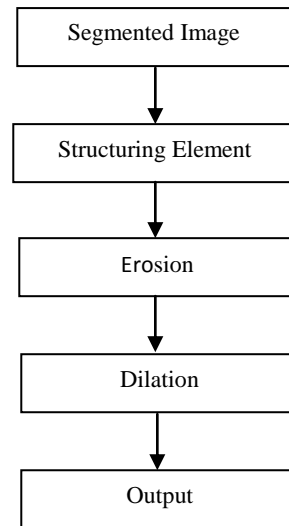


Fig.12 Post processing for segmented image

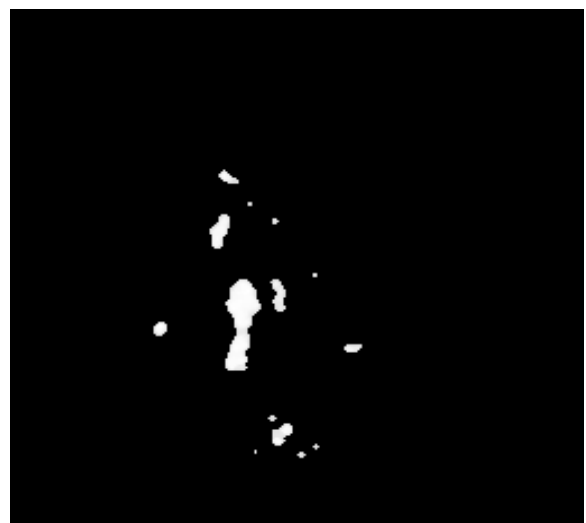


Fig.13 Retinal image with exudates detected

5. Performance Parameters

This parameter is used to find the quality of the input image in a theoretical manner, since after it is contrast enhanced. Using the parameters mean square error and peak signal

to noise ratio, the quality of the image is checked. If there is more error it means that some important details of the image are altered. This helps to find the error between input image and contrast image, in order to find the quality of the image.

$$MSE = \left(\frac{1}{M \times N} \right) \sum_{i=1}^M \sum_{j=1}^N (a_{ij} - b_{ij})^2 \quad (7)$$

$$PSNR = 10 \log_{10} \frac{255^2}{MSE}$$

(8)

Where

MSE – Mean square error,

PSNR – Peak signal to noise ratio,

M, N represents Number of Rows and Columns,

a_{ij} - Original image,

b_{ij} - Enhanced image

MSE must be less than PSNR. PSNR is represented in decibel (db).

Evaluated Parameters values:

Mean square error = 0.0777%

Peak signal to noise ratio = 59.2278db

6. Conclusion

Here the vessels and exudates are extracted successfully for better observations for ophthalmologists. Depending on the area of each feature, the severity of the disease can be classified. Then by finally knowing the severity of the disease corresponding treatment measures can be analyzed. It will

surely help to reduce the risk and increase efficiency for ophthalmologists.

7. References

- [1] Jayakumari and T. Santhanam, "Detection of Hard Exudates for Diabetic Retinopathy Using Contextual Clustering and Fuzzy Art Neural Network", Asian Journal of Information Technology, Vol. 6, No.8, pp. 842-846, 2007.
- [2] R.C.GonzaJez, Digital Image Processing, 2nd ed. PHI, New Delhi-110001: Prentice Hall of India, 2006.
- [3] <http://www.kellogg.umich.edu/theeyeshaveit/optic-fundus/hard-exudates.html>
- [4] Kshetrimayum Lochan , Puspala Sah and Kandarpa Kumar Sarma, “Innovative Feature set for Retinopathic Analysis of Diabetes and its Detection,” 978-1-4577-0748-3/12/\$26.00 © 2012 IEEE.
- [5] M. E. Martinez-Perez, A. D. Hughes, S. A. Thom, and K. H. Parker, “Improvement of a retinal blood vessel segmentation method using the insight segmentation and registration toolkit (ITK),” in *Proc. IEEE 29th Annu. Int. Conf. EMBS*. Lyon, IA, France, 2007, pp. 892–895.
- [6] S. Dua, N. Kandiraju, and H.W. Thompson, “Design and implementation of a unique blood-vessel detection algorithm towards early diagnosis of diabetic retinopathy,” in *Proc. IEEE Int. Conf. in Inf. Technol., Coding Comput.*, 2005, pp. 26–31.
- [7] A.M.Mendonc,a and A. Campilho, “Segmentation of retinal blood vessels by combining the detection of centerlines and

morphological reconstruction,"*IEEE Trans. Med. Imag.*, vol. 25, no. 9, pp. 1200–1213, Sep. 2006

- [8] <http://www.simovision.be/en/producten/dr-s-en/>
- [9] <http://eyepacs.com/camera>

Gabor Image Enhancement Algorithm for AFIS and Machine Vision Applications

M. Selva Kumar, D. Nedumaran

Dept. of Central Instrumentation and Service Lab.
University of Madras, Chennai.

dnmaran@gmail.com, 27selva@gmail.com

Abstract

The performance of an automatic fingerprint identification system (AFIS) mainly depends on the type and efficiency of the fingerprint matching technique. Most of the AFIS system performs the matching operation based on the minutiae marking, which mainly relies on the separation and identification of ridge ending or ridge bifurcation. The efficiency of minutiae marking of AFIS can be improved by developing novel image pre-processing algorithm for image enhancement, segmentation, thinning, and Binarization. This paper presents a fast Gabor filter based fingerprint image enhancement algorithm. The proposed algorithm performs the enhancement operation effectively through the estimation of ridge frequency and ridge orientation. After the separation of the ridge and valley patterns, Gabor filter was implemented to smooth the image. From the estimated and smoothed ridge frequency and ridge orientation information, a convolution template was designed to produce the binarized image. Further, the binarized

image was converted into thinned image using the single pixel method for performing the minutiae marking. The algorithm was developed in the MATLAB and tested on several scratched images obtained from FVC2004 database DB1_A. The performance of the proposed algorithm was carried by visual inspection and estimation of metrics. The outcome of this study reveals that the proposed algorithm better performed and hence it may be suggested as a suitable pre-processing method for AFIS and machine vision applications.

Keywords

Fingerprint enhancement, Gabor filter, AFIS, orientation-field estimation, ridge frequency estimation, Binarization.

1. Introduction

Presently, Fingerprints are the most widely accepted and well-established biometric identification technique for commercial as well as security applications. Fingerprint images comprise of the ridge and valley

patterns, which are unique for an individual [1]-[3]. For the identification of fingerprints of a person, the ridge structures are commonly used. The most predominant ridge structures are ridge endings and ridge bifurcations. Ridge endings refer to the termination of ridge lines and ridge bifurcations are the branching points of ridges, which are known as minutiae in fingerprints. The locations and directions of minutiae are unique for every finger of an individual, which form the foundation for fingerprint matching. In fact, minutiae extraction and matching depend on the quality of the fingerprint images [4]-[10]. The quality of the fingerprints may be degraded due to a variety of reasons such as, skin condition (dry or wet), sensor noise, incorrect finger pressure, and wear and tear of fingerprint patterns. These poor quality images can result in a considerable number of false minutiae identification and true minutiae rejection. Thus, the quality of the fingerprint images plays a predominant role in deciding the AFIS performance, which can be improved through image enhancement techniques [10] [11] for proper identification of minutiae. Several algorithms based on Fast Fourier Transform (FFT), Wavelet, Gaussian filter, etc. techniques have been proposed and implemented in automated fingerprint systems for enhancing the quality of the fingerprint images [12]-[17].

This paper presents a Gabor filter method to improve image quality and a convolution based binarization technique to separate the parallel ridges and valleys in equal distance to make a clear visual observation between the ridges and valleys. The Gabor filter and convolution based enhanced binarized images can be used to perform the post-processing

operation to extract proper minutiae locations accurately. The proposed algorithm was tested on several poor quality fingerprint images obtained from FPC2002 and FPC2004 database [32] [33]. This paper is organized as follows: Overview of Gabor Filter, Convolution based Binarization, Final Thresholding, Experimental result and Conclusion and future work.

2. Overview Of Gabor Filter

Gabor filters have been employed in many signal and image processing applications due to its optimal resolution in both the spatial and frequency domains. Its frequency and orientation selective properties found to be the most important criteria for using in many fingerprint image enhancement applications [18-23]. In this work, the Gabor filter algorithm proposed by Hong et al [24] was employed for fingerprint image enhancement, which involves the following three steps.

- Local Ridge Orientation estimation: The orientation field, which represents the local ridge orientation of the parallel ridges found in the fingerprint image.
- Local Ridge Frequency estimation: The frequency image, which represents the local ridge frequency of the parallel ridges present in a fingerprint image.
- Gabor filter: Gabor filter allows tuning of the filter characteristics to identify the maximal response to parallel ridges and valleys based on the ridge field orientation and ridge frequency characteristics.

2.1 Local Ridge Orientation Estimation

The orientation estimation is an essential step in the enhancement process as the following Gabor filtering stage relies on the ridge



orientation [25]-[28] in order to effectively enhance the fingerprint image. The least mean square estimation method employed in a pixel-wise [24] sequence to produces an accurate estimation of the orientation field. A block of size $w \times w$ is centered at pixel (i, j) for calculating the gradients $\partial_x(i, j)$ and $\partial_y(i, j)$ for every pixel in each block. The local orientation at pixel (i, j) is calculated using Eq. 1.

$$\theta(i, j) = \frac{1}{2} \tan^{-1} \left(\frac{\sum_{u=i-\frac{w}{2}}^{i+\frac{w}{2}} \sum_{v=j-\frac{w}{2}}^{j+\frac{w}{2}} 2\partial_x(u, v)\partial_y(u, v)}{\sum_{u=i-\frac{w}{2}}^{i+\frac{w}{2}} \sum_{v=j-\frac{w}{2}}^{j+\frac{w}{2}} \partial_x^2(u, v)\partial_y^2(u, v)} \right) \dots \quad (1)$$

where $\theta(i, j)$ is the least mean square estimation of the local ridge orientation at the block centered at pixel (i, j) . Smoothing the orientation field in a local neighborhood using Gaussian filter must satisfy the continuous vector field condition represented by the Eq. 2 and Eq. 3.

$$\phi_x(i, j) = \cos(2\theta(i, j)) \quad \dots \quad (2)$$

$$\phi_y(i, j) = \sin(2\theta(i, j)) \quad \dots \quad (3)$$

where ϕ_x and ϕ_y are the x and y components of the vector field. After marking the x and y component of the vector field, Gaussian smoothing is performed using the Eq. 4 and Eq. 5.

$$\phi'_x(i, j) = \sum_{u=-\frac{W\phi}{2}}^{\frac{W\phi}{2}} \sum_{v=-\frac{W\phi}{2}}^{\frac{W\phi}{2}} G(u, v)\phi_x(i-uW, j-vW) \dots \quad (4)$$

$$\phi'_y(i, j) = \sum_{u=-\frac{W\phi}{2}}^{\frac{W\phi}{2}} \sum_{v=-\frac{W\phi}{2}}^{\frac{W\phi}{2}} G(u, v)\phi_y(i-uW, j-vW) \dots \quad (5)$$

$$O(i, j) = \frac{1}{2} \tan^{-1} \left(\frac{\phi'_x(i, j)}{\phi'_y(i, j)} \right) \dots \quad (6)$$

where G is Gaussian low-pass filter of size $W\phi \times W\phi$. The results obtained using Eq. 6 provide the smoothed orientation field O at pixel (i, j) . Fig 1 shows the orientation mapping process of the scratched fingerprint image using Guassian smoothing.

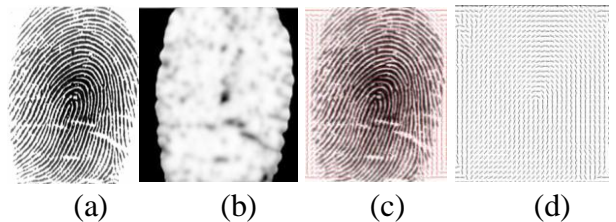


Fig. 1. (a) Original scratched image (b) Reliability representation of Orientation field (c) Orientation mapped over the ridges and (d) Orientation mapped image

2.2 Ridge Frequency Estimation

In ridge frequency estimation, the projection of sinusoidal-shape [9] wave on the local minimum points corresponding to the ridges are identified. This involves smoothing the sinusoidal waveform using a Gaussian low-pass filter [21]-[24] of size $w \times w$ to reduce the noise in the image. The ridge spacing $S(i, j)$ is then calculated by counting the number of pixels between consecutive minima points in the projected waveform. The ridge frequency $F(i, j)$ for a block centered at pixel (i, j) can be defined as

$$F(i, j) = \frac{1}{S(i, j)} \dots \quad (7)$$

The fingerprint scans at a fixed resolution, and therefore, the local ridge frequency estimation values should lie within a certain range. When no consecutive peaks are detected from the projection of the blocks where minutiae points appear, the projected waveform does not produce a well-defined sinusoidal shape wave, which leads to an inaccurate estimation of the ridge frequency. Thus, the out of range frequency values are interpolated using values from neighboring blocks that have a well-defined frequency.

2.3 Gabor Filter

After determining the values of the local ridge orientation and frequency parameters of a fingerprint image, the values are used to construct the even-symmetric Gabor filter. The even-symmetric Gabor filter is the real part of the Gabor function, which is given by a cosine wave modulated by Gaussian method. Even-symmetric Gabor filter in the spatial domain is defined as

$$G(x, y; \theta, f) = \exp \left\{ -\frac{1}{2} \left[\frac{x^2}{\sigma_x^2} + \frac{y^2}{\sigma_y^2} \right] \right\} \cos(2\pi f x_0) \quad \dots \quad (8)$$

where θ is the orientation of the Gabor filter, f is the frequency estimation of the cosine wave, σ_x and σ_y are the standard deviations of the Gaussian envelope along the x and y direction and x_0 and y_0 define the x and y axes of the Gabor filter.

Therefore, the enhanced image $E(i, j)$ can be obtained after applying the Gabor filter G represented by the Eq. 9.

$$E(i, j) = \sum_{u=-\frac{w_x}{2}}^{\frac{w_x}{2}} \sum_{v=-\frac{w_y}{2}}^{\frac{w_y}{2}} G(u, v; O(i, j), F(i, j)) \quad \dots \quad (9)$$

where O is the orientation image, F is the ridge frequency image, and w_x and w_y are the width and height of the Gabor filter mask. The filter bandwidth is determined by the standard deviation parameters σ_x and σ_y , which specifies the range of frequency of the filter.

3. Convolution Based Binarization

Binarization is the process that converts a gray-level fingerprint image into a binary image [9] [22] for marking the minutia effectively. In binarization process, the contrast stretching between the ridges and valleys in the fingerprint image is increased. As a result, the binary image contains two levels of information, i.e., 0 and 1, where the foreground fingerprint image reads „1“ as ridges and the background fingerprint image reads „0“ as valleys.

Further, the property of the Gabor filter produces DC component of the resulting filtered fingerprint image having mean pixel value of zero [22]. Using global threshold pixel value, a straightforward binarization of fingerprint image can be performed. This type of the straightforward binarization method is known as adaptive threshold binarization. This algorithm performs an operation after the Gabor filter which produces the result as broken ridges as shown in Fig. 2(b) due to over threshold in light gray pixel area in a low quality fingerprint image.

To stay away from this type of problems in binarization operation, we have implemented a



convolution template based binarization algorithm using local ridge frequency and local ridge orientation estimation [29] from the smoothed image. A convolution template is designed to separate the ridges and valleys in equal percentage.

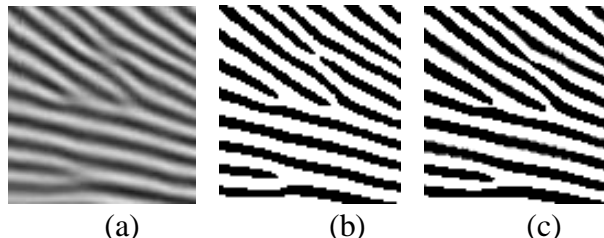


Fig 2 Comparison between Adaptive threshold and Convolution template based Binarization methods. (a) Image enhanced by Gabor filter (b) Image Binarized by Adaptive threshold method (c) Image Binarized by Convolution template method

The convolution template $T(x, y)$ of size $m \times n$ taken from the Gaussian smoothed (i.e. ridge orientation and ridge frequency processed) image $I(x, y)$ of size $W \times W$ (the size $W \times W$ should be equal to the convolution template of size $m \times n$) is binarized using the convolution product given in Equation 10.

$$I * T = \sum_{x=1}^m \sum_{y=1}^n I(x, y)T(x, y) \\ \dots (10)$$

The output image after binarization using the threshold conditions is given by Eq.11.

$$T(p, q) = \begin{cases} 1, & \text{if } (\cos(2\pi p' / f) \geq T_r) \\ 0, & \text{if } (\cos(2\pi p' / f) < T_r) \end{cases} \\ \dots \\ (11)$$

$$p' = p \cos\theta + q \sin\theta$$

where (p, q) is the convolution template size with respect to the block size of $W \times W$, p' is the local ridge orientation at (x, y) in a single

convolution template, and θ is the local ridge orientation at (x, y) . F is the local ridge frequency estimation to fine-tune the average thickness of the ridges and valleys present in the smoothed image, which helps to maintain equal gap distance between the parallel ridges and valleys in threshold operation.

Here, the threshold value is used to adjust the distribution of „0“ and „1“ in the convolution template, i.e., higher threshold (T_r) leads to more items in the template being „1“ and lower threshold (T_r) leads to more items in the template being „0“.

For fingerprint image of size $I(x, y)$, the Gaussian smoothed fingerprint image is given in Fig 2(a) and its corresponding adaptive threshold and convolution template based binarization images are shown in Fig 2(b) and 2(c), respectively.

3.1 Final Thresholding

For estimating the final thresholding, [30] the background image is separated from the convolution image $T(p, q)$. The foreground ridge image (pixels having the value of “1”) after removing the background image is represented as $S(x, y)$. The average binary values of the background image $B(x, y)$ (other than the background and foreground image) is computed using the neighboring pixel interpolation method given in Eq.12

$$B(x, y) = \frac{\sum_{x'} \sum_{y'} (B(x, y))(1 - S(x, y))}{\sum_{x'} \sum_{y'} (1 - S(x, y))} \\ \dots \\ (12)$$

In addition, for low contrast regions, the poor quality of the fingerprint image requires a smaller value for the threshold d to maintain

the ridge connectivity. To perform this operation, an average background value $d(B(x,y))$ is calculated using the expression given in Eq.13.

$$d(B(x, y)) = q^\delta \left\{ \frac{(1-p_2)}{1 + \exp\left(\frac{B(x, y)}{(1-p_1)} + \frac{(1+p_\perp)}{(1-p_1)}\right)} + p_2 \right\} \dots$$

(13) For poor quality fingerprint images, the parameter values for $q=0.8$, $p1=0.5$ and $p2=0.8$ are used for averaging the thresholding. Here, δ is the average distance between the foreground region and background region of the fingerprint image that can be calculated using Eq. 14.

$$\delta = \frac{\sum_x \sum_y (B(x, y) - T(p, q))}{\sum_x \sum_y S(x, y)}$$

... (14)

The final binarized image is obtained after applying the thresholding conditions given in Eq.15.

$$T_B(x, y) = \begin{cases} 1 & \text{if } B(x, y) - T(p, q) > d(B(x, y)) \\ 0 & \text{Otherwise} \end{cases} \dots$$

(15)

The image after applying the convolution template binarization is shown in Fig. 2(c). From the Fig 2, it is clear that the convolution template method distinguishes the ridges and valley patterns clearer and better than the adaptive threshold method.

4. Experimental Result

The proposed Gabor filter with convolution based binarization method algorithm was developed in the MATLAB version 2010a and tested on several poor quality fingerprint images obtained from FVC 2002 and FVC 2004 database [32] [33]. Fig 3 shows the various poor quality fingerprint images (a-c)

and its corresponding Adaptive threshold binarized image with false broken ridges and Convolution template based binarization image are shown in Fig. 3(d-f), and Fig. 3(g-i), respectively.

The algorithm was tested over 800 fingerprint images of size 640×480 pixels with 500 dpi resolution obtained from FVC 2004 [36].

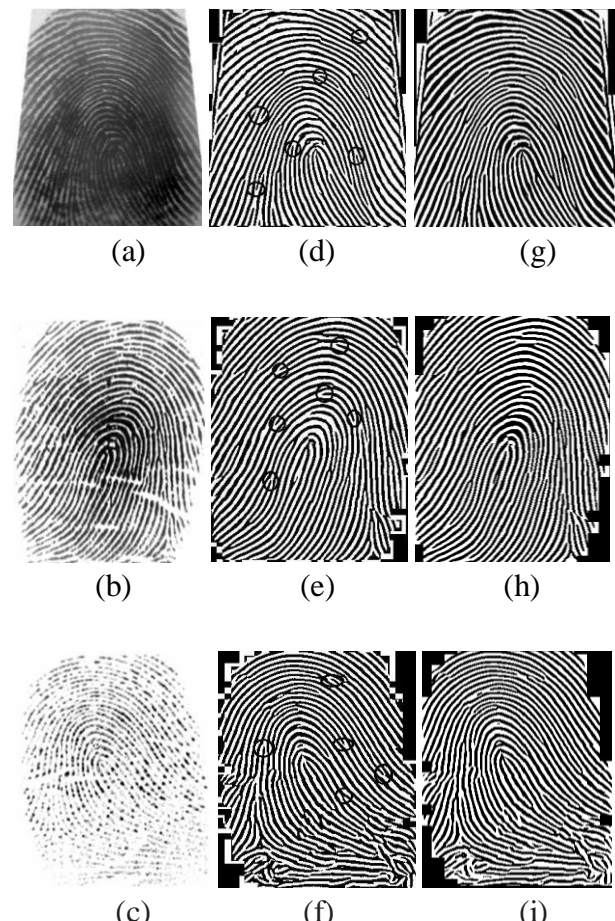


Fig. 3 A comparison between Adaptive threshold and Convolution template binarization methods. (a-c) Original fingerprint images, (d-f) Adaptive threshold binarization with false broken ridges and (g-i) Convolution template binarization without false broken ridges.

From the above Fig. 3 it is observed that the convolution template based binarization images show clear and valid ridge and valley

patterns than the adaptive threshold method. This is clearly shown in Fig 3 (d-f) that the false broken ridges are visible (marked in circle) in the adaptive threshold method where as there are no false broken ridgees found in the convolution method. As a result, the convolution template based binarization algorithm seems to resolve and identify the ridge and valley patterns of the poor quality or smudged fingerprint images better than the adaptive threshold binarization algorithm, which will improve the minutiae detection efficiency.

Further, the performance of the adaptive threshold and convolution template binarization methods in enhancing the quality of the fingerprint images was estimated quantitatively through the calculation of five metrics such as average difference (AD), mean square error (MSE), peak signal to noise ratio (PSNR) normalized absolute error (NAE) and image variance (IV). The estimated metrics values of the three poor and smudged images are given in Table 1. From the Table1, the AD, MSE, and NAE values of the convolution template filtered images are decreased appreciably in comparision with the adaptive threshold method, which implies that the proposed convolution template method reduces the noise and artifacts effectively. Also, the PSNR values of the convolution template images are found to be increasing, which ascertain that the convolution filter retains the details and removes the noise/artifacts found in the images. In addition, the image variances values are slightly increased for the convolution filter, which means the convolution filtered images removes noise/articates effectively than the adaptive filter. Thus, the calculated qualitative

perfromace metrics values substantiated that the convolution template filtered images are found to be better enhanced and resolved than the adaptive threshold filtered images.

Among the evaluated fingerprint image enhancement algorithms, it is proved that the convolution template based enhancement algorithm performed very well over the global adaptive thresholding method in preservering the ridge and valley information found in poor quality and smudged fingerprint images. Further, the following inferences are arrived in this study.

- The global adaptive thresholding technique is not suitable for poor quality fingerprint images that exhibit local variance problems, whereas the convolution template binarization performs well.
- The image usually affected from a great amount of background noise, especially in areas without ridges are well identified and removed by the convolution template binarization method.
- Adaptive thresholding removes the background noise appears in the noisy fingerprint image effectively, which results in false-broken ridges due to over thinning during binarization. Whereas the proposed method removes only the noise without false-broken ridges.
- Further, the quality of the convolution template based binarization image can be improved by using advanced Gabor filter techniques like Log Gabor filter [31].

Images	Average Difference (AD)		Mean Square Error (MSE)		Peak Signal to Noise Ratio (PSNR)		Normalized absolute Error (NAE)		Image Variance (IV)	
	ATB	CTB	ATB	CTB	ATB	CTB	ATB	CTB	ATB	CTB
	0.7821	0.6729	0.7459	0.6367	49.404	50.091	3.0168	2.4362	0.1920	0.1999
	0.6025	0.4760	0.4308	0.3043	51.787	53.297	1.3331	1.2132	0.2477	0.2384
	0.8096	0.5089	0.7318	0.4312	49.486	51.784	2.4461	1.5402	0.2214	0.2212

5. Conclusion And Future Work

In this work, Gabor filter with the convolution template based binarization technique was developed in the MATLAB environment and tested in various poor quality fingerprint images for improving the quality of the fingerprint image for further processing. The results obtained from this study reveals that the proposed method better resolved the fingerprint image than the other adaptive methods, which is required for improving the performance of AFIS and other machine vision applications. Further, this study will be extended to implement the proposed technique for real-time implementation using DSP or embedded processors.

6. References

- [1] P. Komarinski, "Automated Fingerprint Identification System (AFIS)", Elsevier Academic Press, pp, USA2005.
- [2] D. Maltoni, D. Maio, A.K. Jain, and S. Prabhakar "Handbook of Fingerprint Recognition", 2nd ed., pp. 32-49, New Y2003.

[3] E-K. Yun and S-B. Cho, "Adaptive fingerprint imageenhancement with fingerprint image quality analysis", Image and Vision Computing, Elsevier, pp. 101-109, September 2005.

[4] G.Ramaswamy,V.Sreenivasarao, P.Ramesh and D.Ravi Kiran, "A Novel Approach for Human Identification through Fingerprints", International Journal of Computer Applications, Vol 4, Issue No.3, pp 35-40, July 2010.

[5] S. M. Mohsen, S. M. Z. Farhan and M. M. A. Hashem, "Automated Fingerprint Recognition: Using minutiae Matching Technique for the Large fingerprint Database", 3rd International Conference on Electrical & Computer Engineering ICECE, pp 116-118, December 2004.

[6] S. S. Chikkerur, A. N. Cartwright and V. Govindaraju, "Fingerprint Image Enhancement Using STFT Analysis", Unified Biometrics and Sensors, Amherst

- [7] J. Ravi, K.B. Raja, and K.R Venugopal, "Fingerprint Recognition Using Minutia Score Matching", International Journal of Engineering Science and Technology Vol.1(2), pp 35-40, 2009.
- [8] Y. He, J. Tian, X. Luo, and T. Zhang, "Image enhancement and minutiae matching in fingerprint verification", Pattern Recognition, Vol 24, pp 1349-1359.200
- [9] J. S. Bartunek, M. Nilsson, J. Nordberg, and I. Claesson, "Adaptive Fingerprint Binarization by Frequency Domain Analysis", Signals, Systems and Computers, ACSSC '06. Fortieth , pp 598-600, 2006.
- [10] S. S. Patil, G. S. chandel, and R Gupta "Fingerprint Image Enhancement Techniques and Performance Evaluation of the SDC and FFT Fingerprint enhancement techniques", International Journal of Computer Technology and Electronics Engineering (IJCTEE) Vol 2, Issue 2, pp 184-188, April 2012.
- [11] P. Porwik and L.Wieclaw, "A new approach to reference point location in fingerprint recognition", IEICE Electronics Express, Vol.1, Issue No.18, pp 1-7, December 2004.
- [12] S. Hatami, R. Hosseini, M. Kamarei, H. Ahmadi, "Wavelet Based Fingerprint Image Enhancement," Proceedings of the IEEE, pp 4610-4613, 2005.
- [13] A.Cavusoglu and S. Gorguoglu, "A fast fingerprint image enhancement algorithm using a parabolic mask," Computers and Electrical Engineering, pp 250-255, Vol.34, May 2007.
- [14] Y. Wang, J-P. Yu, H-W. Liu and Zhang, "Fingerprint image enhancement based on morphological filter", International Conference on Computational and Information Sciences, pp. 34-36, 2011.
- [15] G. J.Reddy, T. J. C. Prasad and M. N.G. Prasad, "Fingerprint Image Denoising Using Curvelet Transform", ARPN Journal of Engineering and Applied Sciences, Vol. 3, Issue No. 3, pp 31-34, JUNE 2008.
- [16] M. Sepasian, M. R. Bahmanyar, C. Mares, S. M. Azimi and W. Balachandran, "Novel Fingerprint Image Enhancement Algorithm", Advances in Electrical and Electronics Engineering - IAENG Special Edition of the World Congress on Engineering and Computer Science, pp. 244-251, 2008.
- [17] J. S. Bartunek, M. Nilsson, B. Sallberg and I. Claesson, "Adaptive Fingerprint Image Enhancement with Emphasis on Pre-processing of Data", IEEE publication in a future issue of this journal, pp 2-92011.
- [18] J. Wang and X. Sun, "Fingerprint Image Enhancement using a fast Gabor filter", World Congress on Intelligent Control and Automation, pp. 6347-6349, July 2012, China.
- [19] Q. Ye, M. Xiang, and Z. Cui, "Fingerprint Image Enhancement Algorithm Based on Two Dimension EMD and Gabor Filter", International Workshop on Information and Electronics Engineering (IWIEE), Vol. 29, pp 1840 – 1844,2012.

- [20] V. Kakkar, A. Sharma, T. K. Mangalam, P. Kar, "Fingerprint Image Enhancement using Wavelet Transform and Gabor filtering", ACTA Technica Napocensis, Electronics and Telecommunications, Vol. 52, Issue No. 4, pp 17-24, November 2011.
- [21] Y. Hu, X. Jing, B. Zhang and X. Zhu, "Low Quality Fingerprint Image Enhancement Based on Gabor Filter", Advanced Computer Control (ICACC), 2010 2nd International, pp. 196-198, 2010.
- [22] M. Rajinikannan, D. Ashok Kumar and R. Muthuraj, "Estimating the Impact of Fingerprint Image Enhancement Algorithms for Better Minutia Detection", International Journal of Computer Applications, Vol 2, Issue No.1, pp 36-41, May 2010.
- [23] K. Mao, Z. Zhu and H. Jiang, "A Fast Fingerprint Image Enhancement Method", IEEE transaction on Third International Joint Conference on Computational Science and Optimization, pp 222-226, 2010.
- [24] L. Hong, Y. Wan, and A. K. Jain, "Fingerprint image enhancement: Algorithm and performance evaluation", IEEE Transactions on Pattern Analysis and Machine Intelligence Vol. 20, Issue No. 8, 777–789, 1998.
- [25] L. Ji and Z. Yi, "Fingerprint orientation field estimation using ridge projection", Pattern Recognition, Vol. 41, pp 1491-1503, 2008.
- [26] S. Jirachaweng, Z. Hou, W-Y. Yau and V. Areekul, "Residual orientation modeling for fingerprint enhancement and singular point detection", Pattern Recognition, Vol 44, pp 431-442, 2011.
- [27] Y. Mei, G. Cao, H. Sun and R. Hou, "A systematic gradient-based method for the computation of fingerprint's orientation field", Computers and Electrical Engineering, Vol 38 pp 1035–1046. 2012.
- [28] R. Hastings, "Ridge Enhancement in Fingerprint Images Using Oriented Diffusion", Digital Image Computing Techniques and Applications, pp. 246-250, 2007.
- [29] Xi-F. Tong, S-B. Liu, J-H. Huang and X-L. Tang, "A fast image enhancement algorithm for fingerprint", Proceedings of the Sixth International Conference on Machine Learning and Cybernetics, pp-177-179, August 2007
- [30] W. Wang, J. Li, F. Huang and H. Feng, "Design and implementation of Log-Gabor filter in fingerprint image enhancement", Pattern Recognition, Vol 29, pp 301–308, 2008.
- [31] FVC2002,
"<http://bias.csr.unibo.it/fvc2002/>," 2010.
- [32] FVC2004,
"<http://bias.csr.unibo.it/fvc2004/>," 2010.

Finite Element Analysis Of Lumbar Spine With Dynamic Stabilization Device

Abhishek Singh¹, S.Karuppudaiyan², D.Kingsly Jeba Singh³.

School of Mechanical Engineering.

dean.mech@ktr.srmuniv.ac.in

Abstract

The objective of the present work is to perform Biomechanical study of the Lumbar Spine (L2–L5 segments) with dynamic stabilization device using Finite Element Analysis tool. The study is focused to examine the Range of Motion of L2–L5 segments and validate it with intact model. The Range of Motion (ROM) of L2–L5 segments were examined to determine the influence of the dynamic stabilization on the adjacent segments. In the case of the dynamically stabilized spine, the total ROM was similar to that of the intact spine. In particular, the dynamic stabilization device having a stiffness of 10–15 N/mm made the destabilized spine more similar to the intact spine. The Results indicated that the use of dynamic stabilization devices restored functionality closer to that of the intact spine as compared to the fused spine. The stiffness value utilized in the device was determined to be an important design parameter in manufacturing of the dynamic stabilization device.

Keywords:

Dynamic Stabilization, Tetramesh, FEA, ROM, Von-Mises Stress.

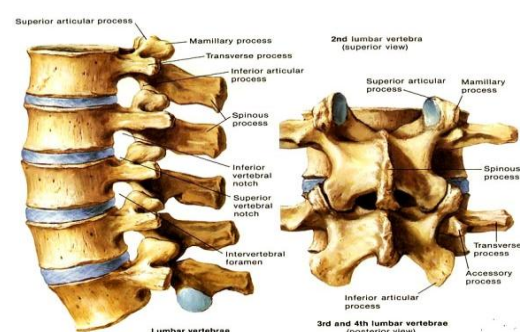
1. Introduction

Biomechanics is the study of the structure and function of biological systems such as humans, animals, plants, organs, and cells by means of the methods of mechanics. The study of biomechanics ranges from the inner workings

of a cell to the movement and development of limbs, to the mechanical properties of soft tissue, and bones. Biomechanics is widely used in orthopedic industry to design orthopedic implants for human joints, dental parts, external fixations and other medical purposes.

2. Lumbar Spine Anatomy

The lumbar spine is the area of the spinal column that comprises the low back. In a human, there are five lumbar vertebrae connecting proximally to the thoracic spine and distally to the sacrum. Each vertebra is often referred to as a ‘level’ and represented with an ‘L’ to define the lumbar spine and a number to specify the particular level. The individual lumbar vertebrae are designated L1 (being the most proximal vertebra), L2, L3, L4 and L5 (being the distal vertebra) [1].



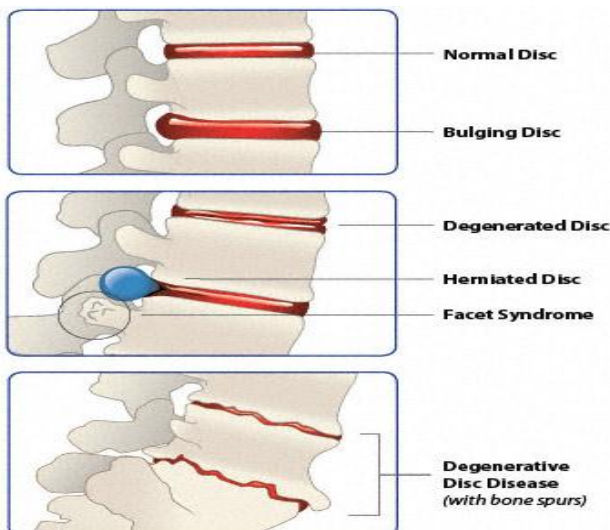
Courtesy: sites.google.com

Figure 1. Lumbar Spine

3. Problem Identification And Treatments

3.1 Low Back Pain

Low back pain (LBP) is a common musculoskeletal disorder and is a widespread problem in modern society both in economics and prevalence. Between 70% of the world's population experiences low back pain at some point of their lives. Hence, there is a necessity to study the origin of pain associated with the lumbar spine and investigate for simple, cost effective, and safe treatment options.



Courtesy: backpain-guide.com

Figure 2: Various Disc Problems

3.1 Nonsurgical Treatment

Several conservative measures may be used to help relieve your pain such as rest, medications, exercises, physical therapy, spinal orthotics and braces. If the conservative treatment fails, surgical treatment is recommended.

3.2 Surgical Treatment Of Low Back Pain

3.2.1 Decompression Surgery

Decompression surgery involves removal of small portion of the bone over the nerve root and/or disc material from under the nerve root to relieve the pressure on the nerve root and allow it to heal, thus alleviating the pain. Various methods of decompression include

unilateral laminectomy, bilateral laminectomy, unilateral facetectomy, bilateral facetectomy. Following the decompression surgery, the stability of the spine is restored with the fixation devices such as fusion devices or posterior dynamic stabilization devices. **Drawbacks:** Recurrent Stenosis or Herniation after Decompression, Missed fragment of the disc can cause pain, Dissection of the nerve root may cause further trauma & continued pain, the cost of spinal decompression therapy.

3.2.2 Fusion

This is essentially a "welding" process. The basic idea is to fuse together the painful vertebrae so that they heal into a single, solid bone. Spinal fusion eliminates motion between vertebral segments. It is an option when motion is the source of pain. For example, your doctor may recommend spinal fusion if you have spinal instability, a bad curvature (scoliosis), or severe degeneration of one or more of your disks. The theory is if the painful spine segments do not move, they should not hurt. A variety of surgical techniques have evolved. In most cases, a bone graft is used to fuse the vertebrae. **Drawbacks:** Adjacent segment degeneration, tedious surgical procedure, Post operative complications (muscle disruption, blood vessel damage or clots).

3.2.3 Disc Replacement

This procedure involves removing the disk and replacing it with artificial parts, similar to replacements of the hip or knee. The goal of disk replacement is to allow the spinal segment to keep some flexibility and maintain more normal motion. An artificial disc serves to replace the symptomatic degenerated disc, restore the functional biomechanical properties of the motion segment, and protect neurovascular structures.. Painful degenerative

disc disease, failed disc syndrome, and transition zone syndrome are clinical indications for total disc arthroplasty.

Drawbacks: Due to the constant motion of the disc, there is a possibility of wear of the implant which may eventually lead to mechanical failure of the device.

3.2.4 Dynamic Stabilization Device

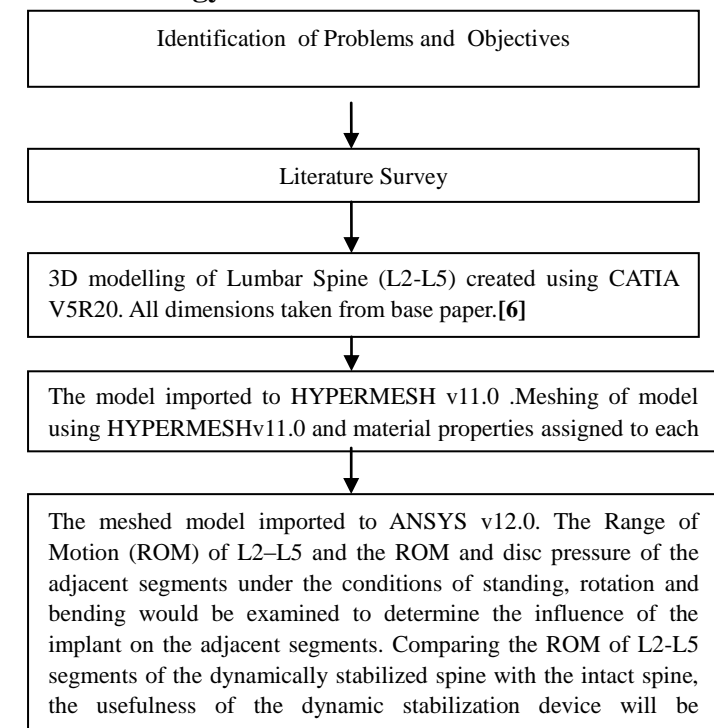
These systems are designed to stabilize the spinal segments by preserving the natural anatomy of the spine. The principle of dynamic stabilization is that the control of spinal instability (abnormal motion under physiological loads), and restoring normal physiological loading pattern through the spinal elements would alleviate pain and prevent degeneration of the adjacent segments. Dynamic stabilization surgery starts much like a typical spine fusion surgery. Once any disc problems have been addressed, your surgeon places a dynamic stabilization device to limit motion at the affected disc level. One commonly implanted device is called Dynesys. Dynesys uses screws to anchor to the vertebrae at two adjacent spinal levels. The screws are connected with rope (to prevent excessive tension) and plastic tubes (to prevent excessive compression).



Courtesy: sites.google.com

Figure 3. Dynesys Dynamic Stabilization Device

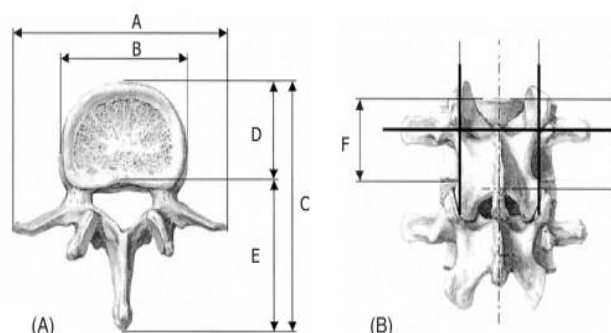
4. Methodology



5. Finite Element Modeling Of Lumbar Spine (L2-L5 Vertebrae)

5.1 Catia Modeling

In this project, 3d model of lumbar spine (L2-L5 vertebrae) was designed by using the software CATIA v5 R20.



Reference Dimensions

FIGURE 4 : Anatomical Parameters Represented In A Cut-Away View Of Vertebra : (A) Dimensions A–E And (B) Dimension F [6]

Table1.Mean values of measured dimensions [6]

Vertebra	Dimension (mm)					
	A	B	C	D	E	F
L1	81.8	40.7	76.0	28.9	49.4	24.9
L2	80.4	39.8	79.1	29.8	48.5	25.4
L3	89.4	43.1	80.1	32.3	48.9	25.6
L4	90.5	44.1	79.6	31.7	47.2	26.5
L5	93.7	48.1	77.1	32.5	43.6	28.6

CAD Models

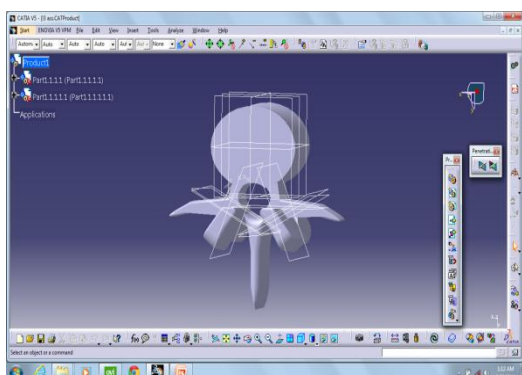


Figure 5. Lumbar Spine Vertebrae

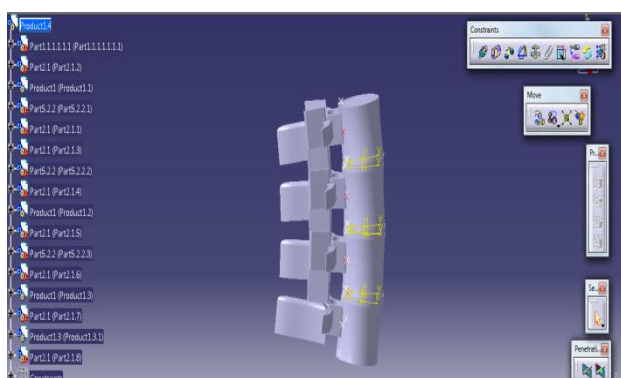


Figure 6. Full Assembly (L2-L5 Vertebrae)

5.2 Meshing Of Lumbar Spine (L2-L5 Vertebrae)

The CATIA V5 R20 model of lumbar spine was imported to HYPERMESH v11.0. The

model consists of 4 cortical bones and 4 cancellous bones, 3 intervertebral discs ,3 superior endplate and 3 inferior endplate. Automesh is done with the 2d elements. For each component geometry cleanup is done by suppressing the free edges. After creating the 2d mesh successfully, now we go for 3d tetramesh, and by selecting the whole geometry we create the tetramesh. After creating the tetramesh now we assign the element type solid 185 (**Advantages:** The element has plasticity, creep, swelling, stress stiffening, large deflection, and large strain capabilities. A reduced integration option with hourglass control is available) for tetrahedral elements. Then by assigning masses to transverse processes on L4 and L5 vertebrae ,we create the spring element i.e. Combin14, between the two vertebrae L4 and L5. A stiffness value of 15 N/mm was chosen for the spring element. Thus, the spring element act as a dynamic stabilizing device. Then we assign material properties to each part of lumbar spine (L3-L5 vertebrae),according to the properties as specified [6]. In the four-level FE model (L2–L5), the inferior surface of the L5 vertebral body was completely fixed in all directions.

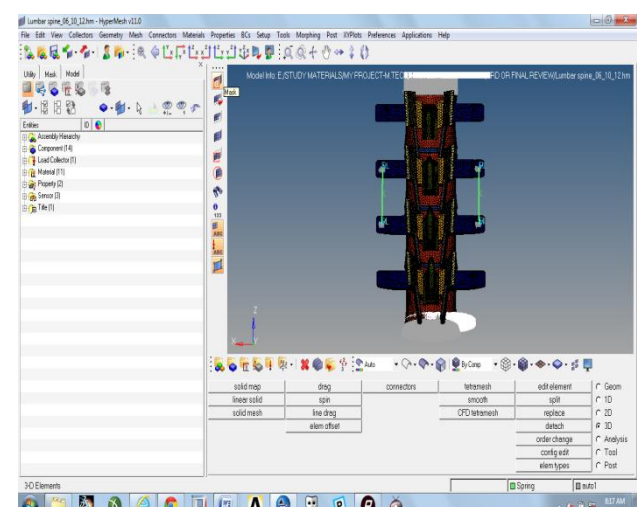


Figure7. Tetramesh Of Dynamically Stabilised Lumbar Spine (L2-L5 Vertebrae) Under Loading Conditions

5.3 Finite Element Analysis Of Lumbar Spine

After assigning all the material properties and element type to lumbar spine model (L2-L5 vertebrae), it is imported to ANSYS v12.0.A moment of 10N/m was applied to L2 vertebrae , with L5 full constrained in all directions. After this ,solution is obtained.This would give us the Range of Motion (ROM) for each vertebrae (L2-L5). Once processing has been completed, the results could be displayed and analyzed by using post processing. This includes displaying two main **results**-Von Mises stress and displacement.[3]



Figure 8. Part File (.cdb format) of Lumbar Spine (L2-L5 Vertebrae) imported from Hypermesh v 11 to Ansys v 12.0 (under loading conditions)

6. Results And Discussions

6.1 FEM Model: The result was obtained from post processing of dynamically stabilized lumbar spine (L2-L5 vertebrae),under moment of 10 N m. Figure 9 and Figure 10 shows the Range Of Motion (ROM) of each vertebral segments (L2-L5). L5 being full constrained in all directions, a moment of 10N/m was applied to L2 vertebrae [5].

6.2 Result Of Dynamically Stabilized Model

6.2.1 Standing Condition

The moment values of 10 N/m are directly applied to L2 vertebrae fixing the L5 vertebrae

in all directions, and material properties are assigned accordingly, as to compare and validate the model with the literature [6].

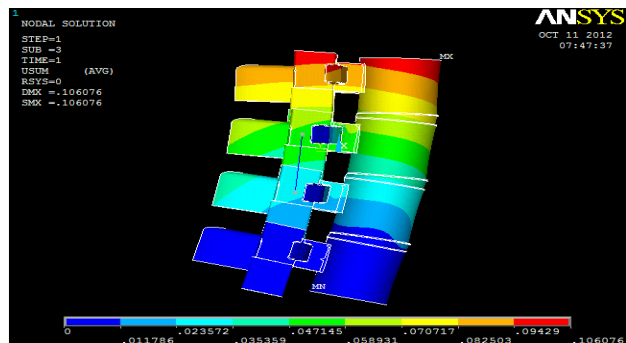


Figure 9 Range of Motion (in radians) of each Vertebral Segments (L2-L5) in standing posture implanted with Dynamic Stabilizer

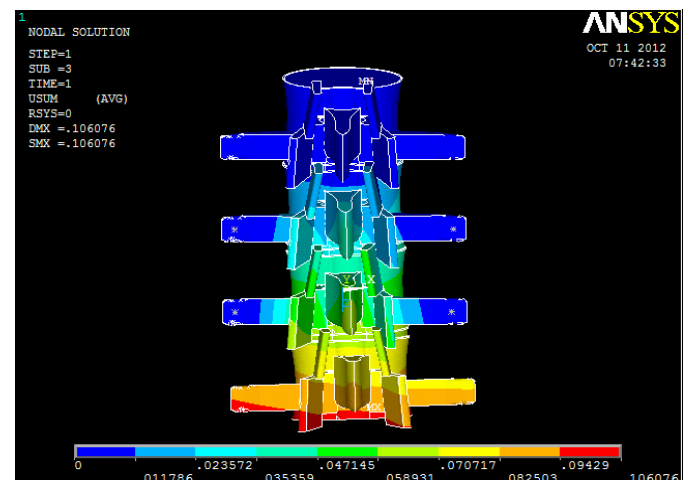


Figure 10 Range of Motion (in radians) of intact (L2-L5 Vertebrae)

6.3 Table Comparing The Values of ROM(Range of Motion)of Present Analysis With The Literature in standing condition

Table 2

Range of Motion(ROM) in degrees	L2-L3 Vertebra e	L3-L4 Vertebra e	L4-L5 Vertebra e
Literature	6.4	6.3	6.4

values for intact model(L2-L5 vertebrae)			
Analysis values for intact model(L2-L5 vertebrae)	6.28	6.1	6.2
Literature for dynamically stabilized model(L2-L5 vertebrae)	6.6	6	6.4
Analysis values for dynamically stabilized model(L2-L5 vertebrae)	6.4	5.91	6.25

6.2.2 Rotational Effect:

For producing rotational effect , we need to rotate the nodes at the top of L2 Vertebrae ,constraining the L5 Vertebrae in all directions. Thus we need to change the Cartesian coordinate system to cylindrical coordinate system [2].

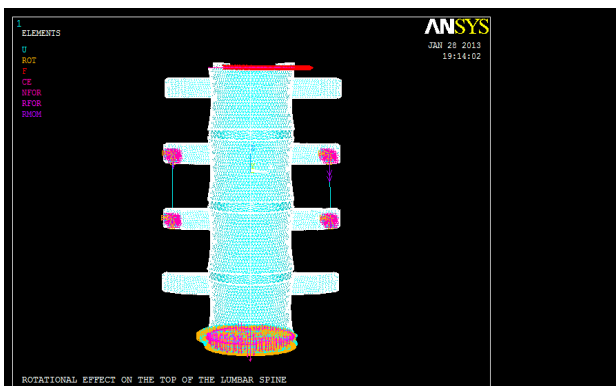


Figure 9 Rotational effect at the top of lumbar spine (L2-L5 vertebrae)

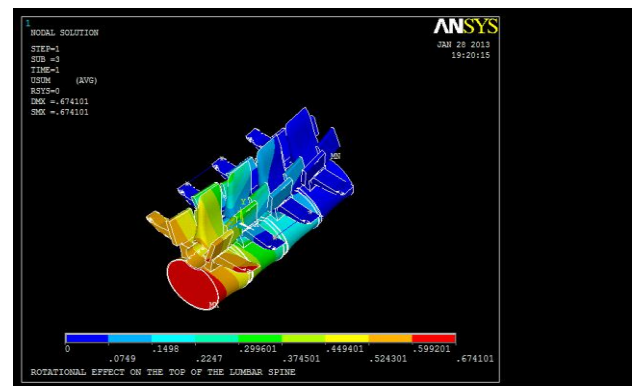


Figure 10 Range of Motion (in radians) due to Rotational effect of each Vertebral Segments (L2-L5) implanted with Dynamic Stabilizer

6.4 Table Comparing The Values of ROM(Range of Motion)of Present Analysis With The Literature due to Rotational effect

Table 3

Range of Motion(ROM) in degrees	L2-L3 Vertebra e	L3-L4 Vertebra e	L4-L5 Vertebra e
Literature values for intact model(L2-L5 vertebrae)	6.4	6.3	6.4
Analysis values for intact model(L2-L5 vertebrae)	6.28	4.6	4.29
Literature for dynamically stabilized model(L2-L5 vertebrae)	6.6	6	6.4
Analysis values for dynamically stabilized model(L2-L5 vertebrae)	6.08	4.3	4.5

6.2.3 Bending Effect:

For producing bending effect, we need to create a dummy node at the front of Lumbar Spine (L2-L5 vertebrae) and then by means of contact manager attach all the nodes of the spine to the dummy node. Then apply a moment of 10N/m to the dummy node.

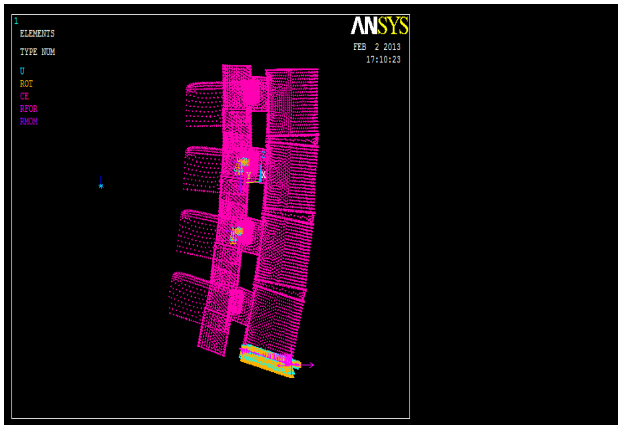


Figure 11 Contact pair creation for bending

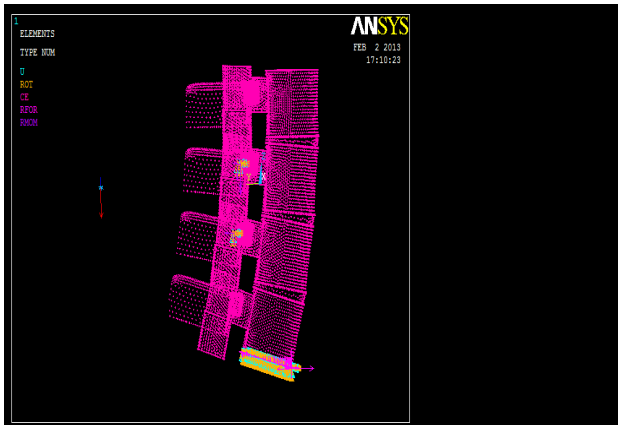


Figure 12 Applying moment of 10 N/m under bending

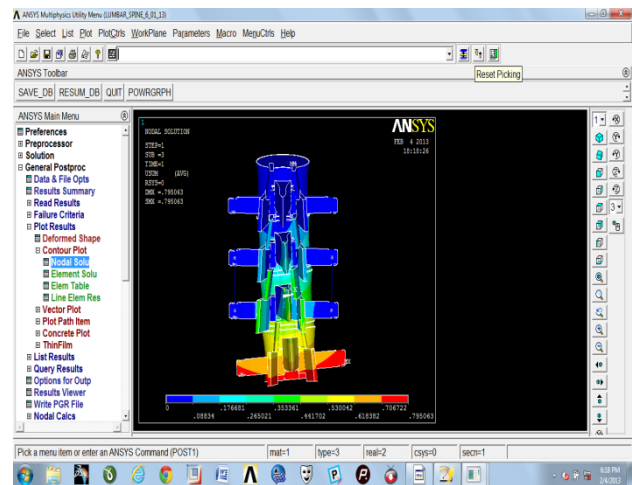


Figure 13 Displacement vector sum due to bending

6.3 Table Comparing The Values of ROM(Range of Motion)of Present Analysis With The Literature due to bending

Table 4

Range of Motion(ROM) in degrees	L2-L3 Vertebrae	L3-L4 Vertebrae	L4-L5 Vertebrae
Literature values for intact model(L2-L5 vertebrae)	6.4	6.3	6.4
Analysis values for intact model(L2-L5 vertebrae)	5.5	4.6	5.5
Literature for dynamically stabilized model(L2-L5 vertebrae)	6.6	6	6.4
Analysis values for dynamically stabilized model(L2-L5 vertebrae)	6.08	5.3	4.8

6.4 Discussion

It is observed that the Range of Motion(ROM) of lumbar spine under conditions of standing, rotation and bending(L2-L5 vertebrae) is similar to that of the intact spine. The maximum values from the literature [6] for Dynamically stabilized model is 6.6 degrees and the maximum obtained result is 6.4 degrees.

7. Conclusions

A three-dimensional FE analysis was performed to investigate the advantages of dynamic stabilization and its influence on the adjacent intervertebral motion segments. The modeling has been done using the CATIA v5 R20 and the meshing is done using HYPERMESH v11 and the same has been imported to ANSYS 12.0. The goal of this study was to calculate the Range of Motion (ROM) of lumbar spine (L2-L5 vertebrae) under the moment of 10N/m under cases of standing, rotation and bending and thus to determine the usefulness of dynamic stabilization device. Results indicated that the use of dynamic stabilization devices restored functionality similar to that of the intact spine. The maximum values from the literature for Dynamically stabilized model is 6.6 degrees and the obtained result for Dynamically stabilized model is 6.4 degrees. The maximum ROM(Range of Motion) is exhibited in L2 vertebrae and the minimum Range of motion is exhibited in L5 vertebrae. The bending motion was limited most and the axial rotation was limited the least, after device implantation. From the completion of this project ,a number of conclusions can be made that will help understand the Range of Motion (ROM) exhibited by a lumbar spine implanted with dynamic stabilization device. The stiffness value utilized in the device would be determined to be an important design parameter in manufacturing of the dynamic stabilization

device. Further research into these areas could prove to be valuable in leading towards a more detailed understanding of low back pain and usefulness of dynamic stabilization device.

8. References

- [1].Tobias Pitzen , Fred Geisler “ A finite element model for predicting the biomechanical behaviour of the human lumbar spine” Spine 1984;9(6):374–81.
- [2].Jia-can SU, Zhuo-dong LI “Three-dimensional finite element analysis of lumbar vertebra loaded by static stress and its biomechanical significance” Spine 1984;9(6):404–61.
- [3].F Nabhani, M Wake “Computer modelling and stress analysis of the lumbar spine” [http://dx.doi.org/10.1016/S0924-0136\(02\)00195-4](http://dx.doi.org/10.1016/S0924-0136(02)00195-4)
- [4].Zheng-Cheng Zhonga, Shun-Hwa Weia “Finite element analysis of the lumbar spine with a new cage using a topology optimization method” . Spine 2004; 29(22):2527–32.
- [5].Jia-can SU, Zhuo-dong LI, Lie-hu CAO “Three-dimensional finite element analysis of lumbar vertebra loaded by static stress and its biomechanical significance” Spine 2005;30(3):324–31
- [6].Dong Suk Shin, Kunwoo Lee “Biomechanical study of lumbar spine with dynamic stabilization device using finite element method” . Computer-Aided Design 39 (2007) 559–567.

Patient Safety Automation Using Secured Steganography and DSP Automatic Control

Prabaharan Rajagopal ¹, Subha Austalakshmi²

Sathyabama University,Chennai.

¹prabaharan.arul@gmail.com, ²subharuthra@gmail.com

Abstract

The goal of this paper is to hide the patient disease information as secret, not visible to others, additionally this paper also explains keep monitoring patient condition and provide automatic control during Emergency ward treatment. This is introduced here mainly for patient safety. Keeping patient disease information as secret and not visible to others - the best way to use steganography, which will be very useful to hide the patient disease text information or scanning image information in patient's photo itself without altering their photo. Advantage of this technology is that only doctors and authorised person's can be able to decrypt and identify disease information by disease info embedded patient's photo. Ultimate aim of this paper is to keep monitoring the patient's critical condition like Heart Beat, Blood pressure, Brain condition, diabetics during emergency ward treatment and provide the control for Glucose, medicines, blood kind of liquid flow. Also provide warning alarm and warning message display, if patient body is going abnormal or right treatment is not given at right time. Steganography is used to prevent the detection of information leakage, from unauthorized. To hide the secret information in Patient images, huge no of steganographic techniques are available. With existing

methods of analysis, I propose a new method called PCT based steganography. PCT is the advanced method of DCT, which will improve the reconstructed image resolution than DCT. Since there is no specific algorithm for monitoring and control, based on standard or doctor's data base both monitoring and controlling will be done. Another Highlight of this paper is that Image kind of signal processing, signal processing and automatic control has been done with high end fixed point (DSP) Digital Signal Processor (ADI processor - BF533) which will be compatible for both signal processing and controlling.

Keywords

Steganography, Steganographic, Least Significant Bit (LSB), Discrete Cosine Transform (DCT), Photo Core Transform (PCT), Digital Signal Processor (DSP).

1. Introduction

The word steganography is originally derived from Greek words which mean "Covered Writing" [4]. In this paper patient automation safety system contains two parts of implementation. First one is Steganography algorithm implementation using PCT tech to make personal secret disease info of the patient. Second one is monitoring and Emergency ward automatic control system for



patient life safety. Both the implementation will be done in single high end DSP processor.

Fig 1 explains all the mechanism involved in steganography tech, patient condition monitoring and Automatic time based control that might be flow control or timing control. Here Mainly automation control will be performed based on the doctor's instruction on medicine and patient condition monitoring.

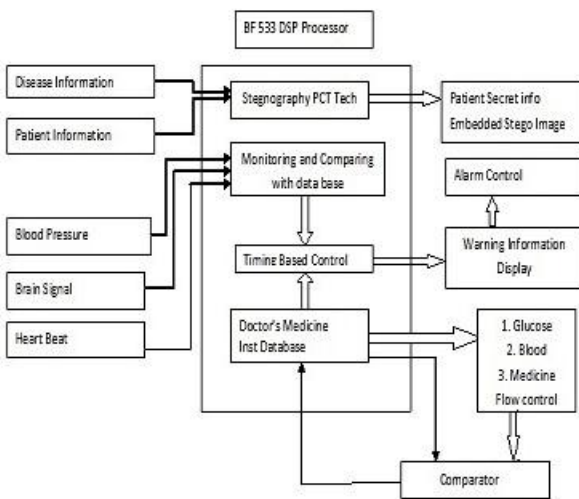


Fig 1: Block diagram of patient safety automation system

1.1 Steganography

Steganography is a technique of hiding secret information within carrier digital media, such as a digital image, audio, video, etc. Also steganography is the technology of invisible communication. This is accomplished through hiding secret information in other carrier information. In digital image steganography the information is hidden exclusively in images. The important requirement of a steganographic algorithm is that embedded image should be identical to the original cover image. Extremely difficult to detect, a normal cover message, which was sent over an insecure channel with one of the periods on the paper containing hidden information.

As of today steganography is mostly used on computers and networks, with digital data being the carriers and high speed delivery protocol channels. Steganography differs from cryptography, cryptography focuses on keeping the contents of a message secret, steganography focuses on keeping the contents of a message secret as well as existence of the message secret. Steganography and cryptography are two ways to protect information from unauthorized parties. Once the presence of hidden information is revealed or even suspected, the purpose of steganography is partly defeated. The strength of steganography can thus be amplified by combining it with cryptography. This proposed analysis in steganography is made for the lack of strength in cryptographic systems. The main goal of steganography is to communicate securely in a completely undetectable manner and to avoid drawing suspicion to the transmission hidden data[2].

Here Fig 2 explains that How disease information to be hidden inside the patient photo. Important thing is only doctor and secret code authorized person can able to decode and identify the disease information. So that patient information to be kept secured.

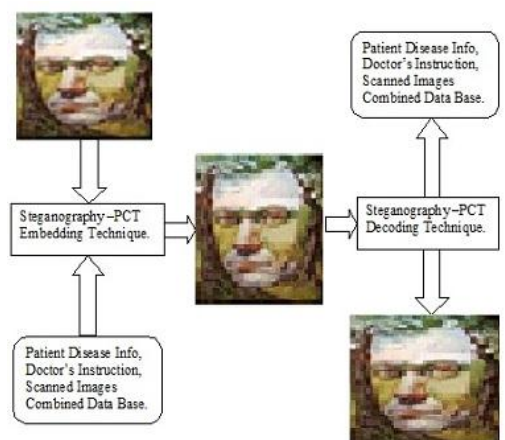


Fig2: Patient disease information hidden & extraction.

Regarding steganography , In rest of this paper we represent the analysis of existing methods and techniques of steganography. Additionally performance comparison of existing different domain techniques and the implementation of newly proposed PCT based steganography also done here.

1.2 Automatic control and Monitoring

Mainly for patient real life safety - automatic control and monitoring implementations has been introduced in this paper. Monitoring will include the patient heart beat, Brain signal, blood pressure measurement and comparison along with threshold data base. Along with the monitoring automatic control also will be done to ensure the patient safety.

1.3 DSP Processor Introduction:

Image processing, Signal processing & controlling all three operations needs to be done here for patient safety. So BF 533 high end DSP processor will be selected to do all three processing at continuous manner. Specifically Analog Device Blackfin DSP Processor is used (BF – 535), which is better for signal processing and controlling.The ADSP-BF535 processor is a member of the Blackfin family of products.The core architecture combines a dual-MAC signal processing engine, an orthogonal RISC-like microprocessor instruction set, and single instruction multiple data (SIMD), multimedia capabilities into a single instruction set architecture. Blackfin processors feature dynamic power management, the ability to vary both the voltage and frequency of operation to provide lower overall power consumption than other DSPs. Additionally it has 533 MHz clock frequency to perform the process very faster.

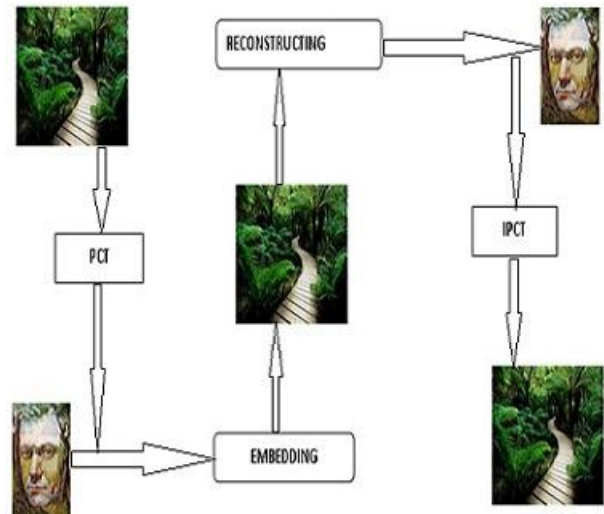


Fig3: Embedding and Reconstruction Algorithm

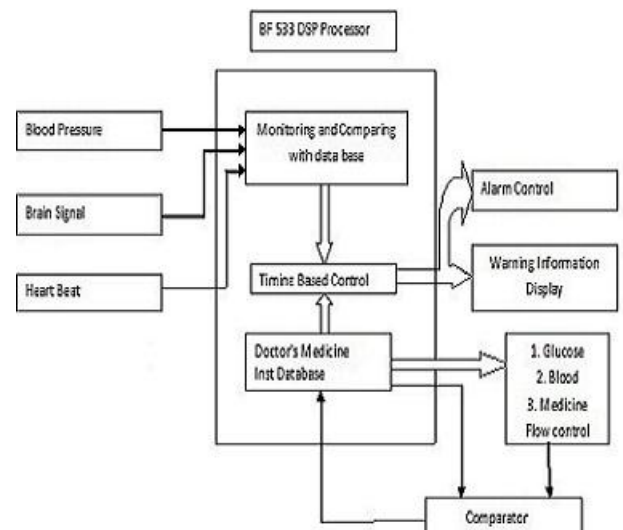


Fig4: Monitoring and automatic control system blocks.

2. Steganography Methods

Three different types of steganography methods are available.

2.1 Physical Kind of Steganography

Physical Steganography has been widely used earlier. In ancient time, people wrote message on wood and then covered it with wax. Message was written on the back of postage stamps. Message was written on paper by secret inks.

2.2 Digital Kind of Steganography

Digital Steganography is the technique of invisibly hiding data within cover data. It conceals the fact that message exists by hiding the secret message. In this, secret message can be hidden inside the image, text, audio clip which can be represented in binary.

2.3 Printed Kind of Steganography

Digital Steganography output can be in the form of printed document formats. The letter size, spacing and other characteristics of a cover text can be manipulated to carry the hidden message. A recipient who knows the hidden technique used can recover the message and then decrypt it.

Almost all digital file formats can be used for steganography, but the formats that are more suitable are those with a high degree of redundancy. Redundancy can be defined as the bits of an object that provide accuracy far greater than necessary for the object's use and display. The redundant bits of an object are those bits that can be altered without the alteration being detected easily. Image and audio files especially comply with this requirement, while research has also uncovered other file formats that can be used for information hiding. Figure2 shows the four main categories of file formats that can be used for steganography

Digital Steganography applicable in different areas like audio, video, text and image. Digital Steganography output can be in the form of

printed document formats. The letter size, spacing and other characteristics of a cover text can be manipulated to carry the hidden message. A recipient who knows the hidden technique used can recover the message and then decrypt it.

Almost all digital file formats can be used for steganography, but the formats that are more suitable are those with a high degree of redundancy. Redundancy can be defined as the bits of an object that provide accuracy far greater than necessary for the object's use and display. The redundant bits of an object are those bits that can be altered without the alteration being detected easily. Image and audio files especially comply with this requirement, while research has also uncovered other file formats that can be used for information hiding. Figure2 shows the four main categories of file formats that can be used for steganography.

3. Diff Domain Techniques

As stated earlier, digital images are the most popular cover objects used for steganography. In the domain of digital images many different image file formats exist, most of them for specific applications. Digital Image Steganography techniques can be divided into two groups: those in the Spatial or Image Domain and those in the Transform Domain. Image – also known as spatial – domain techniques embed messages in the intensity of the pixels directly. In transform domain technique, images are first transformed into frequency domain and then the message is embedded in the image. Image domain techniques encompass bit-wise methods that apply bit insertion and extraction.

The image format that, mostly suitable for image domain steganography are lossless and the techniques are typically dependent on the



image format. Steganography in the transform domain involves the manipulation of algorithms and image transforms. These methods hide messages in more compatible areas of the cover image, making it more robust. Many transform domain methods are independent of the image format and the embedded message that may survive conversion between loss and lossless compression.

4. Spatial Domain –LSB

Least significant bit (LSB) insertion is a generic, simple approach of hiding information in a cover image. The least significant bit of some or all of the bytes inside cover image is changed to a bit of the secret message[1]. When using a 24-bit image, a bit of each of the red, green and blue colour components can be used, since they are each represented by a byte. In other words, one can store 3 bits in each pixel. An 80×60 pixel image, can thus store a total amount of 1, 4400 bits or 1800 bytes of embedded data. For example a grid for 3 pixels of a 24-bit image can be as follows: a. (00101101 00011100 11011101), b. (10100110 11000100 00001100), c. (11010010 10101101 01100011).

When the number 201, which binary representation is 11001001, is embedded into the least significant bits of this part of the image, the resulting grid is as follows: a. (00101101 00011101 11011101), b.(10100110 11000101 00001100), c,(11010010 10101100 01100011).

Although the number was embedded into the first 8 bytes of the grid, only the 4 underlined bits needed to be changed according to the embedded message. So only half of the bits in an image will need to be modified to hide a

secret message using the maximum cover size. Changes in LSB of a pixel results in small changes in the intensity of the colour. These changes cannot be identified by the human eye - thus the message is successfully hidden. With a good image, one can hide the message in the least as well as second to least significant bit and still not see the difference. This approach is very easy to detect.Instead of using the LSB-1 of the cover

for embedding the message, LSB-2 has been used to increase the robustness[1].

A slightly more secure system is for the sender and receiver to share a secret key that specifies only particular pixels to be changed. Should an Adversary suspect that LSB Steganography has been used, he has no way of knowing which pixels to target without the secret key. In its simplest form, LSB makes use of BMP images, since they use lossless compression. Unfortunately to be able to hide a secret message inside a BMP file, one would require a very large cover image. The LSB based Steganography is one of the steganographic methods, used to embed the secret data in to the least significant bits of the pixel values in a cover image. e.g. 240 can be hidden in the first eight bytes of three pixels in a 24 bit image.

Original data: (00100111 11101001 11001000) (00100111 11001000 11101001) (11001000 00100111 11101001) Embed data: 242: 11110010 & Result: (00100111 11101001 11001001) (00100111 11001000 11101000) (11001001 00100110 11101001). Here number 242 is hidden into first eight bytes of the grid and only 6 bits are changed.

4.1 LSB Algorithm

4.1.1 Embed secret image:



Step 1: Read the cover image and secret image which is to be hidden in the cover image.

Step 2: Convert text message in binary.

Step 3: Calculate LSB of each pixels of cover image.

Step 4: Replace LSB of cover image with each bit of secret image one by one.

Step 5: Write stego image

4.1.2 Retrieve secret image:

Step 1: Read the stego image.

Step 2: Calculate LSB of each pixels of stego image.

Step 3: Retrieve bits and convert each 8 bit into image.

5. Frequency Domain - Dct

Discrete Cosine Transform (DCT) is same as like Discrete Fourier Transform (DFT), which is used for signal frequency analysis. These Mathematical transforms convert the pixels to provide the effect of “spreading” the location of the pixel values over part of the image. The DCT transforms a signal from an spatial domain representation into a frequency domain representation, by grouping the pixels into 8×8 pixel blocks and transforming the pixel blocks into 64 DCT coefficients each. A modification of a single DCT coefficient will affect full 64 image pixels in that block.

A DCT coefficient separates the image into parts of differing importance. It transforms a signal or image from the spatial domain to the frequency domain. It can separate the image into high, middle and low frequency components. Signal energy lies at low frequency in image; it appears in the upper left corner of the DCT. Compression can be achieved since the lower right values represent higher frequencies, and generally small enough to be neglected with little visible

distortion. DCT is used in steganography as Image is broken into 8×8 blocks of pixels. Working from left to right, top to bottom, the DCT is applied to each block. Each block is compressed through quantization table to scale the DCT coefficients and message is embedded in DCT coefficients.

5.1. Dct Algorithm:

5.1.1 Embed secret image:

Step 1: Read cover image.

Step 2: Read secret image and convert it in binary.

Step 3: The cover image is broken into 8×8 block of pixels.

Step 4: Working from left to right, top to bottom subtract 128 in each block of pixels.

Step 5: DCT is applied to each block. Step 6: Each block is compressed through quantization table.

Step 7: Calculate LSB of each DC coefficient and replace with each bit of secret image.

Step 8: Write stego image.

5.1.2 Retrieve secret image:

Step 1: Read stego image.

Step 2: Stego image is broken into 8×8 block of pixels.

Step 3: Working from left to right, top to bottom subtract 128 in each block of pixels.

Step 4: DCT is applied to each block.

Step 5: Each block is compressed through quantization table.

Step 6: Calculate LSB of each DC coefficient.

Step 7: Retrieve and convert each 8 bit into Image.

Table1 represents existing methods performance analysis and comparison..

6. Proposed Method - Pct



Finally new proposed PCT based steganography implementation has been started for further implementation and improvements on DCT. PCT – Similar to DCT and IPCT – Similar to IDCT [5], but it is lossless. Series of The PCT is a series of Hadamard, odd, and odd-odd transforms. It is similar to the DCT. Compared to DCT, it is linear, reversible in case image is integer. Divides image in DC, LP and HP Coefficients. In the LSB of the transformed image secret image will be embedded, odd, and odd-odd transforms [5]form PCT algorithm.

6.1 Pct - Algorithm

6.1.1 Embed secret image:

Read the Cover and secret image

- a) Convert the secret image in to binary bits.
- b) Apply PCT on the Cover image by splitting in to that in to 4x4 block size
- c) Do quantization on the received PCT coefficients
- d) Insert the secret image to the quantized PCT coefficients other than 0, 1, and -1 values
- e) Apply de-quantization and inverse PCT to get the stego image.
- f) On the stego image perform quantization and PCT.
- g) Then extract the bits from the stego image other than 0, 1, -1 coefficients to get the secret image.

6.1.2 Retrieve secret image:

- a. Read the Stego image
- b. Apply PCT on the Stego image by splitting in to that in to 4x4 block size

- c. Do quantization on the received PCT coefficients
- d. Extract the secret image bits in the quantized PCT coefficients other than 0, 1, and -1 values
- e. Get the secret image by combining the received secret bits.

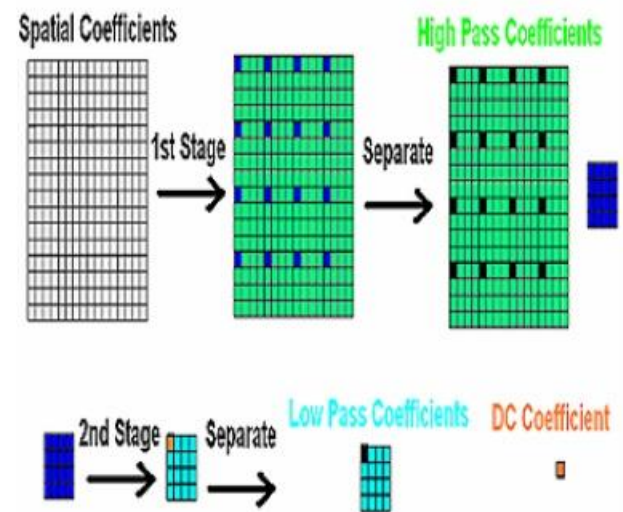


Fig5: PCT Steganography algorithm[6].

Within the spatial layout the data is orthogonally represented in the frequency domain as well. As a result of the transform stage the coefficients are grouped into three groups, DC, lowpass (LP), and highpass (HP). A flow of this process is illustrated in Figure 5 and depicts how in two separate stages one macroblock contains one DC, 15 LP, and 240 HP coefficients. Even though it might appear that these pixels are then grouped separately, they are in fact still within

their spatial layout algorithm[6].

7. Patient Condition Monitoring

There is no specific algorithm for patient condition monitoring. Blood pressure, Heart beat and Brain signal all are measured and compared with the known standard database

threshold value. If patient condition is identified as abnormal by database comparison then alarm sound will be notified and Warning message will be displayed at parallel.

8. Automatic Control

Based on patient monitoring status - alarm and warning message will be notified. For this also no specific algorithm, But based on Doctors instruction and Timing control will be done on blood, glucose, medicine below control. Advantage of this method is to avoid the manual human error, which will make human life's death.

9. Future Scope

In future apart from emergency ward treatment, I hope to add support for all kind of treatment like operation theatre & Artificial treatment monitoring and automatic control according to the patient condition. This allows for a much broader range of patient safety monitoring and control. Depending on the type of the cover object, definite and appropriate technique is followed in order to obtain security[3]. For additional control also will be handled by the same BF-533 DSP processor.

10. Conclusion

Still Steganography is on research. It is good and effective method of hiding data that has been used throughout history. Methods that can be employed to uncover such devious tactics, but the first step are awareness that such methods even exist. There are so many good reasons as well to use this type of data hiding, including watermarking or a more secure central storage method for such things as passwords, or key processes. All the major image file formats have different methods of hiding secret images, with different strong and weak points respectively. Where one technique lacks in memory capacity, the other

lacks in security. Steganography and its various implementations need to be further investigated. In this paper analyzed information of existing spatial and transform domain steganography techniques are given. Additionally implementation of proposed PCT steganography information also added to have more secure digital image steganography. Thus our new proposed method will reduce all demerits which exist in the existing steganography system. Automatic monitoring and control still applied only in limited medical treatments, So with this paper analysis, I propose that this can be extended to broader range of medical treatment. This will help us to avoid manual mistakes in treatment , where small mistake will lead to patient's death. Main advantage of this implementation is that same BF 533 DSP processor is enough, even there is future algorithm implementation.

11. Reference

- [1] A.E.Mustafa,A.M.F.ElGamal,M.E.ElAlmi, Ahmed.BD (2011): Aproposed Algorithm For Steganography In Digital Image Based on Least Significant , Research Journal Specific Education, Issue No. 21, April. 2011.
- [2] M.I.Khalil(2011),Image Steganography: Hiding Short Audio Messages with in Digital Images, JCS&T Vol. 11 No. 2, October 2011.
- [3] Samir Kumar Bandyopadhyay : An Alternative Approach of Steganography using Reference Image, International Journal of Advancements in Technology <http://ijict.org/> ISSN 0976-4860, Vol 1, No 1 (June 2010).
- [4] Abbas Cheddad JoanCondell, KevinCurran, PaulMcKevitt, Digital image steganography: Survey and analysis of

- current methods,
www.elsevier.com/locate/sigpro,
10.1016/j.sigpro.2009.08.010 August
2009.
- [5] VHDL Modeling and Synthesis of the JPEG-XR Inverse Transform by Peter Frandina, Rochester Institute of Technology Rochester, New York August 2009.
- [6] Modeling and Synthesis of the HD Photo Compression Algorithm By Seth Groder, Rochester Institute of Technology, Rochester, New York August 2008.

Design and Implementation of Micro Thermo Electric Generator for Bio Implantable Devices

Y. Jeyashree¹, Pheba Cherian², A.Vimala Juliet³, E. Paul Braineard⁴

ICE Department, SRM University, Chennai, India

¹jeyashree_christley@yahoo.co.in, ²phebacherian@gmail.com, ³vimlala@yahoo.co.in,

⁴ebpaul@gmail.com

Abstract

This work presents the design, simulation and performance of Micro Thermoelectric Generator (micro TEG) for power generation from body heat. For analysis we used P and N silicon Thermo elements and Graphene as the interconnect between the two legs. The output voltage obtained per device is 1.28mV, for a temperature difference of 10K. By using SiO₂ insulation over the cold side the performance is further improved. The size of the each leg of thermocouples in this analysis is length 123 μm by breadth 2 μm by height 0.5μm and distance between two legs, 7.5 μm. This gives a power density of $2.214 \times 10^{-3} \mu\text{W.cm}^{-2}\text{K}^{-2}$. The power can be efficiently used for the working of bio-implantable devices.

General Terms:

Power Source for Bio-Implantable device.

Keywords:

Micro Thermoelectric Generator, Power Source for Bio Implantable devices.

1. Introduction

In the last decade, various miniaturized thermoelectric converters fabricated using MEMS technology are developed [1-6]. The main applications of μ-TEG are electronic heat-cost monitors, active transponders and self-powered temperature warning systems

[1]. The first commercial μ-TEG product is developed for wrist watch application driving by human body heat [2]. Bi₂Te₃-Based flexible micro TEG for providing electrical energy to autonomous micro systems, which up to now are powered by bulky batteries with a limited life time[3]. A new concept of heat dissipation path (HOP) for enhancing the temperature difference between hot and cold junctions [4]. Heat Energy Conversion using μTEG is introduced [6]. The new TEG is developed for the purpose of providing power to Bio-Implantable devices. Since most of the Bio-Implantable devices are powered by batteries that needs replacement, Thermoelectric power generator is a solid state device that provides direct energy conversion from thermal energy (Body heat) due to a temperature gradient into electrical energy based on “Seebeck effect”. This thermoelectric device can act as electrical power generators. A typical thermoelectric power module is shown schematically. In the figure1: n-type and p-type semiconductor thermo elements are connected in series by highly-conducting metal strips to form a thermocouple. The two sides of the thermocouple are maintained at two different temperatures. Due to this temperature difference, flow of the charge carrier's takes place in both n and p-type pellets constituting to the voltage difference across the load resistance. The

semiconductor thermo elements that are sandwiched between the ceramic plates are connected thermally in parallel and electrically in series to form a thermoelectric device (module). More than one pair of semiconductors are normally assembled together to form a thermoelectric module and within the module a pair of thermo elements is called a thermocouple. The junctions connecting the thermo elements between the hot and cold plates are interconnected using highly conducting metal (e.g. copper) strips.

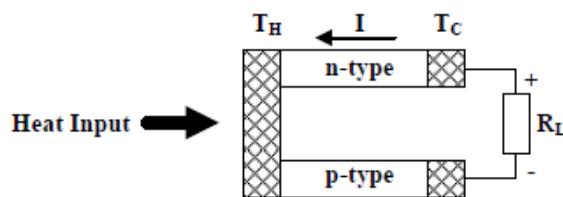


Figure 1: Single Thermo couple producing output power

In this paper, we present a micro thermoelectric generator which can utilize the body heat to produce Electrical power that can be used to drive bio-implantable devices like pacemakers. Poly Si is selected since it is easily available and also more compatible to fabrication procedures compared to highly efficient thermoelectric material Bi₂Te₃.

2. Performance Of Teg

Seebeck coefficient or the thermo power, represented by ‘S’, of a material measures the magnitude of an induced thermoelectric voltage in response to a temperature difference across that material. If the temperature difference ΔT between the two ends of a material is small, then the thermo power of a material is defined approximately as,

$$S = -\Delta V / \Delta T. \quad (1)$$

The figure of merit Z for thermoelectric devices is defined as,

$$Z = \sigma S^2 / \kappa. \quad (2)$$

Where σ is the electrical conductivity, κ is the thermal conductivity, and S is the Seebeck coefficient. The dimensionless figure of merit ZT is formed by multiplying Z with the average temperature.

3. Design Of The Teg

Figure 2 illustrates a schematic of the thermoelectric micro generator. The generator consists of 32 thermocouples in series. The materials of the thermocouples are n-type and p-type polysilicons. Each thermocouple is constructed by two strips; one strip is p-type polysilicon and the other is n-type polysilicon. The dimensions of each thermocouple are 246 μm long, 2 μm wide and 0.3 μm thick. The area of the generator is about 430 * 430 μm^2 .

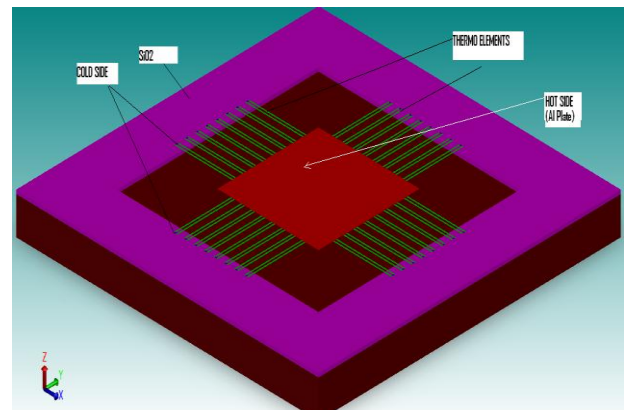


Figure 2 : Thermoelectric Generator - Post processing

As shown in Figure 2, one junction of p-type and n-type polysilicon strips covered with silicon dioxide is the cold part of the thermocouples and the other junction of p-

type and n-type polysilicon strips to be suspended is the hot part of the thermocouples. In order to increase the temperature difference between the hot and cold parts, silicon dioxide with low thermal conductivity is utilized to cover the cold part. In addition to being suspended, the hot part is connected to an aluminum plate, which is used to conduct heat and increase the heat-receiving area. The finite element method (FEM) software, Coventorware, is employed to simulate the temperature distribution of the micro generator. The model of the generator was established in accordance with Figure 2, and the Manhattan brick was used to mesh the model. The parabolic element was adopted.

Table1: Thickness and thermal conductivity of the materials

Material	Thickness(μm)	Thermal Conductivity ($\text{pW}/\mu\text{m}\cdot\text{K}$)
Al	0.6	2.36×10^8
SiO_2	5	1.42×10^6
Poly Si	0.3	3.2×10^7

The initial temperature of 300K (room temperature) was set, and the heat source of 310 K (outside temperature) was applied to the aluminium plate of the generator. Figure 3 shows the simulated results of temperature distribution for the micro generator. The results showed that the suspended aluminum plate had a uniform temperature of 310 K. The silicon dioxide layer over the cold part of the thermocouples successfully isolates the heat source.

4. Simulation In Coventorware

4.1 Process Steps

Simulation is done using Coventorware software using

- Process Editor

- Layout Editor
- Mem Mech Analysis

Design of the generator is done using Layout editor and material properties are defined in process editor and analysis were carried out in Mem Mech Analysis.

The output voltage depends on the number of thermocouples. The relationship between the output voltage and the number of thermocouples is given by

$$V_{out} = n(\alpha_1 - \alpha_2)(T_h - T_c). \quad (3)$$

where V_{out} represents the output voltage generated by the thermoelectric effect; n is the number of thermocouples connected in series; α_1 and α_2 are the Seebeck coefficients of p-type and n-type polysilicons, respectively; and T_h and T_c are the temperatures of the hot and cold parts, respectively. According to Equation (3), we know that the output voltage relies on the number of thermocouples, the Seebeck coefficient of materials and the temperature difference. The output voltage, V_{out} , is proportional to the number of thermocouples, n , and the relative Seebeck coefficient, $\alpha_1 - \alpha_2$. In this work, the n-type and p-type polysilicons are adopted as the materials of the thermocouples owing to their large relative Seebeck coefficient. In this design, the number of thermocouples is 32, and the relative Seebeck coefficient of the n-type and p-type polysilicons is about 0.004 mV/K. The output voltage of the generator can be evaluated by substituting the values $n = 32$ and $\alpha_1 - \alpha_2 = 0.004 \text{ mV/K}$ into Equation (3), and the results are plotted in Figure 4. The calculated results show that the output voltage of the generator was 1280 μV at the temperature difference of 10 K. If the external load, R , that is the same the inertial load is connected, the maximum output power of the generator can be



obtained,

$$P_{\max} = V_{\text{out}}^2 / 4R. \quad (4)$$

Furthermore, substituting Equation (3) into Equation (4), the maximum output power of the generator can be written as,

$$P_{\max} = n^2 (\alpha_1 - \alpha_2)^2 (T_h - T_c)^2 / 4R. \quad (5)$$

In this design, the parameters are $n = 32$, $\alpha_1 - \alpha_2 = 0.004$ mV/K and $R = 1$ kΩ. Substituting the values into Equation (5), the maximum output power of the generator can be yielded and the results are plotted in Figure 5. The output power of the generator was about 409.6 pW at the temperature difference of 10 K.

4.2 Results

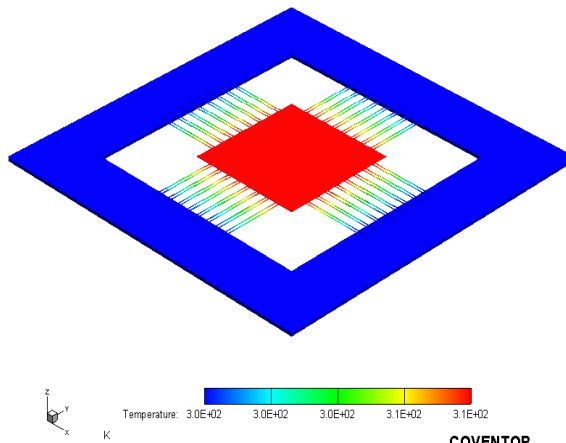


Figure 3: Simulation of temperature distribution for the Thermoelectric generator

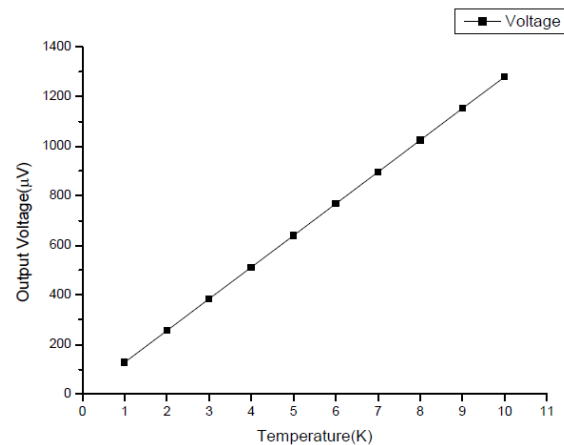


Figure 4: Output Voltage

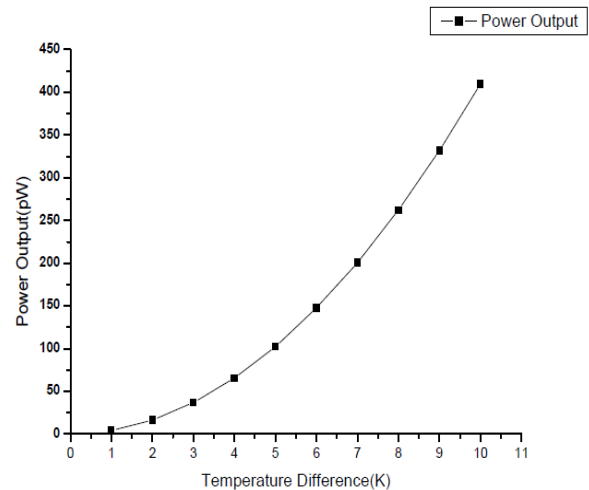


Figure 5: Output Power

5. Conclusion

With a view to replace the batteries in implantable devices, that needs replacement, we have designed and simulated a thermo electric generator using MEMS technology. It is done with a simple structure designed in Coventorware simulation tool and a considerable voltage and output power is obtained. For further improvement we can design a μTEG using a polymer substrate and high conductivity thermoelements and interconnect material.

6. References

- [1] Rowe, D.M., ed., *Thermoelectrics Handbook: Macro to Nano*, CRC Press, BocaRaton, London/New York, 2006.
- [2] M. Kishi, H. Nemoto, T. Hamao, M. Yamamoto, S. Sudou, M. Mandai, S. Yamamoto, Micro thermoelectric modules and their application to wrist watches as an energy source, in: 18th International Conference on Thermoelectrics. Proceedings-ICT'99
- [3] Wolf Glatz, Etienne Schwyter, Lukash Durrer, and Christopher Hierold , Bi_2Te_3 - Based Flexible Micro Thermoelectric Generator with optimized Design , Journal of Microelectromechanical Systems, June 2009
- [4] Chengkuo Lee, Jin Xie ,Development of Vacuum Packaged CMOS Thermoelectric Energy Harvester IEEE International Conference, 117685, 08-01-2009, Shenzhen, China
- [5] Pin-Hsu Kao , Po-Jen Shih , Ching-Liang Dai and Mao-Chen Liu.' Fabrication and Characterization of CMOS-MEMS Thermoelectric Micro Generators. Journal of Sensors 2010, 10, 1315-1325; doi:10.3390/s100201315 ISSN 1424-8220
- [6] Development of a Novel Transparent Microthermoelectric Generator for Solar Energy Conversion. Proceedings of the 2011 6th IEEE International Conference on Nano/Micro Engineered and Molecular Systems February 20-23, 2011, Kaohsiung, Taiwan

Neural Network based Handwritten Script Recognition

Jose Anand, Helen Samuel, and H. C. Parimala

Department of Electronics and Communication Engineering,

KCG College of Technology, Karapakkam.

joseanandme@yahoo.co.in, helensam90@gmail.com, parimala.hc1991@yahoo.com

Abstract

One of the basic requirements in document processing automation is the script identification among multi-script and multi-lingual environments. The existing handwritten script recognition procedures depends on features extracted from the document images at various levels like character, word, text line or block level. This paper describes a neural network based script recognition system which can be used in the machine reading of documents written in capital English alphabets and numerals using the block level extraction method. The proposed system can recognize any number of scripts which are developed from a set of representative symbols or templates. Each script has a clustering textual symbol obtained from a set of neural trained documents and each cluster is represented by its centroid. To recognize a new script, the proposed system compares a subset of symbols from the trained template and selects the script whose template gives the best match.

Key Words – feature extraction, multi-lingual, neural network, OCR, script identification.

I. Introduction

With the recent emergence and widespread application of multimedia technologies, the world moves ever closer to the concept of the “paperless office,” more and more communication and storage of documents is performed digitally. Documents and files that were once stored physically on paper are now being converted into electronic form in order to facilitate quicker additions, searches, and modifications, as well as to prolong the life of such records.

As a result, automatic script recognition has been a challenging research problem in a multi-script environment and has acquired importance through the years [1]. The documents in electronic form can be easily accessible and has more privacy and security. In transforming the document from the existing handwritten based document to the paperless electronic information system, document image processing and OCR will play an important role [2].

As India is a multi-lingual country, multi-script identification plays an important role in the design of an Optical Character Reader (OCR) system for the analysis and recognition of the page in the document. The automatic identification of handwritten script facilitates many important applications such as automatic transcription of multi-lingual documents and



search for documents on the Web containing a particular script. The increase in usage of handheld devices, which accepts handwritten input has created a growing demand for algorithms that can efficiently analyze and retrieve handwritten data.

For the paperless electronic information system, one of the important tasks in document image analysis is the automatic reading or identification of text information from the document format. This can be done by the OCR, which reads the optically scanned document text by the character reader machine. The drawback in OCR is that, it makes an implicit assumption that the multi-script document has to be processed is known beforehand. So this needs human intervention to select the correct OCR package, which is clearly inefficient and undesirable. Thus automatic identification of scripts facilitates more importance.

Different people have very different writing style and even the digits of a same person written in different time are not identical [3]. For automatic processing of documents, a pre-processing is necessary and this will identify the script of the text lines. Thus the data obtained needs a lot of pre-processing including filtering, smoothing, and normalization before the recognition process [4]. This is also a lengthy process, and this paper proposed an automatic document recognition system using a feature extractor and a modular neural network.

The process of digital documentation is becoming popular for applications to office and library automation, banking applications, publishing houses communication technology, postal services and many related fields [15].

Optical Character Reading (OCR) has been implemented for several commercial operations. The Canada postal system has been using OCR systems since 1971. The system read the name and address to sort the post and print a routing bar code on the envelope.

The rest of the paper is organized as follows. Related literature survey is described in Section 2. Section 3 presents the proposed script identification system. The details of experimental setup and results are illustrated in Section 4. Finally, conclusion is given in Section 5.

II. Related Work

Handwriting script processing is a domain with more expansion and this field is not only explained by the exciting challenges involved, but also the huge benefits that a system, designed in the context of all world class application [5]. Pal et al (2003) [6] have reported the majority of the work on Indian language identification. The script identification technique explored uses a binary tree classifier for 12 Indian scripts using a large set of features.

Lijun et al (2006) [7] proposed the binary tree classifier seems to be complex since the features are extracted at line, word and even at character level. Dhandra et al (2006) [8] proposed the word level script identification in bilingual documents through discriminating features. Their work also exploited the use of discriminating features such as aspect ratio, strokes, eccentricity, etc. as a tool for determining the script at word level in a bilingual document containing multi-lingual languages.

Hiremath (2008) [9] proposed a global approach for identification of Indian languages by combining Gabor filter based technique and direction distance histogram classifier considering multi-linguistic languages. Gopal et al (2006) [10] presented a script identification technique for ten different Indian scripts using a set of feature extraction from log-Gabor filter based technique.

Nagabhushan et al (2005) [11] proposed an intelligent pin code based script identification technique based on texture analysis using modified invariant moments. Andrew et al (2005) [12] proposed the use of texture features using gray level co-occurrence matrix and Gabor filter based energy features for determining the script of a document image.

Shivakumar et al (2006) [14] proposed the skew detection and correction technique which uses a global thresholding approach to binarize the scanned gray scale images where black pixels having the value 0's correspond to object and white pixels having value 1's correspond to background. Pradeep et al (2012) [16] identified a Neural Network for the design of hand written character recognition system for the English Language. The system uses back propagation neural network, nearest neighbour network and radial basis function network to classify the characters. The performance of the system is tested for all the twenty six characters.

III. Proposed Script Identification

The Script identification consists of some basics steps pre-processing, feature extraction, classification algorithm to identify the pattern, and testing with the trained set. There are

many analyses based on the character sets or strokes of each script. They are character, word or line analysis, text block analysis and hybrid analysis [13].

In our approach, for the identification of the script of a word, the features that play a major role are the spatial spread of the words formed by the scripts and the direction of orientation of the structural elements of the characters in the word. So, a brief description of the properties of the associated scripts is in order, for the clear understanding that leads to the proper design of an identifier system.

A. Character, word or line analysis

Various methods based on the analysis of character, word or line, have been proposed for language identification. The proposed a scheme for multilingual, multi-font, and multi-size large-set character recognition using self organizing neural network. They determine not the script of the entire document, but the script of individual characters within the document.

In order to improve the performance of the proposed scheme, non-linear shape normalization based on dot density and three kinds of hierarchical features are introduced. For coarse classification, two kinds of classifiers are proposed. One is a hierarchical tree classifier [13], and the other is a SOFM/LVQ based classifier which is composed of an adaptive SOFM coarse classifier and LVQ4 language-classifiers.

For fine classification, an LVQ4 classifier has been adopted. Three efficient techniques for identifying Arabic script and English script were presented and evaluated. These



techniques address the language identification problem on the word level and on text line level. The characteristics of horizontal projection profiles as well as run-length histograms for text written in both languages are the basic features underlying these techniques.

B. Text block analysis

Since visual appearances of different scripts are often distinctive from each other, a text block in each script class may be considered as a unique texture pattern. Thus, texture classification algorithms may be employed to perform script identification. A new scheme based on texture analysis for script identification which did not require character segmentation. Via simple processing, a uniform text block on which texture analysis can be performed is obtained from a document image.

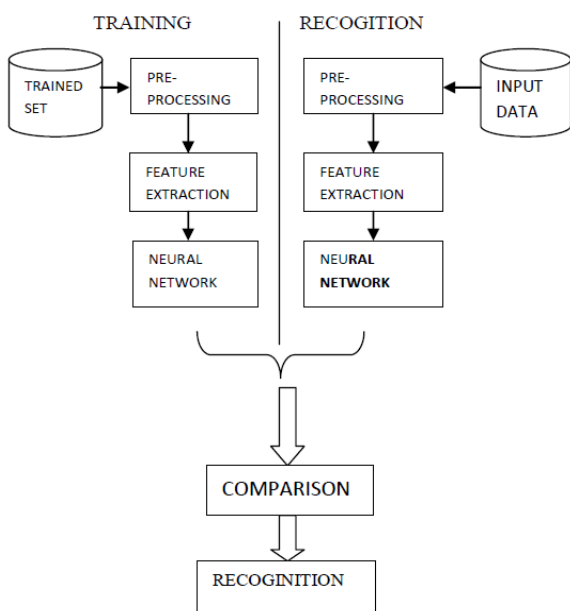


Figure 1 Recognition Process

Multiple channel (Gabor) filters and grey level co-occurrence matrices are used in order

to extract texture features [1]. This uses the K-NN classifier to classify the test documents. Also, an approach on script-based classification of hand-written text documents in a multilingual environment was used. This applies de-noising, thinning, pruning, m-connectivity and text size normalization in sequence to produce a unique text block. Moreover, this uses multi-channel Gabor filtering to extract text features.

C. Hybrid analysis

Most comparatively complex methods are based on hybrid feature analysis. These schemes try to combine the different features extracted from global (text block) and local (text line, word, character and connected components) document entities. Most comparatively complex methods are based on hybrid feature analysis. These schemes try to combine the different features extracted from global (text block) and local (text line, word, character and connected components) document entities.

D. Proposed framework

In this, a concept of identifying the handwritten scripts and convert them to an electronic document is proposed. Before identification the input is scanned by OCR. The identification consists of components like pre-processing, feature extraction and neural network. The figure 1 represents how the recognition process is been done by neural network.

IV. Simulation Results

The implementation will mainly focus on identifying 0 - 9 from segmented pictures of

handwritten digits and the capital letters in English. The input of the program is a gray level image, the intensity level of which varies from 0 to 255. For simplicity, input images are pre-treated to be of certain fixed size, and each input image should contain only one unknown digit in the middle.

A. Pre-processing

Any script identification method requires conditioned image input of the document, which implies that the document should be noise free and skew free, as shown in figure 2. Apart from these, some recognition techniques require that the document image should be segmented and threshold.

All these methods, help in obtaining appropriate features for script identification processes. The preprocessing techniques such as noise removal and skew correction are not necessary for the datasets that are manually constructed by downloading the documents from the Internet. As the cell of codes gets executed the image is read into the Matlab workspace.

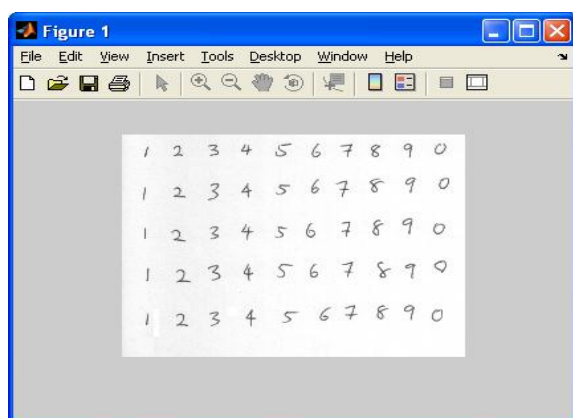


Figure 2 Reading Image

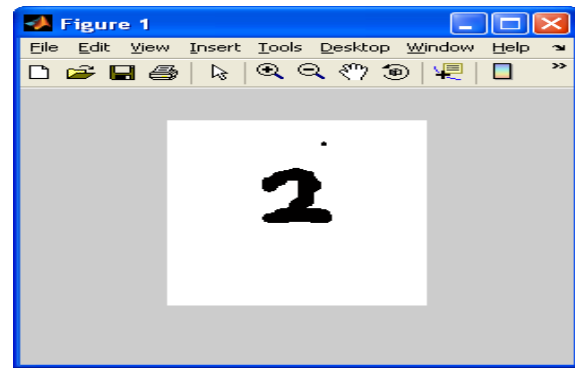


Figure 3 Selecting a particular image

However, for the datasets that is constructed from the scanned document images, preprocessing steps such as removal of non-text regions, skew-correction, noise removal and binarization is necessary. Figure 3 shows the selection of a single segment and figure 4 shows the grabbing of the values into the grid format. After the cell of codes read the image, a particular number is been cropped or selected.

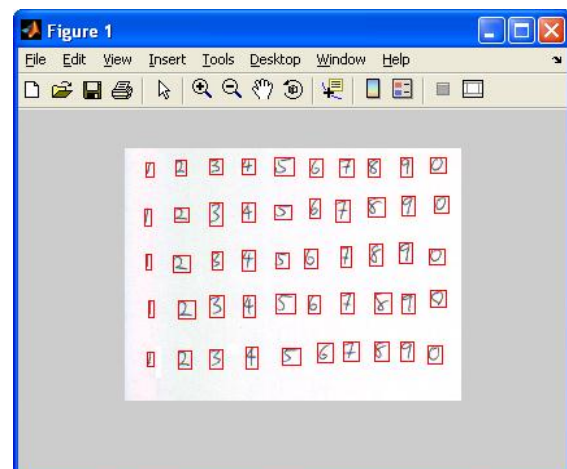


Figure 4 Grabbing the values into the grid

B. Feature Extraction

A feature extraction method is used to reduce the bitmap image of a sample pattern corresponding to pixel distribution into a vector of real numbers required for classification. In pattern recognition and in image processing, feature extraction is a special form of dimensionality reduction [2].

When the input data to an algorithm is too large to be processed and it is suspected to be notoriously redundant (much data, but not much information) then the input data will be transformed into a reduced representation set of features (also named features vector). Transforming the input data into the set of features is called feature extraction. If the features extracted are carefully chosen it is expected that the features set will extract the relevant information from the input data in order to perform the desired task using this reduced representation instead of the full size input.

C. Neural Network Training:

Neural networks, with their remarkable ability to derive meaning from complicated or imprecise data, can be used to extract patterns and detect trends that are too complex to be noticed by either humans or other computer techniques [4]. A trained neural network can be thought of as an "expert" in the category of information it has been given to analyse.

Neural network classifiers exhibit powerful discriminative properties and they have been used in handwriting recognition particularly with digits, isolated characters, and words in small vocabularies. The

training by neural network is shown in figure 5.

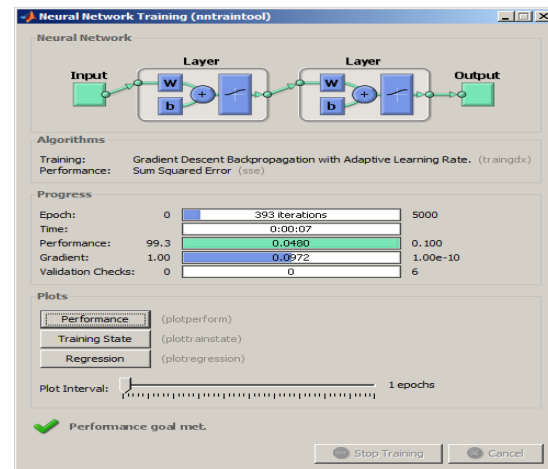


Figure 5 Training by neural network

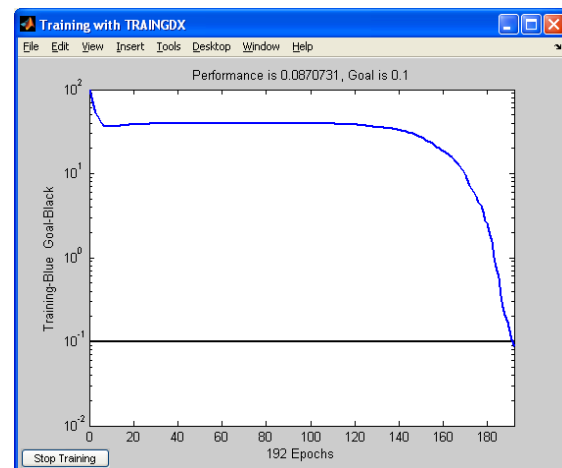


Figure 6 Graph showing performance measure

This training stops when the validation error is increased for six iterations. Figure 6 shows the performance measures of training and goal. The performance of goal is always constant.

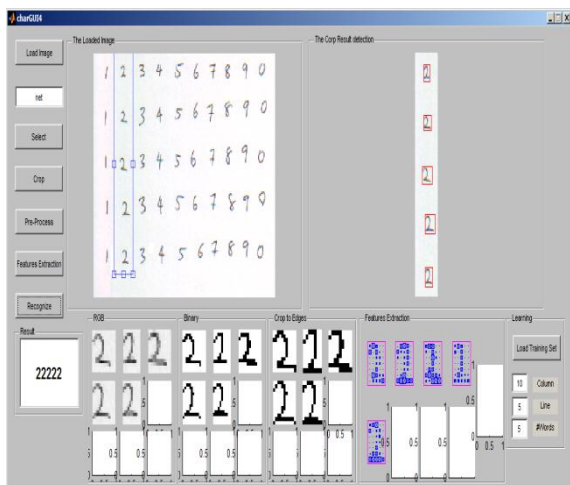


Figure 7 Selection of same values in vertical form

Character Detection - As stated earlier that character is written with white digital ink, so the algorithm for character detection is quite simple. It searches from left to right for white pixels starting from left top corner of the area specified for writing. A trace of a white pixel is the indication of the presence of a character.

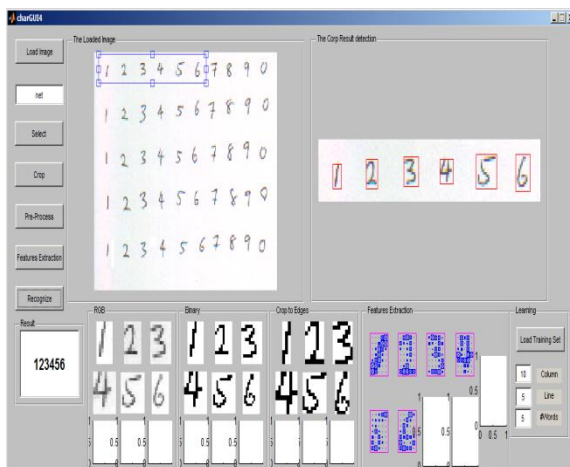


Figure 8 Selection of different values in horizontal form

The figure 7 represent the same number (2) with different hand written inputs is been identified but where as in figure 8 different number (1, 2, 3, 4, 5, 6) is been identified.

Figure 9 shows the output on the command window.

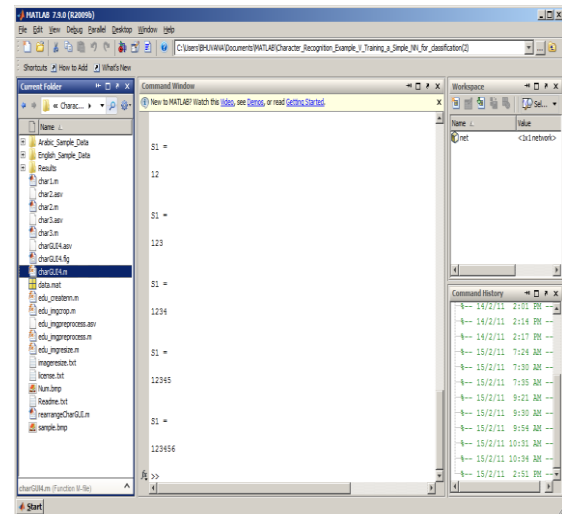


Figure 9 Output on the command window

Figure 10 and 11 shows the various test inputs considered in the simulation.

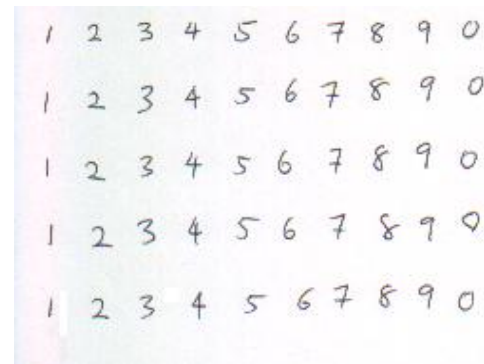


Figure 10 Test input

JUDAS
PRIEST
775758
HOLA
DIEGO
12312
367945

Figure 11 Test input

ssn

V. Conclusion

In this paper, a new method to identify the handwritten script type of the document containing capital English alphabets and numerals are presented. The proposed model is developed based on the classifier called Neural Networks. The method is not only useful for script identification but also for simple and non uniform sized character recognition tasks. Experimental results shows that the proposed method has a recognition rate of 99.5% for the data set constructed from scanned document images. Character recognition for the English character is studied and progressed to a level, but the same is much lagging in the regional languages. This is because of the complications in terms of structure and computations. The future work can be proceeded with the multi-lingual documents. The error rate can be reduced by changing the feature extraction module to increase the number of features.

VI. Reference

- [1] M. C. Padma, and P. A. Vijaya, "Script Identification from Trilingual Documents using Profile based Features", International Journal of Computer Science and Applications, Technomathematics Research Foundation, Vol. 7, No. 4, pp. 16-33, 2010.
- [2] S. Basavaraj Patil, and N. V. Subbareddy, "Neural Network-based system for Script Identification in Indian Documents", Sadhana, Vol. 27, Part 1, pp. 83-97, February 2002.
- [3] Weiran Wang, "ANN for Handwritten Digits Recognition", Final Report of Term Project, May 5, 2009.
- [4] Muhammad Faisal Zafar, Dzulkifli Mohamad, and Razib M. Othman, "Online Handwritten Character Recognition: An Implementation of Counter Propagation Neural Net", World Academy of Science, Engineering and Technology, 10, 2005.
- [5] Morita M., Sabourin R., Bortolozzi F., and Suen C. Y., "A Recognition and Verification Strategy for Handwritten Word Recognition", (ICDAR'03), Edinburgh, Scotland, pp. 482-486, 2003.
- [6] Pal U., Sinha S., and Chaudhuri B. B., "Multi-script Line Identification from Indian Documents", Proceedings of the Seventh International Conference on Document Analysis and Recognition, pp. 880-884, 0-7695-1960-1/03 © IEEE 2003.
- [7] Lijun Zhou, Yue Lu and Chew Lim Tan, "Bangla/English Script Identification based on Analysis of Connected Component Profiles", Proceedings of the 7th IAPR Workshop on Document Analysis System, New Land, pp. 234-254.
- [8] Dhandra B. V., Nagahushan P., Mallikarjun Hagarge, Ravindra Hegadi, and Malemath V. S., "Script Identification based on Morphological Reconstruction in Document Images", Proceedings of the 18th International Conference on Pattern Recognition (ICPR'06), Vol. No. 11-3, pp. 950-953, 2006.
- [9] Hiremath P. S., and Shivashankar S., "Wavelet Based Co-occurrence Histogram Features for Texture Classification with an Application to Script Identification in a Document Image", Pattern Recognition Letters, pp. 1182-1189, 29, 2008.



- [10] Gopal Datt Joshi, Saurabh Garg, and Jayanthi Sivaswamy, “Script Identification from Indian Documents”, H. Bunke and A. L. Spitz editions: DAS 2006, LNCS 3872, pp. 255-267.
- [11] Nagabhushan P., Angadi S. A., and Anami B. S., “An Intelligent Pin Code Script Identification Methodology Based on Texture Analysis using Modified Invariant Moments”, Proceedings of ICCR, pp. 615-623.
- [12] Andrew Busch, Wageeh W. Boles, and Sridha Sridharan, “Texture for Script Identification”, IEEE Transactions of Pattern Analysis and Machine Intelligence, Vol. 27, No. 11, pp. 1720-1732, 2005.
- [13] Lijun Zhou, Yue Lu, and Chew Lim Tan, “Bangla/English Script Identification Based on Analysis of Connected Component Profiles”, East China Normal University, Shanghai – 200062.
- [14] Shivakumar, Nagabhushan, Hemanthkumar, and Manjunath, “Skew Estimation by Improved Boundary Growing for Text Documents in South Indian Languages”, VIVEK – International Journal of Artificial Intelligence, Vol. 16, No. 2, pp. 15-21, 2006.
- [15] Madhu Shahi, Anil K Ahalwat, and B. N. Pandey, “Literature Survey on Offline Recognition of Handwritten Hindi Curve Script Using ANN Approach’, International Journal of Scientific and Research Publications, Vol. 2, Issue 5, pp. 1-6, May 2012, ISSN: 2250-3153.
- [16] J. Pradeep, E. Srinivasan, and S. Himavathi, “Neural Network Based Recognition System Integrating Feature Extraction and Classification for English Handwritten”, IJE Transactions B: Applications, Vol. 25, No. 2, pp. 99-106, May 2012.

Bedside Fall Detection and Patient Limb Movement Detection using Near Infrared Sensor

SubashPadmanaban¹, SuryahSuresh¹

¹ Department of Biomedical Engineering,
SRM University, Kattankulathur.
subashpadmanaban@srmuniv.edu.in

Abstract

Patient falls are inevitable events that occur during various instances often resulting in mild to severe injuries. Further, bedridden patients are always at risk to such unprecedented mishaps. The impact of such falls and the inability to provide immediate medical attention leads to further complications. Thus, it is now imperative for hospitals and places that house bedridden patients to use patient fall detectors to stay updated with the status of the patient. Near Infrared sensor provides an efficient and facile technique to detect bedside falls and alert the caretaker. Using simple electronics obviates the signal processing glitches and non-real time detection encountered by contemporary models. Detecting bedside falls with Near Infrared sensor is a simple and cost-effective alternative. The prototype was fabricated to work as a robust substitute to human caretaking of bedridden patients.

General Terms

Biomedical Instrumentation, Fall detection

Keywords

Fall detection, Near Infrared, Bedside fall, limb movement detection, Biomedical Instrumentation

1. Introduction

In today's modern healthcare facilities, monitoring the status of bedridden patients is given utmost importance. Patient monitoring constitutes of keeping check on the physical status of the patient. Oftentimes, obscure and inadequate knowledge of the physical status of the patient increases the risk of unprecedented events going unnoticed. Patient falls off the bed have become common among household mishaps. A research by Triangle Research and Development Corporation shows that the number of patient falls for a year range from 150,000 to 200,000 for a median population age of 79[1]. We believe that with proper detection systems and effective alarms, the caretaker can be alerted. To build a robust system capable of detecting such falls requires evading artifacts and signal processing errors often encountered in other contemporary models. Previous research has shown that, as people grow old the probability of falls increases[2]. Often, patient falls off the bed are underrated and unreported. But, in nursing home facilities and hospitals, fall rates are three times higher for patients aged 65 or more with an annual rate of 1.5 falls per bed [3]. This calls for technology that can detect such events in order to better the healthcare prospects for the elderly and bedridden.

Variegated approaches have been adopted to detect patient falls. CharalamposDoukas et al[7] developed a novel method using Support Vector machines. Patient falls were detected using data acquired from accelerometers placed on the subject's body. Miguel Angel Estudillo-Valderrama et al [8] also used accelerometers and other biosensors to acquire data. The whole algorithm was developed to cater to the needs of patients who had a high risk of falls and those suffering from chronic illness. [12] and [13] collect vibrations and acoustic information to detect patient falls. [9] [10] use video monitoring and processing to check the status of the patient. In [11], a wearable sensor was fabricated which housed accelerometers and gyroscopes. Machine learning approaches were developed to discriminate between daily activities and a fall.

While these methods prove efficient, numerous practical limitations make them unsuitable for continuous and repeated use. Often, the sensor needs to be calibrated or post processed to detect falls. This prevents real time fall detection. Also, using computer vision to acquire data has its shortcomings. They are ambiguous; require large data processing and extensive pre-processing. Pre-processing involves various techniques such as Histogram Equalization, De-blurring which account for more processing time. Also, significant data can be lost in this process.

Near Infrared sensors are cost-effective alternatives to detect patient falls. Insulation to a range of artefacts improves its efficacy.

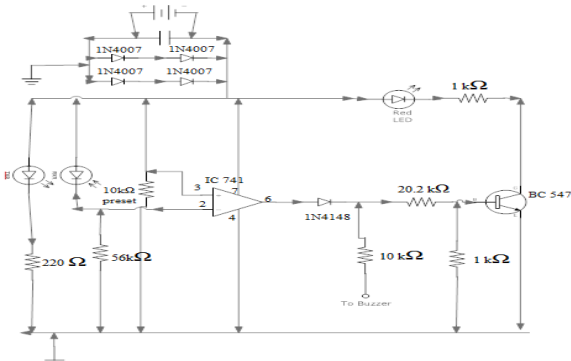
2. System Description

Infrared rays are known to heat surfaces they are incident on. However, the effect to which

these radiations heat the surfaces is directly related to the temperature of the source emitting this radiation and frequency of the rays. Infrared radiations are broadly classified as IR-A (760-1400nm), IR-B (1400-3000nm) and IR-C (3000nm-1μm). The IR-A radiations, also called as Near Infrared rays (NIR) have been clinically proven to penetrate epidermal and dermal layers, even reaching subcutaneous tissues without increasing the skin temperature significantly [4]. Thus, the effect of any stray radiation from the system is significantly harmless to the patient and do not cause damage to the skin.

The patient fall detection system works on the principle that, an alarm is produced when the transmitter (txr) –receiver (rxr) line of transmission is cut. The NIR transmitter continuously transmits the radiation when switched ON. When the line of transmission is cut, the receiver senses this external disturbance and triggers an alarm which is produced by other electronic circuits that work in association. This method is used to detect patient falls off the bed and to detect patient limb movements. Falls off the bed can be detected by placing a NIR txr-rxr pair at either side of it. The maximum distance of separation between the transmitter and receiver can be approximated as 60cm. Parallel to the edge of the bed, the sensor module is setup and monitored for patient falls. Limb movement can be detected by placing the same sensor module at anatomical joints that move perpendicular to the plane of transmission of the near Infrared rays. The degree of freedom of that joint allows the effector muscles to move the limb in a direction that passes across the line of transmission.

3. Materials And Methods



The prototype was fabricated according to the circuit diagram shown above.

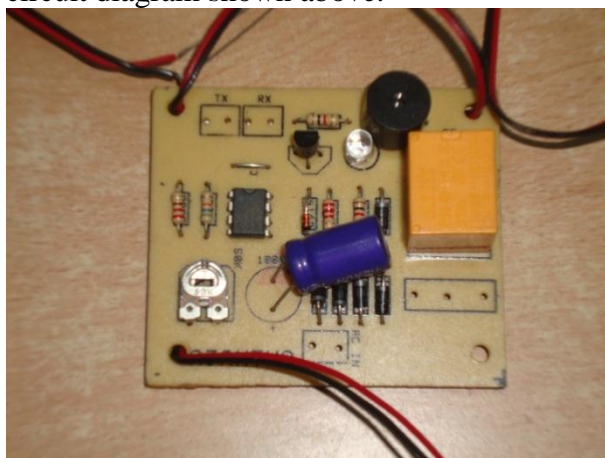


Fig1. Fall Detection prototype

3.1 Rectified Power Supply

The power supply for this prototype is a conventional 9V battery. The power supply is then connected to a rectifier circuit. A parallel circuit consisting of a Capacitor and four Diodes is used to rectify the power supply. The diodes employed are 1N4007 which can produce a rectified forward current up to 1A[5]. Capacitor used has a rating of $1000\mu F$ 25V.

3.2 Core Processing Unit: IC 741

In the circuit, an Operational Amplifier IC 741 acts as the core coordinating equipment. Pin 4 of the IC 741 was grounded while pin 7 was

connected to the power supply to power the amplifier to ON position. Pin 2 (Inverting terminal) of the amplifier was connected to the Receiver photo Diode. Pin 3(Non-inverting terminal) was connected to the input supply voltage tapped from a resistor of $10k\Omega$ pre-set resistance. Pre-set resistance is generally a potentiometer whose value can be adjusted depending on the need of the user. The voltage at the resistor junction connected to pin 3 was 8.98 V (approximately supply voltage). Pin 6 (output) of the operational amplifier was connected to a high speed diode 1N4148.

3.3 Auxiliary Circuit

1N4148 is a high speed diode used for fast switching actions and has a response time of approximately 4ns [6]. The auxiliary circuit that triggers the alarm consists of a transistor BC 547, Buzzer, red LED and other biasing requirements. The diode directly controls the Buzzer. CC1212A buzzer producing monotone sound is used as an auditory alarm. The transistor used, BC 547 (NPN type) controls the red LED which is used as a visual alarm. The transistor works in Common Emitter mode. The switching action of the transistor when in line and out of line can be better explained using the following tabulation:

Table 1.Terminal Voltages of BC 547

	Emitter voltage (mV)	Collector voltage (mV)	Base voltage (mV)
In line	0.5	1.5	6.8
Out of line	7.47	7.35	6.6

For experimental purpose, the distance of separation between the transmitter and

receiver was 2cm. The transistor is out of line when the transmitter and receiver are in line. Once the txr-rxr line of transmission is disrupted, the transistor is said to be in line. The change in Collector and Emitter voltages (as seen in Table 1) is testimony to the switching action and therefore, provides proof for detection of the fall event. The biasing required for the transistor to operate is provided by the $1\text{k}\Omega$ resistor connected to the ground, $20.2\text{k}\Omega$ resistance between the 1N4148 and the Base of the transistor. The Collector terminal is connected the red LED through a $1\text{k}\Omega$ resistor. The Emitter terminal is directly grounded as the transistor works in Common Emitter configuration.

When the line of transmission is cut, the output of the Op-amp IC 741 changed from inverting mode to non-inverting mode. During this transition, the voltage of the 1N4148 diode changed to 5.6 V. The biasing of the diode changed (forward biased) which therefore, triggered the Buzzer. Once the diode is switched ON, the change in transistor terminal voltages triggered the red LED. Thus, an effective alarm system was realized.

3.4 Transmitter and Receiver

The transmitter and receiver are the sensing elements of this prototype. The transmitter employed is an IR LED while the receiver is an IR sensor. A $56\text{k}\Omega$ driving resistor is employed to protect the Receiver and the Op-amp. The transmitter and receiver are placed at the required distance of separation and tested for vital parameters. While detecting patient falls, the distance of separation will be higher (~60cm) than that of detecting limb movement (~10cm).

4. Results

The variation of voltage at the receiver with change in distance from the transmitter is obtained.

Table 2. Receiver Characteristics

Distance (cm)	Transmitter voltage (V)	Receiver voltage (mV)
0.5	1.26	15.0
1.0	1.26	18.5
2.0	1.26	36.0
3.0	1.26	58.0
5.0	1.26	70.0
10.0	1.26	84.0
15.0	1.26	95.0
30.0	1.26	114.0
45.0	1.26	121.0
60.0	1.26	128.0

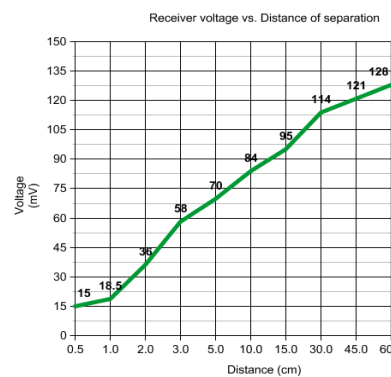


Fig.2. Characteristics of Receiver: Change in receiver voltage (mV) for changes in distance of separation from the Transmitter

The plot and tabulation clearly explain the characteristics of the sensing elements. The receiver voltage is directly proportional to the distance of separation from the transmitter. The prototype was tested for its efficacy up to 60cm as constrained by the length of the wires. The tests were performed in a room devoid of artificial lighting while

accommodating little natural light for working. Therefore, the receiver was able to sense the IR radiation from as far as 60cm and thus establish a line of transmission. This distance offers sufficient separation between the txr-rxr pair in order to monitor the patient falls.

The result from the transistor and txr-rxr characteristics shows that, the prototype can be effectively used as a patient fall detection system. With the above demonstration of the efficacy of the prototype, it is evident that it can be used over short distance (0.5cm-5cm), medium distance (10cm-30cm) and to over 60cm. This makes it suitable to detect limb movement of patients. The limb movements were tested at two anatomical joints: elbow and knee. Movements at these joints are clear signs of movement of the fore and hind limbs.

However, there are a few shortcomings to the prototype. The ambience of the testing laboratories and the actual working environment of the prototype are contrastingly different. It is not possible to conclude that, the line of transmission is purely due to the transmitter itself. There are chances of other external factors that can jeopardize the working and result in false-negative results.

5. Conclusion

This paper describes an alternative to detecting patient falls. Using simple electronics, the fall detector requires no user-input at any stage. Often, fall detectors require patients to press a switch to alert the caretaker. Under traumatic and medically critical conditions, it is not possible for patients to comply with this need. The prototype was fabricated with IC 741 as a core part of the system. The efficacy of the prototype and

extent to which it can be used has been clearly tested. Transparent alarm system ensures that there no glitches in sounding it inappropriately.

In today's world, with technology replacing many mundane and monotonous genres of human work, patient fall detectors arguably substitute for human caretaking. The necessity to depend on human monitoring and attending patients can be evaded to an extent. The prototype was developed to cater the needs of the rural population. Being efficient and cost-effective, Near Infrared patient fall detectors can be an asset to patient monitoring systems.

Encouraged by these results, future works on Near Infrared sensor will focus on building a new Graphic User Interface for monitoring many patients at the same time. Also, a fool-proof design can be devised to ensure maximum accuracy for this fall detector. Adding a LED sensor to this setup, can provide the necessary fool proofing. Currently, visual and auditory alarms are used to alert the event of patient fall. Other alarms such as Wireless transmission of patient fall data from remote locations, SMS alert via cell phones.

6. Acknowledgement

The authors of this paper thank Bilal Ahmed for his contribution in testing the prototype. The authors also thank all the reviewers for their vital support and encouragement.

7. References

- [1] C.J. Lord. "Falls In the Elderly: Detection and Assessment" In Proceedings of the Annual International conference of the



IEEE Engineering in Medicine and Biology Society 1991. Vol.13:1991

[2] Waldron N, Hill AM, Baker A, "Falls prevention in older adults: Assessment and Management", Australian Family Physician, 2012 Dec; 41(12): 930-58

[3] PrabhuRajendran, Amy Corcoran, Bruce Kinosian, and MajdAlwan, "Falls, Fall Prevention, and Fall Detection Technologies", Aging Medicine 2008, pages 187-202

[4] Soyun Cho et al., "Effects of Infrared Radiation and Heat on Human Skin Aging in Vivo", Journal of Investigative Dermatology Proceedings(2009), pages 15-19

[5] Fairchild Semiconductor, "1N4001-1N4007: General Purpose Rectifiers", 2009, Online: <http://www.fairchildsemi.com/ds/1N/1N4001.pdf>

[6] Discrete Semiconductors, "1N4148;1N4448 High Speed Diodes", 2004 Aug 10, Online: http://www.nxp.com/documents/data_sheet/1N4148_1N4448.pdf

[7] CharalamposDoukas, IliasMaglogiannis, FilipposTragkas, DimitrisLiapis, Gregory Yovanof. "Patient Fall Detection using Support Vector Machines". Artificial Intelligence and Innovations 2007: from Theory to ApplicationsVolume 247, pages 147-156

[8] Miguel Angel Estudillo-Valderrama, Laura M. Roa, Javier Reina-Tosina, David Naranjo-Hernandez. "Design and Implementation of a Distributed Fall Detection system- A Personal Server". In

IEEE Transactions on Information Technology in Biomedicine, Vol. 13, No. 6 pages 874-881

[9] H. Foroughi, H. S. Yazdi, H. Pourreza, and M. Javidi, "An eigenspacebasedapproach for human fall detection using integrated time motion image and multi-class support vector machine," in Proc. 4th Int. Conf.Intell. Comput.Commun.Process., 2008, pp. 83–90.

[10] F. Zhengming, E. Culurciello, P. Lichtsteiner, and T. Delbruck, "Fall detection using an address-event temporal contrast vision sensor," in Proc.IEEE Int. Symp. Circuits Syst., May 2008, pp. 424–427.

[11] OlukunleOjetola, Elena I. Gaura, James Brusey. " Fall Detection with Wearable sensors-SAFE(SmArt Fall dEtection)". In 7th Intl Conf. on Intelligent Environments 2011 pages 318-321

[12] D. Litvak, I. Gannot, and Y. Zigel, "Detection of falls at home using floor vibrations and sound," in Proc. IEEE 25th Conv. Electr. Electron. Eng., 2008, pp. 514–518.

[13] M. Popescu, Y. Li, M. Skubic, and M. Rantz, "An acoustic fall detector system that uses sound height information to reduce the false alarm rate," in Proc. 30th Annu. Int. Conf. IEEE EMBS, 2008, pp. 4628–4631

Texture Based Feature Extraction from Mammogram Images to Classify Different Masses & Comparison of Various Classification Techniques

S.Sivarajanji¹ , R.Prem Kumar²

Rajalakshmi engineering college, Thandalam, Chennai.

¹ranjanji.smith@gmail.com, ²indoprem@gmail.com

Abstract

Mammogram images are an important sign for early detection of breast cancer. Segmentation is the first vital step in image processing, which must be successfully taken before subsequent tasks such as feature extraction and classification. In this project Segmentation of Masses will be done using K-Means Clustering Technique and Fuzzy C Means Clustering. Feature extraction procedure relies on the texture, which is the main descriptor for all kinds of mass and non-mass mammograms. Statistical descriptors that include Standard Deviation, Entropy and Gray Level Histogram Moments. The performance of the proposed algorithm is compared with K-means and Fuzzy C-means Clustering and ANN is used to classify the extracted features.

Keywords:Breast cancer, Neural Network, Image segmentation, Classification, Texture Analysis, Mammography Image Processing.

I Introduction

Mammography is currently the most commonly used method for early detection of breast cancer. Texture-analysis methods can be applied to detect clustered micro calcifications in digitized mammograms. A texture-analysis method is performed for the surrounding region-

dependence method. Textural features extracted by these methods are exploited to classify regions of interest (ROI's) into positive ROI's containing clustered micro calcifications and negative ROI's containing normal tissues. The surrounding region-dependence method is shown to be superior to the conventional texture-analysis methods with respect to classification accuracy and computational complexity[1].

Radial-Basis-Function (RBF) networks and Multilayer perceptron (MLP) neural networks are used to classify ROS including all kinds of abnormalities by processing two types of texture features: statistical descriptors based on high-order statistics and the spatial gray-level dependence (SGLD) matrix. The MLP classifier outperforms the score achieved by the RBF networks. MLP is approximately better than that obtained by the RBF networks for the statistical descriptors based on high-order statistics. The radial-basis-function neural networks (RBFNN) have the advantage of fast learning rates[2].

Mammographic mass classification performance between a back propagation neural network (BNN), K nearest neighbors, expert radiologists,



and residents. The Goal is to reduce false negatives during screening of mammograms. Classification performance is measured by computing the sensitivity, specificity, and area under the receiver operating characteristic (ROC) curves. The BNN performance was slightly better than the expert radiologist and significantly better than the residents and the KNN system[3].

The breast cancer detection based on statistical texture features using Support Vector Machine (SVM). These features are then used in conjunction with SVM to detect the breast cancer. Other linear and non-linear classifiers were also employed to be compared to the SVM performance. Algorithm operates by mapping the given training set into a possibly high dimensional feature space. SVM was able to achieve better classification accuracy of 82.5% [4].

The breast tissue is scanned using variable window size, for each sub-image co-occurrence matrices in different orientations are calculated and texture features are estimated for each co-occurrence matrix, then the features are used to train neuro-fuzzy models. A neuro-fuzzy model for detecting candidate circumscribed masses in digitized mammograms is specified by degree of membership [5].

Regions of interest (ROI) containing normal tissue, biopsy-proven malignant masses, and biopsy-proven microcalcification (MCC) clusters using a mix of shape and texture features. Shape features included size, translation, and rotation invariant moments. Texture features included fractal-based features

and spatial gray level dependence (SGLD) matrix features.[6].

Segmentation of breast regions in mammograms according to breast density. Breast cancer usually occurs in the fibro glandular area of breast tissue, which appears bright on mammograms and is described as breast density [7].

The structure of the rest of this paper is as follows: Section II represents the methods that has been carried out. Section III illustrates the experimental results. Section IV outlines the conclusion.

II Methods

Data Acquisition

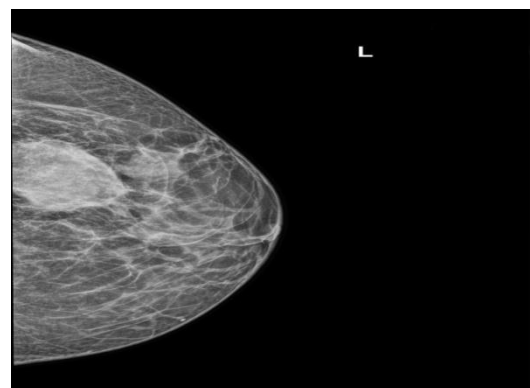
Nearly, 30 images are collected from scans world. Each case contained at least one mass and had an accompanying biopsy result.

Breast imaging reporting and data system(BIRADS)

Grade 1 – Negative.

Grade 2 - Benign.

Grade 3 - Probably benign.



Grade 4 – Suspicious abnormality.

Grade 5 – Highly suggestive of malignancy.
 Grade 6 – Known biopsy proven malignancy.

NORMAL	BENIGN	MALIGNANT
10	15	5

Table 1. Normal, Benign, Malignant cases data are used in this study.

Fig .1 Digital Mammogram of Malignant case Image Digitization

All 30 images were digitized using a 1200 dpi scanner, with 0.37 mm per pixel resolution. The digitized images were 1-2 Mbytes in size.

Image segmentation

The mass/masses in each image were segmented as described in [7] using K-means and Fuzzy C-means starting with the seed pixels which were defined manually by the expert radiologist (DLB). Segmentation of Breast Regions in Mammogram is separating the image into similar constituent parts, including identifying and partitioning regions of interests. A mammogram contains two different regions are exposed breast region and the unexposed air-background (non-breast) region. Background region in a mammogram usually appears as a black region, and it also contains high intensity parts such as bright rectangular labels, opaque markers, and artifacts. In mammogram breast region can be partitioned into dark areas are fatty tissue, light areas are denser tissue which contain ducts, lobes, and other findings. Lighter areas of a mammogram reveal breast tissue that may be glandular or breast masses. These breast regions are segmented by k-means algorithm, is a simple iterative method to partition a given

dataset into a user specified number of clusters, k. Again the breast regions are segmented by Fuzzy C Means algorithm; here each data point belongs to a cluster to a degree specified by a membership grade.

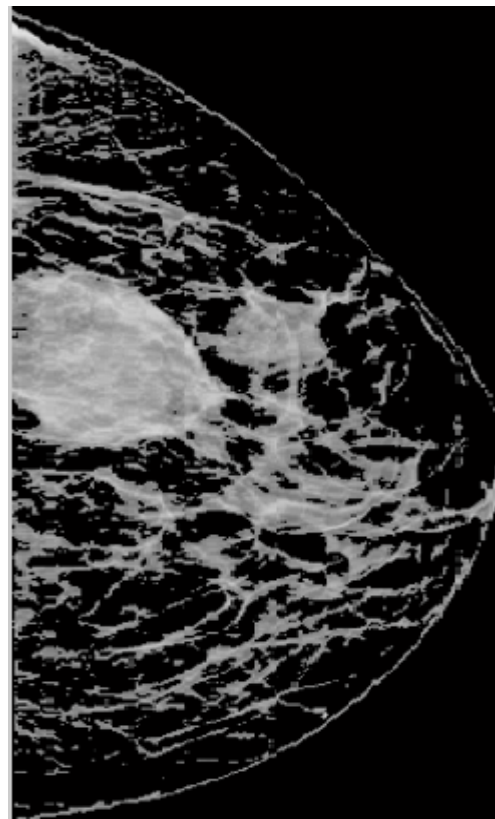


Fig .2 Segmented image for Malignant case

Statistical texture based features

Texture based features were extracted from the masses after segmentation. These features serve as inputs to the BNN, K-means and Fuzzy C-means for mass characterization. These features are mean, standard deviation, smoothness, skewness, entropy, FT-DC and singular vector decomposition, and they were computed as described in [2].

Artificial Neural Network

The extracted features are fed into a neural network classifier which is trained using the ANN algorithm. The performance of the proposed algorithm is compared with K-means and Fuzzy C-means Clustering and they are used to classify masses based on statistical texture features. The system is trained and tested with 10 normal, 15 benign and 5 malignant images.

Classification and Interpretations

After the system is trained, then the input images are given to the trained system to classify the images. It will classify the images based on abnormal, benign and malignant.

III Experimental Results Normal

FEATURES	K-means	Fuzzy C means
Mean	0.5548	0.5560
Standard Deviation	0.0673	0.0661
Smoothness	0.0044	0.0045
Skewness	-496.7334	-331.4791
Entropy	1.5302	1.7080
FT-DC	9.7131	25.8028
SVD	60.2599	64.19891

Benign

FEATURES	K-means	Fuzzy C means
Mean	0.2734	0.2734
Standard Deviation	0.2394	0.2393

Smoothness	0.0427	0.0541
Skewness	-1.0227	-0.9756
Entropy	2.1909	2.6491
FT-DC	4.1984	6.5143
SVD	83.5733	91.5724

Malignant

FEATURES	K-means	Fuzzy C means
Mean	0.3086	0.3127
Standard Deviation	0.2579	0.2840
Smoothness	0.0624	0.0746
Skewness	-0.7059	-0.6220
Entropy	3.6950	3.7178
FT-DC	4.4480	6.1510
SVD	106.4002	113.7739

Discussion

From the Normal, Benign and Malignant tables, we can understand that the statistical parameter values of Entropy, FT-DC and SVD have produced better result in Fuzzy C-Means.

IV Conclusion

The design specifications for the “Texture Based Feature Extraction from Mammogram Images to classify different Masses & Comparison of Various Classification Techniques” have been drafted out. The proposed work is found feasible and is believed that this system can overcome the difficulties prevalent in the existing system. The automatic detection of mass and non-mass breast region and highlight the abnormalities as normal,

benign and malignant is efficient in the proposed work.

V. References

- [1] Jong Kook Kim and Hyun Wook Park “Statistical Textural Features for Detection of Microcalcification in Digitized Mammograms” IEEE TRANS ON MEDICAL IMAGING, VOL. 18, NO. 3 MARCH 1999.
- [2] Claristoyintzni, E. DenizatasanlG. Kokkinakis, “Neural classification of abnormal tissue in digital mammography using statistical features of the texture” WCL, Electrical & Computer Enginccring Dept. University of l'atras, 26100 Patras, I-IELLAS.
- [3] LinaArbach, D.Lee Bennett, Joseph M. Reinhardt, “Mammographic asses classification: comparison between BNN, KNN and human readers” The University of Iowa.
- [4] Al Mutaz M. Abdalla ,SafaaDeris, NazarZaki and Doaa M. Ghoneim, “Breast Cancer Detection Based on Statistical Textural Features Classification” Faculty of Computer Science and Info. Systems, UniversitiTeknologi Malaysia, Malaysia College of Info.Technology, United Arab Emirates University, UAE College of Science, United Arab Emirates University, UAE.
- [5] NafizaSaidin, HarsaAmylia Mat Sakim, UmiKalthumNgah and Ibrahim LutfiShuaib, “Segmentation of Breast Regions in Mammogram Based on Density: A Review” Imaging & Computational Intelligence Group(ICI) School of Electrical and Electronic Engineering UniversitiSains Malaysia, Engineering Campus, 14300 NibongTebal, SeberangPerai Selatan, Pulau Pinang, Malaysia.
- [6] Cynthia Y. Enderwick, EvangeliaMicheli-Tzanakou, “Classification of mammographic using shape and texture features” BME Department, Rutgers University, PO Box 909, Piscataway, NJ 08855-0909 BME Department, Rutgers University, PO Box 909, Piscataway, NJ 08855-0909.
- [7] NohaYoussry', Fatma E.Z. Abou-Chadi' and Alaa' M. El-Sayad, “Early Detection of Masses In Digitized Mammograms Using Texture Features and Neuro-Fuzzy Model” Department of Electronics and Communications Engineering Faculty of Eugineering,Mansoura university Electronics Research Institute.
- [8] C. E. Metz, P. L. Wang, and H. B. Kronman, “A new approach for testing the significance of differences between ROC curves measuredfrom correlated data,” in Proc. Information Processing Medical Imaging8th Conf., Boston, MA, 1984, pp. 432–445.
- [9] D. H. Davies and D. R. Dance, “Automatic computer detection of clustered calcifications in digital mammograms,” Phys. Med. Biol., vol. 35, no. 8, pp. 1111–1118, 1990.
- [10] R. G. Bird, R. G. Wallace, and B. C. Yankaskas, “Analysis of cancers missed at screening mammography,” Radiology, vol. 184, pp. 613–617, 1992.



- [11] Z. Huo, M. Giger, C. Vyhorný, D. Wolverton, R. Schmidt, K. Doi, "Computer-Aided Diagnosis: Automated Classification of Mammographic Mass Lesions", Proc. of the 3rd Int. Workshop OIL Digital Mammography, Chicago, IL, 1996, pp. 207-211
- [12] Harelick R. "Statistical and Structural Approaches to Texture", Proc. IEEE, Vol. 67, No. 4, May 1979, pp 786-804.
- [13] D. Mcersman, P. Schcunders and D. Van Dyck, "Detection of Microcalcifications using Neural Networks". Proc. of the 3rd Int. Workshop on Digital Mammography, Chicago, IL, 1996, pp. 97-103.
- [14] Sahiner, B., Chan H-P., Petrick, N., Wei, D., Helvie, M., Adler, D., and Goodsitt, M., "Classification of Mass and Normal Breast Tissue: A Convolution Neural Network Classifier with Spatial Domain and Texture Images," IEEE Trans. on Med. Imag., 15(5):598-610.